Avogadro Number's-oriented HyperGeometric and ChebyshevT Functions for Black Hole Paradox Generalizations and Turing Machine Ruled Quantum Homeopathy Water Memory Entanglements for the Translation of COVID19 Homeopathy Remedies into the Neprilysin and ACE2/AT1R receptors targeted DRVYIHPFX- ligands.

Ioannis George Grigoriadis *

Posted Date: 11 March 2024

doi: 10.20944/preprints202403.0518.v1

Keywords: COVID19; Chern-Simons Topological; QED (Quantum Electrodynamics); Homeopathic medicine; Water Memory; AI-Quantum computing; Quantum-Inspired Evolutionary Algorithm Predictive Toxicology; QSAR Quantum gates; CS Supergravity Quantum Foam; Cheminformatics artificial intelligence; Phase Data Mining; Machine Learning; Euclid Chemical space exploration; (bosonic) Quantum fields Theory (QFT); Angiotensin Receptor Neprilysin targeted DRVYIHPFX mimetic Holomorphic Ligands; Hidden Entanglement Negativity Translations; Uncertainty Quantum Relationships; Quantum fields theory; Quantum information; HyperGeometric Functions; Chemical Block Systems; Black Hole Paradox Generalizations; SphericalHarmonicY-Supersymmetry breaking foundations; WhittakerM Functions; Hypergeometric1F1 Functions; Turing Machine Learning Ruled Calculations; Avogadro Number's oriented Quantum Homeopathy Hidden Entanglement Negativities; Quantum foam; non-commutative geometry; small molecule ligand engineering; prot

Article

Avogadro Number's-Oriented HyperGeometric and ChebyshevT Functions for Black Hole Paradox Generalizations and Turing Machine Ruled Quantum Homeopathy Water Memory Entanglements for the Translation of COVID19 Homeopathy Remedies into the Neprilysin and ACE2/AT1R Receptors Targeted DRVYIHPFX-Ligands

Grigoriadis Ioannis

[1] Department of BiogenetoligandorolQMMIDDD/QPRPICA/MACHNOT/QIICDNNDCA ADMET/QIICDNNDCA Stations; jgrigoriadis@biogenea. gr, biogeneadrug@gmail.com; tel,306936592686 ORCID ID: https://orcid. org/0000-0002-8443-1777

[2] Cell-Pharmacy Ltd., Personalized SynthocureTM Stations. *

[3] Biogenea Pharmaceuticals Ltd.*

Abstract: SARS-CoV-2 Omicron variant spike RBD epitopes in complex with spike (S) -protein D614G mutations now predominate globally and increase infectivity by assembling more functional S proteins into the virion. On average, homeopathic medicine contains less than one molecule per dose on average. Single variable SphericalHarmonicY, LaguerreL, WhittakerM, SphericalBesselJ, LegendreP, LegendreQ, LaguerreL, ChebyshevT, and Hypergeometric1F1 Functions pFqarise in connection with the power series solution of the Schrodinger equation or in the summation of perturbation expansions in quantum mechanics. A quantum interpretation of the homeopathic method is presented here through a novel algebraic topology approach to supersymmetry and symmetry breaking in quantum fields and quantum gravity theory with the aim of developing a wide range of physical-based drug design applications in a Small Molecule Quantized Water Memory Network suggesting that the Hidden Black Hole Paradox of Information Loss might be solved under suitable conditions.**Keywords:** COVID19; Chern-Simons Topological; QED (Quantum Electrodynamics); Homeopathic medicine; Water Memory; AI-Quantum computing; Quantum-Inspired Evolutionary Algorithm Predictive Toxicology; QSAR Quantum gates; CS Supergravity Quantum Foam; Cheminformatics artificial intelligence; Phase Data Mining; Machine Learning; Euclid Chemical space exploration; (bosonic) Quantum fields Theory (QFT); Angiotensin Receptor Neprilysin targeted DRVYIHPFX mimetic Holomorphic Ligands; Hidden Entanglement Negativity Translations; Uncertainty Quantum Relationships; Quantum fields theory; Quantum information; HyperGeometric Functions; Chemical Block Systems; Black Hole Paradox Generalizations; SphericalHarmonicY-Supersymmetry breaking foundations; WhittakerM Functions; Hypergeometric1F1 Functions; Turing Machine Learning Ruled Calculations; Avogadro Number's oriented Quantum Homeopathy Hidden Entanglement Negativities; Quantum foam; non-commutative geometry; small molecule ligand engineering; protein-folding; entropy; enthalpy; H-bonds; thermodynamic; extended quantum symmetries; groupoids and algebroid; Lie algebras; compact quantum groupoids; quantum C ∗ -algebras; relativistic quantum gravity (RQG); Vaida supergravity and Supersymmetry Theories; Hamiltonians in quantum gravity

 doi:10.20944/preprints202403.0518.v1

Summary

Computer-aided drug discovery/design methods which are broadly classified as either structure-based or ligand-based methods have played a major role in the development of therapeutically important small molecules for over three decades. In this strategy, an innovative Quantum Homeopathy-driven ligand replacement method translated here into a Structure-based evolutionary method which is in principle analogous to high-throughput screening for delocalizing pharmacophoric reconstructions that are perfectly well substituted in a fuzzy sphere shaped druggable scaffolding via an Avogadro Number's-oriented quantum geometry and crowding-based low mass phase protocol for a phenotypic steady-state multiple genetic parental algorithm as a Quantum Geometry-based Dynamic Homeopathic Solution and for a Modified and Restricted Ligand Selection (QuGeDoHoSoMorLiP) approach. It also visualizes an idea that has been invoked in the description of other coherent energy transportations in organic molecules in the purpose of a better Turing Machine learning exploration of the energetic hypergeometric hypersurface for the identification of multiple Quantum Phase Minima Homeopath Solutions in a single Hadamard run while preserving the chemical diversity of the generated RoccustyrnaTM structures. This could be a useful mathematical path for linking Quantum Negative Energy Harnessing from COVID19 Homeopathy remedies with Deep Geometry Sensing as described here which can be Turing Machine translated into Quantized Miasm Moiety metrics that exposed to the water interfaces and has sufficient electronic density data for the same purpose, for the designing of new crystallographic structures following the Steering criteria and conditions whose violation excludes the possibility of describing the observed measurement statistics with local hidden state (LHS) modes. In this case and in addition, important tools such as target/ligand data bases, homology modeling, ligand fingerprint methods, etc., necessary for successful implementation of various computer-aided drug discovery/design methods in this drug discovery campaign are discussed. The article combines quantum field theory with quantum homeopathy entanglement behind these most important Avogadro Number's-oriented HyperGeometric and ChebyshevT Functions for Black Hole Paradox Generalizations where the substances which are not present, that is the homeopathic remedy, could become a kind of receptacle which 'absorbs' the Quantum Information exctracted from COVID19 patient's symptoms, insofar as they are related by similarity of these Turing Machine generated patterns/features, in a Gegenbauerian model which reconfirms the feasibility of our original intention for finding a new model-building recipe in this direction, a prototype Quantum entropy circuit that clearly illustrates a Quantum Homeopathy oriented design principle for a coherent exchange of single energy quanta between electronic and vibrational degrees of freedom with the capacity of calculating the enhanced negative free energy scoring functions from the best-docked poses of the Roccustyrna ligand. Fascinating, although this water quantum memory mimicking topic is exploring the relationship between AdS5 Quantum fields Theory (QFT) Reduction, Vaidya and Kerr metrics for QFT to QM Reduction, Quantum Thermodynamics, and Turing Machine Learning Rules for Quantum Homeopathy Variables and Quantum Biology gives us a greater insight into viral transmissions and thus, SARS-CoV-2 biological complexities?

Introduction

In light of the limited treatment modalities offered by conventional medicine for COVID-19, especially in more severe diseases, the results of the described homeopathic treatment in the cases previously presented are impressive because homeopathy is a well-established form of complementary and traditional medicine that has been used to treat a wide range of conditions, including respiratory illnesses [1–5]. Given the global impact of COVID-19 and despite the lack of a unified methodological standard, a number of healthcare organizations and ministries of health from various countries have recommended homeopathic treatments for the prevention and treatment of SARS-CoV-2 infections [1–7]. Inhibition of the SARS-CoV-2 Omicron variant spike RBD in complex with Fab XGv282 (PDB: 7wlc) binding interface interaction using small molecules or peptides is the most logical and straightforward strategy to block viral cellular entry. Consequently, our research team is committed to generating extended symmetries and quantum groupoid, algebroid, and

 doi:10.20944/preprints202403.0518.v1

functorial Avogadro Number's representations demonstrating the efficacy of translating individualized homeopathy remedies in treating COVID-19 since homeopathic treatments have been employed successfully during major epidemics and pandemics of the 19th century, prompting numerous researchers to investigate the potential of homeopathic interventions to reduce the likelihood of SARS-CoV-2 infection or to alleviate COVID-19 symptoms [1–7,9,10]. Savera et al. 9 and Manchanda et al. reported that the most commonly prescribed homeopathic remedies for COVID-19 were Bryonia alba, Phosphorus, Arsenic album, Gelsemium sempervirens, and (Carboneum oxygenisatum or Pulsatilla nigricans). Clapers et al. conducted a prospective case series study of 103 mild-to-moderately ill COVID-19 patients in Spain, of whom 22 had concomitant diseases. The most frequently prescribed drugs were Bry, Ars, Phos, and Gels, whereas the drugs with the highest rate of "good response" were Sulphur (6/6 = 100%), Pulsatilla (4/5 = 85%), and Bryonia alba (21/29 = 72%) [1–13]. The time to complete recovery after homeopathic treatment ranged from 3.5 to 14.4 days, and potency 200c achieved the fastest rates of complete recovery and the least need to change the remedy. [1–14] Finally, very low response rates of 20% and 0% were observed with the use of Gelsemium and China officinalis, respectively, despite the broad recommendation emphasized in several studies. [9–16] Other controlled randomized studies corroborated these encouraging early findings and facilitated evidence-based decision-making regarding the role of homeopathy in treating COVID-19, adding a potentially quick and effective treatment modality that is both safe and inexpensive. [1–13,17,18] Pre-hypertension (ICD-10-CM R03.0) is a sub-clinical condition, but remains a public health challenge globally. Appropriate intervention is needed to stop its progression to hypertension and other cardiovascular diseases. According to 8th Joint National Committee (JNC-8), blood pressure (BP) is classified as normotensive (≤ 120/80 mm Hg), high normal blood pressure or pre-hypertensive (120–139/80–89 mm Hg) and hypertensive (≥ 140/90 mm Hg). [1–13,19,20] Recent study has shown that during 2011–2012, 28.2% of the US adults (≥ 20 years old) were pre-hypertensive. In 2014, a study in West Bengal police personnel showed that around 42.9% police of various district of West Bengal have pre-hypertension with increased risk of cardiovascular disease conditions. [1–21] Another study showed that pre-hypertension was present in 41.1% of Indian urban population of Belgaum city and recognized the necessity for detecting pre-hypertension and emphasizing on dietary and lifestyle modification (LSM) to prevent further progression to hypertension and its complications. [1–21] Controlling pre-hypertension is basically a primary prevention managed with diet, exercise, and life style modifications. Now-a-days, complementary and alternative medicine (CAM) therapies are increasingly becoming popular in various chronic diseases including hypertension. Selective and integrative use of different CAM therapies has also been recommended in hypertension. Hypertension is a frequently encountered condition in routine homeopathy practice as well. Literature search revealed 13 published trials of homeopathy in hypertension; however, none on pre-hypertension. In the other trials, they hypothesized that there might be a significant difference between individualized homeopathic medicines (IH) and placebo in intervening with the progression of pre-hypertension to hypertension over 3 months of intervention while both groups received standardized recommendations for dietary and lifestyle modifications (LSM). [1–23] Recent calorimetric studies of small molecule interactions with biomolecular targets have generated renewed interest in the phenomenon of entropy-enthalpy compensation and can be used as a lively discussion how the effect of extreme time-dilution in the case of homeopathic exercise may be guided by multistage entropy-enthalpy compensations of a chemogenomic system's polypeptide chains and water molecules under similar solution conditions. [1–23] Despite objections and controversies against homeopathy, its popularity has been increasing worldwide. It has been practiced virtually in every country in the world for the past 200 years and has been widely used by medical doctors and numerous other health and medical professionals as a complement and as an alternative to conventional medical care to treat a wide variety of physical, emotional, and mental health complaints. It is also used in self-treatment by the general public for minor, self-limiting complaints. [1–21,24] During the 1880s, a German pharmacologist Hugo Schultz observed a biphasic dose response characterized by a low dose stimulationand high dose inhibition, indicating that this initial dose dependent toxicity response, which is frequently observed in homoeopathy too could provoke

 doi:10.20944/preprints202403.0518.v1

an initial aggravation of symptoms of the patient followed by a compensatory/rebound response. [1–25] In the beginning, he diluted his drugs simply up to the level that ended their toxicity, and indications to administer them according to the principle of similars were not known enough except fortoxicity they cause when using plant substances and liquids, Hahnemann diluted the solution with water or a mixture of alcohol and water. He then used accordingly the centesimal (1:99) scale for standardization. After each dilution, he vigorously shaked (he used the term "succuss" which is a type of more forceful shaking) the mixture at least 40 times. When he used mineral agents and various chemicals that were insoluble in water/alcohol, he diluted them with lactose (milk sugar) and triturated (i.e., grinded) the mixture since in the 1960s, Cyrus Levinthal pointed out that the apparent contradiction between the astronomical number of possible conformations for a protein chain and the fact that proteins can fold quickly into their native structures should be regarded as a paradox, known as Levinthal's paradox [2–9,22–26]. Calabrese states it more accurately as, "It is a dose-time-response relationship in which there is such that at low doses the response becomes greater than the original background state or control group value in an initial dose-dependent toxicity response". Given the tremendous impact of Quantum Mechanics (QM) in this research area of generalizing Protein-Ligand complexes which are the building blocks of life on Earth and they perform a vast array of biological functions within organisms and have revolutionized more innovative Quantum Functions have to be introduced in order to overcome the main drawback of this understanding of the structure and reactivity of small molecular system approaches which is the large memory footprint of these numerical representations of the molecular orbitals when are much larger in terms of the number of coefficients, with a significant computational overhead [16–25]. Hormesis and homeopathy are interrelated in many ways and since the robust research methodology developed in hormesis can help in carrying out research work in homeopathy toxic substances that do not exhibit hormesis can do so after their potentization, at least those with which life evolved. [1–21,24,25] While these methods can be less expensive than classical approaches, they make up for this deficiency by the more realistic modeling of the electronic nature of biological systems and in their ability to be broadly applied. Advent of nanoscience and new understanding about water can help to answer this question. Schultz claimed that the phenomenon of biphasic dose response explained the principle of homeopathy assertions which could also be brought into the biological realm where quantum systems of a few thousand atoms and beyond are routine. [1–22,26] Since this was his important discovery's marginalization and has characterized as a schism developed in medicine after the advent of homeopathy, Calabrese and colleagues noted the problem, this intrinsic homeopathy phenomenon of biological functions of a nascent protein that exists as an unfolded polypeptide when translated from a sequence of mRNA to a polypeptide chain in a ribosome could be determined by its native three-dimensional (3D) structure derived from the physical process of protein folding [1,2,26,27], by which means a polypeptide folds into its native characteristic and functional 3D structure in an spontaneous manner when applying QM methods to biological problems. Such Protein folding which can thus be considered as the most important mechanism, principle, and motivation for biological existence, fictionalization, diversity, and evolution [27–29] brings an improved representation to these LegendreP Quantum Function Systems by the direct inclusion of inherently QM effects such as polarization and charge transfer. The QM effects will generate a homeopathic pharmaceutical drug designs when translating the dilution, succussion or trituration processes, the "potentization" phenomenon in which the greater number of potentizations led to longer and deeper effects of the drugs, and the need for reduced repetition of them once a medicinal agent is diluted in the ratio of 1:99 12 times (i.e., in its12C potency) or in the ratio of 1:9 24 times (i.e., in its 24X potency). There would be in high probability no remaining molecules of the original medicinal agent (i.e., source-drug) in the solution. These improved representations and novel insights of ultra low dilutions of nanoparticles can cause a hormetic dose-response that can be gleaned from the application of QM tools to biomacromolecules in ultra low aqueous solutions indicating that these ultrahigh dilutions of drugs/toxic substances used in homeopathy as medicines, such nanoparticles are present as an evidence confirming the hormesis as a generalized adaptive response, which may be further generalized to nanoscale druggable scaffolding, drug design, and chemical geometric

 doi:10.20944/preprints202403.0518.v1

challenges. Herein, through the examples chosen, I show the power of QM to provide novel insights into SARS-COV-2 biological systems, while also impacting practical hermetic applications such as structure refinement for providing drug designing examples of QM studies on biological systems that focus on ACE2 protein solvation as viewed by QM, QM enabled structure-based drug design, and NMR and X-ray biological structure refinements using QM derived restraints. These QM and QM enabled structure-based drug designs are based on Turing Machine Learning Relationships by translating quantum entanglement negativities occurred in homeopathic practices where far higher dilutions than N number are used regularly in daily practice. Discussions on how these translational effects can happen will be discussed later. Of the tools and applications discussed in this paper, X-ray structure refinements from many different research groups have shown that various chemicals/drugs diluted homeopathically even beyond Avogadro's limit can stimulate hormetic responses in living cells from medicinal effects of serially diluted solutions that are not confined to substances conventionally used in homeopathy as source-drugs. These hormetic responses are exctracted from Chemicals like histamine,-thyroxin, and aspirin that are diluted homeopathically, even far beyond Avogadro's limit showing opposite effects to those from their pharmacological doses when using QM models. In particular, QM biological models of quantum entanglement are borrowed from physics and developed into an algebraic argument to explain how double-blinding randomized controlled trials could lead to equivocal evidence for the efficacy of homeopathy by proving these quantum homeopathic calculations as a protein-ligand folding problem which was brought to light over 60 years ago. These quantum entanglements distanced hormesis from homeopathy in an effort to establish hormesis well in modern science which is based on Calabrese along with Jona's debate on possible links between these 2 systems when studying hormesis and the dose is conventionally kept just below the toxic threshold, while in homeopathic practice it is usually lower than this and can even be beyond the physical existence of the original agent if prepared in a typical way. These quantum entanglements accurately and efficiently include electron correlation effects and will facilitate our AT1R drug design modeling of new ligands and dispersive interactions, which is also a major hurdle that a broad range of groups are addressing. By analogy with the famous double-slit experiment of quantum physics, and more modern notions of quantum information processing, these failings are understood as blinding causing information loss resulting from a kind of quantum superposition between the remedy and placebo in these Quantum Homeopathy experimental methods that will currently be used to determine the structure of an annotated drug design. Entangled entities are generally applied to static structures, so ways in which to include sampling is an ongoing challenge because they behave as one inseparable holistic unit, whose totality cannot be deduced from any of its parts of QM models in biology is in its infancy, leading to the expectation that the most significant use of these tools to address biological problems will be seen in the coming years. It is hoped that while this account summarizes where I have been, it will also help set the stage for future research directions at the interface of quantum mechanics and biology. In the beginning I consider non-locality which has been defined as 'the mysterious ability of nature to enforce protein folding correlations between separated but entangled parts of a Quantum Homeopathy system that are out of speed-of-light contact to reach instantaneously across vast spatial distances, or even across time itself, and to ensure that the parts of a quantum system are made to match [19–28] of chemical spaces since protein folding is assumed to be one of the miracles of nature that human technology finds quite difficult to follow, due to the very large number of degrees of rotational freedom in an unfolded polypeptide chain. Commenting on the work of Chikramane et al., Calabrese suggested it as a step forward toward unification of hormesis and homeopathy in the early treatments of Hahnemann which can now be identified as hormetic in nature of atom-centered Gaussians which have traditionally been the most common and widespread choice of basis set for molecules [1–10]. This means that observation of one part of an entangled system instantaneously provides information about the rest, provided one knows how the system is entangled. However, attempts to observe the parts of an entangled system as separate entities, destroys the whole despite a lot of progress being made in the prediction of protein native structures through the use of artificial intelligence [2–11], understanding the physical folding mechanisms and laws still remains the most fundamental task in

 doi:10.20944/preprints202403.0518.v1

molecular biology and biophysics. Levinthal also pointed out there should be pathways for protein folding [4–9,11,12]. Several strong arguments are in favor of such a choice: the compactness of the representation which is defined by a handful of coefficients, the ability to represent atomic orbitals well (Slater functions are in theory superior due to the cusp at the nuclear position and the correct asymptotic), the simplification in the computation of molecular integrals which are often obtained analytically (this is the weak point of Slater orbitals which require expensive numerical evaluations) [1–11,13] while non-locality and entanglement have been experimentally demonstrated at the nanoscopic level of particles, atoms and even molecules [2–20] where macroentanglement between ultra small doses in water solutions and water memory is still a matter of Protein folding conjecture which can therefore be considered as an organized reaction as stated in Anfinsen's Dogma, the "thermodynamic hypothesis". That means that the three-dimensional structure of a native protein in its normal physiological milieu (solvent, pH, ionic strength, presence of other components such as metal ions or prosthetic groups, temperature, and other) which is the one in which the Gibbs free energy of the whole system is lowest; that is, that the native conformation is determined by the totality of interatomic interactions and hence by the amino acid sequence, in a given environment [6,12,14]. Indeed, the non-commuting algebraic formulation of orthodox quantum theory which contains the extremely small number called Planck's constant, $h = 6.626 * 10^{-34}$ J s^{-1} would appear to preclude such quantum effects between macroscopic objects/entities where their main disadvantage is the non-orthogonality of the basis which can become a severe problem especially for large bases leading to a computational bottleneck when orthonormalization is required or worse numerical instabilities due to near linear-dependency in the basis [2–14] of well-defined native 3D structures of small globular proteins and are uniquely encoded in their primary structures (i.e., the amino acid sequences), and are kinetically reproducible and stable under a range of physiological conditions that must there be physical mechanisms and allow polypeptide mimicking small molecules to find the native states encoded in their sequence. Nevertheless, it is proving increasingly possible to conceive non-locality and entanglement in a similar but less restricting algebraic [21,22] or, indeed non-algebraic context [23], and usefully apply these concepts to phenomenological problems arising out of CAM research of the spectrum of the plane waves (PWs) that are ideally suited for periodic systems and are orthonormal by construction. However a very large number of them needs to be employed in order to achieve good precision, especially if one is interested in high resolution in the nuclear-core regions [3–12,15]. Lately, the use of projector augmented wave (PAW) [5–16] and linearized augmented plane wave (LAPW) [6–17] techniques, has made this issue less critical for PW calculations. Another challenge for PWs is constituted by non-periodic systems, which can only be dealt with by using a supercell approach [7–18]. Thus, Gernert [24] defines a 'common pre-arranged context' which he suggests characterizes the preparation to be made in advance (or naturally given conditions) in order to enable entanglement for Quantum Chemical modeling which is constantly expanding its horizons: cutting edge research is focused on achieving good accuracy (either in energetics or molecular properties) on large non-periodic systems such as large biomolecules or molecular nanosystems. The present paper explores this possibility along with the relationship between hormesis, homeopathy, Entanglement for Quantum Chemical modeling as a popular choice to circumvent the problem of using pseudopotentials [4–12,16] in the core region by reducing the number of electrons to be treated and at the same time removing the need for very high-frequency components. The black hole solution of the four-dimensional spacetime Einstein–Maxwell functions of classical general relativity has the following physical characteristics: mass (M), electric charge (Q), and angular momentum (J) supporting the idea that lead us to ways of considering macroentanglement as a possible explanation of significant correlations found between carefully performed Quantum Homeopathy Function Experiments on spatially separated pairs of small molecules [25,26] which is essential for an all-electron description where varying resolution is a prerequisite for efficiency. The price to pay, to provide a representation with a given number of vanishing moments, is a basis consisting of several wavelet functions per node as the most common choice of basic functions in the Euclid Space framework which is a generic orthonormal polynomial basis of order k, providing a second possibility to increase the resolution of the representation

 doi:10.20944/preprints202403.0518.v1

alongside the adaptive grid refinement [15–19]. Weather ley-Jones *et al.* had already suggested the reason DBRCTs apparently fail to unequivocally demonstrate the efficacy of homeopathy, is because specific and non-specific effects of the therapeutic process are actually interdependent and mutually correlated with the static spherically symmetric solution as a Schwarzschild metric with mass as its only physical characteristic [1–20]. The static spherically symmetry solution with electric charge is the Reissner–Nördstrom metric [2–19,21,22], and the axisymmetric generalization of the Schwarzschild metric with angular momentum is known as the Kerr metric [4–24] and localizes the orthonormal basis as an ideal match for modern massively-parallel architectures [18–24]. I am confident that this static spherically symmetric solution as a Schwarzschild metric with mass as its only physical characteristic will become competitive with or even superior to traditional ones as an axisymmetric solution of the Reissner–Nördstrom metric has been generalized by incorporating angular momentum to the Kerr–Newman metric [5–26]. Thus, according to this holistic paradigm, the methodologies used in this axisymmetric generalization of the Schwarzschild metric with angular momentum, and the loss of information must necessarily destroy the very thing when they are trying to investigate the basis functions that are localized as Gaussian-type orbitals yet orthonormal as plane waves. One crucial property of Euclid Spaces is the disjoint support (zero overlap) between basis functions in adjacent nodes [14–27], paving the way for adaptive refinement of the mesh, tailored to each given function. Considering these four metrics that are often referred to as the "black hole" exact solutions of general relativity in 1943, Vaidya proposed a radiating spherically symmetric solution. [6–28] These are the solutions where I am developing further in this theme into a critique of cryptomethodology [27] of quantum function series couched in terms of a developing algebraic metaphors of the homeopathic therapeutic process called PPR entanglement [22] in order to achieve high precision and keep the memory footprint at a manageable level. This is an adaptive strategy which refines grids only if needed is necessary [19–29] and is referred to a choice that has a profound impact on the minimization strategies that can be adopted in order to solve SCF problems such as the Roothaan–Hall functions of the Hartree–Fock (HF) method. In other words, these strategies which rely upon having a fixed basis, such as the most common atomic orbital based methods [20–29] are excluded beyond the Vaidya metric, which was originally applied to radiating stars, and can be regarded as the simplest generalization of the Schwarzschild metric. In 1974, Hawking applied Quantum theory to determine that black holes emitted heat radiation [7–30] only for the occupied molecular orbitals are needed both in HF and DFT to describe the wavefunction/electronic density. It is the Quantum theory which predicts that black-hole mass will gradually evaporate through radiation and therefore, the black hole solutions in this project may have a fourth physical characteristic in this macroentanglement as inputs for our innovative Quantum Functions and Turing Machine Learning Rule Relationships. [7–30] This macroentanglement interpretation between the patient, practitioner, and homeopathy remedies can facilitate the design of new druggable scaffolds and chemicalized structures by translating these therapeutic processes into a direct minimization of the orbitals without requiring a fixed basis representation which also must be considered. Additionally, using Euclid Spaces on an adaptive grid generates representations with discontinuities at the nodal surfaces, that poses a challenge when differential operators are considered the Vaidya solution which have been already applied to black holes when studying the Hawking radiation phenomenon. [7–33] As will be shown in the paper, if the Hartree–Fock functions are reformulated as coupled integral functions, it becomes possible to minimize the occupied orbitals, without ever recurring to differential operators like celestial bodies that are present in the nature and require the Vaidya–Kerr solution which always have rotational angular momentum and radiation, including radiating rotating stars and black holes. [7–34] Einstein's field functions are nonlinear differential functions and can obtain accurate analytical solutions by using hypergeometric and symmetry mimicking functions that are envisaged as expressible in terms of wave functions; ψ_{Px}, ψ_{Pr}, ψ_{Rx}, each expressing a multitude states and corresponding to the macroentanglement states from patient (Px) and practitioner (Pr) quantum systems, and remedy (Rx) atomic orbitals. [2–30,35,36] I further define the biological counterparts of this evolutionary drug design macroentanglement as the measure of stochasticity of an evolutionary process of chemical potential (evolutionary potential) as the amount

 doi:10.20944/preprints202403.0518.v1

of evolutionary work required to add a new trainable variable (such as an additional atomic orbits and atomic charges) [Supplementary material (PLIP Reports1-8)] into these Quantum Electrodynamics Subsystems from Quantized Water Memory and Hormetic Networks. Second, the Papapetrou gauge and Ernst functions can also be applied to solve the axisymmetric Einstein's field functions [12–29,37,38], [13-30,39,40] with wave function ψ_n, in any potentially macroentanglenment state that corresponds to the quantum subsystems of each therapeutic situation whereas Px may be considered in a state of wellness ($|\mathbf{Px}\uparrow\rangle$) or unwellness ($|\mathbf{Px}\downarrow\rangle$); Pr may be helpful ($|\mathbf{Pr}\uparrow\rangle$) or unhelpful ($|\mathbf{Pr}\downarrow\rangle$); and the remedy may be curative ($|\mathbf{Rx}\uparrow\rangle$) or non-curative ($|\mathbf{Rx}\downarrow\rangle$). [7–29–41] In addition, previously conducted studies have demonstrated that the Kerr and Kerr–Newman metric can be derived from the orthogonal ansatz by applying an ellipsoidal-coordinate transformation [14–30], [15–42] for the development of a phenomenological approach and for the description of ChebyshevT-adS5 Quantum fields theory (QFT) Reductions, which involves modeling of intregralized chemical Block Systems based on Black Hole Paradox Generalizations and Supersymmetry breaking foundations for Turing Machine Learning Ruled Calculations as a grand potential and as a function of an evolutionary macroentanglement potential, a Hidden MacroEntanglement Evolutionary Potential. [7–40] The World Health Organization considers homeopathy to be a part of "traditional medicine." How can ultra-high dilutions, as used in homeopathy, be effectively translated into methods known for solving axisymmetric problems in the literature are as follows while also exhibiting hormesis at least mathematecically?

The Nature of Significance

We employ the conceptual apparatus of Quantum Thermodynamics to develop a Quantum Hormesis Phenomenological Translational Theory of evolution and of the origin of life that incorporates both equilibrium and nonequilibrium evolutionary processes within a Avogadro Number's based mathematical framework of the theory of learning based on Turing Machine Learning Relationships that takes account of Quantum Mechanics which is a basic theory of physics [7–41]. The threefold correspondence is traced between the fundamental quantities of quantum thermodynamics, the theory of learning, and the theory of evolution. Under this theory, and since in quantum mechanics, physical states of some objects are changed by observations and major transitions in evolution, including the origin of life, represent specific types of physical phase transitions[29–45]. The observer can only know the states after the observations but can not know the states before the observations from [1–46] the COVID-19 viral infectious which emerged in China at the end of 2019 and was accountable for many fatal cases. The physical states correspond to configurations in these Turing Machine Ruled computations [2,4,35] refer to what the WHO committee declared a global health emergency [3,4–36,46,48] and are based on the rate of the increasing spread of the infection [4,5–37] in the range 2.0-6.0 with a reproductive number (rN) 5,4 higher than SARS and Middle East respiratory Syndrome Coronavirus (MERS) respectively, and [8–47] with fatality rate of about 4% that also will be referred to the all observed configurations and inputs in our Turing Machine Ruled experiment. In order to introduce quantum mechanics into the computation theory, and since Deutsch [2–48] has proposed the quantum computer studies in the quantum computers, as in quantum mechanics, a configuration is defined as a base vector in Hilbert space and a transition is described by a unitary matrix. [7–49] A computation is here defined to operate a unitary matrix to vectors of atomic charges from targeted antiviral drugs against the viral main protease Mpro (or 3CL protease), a cysteine protease which cleaves the two polyproteins (pp1a and pp1ab) of SARS-CoV-2 at multiple locations, resulting in the various non-structural proteins, which are the key for viral replication. Nirmatrelvir (PF-07321332), is an irreversible inhibitor of SARS-CoV-2 Mpro that is co-formulated with ritonavir allowing an oral route of administration (known as PAXLOVID). [6–50] When treatment is initiated during the first days after symptom onset, it results in roughly a 90% protection against severe COVID-19 and hospitalization (Owen et al.,2021). Even though the Mpro-gene can be slightly affected by evolutionary mutations, the antiviral potency does not seem to be compromised (Sven Ullrich et al., 2021), [1–59] in terms of matrices and vectors is less comprehensible than that in terms of transition functions. Bernstein & Vazirani [I] have

 doi:10.20944/preprints202403.0518.v1

formulated the quantum computers called Quantum Turing Machines in terms of the transition functions for Genomic characterization by using a simple DNA cryptography genetic code according to the main dogma of biology through a process of DNA, RNA, Amino Acid are underway from scientists worldwide to understand the rapid spread of the novel coronavirus (CoVs), and to develop effective coding drug-protein-gene personalized intervention options. The definition of computations by their Quantum Turing Machines is exactly the same as by quantum mechanics, so that they do not make full use of their own definition on the Quantum Turing Machines so far published make use of vectors and matrices [3–68]. [4,6–69] However, a condition for the transition functions is still written in terms of vectors and it is hard to check, given a transition function, whether it satisfies the condition or not. [2–70] The Quantum Turing Machine defined by Bernstein & Vazirani behaves according to a probabilistic distribution. Hence it is natural to take a Quantum Turing Machine as an extended probabilistic Turing Machine Learing relationship in a major part of the biological and chemical biodiversity in Brazil's natural products remains unexplored [2–70] by removing these restrictions by modifying the Quantum Turing Machines so that they can the.mol2 files from Brazil's natural products natural products and their computations. In order to show the power of the new Quantum Turing Machines, I prove that a class of.mol2 and SMILES accepted by the new machines in polynomial time includes both NP and co-NP. In Section 2, I introduce the concepts of superpositions of chemical configurations and biological observations into the probabilistic Turing Machines. [7–74] The SARS-CoV-2 virus enters the airway and binds, by means of the S (Spike) protein on its surface (after whose image the term coronavirus is coined), to the membrane protein ACE2 in type 2 alveolar cells since these S protein-ACE2 complexes are internalized by endocytosis and facilitates the entry of each virion into the cytoplasm by initiating an inflammatory process with release of proinflammatory cytokines, and establishing a self-powered cascade event which were inserted as inputs into a Quantum Turing Machine, an extension of a probabilistic Turing Machine showing a difference between Bernstein & Vazirani's definition and ours. In Section 1, I point out a difficulty which lies in both types of the Quantum Turing Machines, and solve it by introducing new machines called halting Quantum Turing Machines. In Sections 2 & 3, I show the power of the halting Quantum Turing Machines [2–74] which could be beneficial for the generation of COVID-19 new chemical geometrics. [2–77] NEP activity is elevated in acute respiratory distress syndrome and it is conceivable that it is also high in COVID-19. Multiple clinical studies are in progress to determine the effect of ARB therapy in COVID-19 patients Controlled evaluation of Angiotensin Receptor Blockers for COVID-19 respIraTorY Disease-Full Text View-ClinicalTrials.gov and preliminary evidence indicates a reduction of critical prognosis and a lower death rate in ARB-treated COVID-19 patients (4). [2–16,19–80] I then define Quantum Turing Machines by extending their probabilistic Turing Machine Rules and show that the proposed Quantum Turing Machines have the same powers as those by Bernstein & Vazirani. Both Bernstein & Vazirani's machines. Since Quantum physics and biology over the past decades have long been regarded as unrelated disciplines, describing nature at the inanimate micro-level on the one hand and living species on the other that are required to be time-bounded we get explicitly results from the machines by using QFT to QM methods, vertex prizes, and edge costs including ab initio Density Field Theories (DFT) [23–83] incorporated in a common Quantum-many body premium technique and a semi-empirical computational scheme for translating in-vitro data from SARS-CoV-2 biological systems in an attempt to control, characterize, and prevent this devastating viral disease. Density Field Theories (DFT) are implemented here as more systematic and less expensive methods [2–85] to describe the rich complexity of SARS-CoV-2 variant biosystems that were strikingly correlating with important risk factors for COVID-19, not only in the brain but also in peripheral tissues. [2–16,26–87] Protein–ligand binding affinity calculation is crucial to the discovery and optimization of lead compounds based on the protein structure. [17–89,90] With the recent advancements in data storage and computing power, various computational methods have been developed to calculate the binding affinity of a given protein–ligand complex,1 including molecular docking, molecular dynamics simulation and molecular mechanics/quantum mechanics particularly when focusing on the COVID19 disease since the behavior of SARS-CoV-2 biological complexities do not differ essentially

 doi:10.20944/preprints202403.0518.v1

from the behavior of the mechanical systems of rigid bodies, gas molecules, and fluids similar. [4–94] These combinations of Quantum Mechanical and Quantum Homeopathy mathematical methods are preferably implemented in this project for translating COVID-19 biosystems quantitative observables and peculiarities of theirs behavior in an attempt to generate the Quantum Information required for the entanglement between two non complementary pharmacophoric parts A1 and A2. It is widely known that molecular dynamics simulation methods and molecular mechanics/quantum mechanics methods can calculate the protein–ligand binding affinity with high accuracy [2–17,27–49] where A1 refers to the electron states involved in the mechanisms of injury common to age-related disorders and A2 to those present after SARS-CoV-2 infection, both in the brain and the periphery. Nevertheless, the extensive computational resources required by these methods greatly limit the ligand search space in the process of drug design based on Bohmer and Hogan proposed method for obtaining the Vaidya–Kerr spacetime [20–39]. They utilized a retarded u, t−r coordinate transformation to rewrite the non-static mass function and rotating parameter as m (u) and a (u), respectively in terms of the Kerr–Schild coordinates, which express the Kerr solution using Cartesian coordinates [21–96]. All results of these previously conducted studies involve radiating rotating black hole solution. My derivation is a nonstationary generalization of previous researches [14–98] ; however, this paper presents an improved version of the orthogonal ansatz as well as a more concise and intuitive derivation method. Until the 1950s, the common opinion was that quantum fields theory (QFT) was just quantum mechanics (QM) plus special relativity. But that is not the whole story, as is described in [1,2–99]. There, the authors mainly say that the fact that QFT was "discovered" in an attempt to extend QM to the relativistic regime is only historically accidental. Indeed, QFT is necessary and applied also in the study of condensed matter, e.g., in the case of superconductivity, superfluidity, ferromagnetism, etc. The substantial difference between QM and QFT was understood around the 1950s [3–100], the Haag's theorem [4,–101], the breaking of spontaneous symmetry, the dynamic generation of collective modes (long range correlations). In QM the Stone-von Neumann theorem [7–104] holds: for systems with a finite number of degrees of freedom the representations of the CCRs are "unitarily equivalent", and therefore physically equivalent. The theorem of Stone-von Neumann does not apply to QFT because the fields by their nature introduce an infinite number of degrees of freedom, and so therefore the hypothesis on which the theorem of Stone-von Neumann is based fails: in QFT there are infinitely many unitarily inequivalent representations. There are physically different "stages" or dynamic regimes. For a review on these topics, see, for example, foundational works in [9–105]. Another common opinion is that QFT does not have quantum information content, differing from QM (for example, in the case of a two-levels quantum system). This is a very important point, of great interest to us. In fact, I don't fully agree with this common opinion, in the sense that I believe that there is hidden quantum information in QFT. I instead agree that the quantum information content is not explicit in QFT, and, put in these terms, this can be taken as one of the main differences between QFT and QM. Then, I maintain the following main differences between QFT and QM: (1). The number of degrees of freedom is infinite in QFT and finite in QM. (2) The representations of the canonical commutation relation (CCR) are all unitarily equivalent in QM (for the Stone-von Neumann's theorem). Instead, QFT admits unitarily inequivalent representations (uir) of the CCR. In the case of QFT with interactions, Haag's theorem states that the representation of the interacting fields is unitarily inequivalent to that of the free fields. (3) QFT does not seem to have explicit quantum information content, differing from QM. (4) From point 3 it follows that, while QM can be simulated directly by a quantum computer (QC), QFT cannot. The QFT must first be adjusted before being simulated, and the regulator is typically a lattice, which, however, breaks Lorentz's invariance. For the topic of quantum simulation of QFT, see, for example [13–106]. The various stages of the reduction mechanism are illustrated below, which is quite complex and requires sophisticated mathematics. I considered a boson field operator, over which I performed an ansatz that admits an attractor in whose basin there is a flow of spatial degrees of freedom, an analogous ansatz was used for an SU (2) gauge field in [15–109]). The ansatz I perform in this work corresponds to a boson translation in terms of the annihilation operator in momentum space. This defines a new vacuum and, in the case of infinite

 doi:10.20944/preprints202403.0518.v1

volume, the two Quantum Homeopathy Representations are unitarily inequivalent. However, in the finite volume of the basin of the attractor, the two Avogadro Number's representations become equivalent, indicating that the bosonic Quantum fields Theory has been reduced to Quantum Mechanics. Within this attractor basin it is possible to define a new metric, quantized in Planck units, that undergoes quantum fluctuations, the quantum foam [16–50], which induce uncertainties in the position states. The latter can be interpreted as maximally entangled qubits on the surfaces of the spheres centered at the attractor point. This is possible if an adequate non-commutative space, which is a generalization of the fuzzy sphere [18–51,110–120] is taken as the geometrical representation of the state space of the maximally entangled n-qubits states. Within these fuzzy spheres, instead, the position states are fully mixed states, and represent the spatial degrees of freedom which have been released. The entanglement entropy of the maximally entangled states equals the total quantum entropy (the von Neumann entropy) of the fully mixed states, so that quantum information is conserved. The study of representing qubit states by non-commutative geometry started a few years ago. In [19–122] I looked for a quantum system, on a quantum (non-commutative) space, which could mimic (simulate) space-time at the Planck scale. For a review on quantum spaces, see, for example [20], and for the relation with QFT, see [21–53,123–130]. In contrast to what happens in QM, the von Neumann theorem does not hold in QFT, and the choice of a particular representation of the field algebra can have a physical meaning. From a mathematical point of view, this fact is due to the existence in QFT of unitarily inequivalent representations (uir) of the CCR (in the infinite volume or thermodynamic limit). The two particularly important cases of linear transformations are the boson translation [2,9,23–131] and the Velatin-Bogoliubov transformation (for bosons) [26,27–132]. In this conventional approach of Quantum fields Theory, where I try to explain the interacting theories, more than one class of representations is needed. The said phenomena was observed bay Haag and sometimes is called the Haag's no-go theorem, which states that free and interacting fields must necessarily be defined on different unitarily inequivalent Hilbert spaces. According to Einstein, "It is the only physical theory of universal content, which I am convinced, that within the framework of applicability of its basic concepts will never be overthrown" [3–42,47–133]. The main problem is that when I try to construct a physical theory, by considering, e.g., the Poincare symmetry, I select just one of these classes and simply forget about the existence of others. This causes some problems, such as Haag's no-go theorem. On the other hand, the formulation of S-Matrix is such that one can find the final state by operating S-Matrix on the initial state without taking into account the moment of interaction, regarding it as a black box. But it is the moment of interaction that all of these classes may become equally important with the basic laws of thermodynamics which were established at a time when the atomistic theory of matter was only in its infancy, and even the existence of atoms has not yet been demonstrated unequivocally. The fact of ignoring the moment of interaction derives from the common attitude of the practitioners to adopt ontology of events, instead of ontology of processes since in many domains of Physics, this ontology of events seems to be the only possible one, or at least the most convenient. Nevertheless, these laws remained untouched by all subsequent developments in physics, with the important qualifier "within the framework of applicability of its basic concepts." This framework of applicability is known as the "quantum thermodynamic limit, " the limit of a large number of particles when fluctuations are assumed to be small [4–135] as a process of a temporal sequence of events that is ruled by some dynamical law which characterizes the process itself. This is exactly the structural content of QFT, as stressed and explained in [1,2,9–55,56,136–138], where it is clarified that the dynamics, expressed by the functions for the interacting fields also called Heisenberg fields, that defines and characterizes the theory under this study and manifests itself in the observable physical fields at the level of these Quantum Homeopathy translations. Events are thus the manifestations of the underlying Turing Machine Learning Ruled dynamics (the process). Moreover, this concept of entropy negativity that is central to quantum thermodynamics was further generalized to become the cornerstone of information theory [Shannon's entropy [25–48,139,140] and is currently considered to be one of the most important concepts in all of science, reaching far beyond physics [26–49,100–141]. For example, Black Hole Paradox Generalizations and Supersymmetric breaking foundations for Turing Machine Learning Ruled Calculations are ruled on by these

 doi:10.20944/preprints202403.0518.v1

implemented algorithms. Ontology of Quantum Homeopathy processes does not deny that Hidden Entanglement observations are about events, but hold that events are explained only in terms of the underlying process, and that the descriptions of these events and processes are somehow inseparable. The expression “ontology of processes” has been borrowed from information science, where it has been introduced within the context of space-temporal databases (see, for instance, Kuhn [28–144]). The conventional presentation of Quantum Thermodynamics starts with the analysis of thermal machines. However, a more recently promoted and apparently much deeper approach is based on the understanding of entropy as a measure of our knowledge (or, more accurately, our ignorance) of a quantized subsystem [6–58,67–145]. A theoretical construction of cluster of Hypergeometric Functions to integralize chemical Block Systems developed here, where I found a model for quantum-computational gravity on a quantum space background; namely, the fuzzy sphere. A few words should also be spared for the important role played in this paper by the uir of the CCR in QFT. Thus, the choice of a particular representation in which to work reduces to a pure matter of convenience. The situation changes drastically when I consider systems with an infinite number of degrees of freedom. This is the case of QFT, where systems with a very large number of degrees of freedom are considered. In a sense, there is no entropy other than information entropy, and the loss of information resulting from summation over a subset of the degrees of freedom is the only necessary condition to derive the Gibbs distribution and hence all the laws of quantum thermodynamics [9,10–57,146–154]. In QM, i.e., for systems with a finite number of degrees of freedom, the choice of representation is inessential to the physics, since all the irreducible representations of the canonical commutation relations (CCR) are each unitarily equivalent: this is the content of the Stone-von Neumann theorem. Ludwig Boltzmann prophetically espoused the connection between entropy and biological evolution: “If you ask me about my inner most conviction whether our century will be called the century of iron or the century of steamor electricity, I answer without hesitation: it will be called the century of the mechanical view of nature, the century of Darwin” [11–157]. In particular, in this reduction mechanism of QFT to QM illustrated in this paper, it is extremely important to take due account of the moment of interaction; that is, to assume an ontology of processes, as I will see in the Conclusions. More specifically, the link between thermodynamics and evolution of biological populations was clearly formulated for the first time by Ronald Fisher, the principal founder of theoretical population genetics [60–158]. Subsequently, extended efforts aimed at establishing detailed mapping between the principal quantities analyzed by thermodynamics, such as entropy, temperature, and free energy, and those central to population genetics, such as effective population size and fitness, were undertaken by Sellaand Hirsh [13–61,159–161] and elaborated by Barton and Coe [14–162]. Avoiding doing so would lead to an internal classical computational structure of QFT, which is itself of no real help in the simulation of the latter. It is therefore no surprise that many attempts have been made to apply concepts of thermodynamics to problems of biology, especially to population genetics and the theory of evolution. Theoretical research on quantum simulation of QFT is very urgent nowadays, because it should support important experimental applications, mainly in high energy physics (HEP), and also for setting up the fundaments of theoretical computer science (TCS) [29–163]. The parallel is indeed clear: The smaller the ultra low drug doses the stronger are the effects of random processes (genetic drift), which in physics associates naturally with temperature increase. Among other attempts to conceptualize the relationships between quantum thermodynamics and evolution, of special notices the work of Frank [15,16–165] on applications of the maximum entropy principle, according to which the distribution of any quantity in a large ensemble of entities tends to the highest entropy distribution subject to the relevant constraints (6). [2–166] The mutual information SA1, SA2 − SA1 ∪ A2 measures the correlations between the two parts, but gives only an upper bound on the entanglement between them as a more useful measure of entanglement in the recent Transcriptome analysis of samples from COVID-19 patients [2–6,31–51,62–167] providing an opportunity to correlate their findings with those obtained earlier when reporting ARBs anti-inflammatory and anti-aging protective effects [4–17,32–52,63–168]. [2–13,17,33–53,64] Molecular docking uses a scoring function to evaluate the binding conformation obtained by each docking to predict binding affinity and uses significantly fewer computational resources. One corresponds to the pure electronic states

 doi:10.20944/preprints202403.0518.v1

of the interacted viral proteins involved in the Transcriptomic analysis of samples from COVID-19 patients and SARS-CoV-2-infected primary human alveolar cells where revealed unique inflammatory profiles with excessive inflammatory cytokine release [2–6,34–54,65–169] and the other to the ones reported in the neuronal cultures injured by excitotoxic glutamate concentrations, a major injury factor in the brain that normalized by treatment with the ARB Candesartan [1–170]. Quantum Mechanics (QM) has revolutionized the understanding of the structure and reactivity of small molecular systems in a large ensemble of ultra low drug dose entities that tend to the highest of negative entropy distribution subject to the relevant constraints. Molecular docking can thereby quickly calculate the binding affinity between multiple ligands and proteins and is commonly used for high-throughput virtual screening of drug molecules based on the protein structure. Nonetheless, the computational efficiency of molecular docking comes at the expense of accuracy. For example, QM based methods provide structural information in excellent agreement with experiment, match experimental barrier heights for chemical reactions, and provide chemically accurate interaction energies for hydrogen-bonded or dispersive systems.[1,2–66] Given the tremendous impact QM has had for ultra low drug dose systems I then hypothesized the partial transpose of HermiteH [n, x] HeunT [q, α, γ, δ, ϵ, z] LaguerreL [n, x] HeunT [q, α, γ, δ, ϵ, z] and then the logarithmic negativity as (1) where he refers to the trace norm ||ϱT2|| of the pure electron transition states exctracted from the translation of the cytokine storm signal transduction of the SARS that follows pneumonia and other coronavirus infections. The attention mechanism [12–55,171] is one of the most powerful approaches to solve this problem. By introducing an attention mechanism, this prediction model can focus on features that are most relevant to the prediction target and at the same time improve the accuracy and interpretability of this drug designing model. [2–6,34,35–56,68–172] The key Hypergeometric Functions refer to the geometry shaping of the atom orbitals and atomic charges during the signal transduction of these effects in cardiovascular and metabolic disorders that are frequently comorbid with COVID-19 including alterations in interferon responses, macrophage and neutrophil infiltration, increased apoptosis, and p53 signaling associated with lymphopenia. [13–57,69–173] In this study, in order to predict protein–ligand binding affinities and structures of proteins and ligands, I developed a Quantum Turing Machine Learning Deep Neural Network SEGSA_DTA, a SuperEdge Graph convolution-based and Supervised Attention-based Drug–Target Affinity prediction method. Super edge graph convolution was adopted to learn feature representations of both nodes and edges from graph structures of proteins and ligands. The sum E, ln||E (y) ϱT2∇ ⊗ (Rx (π), [H] ⊗̂ [Ho] ∯I) ⊕ CZeiπ/2 refers to pure Quantum states of the Angiotensin Receptor Blockers (ARBs) where ϱT2 corresponds to the discrete particles that are bound in finite systems such as the protein-drug systems involved in the excessive activation of Angiotensin II AT1 receptors (AT1R). However, because of the small size of the structure dataset and the lack of detailed knowledge concerning protein–ligand interactions, most of the existing methods are not yet able to effectively learn the attention distribution and accurately capture the true interaction information between proteins and ligands, limiting the predictive performance.[16–58,70] Several studies in the fields of visual question answering [17,18–59,71–174] and natural language processing [19,20–60,72–175] have demonstrated that training attention mechanism in a supervised manner can result in more effective attention distribution and improve model performance significantly, but its effectiveness in building a better protein–ligand binding affinity prediction model remains unclear. [16,37,38–61,73–176] These E (y) Quantum Homeopathy wave effects will allow tunneling through an energy barrier for the generation of chemical mappings against the (AT1R) receptor which is a major injury factor and plays a significant role in the development of disorders of the brain, the cardiovascular system, the kidney, lipid and glucose metabolism and the immune system that are linearly associated with viral load and lung injury in COVID-19 patients [1,2,3,4,5–62,74–177]. In recent years, Quantum Turing Machine Deep Learning has achieved great success in many fields such as computer vision, speech recognition and natural language processing. Deep learning is also widely used in numerous aspects of drug design,3 including de novo molecule design and chemical synthesis. Randomness is often an important resource in information processing. This is true even in the quantum regime, where quantum randomness is often represented by a random state, a quantum pure state that is

 doi:10.20944/preprints202403.0518.v1

drawn uniformly at random from a Hilbert space. Currently, most deep learning-based protein–ligand binding affinity prediction models, such as DeepDTA,4 DeepAffinity5 and DeepDTAF, only use protein and ligand sequence information to predict protein–ligand binding affinity. It is known that protein structure information is essential for protein-ligand binding, yet these sequence-based methods lack sufficient structure information. Alternatively, several studies have utilized co-crystal structures of protein–ligand complexes to predict binding affinity. Nevertheless, obtaining co-crystal structure in protein–ligand complexes is a time-consuming practice, and thus the protein structure-based model is still needed. Moreover, with the recent development of Quantum Homeopathy Neural Networks, the advantages of using Quantum Functions to represent proteins and ligands are gradually being highlighted in deep Turing Machine learning-based models. Accordingly, it makes sense to investigate the extent to which peculiarly quantum effects such as coherence and entanglement play an important role in living systems. [8–179,180] The Turing Machine learning representation retains the structure information of proteins and ligands, [9,10–175,181] and quantum hypergeometric functions convolution neural network (GCN) are commonly used to learn the structure pattern. Before turning to these drug designing efforts, I will review the evidence for quantum effects in these hypertension biological mechanisms as [5–76,182] [2–17,23–183] similar mathematical formalisms of QFT to QM Quantum Mechanics for Quantum Homeopathy reduction methodologies for the modeling biosystems of the molecular structures that are associated in these inflammations and viral injuries in the lung will be inserted as a protein code (cipher-protein), and be determined, and be prepared in heterodox interpretations [22–184] when solving the time-independent [21–185] Schrödinger function over a Boson Field Operator for a Poly-Triangle Shaped Fragmentation Scheme. [26,27,28–186] However, these Schrödinger functions in Markovian and [27–81,94–187] non-Markovian scenarios cannot be solved for any but a one-data-driven [29–82,95–188] electron system method (the hydrogen atom) a family of solutions of [28,30–83,96–189] quantum functions and approximations need to be made [33,34–84,97–190] since most applications of these methods in protein systems have been largely limited to semi-empirical, HF, and DFT calculations. Among these approaches, FMO has been applied to higher level ab initio calculations such as second-order Møller−Plesset perturbation theory (MP2) and coupled cluster theory (CC) as Nakai and co-workers have described D&C-MP222, [25,37–191] and D&C-CCSD38 approaches and applied them to linear or near-linear systems. QM excels at the static modeling of a molecular system however, in chemistry and biology, fluctuations are important to describe a broad range of effects. Thus, the ensemble picture of a molecular system is more appropriate, and while molecular dynamics (MD) methods are beginning to address dynamical issues using classical potentials, how to address this "sampling" issue when using more expensive QM based approaches which will need to be addressed in this Quantum Homeopathy approximation, as it is assumed that the atoms that are far away from the region of interest regarding only weakly influence local regions of a protein.

Divide-and-Conquer Approach for Hartree−Fock Based Calculations

[22–67] In this Drug Design Modeling, I explore the relationship between clinical statistical data from COVID-19 symptoms such as Fever or chills, Cough, Shortness of breath or difficulty breathing, Fatigue, Muscle or body aches, Headache, New loss of taste or smell, Sore throat, Congestion or runny nose, Nausea or vomiting, Diarrhea inflammation as well as with ontology of Quantum Homeopathy Thermodynamics processes and Quantum Physics, and propose that these side effects echo the oldest of adaptive solutions and will give us the ability to consider these self-measurements of the Weighted KNN Positioning Matched Bemis and Murko (BM) driven eigenvalue statements as the basic features of these biological functions which could be translated into Molecular Pairs (MMP) and Quantum Foam Like Chemical Spaces. After the local MO coefficient matrices Cα are obtained, the total density matrix system is given by HermiteH [n, x] HeunT [q, α, γ, δ, ϵ, z] LaguerreL [n, x] HeunT [q, α, γ, δ, ϵ, z] LaguerreL [n, a, x] HeunTPrime [q, α, γ, δ, ϵ, z] SphericalHarmonicY [l, m, θ, ϕ] HeunB [q, α, γ, δ, ϵ, z] HeunD [q, α, γ, δ, ϵ, z]. [22–68] Since one of the main Quantum like bio-specialties is consideration of *self-measurements that biosystems perform on themselves, Quantum biology as a separate field of science could thus be described as the application of Quantum mechanical theory to help explain life and*

 doi:10.20944/preprints202403.0518.v1

its complexity. [22–69] It is recently pointed out that a certain property of generic entanglement is responsible for this revealing of properties of generic entanglement which will help our understanding of why quantum error correction works well, even providing real applications of generic entanglement in quantum information science. [22–79] Most of these studies of generic entanglement focus on the random state that is uniformly distributed over the *whole* Hilbert space defined quantum many-body systems which often have symmetry, restricting the distribution of states into that over the invariant subspace of the symmetry. [12–81] Hence, the aforementioned results about generic entanglement cannot be directly applied to complex quantum many-body systems with symmetry it is also worth of pointing out that these SphericalHarmonic hypersymmetric guiding these principles in many-body physics could allow us to understand intriguing many-body phenomena, such as thermal and quantum phase transitions, in a unified manner. [28–82] Thus, it will be interesting to take symmetry into account in this study of generic entanglement for a Quantum-Foam like molecular modeling from this viewpoint of Quantum theory which is considered here as a measurement theory and for guiding us to the generation of tetrahedron shaped ligands after translating them into generalized pharmacological data as a reflection of the features of the COVID-19 Homeopathy Remedies that naturally match the Quantum Homeopathy Formalism. [27–85] In such modeling, it is useful to explore *Quantum Information Theory*, which is proposed to be applied in this micro-world of Quantum systems as a well-defined translation of the function of these ACE2 and AT1R blockers superpositions. [22–36,77–89] Furthermore, the number of entangled qubits is limited in this experiment. To tackle this problem, in this paper I propose a universal cluster of Quantum Functions based on cryptographic measurements with minor pharmacological resources for each one fragmented pharmacophore which is directly related to a partial decrease or total loss of the enzymatic function in the alveolar cells and the viral load of the air inoculums. These showed to me that these Quantum Entropy Negativity Translations which are tightly linked into the availability of energy will allow pure mechanical computations both for re-generating Lipinski rules and Quantum Inferences for bridging the gap between practical in vitro testing implementations and theoretical docking scalability predictions of Angiotensin II conformers inside the AT1R receptors. Because these Angiotensin transformations are considered to play key role in these electron transfer networks [1–87,101–111] of vasoconstriction, apoptosis, proinflammatory effects, and fibrosis these ACE2 functions in alveolar cells that result in a deviation of the homeostatic balance of the Renin Angiotensin System in favor of the angiotensin II-AT1 receptor axis will be replicated into signal transformative applications in this Quantum computing effort for the design of novel small molecule-like drug designs. [7–25,27,28–88,102–113] Since it has been shown that Path selection into a nonlinear Riemann-Hilbert simple problem of any formula φ for Quantum repeater networks towards the determination of the exact interpolating function of h **(**λ**)** can be geometrically represented by Chern-Simons logical spaces and subspaces I decided in this QFT to QM ansatz reduction mechanism of infinite volume for unitarily screening methods by taking advantage ecosystem's capacity to evolve complexity and increase dissipation of energy in a dynamic quasi-stable state, to implement Supersymmetric Solutions and Borel Singularities for N,**2** allowing a Quantum repeater based vectorial supersymmetric representation. [20,26–89,103–112] In general, the notions of Lindenbaum matrix and associated axiomatic formulations **(**AQFT**)** for QNN-Adaptive Weighted KNN Positioning are continuing to shape the field of its relative algebraic logic by introducing the CS topology on a set when defining the [31–90,104–113] Cartesian product for parallel topological spaces. Additionally, subbase supersymmetric solutions from these thermodynamic interpretations of life led me to further algebraization of chemical topology products, which had been begun by George Boole in the 19th century, as well as to an innovative language of logic, in a symmetric model theory containing no other constants but only one connective Philosophical interpretation of QM Molecular Pairs **(**MMP**)** as a core part of contemporary physics **(**Minkowski-type, wave-edge, etc**)**, [20,27,32–91,105–115]. Since generally, systems processing information in a Quantum-like manner need not be only Quantum physical systems in particular but they can be macroscopic biosystems Quantum Theory is considered here as calculus for predictions, measurements, and transformations of Murko **(**BM**)** driven Probabilistic Eigenvalue Statements into

 doi:10.20944/preprints202403.0518.v1

Quantum Negative Probabilities for algebraic multi-metrics (Triangle area, Bond-angle, etc) to treat Tipping–Ogilvie and Turing Machine Learning observables foundationally as an Interaction Information Theory for Quantum Reference Frames. [20,33–92,106–116] In this paper, we address the question of how symmetry in Quantum Homeopathy Systems changes the properties of generic entanglement and specifically investigates bipartite entanglement of random states in invariant subspaces after providing a general formula that is useful to analyze the distribution of entanglement over a random state in any subspace in very small doses. I then apply the formula to investigate the generic entanglement in invariant subspaces associated with a given symmetry which is especially considered to be divided into three symmetries: 1. Axial symmetry that leads to the conservation law of a component of angular momentum, 2. Permutation symmetry that characterizes indistinguishable bosons and fermions, and 3. Translation symmetry that defines the structure of a lattice. We particularly focus on these symmetries since the axial symmetry is the one used in Refs. [2–100] pointed out the relation between generic entanglement and quantum error correction. The permutation symmetry is commonly believed to result in weak entanglement, and the translation symmetry is important in relation to the area law of entanglement. We however note that the annotated formulas we derive can be applied to any symmetries. In this project, I show an original strategy and demonstrate the utility and the mechanics of this [32–93,107–120] unified molecular formalism as a von Neumann and Dirac formulation states application within a Tipping–Ogilvie and Machine Learning (TOML) Quantum Computing Context as perturbed asymptotically through the example of coupled anti-de Sitter black harmonic black-hole LegendreP oscillators (Sqrt[Pi] /(Gamma[(-(G h^ν n Pi Q δ μ σ Sin[ω]))/2] Gamma[3/2 + (G h^ν n Pi Q δ μ σ Sin[ω])/2]) - LegendreP[-1 + G h^ν n Pi Q δ μ σ Sin[c], 0])/(1 + 2 G h^ν n Pi Q δ μ σ Sin[ω]) + (x ((Sqrt[Pi] (1 + G h^ν n Pi Q δ μ σ Sin[ω]) (2 + G h^ν n Pi Q δ μ σ Sin[ω]))/(2 Gamma[1/2 - (G h^ν n Pi Q δ μ σ Sin[ω])/2] Gamma[2 + (G h^ν n Pi Q δ μ σ Sin[ω])/2]) + G h^ν n Pi Q δ μ σ Sin[c] (LegendreP[G h^ν n Pi Q δ μ σ Sin[c], 0] - Log[Sin[ω]] Derivative[1,0] [LegendreP] [-1 + G h^ν n Pi Q δ μ σ Sin[c], 0]))))/(1 + 2 G h^ν n Pi Q δ μ σ Sin[ω]) + (x^2 ((G h^ν n Pi^(3/2) Q δ μ σ Sin[ω] (1 + G h^ν n Pi Q δ μ σ Sin[ω]) (2 + G h^ν n Pi Q δ μ σ Sin[ω]) (3 + G h^ν n Pi Q δ μ σ Sin[ω]))/(8 Gamma[1 - (G h^ν n Pi Q δ μ σ Sin[ω])/2] Gamma[5/2 + (G h^ν n Pi Q δ μ σ Sin[ω])/2]) - (G h^ν n Pi Q δ μ σ Sin[c] (LegendreP[-1 + G h^ν n Pi Q δ μ σ Sin[c], 0] + LegendreP[1 + G h^ν n Pi Q δ μ σ Sin[c], 0] + G h^ν n Pi Q δ μ σ LegendreP[1 + G h^ν n Pi Q δ μ σ Sin[c], 0] Sin[c] + Log[Sin[ω]] ^2 Derivative[1,0] [LegendreP] [-1 + G h^ν n Pi Q δ μ σ Sin[c], 0] + 2 Log[Sin[ω]] Derivative[1, 1] [LegendreP] [-1 + G h^ν n Pi Q δ μ σ Sin[c], 0] + G h^ν n Pi Q δ μ σ Log[Sin[ω]] ^2 Sin[c] Derivative[2, 0] [LegendreP] [-1 + G h^ν n Pi Q δ μ σ Sin[c], 0]))/2))/(1 + 2 G h^ν n Pi Q δ μ σ Sin[ω]) + (x^3 ((2 G h^ν n Pi Q δ μ σ LegendreP[G h^ν n Pi Q δ μ σ Sin[c], 0] Sin[c] + 2 G^2 h^(2 ν) n^2 Pi^2 Q^2 δ^2 μ^2 σ^2 LegendreP[G h^ν n Pi Q δ μ σ Sin[c], 0] Sin[c] ^2 - G h^ν n Pi Q δ μ σ Sin[c] (LegendreP[G h^ν n Pi Q δ μ σ Sin[c], 0] (-1 - G h^ν n Pi Q δ μ σ Sin[c]) - LegendreP[2 + G h^ν n Pi Q δ μ σ Sin[c], 0] (1 + G h^ν n Pi Q δ μ σ Sin[c]) (2 + G h^ν n Pi Q δ μ σ Sin[c]))))/6 + (G h^ν n Pi^(3/2) Q δ μ σ Sin[ω] (-1 + G h^ν n Pi Q δ μ σ Sin[ω]) (1 + G h^ν n Pi Q δ μ σ Sin[ω]) (2 + G h^ν n Pi Q δ μ σ Sin[ω]) (3 + G h^ν n Pi Q δ μ σ Sin[ω]) (4 + G h^ν n Pi Q δ μ σ Sin[ω]))/(48 Gamma[3/2 - (G h^ν n Pi Q δ μ σ Sin[ω])/2] Gamma[3 + (G h^ν n Pi Q δ μ σ Sin[ω])/2]) - (G h^ν n Pi Q δ μ σ Log[Sin[ω]] ^3 Sin[c] Derivative[1, 0] [LegendreP] [-1 + G h^ν n Pi Q δ μ σ Sin[c], 0])/6 - (G h^ν n Pi Q δ μ σ Log[Sin[ω]] ^2 Sin[c] Derivative[1, 1] [LegendreP] [-1 + G h^ν n Pi Q δ μ σ Sin[c], 0])/2 - (G h^ν n Pi Q δ μ σ Log[Sin[ω]] Sin[c] Derivative[1, 2] [LegendreP] [-1 + G h^ν n Pi Q δ μ σ Sin[c], 0])/2 - (G^2 h^(2 ν) n^2 Pi^2 Q^2 δ^2 μ^2 σ^2 Log[Sin[ω]] ^3 Sin[c] ^2 Derivative[2, 0] [LegendreP] [-1 + G h^ν n Pi Q δ μ σ Sin[c], 0])/2 - (G^2 h^(2 ν) n^2 Pi^2 Q^2 δ^2 μ^2 σ^2 Log[Sin[ω]] ^2 Sin[c] ^2 Derivative[2, 1] [LegendreP] [-1 + G h^ν n Pi Q δ μ σ Sin[c], 0])/2 - (G^3 h^(3 ν) n^3 Pi^3 Q^3 δ^3 μ^3 σ^3 Log[Sin[ω]] ^3 Sin[c] ^3 Derivative[3, 0] [LegendreP] [-1 + G h^ν n Pi Q δ μ σ Sin[c], 0])/6))/(1 + 2 G h^ν n Pi Q δ μ σ Sin[ω]) + (x^4 ((G h^ν n Pi^(3/2) Q δ μ σ Sin[ω] (-2 + G h^ν n Pi Q δ μ σ Sin[ω]) (-1 + G h^ν n Pi Q δ μ σ Sin[ω]) (1 + G h^ν n Pi Q δ μ σ Sin[ω]) (2 + G h^ν n Pi Q δ μ σ Sin[ω]) (3 + G h^ν n Pi Q δ μ σ Sin[ω]) (4 + G h^ν n Pi Q δ μ σ Sin[ω]) (5 + G h^ν n Pi Q δ μ σ Sin[ω]))/(384 Gamma[2 - (G h^ν n Pi Q δ μ σ Sin[ω])/2] Gamma[7/2 + (G h^ν n Pi Q δ μ σ Sin[ω])/2]) + (-6 G h^ν n Pi Q δ μ σ LegendreP[-1 + G h^ν n Pi Q δ μ σ Sin[c], 0] Sin[c] - 12 G h^ν n Pi Q δ μ σ LegendreP[1 + G h^ν n Pi Q δ μ σ Sin[c], 0] Sin[c] - 6 G h^ν n Pi Q δ μ σ LegendreP[3 + G h^ν n Pi Q δ μ σ Sin[c], 0] Sin[c] - 3

 doi:10.20944/preprints202403.0518.v1

G^2 h^(2 ν) n^2 Pi^2 Q^2 δ^2 μ^2 σ^2 LegendreP[-1 + G h^ν n Pi Q δ μ σ Sin[c], 0] Sin[c] ^2 - 18 G^2 h^(2 ν) n^2 Pi^2 Q^2 δ^2 μ^2 σ^2 LegendreP[1 + G h^ν n Pi Q δ μ σ Sin[c], 0] Sin[c] ^2 - 11 G^2 h^(2 ν) n^2 Pi^2 Q^2 δ^2 μ^2 σ^2 LegendreP[3 + G h^ν n Pi Q δ μ σ Sin[c], 0] Sin[c] ^2 - 6 G^3 h^(3 ν) n^3 Pi^3 Q^3 δ^3 μ^3 σ^3 LegendreP[1 + G h^ν n Pi Q δ μ σ Sin[c], 0] Sin[c] ^3 - 6 G^3 h^(3 ν) n^3 Pi^3 Q^3 δ^3 μ^3 σ^3 LegendreP[3 + G h^ν n Pi Q δ μ σ Sin[c], 0] Sin[c] ^3 - G^4 h^(4 ν) n^4 Pi^4 Q^4 δ^4 μ^4 σ^4 LegendreP[3 + G h^ν n Pi Q δ μ σ Sin[c], 0] Sin[c] ^4 - G h^ν n Pi Q δ μ σ Log[Sin[ω]] ^4 Sin[c] Derivative[1, 0] [LegendreP] [-1 + G h^ν n Pi Q δ μ σ Sin[c], 0] - 4 G h^ν n Pi Q δ μ σ Log[Sin[ω]] ^3 Sin[c] Derivative[1, 1] [LegendreP] [-1 + G h^ν n Pi Q δ μ σ Sin[c], 0] - 6 G h^ν n Pi Q δ μ σ Log[Sin[ω]] ^2 Sin[c] Derivative[1, 2] [LegendreP] [-1 + G h^ν n Pi Q δ μ σ Sin[c], 0] - 4 G h^ν n Pi Q δ μ σ Log[Sin[ω]] Sin[c] Derivative[1, 3] [LegendreP] [-1 + G h^ν n Pi Q δ μ σ Sin[c], 0] - 7 G^2 h^(2 ν) n^2 Pi^2 Q^2 δ^2 μ^2 σ^2 Log[Sin[ω]] ^4 Sin[c] ^2 Derivative[2, 0] [LegendreP] [-1 + G h^ν n Pi Q δ μ σ Sin[c], 0] - 12 G^2 h^(2 ν) n^2 Pi^2 Q^2 δ^2 μ^2 σ^2 Log[Sin[ω]] ^3 Sin[c] ^2 Derivative[2, 1] [LegendreP] [-1 + G h^ν n Pi Q δ μ σ Sin[c], 0] - 6 G^2 h^(2 ν) n^2 Pi^2 Q^2 δ^2 μ^2 σ^2 Log[Sin[ω]] ^2 Sin[c] ^2 Derivative[2, 2] [LegendreP] [-1 + G h^ν n Pi Q δ μ σ Sin[c], 0] - 6 G^3 h^(3 ν) n^3 Pi^3 Q^3 δ^3 μ^3 σ^3 Log[Sin[ω]] ^4 Sin[c] ^3 Derivative[3, 0] [LegendreP] [-1 + G h^ν n Pi Q δ μ σ Sin[c], 0] - 4 G^3 h^(3 ν) n^3 Pi^3 Q^3 δ^3 μ^3 σ^3 Log[Sin[ω]] ^3 Sin[c] ^3 Derivative[3, 1] [LegendreP] [-1 + G h^ν n Pi Q δ μ σ Sin[c], 0] - G^4 h^(4 ν) n^4 Pi^4 Q^4 δ^4 μ^4 σ^4 Log[Sin[ω]] ^4 Sin[c] ^4 Derivative[4, 0] [LegendreP] [-1 + G h^ν n Pi Q δ μ σ Sin[c], 0])/24))/(1 + 2 G h^ν n Pi Q δ μ σ Sin[ω]) + O[x] ^5 and brane spacetimes. I expect also this Lindenbaum-Tarski driven and Chern-Simons oriented macro-entanglement representation to generate a valid QSAR modeling, and lead this Quantum Homeopathy Compound Design Formalism for the designing of a novel multi-chemo-structure interacted with Quantum Negative Energies against the crystal structure of AT1R, and COVID-19 protein targets. [12–29,35–94,108–122] The WolframAlpha Kappa-Symmetry Functions of local observables and the DockThor's Docking Webserver are incorporated in this project for the validation of the docking experiments of FDA-approved small molecules, peptide-mimetic, and humanized antibodies against potential SARS-COV-2 protein targets via a generalized procedure of Quantization of Classical Fields which were fused together with QSAR Automating Modeling to lead the commutation and anticommutation relations. [19–37,39,41,42–95,109–129] Dynamic niching and flexible heuristic genetic algorithmic states for automatic molecule re-coring and fragmentation are proposed in this in-silico effort to fragment and re-core a database of molecules against the structure and functions of SARS-CoV-2 binding sites found in GISAID **(**Alpha, EPI_ISL_791333; Beta, EPI_ISL_896474; Gamma, EPI_ISL_1091366; Delta, EPI_ISL_2425097; Omicron, EPI_ISL_6794907**)** at all COVID-19 biological scales from proteins, cells and brains to humans and ecosystems so **we** can speak about Quantum Ontology Information Biology. However, the rationale of these Universal Quasihelical Functional Group Activity Coefficients **(**UNIFAC**)** on free energy docking observables in four dimensions of a rich QFT [20–41,42–96,110–130] were deployed in this pharmacophoric merging example for linking fragments, and condensed chemical block systems D - branes that are wrapped on Lagrangian chemical spaces which are restricted to the anti-inflammatory effects of SAC/VAL for supporting SAC/VAL chemical space as a input [22–38,40,43–97,111–134] in this Hybrid Quantum repeater for the robust creation of entanglement between remote memory qubits. To demonstrate its flexibility, I tackle a hugely different Quantum-like modeling objective that elevates the role of convenience and simplicity of Quantum representation of states and observables issued from a 5 - dimensional submanifold organic molecular domain [22–148] as a transverse holomorphic structure, which means that there is a given 3 - dimensional foliation for each one tangent bundle modulo foliation. I show that my method can generate sets of optimized critical molecules as integrable structure complexes which having high energy or low energy, starting only from penicillamine derivatives. I also set constraints on a synthesizability score and structural features when the GS-441524, remdesivir, EIDD-1931, molnupiravir 3 - brane is a chemical subspace of the 5 - brane, and the flux on the invariant 5 - brane vanishes when restricted to the 3 - brane, the 3 - brane refers to the Roccustyrna's derivatives transverse holomorphic chemical structures. [41,42–159] Flexible Topology Euclidean Geometrics on several parameters are also implemented here, to fragmentize molecules automatically in this molecular modeling and drug designing project while

 doi:10.20944/preprints202403.0518.v1

keeping the definition of the groups as simple as possible. Quantum Uncertainties in $C\hat{}\ \infty$ operations for Maximum Common Substructure **(**MCS**)** topologies are proposed here for Quantum Homeopathy Generalizations of k**-**nearest neighbors for valsartan and olmesartan**,** candesartan, and losartan drugs on a Tipping–Ogilvie and Machine Learning approach for generating Quantum Negative Energies from the classical docking comparative analysis of the available ARBs**,** including the telmisartan drug that gathers properties as an initial pharmacological tool to evaluate the hypothesis that Molecular Pairs **(**MMP**)** and Adaptive Weighted KNN Positioning which could be combined in a Matched Bemis and Murko **(**BM) approach for supercritical entanglements. By introducing an advanced Quantum mechanical inverse docking algorithm and providing further insight to confirm the practicality of negative docking energy predictions in this protocol, several hypergeometric quantum functions will be incorporated in combination with tools from conventional cryptography for wild type and selected mutations for Nsp3 (papain-like, PLpro domain), Nsp5 Nsp15 (NendoU), (Mpro,3CLpro), Nsp12 (RdRp), N protein and Spike which are considered as inputs and key element functions of SARS-CoV-2 protein pathways in understanding and designing possible novel antiviral agents, from both a Quantum algebraic and a cheminformatics perspective along with the generic entanglement principles of the regulation of computer-aided drug discovery methodologies. Molecular scaffolds will be represented here as QuantumDistance [AdsQFTˆC, (Rz (π), QFT [H], ⊗̂ [Ho] ∮IMG) μνi),2 CZC∂CZ (Rz (π), QFT [H] ⊗̂ [Ho] ∮IMG) μνi) orthogonal eigenstates for complex topologies in triangular skeletons that are generally used to generalize the superposition states of the core structures of multi-targeted molecules [25,33,38,39,44–170]. In this Quantum Homeopathy oriented Medicinal Chemistry Project, Quantum fieldss and Quantum Homeopathy Entropy in five dimensions Chern-Simons molecular similarity actions are implemented to generalize the molecular scaffolds from the NuBBEDB phytical libraries and represent the core structure of the core group of the selected active compounds in their homeopathy formulation. Since the compounds from the already approved homeopathy remedies with the same scaffold may influence a particular metabolic pathway, the molecular scaffolds can effectively contribute to the prediction of biological activities near to Avogadro Number's approximations [8,16,40,42,43–181]. In this project the selected herbs in ultra low doses are classified into structural classes using the characteristic scaffolds of each group [14,32,33,42–192].

The Use and Importance of the Nanoscale in ZernikeR, Hypergeometric2F1Regularized, LaguerreL, and ChebyshevU Quantum Homeopathy Translations

Before exploring the possible mechanism behind the working of serially diluted succussed solutions, it is interesting to see the importance of too small in Nature. In this regard, there is a famous quote from Johannes Kepler: "Nature uses as little as possible of anything." Nature is replete with specific examples of the powerful impact that results from extremely small doses of specific substances to significantly change living things and to alter physiologies and behaviors. We all know that every living creature is hypersensitive to whatever it needs to survive. It is widely known that dogs have a truly amazing sense of smell and can follow a human trail despite the fact that a person leaves only approximately 4 billionths of a gram of odorous sweat per step. [4–44] Sharks can detect small concentrations of blood in the water or even slight perturbations that humans create while swimming, despite the great amount of volume that our oceans hold. And then, of course, is the truly awesome sensitivity that various insects have to pheromones, which are sexually attracting hormones. Male night moths can find females on a dark moonless night, and if necessary, even against the wind. A male silkworm will fly many miles to find its female insects. [4–114] It is no simple coincidence that pheromones are sensed only by those in the same species who emit them (akin to the homeopathic principle of similars), as though they have developed exquisite and specific receptor sites for what they need to survive and to propagate their species. Ultimately, we only need to look at the significant influence that various chemicals have in our own human body to be in awe of the remarkable influences that exceedingly small doses have: Interleukin-1 for T-cell clone proliferation: 2.5 × 10−19 mol/L (19X)*, Platelet-activating factor for decrease of luteinizing hormone somatostatin: 10−17 mol/L (17X), β-endorphin to modulate natural killer cell activity: 10−18 mol/L

 doi:10.20944/preprints202403.0518.v1

(18X), Tumor necrosis factor for synergistic action with various drugs: 10−14 mol/L (14X), Leukotrienes for release of luteinizing hormone: 10−20 mol/L (20X). [17–128] These small dose variables refer to the quantum homeopathic notation in terms of its decimal scale (1:99) dilution. The scaffold of molecule groups will be defined in this paper as a common sub-graph of the graphs of the molecule groups derived from the translation of the classical nonlinear quantum electro-dynamics of the ACE2 electrochemical processes in SARS-CoV-2 biosystems. [24–134] These Quantum Homeopathy Electrodynamics will essentially speed up also the Translation of COVID19 Homeopathy Remedies into the Neprilysin and AT1R receptor targeted DRVYIHPFX- holomorphic ligands. Representatively, Maximum Common Substructure (MCS), Matched Molecular Pairs (MMP), and Bemis and Murko (BM) basins are used in these proposed methods to produce molecular scaffolds from the Homeopathy remedies of (Ferrum phosphoricum 6CH, Gelsemium 6CH, and Justicia adhatoda 6CH) [22–30,39,40,42,44–103,111] for comparing and assessing the computational antiviral activities between RoccustyrnaTM drug novelties and the Remdesivir FDA approved Drug and its parent nucleoside GS-441524, Molnupiravir, EIDD-1931, and the viral protease inhibitor Nirmatrelvir against the ancestral SARS-CoV2 strain and the five variants of concern including Omicron. [1–23,45–104,112] **I** then assessed the in-silico antiviral effect of GS-441524, Remdesivir, EIDD-1931, Molnupiravir and Nirmatrelvir against the various SARS-CoV-2 VOCs, including Omicron in a Quantum framework where the "Quantum state" is the Quantum information state of a biosystem's Quantum negative energy used for processing of special Quantum uncertainty. [5–28,50–113] Here, I present an analysis of topologically complex Quantum Homeopathy Networks of chemical quantum repeaters composed of heterogeneous links derived from statistic data from the new coronavirus emerged in Wuhan Province, China, causing lung complications similar to those produced by the SARS coronavirus (SARS-CoV) in the 2002–2003 epidemic. [13–34,56–106,114] Since Quantum Circuits have fundamental behavioral differences from classical networks the delicacy of Quantum States makes a practical path for a pharmacophore merging algorithm where classical notions of resource utilization can be directly applicable for the translation of Quantum Homeopathy Entropy Negativities (QHEN) generated from various pharmaco-therapeutic substances in ultra small doses. [27–107,115] It is important to note that nature cannot select against the Quantum-Mechanical nature of chemistry. [27–125] These results of selection are mediated here through genetic processes that can affect biological subsystems which have been evaluated through clinical trials including in vitro and in vivo results from Recombinant ACE2 therapies, administration of agents aimed at increasing ACE2 levels (e. g., estradiol), and administration of drugs that decrease the elevated activity of angiotensin II including renin release inhibitors, classic ACE inhibitors (ACEI), or Angiotensin Receptor 1 Blockers (ARBs). [29–45,67–108,115–135] This paper concentrates on QFT reduction mechanism as a part of the unification of Quantum Mechanics fundamental theories into 3 - dimensional field wave functions for a N=7 supersymmetric generalized k-nearest molecular oscillators which is devoted to quantification of the Heisenberg uncertainty relations in decision making for combinatorial translations of the aetiopathogenic hypothesis described in most patients who develop COVID-19 disease with fever, indicative of an inflammatory process with systemic release of pyrogenic cytokines. [29–45,67–137] Since even very basic cognitive effects cannot be described in a way consistent with the standard observation model the particular type of entanglement I require is called a Bell pair. [29,56–139] Although that type entanglement is location independent, when I refer to a Bell pair in this paper, I mean a Quantum Mechanically distributed Bell pair consisting of one qubit at one location entangled with a qubit at another chemical space solution since for this Quantum-like chemical biology modeling, not any kind of non-classical bio-statistics can be easily delegated to von Neumann model of observations. Quantum Homeopathy Entanglement comes in many forms and can involve more than two parties-drugs in very small doses, but in this paper I focus on the multi party Bell pairs both as Anti-de Sitter Chern-Simons intermediate resources for Quantum Reference Frame Representations of Quantum Homeopathy Entropy Negativities (QHEN) as exctracted from the hypothesis described here, that this inflammation is induced by the inhibition of ACE2 and the imbalance of the renin angiotensin system in the pulmonary interstitium in favor of the angiotensin

 doi:10.20944/preprints202403.0518.v1

II-AT1 receptor axis. [29–55,77–139] Faced with the onset of this inflammatory process, a rapidly effective treatment is necessary to antagonize the cascading and self-sustaining phenomenon described here involving a pharmacophore merging scheme with negative total docking energy energies. These end goals of these Quantum Communication sessions will be delivered to the boundary solution in a five-dimensional Chern-Simons supergravity application layer. [38–55,87–140] In this effort, I propose QFT to QM Maximally Entangled States to achieve very high accuracy levels as say of the position and momentum, and spin and polarization projections which are represented in this Quantum Homeopathy paradigm, by Hermitian operators for the generation of Quantum Hormetic designed molecules of the Roccustyrna_gs, the Roccustyrna_fr, the Roccustyrna_gs_consv, and the Gissitorviffirna_TM ligands. [49–75,87–141] The biological essence of this scheme is illustrated here by Quantum formalization of Quantum fields Theory (QFT) Uncertainities and Topology Geometric Methods in a Functional Quantum Negative Space for FH0Δ holomorphic functions for the generation of novel drug designs and theirs generalized k-nearest neighbors within this Quantum Homeopathy computing chemical context targeted in a atomistic level the (S) Spike proteins and its aspartic acid (SD614) and glycine (SG614) protein apparatus. Through these Quantum Reduction Mechanisms, QFT mainly generates an ansatz on the boson field operator and reveals its hidden internal structure of Negative Quantum Energies, which take into account Quantum foams and non-commutative Quantum geometries for a Quantum network of maximally entangled atomic states for a complete decision tree search of all possible combinations of fragmentation, re – coring, and merging functions of the given pharmacophoric systems that are targeted inside the SARS-CoV Mpro protein targets. [22–95,84–146] A distinctive feature of this implementation is the incorporation of kinetic energy operator which is something desirable when Quantum Functions are employed, because differential operators such as the Laplacian in the kinetic energy are challenging to represent correctly. [2–57,67–109,115–147] These QFT guided docking energy reduction processes (in particular the ENTROPY regulator) would then play the role of a definitional (QUANTUM FUNCTION), which allows the switch from a Quantum Homeopathy Metalanguage to an object language (the logic) when determining the ground-state electron configuration of the Quantum Homeopathy Characteristics of the latter on a five dimensions entropic equilibrium of fully mixed and maximally entangled of negative energy electronic states. Since every living organism is an open system operating far from thermodynamic equilibrium and exchanging energy, matter and information with an external environment with Quantum Homeopathy exchanges are performed through non-linear interactions of billions of different biological components, at different levels, from the quantum to the macro-dimensional. Coherent phenomena are well explained by quantum fields theory (QFT), a well-established theoretical framework in quantum physics. Water is essential for life, being the medium used by living organisms and can be carried out various biochemical reactions and playing a fundamental role in coherent phenomena for this theoretical framework which is described in detail and the implemented algorithm is both presented in the paper and made available as a Quantum Functions. The concept of quantum coherence is an inherent property of living cells, used for long-range interactions such as synchronization of cell division processes is supported from recent advances in quantum biology demonstrating that coherence, as a state of order of matter coupled with electromagnetic (EM) fields, as one of the key quantum phenomena supporting life dynamics in this new Quantum Homeopathy Crypto-Metalanguage Approach of the Quantum simulation of QFT negative reductions of degrees of infinite freedom which is proposed here to quantize CS operators from AT1Rs blockers required for ACE2 endocytosis in SARS-CoV-2 infection. This is also adjusted before being simulated and are strongly relating to how one clustered pharmacophoric element occupies the same Quantum Energy Phase in an alternative XYZ coordinated smile system for the fragmentation and re-merging of the sacubitril/valsartan (SAC/VAL) angiotensin receptor type 1 (AT1R) inhibitors into the RoccustyrnaTM new Drug Designs with increased levels of Negative Docking Energy Values. Two simple examples are presented, highlighting the main features of these implementations including arbitrary predefined precision, rapid and robust convergence, absence of the kinetic energy operator as a negative docking regulator which is typically a lattice and breaks Lorentz's invariances,

 doi:10.20944/preprints202403.0518.v1

holomorphic twists, and holomorphic BF computational skeletons of the DRVYIHPF-mimetic, Gisitorviffirna_TM, Roccustyrna_gs, and Roccustyrna_fr tetrahedrically quantized drug designs. The Quantum Homeopathy Entropy Negativities (QHEN) generated here through this reduction mechanism from (bosonic) QFT to QM could reveal QFT's Hidden Quantum Information (HQI) with very high accuracy levels when Eigenvalue Statements for Shannon entropy quantities as composed on Tipping–Ogilvie driven Machine Learning potentials are unifying for nonzero Christoffel symbols. [67,68–110,114–149] For this model, I find analytic black hole solutions over the Boson Field Operator for a triangle shaped fragmentation Scheme relevant to addressing a vast variety of small molecule modeling problems that are essential for describing pharmacophore merging phenomena, and for the generation of unique drug designs with the highest docking energies of negative binding values when compared to other known SARS - CoV - 2 homeopathy antivirals in the presence of chemical potentials among others at the locally AdS5 spacetime. [67–150] We then find that compared to generic entanglement of a random state without symmetry, the axial and permutation symmetries reduce the amount of entanglement by a constant and a significant degree, respectively, while the translation symmetry does not lead to a significant reduction. [80–154] We also numerically study whether this distribution in exceedingly small doses of Quantum Homeopathy entanglement over random states in invariant subspaces has phase-transition-like behaviors. Although the Helmholtz equation separates in spheroidal coordinates into particular, and special, examples of such equations (ordinary spheroidal wave equations) [10–164] the earliest physical context of a generalized spheroidal wave equation arose in the consideration of the quantum mechanics of hydrogen molecule-like ions. [10–165] Early investigations into this subject are reviewed by Baber and Hasse,′ 5 and much of the discussion in this and the following two sections is excerpted from their article. [10–166] The combined mathematical and physical appeal of the generic discrete and tridiagonal models (2) seems partially marred by the more or less purely numerical [10–167] or perturbative [11–168] nature of their solution. For this reason, analytically solvable models are often preferred in analysis [12–169]. I here simplified mathematics by paying attention to the effects connected with the restricted, one-parametric variation of the end-site-interaction matrix elements cj and bj+1 with j = 0 and j = N − 2 in Eq. (2) [6,13–178]. Marginally we add that similar discrete solvable models with pairs of point-like interactions that played important role in the recent extensive discussion of some conceptual problems of these cryptohermitian quantum scatterings [14,15–179]. In this context a lot of misunderstandings emerged when people forgot to distinguish between the "formal coordinate" x (often chosen as playing the role of the argument in wave functions $\psi(x)$) and the "observable coordinate" (a position-operator eigenvalue denoted by another symbol, say, q). In a very well written paper [16–180] interested reader may find the nice explanation of this subtlety emerging as highly relevant even on the very elementary level of mathematics used in introductory textbooks on quantum mechanics. Once one move to the more sophisticated cryptohermitian models where the "formal coordinate" x itself ceases to be observable, the concept of "locality" must be reconsidered and used with enhanced care. For example, a very instructive comment given in sections 2 & 3 [17–180] shows that the formal wave function of a physical localized state may look non-local as a function $\psi(x)$ of the formal coordinate x. In opposite direction it has been noticed and emphasized by Jones [14–181] that in virtually any experimentally oriented setup we usually treat interaction V as if it is prepared as a specific function of the measurable coordinate q. In this sense, the crucial role of the specification of observables and of the difference between x and q gets even more important in non-Hermitian setting [18–182] solvability-guaranteeing simplifications may reduce the menu of interesting phenomena. Typically, the simplified models explain the emergence of fragile, unstable components in the spectra [20] but they can hardly compete with realistic models in offering sufficient variability of the parametric dependence of the energies [4–183]. A remedy has been found in Refs. [22–184] revealing that there exist nonnumerical chain models or quantum lattices (2) with a much less restricted qualitative variability of spectra. These models were characterized by a delocalized interaction exhibiting an up-down symmetry pairing of the sites with indices m and N − m as were attached with the same strength of interaction in ultra small concentrations. Although the productivity of such an artificial assumption was reconfirmed, say, in Refs. [6–184] and [23–185], its

 doi:10.20944/preprints202403.0518.v1

physical interpretation remained obscure. One would like to have some exactly solvable quantum-lattice models without such symmetry. This motivated our present analysis during in which we developed another class of solvable quantum-lattice models of form (2) without similar non-local, long-range auxiliary correlation. Generalized spheroidal wave equations also result from the separation of linearized covariant wave equations on black hole background metrics, and the quasi-normal modes of the perturbations of these geometries may be found by the same techniques used to determine the bound-state eigenfunctions of the hydrogen molecule ion. [90–184] This section explores the similarity of the differential equations in the astrophysical problem to corresponding differential equations in the molecular ion problem, and reduces them both to the form of equation (1) [67–185] Thus, I analyze the most general QFT to QM reduction mechanism for unitarily Quantum Homeopathy Screening Methods that are consistent with the local AdS5 generated D614G Binding Site isometrics in Riemann-Cartan space when solved with the time-independent Schrodinger functions of motion in much larger chemical spaces that are currently inaccessible to experimental screening methods. Hence, the entire chemogenomic system is divided into fragments called core regions (Core α) with an associated buffer region (Buffer α) assigned to each pharmacophore's core region to account for the local environmental effects. The combination of every pharmacophoric core regions and its buffer region constitutes a subsystem (Rα) which was shown the probability density function for the Avogadro's Number distribution singularities, when splitting the distribution into three different entanglement phases with different entanglement spectra. Since the entanglement spectrum characterizes topological orders of the state, this implies that there exists yet another intriguing relation between a random state and an exotic quantum many-body physics indicating also a close relation between generic entanglement and quantum error correction, one of the key concepts in quantum information science below the levels of Avogadro 's number approximations. It is well-known that a randomly chosen unitary is typically a good encoder of quantum information [34–182]. Herein I briefly review the work carried out in my laboratory over the past decade in exploiting fully QM methods in the study of biological systems particularly discussing the use of Quantum Homeopathy in Drug Designing techniques to address the matrix diagonalization step in semi-empirical methods and in HF and DT approaches. To achieve this Quantum Homeopathy goal, the computational bottlenecks of QM methods had to be addressed. In this semiempirical theory, matrix diagonalization is rate limiting, while in density functional theory or Hartree–Fock theory electron repulsion integral computation is rate-limiting. These Quantum Homeopathy phase transition approaches require a unified conceptual framework that utilizes extended symmetries and quantum groupoid, algebroid, and functorial representations of non-Abelian higher dimensional structures pertinent to quantized spacetime topology and state space geometry of quantum operator algebras. After summarizing the technical aspects of how to compute the QM energy of many thousands of atoms, I will review several fully QM application and function studies carried out for the first time in my laboratory on biological systems after discussing the future outlook of using QM hypergeometric functions to solve biological problems and the ongoing challenges of using a fully QFT to QM Quantum Mechanics and Quantum Homeopathy reduction mathematical model on large systems by mimicking the Quantum behavior of substances in ultra low doses. First, the Newman–Janis algorithm (NJA) [8–31,42–182], which usually requires Newman–Penrose formalism, is a commonly applied technique based on the use of complex null tetrads with ideas taken from 2-component spinors for general relativity [10–185]. ($|\mathbf{Rx}\uparrow\rangle$) refers to a particle less than a 100 nanometer in size which is called a nanoscale particle or nanoparticle and due to its large surface area in comparison to volume, its properties can be extraordinary in comparison to its bulk form which can even act as a Quantum Homeopathy sensor.-[30–35,45–186] ($|\mathbf{Rx}\downarrow\rangle$) along with interfacial water on their surface, they, as nanoparticle—exclusion zone shells, can retain the information specific to the source-drugs/toxic substances showing that such ultra-high dilutions can be bioactive defying conventional wisdom. [7–43,46–187] There have been 2 significant objections against homeopathy while demonstrating of how this phenomenological approach can be used to study the "ideal mutation" model of evolution and its generalizations where several radiating rotating solutions have been proposed. [7–44,47–188] First, our study discussed the axisymmetric Vaidya–Kerr metric, which

 doi:10.20944/preprints202403.0518.v1

retain the information specific to the source-drugs/toxic substances and admits no perfect quantized structures [16–44,50–189]. First, using fact of its medicines that are often ultra-high dilutions of drug-substances and can hardly contain any remaining molecules I developed an equation/function in a spheroid might which well be translated into the consciousness of the practitioner and the patient and plays another important role, not, as yet, in detail analyzed into one of the key features of quantum processes recently used in Quantum Homeopathy and a kind of sophisticated modern magic based on a generalized version of entanglement states. [7–190] Secondly, using results from old homeopathy remedies, their double-blind type clinical trials, and from large reviews of such research we have found evidence of benefit from homeopathic medicines,-while other reviews haven't through a novel algebraic topology approach to supersymmetry (SUSY) and symmetry breaking in quantum fields and quantum gravity theories with a view to developing a wide range of physical based drug design applications. [7–191] This evidence and other exemplifications of generalized entanglement according to Car−Parrinello or Born−Oppenheimer molecular dynamics approaches will be used as an input in this short time scale sampling issue showing how to effectively use QM to study Black Hole Paradox Generalizations and Supersymmetric breaking phenomenon by covering longer time scales Ghosh and Maharaj when applied the Hayward black-hole solution as a seed metric to obtain a rotating radiating black hole solutions without a singularity [17–192]. These ambiguous ChebyshevT-adS5 Quantum fields theory (QFT) Reduction results stem from the fact that these chemical Block Systems on generalized Supersymmetric Turing Machine Learning Ruled Calculations are designed to use the standard power near to Avogadro's Number for Hypergeometric Quantum Series Solutions to establish their convergence, to determine the eigenvalues of boundary value problems which are completely reliable with high docking accuracy when trying to study the behavior of angular and radial spheroidal functions and design modern medicines as highly individualistic therapeutics. [7–192] Such generalized macroentanglements are suitable to a hormetic agent's efficacy within this quantum thermodynamics framework for sampling major transitions from an ensemble of molecules to an ensemble of organisms, which is the origin of life, and can be modeled as a special case of bonafide physical phase transitions which are associated with the emergence of a new type of grand canonical ensemble of hypergeometric descriptions. The aforementioned studies were based upon the Newman–Janis algorithm and Eddington–Finkelstein coordinates [1–18,33,37–194], [19–37,38–195] ; they comprise a pair of coordinate systems, which are adapted to radial null geodesics for a Schwarzschild geometry. Classical thermodynamics is probably the best example of the efficiency of a purely phenomenological approach for the study of an enormously broad range of physical and chemical phenomena [1,2–195]. Additionally, for a better representation of the realistic potentials of the computated docking free energy eigenvalues these phase resonance generalized Special Fuzzy Shape comparisons between atomic models and 3D density maps allowed the fitting of atomic models into chemicalized maps as were exctracted after unifying Hypergeometric Eigenvalue Solutions into Shannon Entropy Quantities for Solvable Quantum Turing Functions (Highlights Supplementary Material, Maths.1-12) and composed with Tipping–Ogilvie driven Machine Learning potentials for nonzero Christoffel symbols which will then be resulting into the cluster of the Roccuffirna_fr, Roccustyrna_gs, Roccustyrna_consv, and Gissitorviffirna_ TRM drug designs demonstrating its microblack hole docking properties in practice. Finally, a new approach for Quantum Homeopathy Simulations of QFT is proposed through the use of QFT's internal Quantum Homeopathy Network. Single variable SphericalHarmonicY, LaguerreL, WhittakerM, SphericalBesselJ, LegendreP, LegendreQ, LaguerreL, ChebyshevT, and Hypergeometric1F1 Functions pFqarise in connection with the power series solution of the Schrodinger equation or in the summation of perturbation expansions in quantum mechanics. (Highlights Supplementary Material, Maths.1-12) In these studies, entropic and enthalpic contributions to molecular binding were observed to vary substantially and in an opposing manner as the ligand protein complex are modified while the binding free energy varies little. Although the power of this Quantum Turing Approach is manifest, challenges still remain.

 doi:10.20944/preprints202403.0518.v1

Methods & Materials

QFT to QM Reductions, Quantum Thermodynamics, and Turing Machine Learning Ruled Quantum Homeopathy Variables for the Biogenetoligandorol Drug Designing Protocol.

Section 1. Composite systems, and the Partial trace of a maximally entangled state of density operators of the matrix sequences screening as GegenbauerC[ϱ A B, ϱ B, ϱ A] ChebyshevT generalized inputs from the Arsenicum album, Pulsatilla nigricans, Nux vomica, Rhus toxicodendron, and Gelsemium sempervirens Homeopathy remedies including NuBEE Phyto – library, and COVID2019 targets identified between the consensus of 2019-nCoV and representative betacoronavirus genomes (Supplementary Material (METHODS AND MATERIALS) (1),(2)).

Section 2. Biogenetoligandorol AI-heuristic (DFT) Generalized algorithm for Chern-Simons Weighted ℓneuron (ι): φ◦ D◦ r^2◦ S◦ r1 Topologies: A Quantum Hilbert space H attempt to put pharmacophoric elements back together: Density Operators (Matrices), Properties of Density Operators, and a Density matrix of a pure state in a Multiwavelet framework: QFT orthogonal polynomial Ansatzs over the Boson Field Operator for a triangle shaped fragmentation Scheme (Supplementary Material (METHODS AND MATERIALS) (1),(2)).

Section 3. Entanglement-Breaking Effect of Homeopathy like to like phenomenon on Lagrangian driven Hartree–Fock functions with respect to an arbitrary orbital variation δφi: Algebraic Topology Foundations of a Supersymmetry Breaking Quantum Foam Ansantz for a tetrahedron shaped pharmacophoric ligand (Supplementary Material (METHODS AND MATERIALS) (1),(2)).: Vaidya and Kerr like evolution metrics for SphericalHarmonicY phenomenology transformations for generalizing genetic coding from 2019-nCoV, bat-SL-CoVZC45, bat-SL-CoVZXC21, SARS-CoV, and SARS-CoV polymorphisms.

Results

An indirect measurement model is registered here as a general measuring process consisting of a quadruple Hilbert space, a density operator, and a unitary operator on the tensor product of the generalized chemical spaces. In this measurement model, the tensor product represents the quantized chemical space of the final peptide mimetic apparatus, and the unitary operator describes the time-evolution of the protein-drug composite system. As a result these high-dimensional Hilbert space Quantum states provided me with a wealth of data to generate γx, δx and ηx rotations around the X-axis and Z-axis. The Total Energy (Etotal) is calculated as the sum of: (i) intermolecular interaction energy which was calculated as the sum of the van der Waals between the hydroxyl and cyano groups (buffering constant, 0.35) and electrostatic potentials between the (PDB code: 6xs6) protein and my ligand atom pairs, (ii) intramolecular interaction energy of the van der Waals and electrostatic potentials was calculated as the sum between the1-4 atom pairs, and (iii) torsional term of the ligand. [11–90,122–194] All best docking poses generated during all the docking steps in this project were then low mass weight categorized and clustered by my in-house tool BiogenetoligandorolTM. [15–195] The related diagonal-matrix operator of the new chemical coordinates remained merely scaling non-invariant.

 doi:10.20944/preprints202403.0518.v1

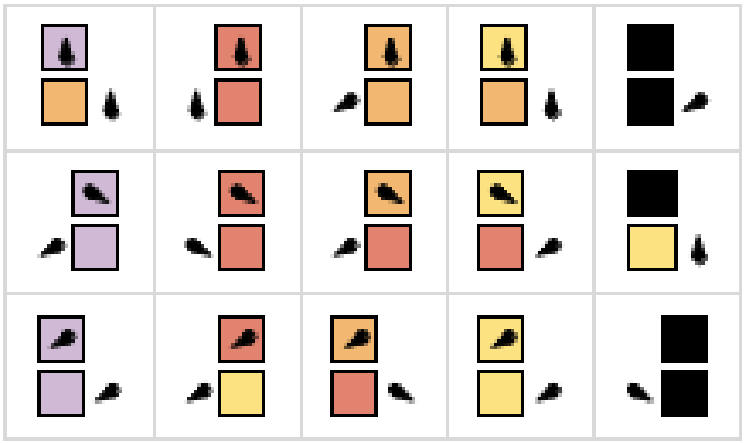

0 | 1 | 2 | 3 | 4

(Ic0a) 1 | 2 | 3

 doi:10.20944/preprints202403.0518.v1

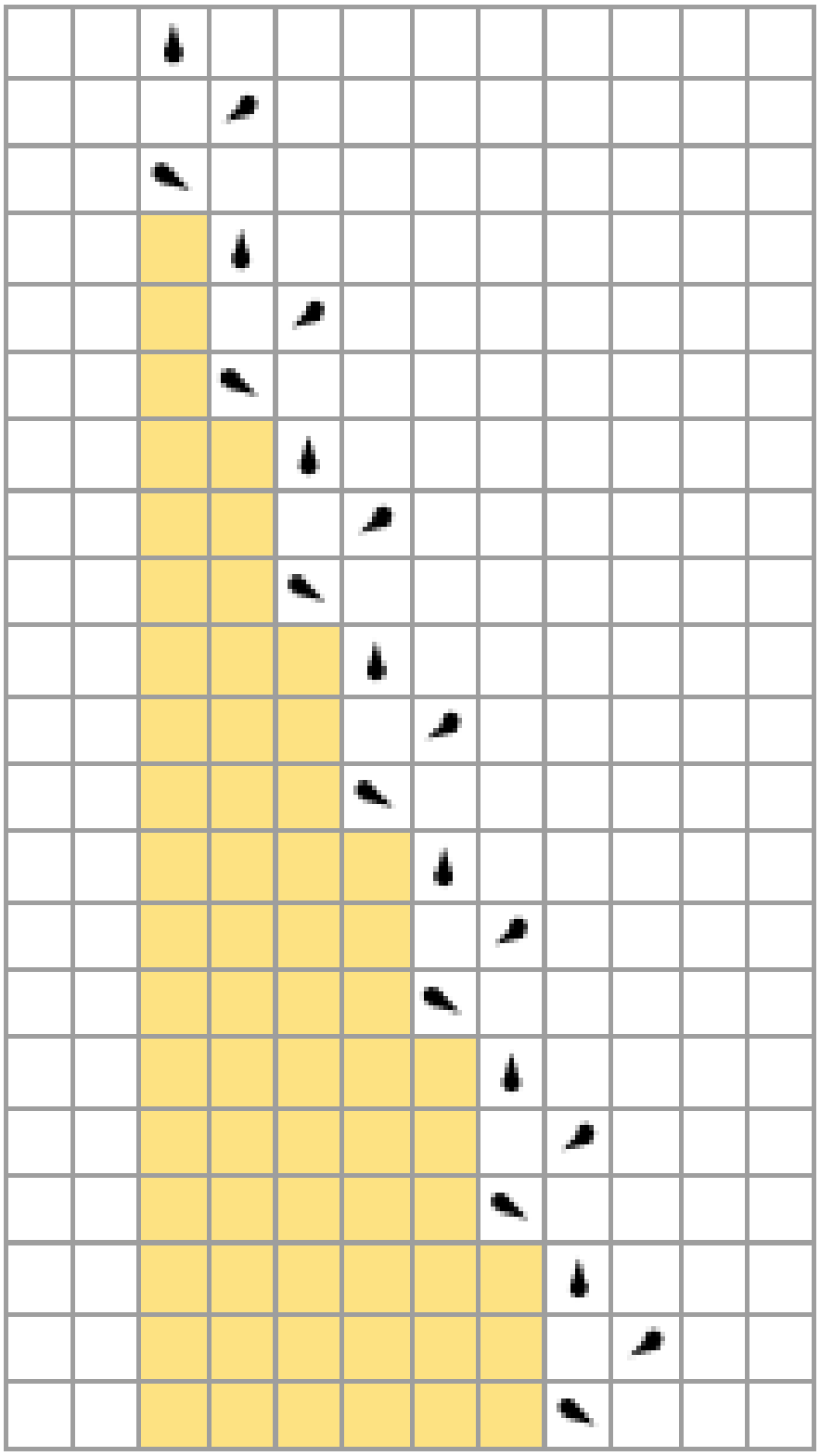

(Ic0b)

 doi:10.20944/preprints202403.0518.v1

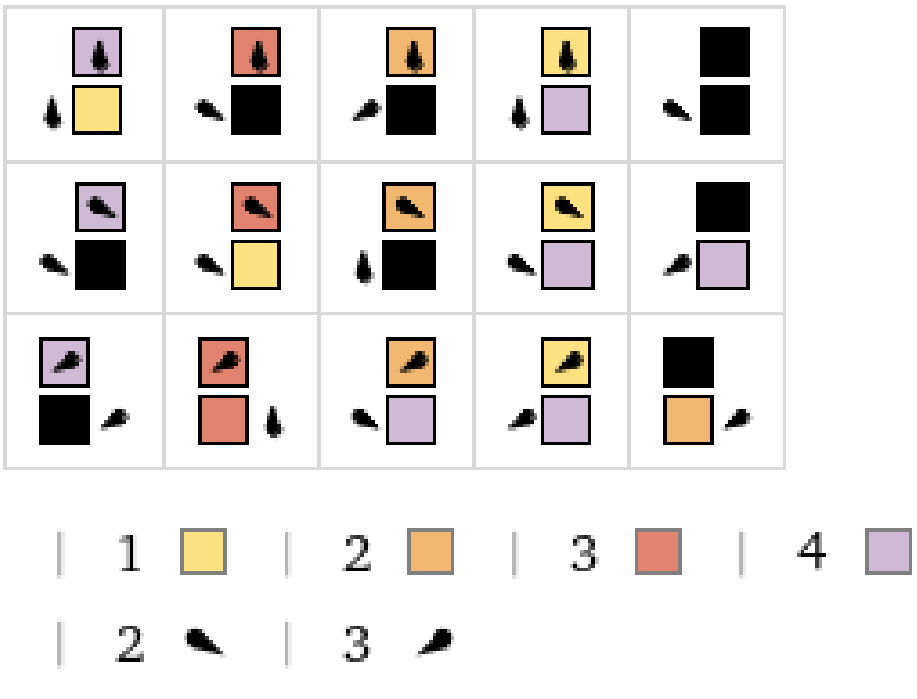

(Ic0c)

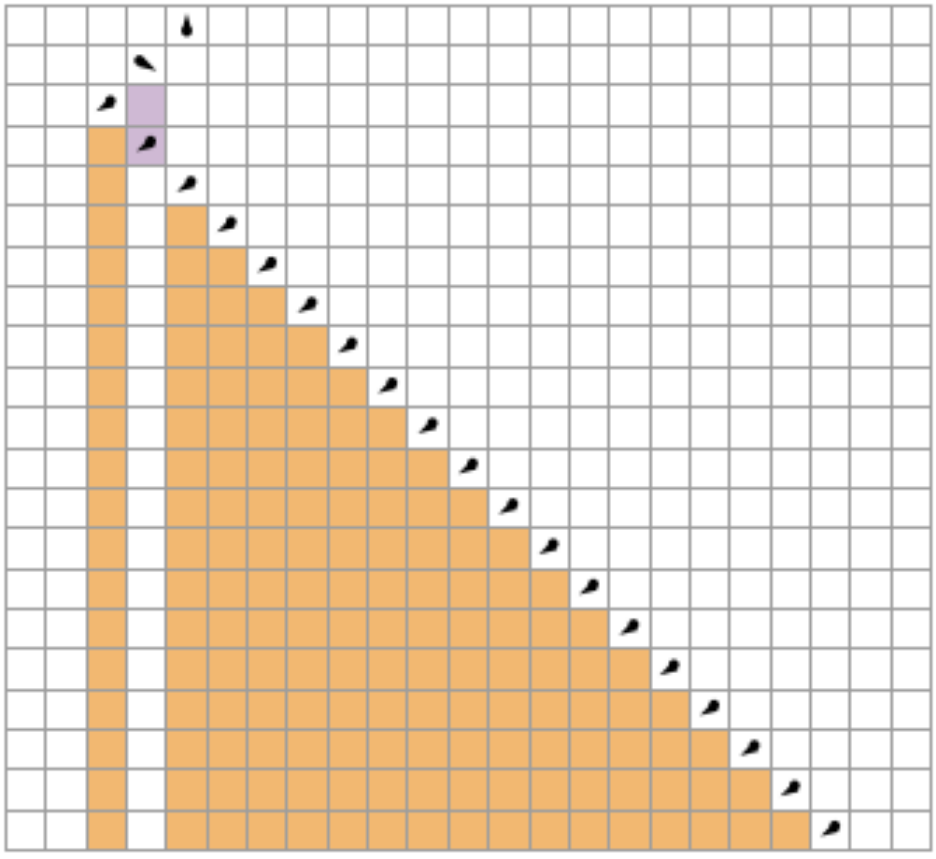

(Ic0d)

 doi:10.20944/preprints202403.0518.v1

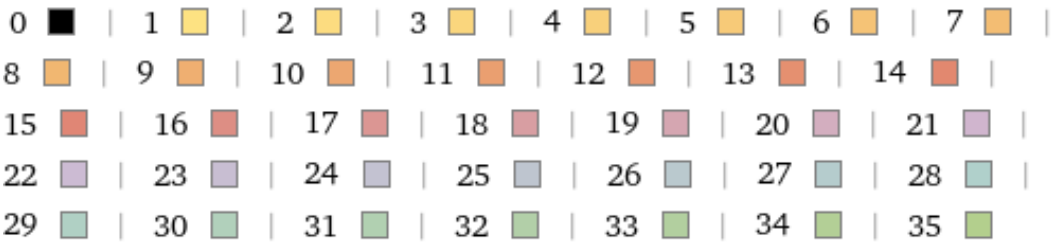

(Ic1a) 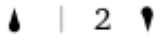

(Ic1b)

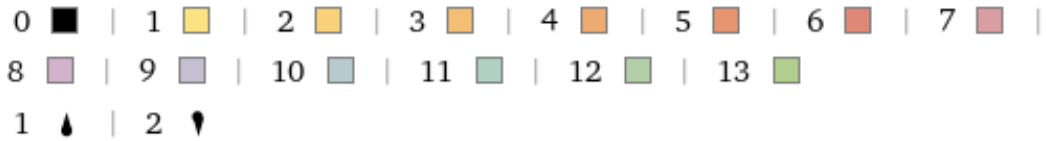

 doi:10.20944/preprints202403.0518.v1

0 | 1 | 2 | 3 | 4 | 5 | 6 | 7 |
8 | 9 | 10 | 11 | 12 | 13 | 14 |
15 | 16 | 17 | 18 | 19 | 20 | 21 |
22 | 23 | 24 | 25 | 26 | 27 | 28 |
29 | 30 | 31 | 32 | 33 | 34 | 35 |
36 | 37 | 38 | 39 |

(Ic1c) 1 | 2

 doi:10.20944/preprints202403.0518.v1

Iconic1. Avogadro's Number LaguerreL, Hypergeometric2F1, and ChebyshevT Potentizations (Ic0a) for Avogadro's Number LaguerreL, Hypergeometric2F1, and ChebyshevT Turing Machine Steps and Quantum Entropy Negativity Translations (Ic0b). Avogadro's Number ChebyshevT and Hypergeometric2F1 Turing Machine Steps for Quantum Entropy Negativity Translations (Ic0c) including Avogadro's Number ChebyshevT and Hypergeometric2F1 Potentizations (Ic0c). Avogadro's Number SphericalHarmonicY (Ic1a), ChebyshevT (Ic1b), and LegendreP (Ic1c) Potentizations. (Ic1d) Avogadro's Number Hypergeometric2F1, ChebyshevT, LegendreP, ChebyshevU, HermiteH, JacobiP, ZernikeR, and ChebyshevT Potentizations.

 doi:10.20944/preprints202403.0518.v1

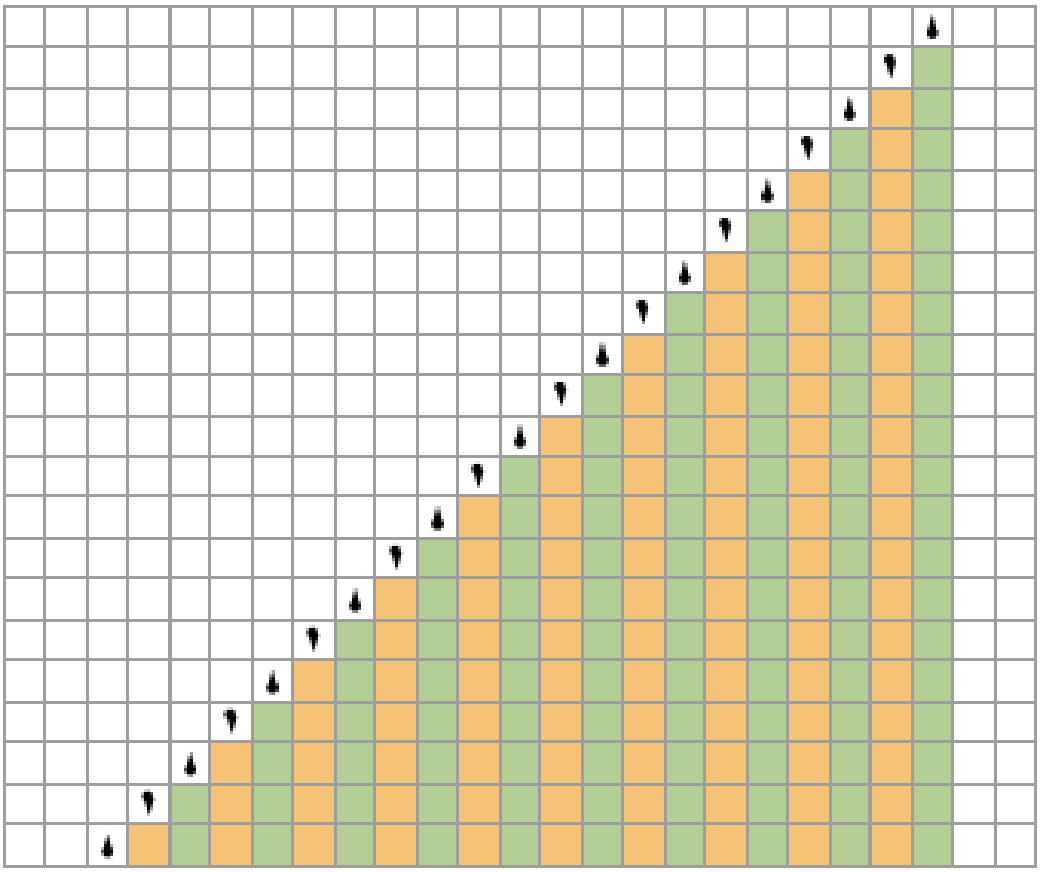

(Ic2a)

 doi:10.20944/preprints202403.0518.v1

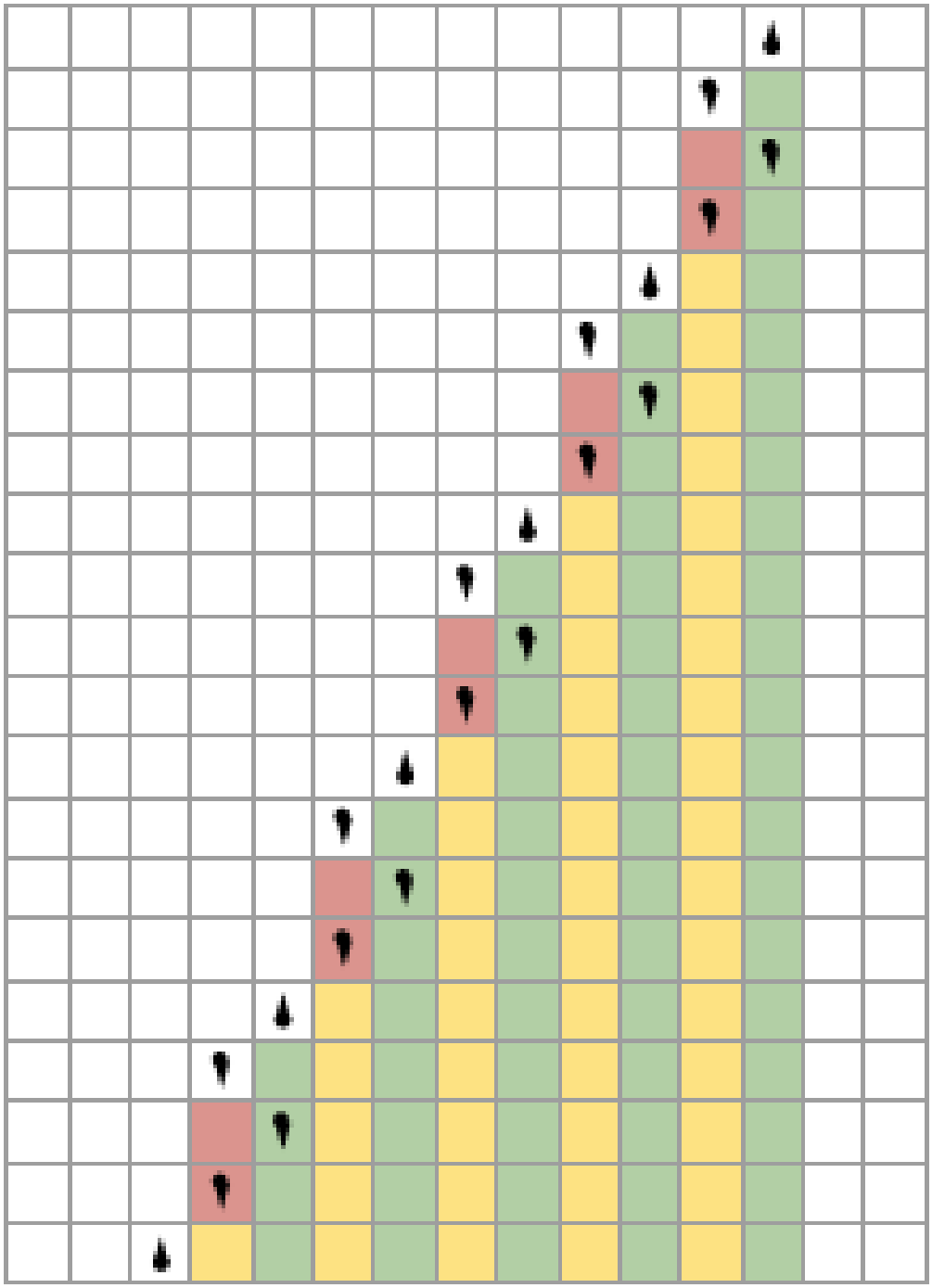

(Ic2b)

 doi:10.20944/preprints202403.0518.v1

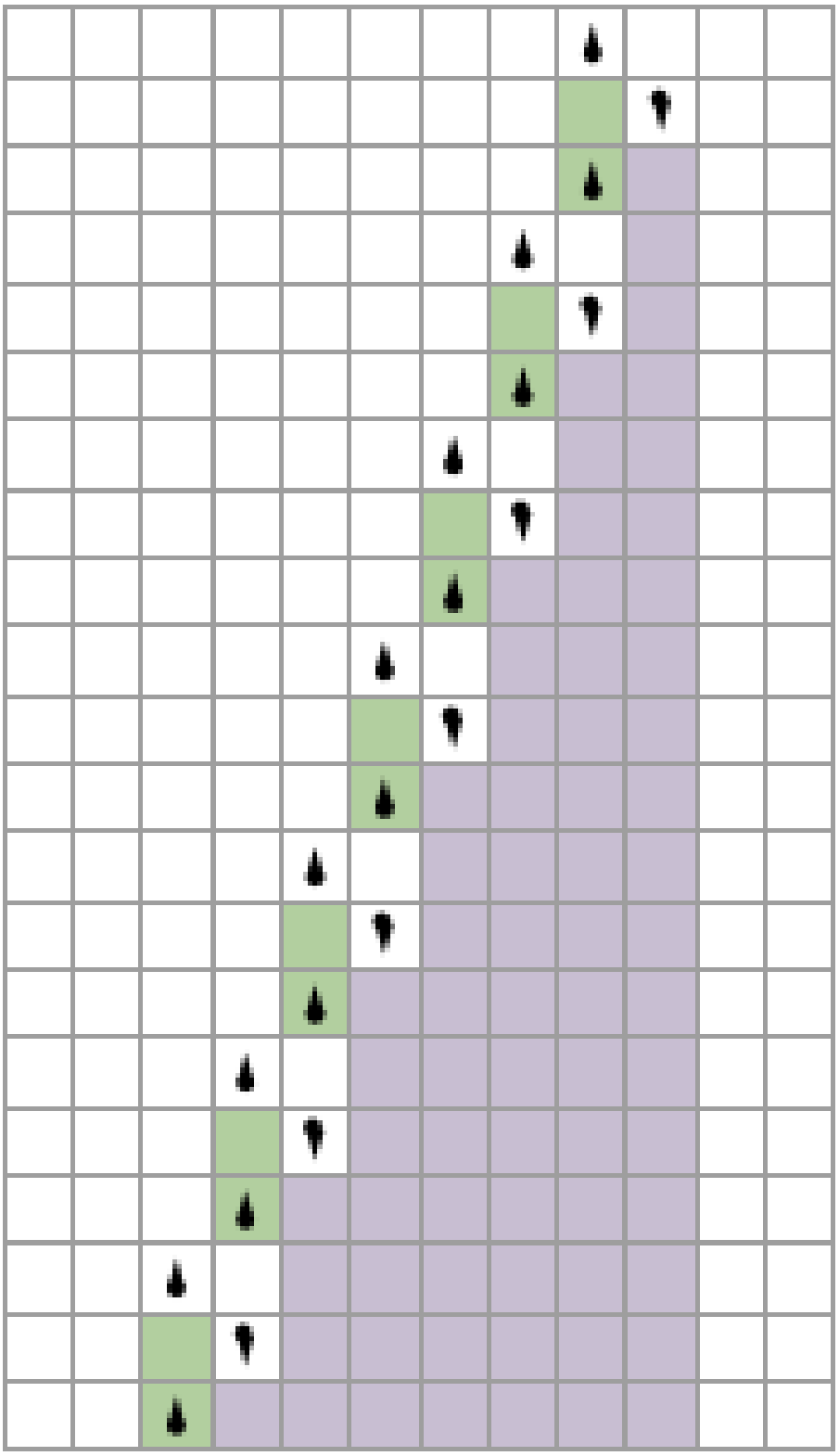

(Ic2c)

 doi:10.20944/preprints202403.0518.v1

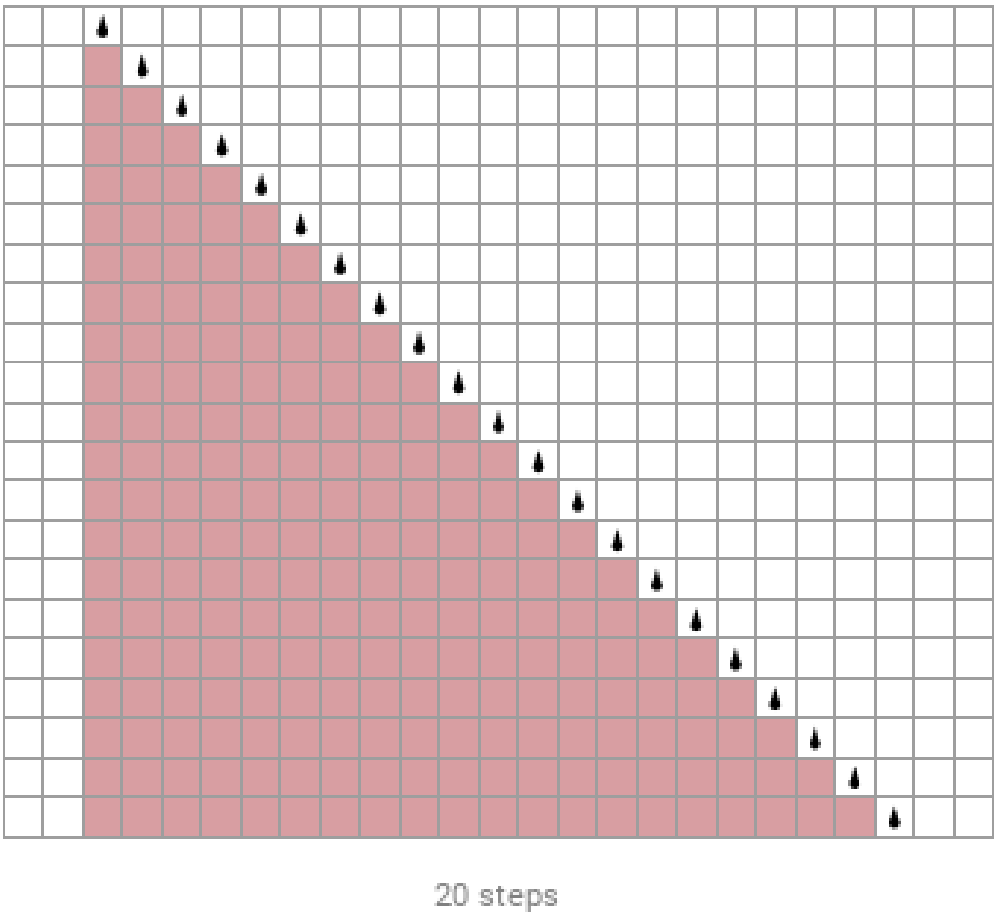

(Ic2d)

Preprints.org (www.preprints.org) | NOT PEER-REVIEWED | Posted: 11 March 2024 doi:10.20944/preprints202403.0518.v1

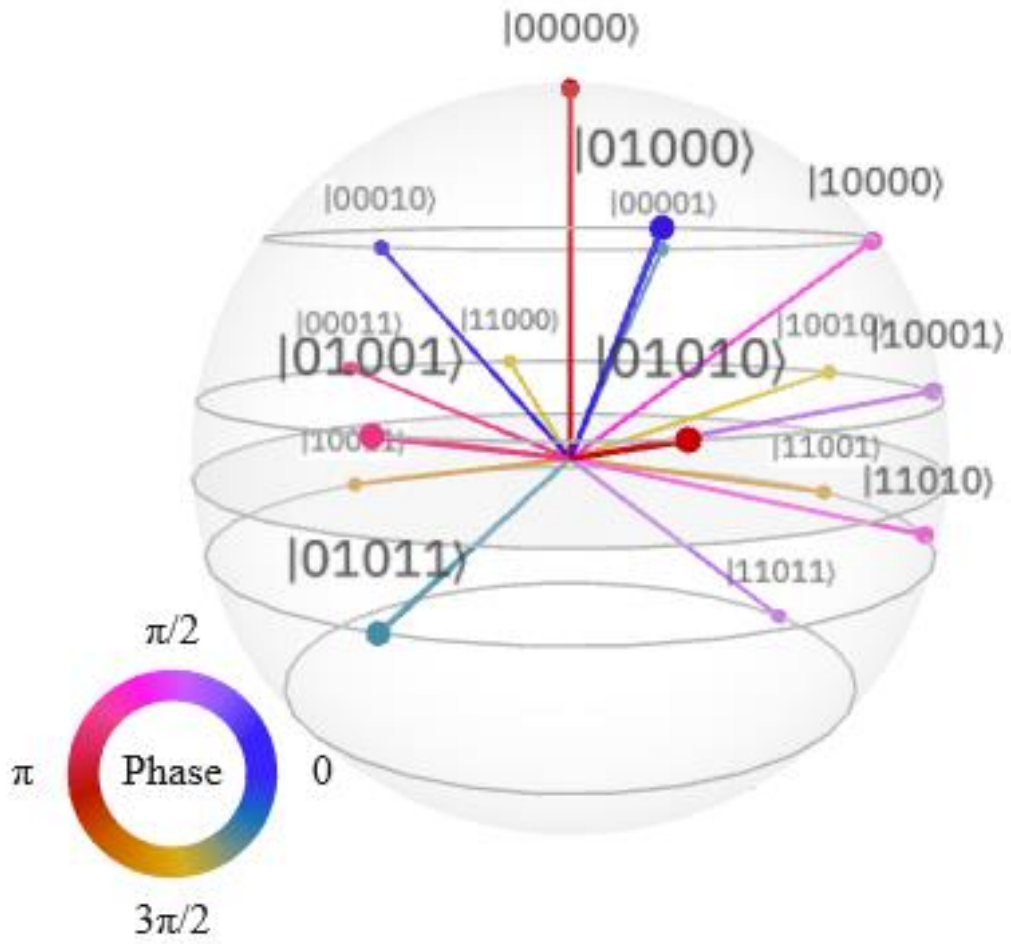

(Ic2e)

Preprints.org (www.preprints.org) | NOT PEER-REVIEWED | Posted: 11 March 2024 doi:10.20944/preprints202403.0518.v1

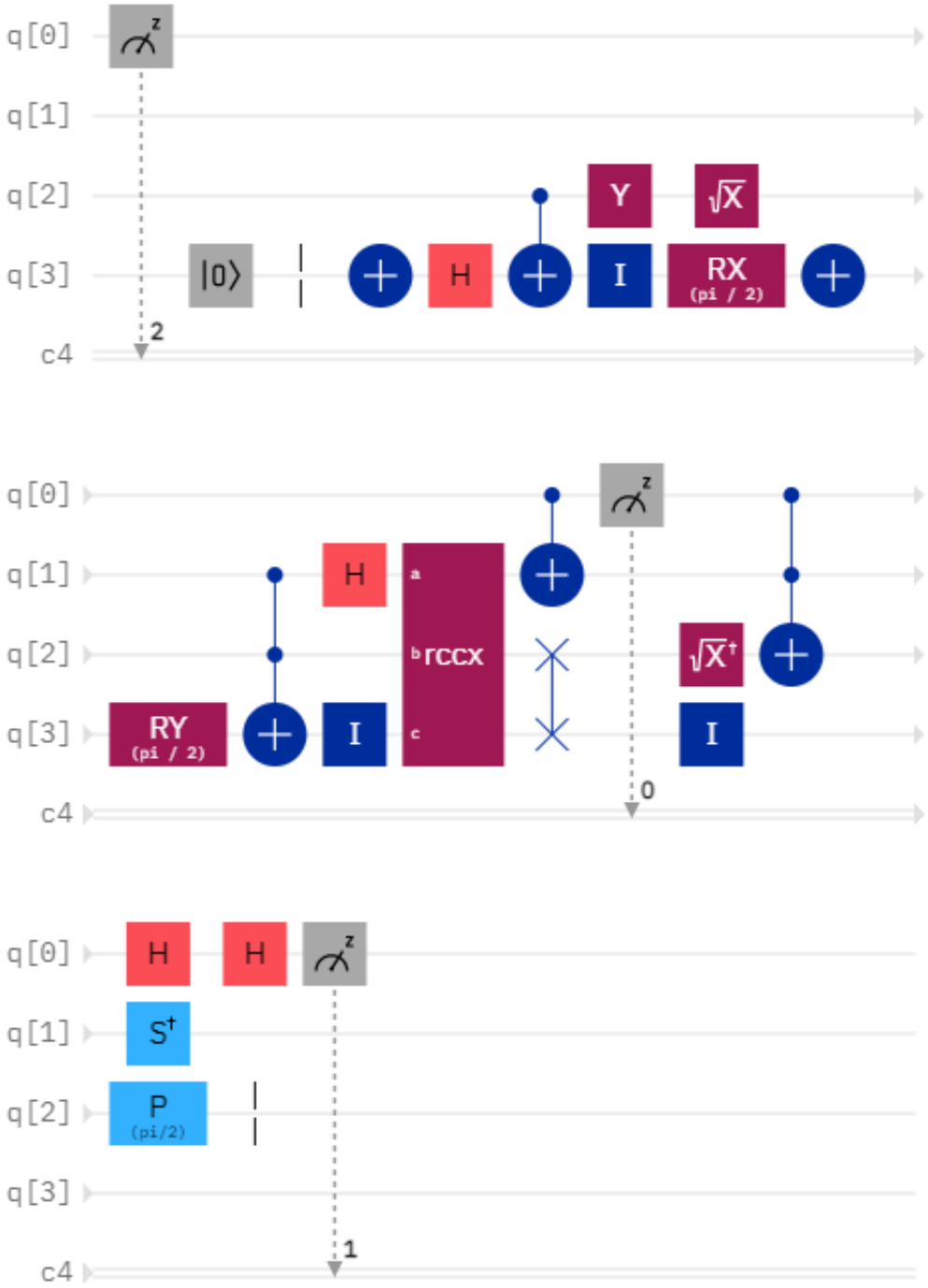

(Ic2f)

 doi:10.20944/preprints202403.0518.v1

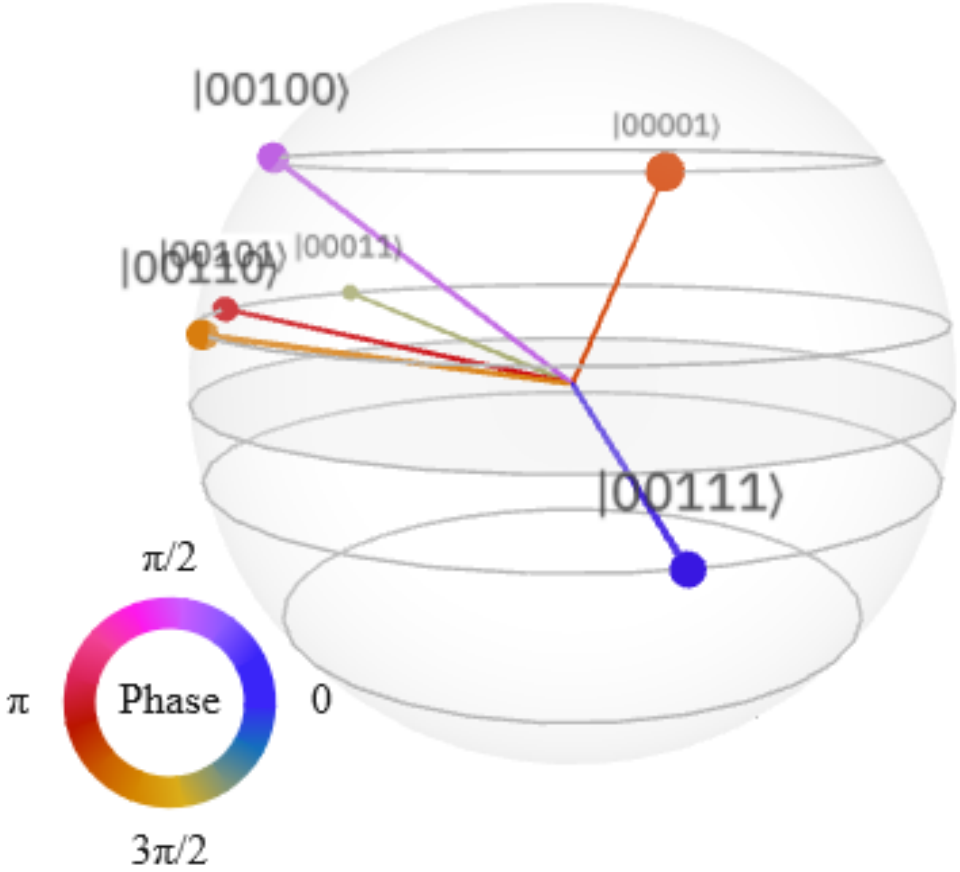

(Ic2g)

Preprints.org (www.preprints.org) | NOT PEER-REVIEWED | Posted: 11 March 2024 doi:10.20944/preprints202403.0518.v1

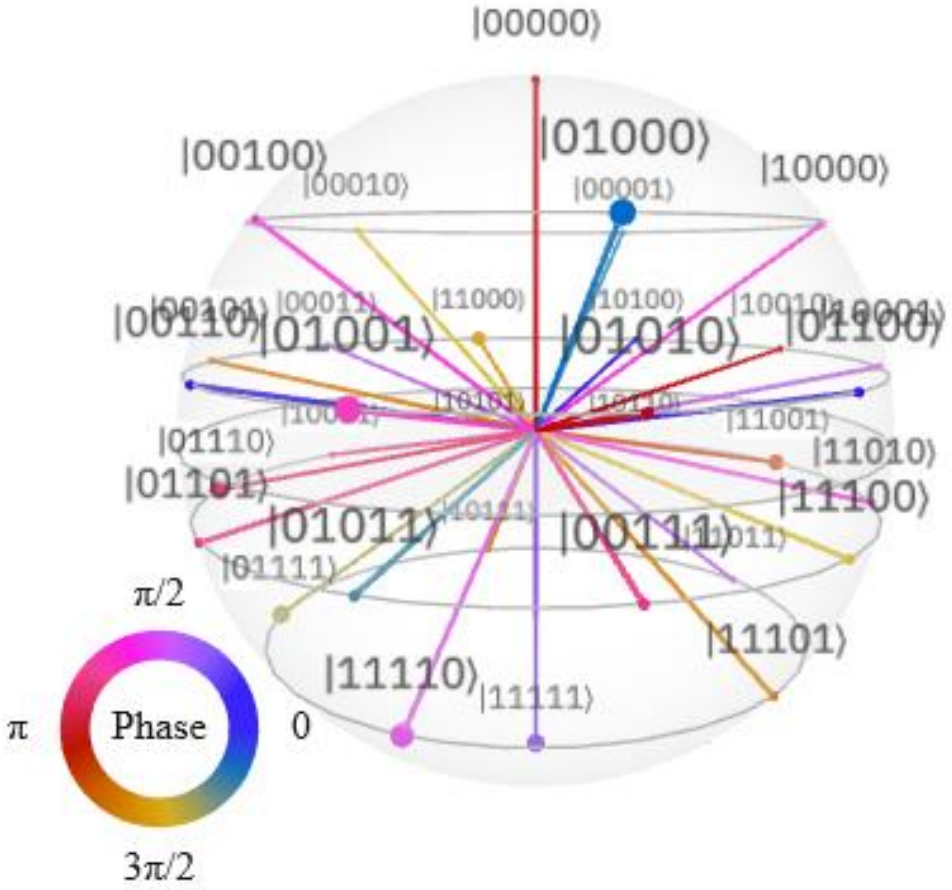

(Ic2h)

 doi:10.20944/preprints202403.0518.v1

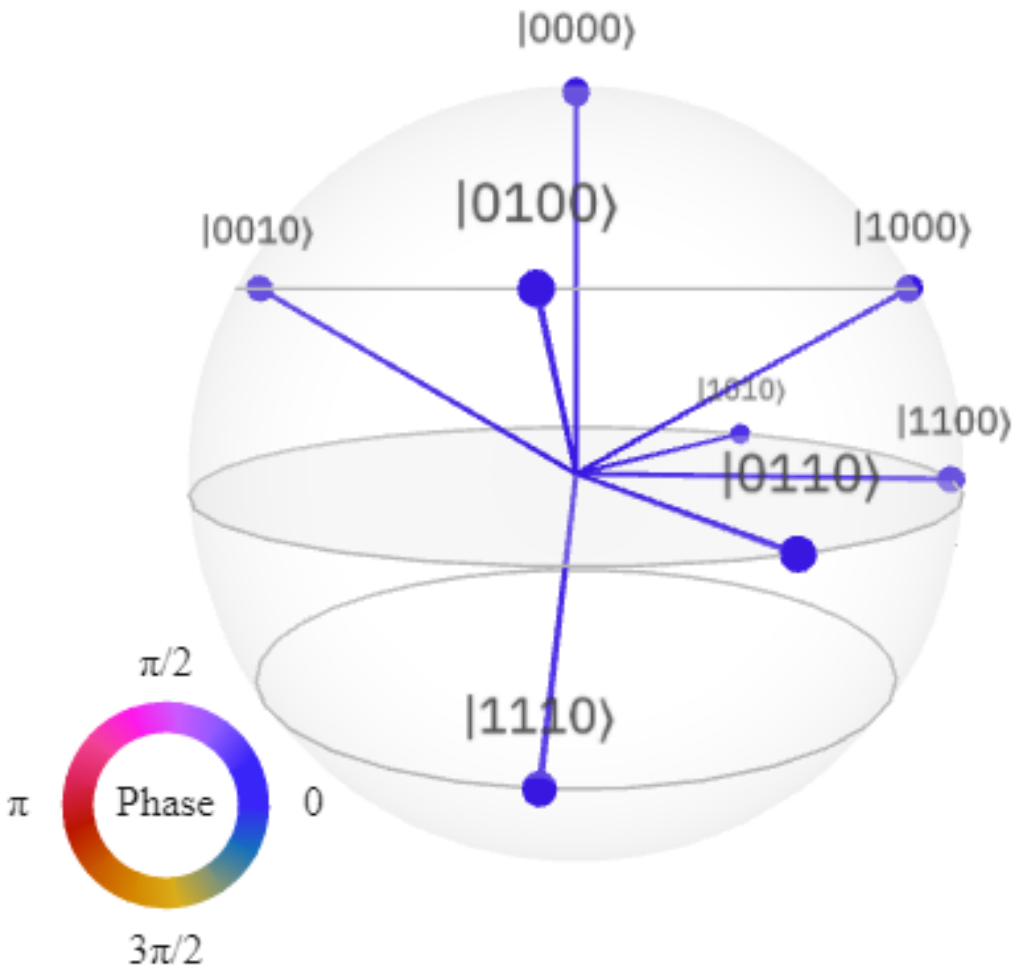

(Ic2i)

 doi:10.20944/preprints202403.0518.v1

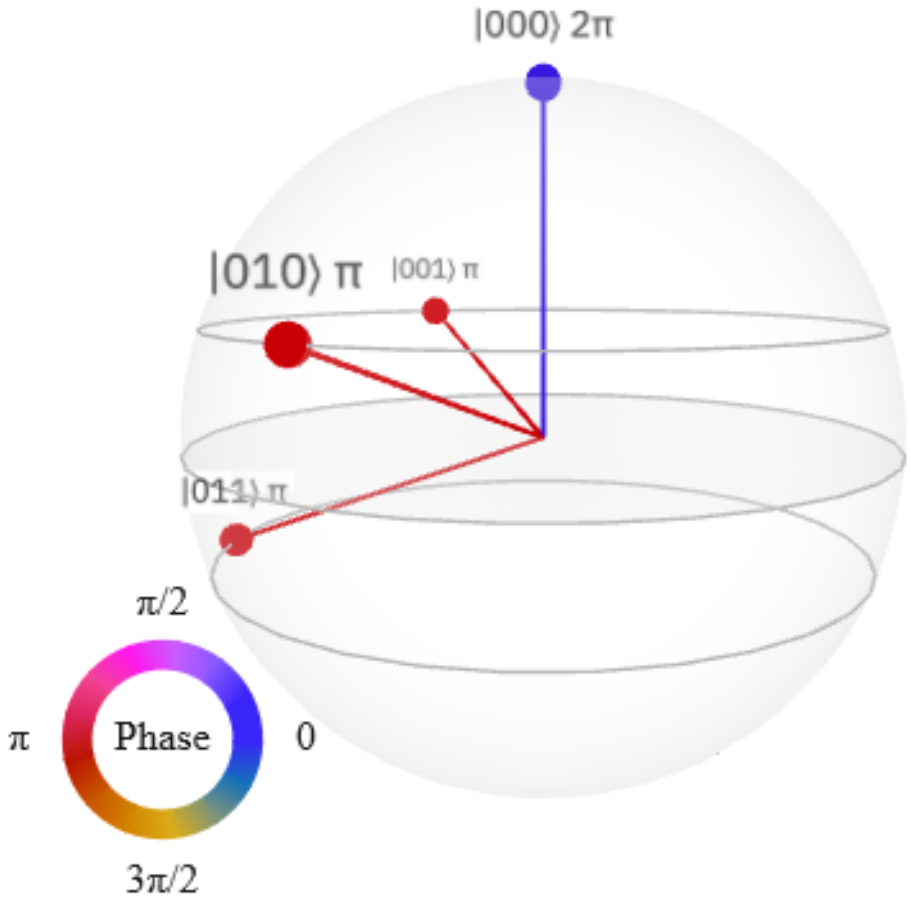

(Ic2j)

 doi:10.20944/preprints202403.0518.v1

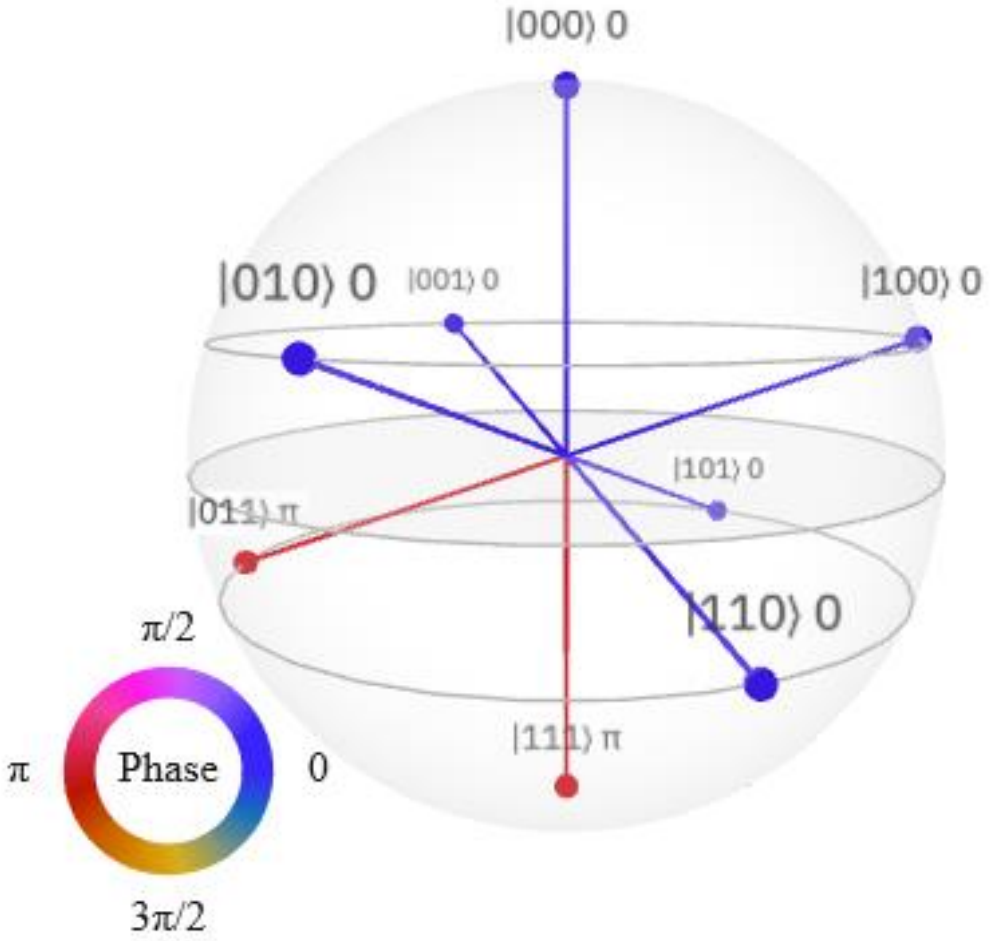

(Ic2k)

Preprints.org (www.preprints.org) | NOT PEER-REVIEWED | Posted: 11 March 2024 doi:10.20944/preprints202403.0518.v1

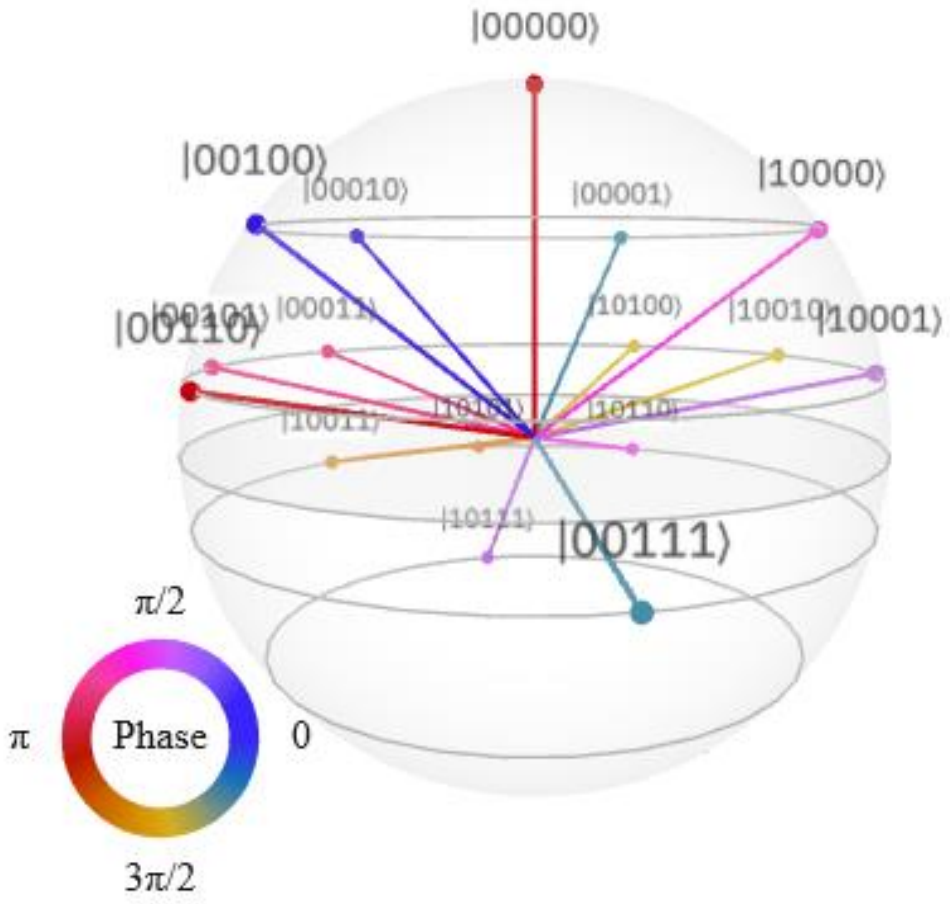

(Ic2l)

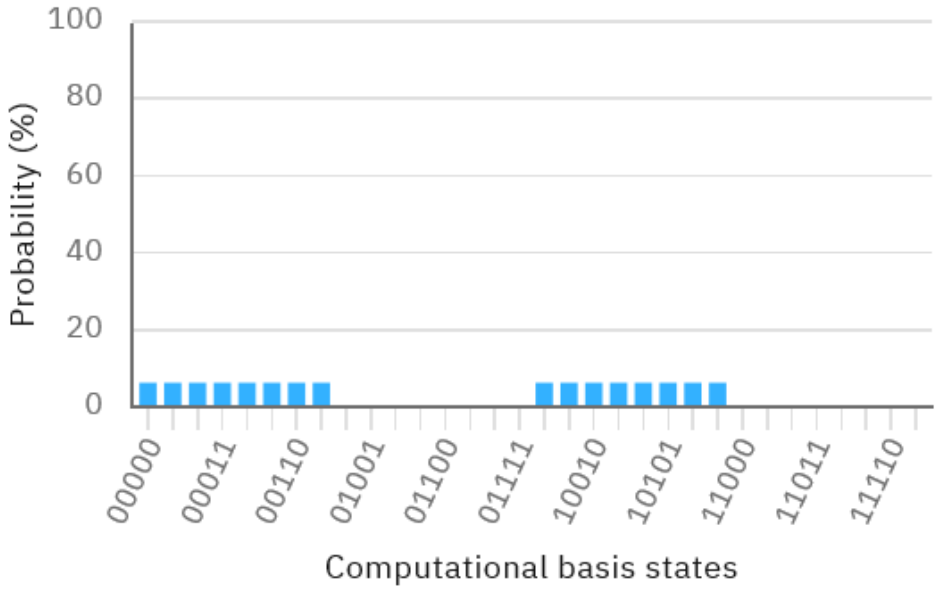

(Ic2m)

Preprints.org (www.preprints.org) | NOT PEER-REVIEWED | Posted: 11 March 2024 doi:10.20944/preprints202403.0518.v1

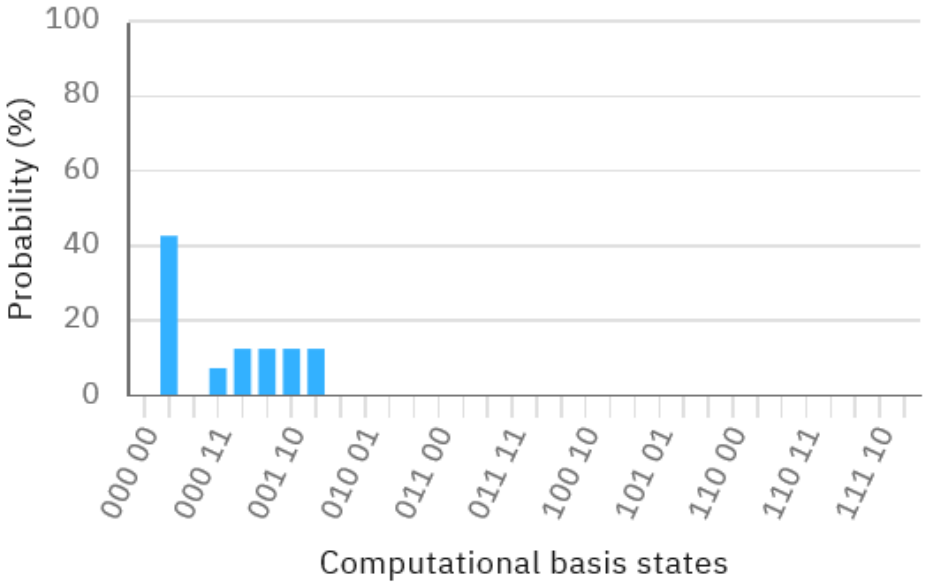

(Ic2n)

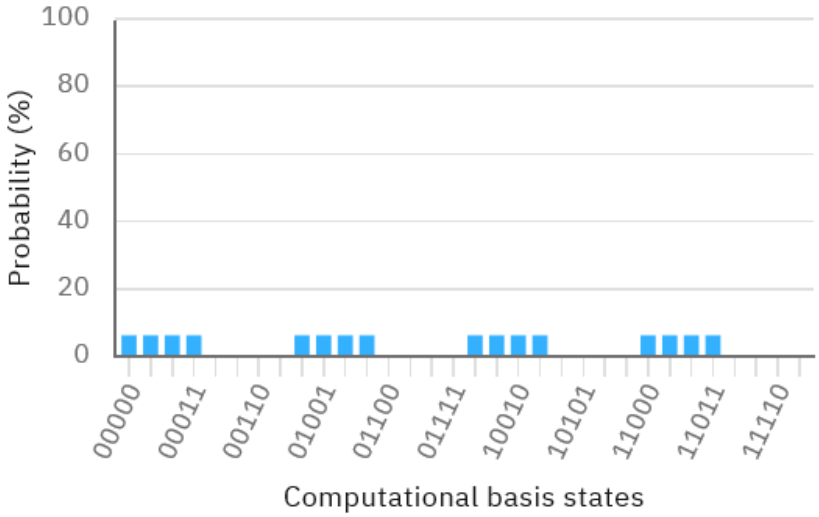

(Ic2o)

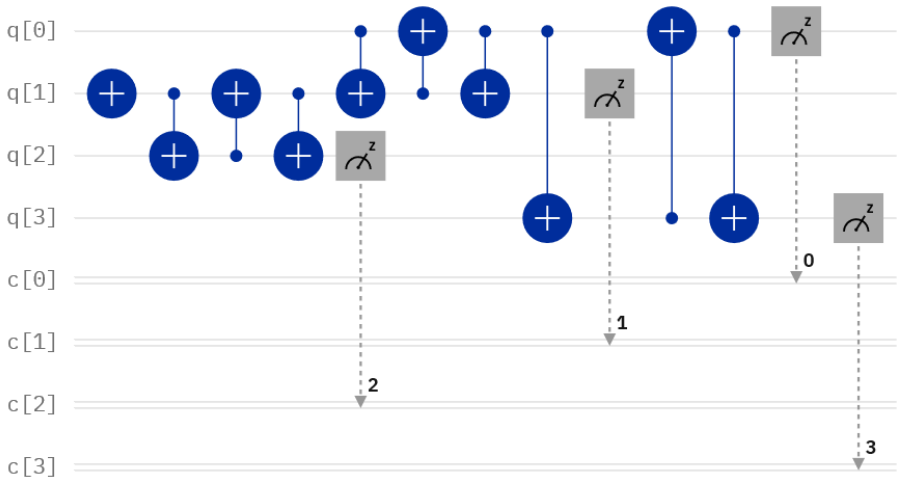

(Ic2p)

 doi:10.20944/preprints202403.0518.v1

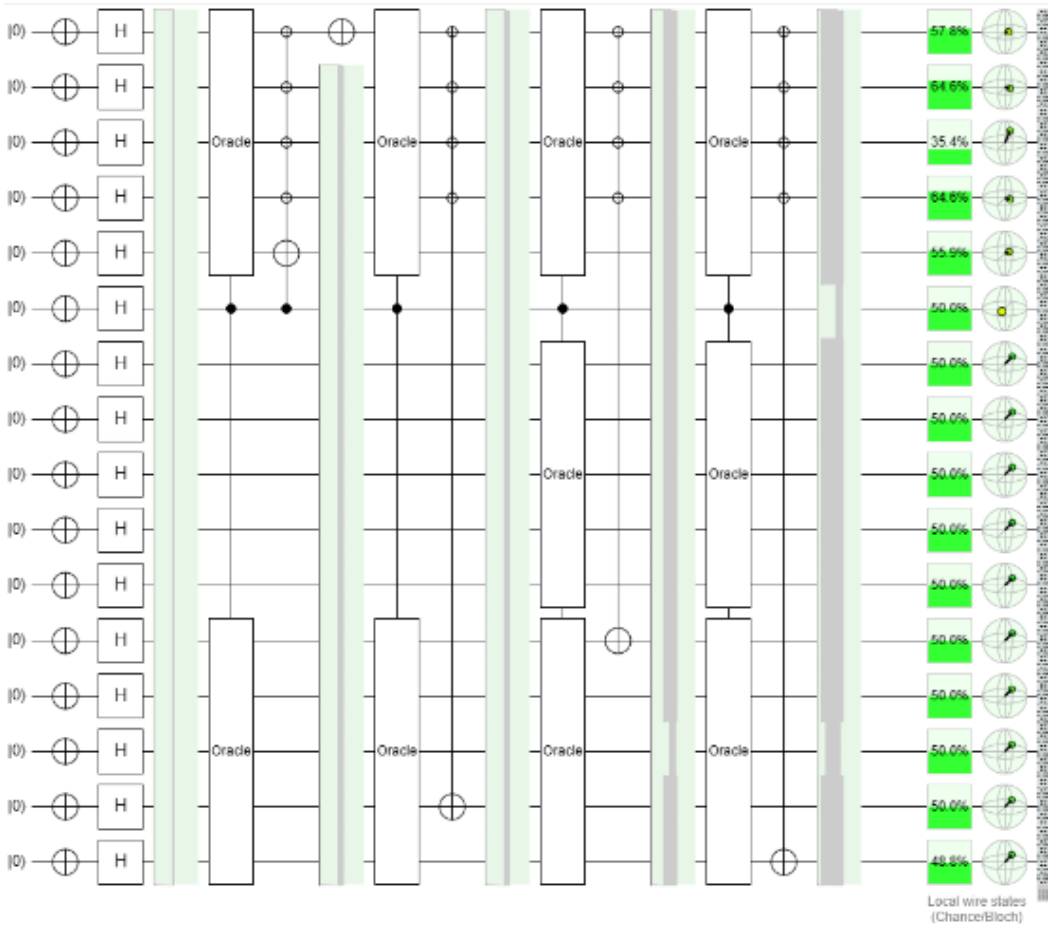

(Ic2q)

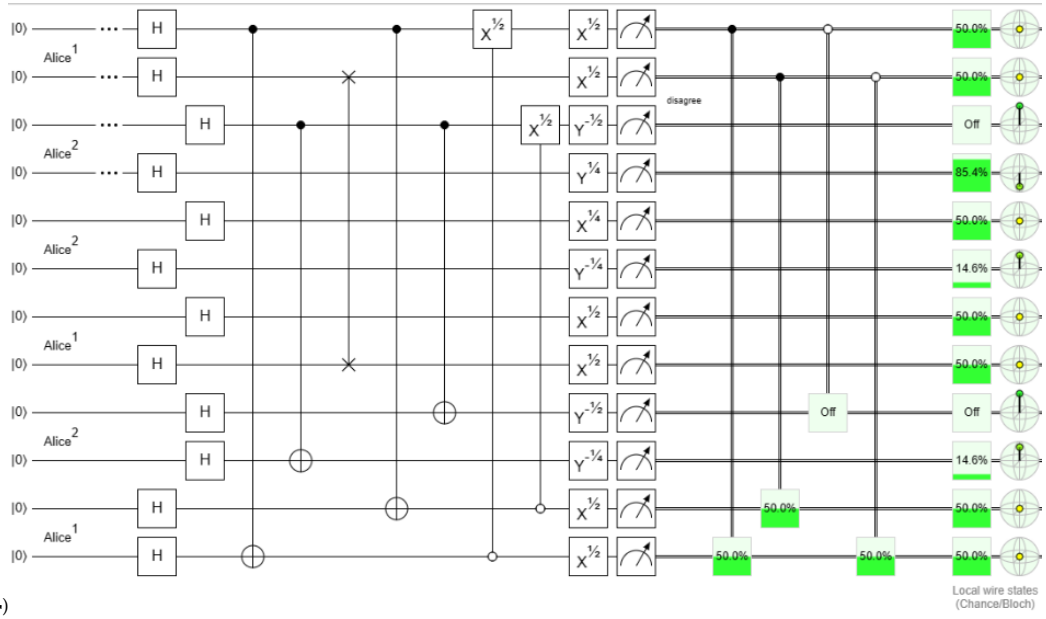

(Ic2r)

Iconic2. Avogadro's Number (Ic2a) SphericalHarmonicY, (Ic2b) ChebyshevT, and (Ic2c) LegendreP Turing Machine Steps for Quantum Entropy Negativity Translations. Avogadro 's number Hypergeometric2F1Regularized ChebyshevU, ChebyshevT, SphericalHarmonicY, LegendreP, and WhittakerM Turing Machine Steps for Quantum Entropy Negativity Translations. (Ic2e,f,g,h,g,k,l,m,o,p,q,r) Quantum Circuit Generative Models of various number of qubits and Grover Quantum Circuit layers for the Roccustyrna peptidemimetic Small Molecule Drug Discoveries.

 doi:10.20944/preprints202403.0518.v1

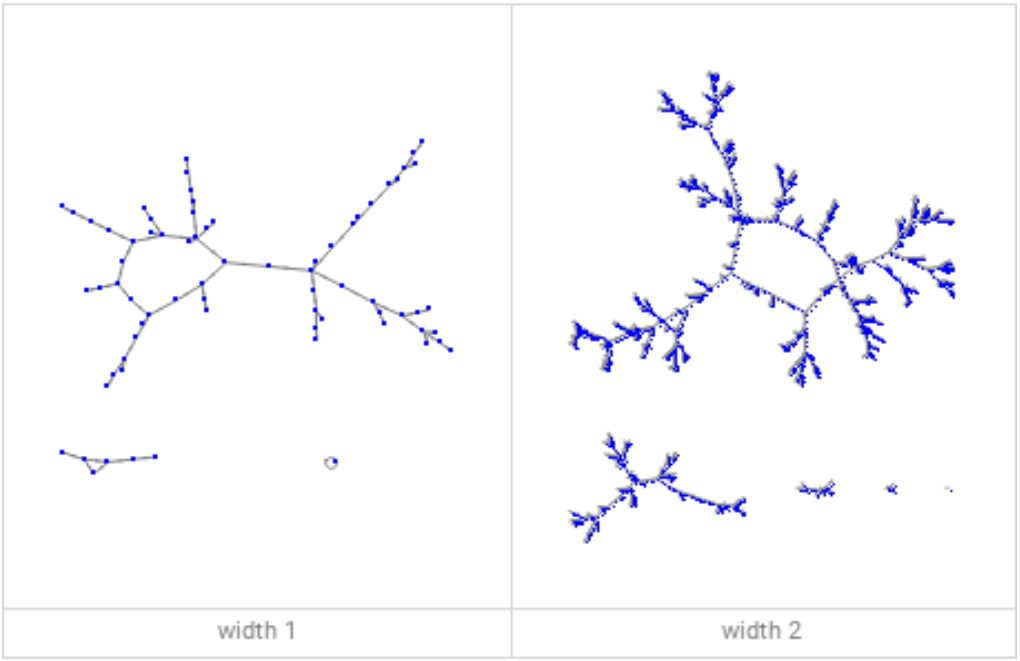

(Ic3a1) (evolution of all possible cyclic initial states)

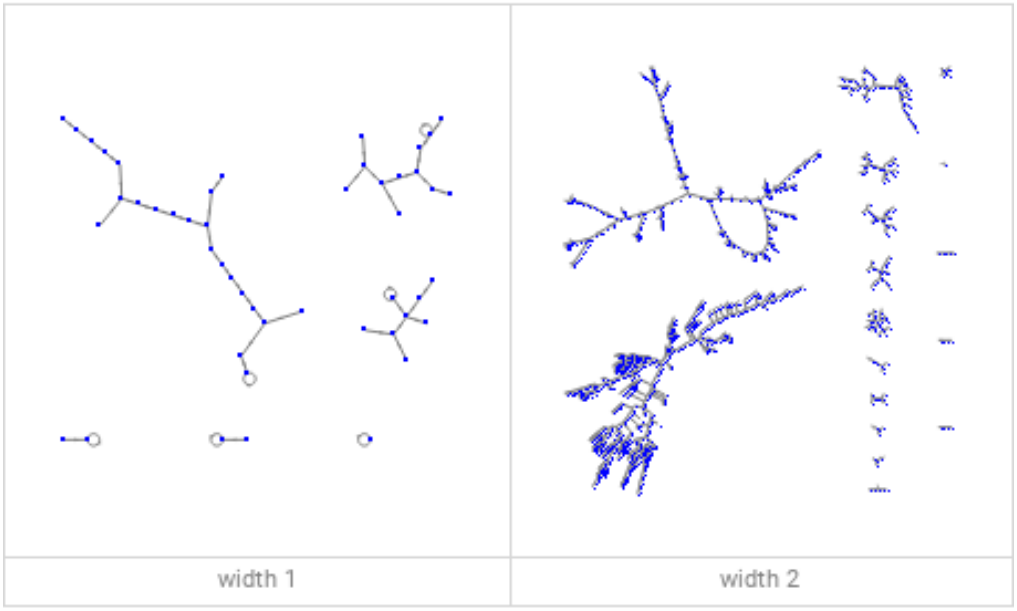

(Ic3a2) (evolution of all possible cyclic initial states)

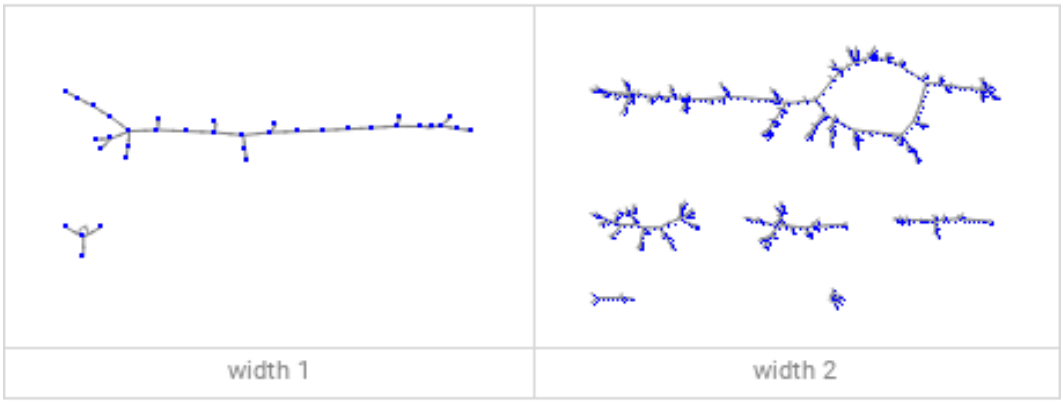

(Ic3b1) (evolution of all possible cyclic initial states)

Preprints.org (www.preprints.org) | NOT PEER-REVIEWED | Posted: 11 March 2024 doi:10.20944/preprints202403.0518.v1

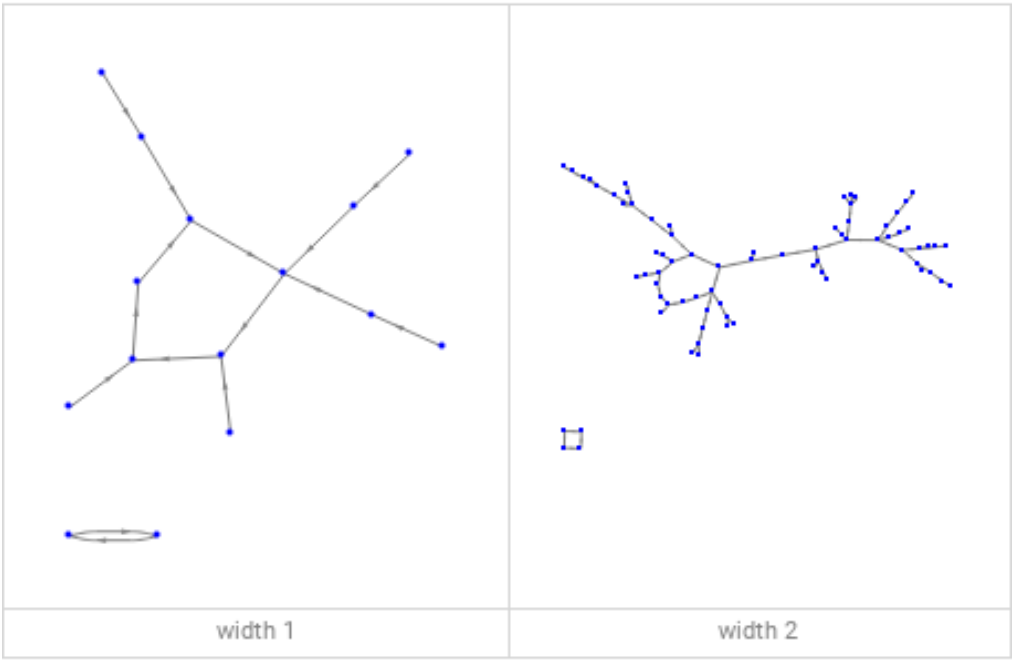

(Ic2b2) (evolution of all possible cyclic initial states)

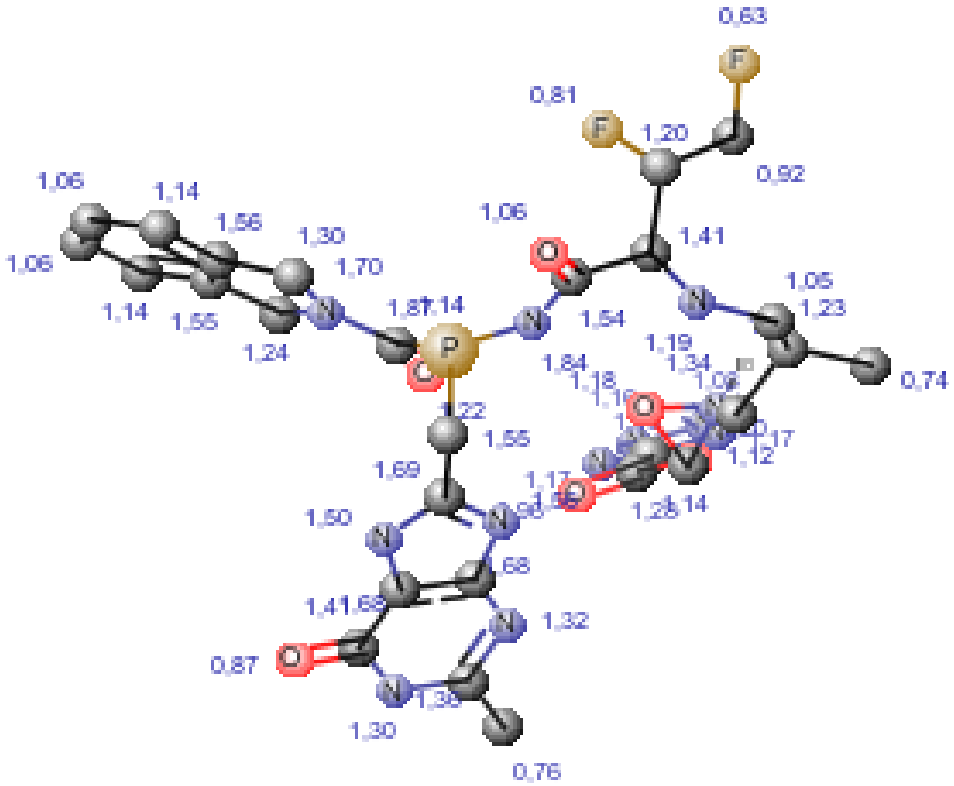

(Ic3c)

Preprints.org (www.preprints.org) | NOT PEER-REVIEWED | Posted: 11 March 2024 doi:10.20944/preprints202403.0518.v1

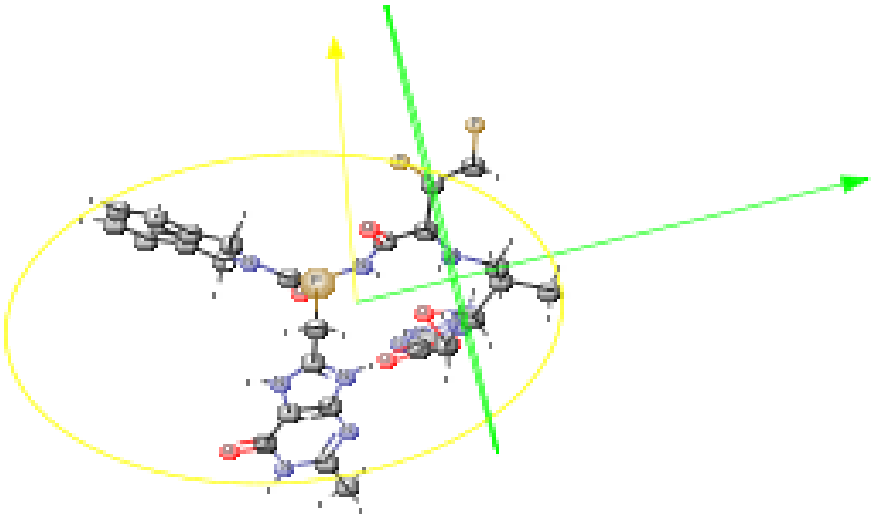

(Ic3d)

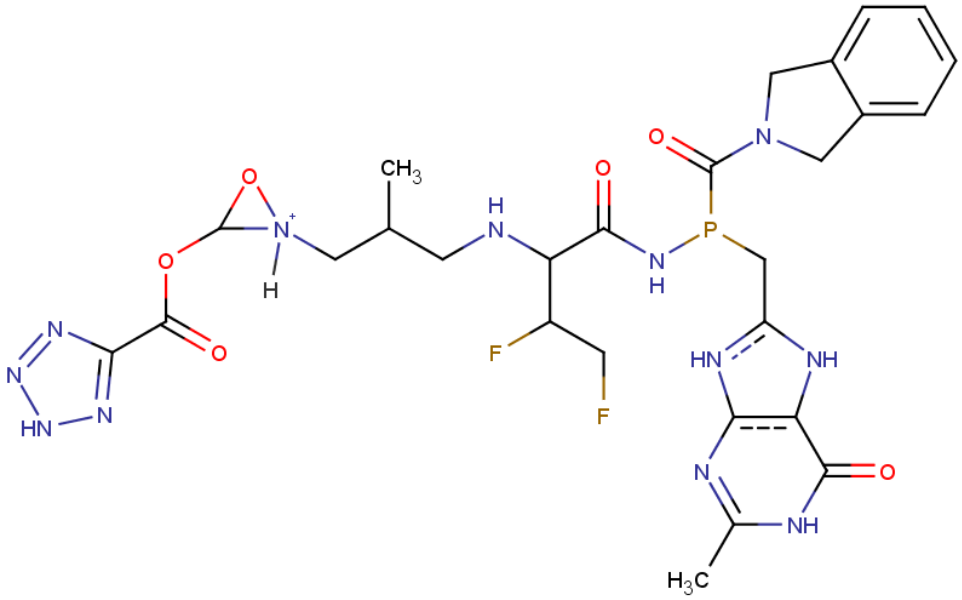

(Ic3e)

 doi:10.20944/preprints202403.0518.v1

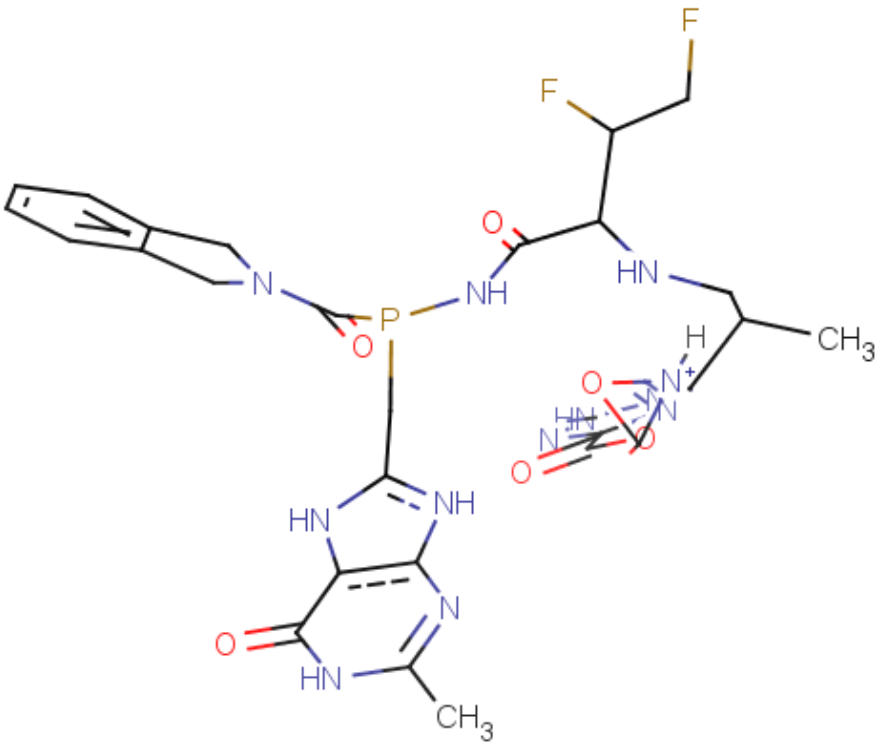

(Ic3f)

 doi:10.20944/preprints202403.0518.v1

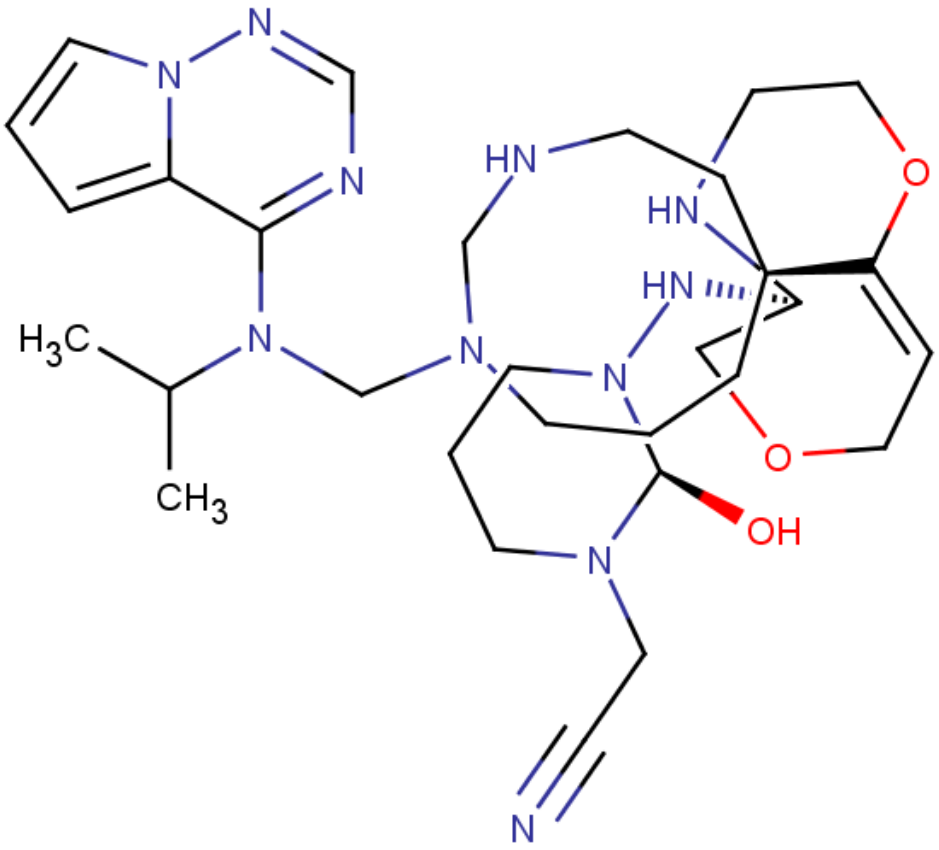

(Ic3g)

 doi:10.20944/preprints202403.0518.v1

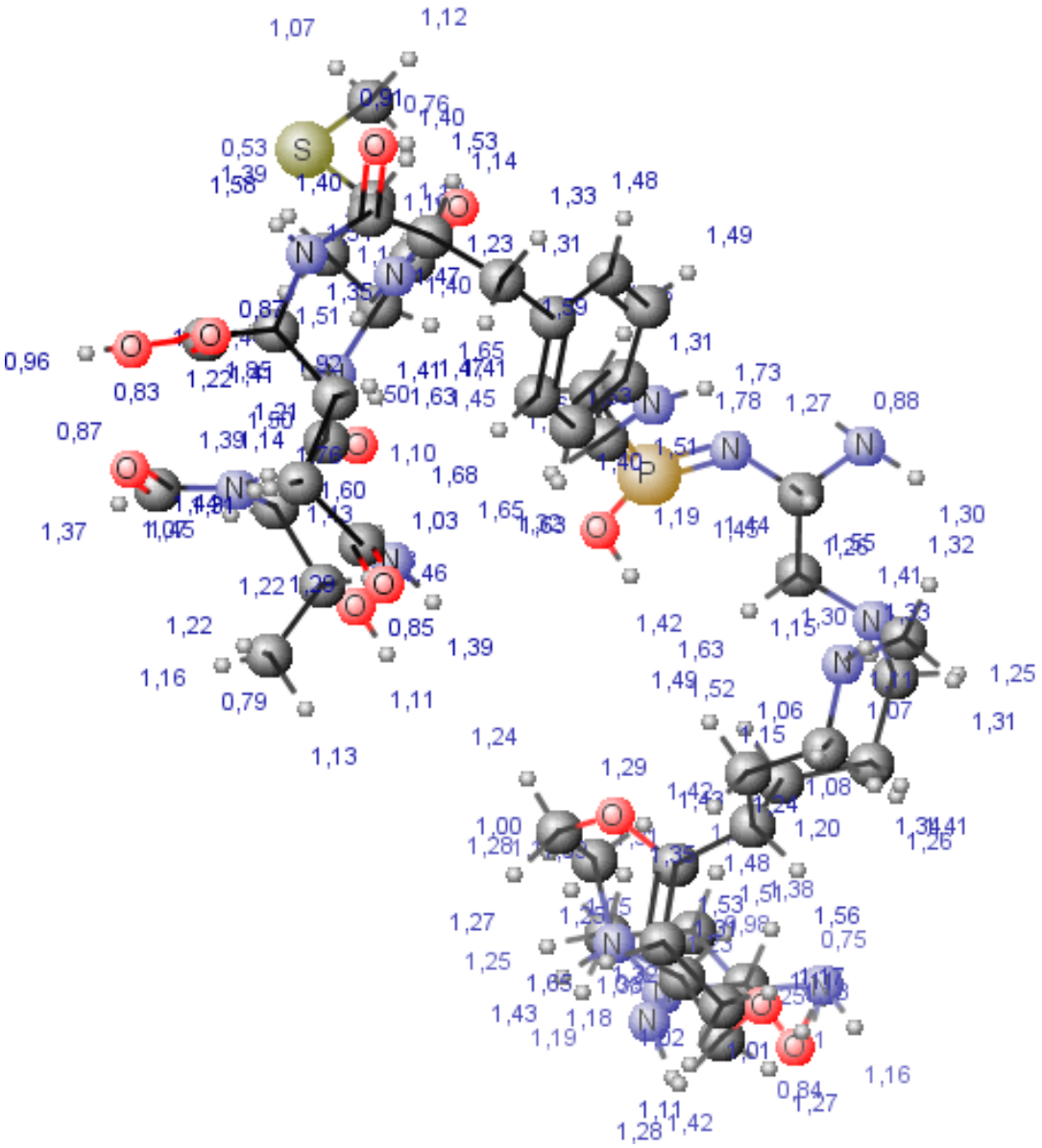

(Ic3h)

 doi:10.20944/preprints202403.0518.v1

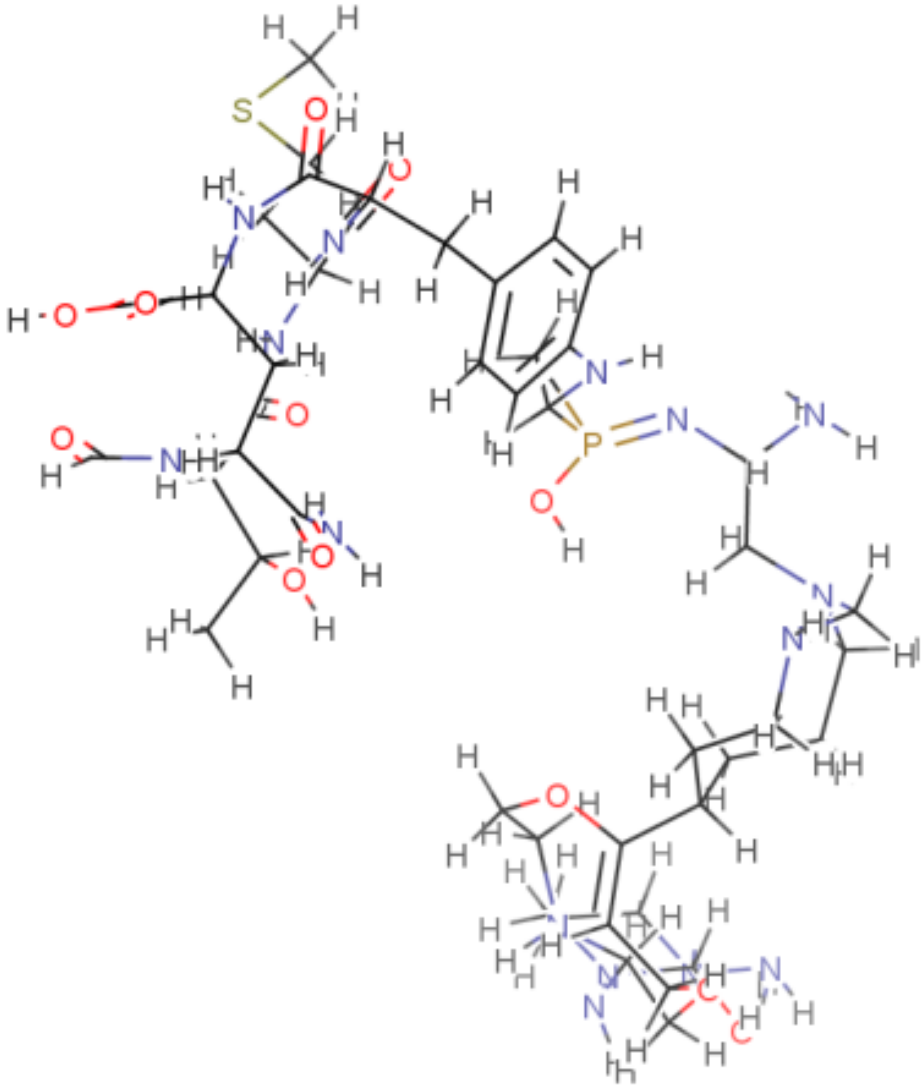

(Ic3i)

 doi:10.20944/preprints202403.0518.v1

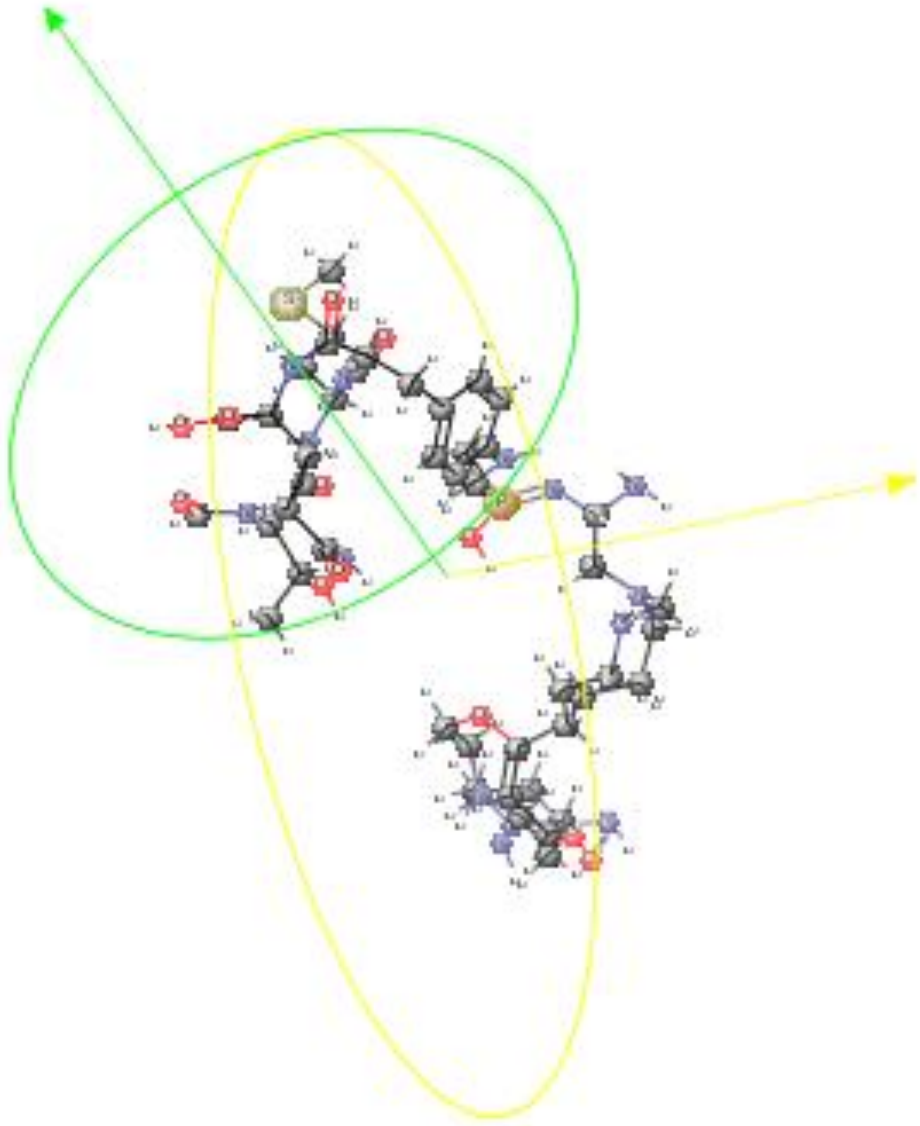

(Ic3j)

 doi:10.20944/preprints202403.0518.v1

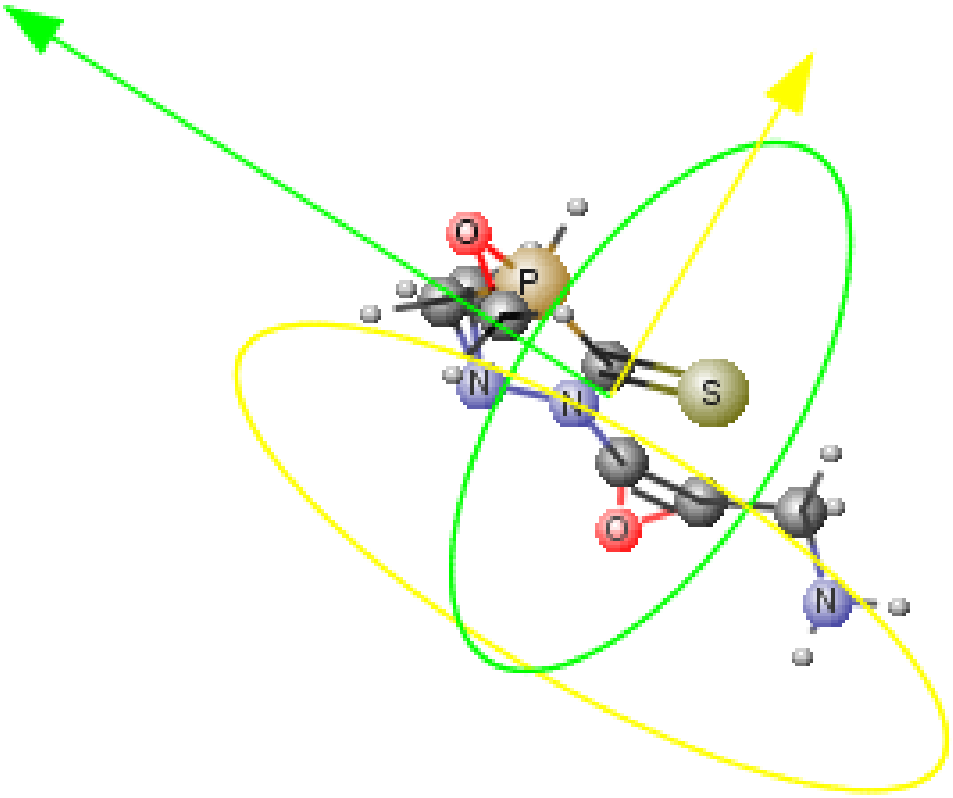

(Ic3k)

Iconic3. Graph Similarities between Avogadro's Number SphericalHarmonicY, ChebyshevT, and LegendreP Turing Machine Ruled Generalizations and Fuzzy Sphere-like small molecules (Ic3a1), (Ic3a2), (Ic3b1), (Ic3b2) and geometrical descriptors (Ic3c), (Ic3d), (Ic3d), (Ic3e), (Ic3f), (Ic3g), (Ic3h), (Ic3i), (Ic3j), (Ic3k) of DRVYIHPFX-mimetic4: Dreiding energy = 320,62 kcal/mol MMFF94 energy = 241,58 kcal/mol Minimal projection area = 100,36 Maximal projection area = 160,51 Minimal projection radius = 7,57 Maximal projection radius = 9,08 Length perpendicular to the max area = 10,90 Length perpendicular to the min area = 17,13 van der Waals volume = 556,04.

 doi:10.20944/preprints202403.0518.v1

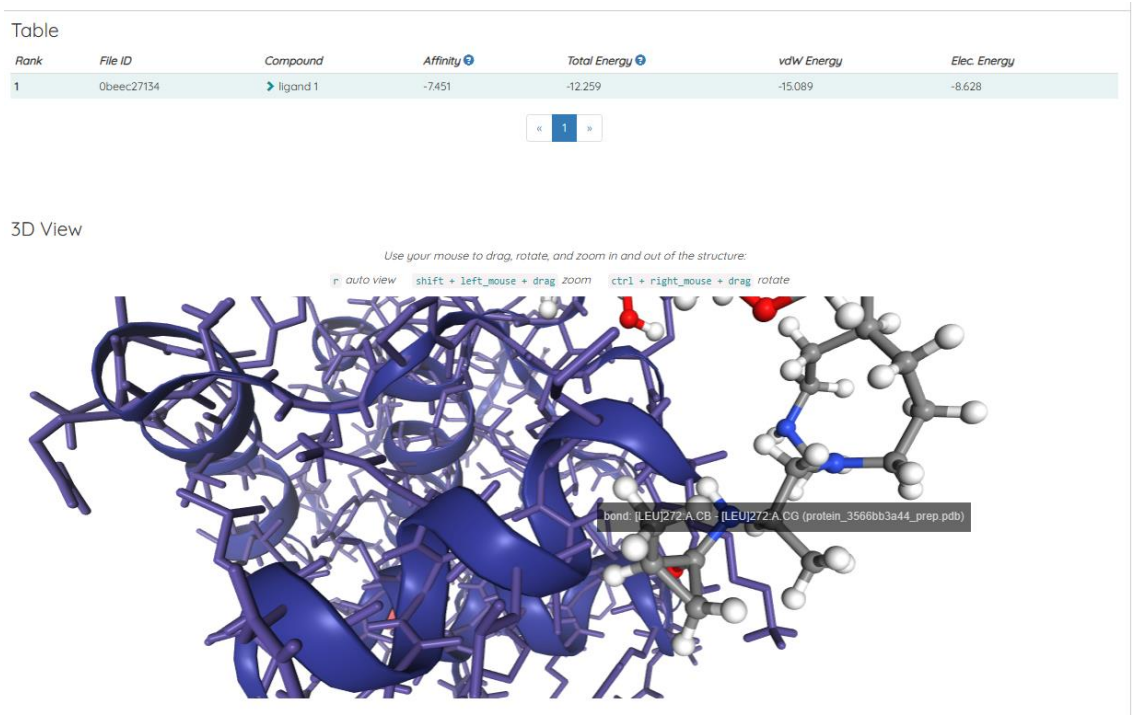

Iconic4. [DockThor] JOB PeptideMimeticIconic1X6wco_653251c21af6b Rank, File ID, Compound, Affinity, Total Energy, vdW Energy, Elec. Energy with 1, 0beec27134 ligand 1, -7.451, -12.259, -15.089, -8.628 scoring values.

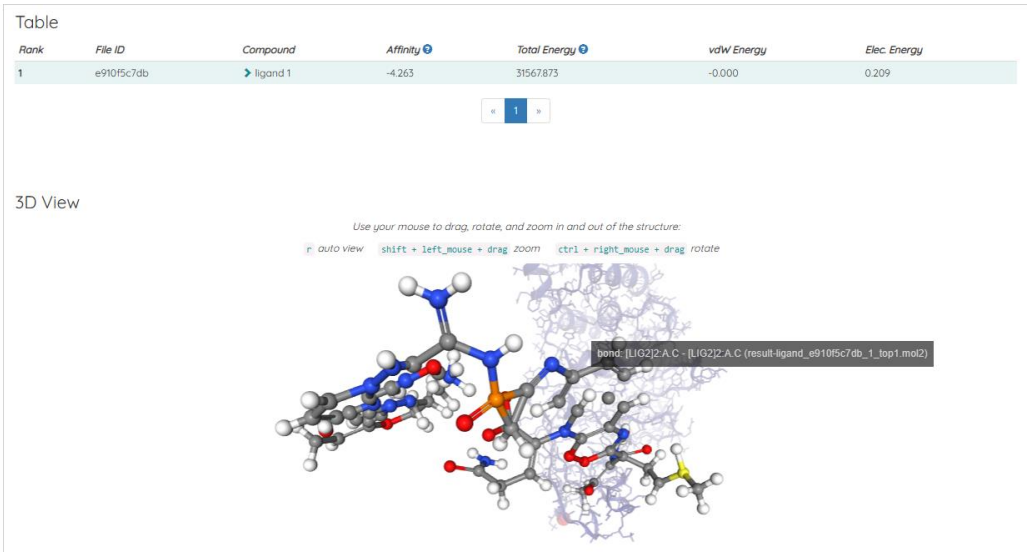

Iconic5. [DockThor] JOB PeptideMimeticIconic36wzu_653252ac8af47 Rank, File ID, Compound, Affinity, Total Energy, vdW Energy, Elec. Energy with 1, e910f5c7db ligand 1, -4.263, 31567.873, -0.000, 0.209 scoring values.

 doi:10.20944/preprints202403.0518.v1

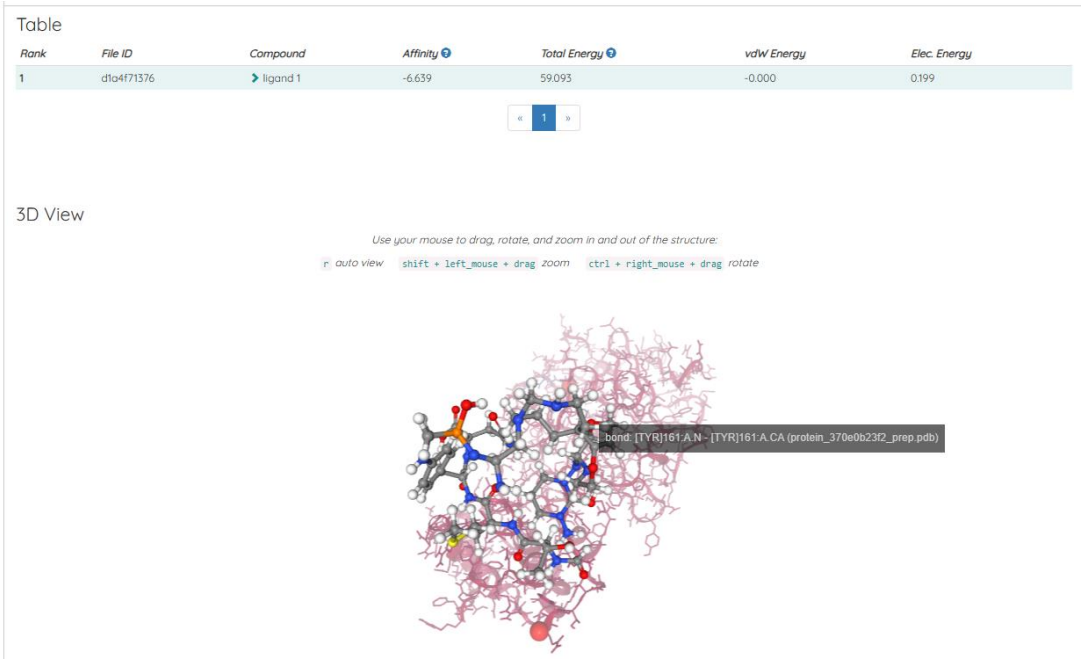

Iconic6. [DockThor] JOB PeptideMimeticIconic26lu7X_6532522a6d5c9 Rank, File ID, Compound, Affinity, Total Energy, vdW Energy, Elec. Energy with 1, d1a4f71376, ligand 1, -6.639, 59.093, -0.000, 0.199 scoring values.

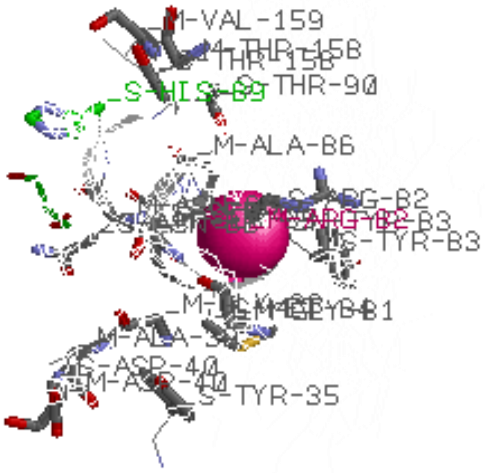

(Schematic1a)

Preprints.org (www.preprints.org) | NOT PEER-REVIEWED | Posted: 11 March 2024 doi:10.20944/preprints202403.0518.v1

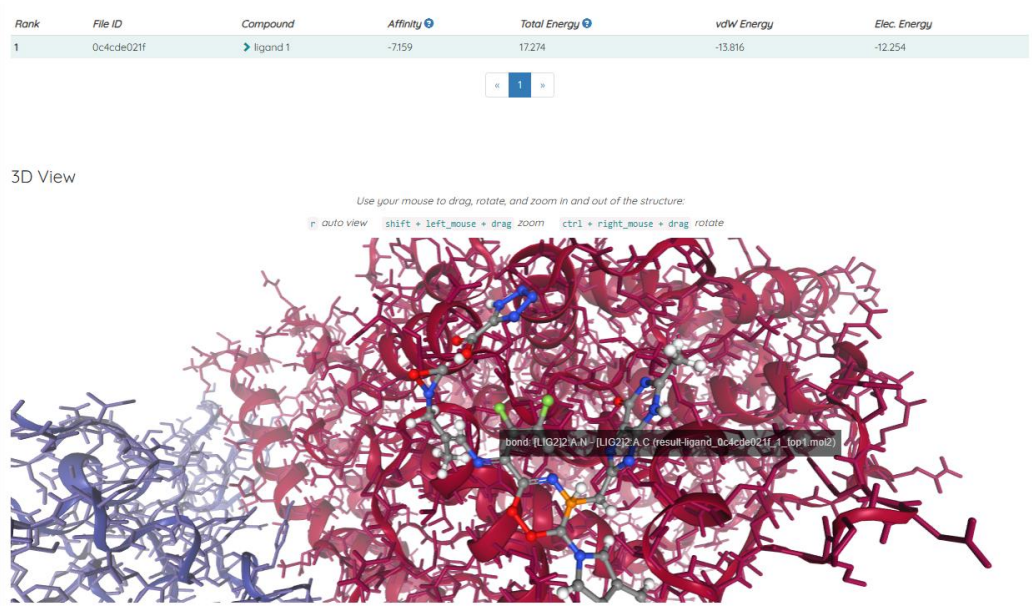

(Schematic1b)

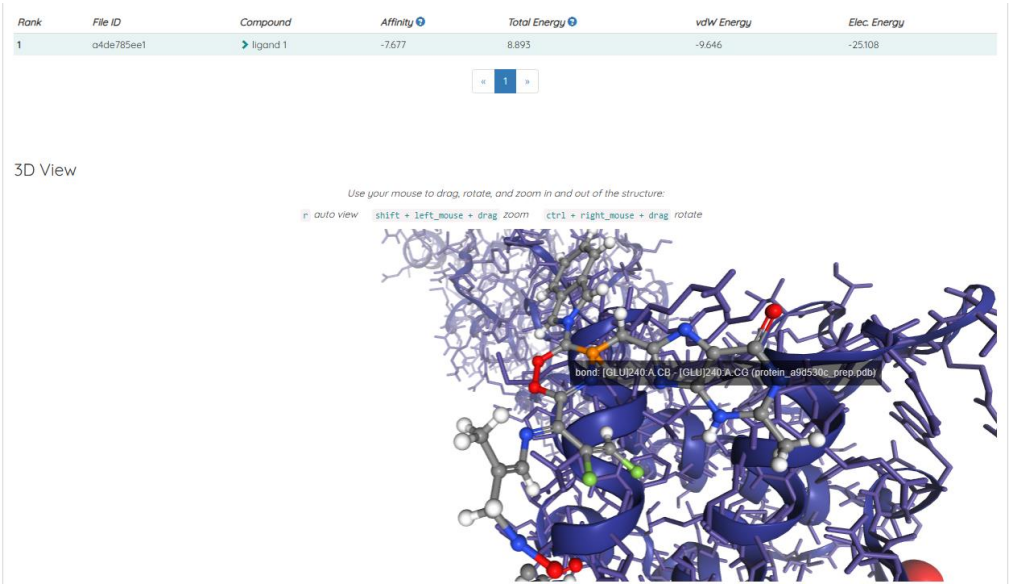

(Schematic1c)

 doi:10.20944/preprints202403.0518.v1

Rank	File ID	Compound	Affinity	Total Energy	vdW Energy	Elec. Energy
1	7d256a6214	ligand 1	-5.885	38.249	-1.317	0.728

« 1 »

3D View

Use your mouse to drag, rotate, and zoom in and out of the structure:

r auto view shift + left_mouse + drag zoom ctrl + right_mouse + drag rotate

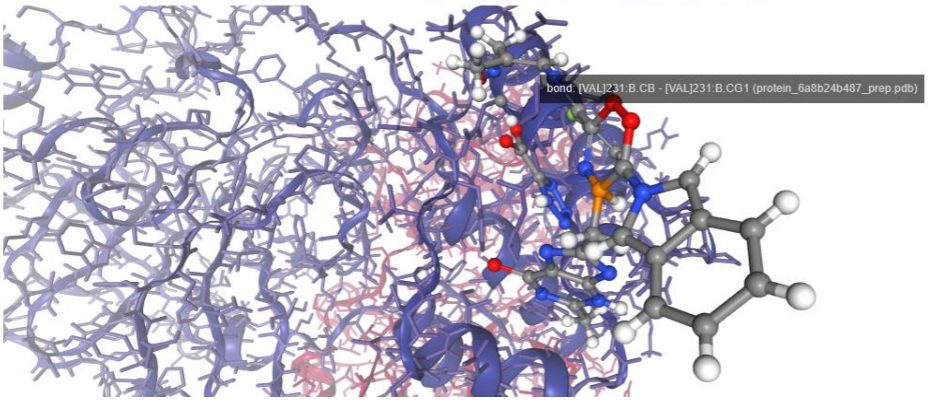

(Schematic1d)

Table

Rank	File ID	Compound	Affinity	Total Energy	vdW Energy	Elec. Energy
1	06ab0e2e50	ligand 1	-6.967	15.471	-7.732	-21.562

« 1 »

3D View

Use your mouse to drag, rotate, and zoom in and out of the structure:

r auto view shift + left_mouse + drag zoom ctrl + right_mouse + drag rotate

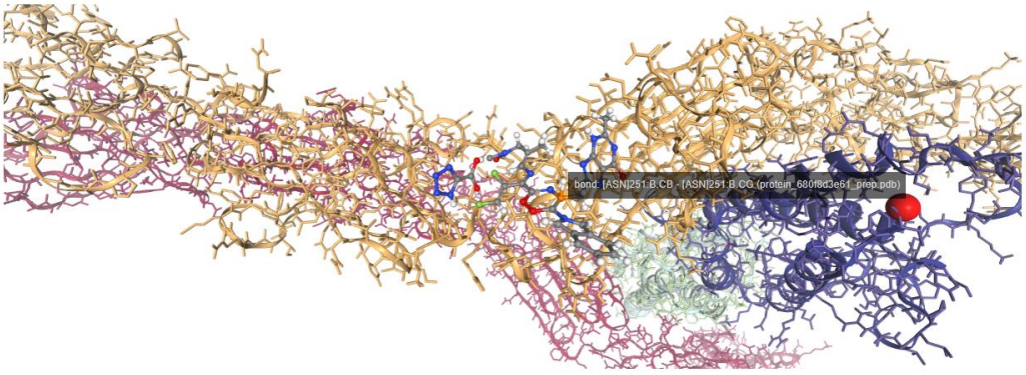

(Schematic1e)

Preprints.org (www.preprints.org) | NOT PEER-REVIEWED | Posted: 11 March 2024 doi:10.20944/preprints202403.0518.v1

Rank	File ID	Compound	Affinity	Total Energy	vdW Energy	Elec. Energy
1	1b4714b9ba	ligand 1	-5.976	23.748	-2.616	-13.576

« 1 »

3D View

Use your mouse to drag, rotate, and zoom in and out of the structure:

r auto view shift + left_mouse + drag zoom ctrl + right_mouse + drag rotate

(Schematic1f)

Table

Rank	File ID	Compound	Affinity	Total Energy	vdW Energy	Elec. Energy
1	3eaf0a881b	ligand 1	-5.323	38.351	-0.002	-0.459

« 1 »

3D View

Use your mouse to drag, rotate, and zoom in and out of the structure:

r auto view shift + left_mouse + drag zoom ctrl + right_mouse + drag rotate

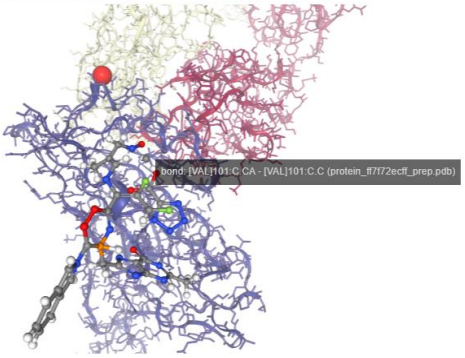

(Schematic1g)

Table

Rank	File ID	Compound	Affinity	Total Energy	vdW Energy	Elec. Energy
1	9ab912b7d2	ligand 1	-7.097	28.414	-12.325	0.313

« 1 »

3D View

Use your mouse to drag, rotate, and zoom in and out of the structure:

r auto view shift + left_mouse + drag zoom ctrl + right_mouse + drag rotate

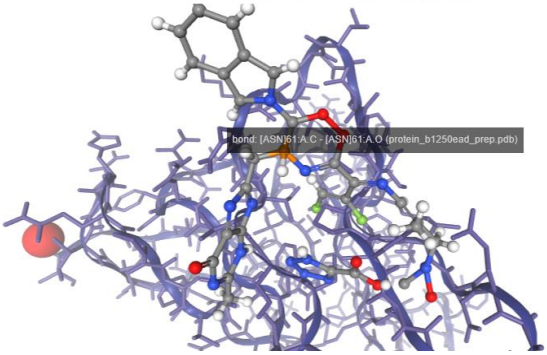

(Schematic1h)

Preprints.org (www.preprints.org) | NOT PEER-REVIEWED | Posted: 11 March 2024 doi:10.20944/preprints202403.0518.v1

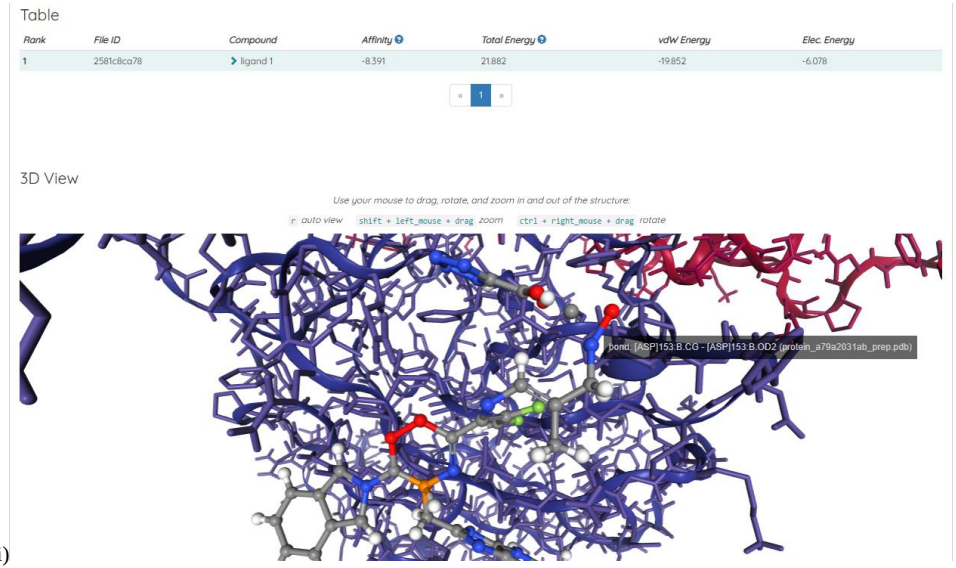

(Schematic1i)

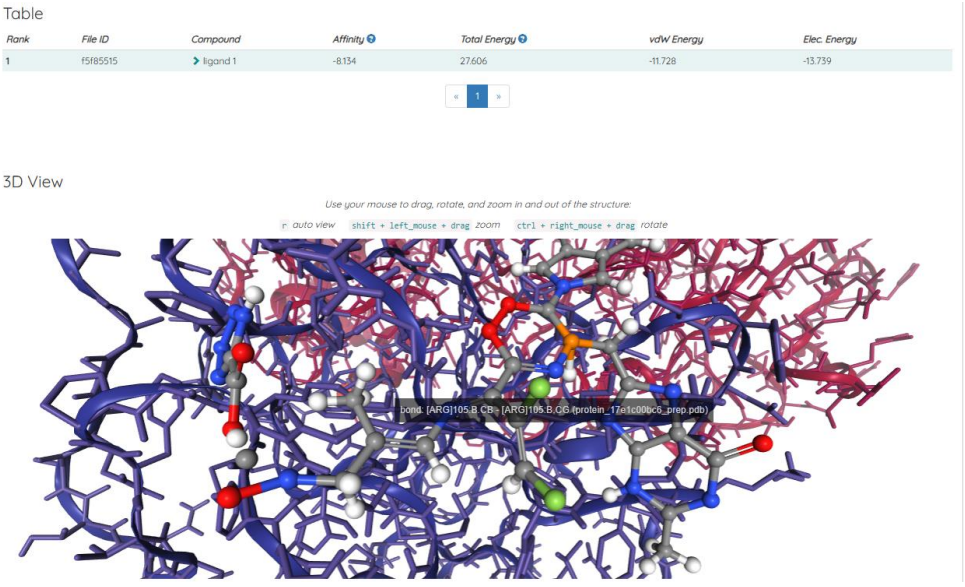

(Schematic1J)

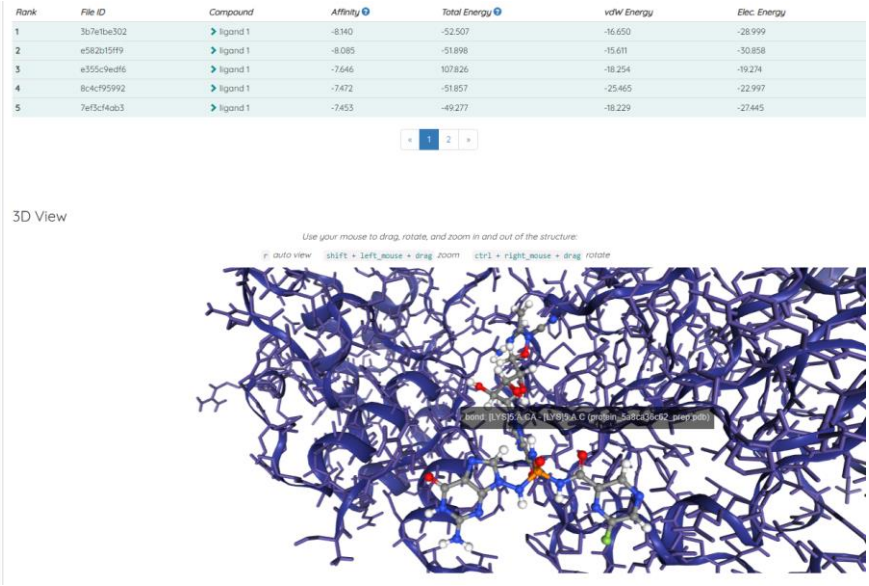

(Schematic1K)

 doi:10.20944/preprints202403.0518.v1

Rank	File ID	Compound	Affinity	Total Energy	vdW Energy	Elec. Energy
1	3b5a9a3e8b	ligand 1	-7.339	144.182	1.571	-78.521
2	830eaf9a02	ligand 1	-6.622	-20.106	4.614	-51.630
3	0d5fdc7d	ligand 1	-6.610	-80.858	3.825	-68.441
4	53ea797731	ligand 1	-6.163	-31.045	-0.986	-25.531
5	1f0f069721	ligand 1	-5.665	-67.797	28.450	-101.974

« 1 »

3D View

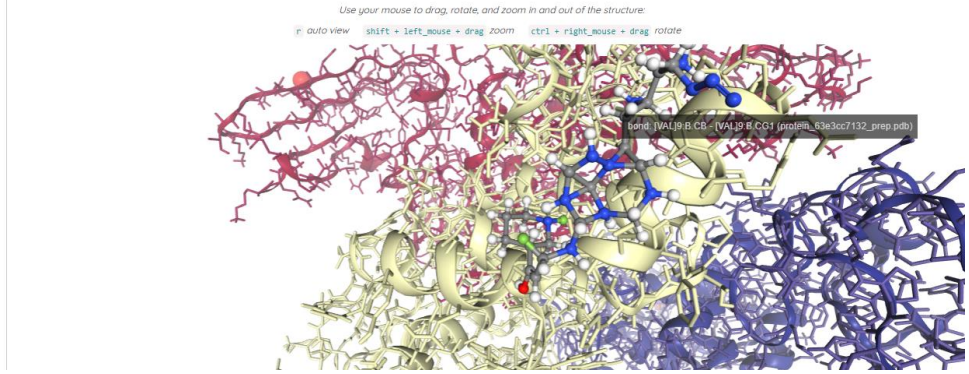

(Schematic1l)

Rank	File ID	Compound	Affinity	Total Energy	vdW Energy	Elec. Energy
1	473af57d23	ligand 1	-7.097	-70.858	-7.638	-34.916
		run 6	-7.097	-70.858	-7.638	-34.916
		run 6	-7.000	-70.087	-7.971	-35.584
		run 12	-7.011	-69.894	-1.237	-42.138
2	4cfb9b20a2	ligand 1	-6.937	-11.995	-2.442	-44.306
3	9df1c0481b	ligand 1	-6.847	2.097	-5.396	-29.754
4	e043fd046e	ligand 1	-6.726	-29.729	-4.881	-42.173
5	818430537f	ligand 1	-6.274	48.482	11.199	-56.474

« 1 2 »

3D View

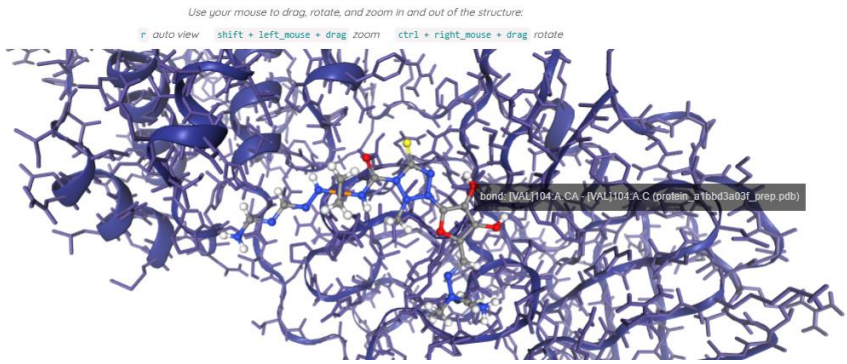

(Schematic1m)

Schematic1. 1a) Docking Composite systems from Fuzzy Sphere-like small molecules, and theirs Partial trace of a maximally entangled state of density operators of the matrix sequences screening as GegenbauerC[ϱ A B, ϱ B, ϱ A] ChebyshevT generalized inputs from the Arsenicum album, Pulsatilla nigricans, Nux vomica, Rhus toxicodendron, and Gelsemium sempervirens Homeopathy remedies including NuBEE Phyto – library, and COVID2019 targets identified between the consensus of 2019-nCoV and representative betacoronavirus genomes. 1b) [DockThor] JOB ROCCUSTYRNAXDRVYIHPFX mimetic2qrcX26lzg_6585a9495b2e8 RoccustyrnaDRVYIHPFXmimetic2 targets into the 6lzg protein cavities. 1c) [DockThor] JOB ROCCUSTYRNAXDRVYIHPF2mimeticXqrcX26WCO_6585aa678f2b6 where RoccustyrnaDRVYIHPFXmimetic2 onto the 6wco binding domains. 1d) [DockThor] JOB ROCCUSTYRNAXDRVYIHPFXmimetic2qrcX22yna_6585ac1538ef9 docking run where RoccustyrnaDRVYIHPFXmimetic2 binds inside the 2yna binding cavities. 1e) [DockThor] JOB ROCCUSTYRNAXDRVYIHPFXmimetic2qrcX22e9w_6585ab11b1474 docking experiment when RoccustyrnaDRVYIHPFXmimetic2 onto the 2e9w binding domains. 1f) [DockThor] JOB ROCCUSTYRNAXDRVYIHPFXmimeticXqrcX24ae3_6585ab87e8be7 docking experiment where

 doi:10.20944/preprints202403.0518.v1

RoccustyrnaDRVYIHPFXmimetic2 against the 4ea3 binding domains. 1g) [DockThor] JOB ROCCUSTYRNAXDRVYIHPFX mimeticXqrcX26w41X_6592b0cf95f01 3D docking trial when RoccustyrnaDRVYIHPFXmimetic2 binds onto the 7W9E SARS-CoV-2 Delta S-8D3 binding domains. 1h) [DockThor] JOB ROCCUSTYRNAXDRVYIHPFX mimeticXqrcX27f5fX_6592b146468cb docking run where RoccustyrnaDRVYIHPFXmimetic2 targets onto the 7F5F SARS-CoV-2 ORF8 S84 binding sites. 1i) [DockThor] JOB ROCCUSTYRNAXDRVYIHPFX mimeticXqrcX27lfpX_6592aee7d8887 docking run when where RoccustyrnaDRVYIHPFXmimetic2 binds inside the 7lfp domains. 1j) [DockThor] JOB 7kfiROCCUSTYRNAXDRVYIHPFXmimeticXqrcX2_6592ad6ebea57 docking experiment where RoccustyrnaDRVYIHPFXmimetic2 binds inside the 7MSW Full length SARS-CoV-2 Nsp2. 1K) [DockThor] JOB 6yb7Roccustyrna_gs_6596e3cde761a docking experiment between and Remdesivir ligand and Roccustyrna_gs_6596e3cde761a (frs1-4) drug designs where Roccustyrna_gs_6596e3cde761a (frs1-4) binds onto the 6yb7 protein targets with negative docking free energies. The Remdesivir drug targets onto the same target with positive docking free energy values of 107.826KcalMolA. 1l) [DockThor] JOB 6w9XXRoccustyrna_frs1X5_6596e1e17c75d parallel docking experiment between Remdesivir ligand and 6w9XXRoccustyrna_frs1X4_6596e1e17c75d (frs1-4) drug designs where Roccustyrna_frs1X4_6596e1e17c75d (frs1-4) druggable designs binds the 6w9c protein target with only negative vDw, Elec.Energy, and Totyal Energy values. On the other hand the Remdesivir targets the same binding domains with positive Total Energy values. 1m) [DockThor] JOB 2zu5GissitorviffirnaTMs(1-9)_659fcd0ad7dc parallel docking experiment between Remdesivir, Nirmatrelvir, Roccustyrnafrs(1-4),and GissitorviffirnaTMs(1-9) ligands. The Remdesivir and Nirmatrelvir Drugs bind into the 2zu5 protein targets with positive docking energy values of 48.482 and 2.097 KcalMolA. Instead of this the Roccustyrnafrs(1-4),and GissitorviffirnaTMs(1-9) drug designs targets into the same protein targets solely with negative docking energy and binding affinity scoring values.

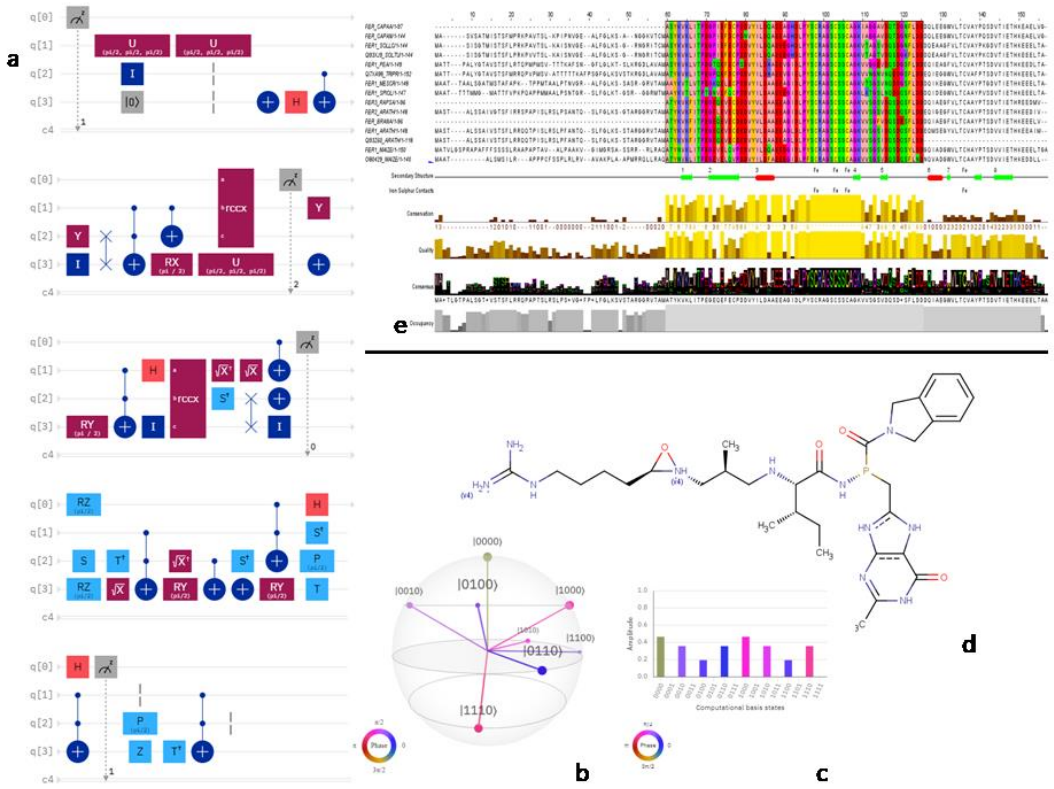

Schematic2. a) Quantum Hidden Entanglement Negativity Translations and Uncertainty Quantum Relationships for Linearized Metric Perturbation Vectors, Scalar Potentials hμν (x) Φ (t, x), A (t, x). Field quantities Linearized for Ricci Tensor Electric and Magnetic fields δRμν E (t, x), B (t, x), and Gauge Transformations hμν hμν − ξμ;ν − ξν;μ A A, ∇ΛΦ Φ − ∂t Λ [0.177-0.427j, 0, 0j, 0.25, 0.25j, 0, 0j, 0.177, 0.073j, 0, 0j, 0.354, 0j, 0, 0j, -0.177, 0.427j, 0, 0j, 0, 0.354j, 0, 0j, 0.177, 0.073j, 0, 0j, -0.25, 0.25j, 0, 0j] OPENQASM 2.0; include "qelib1.inc"; qreg AdS5q [4] ; creg c [4] ; reset AdS5q [3] ; id AdS5q [2] ; u (pi/2, pi/2, pi/2) AdS5q [1] ; barrier

 doi:10.20944/preprints202403.0518.v1

AdS5q [3] ; barrier AdS5q [2] ; u (pi/2, pi/2, pi/2) AdS5q [1] ; x AdS5q [3] ; h AdS5q [3] ; cx AdS5q [2], AdS5q [3] ; measure AdS5q [0] -> c [1] ; id AdS5q [3] ; y AdS5q [2] ; swap AdS5q [2], AdS5q [3] ; ccx AdS5q [1], AdS5q [2], AdS5q [3] ; rx (pi/2) AdS5q [3] ; cx AdS5q [1], AdS5q [2] ; u (pi/2, pi/2, pi/2) AdS5q [3] ; rccx AdS5q [0], AdS5q [1], AdS5q [2] ; y AdS5q [1] ; x AdS5q [3] ; ry (pi/2) AdS5q [3] ; measure AdS5q [0] -> c [2] ; ccx AdS5q [1], AdS5q [2], AdS5q [3] ; h AdS5q [1] ; id AdS5q [3] ; rccx AdS5q [1], AdS5q [2], AdS5q [3] ; sdg AdS5q [2] ; sxdg AdS5q [1] ; swap AdS5q [2], AdS5q [3] ; sx AdS5q [1] ; x AdS5q [2] ; id AdS5q [3] ; cx AdS5q [0], AdS5q [1] ; measure AdS5q [0] -> c [0] ; s AdS5q [2] ; rz (pi/2) AdS5q [3] ; rz (pi/2) AdS5q [0] ; tdg AdS5q [2] ; sx AdS5q [3] ; ccx AdS5q [1], AdS5q [2], AdS5q [3] ; sxdg AdS5q [2] ; ry (pi/2) AdS5q [3] ; cx AdS5q [2], AdS5q [3] ; sdg AdS5q [2] ; x AdS5q [3] ; ry (pi/2) AdS5q [3] ; ccx AdS5q [0], AdS5q [1], AdS5q [2] ; t AdS5q [3] ; h AdS5q [0] ; p (pi/2) AdS5q [2] ; sdg AdS5q [1] ; ccx AdS5q [1], AdS5q [2], AdS5q [3] ; z AdS5q [3] ; p (pi/2) AdS5q [2] ; h AdS5q [0] ; barrier AdS5q [1] ; tdg AdS5q [3] ; ccx AdS5q [1], AdS5q [2], AdS5q [3] ; barrier AdS5q [2] ; measure AdS5q [0] -> c [1] ; b). Computational Basic States for Naive Geometrical Interpretation of the ordinary energy of the Quantum particle-like chemical spaces c). Bloch Sphere Chart embedding and Witten's M-Theory explaining the logical connections and sequential deduction between Quantum Negative Energy interpretations using Einstein relativity and leading to Quantum relativity energy driven chemical spaces in time d).2D DRVYIHPFmimetic small molecule of the IUPAC Name of [amino ({4 - [(2R,3R) - 2 - [(2S) - 3 - { [(1S,2S) - 1 - { [(S) - 1,3 - dihydroisoindole - 2 - carbonyl [(2 - methyl - 6 - oxo - 1,7 - dihydropurin - 8 - yl) methyl] phosphanyl] carbamoyl} - 2 - methylbutyl] amino} - 2 - methylpropyl] oxaziridin - 3 - yl] butyl}amino) methylidene] azaniume) e). Cluster Docking Energy Analysis and In Parallel Cluster Docking Energy Ranking Representations of the NuBEE Phyto – elements inside the PDB IDs: 1xak,7b3o,7khp,6wzu,6w63,6m2q,7kdl,7bv2,6woj,2gt9,6lu7, 6zgg,2ghv,6xs6, and 6yi3 protein targets using Ω, (A [H] ⊗̂ [Ho] AodS5 (Θ) Θ (A [H] ⊗̂ [Ho] AodS5 (Θ) Θ mixed (rboximidoyl - 3 - fluoro - phos phoryl] formonitrile,12, (A [H] ⊗̂ [Ho] AodS5 (Θ) Θ (A [H] ⊗̂ [Ho] AodS5 (Θ) Θ [amino ({4 - [(2R,3R) - 2 - [(2S) - 3 - { [(1S,2S) - 1 - { [(S) - 1,3 - dihydroisoindole - 2 - carbonyl [(2 - methyl - 6 - oxo - 1,7 - dihydropurin - 8 - yl) methyl] phosphanyl] carbamoyl} - 2 - methylbutyl] amino} - 2 - methylpropyl] oxaziridin - 3 - yl] butyl} amino) methylidene] azaniume) (rboximidoyl - 3 - fluoro - phos phoryl] formonitrile ∧, (A [H] ⊗̂ [Ho] AodS5 (Θ) Θ (A [H] ⊗̂ [Ho] AodS5 (Θ) Θ (rboximidoyl - 3 - fluoro - phos phoryl] formonitrile tensor of pharmacophoric elements. after solving the Etotal (SI Appendix XXXIX), (Group of Functions (Cluster of BIOGENEA_ CONSENSUS_Eqs.1-26, (Supplement Material FUNCTIONS.1 - 23)) as a chemical block for the generation of the chemical scaffold of lambda6-sulfanyl}oneboximidoyl-3- (rboximidoyl-3-fluoro- (1S,4S) ((diaminomethylidene) amino) ethenyl}) amino, oxy-methyl) -3,4-dimethyl-7-oxo-4-thia-1-azabicyclo (3.2.0) heptane-2-carbonyloxy) ({((2-amino-6-oxo-6,9-dihydro-3H-purin-9-yl) oxy) (hydroxy) phosphoryl} oxy) phosphinic acid-ylidene, *cyano (2,6-diazabicyclo *3.1.0, hex-1-en-6-yl -) (rboximidoyl-3-fluoro - (1S,4S) ((diamino methylidene) amino) ethenyl}) amino, oxy - methyl) -3,4-dihydroxyoxolan-2-ylo-1,2,4-triazol-3-yl - formamido) dihydroxyoxolan-2-ylo-1,2,4-triazol-3-yl- (formamido) phosphoryl o-6-fluoro-3,4-dihydropyrazine-2-carboxamide (7ar) -5-amino-N-* (S) -,2-* (3-oxabicyclo (2.1.0) (1S,4S) -5-oxabicyclo*2.1.0, pentan-2 ((2S,5r,6r) -6- ((2S) -2-amino-2-phenyl-acetamido) -3,3-dimethyl-7-oxo-4-thia-1-azabicyclo (3.2.0) heptane-2-carbonyloxy) ({((2-amino-6-oxo-6,9-dihydro-3H-purin-9-yl) oxy) (hydroxy) phosphoryl} oxy) phosphinic acid-ylidene, *cyano (2,6-diazabicyclo*3.1.0, hex-1-en-6-yl) (rboximidoyl-3-fluoro- (1S,4S) ((diaminomethylidene) amino) ethenyl}) amino, oxy-methyl) -3,4-dihydroxyoxolan-2-ylo-1,2,4-triazol-3-yl- (formamido) phosphoryl o-6-fluoro-3,4-dihydropyrazine-2-carboxamide (7ar) -5-amino-N-* (S) -,2-* (3-{((1S,4S) -5-oxabicyclo (2.1.0) pentan-2-ylidene) {(cyano ({2,6-diazabicyclo (3.1.0) hex-1-en-6-yl}) phosphanyl- (fluoro) methyl}-lambda6-sulfanyl}one pentan-2-ylidene) {(cyano ({2,6-diazabicyclo (3.1.0) hex-1-en-6-yl}) phosphanyl {((1S,4S) -5-oxabicyclo (2.1.0) pentan-2-ylidene). (METHODS AND MATERIALS), (Cluster of BIOGENEA_ CONSENSUS_Eqs.1-26), (Supplement Material FUNCTIONS.1 - 24), (Cluster of Functions.70) My innovative drug design generated also negatively charged groups within the sequence of the amino acid of the H-M-ASN-33, h-S-ASN-33, h-S-TYR-356, h-M-ASN-424, v-M-ASN-33, v-M-ALA-331, v-M-THR-332, v-S-THR-332, v-S-TYR-356, v-S-TRP-423, v-S-ILE-428, and V-S-ARG-495 with the docking energy values of (-104.7 and-3.45708, -3.5, -3.97711, -3.5, -5.33228, -6.79753, -7.9376, -6.69969, -12.2528, -7.66989, -8.15072, -7.332) Kcalmol respectively (SI Appendix I), (SI Appendix IV), (SI Appendix V), (SI Appendix VI), (SI Appendix VII), (SI Appendix VIII), (SI Appendix XII), (SI Appendix XIII), (SI Appendix IX), (SI Appendix XIV), (SI Appendix XV), (SI Appendix XVI), (SI Appendix XVII), (SI Appendix XVIII), (SI Appendix XIX), (SI Appendix XX), (SI Appendix XXI), (SI Appendix XXII), (SI Appendix XXIII), (SI Appendix XXIV), (SI Appendix XXV) (SI Appendix XXVI), (SI Appendix XXVII). (SI Appendix XXVIII), (SI Appendix XXIX), (SI Appendix XXX), (SI Appendix XXXI), (SI Appendix XXXII), (SI Appendix XXXIII), (SI Appendix XXXIV), (SI Appendix XXXV), (SI Appendix XXXVI), (SI Appendix XXXVII), (SI Appendix XXXV), (SI Appendix

 doi:10.20944/preprints202403.0518.v1

XXXVI), (SI Appendix XXXVII), (SI Appendix XVIII), and ((Cluster Docking Energy TableS1), (SI Appendix I), (Cluster Docking Energy TableS2), SI Appendix I), (Docking Energy TableS1), (SI Appendix I), (Docking Energy TableS2), (SI Appendix I), (Docking Energy TableS3), (SI Appendix I)). The multi-covalent Gissitorviffirna_TM5 4 - [3 - (aminomethyl) oxiren - 2 - yl] - 4,5 - diaza - 2λ⁵ - phosphaspiro [bicycle [3.1.0] hexane - 2,2' - oxaphosphirane] - 3 - thione contact residues generated the Roccustyrna_gs, and the Roccustyrna_fr drug design derived Gissitorviffirna_TM7 (1S,3S,7R) - 7 - amino - 1 - [(R) - {3 - sulfanylidene - 2,4,6 - triazabicyclo [3.1.0] hexa - 1,4 - dien - 6 - yl} [(E) - 2 - [(3R) - 3 - [(2R,5R) - 3,4,5 - trifluoro - 2,5 - dihydrofuran - 2 - yl] - 3H - 1,2,4 - triazol - 5 - yl] diazen - 1 - yl] phosphoroso] - 1,2,4,6 - tetraazaspiro [2.4] heptane - 5 - thione that hits also the entire binding domains of the SARS-COV-2 core elements of (PDB: 6mq2), (PDB: 6woj), (PDB: 7khp), (PDB: 7b3d), (PDB: 7b3o), (PDB: 6w23), and (PDB: 6w9c) protein targets within the amino acid sequence of V-S-PRO-59, v-S-ARG-65, v-M-THR-75, v-S-THR-75, v-M-PRO-77, v-S-PRO-77, v-M-HIS-47, and V-S-HIS-47 with the docking energies of the (-83.9, -4.21999, -12.6164, -7.60372, -6.69528, -5.89416, -6.40663, -5.51621, -7.99273) Kcalmol (SI Appendix), (SI Appendix II), (SI Appendix III), (SI Appendix IV), (SI Appendix V), (SI Appendix VI), (SI Appendix VII), (SI Appendix VIII), (SI Appendix XII), (SI Appendix XIII), (SI Appendix IX), (SI Appendix XIV), (SI Appendix XV), (SI Appendix XVI), (SI Appendix XVII), (SI Appendix XVIII), (SI Appendix XIX), (SI Appendix XX), (SI Appendix XXI), (SI Appendix XXII), (SI Appendix XXIII), (SI Appendix XXIV), (SI Appendix XXV) (SI Appendix XXVI), (SI Appendix XXVII). (SI Appendix XXVIII), (SI Appendix XXIX), (SI Appendix XXX), (SI Appendix XXXI), (SI Appendix XXXII), (SI Appendix XXXIII), (SI Appendix XXXIV), (SI Appendix XXXV), (SI Appendix XXXVI), (SI Appendix XXXVII), (SI Appendix XXXV), (SI Appendix XXXVI), (SI Appendix XXXVII), (SI Appendix XVIII), ((Cluster Docking Energy TableS1), (SI Appendix I), (Cluster Docking Energy TableS2), SI Appendix I), (Docking Energy TableS1), (SI Appendix I), (Docking Energy TableS2), (SI Appendix I), (Docking Energy TableS3), (SI Appendix I)), (Figure S1), (Figure S2a), (Figure S2b), (Figure S2c), (Figure S2d), and (Figure S2e). (Figure S3), (Figure S4f), (Figure S4g), (Figure S4h) (Statue1a), (SI Appendix V), (SI Appendix VI), (Statue1b), (SI Appendix VII), (SI Appendix VIII), (SI Appendix IX), (SI Appendix XVIII) (Statue1c), (SI Appendix X), (SI Appendix XI), (Statue1d), (SI Appendix VIII), (SI Appendix VIII), (SI Appendix XII), (SI Appendix XIII), (Statue1e), (SI Appendix IX), (SI Appendix XIV), (SI Appendix XV), (SI Appendix XVI), (SI Appendix XVII), (SI Appendix XVIII), (SI Appendix XIX), (SI Appendix XX), (SI Appendix XXI), (Statue1f), (SI Appendix XXII), (SI Appendix XXIII), (SI Appendix XXIV), (SI Appendix XXV) (SI Appendix XXVI), (Statue1g), (SI Appendix XXVII). (SI Appendix XXVIII), (Statue1h), (SI Appendix XXIX), (SI Appendix XXX), (Statue1i), (SI Appendix XXXI), (SI Appendix XXXII), (SI Appendix XXXIII), (SI Appendix XXXIV), (Statue1j), (SI Appendix XXXV), (SI Appendix XXXVI), (SI Appendix XXXVII), (Statue1k), (SI Appendix XXXV), (SI Appendix XXXVI), (SI Appendix XXXVII), (SI Appendix XVIII), (Cluster Docking Energy TableS1), (SI Appendix I), (Cluster Docking Energy TableS2), SI Appendix I), (Docking Energy TableS1), (SI Appendix I), (Docking Energy TableS2), (SI Appendix I), (Docking Energy TableS3), (SI Appendix I) In a next step, the Roccustyrna_gs_consv1 chemical structure generated an inhibitory docking effect of high negative binding energy docking values of the (-66,7) KcalmolA when docked onto the cav7bv2_POP binding cavities within the binding sites of the amino acids of V-M-LYS-551, v-S-LYS-551, v-S-ARG-553, v-S-ASP-618, v-M-TYR-619, and V-M-PRO-620 with the docking energy values of (-4.71516, -10.4842, -4.7999, -6.65538, -5.1339, -6.28532) KcalMolA. (Figure S5a), (Figure S5b), (Figure S5c), (Figure S6) On the other hand the Remdesivir drug when combined to the Roccustyrna small molecule interacted at the same binding domains of the amino acids of V-M-LYS-551, v-S-LYS-551, v-S-ARG-553, v-S-ASP-618, v-M-TYR-619, and V-M-PRO-620 with positive and zero docking values of the (42.1, -0.104885, -0.19986,25.0575) Kcalmol. That means that the Remdesivir drug could induce in same the COVID19 disease (Statue1a), (SI Appendix V), (SI Appendix VI), (Statue1b), (SI Appendix VII), (SI Appendix VIII), (SI Appendix IX), (SI Appendix XVIII) (Statue1c), (SI Appendix X), (SI Appendix XI), (Statue1d), (SI Appendix VIII), (SI Appendix VIII), (SI Appendix XII), (SI Appendix XIII), (Statue1e), (SI Appendix IX), (SI Appendix XIV), (SI Appendix XV), (SI Appendix XVI), (SI Appendix XVII), (SI Appendix XVIII), (SI Appendix XIX), (SI Appendix XX), (SI Appendix XXI), (Statue1f), (SI Appendix XXII), (SI Appendix XXIII), (SI Appendix XXIV), (SI Appendix XXV) (SI Appendix XXVI), (Statue1g), (SI Appendix XXVII). (SI Appendix XXVIII), (Statue1h), (SI Appendix XXIX), (SI Appendix XXX), (Statue1i), (SI Appendix XXXI), (SI Appendix XXXII), (SI Appendix XXXIII), (SI Appendix XXXIV), (Statue1j), (SI Appendix XXXV), (SI Appendix XXXVI), (SI Appendix XXXVII), (Statue1k), (SI Appendix XXXV), (SI Appendix XXXVI), (SI Appendix XXXVII), (SI Appendix XVIII), (Cluster Docking Energy TableS1), (SI Appendix I), (Cluster Docking Energy TableS2), SI Appendix I), (Docking Energy TableS1), (SI Appendix I), (Docking Energy TableS2), (SI Appendix I), (Docking Energy TableS3), (SI Appendix I). (PDB: 4ea3). As illustrated in the (Figure S3d), (Figure S3c), (Figure S3e), (Figure S3f), (Figure S3g), and the (Figure S3h) the Roccustyrna small molecule

 doi:10.20944/preprints202403.0518.v1

generated also negative docking energy values with a potential inhibitory effect when docked against the sequence of the amino acids of the protein targets of (PDB: 6YI3) of the N-terminal RNA-binding domain of the SARS-CoV-2 nucleocapsid phosphoprotein which is essential for linking the viral genome to the viral membrane. (Figure S4d), (Figure S4e) In this project for the first time I generated a Comparative Docking Cluster Analysis between the Remdesivir and My prototype chemical library of the Roccustyrna_gs, the Roccustyrna_fr, and the Gissitorviffirna_TM small molecules in combination with the [amino ({4 - [(2R,3R) - 2 - [(2S) - 3 - { [(1S,2S) - 1 - { [(S) - 1,3 - dihydroisoindole - 2 - carbonyl [(2 - methyl - 6 - oxo - 1,7 - dihydropurin - 8 - yl) methyl] phosphanyl] carbamoyl} - 2 - methylbutyl] amino} - 2 - methylpropyl] oxaziridin - 3 - yl] butyl}amino) methylidene] azanium peptide mimetic scaffolding when docked onto the SARS-COV-2 protein targets of (PDB: 7bv2) with the averaged docking energy values of (Num_Members: 40, Total_Energy: 2.103, vdW:-5.122, coulomb:-4.977, internal: 12.203, rmsd: 3.183 and $Number of Clusters: 10, $Seed:-1985, $Leader_Info 1 { Num_Members: 63 Total_Energy:-0.883, vdW:-6.041, coulomb:-7.045, internal: 12.203) KcalMolA respectively. More specifically, in this project I unified generalized Quantum Negative Energies for k-nearest values and Quantum Uncertainities for re-generalizing bosonic formalisms of these k-nearest neighbors of Molecular Pairs (MMP) and von Neumann formulations for Dirac formulation states as a Tipping–Ogilvie and Machine Learning application within this Quantum computing context with algebraic multi-metrics characteristics targeting the atomistic level of the protein apparatus of the SARS-COV-2 viral characteristics. An Adaptive Weighted KNN Positioning approach through nonlinear electrodynamics to simulate an advanced Quantum mechanical inverse docking algorithm was applied in this unified protocol by providing further insight on a ℓneuron (ι), φ D [r2] S [r1] Chern-Simons Topology improver for generating a negative docking energy effect of the highest docking energy values. By performing Euclidean Geometrics driven stationary phase approximations around these [amino ({4 - [(2R,3R) - 2 - [(2S) - 3 - { [(1S,2S) - 1 - { [(S) - 1,3 - dihydroisoindole - 2 - carbonyl [(2 - methyl - 6 - oxo - 1,7 - dihydropurin - 8 - yl) methyl] phosphanyl] carbamoyl} - 2 - methylbutyl] amino} - 2 - methylpropyl] oxaziridin - 3 - yl] butyl} amino) methylidene] azanium pharmacophore merging critical points, I obtained the asymptotic expansions of the Roccustyrna_fr's merged holomorphic chemical block systems against the specific combination of (PDB: 6mq2), (PDB: 6woj), (PDB: 7khp), (PDB: 7b3d), (PDB: 7b3o), (PDB: 6w23), and (PDB: 6XS6) protein targets (SI Appendix), (SI Appendix II), (SI Appendix III), (SI Appendix IV), (SI Appendix V), (SI Appendix VI), (SI Appendix VII), (SI Appendix VIII), (SI Appendix XII), (SI Appendix XIII), (SI Appendix IX), (SI Appendix XIV), (SI Appendix XV), (SI Appendix XVI), (SI Appendix XVII), (SI Appendix XVIII), (SI Appendix XIX), (SI Appendix XX), (SI Appendix XXI), (SI Appendix XXII), (SI Appendix XXIII), (SI Appendix XXIV), (SI Appendix XXV) (SI Appendix XXVI), (SI Appendix XXVII). (SI Appendix XXVIII), (SI Appendix XXIX), (SI Appendix XXX), (SI Appendix XXXI), (SI Appendix XXXII), (SI Appendix XXXIII), (SI Appendix XXXIV), (SI Appendix XXXV), (SI Appendix XXXVI), (SI Appendix XXXVII), (SI Appendix XVIII), and ((Cluster Docking Energy TableS1), (SI Appendix I), (Cluster Docking Energy TableS2), SI Appendix I), (Docking Energy TableS1), (SI Appendix I), (Docking Energy TableS2), (SI Appendix I), (Docking Energy TableS3), (SI Appendix I)). (Illustration1) As a result, Entangled Neural Networks and Quantum-Inspired Kappa-Symmetrizing frameworks were mixed together and by using Chern-Simons P_(δ n)^((d^4 δ n^2 Q^4 r^10 Ψ)/(α G))(G N g^(6^(-d^3)) 1F1(a, b, z) U(exp(QHypergeometricPFQ {{e^x, i y}, 2 y} (Q^cos^4(c X) | sin^(-1)(r)^2)))) normalized Shannon Entropy Quantities through Tipping–Ogilvie potentials I generated the combination of DRVYIHPF-mimetic, Gisitorviffirna_TM, Roccustyrna_gs, and Roccustyrna_fr small molecules. This annotated cluster of Druggable Scaffolds were able of producing the highest rates of Negative Docking Energy scoring values when virtually combined with the Amprenavir, Asunaprevir, Atazanavir, Boceprevir, Cytarabine, Darunavir, ritonavir, Sorivudine, Taribavirin, Tenofovir, Valganciclovir, Vidarabine, Lopinavir, Sofosbuvir, Zanamivir, Penciclovir, Nelfinavir, Merimepodib, Maribavir, Indinavir, Inarigivir, Galidesivir, Famciclovir, and Faldaprevir FDA approved antiviral drugs against the SARS-COV-2 protein binding sites of the (PDB: 6M2Q) SARS-CoV-2 3CL protease (3CL pro) apo structure (space group C21) inside the amino acid sequence oV-M-ARG-4, v-S-ARG-4, v-S-MET-6, v-M-ALA-7, v-S-PHE-8, v-M-GLY-11, v-M-LYS-12, v-S-LYS-12, v-M-GLU-14, v-S-GLU-14, v-M-GLY-15, v-M-THR-24, v-S-THR-24, v-M-THR-25, v-S-THR-25, v-M-THR-26, v-S-THR-26, v-M-VAL-35, v-S-VAL-35, v-S-ARG-40, v-S-HIS-41, v-M-THR-45, v-M-SEr-46, v-S-SEr-46, v-S-MET-49, v-M-ASN-53, v-S-ASN-53, v-S-TYR-54, v-M-ALA-70, v-M-GLY-71, v-M-ASN-95, v-S-LYS-97, v-M-PRO-99, v-S-LYS-102, v-S-VAL-104, v-M-ILE-106, v-S-GLN-107, v-M-PRO-108, v-M-GLY-109, v-S-GLN-110, v-M-THR-111, v-S-ASN-119, v-M-GLY-124, v-S-TYR-126, v-M-GLN-127, v-M-CYS-128, v-S-ARG-131, v-S-LYS-137, v-M-LEU-141, v-M-ASN-142, v-S-ASN-142, v-M-GLY-143, v-M-ASN-151, v-S-ASN-151, v-M-ILE-152, v-M-ASP-153, v-S-ASP-153, v-S-SEr-158, v-M-MET-165, v-S-MET-165, v-M-GLU-166, v-S-GLU-

 doi:10.20944/preprints202403.0518.v1

166, v-M-LEU-167, v-S-PRO-168, v-M-GLU-178, v-M-VAL-186, v-S-VAL-186, v-S-ARG-188, v-M-GLN-189, v-S-GLN-189, v-M-THR-190, v-S-TRP-218, v-M-LEU-220, v-M-ASN-221, v-S-PHE-223, v-M-TYR-237, v-S-TYR-237, v-S-TYR-239, v-M-ASP-245, v-S-ASP-245, v-S-HIS-246, v-S-ILE-249, v-M-GLU-270, v-S-GLU-270, v-S-LEU-271, v-M-LEU-272, v-M-GLN-273, v-M-ASN-274, v-S-ASN-274, v-M-GLY-275, v-M-MET-276, v-M-ASN-277, v-S-ASN-277, v-M-GLY-278, v-M-LEU-286, v-S-LEU-286, v-M-LEU-287, v-S-LEU-287, v-S-ASP-289, v-S-GLU-290, v-S-THR-292, v-S-PRO-293, v-M-PHE-294, v-S-PHE-294, v-S-ARG-298, v-M-GLN-299, v-S-GLN-299, v-M-GLY-302, v-M-VAL-303, v-M-PHE-305 (SI Appendix I), (SI Appendix II), (SI Appendix III), (SI Appendix IV), (SI Appendix V), (SI Appendix VI), (SI Appendix VII), (SI Appendix VIII), (SI Appendix XII), (SI Appendix XIII), (SI Appendix IX), (SI Appendix XIV), (SI Appendix XV), (SI Appendix XVI), (SI Appendix XVII), (SI Appendix XVIII), (SI Appendix XIX), (SI Appendix XX), (SI Appendix XXI), (SI Appendix XXII), (SI Appendix XXIII), (SI Appendix XXIV), (SI Appendix XXV) (SI Appendix XXVI), (SI Appendix XXVII). (SI Appendix XXVIII), (SI Appendix XXIX), (SI Appendix XXX), (SI Appendix XXXI), (SI Appendix XXXII), (SI Appendix XXXIII), (SI Appendix XXXIV), (SI Appendix XXXV), (SI Appendix XXXVI), (SI Appendix XXXVII), (SI Appendix XXXV), (SI Appendix XXXVI), (SI Appendix XXXVII), and (SI Appendix XVIII), ((Cluster Docking Energy TableS1), (SI Appendix I), (Cluster Docking Energy TableS2), SI Appendix I), (Docking Energy TableS1), (SI Appendix I), (Docking Energy TableS2), (SI Appendix I), (Docking Energy TableS3), (SI Appendix I)). Additionally, the same combination of My drug design novelties interacted with the highest docking energy values onto the binding sites of the (PDB: 6WOJ) protein targets of the SARS-CoV-2 macrodomain (NSP3) in complex with ADP-ribose of the targeting sequence of V-M-ALA-21, v-M-ASP-22, v-S-ASP-22, v-M-GLU-25, v-S-GLU-25, v-M-ALA-38, v-M-ALA-39, v-S-ASN-40, v-M-TYR-42, v-M-GLY-46, v-M-GLY-47, v-M-GLY-48, v-M-VAL-49, v-S-VAL-49, v-M-ALA-50, v-M-GLY-51, v-M-ALA-52, v-S-LEU-53, v-M-VAL-95, v-S-VAL-95, v-M-VAL-96, v-M-PRO-98, v-S-ASN-101, v-S-LEU-109, v-S-PRO-125, v-M-LEU-126, v-S-LEU-126, v-M-SEr-128, v-M-ALA-129, v-M-GLY-130, v-M-ILE-131, v-S-ILE-131, v-S-PHE-132, v-M-GLY-133, v-M-ALA-134, v-S-PRO-136, v-M-SEr-139, v-M-ALA-154, v-M-VAL-155, v-S-VAL-155, v-M-PHE-156, v-S-PHE-156, v-M-ASP-157, v-M-LEU-160, v-S-LEU-160, v-M-GLU-120 amino acids respectively when compared with Amprenavir, Asunaprevir, Atazanavir, Boceprevir, Cytarabine, Darunavir, ritonavir, Sorivudine, Taribavirin, Tenofovir, Valganciclovir, Vidarabine, Lopinavir, Sofosbuvir, Zanamivir, Penciclovir, Nelfinavir, Merimepodib, Maribavir, Indinavir, Inarigivir, Galidesivir, Famciclovir, and Faldaprevir FDA approved antiviral drugs while targeting the (PDB: 7khp) (Figure S5), (Figure S6), (Figure S7), (Figure S8), (Figure S9A), (PDB: 6WOJ) (Figure S9B), (PDB: 7B3D) (Figure S9C), (PDB: 6M2Q) Figure S9D), (PDB: 6lu7) (Figure S9E), (PDB: 6wzu) (Figure S9F), (PDB: 1XU9) (Figure S9G), (PDB: 3TWU) (Figure S9H), (PDB: 7BEO) (Figure S9I), (PDB: 1XAK) (Figure S9J) protein targets. More precisely, I generally made use of the vector field ∂/∂t which is globally well defined, as the kernel of dz and dz at each point can be viewed as a topological theory of class H.

A Cluster Comparative Docking Analysis between Gisitorviffirna_TM, Roccustyrna_gs, Roccustyrna_fr, DRVYIHPFXmimetic drug designs and the FDA Molnupiravir and Nirmatrelvir, and the Antihypertensive Drugs of Candesartan, Telmisartan, Losartan, Olmesartan, and the Valsartan Drug inside the angiotensin receptor type 1 (AT1R) protein targets.

Increasingly, and since machine learning models have been used for enabling target-based design, predicting on-or off-target effects and creating scoring functions I have shown in this paper that similar Quantum algorithms can be used to transform Quantum Homeopathy Entropy Negativities (QHEN) into waveforms of non-linear functions for the calculation of the Negative Docking Energies (NDE) engaged in the binding domains of the protein targets of the (PDB: 6mq2), (PDB: 6woj), (PDB: 7khp), (PDB: 7b3d), (PDB: 7b3o), (PDB: 6w23), and (PDB: 1xak) respectively (SI Appendix I), (SI Appendix II), (SI Appendix III), (SI Appendix IV), (SI Appendix V), (SI Appendix VI), (SI Appendix VII), (SI Appendix VIII), and (Figure S1), (Figure S2), (Supplementary Material METHODS AND MATERIALS (1), (2)) Figures S(1-16), ((Iconics1-4), (Eqs1-400), and (Schematics1a,1b,1c,1d,1e,1f,1g,1h,1i,1j,1k,1l,1m), (I-VI) Supplementary Material METHODS AND MATERIALS (1), (2)) with the docking energy values of (T. Energy, I. Energy, vdW, Coul, Numrotors, RMSD, Score), (-19.625, -35.483,7.633, -43.116,7, -5.813) KcalmolA, (Tables S(1-4)), (Table S5). The (S) - { [(S) - [(2R,5R,6S) - 6 - [(2S) - 2 - amino - 2 - phenylacetamido] - 3,3 - dimethyl - 7 - oxo - 4 - thia - 1 - azabicyclo [3.2.0] heptane - 2 - carb onyloxy] (hydroxy) λ^3 - oxidanidyli ene - λ^5 - phosphanyl] oxy} ({ [2 - ({ [(3S) - 3 - [(2R) - 2 - [(2S) - 2 - amino - 4 - carbamoylbutanamido] - 4 - carbamoyl-butanamido] - 4,4 - dihydroxybutyl] sulfanyl}methyl) - 6 - oxo - 8Hpurin-9 - yl] oxy}) hydroxy - λ^5 - phosphanyl-

 doi:10.20944/preprints202403.0518.v1

ideneolate Roccustyrna_fr1 chemical structure's main property is its additivity from the two [O1] [O2], ∯G (events that are joint since the probability of disjunction of these events are equals to the sum of the atomistic probabilities when interacted into the binding sites of the protein targets of (PDB: 6w9c), (Figures S(1-5)) with the negative docking energies of the (T. Energy, I. Energy, vdW, Coul, Numrotors, RMSD, Score), (-36.678, -55.648, -7.519, -48.129,7, -6.762) KcalMolA. The same combination of small molecules generated a vector model of probabilistic reasoning for each complex amplitude that gives the probability by the Born's rule which was obtained as the square of the absolute docking values of a generalized complex amplitude that directs the generation of hydrophobic interactions when docked onto the A1, 02J C binding cavities of the amino acid of 168 PRO with the docking energy values of (-3.53, -2369, -1303, -10.425, -3.42, -72.447, -13.394, -3.19, -70.551) KcalmolA. These QMMM Elec. Pure State Systems designed chemical blocks of Quantum thinking small molecules that are given by normalizing vectors of positive semi-definite operators with unit trace mixed states that are additionally involved in the generation of the hydrogen bonding within the PJE: C: 5 (PJE-010) 010: C: 6 Interacting chain (s) while generating hydrophobic interactions when docked into the A6, 010 C binding domains of the amino acid of the 25THR with the docking energy values of (-3.73, -2415,179, -7.156, -21.406, -66.898, -8.709, -22.779) Kcalmol. This combination of DRVYIHPF-mimetic, Gisitorviffirna_TM, Roccustyrna_gs, and Roccustyrna_fr cluster of active pharmacophoric sites of the 2- ({(fluoro ({((2E) -5-oxabicyclo (2.1.0) pentan-2-ylidene) { [(1S,2S,3S) - 2 - (4 - amino - 5 - sulfanylidene - 4H - 1,2,4 - triazol - 3 - yl) - 2 - carboximidoyl - 3 - fluoro - 1 - oxo - 1λ⁵ - pho-sphirane - 1 - yl] amino} [(Z) - ethylideneamino] diamino ({ [1 - ({ [(2S,3R,4R,5R) - 5 - (3 - { [(R) - [(2 - amino - 6 - oxo - 8,9 - dihydro - 1λ⁴,3λ⁴ - purin - 9 - yl) amino] [(6 - fluoro - 3H - 1λ⁴ - pyrazin - 2 - yl) formamido] phosphoryl] carbamoyl} - 1,5 - dihydro - 1,2,4 - triazol - 1 - yl) - 3,4 - dihydroxy-oxolan - 2 - yl] methoxy} (cyano) amino) ethenyl] imino}) methanium imino-methanium cyano-lambda6-sulfanyl}) methyl) phosphorylidene} amino) -4,6-dihydro-1H-purin-6-one N - ({5 - amino - 7 - oxo - 1H,3aH,4H,5H,6H,7aH - pyrrolo [2,3 - c] pyridin - 3 - yl}amino ({4 - [5 - ({cyano [N - (diaminomethyl) carbamimidoyl] methoxy} methyl) - 3,4 - dihydroxy-oxolan - 2 - yl] - 4,5 - dihydro - 3H - imidazol - 2 - yl}methyl) aminophosphoryl) - 6 - fluoro-piperazine - 2 - carboxamide (methylamino) -1,6-diazabicyclo (3.2.0) heptan-4-yl) oxy} imino) interacted into the A6 010C binding cavities of the amino acid of the 26 THR with the docking energy values of (-3.81, -2415, -186, -7.156, -21.406, -66.898, -6.155, -24.392, -64.757) KcalmolA. The combination of the same cluster of active pharmacophoric sites of the 2- ({(fluoro ({((2E) -5-dimethyl-7-oxo-4-thia-1-azabicyclo (3.2.0) heptane-2-carbonyloxy) ({((2-amino-6-oxo-6,9-dihydro-3H-purin-9-yl) oxy) (hydroxy) phosphoryl} oxy) phosphinic acid-ylidene, *cyano (2,6-diazabicyclo*3.1.0, hex-1-oxabicyclo (2.1.0) pentan-2-ylidene) cyano-lambda6-sulfanyl}) methyl) phosphorrylidene} amino) -4,6-dihydro-1H-purin-6 N - { [(2S) - 3 - (aminomethyl) - 2 - [(1R,2S) - 2 - methyl-diaziridin - 1 - yl] - 1,3 - diazetidin - 1 - yl] ({ [(E) - { [(E) - (amino methyl-idene) amino] methylidene} amino] amino}) aziridin - 1 - yl - λ⁵ - phosphanyl} - 3 - {5 - [(1E) - [2 - (aminomethyl) - 2 - methylhydrazin - 1 - ylidene] methyl] - 3,4 - dihydroxyfuran - 2 - yl} - 2 - methyl - 5 - sulfanylidene - 1,2,3,4 - tetrazole - 1 - carboxone-dihydro-3H-purin-9-yl) -3-hydroxy-oxo-an generated a docking space of density operators which is denoted by the space of all linear operators. This docking space effect is denoted by the linear space and the complex Hilbert space that are considered as the scalar product. The linear operators acting there are called superoperators. The dynamics of the pure state of this isolated Quantum system is described by the Schrödinger function and is involved in the generation of hydrogen bonds when docked into the A6 010C binding cavities of the amino acid of 143 GLY with an averaged docking energy value of (-62.905) KcalmolA. In addition, the CoMFA contour map of the electrostatic regions around the (Roccustyrna_fr1-0., Roccustyrna_fr2-0., Roccu-styrna_fr3-1., Roccustyrna_fr4-1., Roccustyrna_fr5-0., Roccustyrna_gs1-1., Roccu-styrna_gs2-1, Roccustyrna_gs3-0., Roccustyrna_gs4-1., Roccustyrna_gs5-1., Ro-ccustyrna_gs6-1., Roccustyrna_gs7-1., and Roccustyrna_gs8-1) chemical structures indicated to me that contact residues from the N - [({ [(S) - {2 - [(1M) - 2 - amino - 9 - [(2R,3R,4R,5S) - 5 - [({ [(E) - (amino-methylidene) amino] methyl} (methyl) amino) methyl] - 3,4 - dihydroxyoxolan - 2 - yl] - 6 - oxo - 5,8 - dihydro - 1λ⁴,3λ⁴ - purin - 7 - yl] - 2 - oxoethyl}amino (1S) - 2,2 - dimethylaziridin - 1 - ylphosphoryl] amino}methoxy) methyl] - 6 - fluoro - 3 - oxo - 5H - 1λ⁴ - pyrazine - 2 - carboxamide Roccustyrna_gs4-

 doi:10.20944/preprints202403.0518.v1

1 ligand when docked onto the SARS-COV-2 protein targets of (PDB: 2zu5), (PDB: 6mq2), (PDB: 6woj), (PDB: 7khp), (PDB: 7b3d), (PDB: 7b3o), and (PDB: 6w23) (SI Appendix II), (SI Appendix III), (SI Appendix IV), (SI Appendix V), (SI Appendix VI), (SI Appendix VII), and (SI Appendix VIII). (PLIP Report8) In advance more calculated predictions of the noncovalent interactions for (PDB: 6nur-Roccustyrna_fr5-0) protein-ligand complexes indicated to me that the contact residues of the N - [({ [(S) - {2 - [(1M,1M) - 2 - amino - 9 - [(2R,3R,4R,5S) - 5 - [({ [(E) - (amino-methylidene) amino] methyl} (methyl) amino) methyl] - 3,4 - dihydroxyoxolan - 2 - yl] - 6 - oxo - 5,8 - dihydro - 1λ⁴,3λ⁴ - purin - 7 - yl] - 2 - oxoethyl}amino (1S) - 2,2 - dimethyl aziridin - 1 - ylphosphoryl] amino}methoxy) methyl] - 6 - fluoro - 3 - oxo-5H - 1λ⁴ - yrazine - 2 - carbo-xamide Roccustyrna_fr5 chemical structure were able of creating (ZN: A: 1001 (ZN) – ION),295, hIS, A,1001, zN, A,8650, zn,1475, n,4,2.18 protein sidechain, 20.88 tetrahedrals, 1,147.890, 165.413, 131.862, 148.660, 167.274, 131.033, zN: A: 1002 (ZN) – ION),487, CYS, A,1002, zN, A,8651, zn,3002, s,5,2.36 protein sidechain,43.36, square. pyramidal, 1,129.135,163.040,140.828,129.033,162.198,143.028 metal complexes when targeted each one amino acid of the amino acid sequence of V-M-ARG-21, v-S-LEU-28, v-M-MET-62, v-S-MET-62, v-M-GLN-63, v-M-LEU-117, v-M-ASN-118, v-S-ASN-118, v-S-ILE-119 with the total binding energy values of the (-96.1) KcalMolA, and binding free energies of (-4.25129, -5.28591, -6.44116, -10.139, -4.55766, -4.81505, -5.84957, -5.63692, -7.08058, -5.16512, -4.15949, -9.8487, -4.77062, -4.72901, -6.7295, -5.82428, -5.35883, -4.2588, -5.37491) KcalmolA respectively (Statue2a). (PLIP Report3), (SI Appendix I), (Figure S(2a-d)) This K-nearest prototype pharmacophoric element named Roccustyrna_gs4-1 implies that the QFT Pure System States evolves unitarily where one parametric group of unitary operators is associated negatively with the Quantum Negative Energy-observables. However, in these Quantum-like SARS-CoV-2 chemical biosystems, the operator has direct coupling with physical energy and behaves as an evolution-generator information descriptor for calculating the generated noncovalent interactions around the (PDB: 5RLD) protein targets when docked into the A5, pJE C2 binding sites of the amino acid sequence of V-M-ARG-569, v-M-LYS-574, v-S-LYS-574, v-M-SER-667, v-S-SER-667, v-S-GLU-672, and V-S-ASN-678 with the total docking energies of (-71.4) KcalMolA, and binding affinity scoring values of (-6.64579, -9.83087, -13.7842, -5.4447, -4.77112, -4.45958, -6.25956) KcalMolA (Statue2f) while building 283, PRO, A,704, pO4, a,3.36,3.98,124.00,8933, o3,1998, o2, -9.519,9.895, -77.228, -8.677,12.349, -80.248 hydrogen bonds,289, SER, A,704, pO4, a,4.09,3.77,125.16,86.74,2038, o3,8935, o3,9152, -11.112,9.433, -75.222, -11.646,8.055, -70.307, -14.360,8.819, -72.816 water Bridges,288, LYS, A,2032,704, pO4, a,3.77 phosphate interactions bonds,8931,8931,8932,8933,8934,8935, -10.871,9.320, -76.799, -9.398,12.746, -77.378, and salt Bridges inside the cav5lrd (2) _KS2_PO4: A: 704 (PO4) Interacting chains: A with the binding energy values of the (-163.07, -153.73, -2408) KcalmolA, in the coupled atoms of the N3 and O2 with the docking energy values of (-12.282, -14.994, -67.123) Kcal/Mol. (PLIP Report2) Noncovalent interactions for (PDB: 5rem-GissitorviffirnaTM9) protein ligand complexes indicated to me furthermore that the (6R) - 6 - [(3S) - 2 - [(1Z) - amino ({1H - 1,3 - benzodiazol - 2 - yl [(3R) - 3 - ethyloxolan - 3 - yl] methylidene}) - λ⁵ - phosphanyl] - 5 - sulfanylidene - 1,2,4 - triazolidin - 3 - yl] - 4 - oxa - 1 - aza-bicyclo [3.1.0] hexane - 3 - thione contact residues interacted with the binding patterns of the 02J: C: 1 (02J) active sites of the amino acid sequence of V-M-PHE-140, v-M-LEU-141, v-M-ASN-142, v-M-HIS-164, v-M-MET-165, v-S-MET-165, v-M-GLU-166, v-S-GLU-166, v-M-GLN-189 onto the cav5rem (1) _T2J_168 PRO, A1, 02J C binding domains with the total docking values of (-96KcalMolA) and binding free energy affinities of (-4.48079, -8.24714, -5.30157, -4.0643, -11.5094, -8.40631, -12.8568, -11.6458, -10.7448) KcalMolA (Statue2e) while generating 298, ARG, A,402, dMS, A,1.87,2.82,160.70,2331, ng,2377, o2,6.985, -0.666, -7.414,9.778, -1.009, -7.533 hydrophobic Interactions,295, ASP, A,2305,2306,402, dMS, A,5.36 sulfonium bonds,2376,6.138, -0.966, -6.224,10.415,2.164, -5.450 salt Bridges, and 8, PHE, A, 60, 61, 62, 63, 64, 65, 402, dMS, A, 4.66, 1.07, false sulfonium bonds, 2376, 6.138, -0.966, -6.224, 8.375, -4.557, -4.278, pi-Cation Interactions with the docking energy values of (-3.53, -2369, -1303, -10.425, -3.42, -72.447, -13.394, -3.19, -70.551) KcalmolA inside the DMS: A: 401 (DMS) Interacting chains: A. (Figure S3a) 85, SER, A, 502, gOL, A, True, 3.33, 3.77, 109.85, false, 2583, o3, 695, o3, -15.032, 80.245, 20.512, -11.744, 80.847, 18.762 hydrogen Bonds, 165, VAL, A, 507, gOL, A, 3.77, 3.32, 111.74, 85.97, 1342, nam, 2601, o3, 2723, 0.276, 71.899, 40.070, 1.264, 75.312, 35.610, 2.859, 73.799, 38.095 water Bridges, 73, hIS, A, 597, 600, 504, pO4, a, 4.50

 doi:10.20944/preprints202403.0518.v1

phosphate interactions, 2589, 2589, 2593, 2590, 2591, 2592, 11.631, 77.428, 17.813, 10.264, 80.389, 14.716 salt Bridges, and 189, CYS, A, 501, zN, A, 2577, zn, 1546, s, 4, 2.28 protein sidechain, 7.16 tetrahedrals, 1, 20.631, 49.524, 41.020, 21.760, 50.606, 42.681 metal complexes were formed inside the D10-C-1099 DMS: A: 402 (DMS), GOL: A: 502 (GOL), GOL: A: 507 (GOL), PO4: A: 503 (PO4), PO4: A: 504 (PO4), and ZN: A: 501 (ZN) – ION Interacting chains: A (PLIP Report7) binding sites were also constructed when the combined pharmacophoric elements of the combination of Gisitorviffirna_TM9, Roccustyrna_gs2-1, and the Roccustyrna_fr2-0 ligands docked inside the cluster of (PDB: 6wzu), (PDB: 6lu7), (PDB: 6mq2), (PDB: 6woj), (PDB: 7khp), (PDB: 7b3d), (PDB: 7b3o), and (PDB: 6w23) protein targets (SI Appendix II), (SI Appendix III), (SI Appendix IV), (SI Appendix V), (SI Appendix VI), (SI Appendix VII), and (SI Appendix VIII)., 283, PRO, A, 704, pO4, a, False, 3.04, 3.78, 133.85, 8960, o3, 6507, o2, -9.675, 10.581, -77.340, -8.805, 12.626, -80.399, and 285, GLY, A, 704, pO4, a, False, 2.25, 3.11, 145.45, true, 6518, nam, 8959, o2, -12.140, 10.727, -77.514, -11.537, 10.695, -80.565, 404, GLN, A, 705, pO4, a, True, 1.67, 2.60, 156.02, true, 7447, nam, 8966, o3, -14.016, 15.833, -77.917, -12.660, 17.840, -78.871, 285, GLY, B, 705, pO4, b, False, 2.84, 3.72, 149.41, true, 2122, nam, 8947, o3, -18.180, 35.901, -21.271, -18.607, 36.051, -17.574, 285, GLY, B, 706, pO4, b, False, 2.97, 3.59, 122.13, 2122, nam, 8953, o3, -20.472, 33.553, -19.358, -18.607, 36.051, -17.574 hydrogen Bonds, 288, LYS, A, 6541, 704, pO4, a, 3.72 phosphate interactions, 8958, 8958, 8962, 8959, 8960, 8961, -10.980, 9.945, -76.923, -9.741, 13.425, -77.402, 288, LYS, A, 6541, 705, pO4, a, 3.87, true phosphate interactions, 8963, 8963, 8964, 8965, 8966, 8967, -13.431, 14.406, -78.057, -9.741, 13.425, -77.402, 443, ARG, A, 7751, 7753, 7754, 705, pO4, a, 4.75 phosphate interactions, 8963, 8963, 8964, 8965, 8966, 8967, -13.431, 14.406, -78.057, -15.407, 10.811, -80.456, 288, LYS, B, 2145, 705, pO4, b, 3.68 phosphate interactions, 8945, 8945, 8946, 8947, 8948, 8949, -17.168, 37.026, -21.134, -15.854, 33.753, -20.088, 288, LYS, B, 2145, 706, pO4, b, 3.92, true phosphate interactions, 8950, 8950, 8954, 8951, 8952, 8953, -19.641, 32.773, -20.309, -15.854, 33.753, -20.088, 443, ARG, B, 3326, 3328, 3329, 706, pO4, b, 4.45, true phosphate interactions, 8950, 8950, 8954, 8951, 8952, 8953, -19.641, 32.773, -20.309, -22.232, 36.015, -18.698 salt Bridges, 404, GLN, B, 706, pO4, b, 3.85, 3.77, 144.90, 135.44, false, 8954, o3, 3021, o2, 9054, -18.251, 32.582, -19.772, -17.534, 30.180, -18.482, -17.768, 29.838, -22.306water Bridges, 505, ALA, B, 701, vW1, b, 3.60, 8930, 3822, -38.110, 40.085, -11.419, -41.441, 41.447, -11.435, 508, LYS, B, 701, vW1, b, 3.81, 8933, 3854, -37.901, 41.882, -12.998, -37.905, 41.876, -16.807 hydrophobic Interactions, 506, tRP, B, 701, vW1, b, 3828, 3829, 3830, 3831, 3832, 4.96, 70.46, 1.65, t, 8929, 8930, 8931, 8933, 8938, 8939, -37.970, 41.433, -11.690, -38.760, 36.898, -9.853, 543, TYR, B, 701, vW1, b, 4110, 4111, 4112, 4113, 4114, 4115, 3.58, 4.07, 1.59, p, 8929, 8930, 8931, 8933, 8938, 8939, -37.970, 41.433, -11.690, -34.882, 39.750, -12.381 pi-Stackings, 50, CYS, A, 701, zN, A, 8955, zn, 4877, s, 4, 2.37 protein sidechains, 11.31 tetrahedrals, 1, -2.515, 70.172, -52.608, -1.591, 68.518, -51.179, 55, CYS, A, 701, zN, A, 8955, zn, 4907, s, 4, 2.21 protein sidechains, 11.31 tetrahedrals, 1, -2.515, 70.172, -52.608, -4.649, 69.932, -53.149, 16, CYS, A, 702, zN, A, 895, zn, 4618, s, 4, 2.34 protein sidechains, 6.41 tetrahedrals, 1, -2.355, 50.541, -62.574, -2.087, 51.579, -60.493, and metal complexes (PLP Report6) were then produced when the GissitorviffirnaTM2 chemical coupled atoms interacted within the (PDB: 5RLG) protein targets against the amino acid list of V-M-PHE-68, v-M-HIS-69, v-M-ARG-127, v-S-PRO-143, v-M-SER-254, v-S-TRP-257 (Statue2b) into the cav5lrg_73N _402 DMS A Ngo2377 O2, pO4: A: 704 (PO4), PO4: A: 705 (PO4), PO4: B: 705 (PO4), PO4: B: 706 (PO4), VW1: B: 701 (VW1), ZN: A: 701 (ZN), ZN: A: 702 (ZN), ZN: A: 703 (ZN) – ION Interacting chains: A&B with the total docking energy values (-54.4) KcalMolA and binding free energies of (-9.33191, -13.1913, -4.53386, -6.098, -7.8376, -5.65001) KcalmolA., 323, hIS, B, 2427, 243, 9000, 6Q5, b, 3.83, carboxylate, 3872, 3874, -17.172, 25.221, 14.372, -14.312, 26.677, 12.288, 323, hIS, A, 518, 521, 9000, 6Q5, a, 3.76, carboxylate, 3839, 3841, -21.295, 21.829, -14.748, -23.391, 19.443, -12.739 salt Bridges (PLP Report 5) were also shown to be involved in the generation of the Sulfonium bonding when GissitorviffirnaTM3 docked inside the cav5x8s_6Q5_DMS A 5.49 binding cavities within the (PDB: 5X8S) amino acid domains (Statue2c) with the total docking energy values of (-93.9) KcalMolA and binding affinity scoring values of (-11.8231, -7.89889, -11.1795, -5.9969, -4.70955, -6.4492, -4.19167) KcalmolA against the peptide binding pocket of V-S-HIS-323, v-M-MET-365, v-S-MET-365, v-M-PHE-377, v-S-PHE-377, v-S-PHE-388, v-M-HIS-479 (SI Appendix XIX)., 5, tRP, A, 101, c8E, A, 3.50, 1041, 41, -21.433, 12.011, 7.926, -18.708, 10.442, 9.452, 11, PHE, E, 101, c8E, A, 3.74, 1037, 920, -19.381, 14.902, 9.440, -15.879, 15.889, 10.300, 15, LEU,

 doi:10.20944/preprints202403.0518.v1

A, 103, c8E, E, 3.79, 1071, 122, -20.010, 23.787, -0.373, -18.286, 21.060, -2.363, 16, LEU, A, 103, c8E, E, 3.93, 1073, 133, -19.760, 25.967, 0.842, -16.500, 24.202, 2.150, 21, VAL, E, 103, c8E, E, 3.68, 1075, 996, -19.816, 28.170, 2.044, -16.512, 29.531, 2.936, 3, LEU, B, 102, c8E, E, 3.72, 1070, 227, -6.883, 3.854, -0.021, -8.696, 3.315, -3.225, 6, iLE, A, 102, c8E, E, 3.88, 1068, 49, -7.107, 6.345, 0.221, -9.758, 6.834, 3.008, 6, iLE, C, 102, c8E, E, 3.74, 1069, 462, -6.183, 5.199, -0.172, -5.409, 7.165, -3.256, 6, iLE, C, 102, c8E, E, 3.72, 1065, 461, -6.044, 9.930, 0.171, -3.588, 9.143, -2.505, 6, iLE, E, 102, c8E, E, 3.70, 1066, 876, -7.027, 8.839, 0.578, -6.956, 8.974, 4.278, 6, iLE, E, 102, c8E, E, 3.68, 1067, 877, -6.315, 7.510, 0.804, -4.773, 6.924, 4.093, 10, LEU, B, 102, c8E, E, 3.86, 1064, 287, -6.771, 11.133, -0.418, -5.699, 11.708, -4.079, 20, iLE, A, 101, c8E, E, 3.68, 1059, 162, -7.481, 28.197, 0.039, -11.115, 27.605, -0.002, 20, iLE, A, 101, c8E, E, 3.92, 1061, 161, -7.295, 30.590, -0.696, -10.778, 29.614, -2.201, 20, iLE, C, 101, c8E, E, 3.88, 1060, 574, -6.531, 29.359, -0.223, -2.788, 29.748, -1.177, 24, LEU, C, 101, c8E, E, 3.96, 1063, 608, -6.697, 33.024, -0.539, -2.792, 33.623, -0.260 hydrophobic Interactions (PLP Report4) within the GissitorviffirnaTM7 small molecule's whole residue subsurface were also constructed within the amino acid sequence of V-M-GLU-14, v-M-GLY-15, v-M-MET-17, v-M-ALA-70, v-M-GLY-71, v-S-ASN-95, v-S-PRO-96, v-S-LYS-97 inside the Interacting chains: A, B, C of the D402 DMS A, C8E: E: 102 (C8E), and C8E: E: 103 (C8E) pharmacophoric sites while targeting to the (PDB: 6MQ2) protein targets with the total docking energy values of (-90.7) KcalMolA, and binding affinity energy values of (-5.54671, -6.69992, -6.79962, -9.08665, -7.04715, -5.91789, -5.46872, -9.46214) KcalMolA (Statue2d). (Figure S3b), 168, PRO, A, 1, 02J, C, 3.53, 2369, 1303, -10.425, 3.420, 72.447, -13.394, 3.190, 70.551, 25, THR, A, 6, 010, c, 3.73, 2415, 179, -7.156, 21.406, 66.898, -8.709, 22.779, 70.002, 26, THR, A, 6, 010, c, 3.81, 2415, 186, -7.156, 21.406, 66.898, -6.155, 24.392, 64.757 hydrophobic Interactions and 164, hIS, A, 5, pJE, C, 2.16, 3.07, 153.73, false, 2408, n3, 1266, o2, -12.282, 14.994, 67.123, -15.161, 15.336, 68.144, and 166, GLU, A, 5, pJE, C, 2.61, 3.38, 135.52, false, 2405, nam, 1289, o2, -11.386, 11.531, 63.232, -12.536, 8.469, 62.363 hydrogen Bonds were simultaneously generated by the Gissitorviffirna_TM8 {1 - [(R) - [(1S, 3R) - 3 - [(R) - amino (carbamothioylamino) methyl] diaziridin - 1 - yl] ({6 - oxo - 2 - [(2S, 5R) - 3, 4, 5 - trifluoro - 2, 5 - dihydrofuran - 2 - yl] - 6, 7 - dihydro - 1H - purin - 8 - yl}amino) phosphoroso] - 1H - azirin - 2 - yl}thiourea and the Roccustyrna_gs8-1 diamino ({ [1 - ({ [(2S, 3R, 4R, 5R) - 5 - (3 - { [(R) - [(2 - amino - 6 - oxo - 8, 9 - dihydro - 1λ^4, 3λ^4 - purin - 9 - yl) amino] [(6 - fluoro - 3H - 1λ^4 - pyrazin - 2 - yl) formamido] phosphoryl] carbamoyl} - 1, 5 - dihydro - 1, 2, 4 - triazol - 1 - yl) - 3, 4 - dihydroxyoxolan - 2 - yl] methoxy} (cyano) amino) ethenyl] imino}) methanium chemical residues when in parallel docked into the cluster of (PDB: 6mq2), (PDB: 6woj), (PDB: 7khp), (PDB: 7b3d), (PDB: 7b3o), (PDB: 6w23), and (PDB: 6lu7) protein targets (PLP Report), (SI Appendix II), (SI Appendix III), (SI Appendix IV), (SI Appendix V), (SI Appendix VI), (SI Appendix VII), and (SI Appendix VIII) inside the D10-H-1099 X77: A: 401 (X77) conserved side domains within the active sites of the amino acid cavities of the 41 HIS A 401 X77 A, 165 MET A 401 X77 A, and 166 GLU A 401 X77 A with the docking energy values of (-3.75, -4670, -609, -20.444, -13.613, -29.034, -19.778, -13.574, -32.721-3.90, -4673, -2529, -19.389, -17.775, -28.688, -16.611, 16.152, -26.489, -3.86, -4661, -2546, -17.350, -23.138, -25.438-16.439, -20.244, -23.055, -18.9, -3.90, -4657, -2881, -21.763, -15.894, -23.429, -24.934, -13.635, -23.312) KcalmolA showing that my AI-Quantum thinking chemical structures named Roccustyrna_fr are capable of generating Hydrogen Bonds when docked onto the 41 HIS A 401 X77 A, 143 GLY A 401 X77 A, 144 SEr A 401 X77 A, and 166 GLU A 401 X77 A sequence of amino acid residues while targeting the Npl 4680 N2, o3 4679 N2 Nam 4682 O2, and Nam 4683 O2 binding sites with the binding free energy values of the (-3.46, -3.79, -106.13, -611, -20.860, -19.573, -32.52, -19.394, -16.086, -32.767, -2.17, -2.94, -148.03, -2216-19.635, -22.244, -29.036, -18.779, -24.455, -30.773, -3.14, -3.42, -101.78, -2228-16.096, -21.679, -26.816, -14.503, -23.707, -29.056, -1.98, -2.80, -158.32, -2542-18.546, -18.654, -26.028-16.172, -18.348, -24.583) KcalmolA respectively. (Figure S3c) The 2- ({(fluoro ({((2E) -5-oxabicyclo (2.1.0) pentan-2-ylidene) cyano-lambda6-sulfanyl}) methyl) phosphor-rylidene} amino) -4, 6-dihydro-1H-purin-6- (2S, 3S) - 3 - ({ [(1 - { [(3R) - 2 - (dimethylamino) - 3 - [(R) - hydroxy (2R) - oxiran - 2 - ylmethyl] - 2λ^5 - oxaphosphiran - 2 - yl] methyl}hydrazin - 1 - yl) methyl] amino} methyl) oxirane - 2 - carbonitrile one (1Z) -2-{((2S, 3S, 5r) -5- (2-amino- [2 - (aminomethyl) - 2 - { [(2E) - 3 - oxofuran - 2 - ylidene] methyl} - 2λ^5 - azaphosphiridin - 1 - yl] amino (1R, 4S) - 3, 3 - dimethyl - 6 - oxo - 2λ^4 - thia - 5 - aza spiro [bicyclo [3.2.0] heptane - 2, 1' - thiirane] - 4 - carboxylate 6-oxo-6, 9-dihydro-1H-purin-9-yl) -3-hydro-xyoxolan-

 doi:10.20944/preprints202403.0518.v1

2-yl) methylidene}- (Z) - 4 - amino - N - [(1Z) - amino-methyl-idene] - N' - [(Z) - 2 - {6 - [(1Z) - [(fluoromethyl) imino] methyl] - 3 - sulfanylidene - 1, 2, 4 - triazabicyclo [3.1.0] hex - 2 - en - 6 - yl} - N' - methyl ethanimidamido] - 2 - oxobutanimidamide 2-cyano-1- ({((2S, 4r, 5r) -2-methyl-2-(methylamino) -1, 6-diazabicyclo (3.2.0) heptan-4-yl) oxy} imino) -1lambda5, 2lambda5-azaphosphiridin-1-ylium druggable scaffold of the Roccustyrna_gs, and the Roccustyrna _fr small molecule library therefore competes with endogenous SARS-CoV2 PLpro for binding to LYS711 and ARG355 targeting into the binding domains of the critical SARS-CoV2 PLpro residues onto the SARS-COV-2 protein targets of (PDB: 2zu5) within the binding sites of the amino acid of the V-M-THR-25, v-S-THR-25, v-M-THR-26, v-S-HIS-41, v-M-LEU-141, v-M-ASN-142, v-S-ASN-142, v-M-GLY-143, v-S-CYS-145, v-M-MET-165 with the binding energy values of the (-97.2 and-5.16512, -4.15949, -9.8487, -4.77062, -4.72901, -6.7295, -5.82428, -5.35883, -4.2588, -5.37491) KcalmolA respectively. CoMFA analysis of electrostatic regions around the Roccustyrna_gs, and the Roccustyrna_fr small scale chemical libraries indicated to us that Hydrogen bonds, salt Bridges, and Metal complexes containing Diphosphate, dihydrogen and ION binding sites were generated into the Roccustyrna_gs6-1.{ [(1S, 2S, 3S) - 2 - (4 - amino - 5 - sulfanylidene - 4H - 1, 2, 4 - triazol - 3 - yl) - 2 - carboximidoyl - 3 - fluoro - 1 - oxo - 1λ^5 - phosphiran - 1 - yl] amino} [(Z) - ethylideneamino] iminomethanium contact residues of the Roccustyrna_gs, and the Roccustyrna_fr6-1 small molecule when docked onto the SARS-COV-2 protein targets of the (PDB: 2zu5), (PDB: 6mq2), (PDB: 6woj), (PDB: 7khp), (PDB: 7b3d), (PDB: 7b3o), and (PDB: 6w23) within the consensus sequence of the amino acids of V-M-THR-25, v-S-THR-25, v-M-THR-26, v-S-HIS-41, v-M-LEU-141, v-M-ASN-142, v-S-ASN-142, v-M-GLY-143, v-S-CYS-145, v-M-MET-165 with the negative docking values of (-97.2, -5.16512, -4.15949, -9.8487, -4.77062, -4.72901, -6.7295, -5.82428, -5.35883, -4.2588, -5.37491) KcalmolA respectively (SI Appendix), (SI Appendix II), (SI Appendix III), (SI Appendix IV), (SI Appendix V), (SI Appendix VI), (SI Appendix VII), and (SI Appendix VIII). (Figure S4a), (Tables S(1-4)), (Table S5) DMS: A: 402 (DMS) binding sites into the 524 Nam 2578 O2 02J (5-Methylisoxazole-3-carboxylic acid) domains were generated inside the 65 ASN A 402 DMS A cavities when the Roccustyrna_gs5-1. (2R) - 2 - [(2R) - 2 - amino - 4 - [({ [(2S) - 2 - [(2R, 4R, 5S) - 2 - amino - 3 - {2 - [(1R, 2S, 3S, 4R, 5S) - 2, 3 - dihydroxy - 5 - methyl - 4 - ({methyl [(methylideneamino) methyl] amino} methyl) cyclopentyl] - 3H - 1λ^2, 2, 4 - triazole - 5 - carbonyl} - 6 - oxo - hexahydropurin - 1 - yl] propyl] amino}methyl) carbamoyl] butanamido] - N - [(2S) - 1, 1 - dihydroxy - 4 - (methylsulfanyl) butan - 2 - yl] pentanediamide and the Roccustyrna_gs4-1 N - [({ [(S) - {2 - [(1M) - 2 - amino - 9 - [(2R, 3R, 4R, 5S) - 5 - [({ [(E) - (amino-methylidene) amino] methyl} (methyl) amino) methyl] - 3, 4 - dihydroxyoxolan - 2 - yl] - 6 - oxo - 5, 8 - dihydro - 1λ^4, 3λ^4 - purin - 7 - yl] - 2 - oxoethyl}amino (1S) - 2, 2 - dimethylaziridin - 1 - ylphosphoryl] amino}methoxy) methyl] - 6 - fluoro - 3 - oxo - 5H - 1λ^4 - pyrazine - 2 - carboxamide contact residues of the Roccustyrna_gs, and the Roccustyrna_fr drug designs interacted with the (PDB: 6mq2), (PDB: 6woj), (PDB: 7khp), (PDB: 7b3d), (PDB: 7b3o), (PDB: 6w23), and (PDB: 6lu7) protein targets with the docking energy values of (-2.05, -2.94, -148.0, -8.211, -20.857, -29.787, -11.058, -20.242, -30.160, -298) KcalmolA (SI Appendix), (SI Appendix II), (SI Appendix III), (SI Appendix IV), (SI Appendix V), (SI Appendix VI), (SI Appendix VII), and (SI Appendix VIII). Salt Bridges were also constructed when My [amino ({4 - [(2R, 3R) - 2 - [(2S) - 3 - { [(1S, 2S) - 1 - { [(S) - 1, 3 - dihydroisoindole - 2 - carbonyl [(2 - methyl - 6 - oxo - 1, 7 - dihydropurin - 8 - yl) methyl] phosphanyl] carbamoyl} - 2 - methylbutyl] amino} - 2 - methylpropyl] oxaziridin - 3 - yl] butyl}amino) methylidene] azanium prototype's surface sidechains docked inside the DMS-A, Ngo2582 O2 binding pocket cavities of the amino acid of the ARG A 403 with the docking energy values of (-1.93, -2.87, -160.38, -2512, -7.044, -0.753, -7.469, -9.865, -1.270, -7.327) Kcalmol/A. Sulfonium bondings were also constructed when My [amino ({4 - [(2R, 3R) - 2 - [(2S) - 3 - { [(1S, 2S) - 1 - { [(S) - 1, 3 - dihydroisoindole - 2 - carbonyl [(2 - methyl - 6 - oxo - 1, 7 - dihydropurin - 8 - yl) methyl] phosphanyl] carbamoyl} - 2 - methylbutyl] amino} - 2 - methylpropyl] oxaziridin - 3 - yl] butyl}amino) methyl idene] azanium small molecule interacted within the 403 DMS A contact residues of the binding sites of the 295 ASP amino acid with the docking energy values of (-5.31, -2581, -6.227, -1.042, -6.293, -10.460, -2.019, -5.344) Kcalmol/A. (Figure S4b) 999 ZN D 20947 Zn, ZN: A: 998 (ZN), and 998 Zn 470 S Metal Complexes were also constructed into the 02J (5-Methylisoxazole-3-carboxylic acid) PJE-C 5 residues when the Roccustyrna_gs, and the Roccustyrna_fr's chemical

 doi:10.20944/preprints202403.0518.v1

fragment of (1Z) -2-{((2S, 3S, 5r) -5- (2-amino-6-oxo-6, 9-o-6-fluoro-3, 4-dihydropyrazine-2-carboxamide (7aR) -5-amino-N-* (S) -, 2-* (3-oxabicyclo (2.1.0) (1S, 4S) -5-oxabicyclo*2.1.0-pentan-2 ((2S, 5R, 6R) -6- ((2S) -2-amino-2-phenylacetamido) -3, 3-dihydro-1H-purin-9-yl-4-yl) oxy}-imino) -1lambda5, 2-lambda5-azaphosphiridin-1-ylium generated tetrahedral side chains inside the117 CYS D and 74 CYS A amino acids with the docking energy values of (-1103.746, -101.848, -13.968, -103.306, -102.613, -1118.874, -104.964, -32.313-118.938, -103.573, -30.6090 KcalmolA indicating that My [amino ({4 - [(2R, 3R) - 2 - [(2S) - 3 - { [(1S, 2S) - 1 - { [(S) - 1, 3 - dihydroisoindole - 2 - carbonyl [(2 - methyl - 6 - oxo - 1, 7 - dihydropurin - 8 - yl) methyl] phosphanyl] carbamoyl} - 2 - methylbutyl] amino} - 2 - methylpropyl] oxaziridin - 3 - yl] butyl} amino) methylidene] azanium multi-targeted drug design has the ability of generating a self-assembled monolayer inside the1: Mg, NA (1), 1, 10P, G Metal Complexes when docked onto the1, 553A binding cavities of the amino acid of the ARG into the (PDB: 7bv2) protein targets. The combination of DRVYIHPF-mimetic, Gisitorviffirna_TM, Roccustyrna_gs, and Roccustyrna_fr cluster of pharmacophoric active site of (1Z) -2-{((2S, 3S, 5r) -5- (2-amino-6-2-yl) methylidene}-2-cyano-12- ({(fluoro ({((2E) -5-oxabicyclo (2.1.0) pentan-2-ylidene) cyano-lambda6-sulfanyl}) methyl) phosphorylidene} amino) -4, 6-dihydro-1H-purin-6-one- (Z) - 4 - amino - N - [(1Z) - (1S, 3S, 7R) - 7 - amino - 1 - [(R) - {3 - sulfanylidene - 2, 4, 6 - triazabicyclo [3.1.0] hexa - 1, 4 - dien - 6 - yl} [(E) - 2 - [(3R) - 3 - [(2R, 5R) - 3, 4, 5 - trifluoro - 2, 5 - dihydrofuran - 2 - yl] - 3H - 1, 2, 4 - triazol - 5 - yl] diazen - 1 - yl] phosphoroso] - 1, 2, 4, 6 - tetraazaspiro [2.4] heptane - 5 - thione (2R, 4R, 5S) - 2 - amino - 3 - {4 - amino - 1 - [(2R, 3R, 4R, 5R) - 5 - [(2R) - 3 - (aminomethyl) - 2 - (2 - methyl-diaziridin - 1 - yl) - 1, 3 - diazetidin - 1 - yl] - 3, 4 - dihydroxyoxolan - 2 - yl] - 5 - sulfanylidene - 4, 5 - dihydro - 1H - 1, 2, 4 - triazole - 3 - carbonyl} - 1 - [(2S) - 1 - [(3R) - 2 - amino - 1 - methyl - 5 - sulfanylidene - 1, 2, 4 - triazolidin - 3 - yl] propan - 2 - yl] - octahydro - 1H - purin - 6 - one amino-methyl idene] - N' - [(Z) - 2 - {6 - [(1Z) - [(fluoromethyl) imino] methyl] - 3 - sulfanylidene - 1, 2, 4 - triaza-bicyclo [3.1.0] hex - 2 - en - 6 - yl} - N' - methylethanimidamido] - 2 - oxobutanimidamide ({((2S, 4r, 5r) -2-methyl-2-(methylamino) -1, 6-dia-zabicyclo (3.2.0) heptan-4-yl) oxy} imino) -1lambda5, 2lambda5-azaphosphiridin-1-ylium of the Gissitorviffirna_TM0 N - { [(2S) - 3 - (aminomethyl) - 2 - [(1R, 2S) - 2 - methyldiaziridin - 1 - yl] - 1, 3 - diazetidin - 1 - yl] ({ [(E) - { [(E) - (aminomethylidene) amino] methyl-idene}amino] amino}) aziridin - 1 - yl - λ^5 - phosphanyl} - 3 - {5 - [(1E) - [2 - (aminomethyl) - 2 - methylhydrazin - 1 - ylidene] methyl] - 3, 4 - dihydroxyfuran - 2 - yl} - 2 - methyl - 5 - sulfanylidene - 1, 2, 3, 4 - tetrazole - 1 - carboxa2-lambda5-azaphosphiridin-1-ylium is represented here by a Hermitian operator with discrete Schrödinger's Dynamics for it's pure states implying that the Dynamics of mixed states represented by a density operator can be described by the von Neumann function when engaging in hydrogen bonding interactions for the formation of 285 GLY. A, 705, pO4, a, False, 3.11, 3.92, 139.77, 2009, nam, 8938, o3 binding sites of (-11.823, 14.311, -78.571, -11.528, 11.025, -80.682, 404, GLN, A, 705, pO4, a, 1.86, 2.83, 166.54, 2938, nam, 8939, o3, -13.630, 15.838, -77.672, -12.632, 17.988, -79.209, 404, GLN, A, 705, pO4, a, True, 3.21, 3.82, 122.94, 8939, o3, 2937, o2, -13.630, 15.838, -77.672, -10.621, 17.175, -79.613, 404, GLN, A, 705, pO4, a, 2.52, 3.28, 134.34, false, 8938, o3, 2937, o2, -11.823, 14.311, -78.571, -10.621, 17.175, -79.613, 538, GLY, A, 705, pO4, a, 2.52, 3.11, 117.55, true, 3978, nam, 8939, o3, -13.630, 15.838, -77.672, -16.553, 16.235, -76.702) KcalMolA. Hydrogen bonds inside the N3 1266 O2 binding cavities within the amino acid sequence of V - S - HIS - 159, v - S - ARG - 160, v - S - ARG - 112 V - M - GLU - 148 V - M - PHE - 150, v - S - PHE - 150, v - S - HIS - 159, and V - M - TYR - 161 were also constructed here with the docking energy values of (-1.93, -2.80, -145.29, -1105, -3.81, -2415, -186, -7.156, -21.406, -66.898-6.155, -24.392, -64.757, -2411, -8.911, -17.849, -65.703-8.918, -17.918, -62.905, -2.16, -3.07, -153.73, -2408, -12.282, -14.994, -67.123, -15.161, -15.336, -68.144) Kcalmol. The Roccustyrna_gs and the Roccustyrna_fr generated Gissitorviffirna_TM2 [2 - (aminomethyl) - 2 - { [(2E) - 3 - oxofuran - 2 - ylidene] methyl} - 2λ^5 - aza-phosphiridin - 1 - yl] amino (1R, 4S) - 3, 3 - dimethyl - 6 - oxo - 2λ^4 - thia - 5 - azaspiro [bicyclo [3.2.0] heptane - 2, 1' - thiirane] - 4 - carboxylate small molecules involved also in the generation of the hydrophobic interactions within the binding domains of the amino acid sequence of V - M - LYS - 557, v - S - LYS - 557, v - M - ARG - 567, v - M - ASP - 568, v - S - ASP - 574, v - S - PHE - 43, v - M - ARG - 44, v - M - SER - 45, v - S - SER - 45 with the docking energy values of (-3.73, -2415, -179, -7.156, -21.406, -66.898-8.709, -22.779) KcalmolA as illustrated in the (Figure S4c), (SI Appendix I). In this drug designing project the

 doi:10.20944/preprints202403.0518.v1

electrostatic regions around the combination of DRVYIHPF-mimetic, Gisitorviffirna_TM, Roccustyrna_gs, and Roccustyrna_fr conserved pharmacophoric elements of (7ar) - (1S, 3S, 7R) - 7 - amino - 1 - [(R) - {3 - sulfanylidene - 2, 4, 6 - triazabicyclo [3.1.0] hexa - 1, 4 - dien - 6 - yl} [(E) - 2 - [(3R) - 3 - [(2R, 5R) - 3, 4, 5 - trifluoro - 2, 5 - dihydrofuran - 2 - yl] - 3H - 1, 2, 4 - triazol - 5 - yl] diazen - 1 - yl] phosphoroso] - 1, 2, 4, 6 - tetraazaspiro (2R, 4R, 5S) - 2 - amino - 3 - {4 - amino - 1 - [(2R, 3R, 4R, 5R) - 5 - [(2R) - 3 - (aminomethyl) - {1 - [(R) - [(1S, 3R) - 3 - [(R) - amino (carbamothioylamino) methyl] diaziridin - 1 - yl] ({6 - oxo - 2 - [(2S, 5R) - 3, 4, 5 - trifluoro - 2, 5 - dihydrofuran - 2 - yl] - 6, 7 - dihydro - 1H - purin - 8 - yl}amino) phosphoroso] - 1H - azirin - 2 - yl}thiourea 2 - (2 - methyldiaziridin - 1 - yl) - 1, 3 - diazetidin - 1 - yl] - 3, 4 - dihydroxy-oxolan - 2 - yl] - 5 - sulfanyl-idene - 4, 5 - dihydro - 1H - 1, 2, 4 - triazole - 3 - carbonyl} - 1 - [(2S) - 1 - [(3R) - 2 - amino - 1 - methyl - 5 - sulfanylidene - 1, 2, 4 - triazolidin - 3 - yl] propan - 2 - yl] - octahydro - 1H - purin - 6 - one [2.4heptane - 5 - thione 5-amino-N- ((S) -{2- ((S) - ((E) - (amino-methylidene) amino) (cyano) methyl) hydrazin-1-yl} (aziridin-1-yl) phosphoryl) -1- ((2E) -2- ((fluoro-methanimidoyl) imino) acetyl) -7-oxo-1H, 7H, 7aH-pyrazolo (4, 3-d) pyrimidine-3-carboxamide; N-{((2-amino-6-oxo-6, 9-dihydro-1H-purin-9-yl) amino) ({1- (5-({(cyano ({1- ((diamino methylidene) amino) ethenyl}) amino) oxy} methyl) -3, 4-dihydroxyoxolan-2-yl) -1H-1, 2, 4-triazol-3-yl} (formamido) phosphoryl}-6-fluoro-3, 4-dihydropyrazine-2-carboxamide; (3- (2-amino-5-sulfanylidene-1, 2, 4-triazolidin-3-yl) oxaziridin-2-yl) ({3-sulfanylidene-1, 2, 4, 6-tetraaza bicyclo (3.1.0) hexan-6-yl}) phosphoros [ΦˆK (ADS5R) † (o1/7x)] - (3, 4, 5-trifluorooxolan-2-yl) -1H-1, 2, 4-triazole-3-carboxylate 3-hydroxyoxolan-2-yl) -methylidene}-2-cyano-1- ({((2S, 4r, 5r) - 2-methyl-2- (methyl-amino) -1, 6-diazabicyclo (3.2.0) heptan-4-yl) oxy} imino) -1lambda5, 2-lambda5-(1S, 5S) - 4 - [(2R, 3S) - 3 - [(3R) - 2 - amino - (6R) - 6 - [(3S) - 2 - [(1Z) - amino ({1H - 1, 3 - benzodiazol - 2 - yl [(3R) - 3 - ethyloxolan - 3 - yl] methylidene}) - λ^5 - phosphanyl] - 5 - sulfanylidene - 1, 2, 4 - triazolidin - 3 - yl] - 4 - oxa - 1 - azabicyclo [3.1.0] hexane - 3 - thione (Z) - 4 - amino - N - [(1Z) - amino-methylidene] - N' - [(Z) - 2 - {6 - [(1Z) - [(fluoro-methyl) imino] methyl] - 3 - sulfanylidene - 1, 2, 4 - triazabicyclo [3.1.0] hex - 2 - en - 6 - yl} - N' - methyl-ethanimidamido] - 2 - oxobutanimidamide 1 - fluoro - 5 - N - { [(2S) - 3 - (amino-methyl) - 2 - [(1R, 2S) - 2 - methyl-diaziridin - 1 - yl] - 1, 3 - diazetidin - 1 - yl] ({ [(E) - { [(E) - (amino-methylidene) amino] methylidene} amino] amino}) aziridin - 1 - yl - λ^5 - phosphanyl} - 3 - {5 - [(1E) - [2 - (aminomethyl) - 2 - methylhydrazin - 1 - ylidene] methyl] - 3, 4 - dihydroxyfuran - 2 - yl} - 2 - methyl - 5 - sulfanylidene - 1, 2, 3, 4 - tetrazole - 1 - carboxasulfanylidene - 3H - 1, 2, 4 - triazol - 3 - yl] oxiran - 2 - yl] - 4, 5, 6 - triaza - 2λ^5 - phosphaspiro [bicyclo [3.1.0] hexane - 2, 2' - oxaphosphirane] - 3 - thione aza-phosphiridin- [2 - (amino-methyl) - 2 - { [(2E) - 3 - oxofuran - 2 - ylidene] methyl} - 2λ^5 - aza-phosphiridin - 1 - yl] amino (1R, 4S) - 3, 3 - dimethyl - 6 - oxo - 2λ^4 - thia - 5 - azaspiro [bicyclo [3.2.0] heptane - 2, 1' - thiirane] - 4 - carboxylate 1-ylium (Figure S4d), (Figure S4e) showing that the combination of DRVYIHPF-mimetic, Gisitorviffirna_TM, Roccustyrna_gs, and Roccustyrna_fr binding sites hit the (PDB: 6lu7) binding domains of the 02J: C: 1 (02J) regions while co-generating Hydrophobic Interactions and Hydrogen Bonds against the coupled atoms of the Nam 2411 O3 inside the cavities of these crucial entering amino acids of the 25 THR A 6 010 C and 143 GLY A 6 010 C with the averaged docking energy values of (-3.73, -2415, -179, -7.156, - 21.406, -66.898, -8.709, -22.779, -70, -26, -81, -2415, -186, -7.156, -21.406, -66.898, -6.155, -24.392, -64.757, -1.93, -2.80, -145, -29, -1105, -8.911, - 17.849, -65.703, -8.918, -17.918, -62.905) KcalmolA respectively. Electrostatic CoMFA analysis of the contact residues of the best docking poses of the contact chemical residues indicated also that the entire Roccustyrna_gs, and the Roccustyrna_fr chemical structure surfaces when docked onto the aligned SARS-COV-2 protein targets of (PDB: 6mq2), (PDB: 6woj), (PDB: 7khp), (PDB: 7b3d), (PDB: 7b3o), (PDB: 6w23), and (PDB: 3fqq) (Statue1a), (SI Appendix V), (SI Appendix VI), (SI Appendix VII), (SI Appendix VIII), (SI Appendix IX), (SI Appendix XVIII), (SI Appendix X), (SI Appendix XI), (SI Appendix VIII), (SI Appendix VIII), (SI Appendix XII), (SI Appendix XIII), (SI Appendix IX), (SI Appendix XIV), (SI Appendix XV), (SI Appendix XVI), (SI Appendix XVII), (SI Appendix XVIII), (SI Appendix XIX), (SI Appendix XX), (SI Appendix XXI), (SI Appendix XXII), (SI Appendix XXIII), (SI Appendix XXIV), (SI Appendix XXV) (SI Appendix XXVI), (SI Appendix XXVII). (SI Appendix XXVIII), (SI Appendix XXIX), (SI Appendix XXX), (SI Appendix XXXI), (SI Appendix XXXII), (SI Appendix XXXIII), (SI Appendix XXXIV), (SI Appendix XXXV), (SI Appendix XXXVI), (SI Appendix XXXVII), (SI Appendix XXXV), (SI Appendix

 doi:10.20944/preprints202403.0518.v1

XXXVI), (SI Appendix XXXVII), (SI Appendix XVIII), ((Cluster Docking Energy TableS1), (SI Appendix I), (Cluster Docking Energy TableS2), SI Appendix I), (Docking Energy TableS1), (SI Appendix I), (Docking Energy TableS2), (SI Appendix I), (Docking Energy TableS3), (RoccustyrnaTM_PATHS 01-13), (SI Appendix I)) generated the positively charged SARS - CoV Mpro - N1 groups and SARS - CoV Mpro - N3 regions favored by negatively charged groups within the amino acid sequence of the V-S-HIS-159, v-S-ARG-16, v-S-ARG-112, v-M-GLU-148, v-M-PHE-15, v-S-PHE-15, v-S-HIS-159, v-M-TYR-161 with an averaged total docking energy value of (-101), and scoring affinities (-14.0762, -5.11094, -7.98447, -4.17314, -4.43549, -9.66939, -9.42926, -7.32) KcalmolA respectively. Several hydrogen bonding interactions were also built between SARS-CoV-2 main protease (Mpro) (PDB: 7nij) protein targets by the same combination of the RoccustyrnaTM_gs_ convs_1.b7cca856fc, and the RoccustyrnaTM _gs_convs_2.8e15f79d30 ligand conformers with the docking values of (Affinity, Total Energy, vdW Energy Elec. Energy) KcalMolA, (-4.582, -24.675, -0.006, 0.314) KcalMolA, and (-4.917, -102.012, -0.308, -0.183) KcalMolA respectively as a novel conformational state (SI Appendix XXXI). The crystal structure of Papain-Like Protease of SARS CoV-2, p3221 space group is an attractive target because it plays an essential role in cleavage and maturation of viral polyproteins, activates the replicase-transcriptase complex for the disruption of host responses. Other noncovalent intermolecular interactions at the boundary of both proteins involved in polar hydroxyl or carbonyl (C, O) groups with polar amino acid residues such as ARG, ASP, and GLU in either protein targets revealed to me that this combination of RoccustyrnaTM_gs_convs_ 1.c359152ed8 and RoccustyrnaTM_gs_convs_ 2.6f9df35049 conformers were able of co-generating binding affinity and docking values of (Affinity, Total Energy, vdW Energy, Elec. Energy) of (-4.830, -86.676, 0.113) KcalMolA, and (-4.657, -28.226, 0.036) KcalMolA respectively inside the (PDB: 6WZU) protein targets (SI Appendix XXXIV). Aromatic functionality and hydrophobic alkyl chains in the RoccustyrnaTM_gs_ convs_2.617493ae06, and RoccustyrnaTM_ gs_convs_1.dafeb75bd0 conformer ligands are observed to be interacted also with the aromatic PHE, TYR, and HIS amino acids, and with the hydrophobic ALA VAL, LEU and Ile side chains of either the Crystal Structure of the mutant Human ROR gamma Ligand Binding Domains in combination with the Ursolic acid (PDB: 5x8s) small molecule, respectively with the binding affinity values (Affinity, Total Energy, vdW Energy, Elec. Energy) of (-4.883, -101.715, -0.045, -0.082) KcalMolA, and (-4.585, -25.145, -0.006, -0.155) KcalMolA with a potential role for directly controlling the differentiation of Th17 cell and for the production of interleukin-17 that plays an integral role in autoimmune diseases (SI Appendix XXVIII), (SI Appendix XXXV). The Crystal Structure of SARS-CoV-2 helicase in complex with the Z19739650 (PDB: 5rlg) is also targeted by my RoccustyrnaTM_ gs_convs_ 2.1048f4616c and RoccustyrnaTM_ gs_convs_1.dafeb75bd0 ligands in this research article with the binding affinity and docking energy values of (Affinity, Total Energy, vdW Energy, Elec. Energy) of (-4.933, -102.284, -0.464, -0.238) KcalMolA, and (-4.636, -26.339, -0.390, -1.326) KcalMolA, respectively (SI Appendix XXXII). More specifically, the Crystal Structure of SARS-CoV-2 helicase in complex with Z235341991 (PDB: 5rlf) protein targets were also interacted with the same small molecule combination of RoccustyrnaTM_ gs_convs_ 1.4ac5543646 and RoccustyrnaTM_ gs_convs_ 2.54b4ef35cf conformer ligands with the total binding affinity and docking energy values of (Affinity, Total Energy, vdW Energy, Elec. Energy) of (-4.955, -101.280, -0.520, -0.1590) KcalMolA, and (-4.657, -26.459, -0.405, -1.310) KcalMolA respectively (SI Appendix XXII). Atomic structures of the Omicron spike protein in complex with three classes of antibodies that were active against all five variants of concern were also uploaded in the DockThor webserver in the form of a. pdb file. An In-silico Multi-Covalent Inhibitory effect that may alter the local conformation at the SARS-CoV-2 Omicron variant spike RBD in complex with Fab XGv282 (PDB: 7wlc) binding interfaces generated here with the docking values of (Affinity, Total Energy, vdW Energy, Elec. Energy), (-1.087, -23.304, -0.087) KcalMolA, and of (-1.016, -101.602, -0.001) KcalMolA binding affinity and total docking energies which was also reported when the neutralized RoccustyrnaTM_ gs_convs_ 1.2d844d7d75 and RoccustyrnaTM_ gs_convs_2.2ba0c330b4 ligand determinants targeting the key antibody G446S escape site that confers greater resistance to a class of antibodies on the right shoulder of the receptor-binding domains. These affinity predictions and rankings of distinct ligands were performed with

 doi:10.20944/preprints202403.0518.v1

the linear model and DockThor scoring function. To increase the accuracy 30 runs were made with 106 evaluations per run. As is usually done, all the water molecules were removed and the PDB files were separated into two different files, one containing the protein and the other containing the ligand structure. All the molecular force field parameterizations were performed automatically by the programs cited. The remaining settings, conditions and parameters offered by the program were used in the default mode The binding interaction of RoccustyrnaTM_ gs_convs_1.2d844d7d75 and RoccustyrnaTM_ gs_convs_2,2d1105f87c neo-ligand conformers with the (PDB: 5rld) protein targets inside the Crystal Structure of SARS-CoV-2 helicase in complex with Z1429867185 (PDB: 5rle) binding domains revealed three hydrogen bonds with three amino acids (Leu162, tyr264 and Tyr268), one π-π T-shaped interaction between phenyl ring and Tyr268, along with additional π-alkyl interaction between phenyl ring and Pro248 with the calculated Binding Affinity, Total Energy, vdW Energy, and Elec. Energy scoring values of (-4.964, -101.415, -0.634, -0.170) KcalMolA and (-4.644, -26.614, -0.456, -1.264) KcalMolA respectively (SI Appendix XXIII). Notably, the chemical cluster of the Roccustyrna_gs8-1.aa05034965, Roccustyrna_gs6-1.23bbeb63bf, Roccustyrna_gs4-1.c9aea1e4, Roccustyrna_gs2-1.1b9d84b9b5, Roccustyrna_gs3-0.b98f798, Roccustyrna _fr6-1.1ba9aeae36, Roccustyrna_fr5-0.5eacae4, Roccustyrna_fr3-1.d27fb78841, Roccustyrna_fr2-0.d680bf73c5, and Roccustyrna_fr1-0, dcb452aabe chemotypes formed two π-π T-shaped and two π-alkyl interactions when docked inside the (PDB: 7tx5) protein targets with the estimated Binding Affinity, Total Energy, vdW Energy, and Elec. Energy scoring values of (-7.791, -3.354, -20.687, -11.211) KcalMolA, (-7.719, -0.575, -13.995, -5.159) KcalMolA, (-7.012, -50.285, -13.601, -30.682) KcalMolA, (-6.953, -26.135, -8.952, -33.709) KcalMolA, (-6.951, -48.661, -5.089, -38.219) KcalMolA, (-6.638, -47.817, 0.444, -39.210) KcalMolA, (-6.552, -2.305, -1.228, -32.004) KcalMolA, (-6.276, -23.284,34.079, -90.679) KcalMolA, (-6.220, -49.774,7.609, -36.637) KcalMolA, and (-5.422, -34.589,51.705, -100.883) KcalMolA respectively (SI Appendix XXVI). At the same time an additional π-sigma interaction was noticed where the TYR264 amino acid was involved when the RoccustyrnaTM_ gs_convs_ 1.61f0324366 and the RoccustyrnaTM_gs_ convs_ 2.5bc061fb9 neo-ligand conformers in parallel generated Binding Affinity, Total Energy, vdW Energy, and Elec. Energy scoring values of (-4.937, -102.448, -0.504, -0.354) KcalMolA and (-4.644, -26.628, -0.447, -1.278) KcalMolA (SI Appendix XXIV), (SI Appendix XXXVI) within the Neutron crystal structure of SARS-CoV-2 NSP3 macrodomain in complex with the ADP-ribose and the Crystal Structure of SARS-CoV-2 main protease PCM-0103016 (PDB: 5rem) protein targets. Next, I predicted the protein-ligand docking energy complexes and revealed the binding affinity docking value differences, using the DockThor web server regarding the chemical library of the Roccustyrna_ gs8-1.1d0aa1d25a, Roccustyrna_ gs6-1.6fcbb8e547, Roccustyrna_ gs5-1.db51c 934a6, Roccustyrna_ gs201.7888f0b, Roccustyrna_ gs3-0.1dfc0b3f53, Roccustyrna_ fr5-0.6022ed281f, Roccustyrna_ fr4-1.055f7a2bc4, Roccustyrna_fr3-1.a199d4dd7f, Roccustyrna_ fr2-0.d1e 3d76a74, and Roccustyrna_fr1-0.d4f706b9a neo-ligands when docked onto the (PDB: 6wzu) protein targets with the (-7.791, -53.924, -18.678, -29.784) KcalMolA, (-7.565, -5.044, -22.408, -11.859) KcalMolA, (-7.555, -48.956, -24.056, -19.974) KcalMolA, (-7.326, -18.103, -19.360, -12.281) KcalMolA, (-7.310, -1.601, -11.901, -8.362) KcalMolA, (-7.117, -1.400, -12.407, -21.322) KcalMolA, (-7.047, -13.539, -13.168, -22.883) KcalMolA, (-6.878, -48.230, -19.920, -29.503) KcalMolA, (-6.816, -47.779, -5.527, -22.966) KcalMolA, and (-6.396, -19.936, -12.112, -21.848) KcalMolA (Affinity, Total Energy, vdW Energy, Elec. Energy) KcalMolA respectively. Simultaneously, I identified starting points for such pharmacophoric re-generalizations after performing a large-scale virtual screening of theirs electrophile and non-covalent fragments through a DockThor and a Gemdock approach against the SARS-CoV-2 main protease. One of two cysteine viral proteases which are essential for viral replication were then targeted by the re-generalized chemical scaffolds of Roccustyrna_gs2-1.080717cdc, Roccustyrna_fr6-1.445e58e300, Roccustyrna_fr5-0.2037c981cd, Roccustyrna_ fr3-1.109dc80f33, and Roccustyrna_fr1-0.65ae768444 neo-ligand conformers for the construction of a multi-amino acid targeted inhibitory effect with the Binding Affinity, Total Energy, vdW Energy, and Elec. Energy docking values of (-5.190, -20.856, 0.074) KcalMolA, (-4.536, -13.256, 0.076) KcalMolA, (-4.271, -19.620, 0.074) KcalMolA, (-4.089, -18.732, 0.073) KcalMolA, and (-3.610, -13.524, -0.095) KcalMolA respectively (SI Appendix XXVII) inside the (PDB: 5rlh) protein targets. By implementing the DockThor's algorithm as the

 doi:10.20944/preprints202403.0518.v1

search method I identified that the cluster of the Roccustyrna_gs6-1.bd66c 63f88, Roccustyrna_ gs5-1.534067352d, Roccustyrna_gs4-1.498eff9687, Roccustyrna_ gs4-1.498eff9687, Roccustyrna_fr1-0.2ce1332add, Roccustyrna_ gs6-1.fbe206e0d9, Roccustyrna_ gs4-1.f696a07742, Roccustyrna_fr5-0.e3a01e46ea, Roccustyrna_ fr4-1.73f1bd963e, and the Roccustyrna_ fr1-0.cde322 neo-ligands was able of simultaneously generating a large amount of negative binding affinity and negative docking energy scoring values of (-5.712, -20.653, -0.365, 0.642) KcalMolA, (-5.644, -12.890, -0.505, 0.932) KcalMolA, (-5.573, -19.142, -0.422, 0.942) KcalMolA, (-3.407, -6.889, -0.401, -1.201) KcalMolA, (-5.716, -20.781, -0.406, 0.554) KcalMolA, (-5.568, -17.628, -0.484, 0.994) KcalMolA, (-4.599, -12.974, -0.530, 0.883) KcalMolA, (-4.356, -17.396, -0.367, 0.920) KcalMolA, and (-3.406.-10.052, -0.429, -1.281) KcalMolA (Affinity, Total Energy, vdW Energy, Elec. Energy) (SI Appendix XXIX) when docked inside the (PDB: 5rlg) and (PDB: 1xak) protein targets. In this phenotypic crowding-based multiple solution a steady-state genetic strategy is finalized, using DockThor's parental replacement method following Dynamic Modified Restricted Tournament Selections (DMRTS) I provided a better exploration of the energy hypersurface in a single run by preserving the population diversity of the generated structures of Roccustyrna_gs4-1.598e539d1, Roccustyrna_fr6-1.eba009524c, Roccustyrna_ fr5-0.ed0be64fce, Roccustyrna_fr3-1.c6cba8e261, Roccustyrna_fr2-0.d8c1263467 neo-ligand 3D conformers when targeting the Crystal Structure of SARS-CoV-2 main protease in complex with PCM-0103016 (PDB: 5rem) protein targets with the Binding Affinity, Total Energy, vdW Energy, and Elec. Energy scoring values of (-5.236, -20.582, -0.373, 0.720) KcalMolA, (-4.599, -12.779, -0.505,1.012) KcalMolA, (-4.328, -18.497, -0.454,1.047) KcalMolA, (-4.142, -18.231, -0.427, 0.975) KcalMolA, (-3.670, -9.219, -0.233, -1.301) KcalMolA (SI Appendix XXX) respectively. The same scoring function based on the sum of the following terms from the MMFF94S force field was used in section2 to score the docked poses of the small molecules of the Gissitoviffirna_ TM3.79af0ebe97, Gissitoviffirna_TM4.49ec2fbd, Gissitoviffirna_ TM8.dab3914dae, and the Gissitorviffirna_TM9.45076bcfae, neo ligands. As a result these top energy-poses from each Gissitoviffirna_ TM cluster are given by Born's rule in form (5) by transformation as representative outcomes when interacted with the (PDB: 5rem) protein targets with the Binding Affinity, Total Energy, vdW Energy, and Elec. Energy scoring values of (-7.414, -73.496, -16.329, -33.867) KcalMolA, (-7.308, -4.493, -16.344, -18.151) KcalMolA, (-6.904, -32.614, -12.895, -39.697) KcalMolA, and (-6.685, -41.976, -11.421, -29.418) KcalMolA respectively (SI Appendix XXXVII). The above mentioned DockThor molecular force field parameterizations performed automatically and combined to GemDock Program in the original conformation presented in the e-Drug3D dataset for each distinct cluster of the small molecule conformers of the Gissitorviffirna_ TM1.bdc725ca3 and Gissitorviffirna_ TM2. f170 e0c75d neo-ligands with the Binding Affinity, Total Energy, vdW Energy, and Elec. Energy scoring values of (-8.035, -46.133, -18.379, -33.447) KcalMolA, and (-6.904,51.095, -12.834, -23.876) KcalMolA respectively when targeted onto the same protein targets (SI Appendix XXXVIII). In order then to study the In-Silico inhibitory binding mechanisms of the Gissitorviffirna_TM1 I integrated molecular docking GEMDOCK outcomes with DockThor results to ensure that every Quantum instrument is physically realizable and predict the docked conformations in the active site of the (PDB: 1xak) protein targets, based on the calculated binding energies. More accurately, the Gissitorviffirna_TM1 neo-ligand targeted the amino acid sequence of the V-M-TYR-3, v-S-TYR-3, v-M-HIS-4, v-S-TYR-5, v-M-ASN-28, v-S-ASN-28, v-S-THR-44, v-M-SER-45, v-M-THR-46, v-S-THR-46, v-S-HIS-47, v-S-THR-59, v-S-GLN-61amino acids with the total docking energy of (-74.9) KcalMolA, and with the negative docking free energies of (-4.89748, -9.25783, -4.45556, -12.4852, -10.0815, -8.70546, -7.96912, -2.26724) Kcal/Mol/A respectively. The Calculation of the binding free energies from these chemical-biological molecule complexes have been evaluated using MM/GBSA and MM/PBSA methods which are arguably the most frequently employed approaches for accurately investigations of the predicted docking conformations. In this binding model the Gissitorviffirna_TM1 and Gissitorviffirna_TM2 {1 - [(R) - [(1S,3R) - 3 - [(R) - amino (carbamo-thioylamino) methyl] diaziridin - 1 - yl] ({6 - oxo - 2 - [(2S,5R) - 3,4,5 - trifluoro - 2,5 - dihydrofuran - 2 - yl] - 6,7 - dihydro - 1H - purin - 8 - yl}amino) phosphoroso] - 1H - azirin - 2 - yl} thiourea pharmacophores occupied the amino acid sequence of V-M-ALA-331, v-M-THR-332, v-S-THR-332, v-S-LYS-333, v-S-TRP-423, v-S-ILE-428, v-S-ARG-495, v-M-LYS-333, v-S-LYS-333, v-M-ILE-

 doi:10.20944/preprints202403.0518.v1

428, v-M-ASP-429, v-S-ASN-435, v-M-ASN-437, v-S-ASN-437, v-S-TYR-438, by forming hydrogen bonds within multiple (PDB: 2ghv) and (PDB: 1xak) residues, including the catalytic residue C145 and generated total docking energies of (-71.2) and (-93.8) KcalMolA. Binding Affinity, Total Energy, vdW Energy, and Elec. Energy scoring values of (-8.50976, -19.4761, -5.84652, -4.45764, -8.35425, -8.46354, -8.2281) KcalMolA and (-7.19179, -6.35389, -9.90665, -6.45926, -6.89001, -5.45936, -5.05747, -8.80065) KcalMolA which were also respectively produced by the same cluster of distinct ligands against the 22mer conserved binding domains inside the (PDB: 2ghv) and (PDB: 1xak) protein targets. Prior to the DockThor protein-ligand docking, the binding interfaces for both domains were in parallel identified, and a GemDock constraint was applied to achieve accurate co-factor docking experiment against the (PDB: 6nur) protein targets when hitted by the cluster of the Gissitorviffirna_TM1 and Gissitorviffirna_TM2 small molecules with the estimated total docking energy value of (-83.6) Kcal/Mol/A, and the docking energy values of (-4.01959, -11.6821, -5.50052, -6.21887, -6.00567, -4.52625, -11.821, -14.8798) KcalMolA and (-75.3, -5.52846, -14.8044, -9.54718, -11.2557, -6.82854, -8.26477) KcalMolA inside the list of V-S-ASP-452, v-S-TYR-455, v-S-ARG-553, v-S-ASP-623, v-S-ARG-624, v-S-ASP-760 active amino acids (Figure S2b), (Statue1a), (SI Appendix V), (SI Appendix VI), (Statue1b), (SI Appendix VII), (SI Appendix VIII), (SI Appendix IX), (SI Appendix XVIII) (Statue1c), (SI Appendix X), (SI Appendix XI), (Statue1d), (SI Appendix VIII), (SI Appendix VIII), (SI Appendix XII), (SI Appendix XIII), (Statue1e), (SI Appendix IX), (SI Appendix XIV), (SI Appendix XV), (SI Appendix XVI), (SI Appendix XVII), (SI Appendix XVIII), (SI Appendix XIX), (SI Appendix XX), (SI Appendix XXI), (Statue1f), (SI Appendix XXII), (SI Appendix XXIII), (SI Appendix XXIV), (SI Appendix XXV) (SI Appendix XXVI), (Statue1g), (SI Appendix XXVII). (SI Appendix XXVIII), (Statue1h), (SI Appendix XXIX), (SI Appendix XXX), (Statue1i), (SI Appendix XXXI), (SI Appendix XXXII), (SI Appendix XXXIII), (SI Appendix XXXIV), (Statue1j), (SI Appendix XXXV), (SI Appendix XXXVI), (SI Appendix XXXVII), (Statue1k), (SI Appendix XXXV), (SI Appendix XXXVI), (SI Appendix XXXVII), (SI Appendix XVIII), (Cluster Docking Energy TableS1), (SI Appendix I), (Cluster Docking Energy TableS2), SI Appendix I), (Docking Energy TableS1), (SI Appendix I), (Docking Energy TableS2), (SI Appendix I), (Docking Energy TableS3), (SI Appendix I). Other QSAR/CoMFA experiments have shown to us that the entire pharmacophoric residues of the Gissitorviffirna_TM2 [2 - (aminomethyl) - 2 - { [(2E) - 3 - oxofuran - 2 - ylidene] methyl} - 2λ^5 - azaphosphiridin - 1 - yl] amino (1R,4S) - 3,3 - dimethyl - 6 - oxo - 2λ^4 - thia - 5 - azaspiro [bicycle [3.2.0] heptane - 2,1' - thiirane] - 4 - carboxylate chemical design when docked onto the Mpro - N9 binding sites inside the conserved SARS-COV-2 protein targets of (PDB: 6mq2), (PDB: 6woj), (PDB: 7khp), (PDB: 7b3d), (PDB: 7b3o), (PDB: 6w23), and (PDB: 6xs6), interacted negatively with the Cys145 catalytic site of SARS - CoV - 2 Mpro charged groups within the sequence of the amino acid of V-M-LYS-557, v-S-LYS-557, v-M-ARG-567, v-M-ASP-568, v-S-ASP-574, v-S-PHE-43, v-M-ARG-44, v-M-SEr-45, and V-S-SEr-45 with the docking energy values of (-85.8, and-5.56, -8.38956, -5.77168, -6.13664, -12.8661, -5.37546, -6.10391, -5,928) Kcalmol respectively (SI Appendix), (SI Appendix II), (SI Appendix III), (SI Appendix IV), (SI Appendix V), (SI Appendix VI), (SI Appendix VII), (SI Appendix VIII), (SI Appendix XII), (SI Appendix XIII), (SI Appendix IX), (SI Appendix XIV), (SI Appendix XV), (SI Appendix XVI), (SI Appendix XVII), (SI Appendix XVIII), (SI Appendix XIX), (SI Appendix XX), (SI Appendix XXI), (SI Appendix XXII), (SI Appendix XXIII), (SI Appendix XXIV), (SI Appendix XXV) (SI Appendix XXVI), (SI Appendix XXVII). (SI Appendix XXVIII), (SI Appendix XXIX), (SI Appendix XXX), (SI Appendix XXXI), (SI Appendix XXXII), (SI Appendix XXXIII), (SI Appendix XXXIV), (SI Appendix XXXV), (SI Appendix XXXVI), (SI Appendix XXXVII), (SI Appendix XXXV), (SI Appendix XXXVI), (SI Appendix XXXVII), (SI Appendix XVIII), and ((Cluster Docking Energy TableS1), (SI Appendix I), (Cluster Docking Energy TableS2), SI Appendix I), (Docking Energy TableS1), (SI Appendix I), (Docking Energy TableS2), (SI Appendix I), (Docking Energy TableS3), (SI Appendix I)). (Figure S2c) Moreover, Cluster of the QSAR/QMMM/CoMFA map analysis of the electrostatic regions around the (rboximidoyl-3-fluoro- (1S,4S) ((diamino-methylidene) amino) ethenyl}) amino, oxy-methyl) -3,4-dihydroxyoxolan-2-ylo-1,2,4-triazol-3-yl- (formamido) phosphoryl o-6-fluoro-3,4-dihydropyrazine-2-carboxamide (7ar) -5-amino-N-* (S) -,2-* (3-oxabicyclo (2.1.0) (1S,4S) -5-oxabicyclo*2.1.0, pentan-2 ((2S,5r,6r) -6- ((2S) -2-amino-2-phenylacetamido) -3,3-dimethyl-7-oxo-4-

 doi:10.20944/preprints202403.0518.v1

thia-1-azabicyclo (3.2.0) heptane-2-carbonyloxy) ({((2-amino-6-oxo-6,9-dihydro-3H-purin-9-yl) oxy) (hydroxy) phosphoryl} oxy) phosphinic acid-ylidene, *cyano (2,6-diazabicyclo*3.1.0, hex-1-en-6-yl) (rboximidoyl-3-fluoro- (1S,4S) ((diamino-methylidene) amino) ethenyl}) amino, oxy-methyl) -3,4-dihydroxyoxolan-2-ylo-1,2,4-triazol-3-yl- (formamido) phosphoryl o-6-fluoro-3,4-dihydropyrazine-2-carboxamide (7ar) -5-amino-N-* (S) -,2-* (3-{((1S,4S) -5-oxabicyclo (2.1.0) pentan-2-ylidene) {(cyano ({2,6-diazabicyclo (3.1.0) hex-1-en-6-yl}) phosphanyl- (fluoro) methyl}-lambda6-sulfanyl}one pentan-2-ylidene) {(cyano ({2,6-diazabicyclo (3.1.0) hex-1-en-6-yl}) phosphanyl-lambda6- (rboximidoyl-3-{((1S,4S) -5-oxabicyclo (2.1.0) pentan-2-ylidene) {(cyano ({2,6-diazabicyclo (3.1.0) hex-1-en-6-yl}) phosphanyl) (fluoro) methyl}-lambda6-sulfanyl}one (rboximidoyl-3-oxabicyclo (2.1.0) pentan-2-ylidene) {(cyano ({2,6-diazabicyclo (3.1.0) hex-sulfanyl}one-boximidoyl-3-{((1S,4S) -5-oxabicyclo (2.1.0) pentan-2-ylidene) contact residues of the Roccustyrna_gs and the Roccustyrna_fr chemical library derived Gissitorviffirna_TM3 (Z) - 4 - amino - N - [(1Z) - amino-methylidene] - N' - [(Z) - 2 - {6 - [(1Z) - [(fluo romethyl) imino] methyl] - 3 - sulfanyl idene - 1,2,4 - triazabicyclo [3.1.0] hex - 2 - en - 6 - yl} - N' - methyl ethan imidamido] - 2 - oxo-butan-imidamide small molecules when docked onto the combined SARS-COV-2 protein targets of (PDB: 6mq2), (PDB: 6woj), (PDB: 7khp), (PDB: 7b3d), (PDB: 7b3o), (PDB: 6w23), and (PDB: 2ghv) (SI Appendix), (SI Appendix II), (SI Appendix III), (SI Appendix IV), (SI Appendix V), (SI Appendix VI), (SI Appendix VII), (SI Appendix VIII), (SI Appendix XII), (SI Appendix XIII), (SI Appendix IX), (SI Appendix XIV), (SI Appendix XV), (SI Appendix XVI), (SI Appendix XVII), (SI Appendix XVIII), (SI Appendix XIX), (SI Appendix XX), (SI Appendix XXI), (SI Appendix XXII), (SI Appendix XXIII), (SI Appendix XXIV), (SI Appendix XXV) (SI Appendix XXVI), (SI Appendix XXVII). (SI Appendix XXVIII), (SI Appendix XXIX), (SI Appendix XXX), (SI Appendix XXXI), (SI Appendix XXXII), (SI Appendix XXXIII), (SI Appendix XXXIV), (SI Appendix XXXV), (SI Appendix XXXVI), (SI Appendix XXXVII), (SI Appendix XXXV), (SI Appendix XXXVI), (SI Appendix XXXVII), (SI Appendix XVIII), and ((SI APPENDIX I Supplementary Material), (TableS1), (TableS2), (TableS3), (Figures S1), (Figure S2a), (Figure S2b), (Figure S2c), (Figure S2d), (Figure S2d), (Figure S2e), (Figure S3a), (Figure S3b), (Figure S3c), (Figure S3d), (Figure S3e), (Figure S3f), (Figure S3g), (Figure S3h), (Cluster Docking Energy TableS1), (SI Appendix I), (Cluster Docking Energy TableS2), SI Appendix I), (Docking Energy TableS1), (SI Appendix I), (Docking Energy TableS2), (SI Appendix I), (Docking Energy TableS3), (SI Appendix I)).In this effort Quantum Energy Negativities exctracted from the above Quantum Communication Systems ((Supplement Material) Equation Master1-13), ((Iconics1–6), ((Eqs1-400), (Iconics1-4) Supplementary Material METHODS AND MATERIALS (1), (2)), and (Eqs1-325)) that use entanglement in various ways and for different purposes in a reducible manner generated the apparent loss of degrees of freedom of the original theory in terms of Quantum information in a reduced one through the use of QFT's internal Quantum network. These translations have been achieved by generalizing Hidden Gene to Protein Interactions of the Hidden Pharmacophoric Subgroups from two oral antivirals, the Molnupiravir drug and Nirmatrelvir-Ritonavir drugs, and the Antihypertensive Drugs of Candesartan, Telmisartan, Losartan, Olmesartan, and the Valsartan Drug which have been have been used as an outpatient treatment of mild to moderate COVID-19 patients who are at risk for progression. A new Quantum crypto-metalanguage approach of the Quantum simulation of QFT negative reductions of degrees of infinite freedom is proposed here to quantize CS operators from AT1Rs blockers required for ACE2 endocytosis in SARS-CoV-2 infection which is adjusted before being simulated and are strongly relating to how one clustered pharmacophoric element occupies the same Quantum energy phase in an alternative XYZ coordinated smile system for the fragmentazing and the re-merging of the chemical structures of the angiotensin receptor type 1 (AT1R) semi-negative inhibitors of the Candesartan, Telmisartan, Losartan, Olmesartan, and the Valsartan into new Drug Designs with increased levels of Negative Docking Energy Values. More specifically the Antihypertensive Drugs of the Candesartan Conformer of 3D_ CID _ 2541_4ea3_ 637677dbbeFFFTˆUμ (x) superimposed states targets the (PDB: 4ea3) binding domains with semi-negative docking values of (1,3e5dd31abd lig and 1, -5.747, 84.926, 6.790, -29.284) KcalMolA with positive Total Energies of (84.926) KcalMolA due to lack of the so called completely negative superoperator and its natural extension to the tensor product. In addition the Telmisartan Conformer3D_ CID _65999_4ea3_ 6376777d59f4e hits into the

 doi:10.20944/preprints202403.0518.v1

same binding cavities with positive Total Energies of (110.429) KcalMolA with the Docking parameters of Docking scoring values of (1,6375f1a51d lig and 1, -6.026,110.429, 3.919, -20.915) KcalMolA because of its complete positivity characterizing such a non-Triangularized Quantum instrument-like pharmacophore. The same sufficient condition cannot be physically realizable also for the Losartan Conformer3D_ CID_3961_4ea3_ 637675d2e4360 since it is observed that the chemical structure of this antihypertensive drug binds into the (PDB: 4EA3) protein targets with a semi-inhibitory docking effect while generating some of positive Total Energies of (92.247) KcalMolA and related docking outputs of (1,7b462582c3 lig and 1, -6.058,92.247, 0.346, -20.606) KcalMolA. The Olmesartan Conformer3D_ CID _ 158781_4ea3_ 637675667c4a3 also produced positive Total Binding Energies of 87.923KcalMolA when docked onto the (PDB:4ea3) binding residues with (1, f0e83c3c08 lig and 1, -5.863, 87.923, 8.122, -33.252) KcalMolA implying that this Drug represent a positive superoperator, so that Olmesartan's Total Binding Energy is completely positive against all the above mentioned PDB IDs and relative protein targets. Similarly, any non-Triangularized Total Energy measuring system should have its extended measuring system for any realizable docking system. The (PDB: 6lzg) binding cavities were also covered by the FDA approved Drugs of the Valsartan, Candesartan, Losartan, and Olmesartan but with positive Total Energies unfortunately indicating the fact that these Drugs weren't able of blockading the core element of the (PDB: 6lzg) protein targets at least computationally. In detail the Candesartan Conformer3D_CID_ 2541_6lzg_ 637673b72423a targeted the (PDB: 6lzg) binding domains with a positive docking energy effect of positive Total Energies of 84.310KcalMolA with binding affinity values of (1, b4c7c9b174 ligand 1, -7.309, 84.310, -12.684, -10.784) KcalMolA. The Losartan Conformer3D_ CID_3961_6lzg_ 637672e4b963e hitted the (PDB: 6lzg) Protein Targets also with positive Total Energies of 84.310KcalMolA and other parameters of (1,6ab04e92d lig and 1, -7.125, 87.761, -15.975, -7.183) KcalMolA. The Olmesartan Conformer3D_ CID _158781_6lzg_ 6376722b32225 binds onto the (PDB: 6lzg) binding residues with a semi positive inhibitory effect of positive Total Energies of 88.260KcalMolA and binding affinity values of (1,8edd42d737 ligand 1, -6.570, 88.260, -6.692, -18.765) KcalMolA. The Candesartan's Conformer3D_ CID _2541_4ea3_ 637677dbbeFFFTˆUμ (x) produced a semi negative docking effect with positive Total Energy Values of 84.926 KcalMolA and binding affinity energies of (1,3e5dd31abd lig and 1, -5.747, 84.926, 6.790, -29.284) KcalMolA. Finally, the Telmisartan's Conformer3D_ CID_65999_ 4ea3_ 6376777d59f4e interacted with an intermediate negative docking affinities with positive Total Energies of 110.429KcalMoLA and relative DockThor binding affinity scoring values of (1,6375f1a51d lig and 1, -6.026,110.429,3.919, -20.915) KcalMolA. At the same time the Losartan's Conformer3D_ CID_3961_4ea3_ 637675d2e4360 produced some of (92.247) KcalMolA non-negative binding Total Energies. The same type of an in-silico semi inhibitory effect also observed by the Olmesartan's Conformer3D_ CID_158781_ 4ea3_637675667c4a3 when approached the (PDB: 4ea3) protein targets with positive Total Energies of 87.923KcalMolA and generated comparative docking outputs of (1, f0e83c3c08 lig and 1, -5.863,87.923,8.122, -33.252) KcalMolA. The PAXLOVID (Nirmatrelvir) 63737f0dbf777 ligand conformer generated a partial inhibitory effect with positive Total Energy Docking Values of (26.299) KcalMoLA and other less negative vdW and Elec. Energy scoring values of (1, -7.304,26.299, -10.888, -11.924 run 8, -7.304,26.299, -10.888, -11.924, run 5, -7.570,28.015, -14.907, -6.462, run 9, -7.791,28.022, -17.748, -3.806) KcalMolA. The Molnupiravir b4dac186 ligand conformer generated some of low negative binding affinity scoring values with positive Total Free Energies of (6.750) KcalMolA and other binding scoring values of (1, -6.953,6.394, -11.120, -16.458, run 3, -6.953,6.394, -11.120, -16.458, run 7, -6.919,6.750, -9.433, -18.712, run 2, -6.891,8.520, -11.763, -15.567) KcalMolA. On the other hand the DRVYIHPFXmimetic X_4ea3X_63887d6da75a7 Drug design interacted inside the same (PDB: 4ea3) Protein Targets only with negative Total Energies, and vdW and Elec. Energies (Rank, File, ID, Compound, Affinity, Total Energy, vdW Energy, Elec. Energy) of (1, abdd7947 Lig and 1, -6.221, -25.657,2.768, -24.410) KcalMolA. (2,5-42) I have illustrated at this point the power of such a Flexible Heuristic Algorithmic Approach as illustrated in (BIOGENEA.Quantum Function1) and interpreted in a distinct Quantum circuit where LnAdS5 refers to qubit preparations, and certain 1-and 2-N qudit gates for automatic molecule fragmentation as a meaningful application for translating these complex physical-like

 doi:10.20944/preprints202403.0518.v1

devices interacting with virologic functions. That shows the result of AdS5 Quantum fields Theory (QFT) Reduction measurement where M↓ represent the states of the Generalized Chemical Block Systems and the operator representing the interaction-dynamics, the docking system that measures the Quantum Negative Docking Energy outputs as refined by the BIOGENEA (QCS) - (QEN) s apparatus. After this an observer can finally see Hidden Entanglement Negativity Translations and Uncertainty Quantum Relationships revealed after comparing the docking outputs of the Roccustyrna and Gissitorviffirna Drug Designs with Molnupiravir and Nirmatrelvir Oral COVID19 Antiviral Drugs. These outputs consisting of a Hilbert space, a density operator Δx B1Δx C1, and a unitary operator Jacobi P [LnAdS5 [H] ⊗̂ [Ho]] Ê ⩛ ⊕, Ĝ ⊋ Ĥ ⊕ ∂ ∧ ∇ ⊗ σkr | ‖ϱAT2‖ on the tensor product of the state chemical spaces describe the initial state of the BIOGENEA (QEN) s apparatus, where the Hermitian operator describes the meter observable of this (QCS) - (QEN) s apparatus for measuring the Quantum Negative Energy Values of these observables for these biological systems of molecular epidemiology, evolution, and phylogeny of SARS coronavirus pharmacophoric for the designing of the binding components of o-lambda6-dimethyl - 7 - oxo - 4 - thia - 1 - azabicyclo (3.2.0) heptane - 2 - carbonyloxy) ({((2 - amino - 6 - oxo - 6,9 - dihydro - 3H - purin - 9 - yl) oxy) (hydroxy) phosphoryl} oxy) phosphinic acid - ylidene, *cyano (2,6 - diazabicyclo*3.1.0, hex - 1 - en - 6 - yl-) (rboximidoyl - 3 - {((1S,4S) - 5 - oxabicyclo (2.1.0) pentan - 2 - ylidene) {(cyano ({2,6 - diazabicyclo (3.1.0) hex - 1 - en - 6 - yl}) phosphanyl) (fluoro) methyl} - lambda6 - su lfanyl}one1S,4S) - 5 - oxabicyclo (2.1.0) pentan - 2 - ylidene) {(cyano ({2,6 - diazabicyclo (3.1.0) hex - 1 - en - 6 - yl}) phosphanyl) (fluoro) methyl} - lambda6 - su lfanyl}one formonitrile (rboximidoyl - 3 - fluoro - 1 - {5 - oxabicyclo (2.1.0) pentan - 2 - yl} - purin - 2 - yl) amino}) phosphoryl) oxy}) phosphoryl) formonitrile2) sulfanyl}oneboximidoyl after solving the S (BIOGENEA.Quantum Function2), so the general solution is insensitive to the infinitesimal changes δθ,2 [σ] (r), δθt,2Zdrτ (r), and δθr,2Z (dr) [ϱcr. (r)] o2ZdrZr 0 Ĥ ⊕ ds Ĥ ⊕ ∂ τ (s) ⊕ ∂ o2 [σ] (r) while generating the * [1- [(2R,3R,4S,5R) -3,4-dihydroxy-5- (hydroxymethyl) oxolan-2-yl] -1,2,4-triazole-3-carboxamide-ethyl-6-bromo-4- [(di-methyl-amino) methyl] -5-hydroxy-1-methyl-2- (phenyl-sulfanyl-methyl) indole-3-carboxylate] non-vanishing torsion components of the Roccustyrna_gs, the Roccustyrna_fr, and the Gissitorviffirna_TM pharmacophoric structures that targeting simultaneously with negative docking energy values the amino acid sequence of the ASP-187, ARG-188, GLN-189, GLN-189, TYR-237, TYR-239, LEU-272, LEU-286, ARG-298, ARG-298, GLN-299, GLN-299, GLY-302, VAL-303, ASN-142, ASN-142, mET-165, mET-165, GLU-166, GLU-166, LEU-167, PRO-168, PRO-168, VAL-186, ASP-187, ASP-187, GLU-166, LEU-167, PRO-168, PRO-168, GLN-189, THR-190, ALA-191, ALA-2, VAL-3, and VAL-3 and theirs binding domains. The auxiliary expression δχr, [χ], [r] ˆ2 ⟨Ψ1, [ϱcr] .Ψ ⟩ t [σ] ″ − χ [r1] f [χ], [r] ˆ2 oη [ϕ0] 2 ⟨Ψ1, [ϱcr] .Ψ ⟩ 2 t [σ] o [χ], [r] ˆ2 ⟨Ψ1, [ϱcr] .Ψ ⟩ t1 − f 3η [ϕ0] χr ⟨Ψ1, [ϱcr] .Ψ ⟩ tχtτ of 2η [ϕ0] 2χr ⟨Ψ1, [ϱcr] .Ψ ⟩ 2 t χt ϱcr.− [χ], [r] ˆ2 ⟨Ψ1, [ϱcr] .Ψ ⟩ t ϱcr.C generated the following δη [ϕ0], η [ϕ0] f [χ], [r] ˆ2 [σ] or 2f χt τ − η [ϕ0] χt ϱcr.local transformations of the δE (r), E (r), [σ] f [χ], [r] ˆ2 metric, and the Roccustyrna-mixed [mPPIA GAGCT-GTTTGCAG-ACAAAGTTC-CCCTGGCACAT-GAAT-CCTGG] cos,1 2 (Θ)] ∩ [B] aMˆrˆ2 (AdS5νr) ∧ ⊗ pi | FFFTˆUμ (X) |∅ (AoΨo, d) ⩛, [H] ⊗̂ [Ho] ∯∫̄ i [Ψ] [EntanglementEntropy [qstate_ [QFTq] ψoMG)] ˆ(ωsinθ/2), Sˆ MNI,1/2pi˜ (i sin (-1/3 (24r), SphericalHarmonicYHypergeometric0F1 [PolyLog [logi, |ψ˜ [QFTq] (α) ⟩) μ, (x)) J (r′)) Hypergeometric0F1 [PolyLog [logi, |ψ˜ [QFTq] (α) ⟩) μ, [A [Ψo*sinϕ*{Ψ} ⩛ ⊕ G | xi, n, G ⟩ ν]]] ⩛ ⊕ G | xi, n, G ⟩ ν] ⟨FF |∅ (AoΨo, d) ⩛, [H] ⊗̂ [Ho] ∯∫̄ i [Ψ] [Entanglement Entropy [qstate_ [QFTq] ψoMG)] ˆ(ωsinθ/2), Sˆ MNI,1/2pi˜ (i sin (-1/3 (24r), |ψ˜ [QFTq] (α) ⟩) μ, (x)) J (r′)) [A [Ψo*sinϕ*{Ψ}]] ⩛ ⊕ G | xi, μ |, |FF |∅ (AoΨo, d) ⩛, [H] ⊗̂ [Ho] ∯∫̄ i [Ψ] [EntanglementEntropy [qstate_ [QFTq] ψoMG)] ˆ(ωsinθ/2), Sˆ MNI,1/2pi˜ (i sin (-1/3 (24r), |ψ˜ [QFTq] (α) ⟩) μ, (x)) J (r′)) [A [Ψo*sinϕ*{Ψ}]] ⩛ ⊕ G | xi, ξ⟩ ORDER ← Sort_Pharmacophoric_ strings (s) ▹ I sort s, ({E (y) {1 − Jacobi P [LnAdS5 [H] ⊗̂ [Ho]] Ê ⩛ ⊕, Ĝ ⊋ Ĥ ⊕ ∂ ∧ ∇ ⊗ cos (ζ478xσk-iyry)}∇ ⊗ eˆiπ/2, CZ (Rx (π) ⊗, Rz (π) | ln{1 − Jacobi P [LnAdS5 [H] ⊗̂ [Ho]] Ê ⩛ ⊕, Ĝ ⊋ Ĥ ⊕ ∂ ∧ ∇ ⊗ σkr | ‖ϱAT2‖ COS (Θ) |0⟩ ψoi ⊕ √MGQFT [H] ⊗̂ [Ho] ∯Gxi y} | ∇ ⊗ (Rx (π), [H] ⊗̂ [Ho] ∯I) ⊕ CZeiπ/2CZ (Rx (π), [H] ⊗̂ [Ho] ∯, Rz (π))}, -1/367ΨCH, RamanujanTauZ [cosQFTq. [H] ⊗̂ [Ho] ∯ (AdS5νr)] sinˆiπ (-1), log (|ζ (π) [H] ⊗̂ [Ho] (r) (x-iyQFTG) |). ⊗ |xi, M↓ ⊗ ∭∭∭ |∅iΨ | ⩛ ⊕,1/2ˆaLM QFTq. ⩛ ⊕ G | xi, ΨCH QFTq. Λ ∯IMG) μνi), Ψoð ⩛ ⊕ G | xi, H Mrˆ4h0 (r) s1, (AdS5k r) Mrˆ4h0 (r) sn). [PRF3pΔ2ΔG 5′-TGTCAAA-AGCCCT-GTATAC-3′]

 doi:10.20944/preprints202403.0518.v1

* ∧ [[Cd], [GLY-354] *], [(9Z,12Z) -octadeca-9,12-dienoic acid] ∇ [M-PRF3p-G19C5'GATGT-CAAAAG-CCCTGT-ACTAC-3'] 〉 torsion components of [1- [(2R,3R,4S,5R) -3,4-dihydroxy-5-(hydroxy-methyl) oxolan-2-yl] -1,2,4-triazole-3-carbo-xamide-ethyl 6-bromo-4- [(dimethyl amino) methyl] -5-hydroxy-1-methyl-2- (phenyl sulfanylmethyl) indole-3-carboxylate] while constructing an inhibitory docking effect of high negative binding energy docking values of the (-66,7) KcalmolA when docked onto the cav7bv2_POP binding domains within the amino acids of the V-M-LYS-551, v-S-LYS-551, v-S-ARG-553, v-S-ASP-618, v-M-TYR-619, and V-M-PRO-620 with the docking energy values of (-4.71516, -10.4842, -4.7999, -6.65538, -5.1339, -6.28532) KcalmolA. Its axial-torsion solution in general solves functions of the form χpT (r), 0 and [⟨Ψ1, [ϱcr] .Ψ ⟩ p] [χ], [r] T (r), 0, with p, r, t, σ by choosing [⟨Ψ1, [ϱcr] .Ψ ⟩ p] [χ], [r], χp, δf, [σ] f, δAt, k [C] [ℓ] [α] r [σ] ′ o2η [ϕ0] rf [σ] orf [χ], [r] ˆ2 [χ], [t] /2 τ − r ofη [ϕ0] r [χ], [t] /2 [χ], [ϱcr.] (SI Appendix I), (SI Appendix II), (SI Appendix III), (SI Appendix IV), (SI Appendix V), (SI Appendix VI), (SI Appendix VII), (SI Appendix VIII) which generated the density operator for a unitary combination of DRVYIHPF-mimetic, Gisitorviffirna_TM, Roccustyrna_gs, and Roccustyrna _fr small molecules (Scheme1) as a fusion product of chemical space representations when merged into the connection form of ℓ o (SI Appendix XXXIX), ((Iconics1-4), (Eqs1-400), Supplementary Material METHODS AND MATERIALS (1), (2)), (Supplement Material FUNCTIONS.1-25), and (Cluster of BIOGENEA_ CONSENSUS_Eqs.1-26). To obtain docking insights into RORγ, I have determined the first crystal structure of a ternary complex containing RORγ ligand-binding domain (LBD) bound with the RoccustyrnaTM_gs_convs_ 2.617493ae06 inhibitors in combination with the repressor peptide, a 22-mer peptide from silencing mediator of retinoic acid and thyroid hormone receptor (SMRT). This 22-mer peptide mimetic ligand [amino ({4 - [(2R,3R) - 2 - [(2S) - 3 - { [(1S,2S) - 1 - { [(S) - 1,3 - dihydroisoindole - 2 - carbonyl [(2 - methyl - 6 - oxo - 1,7 - dihydropurin - 8 - yl) methyl] phosphanyl] carbamoyl} - 2 - methylbutyl] amino} - 2 - methylpropyl] oxaziridin - 3 - yl] butyl}amino) methylidene] azanium generated also negative docking energy values with a potential inhibitory effect when docked against the (PDB: 4ea3) structure of the N/OFQ Opioid Receptor in Complex with a Peptide Mimetic Members of the opioid receptor family of the G-protein-coupled receptors (GPCRs) which have been found throughout the peripheral and central nervous system and have key roles in analgesia. These NP-peptide mimetics computationally interacted with the GissitorviffirnaTM9 (6R) - 6 - [(3S) - 2 - [(1Z) - amino ({1H - 1,3 - benzodiazol - 2 - yl [(3R) - 3 - ethyloxolan - 3 - yl] methylidene}) - λ^5 - phosphanyl] - 5 - sulfanylidene - 1,2,4 - triazolidin - 3 - yl] - 4 - oxa - 1 - azabicyclo [3.1.0] hexane - 3 - thione ligand inside the Interacting chains A and constructed Hydrophobic Interactions (RESNR, RESTYPE, RESCHAIN, RESNR_LIG, RESTYPE_LIG, RESCHAIN_LIG, DIST, LIGCARBONIDX, PROTCARBONIDX, LIGCOO, PROTCOO) of (127, iLE, A, 1501, 0NN, A, 3.80, 5034, 611, 6.900, 59.959, 3.464, 3.456, 58.734, 4.496, 131, TYR, A, 1501, 0NN, A, 3.47, 5011, 641, 7.105, 52.254, 3.207, 4.723, 54.677, 2.522, 131, TYR, A, 1501, 0NN, A, 3.92, 5032, 644, 7.291, 57.619, 2.710, 5.233, 56.289, 0.349, 134, mET, A, 1501, 0NN, A, 3.21, 5011, 671, 7.105, 52.254, 3.207, 7.459, 49.203, 2.269, 135, PHE, A, 1501, 0NN, A, 3.66, 5011, 684, 7.105, 52.254, 3.207, 4.196, 51.520, 5.303, 219, iLE, A, 1501, 0NN, A, 3.40, 5010, 1247, 7.964, 52.247, 4.430, 7.257, 54.433, 6.935, 276, tRP, A, 1501, 0NN, A, 3.83, 5018, 1691, 10.228, 52.693, 0.305, 12.965, 50.175, 1.202) KcalMolA, hydrogen Bonds (RESNR, RESTYPE, RESCHAIN, RESNR_LIG, RESTYPE_LIG, RESCHAIN_LIG, SIDECHAIN, DIST_H, A, DIST_D, A, DON_ANGLE, PROTISDON, DONORIDX, DONORTYPE, ACCEPTORIDX, ACCEPTORTYPE, LIGCOO, PROTCOO) of (107, GLN, A, 1501, 0NN, A, True, 2.32, 3.15, 142.09, false, 5027, nam, 460, o2, 10.643, 57.235, 6.108, 10.149, 54.857, 8.120) KcalMolA, salt Bridges (RESNR, RESTYPE, RESCHAIN, PROT_IDX_LIST, RESNR_LIG, RESTYPE_LIG, RESCHAIN_LIG, DIST, PROTISPOS, LIG_GROUP, LIG_IDX_LIST, LIGCOO, PROTCOO) of (130, ASP, A, 633, 634, 1501, 0NN, A, 2.95, false, Tertamine, 5016, 10.495, 54.509, 2.009, 7.967, 53.234, 2.822) KcalMolA, within the 0NN:B:1501 (0NN) binding domains. By performing stationary phase approximations on and between the chemical spaces of these NP-peptide mimetic a Hermitian operator is generalized to describe the Quantum Negative Meter Observables of the BIOGENEA (QEN) s apparatus. In this measurement model, the Hilbert space describes the Negative Energy States, the unitary operator H describes the time-evolution of the composite system M, S, and the density operator σ describes the generalized chemical spaces around the pharmacophore merging

 doi:10.20944/preprints202403.0518.v1

critical points as obtained by the asymptotic expansions of the [amino ({4 - [(2R, 3R) - 2 - [(2S) - 3 - { [(1S, 2S) - 1 - { [(S) - 1, 3 - dihydroisoindole - 2 - carbonyl [(2 - methyl - 6 - oxo - 1, 7 - dihydropurin - 8 - yl) methyl] phosphanyl] carbamoyl} - 2 - methylbutyl] amino} - 2 - methylpropyl] oxaziridin - 3 - yl] butyl}amino) methylidene] azanium against the nociceptin/orphanin FQ (N/OFQ) peptide receptor (NOP, also known as ORL-1) which was discovered relatively recently by molecular cloning and characterization of an orphan GPCR and has a markedly distinct pharmacology, featuring activation by the endogenous peptide N/OFQ, and a unique selectivity for exogenous ligands. This NP-peptide mimetic ligand that represents the projector onto the subspace of that system's state is mathematically represented by a density operator. Then the probability to get the answer is given by the Born rule corresponding to the eigenvalues of the interacted chemical spaces inside its Interacting chains B while generating Hydrophobic Interactions (RESNR, RESTYPE, RESCHAIN, RESNR_LIG, RESTYPE_LIG, RESCHAIN_LIG, DIST, LIGCARBONIDX, PROTCARBONIDX, LIGCOO, PROTCOO) of (110, ASP, B, 1501, 0NN, B, 3.64, 5093, 3404, 15.850, 36.473, 30.032, 15.376, 35.646, 26.515, 127, iLE, B, 1501, 0NN, B, 3.61, 5101, 3538, 12.580, 36.226, 35.455, 9.104, 37.184, 35.216, 131, TYR, B, 1501, 0NN, B, 3.51, 5078, 3568, 13.188, 43.376, 42.938, 10.614, 41.084, 42.268, 134, mET, B, 1501, 0NN, B, 3.30, 5078, 3598, 13.188, 43.376, 42.938, 13.442, 46.541, 42.054, 135, PHE, B, 1501, 0NN, B, 3.78, 5078, 3611, 13.188, 43.376, 42.938, 10.230, 44.214, 45.129, 219, iLE, B, 1501, 0NN, B, 3.19, 5077, 4193, 14.006, 43.126, 44.162, 13.306, 41.235, 46.635) KcalMolA, hydrogen Bonds (RESNR, RESTYPE, RESCHAIN, RESNR_LIG, RESTYPE_LIG, RESCHAIN_LIG, SIDECHAIN, DIST_H, A, DIST_D, A, DON_ANGLE, PROTISDON, DONORIDX, DONORTYPE, ACCEPTORIDX, ACCEPTORTYPE, LIGCOO, PROTCOO) of (107, GLN, B, 1501, 0NN, B, True, 2.17, 3.03, 145.56, false, 5094, nam, 3387, o2, 16.420, 38.706, 33.233, 15.800, 41.083, 31.453) KcalMolA, and Salt Bridges (RESNR, RESTYPE, RESCHAIN, PROT_IDX_LIST, RESNR_LIG, RESTYPE_LIG, RESCHAIN_LIG, DIST, PROTISPOS, LIG_GROUP, LIG_IDX_LIST, LIGCOO, PROTCOO) of (110, ASP, B, 3406, 3407, 1501, 0NN, B, 5.15, false, Tertamine, 5103, 14.303, 37.179, 31.615, 15.465, 33.941, 27.776, 130, ASP, B, 3560, 3561, 1501, 0NN, B, 3.03, false, Tertamine, 5083, 16.264, 41.067, 37.553, 13.753, 42.618, 36.849) KcalMolA within the OLA:A:1503 (OLA) binding domains when combined at least virtually with the GissitorviffirnaTM8 {1 - [(R) - [(1S, 3R) - 3 - [(R) - amino (carbamothioylamino) methyl] diaziridin - 1 - yl] ({6 - oxo - 2 - [(2S, 5R) - 3, 4, 5 - trifluoro - 2, 5 - dihydrofuran - 2 - yl] - 6, 7 - dihydro - 1H - purin - 8 - yl}amino) phosphoroso] - 1H - azirin - 2 - yl}thiourea druggable pharmacophoric compounds according to the projection postulate since the post-measurement state is obtained via each molecular complex state-transformation. Here, the observable-operator and its spectral decomposition uniquely determine the feedback Quantum State Negativity Transformations for Negative Docking Energy Outcomes by revealing atomic details of these ligand-receptor recognitions and selectivities. This NP-Peptide mimetic Compound mimics the first four amino-terminal residues of the NOP-selective peptide antagonist UFP-101, a close derivative of N/OFQ, and provides important clues to the binding of these peptides against the Interacting chains A, B when generating Hydrophobic Interactions (RESNR, RESTYPE, RESCHAIN, RESNR_LIG, RESTYPE_LIG, RESCHAIN_LIG, DIST, LIGCARBONIDX, PROTCARBONIDX, LIGCOO, PROTCOO) of (55, VAL, A, 1503, oLA, A, 3.14, 5076, 61, 12.465, 54.202, 19.220, 15.257, 53.858, 17.827, 74, TYR, B, 1503, oLA, A, 3.70, 5063, 3120, 6.092, 66.908, 21.039, 4.974, 67.226, 24.547, 74, TYR, B, 1503, oLA, A, 3.84, 5065, 3118, 7.494, 65.194, 22.260, 5.480, 66.235, 25.364, 109, THR, A, 1503, oLA, A, 3.63, 5073, 472, 10.848, 56.661, 21.596, 9.256, 56.761, 18.335, 112, LEU, A, 1503, oLA, A, 3.47, 5074, 495, 12.017, 56.000, 20.882, 14.754, 57.769, 19.695, 113, LEU, A, 1503, oLA, A, 3.87, 5066, 503, 7.687, 63.702, 22.516, 9.534, 62.781, 19.239, 113, LEU, A, 1503, oLA, A, 3.61, 5069, 504, 9.319, 61.337, 22.560, 11.679, 63.141, 20.513, 115, PHE, A, 1503, oLA, A, 3.69, 5061, 517, 4.783, 68.177, 19.295, 7.499, 66.406, 17.540, 115, PHE, A, 1503, oLA, A, 3.50, 5063, 519, 6.092, 66.908, 21.039, 8.474, 66.519, 18.510, 117, PRO, A, 1503, oLA, A, 3.68, 5064, 538, 6.405, 65.426, 21.218, 5.582, 63.725, 18.059) KcalMolA against the OLB:A:1502, (OLB) binding cavities. These structures also show substantial conformational differences in the pocket regions between NOP and the classical opioid receptors κ (ref.5) and μ (ref.6), and these are probably due to a small number of residues that vary between these receptors. This NP-mimetic structure explains the divergent selectivity profile of NP and provides a new structural template for the design of NP mimetic ligands that are capable of

 doi:10.20944/preprints202403.0518.v1

generating Hydrophobic Interactions (RESNR, RESTYPE, RESCHAIN, RESNR_LIG, RESTYPE_LIG, RESCHAIN_LIG, DIST, LIGCARBONIDX, PROTCARBONIDX, LIGCOO, PROTCOO) of (139, PHE, A, 1502, oLB, A, 3.86, 5056, 712, 1.882, 42.380, 11.862, 3.617, 44.197, 8.925, 143, ALA, A, 1502, oLB, A, 3.87, 5043, 743, 0.721, 36.187, 11.552, 2.432, 36.184, 8.080, 177, LEU, A, 1502, oLB, A, 3.88, 5055, 946, 0.935, 41.513, 11.040, 1.583, 44.430, 10.614) KcalMolA, hydrogen Bonds (RESNR, RESTYPE, RESCHAIN, RESNR_LIG, RESTYPE_LIG, RESCHAIN_LIG, SIDECHAIN, DIST_H, A, DIST_D, A, DON_ANGLE, PROTISDON, DONORIDX, DONORTYPE, ACCEPTORIDX, ACCEPTORTYPE, LIGCOO, PROTCOO) of (89, TYR, A, 1502, oLB, A, True, 1.50, 2.37, 151.58, true, 320, o3, 5053, o3, 0.659, 30.781, 8.969, 0.323, 32.597, 7.489) KcalMolA inside the OLC:B:1502, (OLC) targeted binding residues of the Interacting chains B, while constructing Hydrogen Bonds (RESNR, RESTYPE, RESCHAIN, RESNR_LIG, RESTYPE_LIG, RESCHAIN_LIG, SIDECHAIN, DIST_H, A, DIST_D, A, DON_ANGLE, PROTISDON, DONORIDX, DONORTYPE, ACCEPTORIDX, ACCEPTORTYPE, LIGCOO, PROTCOO) of (147, ASP, B, 1502, oLC, B, True, 1.69, 2.58, 155.79, true, 3698, o3, 5123, o3, 6.436, 65.958, 49.872, 8.468, 67.082, 48.754) KcalMolA. On the other hand this innovative Drug Design Conformer, the GissitorviffirnaTM-d5dc2541d4 ligand generated an in-silico blocking effect only interacted with Negative Total Free Energy Docking values of (1, -6.725, -38.697, -6.406, -35.072, run 12, -6.725, -38.697, -6.406, -35.072, run 12, -6.918, -38.398, -16.867, -17.322, run 8, -6.637, -37.566, -9.611, -22.509) KcalMolA inside the (PDB: 6wzu) protein targets. At the same time a semi-negative docking effect was detected from the Nirmatrelvir compound with positive Total Energy Interaction docking values of (1, PAXLOVID (Nirmatrelvir) e92b8739e1 ligand of (1, -5.957, 49.082, -0.000, -0.001, run 1, -5.957, 49.082, -0.000, -0.001, run 1, -5.957, 49.082, -0.000, -0.001, run 1, -5.957, 49.082, -0.000, -0.001) KcalMolA when combined with the Molnupiravira0932ea8a7 ligand against the same binding domains. More precisely the Molnupiravir conformer interacted with Positive Total Energy Interactions of (1, -5.428, 32.769, -0.000, -0.003, run 2, -5.428, 32.769, -0.000, -0.003, run 2, -5.428, 32.769, -0.000, -0.003, run 2, -5.428, 32.769, -0.000, -0.003) KcalMolA due to the missing of the (1S, 3S, 7R) - 7 - amino - 1 - [(R) - {3 - sulfanylidene - 2, 4, 6 - triazabicyclo [3.1.0] hexa - 1, 4 - dien - 6 - yl} [(E) - 2 - [(3R) - 3 - [(2R, 5R) - 3, 4, 5 - trifluoro - 2, 5 - dihydrofuran - 2 - yl] - 3H - 1, 2, 4 - triazol - 5 - yl] diazen - 1 - yl] phosphoroso] - 1, 2, 4, 6 - tetraazaspiro [2.4] heptane - 5 - thione pharmacophoric substitutions. In addition the GissitorviffirnaTM8ac33ef19 ligand conformer of (1, -4.598, -7.504, -0.000, 0.076, run 10, -4.598, -7.504, -0.000, 0.076, run 10, -4.598, -7.504, -0.000, 0.076, run 10, -4.598, -7.504, -0.000, 0.076) KcalMolA. The Molnupiravir_5vyh_ 6372632b98921 ligand conformer generated an intermediate inhibitory outcome inside the (PDB: 5vyh) binding domains since it was interacted with positive Total Energies of (34.068) KcalMolA and docking activities of (1, molnupiravirac1e1b4022 lig and 1, -1.667, 34.068, -0.000, -0.013) KcalMolA due to the lack of the 4 - [3 - (aminomethyl) oxiren - 2 - yl] - 4, 5 - diaza - 2λ⁵ - phosphaspiro [bicyclo [3.1.0] hexane - 2, 2' - oxaphosphirane] - 3 - thione druggable scaffoldings. The same partial inhibitory effect was observed when the Molnupiravir_6lu7_ 637265a213f4d ligand conformer generated a partial negative docking effect of less positive docking energy values when docked into the (PDB: 6lu7) protein targets with the binding affinity scoring values of (1, molnupiravir7b59c1 lig and 1, -5.428, 34.075, -0.000, -0.005) KcalMolA due to the absence of the (1S, 5S) - 4 - [(2R, 3S) - 3 - [(3R) - 2 - amino - 1 - fluoro - 5 - sulfanylidene - 3H - 1, 2, 4 - triazol - 3 - yl] oxiran - 2 - yl] - 4, 5, 6 - triaza - 2λ⁵ - phosphaspiro [bicyclo [3.1.0] hexane - 2, 2' - oxaphosphirane] - 3 - thione substituted ligand. The Molnupiravir_1xak_ 637265fc11b93 ligand also interacted with intermediate docking affinities and positive Total Energies against the (PDB: 1xak) Protein Targets with the scoring values of (1, molnupiravir 531711241a lig and 1, -5.591, 12.564, 4.722, -29.328) KcalMolA because of the missing pharmacophoric groups of the (Z) - 4 - amino - N - [(1Z) - amino-methylidene] - N' - [(Z) - 2 - {6 - [(1Z) - [(fluoromethyl) imino] methyl] - 3 - sulfanylidene - 1, 2, 4 - triazabicyclo [3.1.0] hex - 2 - en - 6 - yl} - N' - methyl-ethanimidamido] - 2 - oxobutanimidamide chemical element. At the same time the Molnupiravir_5rgw_ 63726ae391d65 ligand generated again positive Total Energies when interacted with the SARS-CoV-2 protein targets of (PDB:1xak) with the docking values of (1, molnupiravird26f2bece9 lig and 1, -6.867, 7.794, -7.938, -19.751) KcalMolA due to missing pharmacophoric elements of [2 - (aminomethyl) - 2 - { [(2E) - 3 - oxofuran - 2 - ylidene] methyl} - 2λ⁵ - azaphosphiridin - 1 - yl] amino (1R, 4S) - 3, 3 - dimethyl - 6 - oxo - 2λ⁴ - thia - 5 - azaspiro

 doi:10.20944/preprints202403.0518.v1

[bicyclo [3.2.0] heptane - 2, 1' - thiirane] - 4 - carboxylate. The FDA drug of the Molnupiravir_5rf6_63726b4acf0fd ligand conformer generated finally positive Total Energies of 7.385KcalMolA with the docking values of (1, molnupiravir28276be760 lig and 1, -7.051, 7.385, -12.069, -16.022) KcalMolA while co-interacting with the Valsartan_ 1y8jX_6348460bb635e ligand conformer for the generation again of an intermediate docking effect with positive docking values of 73.198KcalMolA and observed docking parameters of some of (1, valsartan ea8754f6fa lig and 1, -7.005, 73.198, -10.604, -20.20) KcalMolA. That Positive Docking Energy effect produced from the combination of the Molnupiravir and Valsartan Drugs means that these two chemical structures weren't able of generalizing the Quantum Negative state Transformations generated by docking measurements' feedback due to the missing of the Triangularized pharmacophoric group of N - { [(2S) - 3 - (aminomethyl) - 2 - [(1R, 2S) - 2 - methyldiaziridin - 1 - yl] - 1, 3 - diazetidin - 1 - yl] ({ [(E) - { [(E) - (aminomethylidene) amino] methylidene} amino] amino}) aziridin - 1 - yl - λ^5 - phosphanyl} - 3 - {5 - [(1E) - [2 - (aminomethyl) - 2 - methylhydrazin - 1 - ylidene] methyl] - 3, 4 - dihydroxyfuran - 2 - yl} - 2 - methyl - 5 - sulfanylidene - 1, 2, 3, 4 - tetrazole - 1 - carboxa-diamino ({ [1 - ({ [(2S, 3R, 4R, 5R) - 5 - (3 - { [(R) - [(2 - amino - 6 - oxo - 8, 9 - dihydro - 1λ^4, 3λ^4 - purin - 9 - yl) amino] [(6 - fluoro - 3H - 1λ^4 - pyrazin - 2 - yl) formamido] phosphoryl} carbamoyl} - 1, 5 - dihydro - 1, 2, 4 - triazol - 1 - yl) - 3, 4 - dihydroxyoxolan - 2 - yl] methoxy} (cyano) amino) ethenyl] imino}) methanium derivatives. On the hand my DRVYIHPFXmimetic_ 6gid_63887f917804a Drug Design interacted solely with negative docking energy values (Rank, File, ID, Compound, Affinity, Total Energy, vdW Energy, Elec. Energy) of (1, 8f357f6ad2 Lig and 1, -7.178, -36.112, -14.305, -17.511) KcalMolA inside the same (PDB: 6gid). This DRVYIHPFX mimetic ligand generated once more noncovalent interactions for (PDB: 6gid) protein structure of the substrate-free human neprilysin Neprilysin inside it's transmembrane M13 zinc metalloprotease binding sites which are responsible for the degradation of several biologically active peptides including insulin, enkephalin, substance P, bradykinin, endothelin-1, neurotensin and amyloid-β while targeting the EDO:A:806 (EDO) binding sites when conjoined with the GissitorviffirnaTM7 (1S, 3S, 7R) - 7 - amino - 1 - [(R) - [amino ({4 - [(2R, 3R) - 2 - [(2S) - 3 - { [(1S, 2S) - 1 - { [(S) - 1, 3 - dihydroisoindole - 2 - carbonyl [(2 - methyl - 6 - oxo - 1, 7 - dihydropurin - 8 - yl) methyl] phosphanyl] carbamoyl} - 2 - methylbutyl] amino} - 2 - methyl propyl] oxaziridin - 3 - yl] butyl}amino) methylidene] azanium {3 - sulfanylidene - 2, 4, 6 - triazabicyclo [3.1.0] hexa - 1, 4 - dien - 6 - yl} [(E) - 2 - [(3R) - 3 - [(2R, 5R) - 3, 4, 5 - trifluoro - 2, 5 - dihydrofuran - 2 - yl] - 3H - 1, 2, 4 - triazol - 5 - yl] diazen - 1 - yl] phosphoroso] - 1, 2, 4, 6 - tetraazaspiro [2.4] heptane - 5 - thione neo-ligand (SI Appendix XL) within the Interacting chains A. Hydrogen Bonds (RESNR, RESTYPE, RESCHAIN, RESNR_LIG, RESTYPE_LIG, RESCHAIN_LIG, SIDECHAIN, DIST_H, A, DIST_D, A, DON_ANGLE, PROTISDON, DONORIDX, DONORTYPE, ACCEPTORIDX, ACCEPTORTYPE, LIGCOO, PROTCOO) of (195, GLY, A, 806, eDO, A, False, 2.75, 3.44, 128.85, false, 5605, o3, 1098, o2, 16.140, 26.425, 9.139, 18.810, 24.341, 8.535, 196, LYS, A, 806, eDO, A, True, 2.29, 3.30, 169.26, true, 1107, n3, 5603, o3, 13.414, 27.389, 11.321, 14.171, 24.687, 13.061, 197, LYS, A, 806, eDO, A, False, 2.11, 3.07, 165.00, true, 1108, nam, 5605, o3, 16.140, 26.425, 9.139, 15.191, 23.894, 7.679, 373, ARG, A, 806, eDO, A, True, 2.49, 2.91, 105.37, true, 2541, ng, 5603, o3, 13.414, 27.389, 11.321, 10.731, 26.906, 12.352) KcalMolA were generated inside the EDO:A:807 (EDO) binding sites when the amino ({4 - [(2R, 3R) - 2 - [(2S) - 3 - { [(1S, 2S) - 1 - { [(S) - 1, 3 - dihydro-isoindole - 2 - carbonyl [(2 - methyl - 6 - oxo - 1, 7 - dihydropurin - 8 - yl) methyl] phosphanyl] carbamoyl} - 2 - methylbutyl] amino} - 2 - methylpropyl] oxaziridin - 3 - yl] butyl}amino) methylidene] azanium small molecule conducted with the GissitorviffirnaTM6 (2R, 4R, 5S) - 2 - amino - 3 - {4 - amino - 1 - [(2R, 3R, 4R, 5R) - 5 - [(2R) - 3 - (aminomethyl) - 2 - (2 - methyldiaziridin - 1 - yl) - 1, 3 - diazetidin - 1 - yl] - 3, 4 - dihydroxyoxolan - 2 - yl] - 5 - sulfanylidene - 4, 5 - dihydro - 1H - 1, 2, 4 - triazole - 3 - carbonyl} - 1 - [(2S) - 1 - [(3R) - 2 - amino - 1 - methyl - 5 - sulfanylidene - 1, 2, 4 - triazolidin - 3 - yl] propan - 2 - yl] - octahydro - 1H - purin - 6 - one drug design (SI Appendix XL) inside the same Interacting chains A. Additional Hydrogen Bonds (RESNR, RESTYPE, RESCHAIN, RESNR_LIG, RESTYPE_LIG, RESCHAIN_LIG, SIDECHAIN, DIST_H, A, DIST_D, A, DON_ANGLE, PROTISDON, DONORIDX, DONORTYPE, ACCEPTORIDX, ACCEPTORTYPE, LIGCOO, PROTCOO) of (206, THR, A, 807, eDO, A, False, 2.18, 3.02, 143.00, true, 1178, nam, 5609, o3, 22.347, 34.983, 0.162, 23.986, 33.907, 2.135) KcalMolA and water Bridges (RESNR,

 doi:10.20944/preprints202403.0518.v1

RESTYPE, RESCHAIN, RESNR_LIG, RESTYPE_LIG, RESCHAIN_LIG, DIST_A, W, DIST_D, W, DON_ANGLE, WATER_ANGLE, PROTISDON, DONOR_IDX, DONORTYPE, ACCEPTOR_IDX, ACCEPTORTYPE, WATER_IDX, LIGCOO, PROTCOO, WATERCOO) of (346, TYR, A, 807, eDO, A, 3.45, 3.70, 153.83, 117.07, false, 5607, o3, 2314, o3, 5885, 19.543, 35.634, 0.353, 17.673, 37.051, 2.268, 17.274, 38.520, 0.831) KcalMolA inside the EDO:A:808 (EDO) binding domains were constructed when the pharmacophoric scaffold of [amino ({4 - [(2R, 3R) - 2 - [(2S) - 3 - { [(1S, 2S) - 1 - { [(S) - 1, 3 - dihydroisoindole - 2 - carbonyl [(2 - methyl - 6 - oxo - 1, 7 - dihydropurin - 8 - yl) methyl] phosphanyl] carbamoyl} - 2 - methylbutyl] amino} - 2 - methylpropyl] oxaziridin - 3 - yl] butyl}amino) methylidene] azanium combined with the GissitorviffirnaTM4 (1S, 5S) - 4 - [(2R, 3S) - 3 - [(3R) - 2 - amino - 1 - fluoro - 5 - sulfanylidene - 3H - 1, 2, 4 - triazol - 3 - yl] oxiran - 2 - yl] - 4, 5, 6 - triaza - 2λ^5 - phosphaspiro [bicyclo [3.1.0] hexane - 2, 2' - oxaphosphirane] - 3 - thione small molecule. These novel pharmacophoric designs could received attention in near for its potential role in modulating blood pressure responses with its inhibition producing an antihypertensive response since to date, several inhibitor bound crystal structures of the human neprilysin extracellular domain have been determined, but, a structure free of bound inhibitor or substrate has yet to be reported. Moreover Hydrogen Bonds (RESNR, RESTYPE, RESCHAIN, RESNR_LIG, RESTYPE_LIG, RESCHAIN_LIG, SIDECHAIN, DIST_H, A, DIST_D, A, DON_ANGLE, PROTISDON, DONORIDX, DONORTYPE, ACCEPTORIDX, ACCEPTORTYPE, LIGCOO, PROTCOO) of (264, ASP, A, 808, eDO, A, False, 1.87, 2.82, 160.29, true, 1647, nam, 5611, o3, 0.117, 9.051, 23.843, 1.328, 8.662, 26.357) KcalMolA including water Bridges (RESNR, RESTYPE, RESCHAIN, RESNR_LIG, RESTYPE_LIG, RESCHAIN_LIG, DIST_A, W, DIST_D, W, DON_ANGLE, WATER_ANGLE, PROTISDON, DONOR_IDX, DONORTYPE, ACCEPTOR_IDX, ACCEPTORTYPE, WATER_IDX, LIGCOO, PROTCOO, WATERCOO) of (267, GLN, A, 808, eDO, A, 2.97, 4.00, 153.01, 97.25, true, 1680, nam, 5613, o3, 5702, 1.188, 7.266, 20.727, 3.305, 10.037, 17.948, 0.386, 9.369, 19.348) KcalMolA against the EDO:A:809 (EDO) binding residues were produced when the clustered pharmacophoric element of [amino ({4 - [(2R, 3R) - 2 - [(2S) - 3 - { [(1S, 2S) - 1 - { [(S) - 1, 3 - dihydroisoindole - 2 - carbonyl [(2 - methyl - 6 - oxo - 1, 7 - dihydropurin - 8 - yl) methyl] phosphanyl] carbamoyl} - 2 - methylbutyl] amino} - 2 - methylpropyl] oxaziridin - 3 - yl] butyl}amino) methylidene] azanium concerted in these parallel docking experiments with the GissitorviffirnaTM3 (Z) - 4 - amino - N - [(1Z) - amino-methylidene] - N' - [(Z) - 2 - {6 - [(1Z) - [(fluoromethyl) imino] methyl] - 3 - sulfanylidene - 1, 2, 4 - triazabicyclo [3.1.0] hex - 2 - en - 6 - yl} - N' - methylethanimidamido] - 2 - oxobutanimidamide ligand (SI Appendix XL) inside the Interacting chains A while Hydrogen Bonds (RESNR, RESTYPE, RESCHAIN, RESNR_LIG, RESTYPE_LIG, RESCHAIN_LIG, SIDECHAIN, DIST_H, A, DIST_D, A, DON_ANGLE, PROTISDON, DONORIDX, DONORTYPE, ACCEPTORIDX, ACCEPTORTYPE, LIGCOO, PROTCOO) of (292, ARG, A, 809, eDO, A, True, 3.34, 3.78, 109.41, true, 1876, ng, 5615, o3, 15.143, 37.396, 2.310, 11.668, 36.021, 2.905) KcalMolA and water Bridges (RESNR, RESTYPE, RESCHAIN, RESNR_LIG, RESTYPE_LIG, RESCHAIN_LIG, DIST_A, W, DIST_D, W, DON_ANGLE, WATER_ANGLE, PROTISDON, DONOR_IDX, DONORTYPE, ACCEPTOR_IDX, ACCEPTORTYPE, WATER_IDX, LIGCOO, PROTCOO, WATERCOO) of (292, ARG, A, 809, eDO, A, 3.92, 3.82, 110.03, 125.26, false, 5617, o3, 1869, o2, 5787, 14.114, 40.643, 3.719, 11.441, 42.049, 0.919, 10.866, 42.346, 4.789) KcalMolA redirected into the EDO:A:810 (EDO) binding domains. The active pharmacophoric element of [amino ({4 - [(2R, 3R) - 2 - [(2S) - 3 - { [(1S, 2S) - 1 - { [(S) - 1, 3 - dihydroisoindole - 2 - carbonyl [(2 - methyl - 6 - oxo - 1, 7 - dihydropurin - 8 - yl) methyl] phosphanyl] carbamoyl} - 2 - methylbutyl] amino} - 2 - methylpropyl] oxaziridin - 3 - yl] butyl}amino) methylidene] azanium when combined with the GissitorviffirnaTM1 (2S, 3S) - 3 - ({ [(1 - { [(3R) - 2 - (dimethylamino) - 3 - [(R) - hydroxy (2R) - oxiran - 2 - ylmethyl] - 2λ^5 - oxaphosphiran - 2 - yl] methyl}hydrazin - 1 - yl) methyl] amino} methyl) oxirane - 2 - carbonitrile (SI Appendix XL) covered the whole binding surfaces in Interacting chains A while constructing Hydrogen Bonds (RESNR, RESTYPE, RESCHAIN, RESNR_LIG, RESTYPE_LIG, RESCHAIN_LIG, SIDECHAIN, DIST_H, A, DIST_D, A, DON_ANGLE, PROTISDON, DONORIDX, DONORTYPE, ACCEPTORIDX, ACCEPTORTYPE, LIGCOO, PROTCOO) of (448, GLU, A, 810, eDO, A, False, 3.25, 3.71, 110.69, true, 3124, nam, 5621, o3, 37.123, 59.496, 3.334, 33.639, 60.589, 3.993) KcalMolA and water Bridges (RESNR,

 doi:10.20944/preprints202403.0518.v1

RESTYPE, RESCHAIN, RESNR_LIG, RESTYPE_LIG, RESCHAIN_LIG, DIST_A, W, DIST_D, W, DON_ANGLE, WATER_ANGLE, PROTISDON, DONOR_IDX, DONORTYPE, ACCEPTOR_IDX, ACCEPTORTYPE, WATER_IDX, LIGCOO, PROTCOO, WATERCOO) of (444, ALA, A, 810, eDO, A, 3.98, 3.66, 101.99, 89.29, true, 3091, nam, 5619, o3, 5675, 38.720, 56.570, 3.135, 37.118, 57.120, 7.660, 39.164, 54.352, 6.410) KcalMolA inside the EDO:A:811 (EDO) binding sites in conjunction with the [amino ({4 - [(2R, 3R) - 2 - [(2S) - 3 - { [(1S, 2S) - 1 - { [(S) - 1, 3 - dihydroisoindole - 2 - carbonyl [(2 - methyl - 6 - oxo - 1, 7 - dihydropurin - 8 - yl) methyl] phosphanyl] carbamoyl} - 2 - methylbutyl] amino} - 2 - methylpropyl] oxaziridin - 3 - yl] butyl}amino) methylidene] azanium Interacting chains GOL:A:817, (GOL), [amino ({4 - [(2R, 3R) - 2 - [(2S) - 3 - { [(1S, 2S) - 1 - { [(S) - 1, 3 - dihydroisoindole - 2 - carbonyl [(2 - methyl - 6 - oxo - 1, 7 - dihydropurin - 2 - [(2S) - 3 - { [(1S, 2S) - 1 - { [(S) - 1, 3 - dihydroisoindole - 2 - carbonyl [(2 - methyl - 6 - oxo - 1, 7 - dihydropurin - 8 - yl) methyl] phosphanyl] carbamoyl} - 2 - methylbutyl] amino} - 2 - methylpropyl] oxaziridin - 3 - yl] butyl}amino) methylidene] azanium Interacting chains GOL:A:817, (GOL), [amino ({4 - [(2R, 3R) - 2 - [(2S) - 3 - { [(1S, 2S) - 1 - { [(S) - 1, 3 - dihydroisoindole - 2 - carbonyl [(2 - methyl - 6 - oxo - 1, 7 - dihydropurin - 8 - yl) methyl] phosphanyl] carbamoyl} - 2 - methylbutyl] amino} - 2 - methylpropyl] oxaziridin - 3 - yl] butyl}amino) methylidene] azanium when docked in parallel with the Roccustyrna_gs8-1 diamino ({ [1 - ({ [(2S, 3R, 4R, 5R) - 5 - (3 - { [(R) - [(2 - amino - 6 - oxo - 8, 9 - dihydro - 1λ^4, 3λ^4 - purin - 9 - yl) amino] [(6 - fluoro - 3H - 1λ^4 - pyrazin - 2 - yl) formamido] phosphoryl] carbamoyl} - 1, 5 - dihydro - 1, 2, 4 - triazol - 1 - yl) - 3, 4 - dihydroxyoxolan - 2 - yl] methoxy} (cyano) amino) ethenyl] imino}) methanium neo-ligand (SI Appendix XL) as a first crystal structured inhibitor targeted the extracellular catalytic domain of human neprilysin at 1.9 Å resolution. This structure will provide a reference point for comparisons to future inhibitor substrate bound structures. These neprilysin mimicking structures also revealed that these closed protein-ligand conformations can be adopted in protein crystals absent of bound substrate or inhibitor. The same combination of small molecules also generated hydrophobic interactions when docked onto the Interacting chains A and Hydrogen Bonds (RESNR, RESTYPE, RESCHAIN, RESNR_LIG, RESTYPE_LIG, RESCHAIN_LIG, SIDECHAIN, DIST_H, A, DIST_D, A, DON_ANGLE, PROTISDON, DONORIDX, DONORTYPE, ACCEPTORIDX, ACCEPTORTYPE, LIGCOO, PROTCOO) of (174, GLU, A, 817, gOL, A, True, 2.40, 3.26, 148.13, false, 5653, o3, 935, o2, 3.153, 6.821, 12.306, 0.311, 7.099, 10.730, 271, GLU, A, 817, gOL, A, True, 3.16, 3.58, 108.05, false, 5657, o3, 1710, o3, 2.370, 7.789, 16.473, 0.738, 10.772, 17.605) KcalMolA inside the NAG:A:801 (NAG) binding cavities when joint docking activities with the Roccustyrna_gs6 – 1 { [(1S, 2S, 3S) - 2 - (4 - amino - 5 - sulfanylidene - 4H - 1, 2, 4 - triazol - 3 - yl) - 2 - carboximidoyl - 3 - fluoro - 1 - oxo - 1λ^5 - phosphiran - 1 - yl] amino} [(Z) - ethylideneamino] iminomethanium ligand. Additionally, more Hydrogen Bonds (RESNR, RESTYPE, RESCHAIN, RESNR_LIG, RESTYPE_LIG, RESCHAIN_LIG, SIDECHAIN, DIST_H, A, DIST_D, A, DON_ANGLE, PROTISDON, DONORIDX, DONORTYPE, ACCEPTORIDX, ACCEPTORTYPE, LIGCOO, PROTCOO) of (144, ASN, A, 801, nAG, A, True, 3.31, 3.68, 104.43, true, 702, nam, 5558, o2, 34.971, 17.263, 33.043, 31.545, 16.322, 32.067) KcalMolA were reconstructed around the NAG:A:802 (NAG) binding surfaces when the [amino ({4 - [(2R, 3R) - 2 - [(2S) - 3 - { [(1S, 2S) - 1 - { [(S) - 1, 3 - dihydroisoindole - 2 - carbonyl [(2 - methyl - 6 - oxo - 1, 7 - dihydropurin - 8 - yl) methyl] phosphanyl] carbamoyl} - 2 - methylbutyl] amino} - 2 - methylpropyl] oxaziridin - 3 - yl] butyl}amino) methylidene] azanium neo-ligand in parallel combined with the Roccustyrna_gs4-1 N - [({ [(S) - {2 - [(1M) - 2 - amino - 9 - [(2R, 3R, 4R, 5S) - 5 - [({ [(E) - (aminomethylidene) amino] methyl} (methyl) amino) methyl] - 3, 4 - dihydroxyoxolan - 2 - yl] - 6 - oxo - 5, 8 - dihydro - 1λ^4, 3λ^4 - purin - 7 - yl] - 2 - oxoethyl}amino (1S) - 2, 2 - dimethylaziridin - 1 - ylphosphoryl] amino}methoxy) methyl] - 6 - fluoro - 3 - oxo - 5H - 1λ^4 - pyrazine - 2 - carboxamide drug design (SI Appendix XL) while generating Hydrophobic Interactions (RESNR, RESTYPE, RESCHAIN, RESNR_LIG, RESTYPE_LIG, RESCHAIN_LIG, DIST, LIGCARBONIDX, PROTCARBONIDX, LIGCOO, PROTCOO) of (327, ASN, A, 802, nAG, A, 3.64, 5566, 2162, 18.267, 12.140, 6.115, 18.535, 15.554, 7.344) KcalMolA, and Hydrogen Bonds (RESNR, RESTYPE, RESCHAIN, RESNR_LIG, RESTYPE_LIG, RESCHAIN_LIG, SIDECHAIN, DIST_H, A, DIST_D, A, DON_ANGLE, PROTISDON, DONORIDX, DONORTYPE, ACCEPTORIDX, ACCEPTORTYPE, LIGCOO, PROTCOO) of (324, ASN, A, 802, nAG, A, True, 2.65, 3.19, 115.43, true, 2139, nam, 5572, o2, 16.708,

 doi:10.20944/preprints202403.0518.v1

11.643, 7.870, 13.718, 11.868, 6.767, 328, GLU, A, 802, nAG, A, True, 2.24, 3.07, 140.89, false, 5567, nam, 2174, o2, 16.379, 10.675, 5.864, 16.025, 10.984, 2.833) KcalMolA around the NAG:A:803 (NAG) binding areas. Furthermore hydrogen Bonds (RESNR, RESTYPE, RESCHAIN, RESNR_LIG, RESTYPE_LIG, RESCHAIN_LIG, SIDECHAIN, DIST_H, A, DIST_D, A, DON_ANGLE, PROTISDON, DONORIDX, DONORTYPE, ACCEPTORIDX, ACCEPTORTYPE, LIGCOO, PROTCOO) of (627, ASN, A, 803, nAG, A, True, 3.51, 3.89, 105.29, true, 4579, nam, 5586, o2, 1.610, 55.515, 10.683, 1.499, 58.825, 12.720, 744, LYS, A, 803, nAG, A, True, 3.44, 3.99, 115.41, true, 5495, n3, 5585, o3, 1.466, 62.342, 9.676, 4.427, 64.565, 8.191, 744, LYS, A, 803, nAG, A, True, 3.28, 3.99, 131.73, false, 5585, o3, 5495, n3, 1.466, 62.342, 9.676, 4.427, 64.565, 8.191) KcalMolA were generated inside the NAG:A:804 (NAG) binding surfaces when the active pharmacophoric elements of [amino ({4 - [(2R, 3R) - 2 - [(2S) - 3 - { [(1S, 2S) - 1 - { [(S) - 1, 3 - dihydroisoindole - 2 - carbonyl [(2 - methyl - 6 - oxo - 1, 7 - dihydropurin - 8 - yl) methyl] phosphanyl] carbamoyl} - 2 - methylbutyl] amino} - 2 - methylpropyl] oxaziridin - 3 - yl] butyl}amino) methylidene] azanium interacted inside the Interacting chains A while Hydrogen Bonds (RESNR, RESTYPE, RESCHAIN, RESNR_LIG, RESTYPE_LIG, RESCHAIN_LIG, SIDECHAIN, DIST_H, A, DIST_D, A, DON_ANGLE, PROTISDON, DONORIDX, DONORTYPE, ACCEPTORIDX, ACCEPTORTYPE, LIGCOO, PROTCOO) of (284, ASN, A, 804, nAG, A, True, 2.78, 3.18, 104.95, false, 5595, nam, 1814, o2, 6.788, 33.598, 6.796, 3.683, 34.293, 6.875, 353, LYS, A, 804, nAG, A, True, 2.41, 3.12, 125.94, true, 2371, n3, 5599, o3, 4.465, 33.145, 1.099, 1.907, 34.549, 0.012) KcalMolA in combination with water Bridges (RESNR, RESTYPE, RESCHAIN, RESNR_LIG, RESTYPE_LIG, RESCHAIN_LIG, DIST_A, W, DIST_D, W, DON_ANGLE, WATER_ANGLE, PROTISDON, DONOR_IDX, DONORTYPE, ACCEPTOR_IDX, ACCEPTORTYPE, WATER_IDX, LIGCOO, PROTCOO, WATERCOO) of (284, ASN, A, 804, nAG, A, 2.83, 3.93, 119.89, 88.41, true, 1815, nam, 5599, o3, 5891, 4.465, 33.145, 1.099, 4.326, 32.612, 5.533, 3.162, 30.887, 2.205, 284, ASN, A, 804, nAG, A, 3.32, 3.93, 119.89, 135.09, true, 1815, nam, 5598, o3, 5891, 5.265, 33.122, 3.473, 4.326, 32.612, 5.533, 3.162, 30.887, 2.205) KcalMolA against the NO3:A:812 (NO3) binding surfaces. As a result the active pharmaco-element of [amino ({4 - [(2R, 3R) - 2 - [(2S) - 3 - { [(1S, 2S) - 1 - { [(S) - 1, 3 - dihydroisoindole - 2 - carbonyl [(2 - methyl - 6 - oxo - 1, 7 - dihydropurin - 8 - yl) methyl] phosphanyl] carbamoyl} - 2 - methylbutyl] amino} - 2 - methylpropyl] oxaziridin - 3 - yl] butyl}amino) methylidene] azanium when incorporated with the Roccustyrna_gs2-1.4 - amino - 5 - [(1'R, 2S, 3''S, 5'R, 6'R) - 3' - methyldispiro [oxirane - 2, 2' - bicyclo [3.1.0] hexane-6', 2'' - oxiran] - 3' - en - 3'' - ylmethyl] - 1, 2, 4 - triazole - 3 - thione multi-covalent ligand (SI Appendix XL) for the construction of Hydrogen Bonds (RESNR, RESTYPE, RESCHAIN, RESNR_LIG, RESTYPE_LIG, RESCHAIN_LIG, SIDECHAIN, DIST_H, A, DIST_D, A, DON_ANGLE, PROTISDON, DONORIDX, DONORTYPE, ACCEPTORIDX, ACCEPTORTYPE, LIGCOO, PROTCOO) of (199, LEU, A, 812, nO3, a, False, 1.94, 2.89, 162.76, true, 1124, nam, 5629, o2, 8.490, 25.127, 8.199, 8.646, 23.805, 5.629, 373, ARG, A, 812, nO3, a, True, 1.93, 2.58, 120.99, true, 2540, ng, 5627, o2, 6.894, 25.493, 9.659, 8.897, 26.058, 11.187) KcalMolA into the NO3:A:813 (NO3) binding residues. The [amino ({4 - [(2R, 3R) - 2 - [(2S) - 3 - { [(1S, 2S) - 1 - { [(S) - 1, 3 - dihydroisoindole - 2 - carbonyl [(2 - methyl - 6 - oxo - 1, 7 - dihydropurin - 8 - yl) methyl] phosphanyl] carbamoyl} - 2 - methylbutyl] amino} - 2 - methylpropyl] oxaziridin - 3 - yl] butyl}amino) methylidene] azanium holomorphic ligand when merged with Roccustyrna_gs1-1.N - [(R) - {1 - [(2R, 3R, 4R, 5S) - 5 - (4 - amino - 5 - sulfanylidene - 1, 2, 4 - triazol - 3 - yl) - 3, 4 - dihydroxyoxolan - 2 - yl] - 5H - 1, 2, 4 - triazol - 3 - yl}formamido (2 - amino - 6 - oxo - 8H - 1λ^4, 3λ^4 - purin - 9 - yl) aminophosphoryl] - 6 - fluoro - 3H - 1λ^4 - pyrazine - 2 - carboxamide structure (SI Appendix XL) constructed Hydrogen Bonds (RESNR, RESTYPE, RESCHAIN, RESNR_LIG, RESTYPE_LIG, RESCHAIN_LIG, SIDECHAIN, DIST_H, A, DIST_D, A, DON_ANGLE, PROTISDON, DONORIDX, DONORTYPE, ACCEPTORIDX, ACCEPTORTYPE, LIGCOO, PROTCOO) of (401, THR, A, 813, nO3, a, False, 3.47, 3.97, 115.65, false, 5633, o2, 2760, o2, 11.869, 30.592, 32.137, 12.673, 31.473, 35.921) KcalMolA, water Bridges (RESNR, RESTYPE, RESCHAIN, RESNR_LIG, RESTYPE_LIG, RESCHAIN_LIG, DIST_A, W, DIST_D, W, DON_ANGLE, WATER_ANGLE, PROTISDON, DONOR_IDX, DONORTYPE, ACCEPTOR_IDX, ACCEPTORTYPE, WATER_IDX, LIGCOO, PROTCOO, WATERCOO) of (391, ASN, A, 813, nO3, a, 3.90, 4.08, 118.53, 110.49, true, 2684, nam, 5631, o2, 6075, 13.587, 29.331, 31.701, 14.670, 25.656, 32.405, 12.921, 27.952, 35.290, 400, THR, A, 813,

 doi:10.20944/preprints202403.0518.v1

nO3, a, 3.58, 2.62, 159.65, 133.83, true, 2755, o3, 5632, o2, 5746, 13.102, 31.019, 30.332, 12.693, 33.765, 29.626, 14.518, 33.171, 27.843) KcalMolA, PEG:A:814 (PEG) binding residues were also reshaped by [amino ({4 - [(2R, 3R) - 2 - [(2S) - 3 - { [(1S, 2S) - 1 - { [(S) - 1, 3 - dihydroisoindole - 2 - carbonyl [(2 - methyl - 6 - oxo - 1, 7 - dihydropurin - 8 - yl) methyl] phosphanyl] carbamoyl} - 2 - methylbutyl] amino} - 2 - methylpropyl] oxaziridin - 3 - yl] butyl}amino) methylidene] azanium Interacting chains PEG:A:815, (PEG), [amino ({4 - [(2R, 3R) - 2 - [(2S) - 3 - { [(1S, 2S) - 1 - { [(S) - 1, 3 - dihydroisoindole - 2 - carbonyl [(2 - methyl - 6 - oxo - 1, 7 - dihydropurin - 8 - yl) methyl] phosphanyl] carbamoyl} - 2 - methylbutyl] amino} - 2 - methylpropyl] oxaziridin - 3 - yl] butyl}amino) methylidene] azanium chemical structure when conjoint negative docking energies with the Roccustyrna_fr5-0.N - [({ [(S) - {2 - [(1M, 1M) - 2 - amino - 9 - [(2R, 3R, 4R, 5S) - 5 - [({ [(E) - (aminomethylidene) amino] methyl} (methyl) amino) methyl] - 3, 4 - dihydroxyoxolan - 2 - yl] - 6 - oxo - 5, 8 - dihydro - 1λ⁴, 3λ⁴ - purin - 7 - yl] - 2 - oxoethyl}amino (1S) - 2, 2 - dimethylaziridin - 1 - ylphosphoryl] amino}methoxy) methyl] - 6 - fluoro - 3 - oxo-5H - 1λ⁴ - pyrazine - 2 - carboxamide ligand (SI Appendix XL) inside the Interacting chains A by formulating water Bridges (RESNR, RESTYPE, RESCHAIN, RESNR_LIG, RESTYPE_LIG, RESCHAIN_LIG, DIST_A, W, DIST_D, W, DON_ANGLE, WATER_ANGLE, PROTISDON, DONOR_IDX, DONORTYPE, ACCEPTOR_IDX, ACCEPTORTYPE, WATER_IDX, LIGCOO, PROTCOO, WATERCOO) of (394, ARG, A, 815, pEG, A, 3.22, 3.72, 153.38, 101.62, true, 2710, ng, 5645, o3, 6038, 17.348, 36.136, 23.420, 15.147, 32.782, 24.310, 15.874, 35.859, 26.266) KcalMolA, PEG:A:816 (PEG) active residues were targeted by the [amino ({4 - [(2R, 3R) - 2 - [(2S) - 3 - { [(1S, 2S) - 1 - { [(S) - 1, 3 - dihydroisoindole - 2 - carbonyl [(2 - methyl - 6 - oxo - 1, 7 - dihydropurin - 8 - yl) methyl] phosphanyl] carbamoyl} - 2 - methylbutyl] amino} - 2 - methylpropyl] oxaziridin - 3 - yl] butyl}amino) methylidene] azanium chemical analogue when amalgamated its negative Quantum energies with the Roccustyrna_fr3-1. (2R, 4R, 5S) - 2 - amino - 3 - {4 - amino - 1 - [(2R, 3R, 4R, 5S) - 3, 4 - dihydroxy - 5 - methyloxolan - 2 - yl] - 5 - sulfanylidene - 1, 2, 4 - triazole - 3 - carbonyl} - 1 - [(2S) - 1 - [(3R) - 2 - amino - 1 - methyl - 5 - sulfanylidene - 3H - 1, 2, 4 - triazol - 3 - yl] propan - 2 - yl] - hexahydropurin - 6 - one ligand (SI Appendix XL). Hydrogen Bonds (RESNR, RESTYPE, RESCHAIN, RESNR_LIG, RESTYPE_LIG, RESCHAIN_LIG, SIDECHAIN, DIST_H, A, DIST_D, A, DON_ANGLE, PROTISDON, DONORIDX, DONORTYPE, ACCEPTORIDX, ACCEPTORTYPE, LIGCOO, PROTCOO) of (717, ARG, A, 816, pEG, A, True, 3.03, 3.94, 154.00, true, 5287, ng, 5648, o3, 22.023, 47.994, 15.687, 18.908, 49.952, 17.090, 717, ARG, A, 816, pEG, A, True, 3.04, 3.94, 153.38, true, 5288, ng, 5648, o3, 22.023, 47.994, 15.687, 19.893, 51.304, 15.511) KcalMolA inside the PO4:A:818 (PO4, zN) binding surfaces including ION, and ZN:A:805 Interacting chains A and additional Hydrogen Bonds (RESNR, RESTYPE, RESCHAIN, RESNR_LIG, RESTYPE_LIG, RESCHAIN_LIG, SIDECHAIN, DIST_H, A, DIST_D, A, DON_ANGLE, PROTISDON, DONORIDX, DONORTYPE, ACCEPTORIDX, ACCEPTORTYPE, LIGCOO, PROTCOO) of (543, ALA, A, 818, pO4, a, False, 1.86, 2.81, 164.23, false, 5662, o3, 3910, o2, 23.676, 47.229, 13.685, 26.001, 45.930, 12.796) KcalMolA, and Salt Bridges (RESNR, RESTYPE, RESCHAIN, PROT_IDX_ LIST, RESNR_LIG, RESTYPE_LIG, RESCHAIN_LIG, DIST, PROTISPOS, LIG_GROUP, LIG_IDX_LIST, LIGCOO, PROTCOO) of (583, hIS, A, 4212, 4215, 818, pO4, a, 4.81, true phosphate interactions, 5658, 5658, 5659, 5660, 5661, 5662, 22.665, 47.117, 12.567, 21.765, 51.812, 12.072, 587, hIS, A, 4246, 4249, 818, pO4, a, 5.29, true phosphate interactions, 5658, 5658, 5659, 5660, 5661, 5662, 22.665, 47.117, 12.567, 20.991, 49.448, 8.128, 711, hIS, A, 5238, 5241, 818, pO4, a, 4.76, true phosphate interactions, 5658, 5658, 5659, 5660, 5661, 5662, 22.665, 47.117, 12.567, 18.364, 46.404, 14.482) KcalMolA, In addition Metal Complexes (RESNR, RESTYPE, RESCHAIN, RESNR_LIG, RESTYPE_LIG, RESCHAIN_LIG, METAL_IDX, METAL_TYPE, TARGET_IDX, TARGET_TYPE, COORDINATION, DIST, LOCATION, RMS, GEOMETRY, COMPLEXNUM, METALCOO, TARGETCOO) of (583, hIS, A, 805, zN, A, 5601, zn, 4215, n, 5, 2.02 protein sidechains, 28.23 trigonal bipyramidal, 1, 21.141, 48.946, 11.217, 21.746, 50.786, 11.773, 587, hIS, A, 805, zN, A, 5601, zn, 4249, n, 5, 2.10 protein sidechains, 28.23 trigonal bipyramidal, 1, 21.141, 48.946, 11.217, 21.242, 49.165, 9.132, 646, GLU, A, 805, zN, A, 5601, zn, 4721, o, 5, 1.93 protein sidechains, 28.23 trigonal bipyramidal, 1, 21.141, 48.946, 11.217, 19.304, 49.301, 11.670, 646, GLU, A, 805, zN, A, 5601, zn, 4722, o, 5, 2.77 protein sidechains, 28.23 trigonal bipyramidal, 1, 21.141, 48.946, 11.217, 18.873, 47.551, 10.443, 818, pO4, a, 805, zN, A, 5601, zn, 5661, o, 5, 2.36, lig and 28.23 trigonal bipyramidal, 1,

 doi:10.20944/preprints202403.0518.v1

21.141, 48.946, 11.217, 21.337, 47.575, 13.123) KcalMolA generated by the DRVYIHPFX-mimetic ligand against the (PDB: 6lzg) protein targets. More precisely, this mimetic analogue interacted inside these (PDB: 6LZG) Protein Structure of novel coronavirus spike receptor-binding domain complexed with its receptor ACE2 with (1, dRVYIHPFX-mimetic2895ec5f lig and 1, -7.064, -31.184, -13.178, -14.887) KcalMolA, NAG:A:701 (NAG), NAG:A:702 (NAG) binding surfaces were also Quantum electronically affected by the [amino ({4 - [(2R, 3R) - 2 - [(2S) - 3 - { [(1S, 2S) - 1 - { [(S) - 1, 3 - dihydroisoindole - 2 - carbonyl [(2 - methyl - 6 - oxo - 1, 7 - [amino ({4 - [(2R, 3R) - 2 - [(2S) - 3 - { [(1S, 2S) - 1 - { [(S) - 1, 3 - dihydroisoindole - 2 - carbonyl [(2 - methyl - 6 - oxo - 1, 7 - dihydropurin - 8 - yl) methyl] phosphanyl] carbamoyl} - 2 - methylbutyl] amino} - 2 - methylpropyl] oxaziridin - 3 - yl] butyl}amino) methylidene] azanium dihydropurin - 8 - yl) methyl] phosphanyl] carbamoyl} - 2 - methylbutyl] amino} - 2 - methylpropyl] oxaziridin - 3 - yl] butyl}amino) methylidene] azanium ligand by formatting Interacting chains A and Hydrogen Bonds (RESNR, RESTYPE, RESCHAIN, RESNR_LIG, RESTYPE_LIG, RESCHAIN_LIG, SIDECHAIN, DIST_H, A, DIST_D, A, DON_ANGLE, PROTISDON, DONORIDX, DONORTYPE, ACCEPTORIDX, ACCEPTORTYPE, LIGCOO, PROTCOO) of (53, ASN, A, 701, nAG, A, True, 2.75, 3.26, 112.74, true, 293, nam, 6427, o2, 44.208, 2.590, 5.010, 46.107, 3.597, 7.463, 57, GLU, A, 701, nAG, A, True, 2.49, 3.22, 131.58, false, 6426, o3, 325, o. co2, 50.309, 5.709, 7.679, 52.218, 7.787, 6.133, 58, ASN, A, 701, nAG, A, True, 2.96, 3.74, 137.05, true, 334, nam, 6425, o3, 48.217, 4.262, 6.844, 46.986, 7.085, 8.973) KcalMolA when fused in a parallel docking run with the RoccustyrnaTM_gs_convs_ (2). ({3 - methyl - 2H - 4λ^4, 6λ^4 - [1,2,3] triazolo [4, 5 - d] pyrimidin - 5 - yl}methyl) amino [(R) - (3H - 1λ^4 - pyridin - 4 - ylamino) ({ [(5H - 1, 3λ^4 - thiazol - 5 - ylmethoxy) carbonyl] amino}) methyl] aminophosphinic acid drug design (SI Appendix XL). After that it was observed that the crystal structure of the C-terminal domain of SARS-CoV-2 (SARS-CoV-2-CTD) spike (S) protein in complex with human ACE2 (hACE2), which reveals a hACE2-binding mode similar overall to that observed for SARS-CoV generated Hydrogen Bonds (RESNR, RESTYPE, RESCHAIN, RESNR_LIG, RESTYPE_LIG, RESCHAIN_LIG, SIDECHAIN, DIST_H, A, DIST_D, A, DON_ANGLE, PROTISDON, DONORIDX, DONORTYPE, ACCEPTORIDX, ACCEPTORTYPE, LIGCOO, PROTCOO) of (26, LYS, A, 702, nAG, A, True, 1.61, 2.58, 156.62, true, 62, n3, 6440, o3, 24.113, 38.926, 0.412, 23.783, 41.447, 0.011) KcalMolA, water Bridges (RESNR, RESTYPE, RESCHAIN, RESNR_LIG, RESTYPE_LIG, RESCHAIN_LIG, DIST_A, W, DIST_D, W, DON_ANGLE, WATER_ANGLE, PROTISDON, DONOR_IDX, DONORTYPE, ACCEPTOR_IDX, ACCEPTORTYPE, WATER_IDX, LIGCOO, PROTCOO, WATERCOO) of (90, ASN, A, 702, nAG, A, 3.70, 3.10, 153.75, 117.07, true, 592, nam, 6441, o2, 6475, 18.602, 41.843, 2.243, 21.601, 40.530, 2.905, 21.912, 43.467, 1.953) KcalMolA within the NAG:A:703 (NAG) binding cavities when targeted by the [amino ({4 - [(2R, 3R) - 2 - [(2S) - 3 - { [(1S, 2S) - 1 - { [(S) - 1, 3 - dihydroisoindole - 2 - carbonyl [(2 - methyl - 6 - oxo - 1, 7 - dihydropurin - 8 - yl) methyl] phosphanyl] carbamoyl} - 2 - methylbutyl] amino} - 2 - methylpropyl] oxaziridin - 3 - yl] butyl}amino) methylidene] - [amino ({4 - [(2R, 3R) - 2 - [(2S) - 3 - { [(1S, 2S) - 1 - { [(S) - 1, 3 - dihydroisoindole - 2 - carbonyl [(2 - methyl - 6 - oxo - 1, 7 - dihydropurin - 8 - yl) methyl] phosphanyl] carbamoyl} - 2 - methylbutyl] amino} - 2 - methylpropyl] oxaziridin - 3 - yl] butyl}amino) methylidene] azanium mimetic compound, and when merged electronically with the RoccustyrnaTM_gs_ convs_ (1). [({4 - [methyl (2 - methylpropyl) sulfamoyl] phenyl} (3S) - oxolan - 3 - ylamino) methyl] amino ({3 - methyl - 2H - 4λ^4, 6λ^4 - [1,2,3] triazolo [4, 5 - d] pyrimidin - 5 - yl}methyl) aminophosphinic acid ligand (SI Appendix XL). Between NAG:B:601 (NAG) Interacting chains A Hydrogen Bonds, (RESNR, RESTYPE, RESCHAIN, RESNR_LIG, RESTYPE_LIG, RESCHAIN_LIG, SIDECHAIN, DIST_H, A, DIST_D, A, DON_ANGLE, PROTISDON, DONORIDX, DONORTYPE, ACCEPTORIDX, ACCEPTORTYPE, LIGCOO, PROTCOO) of (322, ASN, A, 703, nAG, A, True, 2.15, 2.82, 124.20, true, 2484, nam, 6455, o2, 20.208, 4.529, 3.037, 18.772, 6.953, 2.937) KcalMolA were produced when the [amino ({4 - [(2R, 3R) - 2 - [(2S) - 3 - { [(1S, 2S) - 1 - { [(S) - 1, 3 - dihydroisoindole - 2 - carbonyl [(2 - methyl - 6 - oxo - 1, 7 - dihydropurin - 8 - yl) methyl] phosphanyl] carbamoyl} - 2 - methylbutyl] amino} - 2 - methylpropyl] oxaziridin - 3 - yl] butyl}amino) methylidene] azanium when incorporated with the Roccustyrna_fr.0. (E) - N' - [(1S) - 2 - { [(S) - ({1 - [(3R, 7R, 7aR) - 3 - amino - 7 - [(2E) - 4 - fluoropenta - 2, 4 - dienoyl] - 1H, 2H, 3H, 7H, 7aH - pyrrolo [3, 4 - e] [1,2,4] triazin - 5 - yl] ethenyl}amino) [(1R, 2R) - 2 - fluoroaziridin - 1 - yl]

 doi:10.20944/preprints202403.0518.v1

phosphoryl] amino} - 1 - cyanoethyl] methanimidamide ligand while constructing (SI Appendix XL) within Interacting chains B Hydrophobic Interactions (RESNR, RESTYPE, RESCHAIN, RESNR_LIG, RESTYPE_LIG, RESCHAIN_LIG, DIST, LIGCARBONIDX, PROTCARBONIDX, LIGCOO, PROTCOO) of (338, PHE, B, 601, nAG, B, 3.85, 6464, 4904, 33.695, 12.828, 30.337, 33.521, 15.679, 32.915, 342, PHE, B, 601, nAG, B, 3.69, 6464, 4935, 33.695, 12.828, 30.337, 34.428, 14.731, 27.264, 368, LEU, B, 601, nAG, B, 3.98, 6464, 5152, 33.695, 12.828, 30.337, 29.754, 13.278, 30.619) KcalMolA, and Hydrogen Bonds (RESNR, RESTYPE, RESCHAIN, RESNR_LIG, RESTYPE_LIG, RESCHAIN_LIG, SIDECHAIN, DIST_H, A, DIST_D, A, DON_ANGLE, PROTISDON, DONORIDX, DONORTYPE, ACCEPTORIDX, ACCEPTORTYPE, LIGCOO, PROTCOO) of (343, ASN, B, 601, nAG, B, True, 3.51, 4.05, 116.38, false, 6465, nam, 4948, o2, 34.670, 10.870, 29.329, 36.829, 11.053, 25.908) KcalMolA when docked inside the ZN:A:704 (ZN) ION Interacting chains A against SARS-CoV-S1/receptor-binding domain (RBD) indicating notable differences in antigenicity between SARS-CoV and SARS-CoV-2. These DRVYIHPFXmimetic DockThor experiments findings shed light on the viral pathogenesis and provide important structural information regarding development of therapeutic countermeasures against the emerging virus since Metal Complexes of (RESNR, RESTYPE, RESCHAIN, RESNR_LIG, RESTYPE_LIG, RESCHAIN_LIG, METAL_IDX, METAL_TYPE, TARGET_IDX, TARGET_TYPE, COORDINATION, DIST, LOCATION, RMS, GEOMETRY, COMPLEXNUM, METALCOO, TARGETCOO, 374, hIS, A, 704, zN, A, 6456, zn, 2894, n, 5, 2.09 protein sidechains, 37.21 trigonal bipyramidal, 1, 24.694, 12.184, 18.492, 23.354, 10.579, 18.391, 378, hIS, A, 704, zN, A, 6456, zn, 2925, n, 5, 2.10 protein sidechains, 37.21 trigonal bipyramidal, 1, 24.694, 12.184, 18.492, 24.236, 12.925, 16.583, 402, GLU, A, 704, zN, A, 6456, zn, 3118, o, 5, 2.76 protein sidechains, 37.21 trigonal bipyramidal, 1, 24.694, 12.184, 18.492, 24.944, 14.617, 19.778, 402, GLU, A, 704, zN, A, 6456, zn, 3119, o, 5, 2.00 protein sidechains, 37.21 trigonal bipyramidal, 1, 24.694, 12.184, 18.492, 23.365, 13.098, 19.667, 911, hOH, A, 704, zN, A, 6456, zn, 6581, o, 5, 2.47, water, 37.21 trigonal bipyramidal, 1, 24.694, 12.184, 18.492, 26.940, 11.221, 18.145) KcalMolA were shaped when this peptide mimetic ligand targeted inside the (PDB:6wco) with (DRVYIHPFXmimetic_ 6wco_63887dfc2642b (Rank, File, ID, Compound, Affinity, Total Energy, vdW Energy, Elec. Energy) of (1, ffb8fa6a Lig and 1, -7.144, -25.017, -13.111, -8.558) KcalMolA. (SI Appendix XL). Noncovalent interactions for (PDB:6wco) Protein Structures of SARS main protease bound to inhibitor X47 indicated that DMS:A:404 (DMS) binding domains constructed when the [amino ({4 - [(2R, 3R) - 2 - [(2S) - 3 - [amino ({4 - [(2R, 3R) - 2 - [(2S) - 3 - { [(1S, 2S) - 1 - { [(S) - 1, 3 - dihydroisoindole - 2 - carbonyl [(2 - methyl - 6 - oxo - 1, 7 - dihydropurin - 8 - yl) methyl] phosphanyl] carbamoyl} - 2 - methylbutyl] amino} - 2 - methylpropyl] oxaziridin - 3 - yl] butyl}amino) methylidene] azanium{ [(1S, 2S) - 1 - { [(S) - 1, 3 - dihydroisoindole - 2 - carbonyl [(2 - methyl - 6 - oxo - 1, 7 - dihydropurin - 8 - yl) methyl] phosphanyl] carbamoyl} - 2 - methylbutyl] amino} - 2 - methylpropyl] oxaziridin - 3 - yl] butyl}amino) methylidene] azanium ligand interacted within chains A by formatting Hydrogen Bonds (RESNR, RESTYPE, RESCHAIN, RESNR_LIG, RESTYPE_LIG, RESCHAIN_LIG, SIDECHAIN, DIST_H, A, DIST_D, A, DON_ANGLE, PROTISDON, DONORIDX, DONORTYPE, ACCEPTORIDX, ACCEPTORTYPE, LIGCOO, PROTCOO) of (40, ARG, A, 404, dMS, A, True, 3.49, 3.84, 103.57, true, 305, ng, 2656, o2, 18.411, 32.569, 6.766, 20.537, 33.919, 9.664, 40, ARG, A, 404, dMS, A, True, 3.62, 3.96, 103.11, true, 306, ng, 2656, o2, 18.411, 32.569, 6.766, 20.165, 31.715, 10.208) KcalMolA. In addition, MES:A:401 (MES) binding surfaces were also reproduced when the [amino ({4 - [(2R, 3R) - 2 - [(2S) - 3 - { [(1S, 2S) - 1 - { [(S) - 1, 3 - dihydroisoindole - 2 - carbonyl [(2 - methyl - 6 - oxo - 1, 7 - dihydropurin - 8 - yl) methyl] phosphanyl] carbamoyl} - 2 - methylbutyl] amino} - 2 - methylpropyl] oxaziridin - 3 - yl] butyl}amino) methylidene] azanium ligand merged with the chemical scaffold of lambda6-sulfanyl}oneboximidoyl-3- (rboximidoyl-3-fluoro- (1S, 4S) ((diaminomethylidene) amino) ethenyl}) amino, oxy-methyl) -3, 4-dimethyl-7-oxo-4-thia-1-azabicyclo (3.2.0) heptane-2-carbonyloxy) ({((2-amino-6-oxo-6, 9-dihydro-3H-purin-9-yl) oxy) (hydroxy) phosphoryl} oxy) phosphinic acid-ylidene, *cyano (2, 6-diazabicyclo *3.1.0, hex-1-en-6-yl -) (rboximidoyl-3-fluoro - (1S, 4S) ((diamino methylidene) amino) ethenyl}) amino, oxy - methyl) -3, 4-dihydroxyoxolan-2-ylo-1, 2, 4-triazol-3-yl - formamido) dihydroxyoxolan-2-ylo-1, 2, 4-triazol-3-yl-(formamido) phosphoryl o-6-fluoro-3, 4-dihydropyrazine-2-carboxamide (7ar) -5-amino-N-* (S) -, 2-* (3-oxabicyclo (2.1.0) (1S, 4S) -5-oxabicyclo*2.1.0, pentan-2 ((2S, 5r, 6r) -6- ((2S) -2-amino-2-

 doi:10.20944/preprints202403.0518.v1

phenylacetamido) -3, 3-dimethyl-7-oxo-4-thia-1-azabicyclo (3.2.0) heptane-2-carbonyloxy) ({((2-amino-6-oxo-6, 9-dihydro-3H-purin-9-yl) oxy) (hydroxy) phosphoryl} oxy) phosphinic acid-ylidene, *cyano (2, 6-diazabicyclo*3.1.0, hex-1-en-6-yl) (rboximidoyl-3-fluoro- (1S, 4S) ((diaminomethylidene) amino) ethenyl}) amino, oxy-methyl) -3, 4-dihydroxyoxolan-2-ylo-1, 2, 4-triazol-3-yl- (formamido) phosphoryl o-6-fluoro-3, 4-dihydropyrazine-2-carboxamide (7ar) -5-amino-N-* (S) -, 2-* (3-{((1S, 4S) -5-oxabicyclo (2.1.0) pentan-2-ylidene) {(cyano ({2, 6-diazabicyclo (3.1.0) hex-1-en-6-yl}) phosphanyl-(fluoro) methyl}-lambda6-sulfanyl}one pentan-2-ylidene) {(cyano ({2, 6-diazabicyclo (3.1.0) hex-1-en-6-yl}) phosphanyl {((1S, 4S) -5-oxabicyclo (2.1.0) pentan-2-ylidene) cluster of my innovative drug design (SI Appendix XL). The density operator describes the initial state of the Quantum negative energies of the Roccustyrna pharmacophoric apparatus, and the Hermitian operator corresponds to the negative docking observables of these pharmaco-ligand apparatuses when generated Hydrogen Bonds (RESNR, RESTYPE, RESCHAIN, RESNR_LIG, RESTYPE_LIG, RESCHAIN_LIG, SIDECHAIN, DIST_H, A, DIST_D, A, DON_ANGLE, PROTISDON, DONORIDX, DONORTYPE, ACCEPTORIDX, ACCEPTORTYPE, LIGCOO, PROTCOO) of (105, ARG, A, 401, mES, A, True, 3.70, 4.08, 105.94, true, 882, ng, 2545, n3, 11.608, 25.558, 4.564, 7.925, 26.479, 6.055, 183, GLY, A, 401, mES, A, False, 1.92, 2.90, 178.32, true, 1507, nam, 2553, o3, 8.130, 23.631, 6.141, 9.757, 23.092, 8.482) KcalMolA, water Bridges of (RESNR, RESTYPE, RESCHAIN, RESNR_LIG, RESTYPE_LIG, RESCHAIN_LIG, DIST_A, W, DIST_D, W, DON_ANGLE, WATER_ANGLE, PROTISDON, DONOR_IDX, DONORTYPE, ACCEPTOR_IDX, ACCEPTORTYPE, WATER_IDX, LIGCOO, PROTCOO, WATERCOO) of (181, PHE, A, 401, mES, A, 3.61, 2.95, 177.22, 93.39, true, 1484, nam, 2542, o3, 2901, 13.161, 27.871, 4.385, 11.950, 28.811, 8.607, 14.667, 28.983, 7.469) KcalMolA, and Salt Bridges of (RESNR, RESTYPE, RESCHAIN, PROT_IDX_LIST, RESNR_LIG, RESTYPE_LIG, RESCHAIN_LIG, DIST, PROTISPOS, LIG_GROUP, LIG_IDX_LIST, LIGCOO, PROTCOO) of (105, ARG, A, 879, 881, 882, 401, mES, A, 5.07, true, Sulfonicacid, 2550, 2550, 2553, 2551, 2552, 8.782, 22.872, 5.064, 7.314, 27.648, 5.918, 134, hIS, A, 1129, 1132, 401, mES, A, 4.04, true, Sulfonicacid, 2550, 2550, 2553, 2551, 2552, 8.782, 22.872, 5.064, 7.140, 20.014, 7.403) KcalMolA while inside the MES:A:402 (MES) binding residues co-generating Hydrogen Bonds of (RESNR, RESTYPE, RESCHAIN, RESNR_LIG, RESTYPE_LIG, RESCHAIN_LIG, SIDECHAIN, DIST_H, A, DIST_D, A, DON_ANGLE, PROTISDON, DONORIDX, DONORTYPE, ACCEPTORIDX, ACCEPTORTYPE, LIGCOO, PROTCOO) of (53, ASN, A, 402, mES, A, True, 3.51, 3.99, 111.85, true, 411, nam, 2578, o3, 32.123, 32.195, 10.616, 28.968, 33.145, 8.374), water Bridges (RESNR, RESTYPE, RESCHAIN, RESNR_LIG, RESTYPE_LIG, RESCHAIN_LIG, DIST_A, W, DIST_D, W, DON_ANGLE, WATER_ANGLE, PROTISDON, DONOR_IDX, DONORTYPE, ACCEPTOR_IDX, ACCEPTORTYPE, WATER_IDX, LIGCOO, PROTCOO, WATERCOO) of (60, ARG, A, 402, mES, A, 3.84, 3.50, 121.68, 95.14, true, 480, ng, 2567, o3, 2712, 36.676, 35.450, 14.696, 34.278, 39.200, 13.589, 35.065, 36.588, 11.400, 60, ARG, A, 402, mES, A, 2.63, 3.50, 121.68, 75.06, true, 480, ng, 2570, n3, 2712, 34.945, 34.379, 12.813, 34.278, 39.200, 13.589, 35.065, 36.588, 11.400) KcalMolA, and Salt Bridges of (RESNR, RESTYPE, RESCHAIN, PROT_IDX_LIST, RESNR_LIG, RESTYPE_LIG, RESCHAIN_LIG, DIST, PROTISPOS, LIG_GROUP, LIG_IDX_LIST, LIGCOO, PROTCOO) of (56, ASP, A, 439, 440, 402, mES, A, 4.62, false, Tertamine, 2570, 34.945, 34.379, 12.813, 32.279, 37.922, 11.524) KcalMolA. X47:A:403 (X47) binding domains which were also activated by the [amino ({4 - [(2R, 3R) - 2 - [(2S) - 3 - { [(1S, 2S) - 1 - { [(S) - 1, 3 - dihydroisoindole - 2 - carbonyl [(2 - methyl - 6 - oxo - 1, 7 - dihydropurin - 8 - yl) methyl] phosphanyl] carbamoyl} - 2 - methylbutyl] amino} - 2 - methylpropyl] oxaziridin - 3 - yl] butyl}amino) methylidene] azanium ligand when electronically co-interacted with the GissitorviffirnaTM9 (6R) - 6 - [(3S) - 2 - [(1Z) - amino ({1H - 1, 3 - benzodiazol - 2 - yl [(3R) - 3 - ethyloxolan - 3 - yl] methylidene}) - λ^5 - phosphanyl] - 5 - sulfanylidene - 1, 2, 4 - triazolidin - 3 - yl] - 4 - oxa - 1 - azabicyclo [3.1.0] hexane - 3 - thione ligand (SI Appendix XL). Hydrophobic Interactions (RESNR, RESTYPE, RESCHAIN, RESNR_LIG, RESTYPE_LIG, RESCHAIN_LIG, DIST, LIGCARBONIDX, PROTCARBONIDX, LIGCOO, PROTCOO) of (41, hIS, A, 403, x47, a, 3.96, 2599, 311, 19.683, 28.503, 18.586, 19.425, 32.404, 17.978, 166, GLU, A, 403, x47, a, 3.97, 2606, 1382, 12.713, 25.212, 25.953, 13.400, 22.628, 23.023) KcalMolA, hydrogen Bonds (RESNR, RESTYPE, RESCHAIN, RESNR_LIG, RESTYPE_LIG, RESCHAIN_LIG, SIDECHAIN, DIST_H, A, DIST_D, A, DON_ANGLE, PROTISDON, DONORIDX,

 doi:10.20944/preprints202403.0518.v1

DONORTYPE, ACCEPTORIDX, ACCEPTORTYPE, LIGCOO, PROTCOO) of (143, GLY, A, 403, x47, a, False, 2.09, 3.03, 159.23, true, 1194, nam, 2623, o2, 15.543, 28.616, 26.154, 13.714, 30.367, 27.818, 166, GLU, A, 403, x47, a, False, 2.07, 3.04, 167.82, true, 1378, nam, 2624, o2, 16.230, 25.173, 22.680, 13.910, 24.033, 21.074) KcalMolA, and water Bridges (RESNR, RESTYPE, RESCHAIN, RESNR_LIG, RESTYPE_LIG, RESCHAIN_LIG, DIST_A, W, DIST_D, W, DON_ANGLE, WATER_ANGLE, PROTISDON, DONOR_IDX, DONORTYPE, ACCEPTOR_IDX, ACCEPTORTYPE, WATER_IDX, LIGCOO, PROTCOO, WATERCOO) of (41, hIS, A, 403, x47, a, 2.89, 2.74, 153.51, 74.63, true, 313, nar, 2621, n2, 2765, 17.877, 31.984, 24.334, 18.095, 32.186, 20.123, 19.686, 32.846, 22.253) KcalMolA noncovalent interactions were produced for the (PDB:5rgw) Protein Structures inside the DMS:A:1002 (DMS) binding residues when positioned with the GissitorviffirnaTM8 {1 - [(R) - [(1S, 3R) - 3 - [(R) - amino (carbamothioyl amino) methyl] diaziridin - 1 - yl] ({6 - oxo - 2 - [(2S, 5R) - 3, 4, 5 - trifluoro - 2, 5 - dihydrofuran - 2 - yl] - 6, 7 - dihydro - 1H - purin - 8 - yl}amino) phosphoroso] - 1H - azirin - 2 - yl}thiourea ligand. (SI Appendix XL) Since the basic model of this scheme formalizes the entanglemment negative energy measurement's outputs which were generated via interaction of this pharmacophoric system with the BIOGENEA measurement apparatus (Schematics1a,1b,1c,1d,1e,1f,1g,1h,1i,1j,1k,1l,2a,2b,2c,2d,2e) for construction of these Quantum chemical spaces is based on the scheme of indirect Quantum measurements in this apparatus that consists of a complex chemical space device when co-interacted into the Interacting chains A for the development of Hydrogen Bonds (RESNR, RESTYPE, RESCHAIN, RESNR_LIG, RESTYPE_LIG, RESCHAIN_LIG, SIDECHAIN, DIST_HA, DIST_DA, DON_ANGLE, PROTISDON, DONORIDX, DONORTYPE, ACCEPTORIDX, ACCEPTORTYPE, LIGCOO, PROTCOO) of (298, ARG, A, 1003, dMS, A, True, 1.82, 2.75, 156.45, true, 2321, ng, 2385, o2, 7.152, 0.701, 7.418, 9.838, 1.276, 7.447) KcalMolA, salt Bridges (RESNR, RESTYPE, RESCHAIN, PROT_IDX_LIST, RESNR_LIG, RESTYPE_LIG, RESCHAIN_ LIG, DIST, PROTISPOS, LIG_GROUP, LIG_IDX_LIST, LIGCOO, PROTCOO) of (295, ASP, A, 2295, 2296, 1003, dMS, A, 5.35, false sulfonium bonds, 2384, 6.214, 1.061, 6.358, 10.457, 2.056, 5.399) KcalMolA, piCation Interactions (RESNR, RESTYPE, RESCHAIN, PROT_IDX_LIST, RESNR_LIG, RESTYPE_LIG, RESCHAIN_LIG, DIST, OFFSET, PROTCHARGED, LIG_GROUP, LIG_IDX_LIST, LIGCOO, PROTCOO) of (8, PHE, A, 60, 61, 62, 63, 64, 65, 1003, dMS, A, 4.71, 0.93) KcalMolA, and sulfonium bonds of (2384, 6.214, 1.061, 6.358, 8.434, 4.678, 4.314) KcalMolA against the DMS:A:1004 (DMS) residues. The [amino ({4 - [(2R, 3R) - 2 - [(2S) - 3 - { [(1S, 2S) - 1 - { [(S) - 1, 3 - dihydroisoindole - 2 - carbonyl [(2 - methyl - 6 - oxo - 1, 7 - dihydropurin - 8 - yl) methyl] phosphanyl] carbamoyl} - 2 - methylbutyl] amino} - 2 - methylpropyl] oxaziridin - 3 - yl] butyl}amino) methylidene] azanium Interacting chains DMS:A:1005, (DMS), [amino ({4 - [(2R, 3R) - 2 - [(2S) - 3 - { [(1S, 2S) - 1 - { [(S) - 1, 3 - dihydroisoindole - 2 - carbonyl [(2 - methyl - 6 - oxo - 1, 7 - dihydropurin - 8 - yl) methyl] phosphanyl] carbamoyl} - 2 - methylbutyl] amino} - 2 - methylpropyl] oxaziridin - 3 - yl] butyl}amino) methylidene] azanium substituted ligand when combined with the GissitorviffirnaTM7 (1S, 3S, 7R) - 7 - amino - 1 - [(R) - {3 - sulfanylidene - 2, 4, 6 - triazabicyclo [3.1.0] hexa - 1, 4 - dien - 6 - yl} [(E) - 2 - [(3R) - 3 - [(2R, 5R) - 3, 4, 5 - trifluoro - 2, 5 - dihydrofuran - 2 - yl] - 3H - 1, 2, 4 - triazol - 5 - yl] diazen - 1 - yl] phosphoroso] - 1, 2, 4, 6 - tetraazaspiro [2.4] heptane - 5 - thione small molecule for Interacting chains A generated Salt Bridges (RESNR, RESTYPE, RESCHAIN, PROT_IDX_LIST, RESNR_LIG, RESTYPE_LIG, RESCHAIN_LIG, DIST, PROTISPOS, LIG_GROUP, LIG_IDX_LIST, LIGCOO, PROTCOO) of (240, GLU, A, 1886, 1887, 1005, dMS, A, 5.49, false sulfonium bonds, 2392, 21.115, 14.615, 7.890, 20.932, 13.628, 2.497) KcalMolA when docked onto the UGM:A:1001 (UGM) conserved domains when combined with the [amino ({4 - [(2R, 3R) - [amino ({4 - [(2R, 3R) - 2 - [(2S) - 3 - { [(1S, 2S) - 1 - { [(S) - 1, 3 - dihydroisoindole - 2 - carbonyl [(2 - methyl - 6 - oxo - 1, 7 - dihydropurin - 8 - yl) methyl] phosphanyl] carbamoyl} - 2 - methylbutyl] amino} - 2 - methylpropyl] oxaziridin - 3 - yl] butyl}amino) methylidene] azanium-2 - [(2S) - 3 - { [(1S, 2S) - 1 - { [(S) - 1, 3 - dihydroisoindole - 2 - carbonyl [(2 - methyl - 6 - oxo - 1, 7 - dihydropurin - 8 - yl) methyl] phosphanyl] carbamoyl} - 2 - methylbutyl] amino} - 2 - methylpropyl] oxaziridin - 3 - yl] butyl}amino) methylidene] azanium fragment for the reproduction of Hydrophobic Interactions (RESNR, RESTYPE, RESCHAIN, RESNR_LIG, RESTYPE_ LIG, RESCHAIN_LIG, DIST, LIGCARBONIDX, PROTCARBONIDX, LIGCOO, PROTCOO) of (166, GLU, A, 1001, uGM, A, 3.99, 2369, 1285, 4.840,

 doi:10.20944/preprints202403.0518.v1

1.307, 18.869, 7.863, 3.905, 18.705) KcalMolA. Hydrogen Bonds (RESNR, RESTYPE, RESCHAIN, RESNR_LIG, RESTYPE_LIG, RESCHAIN_LIG, SIDECHAIN, DIST_HA, DIST_DA, DON_ANGLE, PROTISDON, DONORIDX, DONORTYPE, ACCEPTORIDX, ACCEPTORTYPE, LIGCOO, PROTCOO) of (142, ASN, A, 1001, uGM, A, True, 2.98, 3.78, 138.93, false, 2376, nam, 1103, o2, 7.255, 0.025, 21.247, 3.791, 0.187, 22.752, 164, hIS, A, 1001, uGM, A, True, 3.36, 4.10, 132.60, true, 1269, nar, 2362, n1, 14.398, 1.975, 20.469, 15.182, 4.645, 17.464, 166, GLU, A, 1001, uGM, A, False, 2.02, 2.95, 157.71, true, 1281, nam, 2375, o2, 9.321, 0.870, 20.936, 9.925, 2.614, 18.631) KcalMolA, pi Stacking (RESNR, RESTYPE, RESCHAIN, RESNR_LIG, RESTYPE_LIG, RESCHAIN_LIG, PROT_IDX_LIST, CENTDIST, ANGLE, OFFSET, TYPE, LIG_IDX_LIST, LIGCOO, PROTCOO) of (41, hIS, A, 1001, uGM, A, 308, 309, 310, 311, 312, 4.96, 62.77, 0.60, t, 2364, 2365, 2367, 2370, 2371, 2372, 11.890, 0.316, 23.057, 11.899, 4.967, 21.322) KcalMolA co-generated when the DRVYIHPFX-mimetic ligand produced (DRVYIHPFX-mimeticX_5rf6_ 63887e6f8dea9, rank, File, ID, Compound, Affinity, Total Energy, vdW Energy, Elec. Energy) of (1, 6291316fb3 ligand 1, -8.240, -40.737, -16.590, -35.518) KcalMolA (SI Appendix XL) onto the (PDB:5rf6) Crystal Structure of SARS-CoV-2 main protease in complex with Z1348371854. It was also observed that the DMS:A:401 (DMS) molecular surfaces were hit by the [amino ({4 - [(2R, 3R) - 2 - [(2S) - 3 - { [(1S, 2S) - 1 - { [(S) - 1, 3 - dihydroisoindole - 2 - carbonyl [(2 - methyl - 6 - oxo - 1, 7 - dihydropurin - 8 - yl) methyl] phosphanyl] carbamoyl} - 2 - methylbutyl] amino} - 2 - methylpropyl] oxaziridin - 3 - yl] butyl}amino) methylidene] azanium Interacting chains DMS:A:402, (DMS), [amino ({4 - [(2R, 3R) - 2 - [(2S) - 3 - { [(1S, 2S) - 1 - { [(S) - 1, 3 - dihydroisoindole - 2 - carbonyl [(2 - methyl - 6 - oxo - 1, 7 - [amino ({4 - [(2R, 3R) - 2 - [(2S) - 3 - { [(1S, 2S) - 1 - { [(S) - 1, 3 - dihydroisoindole - 2 - carbonyl [(2 - methyl - 6 - oxo - 1, 7 - dihydropurin - 8 - yl) methyl] phosphanyl] carbamoyl} - 2 - methylbutyl] amino} - 2 - methylpropyl] oxaziridin - 3 - yl] butyl}amino) methylidene] azanium-dihydropurin - 8 - yl) methyl] phosphanyl] carbamoyl} - 2 - methylbutyl] amino} - 2 - methylpropyl] oxaziridin - 3 - yl] butyl}amino) methylidene] azanium quantized structure when combined with the GissitorviffirnaTM6 (2R, 4R, 5S) - 2 - amino - 3 - {4 - amino - 1 - [(2R, 3R, 4R, 5R) - 5 - [(2R) - 3 - (aminomethyl) - 2 - (2 - methyldiaziridin - 1 - yl) - 1, 3 - diazetidin - 1 - yl] - 3, 4 - dihydroxyoxolan - 2 - yl] - 5 - sulfanylidene - 4, 5 - dihydro - 1H - 1, 2, 4 - triazole - 3 - carbonyl} - 1 - [(2S) - 1 - [(3R) - 2 - amino - 1 - methyl - 5 - sulfanylidene - 1, 2, 4 - triazolidin - 3 - yl] propan - 2 - yl] - octahydro - 1H - purin - 6 - one ligand (SI Appendix XL) inside the Interacting chains A. As a consequence some of Hydrogen Bonds (RESNR, RESTYPE, RESCHAIN, RESNR_LIG, RESTYPE_LIG, RESCHAIN_LIG, SIDECHAIN, DIST_H, A, DIST_D, A, DON_ANGLE, PROTISDON, DONORIDX, DONORTYPE, ACCEPTORIDX, ACCEPTORTYPE, LIGCOO, PROTCOO) of (298, ARG, A, 402, dMS, A, True, 1.81, 2.75, 160.37, true, 2331, ng, 2377, o2, 7.108, 0.748, 7.301, 9.817, 1.236, 7.202) KcalMolA, salt Bridges (RESNR, RESTYPE, RESCHAIN, PROT_IDX_LIST, RESNR_LIG, RESTYPE_LIG, RESCHAIN_LIG, DIST, PROTISPOS, LIG_GROUP, LIG_IDX_LIST, LIGCOO, PROTCOO) of (295, ASP, A, 2305, 2306, 402, dMS, A, 5.37, false sulfonium bonds, 2376, 6.127, 1.013, 6.220, 10.436, 2.068, 5.316) KcalMolA, and pi Cation Interactions (RESNR, RESTYPE, RESCHAIN, PROT_IDX_LIST, RESNR_LIG, RESTYPE_LIG, RESCHAIN_LIG, DIST, OFFSET, PROTCHARGED, LIG_GROUP, LIG_IDX_LIST, LIGCOO, PROTCOO) of (8, PHE, A, 60, 61, 62, 63, 64, 65, 402, dMS, A, 4.74, 0.85, false sulfonium bonds, 2376, 6.127, 1.013, 6.220, 8.426, 4.631, 4.196) KcalMolA were co-formatted into these DMS:A:403 (DMS) binding sites. The same clustered pharmaco ligand [amino ({4 - [(2R, 3R) - 2 - [(2S) - 3 - { [(1S, 2S) - 1 - { [(S) - 1, 3 - dihydroisoindole - 2 - carbonyl [(2 - methyl - 6 - oxo - 1, 7 - dihydropurin - 8 - yl) methyl] phosphanyl] carbamoyl} - 2 - methylbutyl] amino} - 2 - methylpropyl] oxaziridin - 3 - yl] butyl}amino) methylidene] azanium was then combined with the GissitorviffirnaTM5_ 4 - [3 - (aminomethyl) oxiren - 2 - yl] - 4, 5 - diaza - 2λ^5 - phosphaspiro [bicyclo [3.1.0] hexane - 2, 2' - oxaphosphirane] - 3 - thione (SI Appendix XL) and generated electrophile and non-covalent fragments in this combined mass spectrometry and X-ray approach against the SARS-CoV-2 main protease by targeting two cysteine viral proteases that essential for viral replication. The Interacting chain of DMS:A:405 (DMS) was also observed to be contacted by the [amino ({4 - [(2R, 3R) - 2 - [(2S) - 3 - { [(1S, 2S) - 1 - { [(S) - 1, 3 - dihydroisoindole - 2 - carbonyl [(2 - methyl - 6 - oxo - 1, 7 - dihydropurin - 8 - yl) methyl] phosphanyl] carbamoyl} - 2 - methylbutyl] amino} - 2 - methylpropyl] oxaziridin - 3 - yl] butyl}amino) methylidene] azanium active

 doi:10.20944/preprints202403.0518.v1

chemical structure for the generation of Salt Bridges (RESNR, RESTYPE, RESCHAIN, PROT_IDX_LIST, RESNR_LIG, RESTYPE_LIG, RESCHAIN_LIG, DIST, PROTISPOS, LIG_GROUP, LIG_IDX_LIST, LIGCOO, PROTCOO) of (166, GLU, A, 1295, 1296, 405, dMS, A, 4.68, false sulfonium bonds, 2399, 5.710, 0.278, 18.104, 5.136, 4.918, 18.220) KcalMolA inside the NTG:A:404 (NTG) binding residues. These pharmacophoric fragments [amino ({4 - [(2R, 3R) - 2 - [(2S) - 3 - { [(1S, 2S) - 1 - { [(S) - 1, 3 - dihydroisoindole - 2 - carbonyl [(2 - methyl - 6 - oxo - 1, 7 - dihydropurin - 8 - yl) methyl] phosphanyl] carbamoyl} - 2 - methylbutyl] amino} - 2 - methylpropyl] oxaziridin - 3 - yl] butyl}amino) methylidene] azanium when combined with the GissitorviffirnaTM4 (1S, 5S) - 4 - [(2R, 3S) - 3 - [(3R) - 2 - amino - 1 - fluoro - 5 - sulfanylidene - 3H - 1, 2, 4 - triazol - 3 - yl] oxiran - 2 - yl] - 4, 5, 6 - triaza - 2λ⁵ - phosphaspiro [bicyclo [3.1.0] hexane - 2, 2' - oxaphosphirane] - 3 - thione chemical structure (SI Appendix XL) are the outcomes of the Neumann's formulation (Schemiatic2a) since their computational properties and docking measurements are uniquely determined by Born's rule (2-5) and its projection postulate (2-6). These substituted fragments are represented by a Quantum entropy negativity Function Map (2-7) and considered as an instrument of a generalized von Neumann type (Schematic2d) when targeted the Interacting chains A and generated Hydrophobic Interactions (RESNR, RESTYPE, RESCHAIN, RESNR_LIG, RESTYPE_LIG, RESCHAIN_LIG, DIST, LIGCARBONIDX, PROT CARBONIDX, LIGCOO, PROTCOO) of (25, THR, A, 404, nTG, A, 3.38, 2390, 179, 8.975, 5.856, 23.587, 7.829, 8.893, 24.538) KcalMolA, hydrogen Bonds (RESNR, RESTYPE, RESCHAIN, RESNR_LIG, RESTYPE_LIG, RESCHAIN_LIG, SIDECHAIN, DIST_H, A, DIST_D, A, DON_ANGLE, PROTISDON, DONORIDX, DONORTYPE, ACCEPTORIDX, ACCEPTORTYPE, LIGCOO, PROTCOO) of (166, GLU, A, 404, nTG, A, False, 2.07, 3.03, 164.49, true, 1288, nam, 2384, n1, 9.978, 1.480, 21.333, 9.961, 2.675, 18.544) KcalMolA, and pi Stacking molecular interactions (RESNR, RESTYPE, RESCHAIN, RESNR_LIG, RESTYPE_LIG, RESCHAIN_LIG, PROT_IDX_LIST, CENTDIST, ANGLE, OFFSET, TYPE, LIG_IDX_LIST, LIGCOO, PROTCOO) of (41, hIS, A, 404, nTG, A, 308, 309, 310, 311, 312, 4.77, 89.87, 1.34, t, 2386, 2387, 2388, 2394, 2395, 2397, 9.588, 1.712, 23.544, 11.975, 5.032, 21.091) KcalMolA. In accordance with previous docking energy observations the DMS:A:401 (DMS), binding cavities were also covered by the [amino ({4 - [(2R, 3R) - 2 - [(2S) - 3 - { [(1S, 2S) - 1 - { [(S) - 1, 3 - dihydroisoindole - 2 - carbonyl [(2 - methyl - 6 - oxo - 1, 7 - dihydropurin - 8 - yl) methyl] phosphanyl] carbamoyl} - 2 - methylbutyl] amino} - 2 - methylpropyl] oxaziridin - 3 - yl] butyl}amino) methylidene] azanium pharmacophoric element when approaching the DMS:A:402 (DMS), Interacting chains when its Quantum negative binding energies integrated with the GissitorviffirnaTM3 (Z) - 4 - amino - N - [(1Z) - amino-methylidene] - N' - [(Z) - 2 - {6 - [(1Z) - [(fluoromethyl) imino] methyl] - 3 - sulfanylidene - 1, 2, 4 - triazabicyclo [3.1.0] hex - 2 - en - 6 - yl} - N' - methyl-ethanimidamido] - 2 - oxobutanimidamide topological descriptor energy at the dimer interface. Hydrogen Bonds (RESNR, RESTYPE, RESCHAIN, RESNR_LIG, RESTYPE_LIG, RESCHAIN_LIG, SIDECHAIN, DIST_H, A, DIST_D, A, DON_ANGLE, PROTISDON, DONORIDX, DONORTYPE, ACCEPTORIDX, ACCEPTORTYPE, LIGCOO, PROTCOO) of (298, ARG, A, 402, dMS, A, True, 1.81, 2.75, 160.37, true, 2331, ng, 2377, o2, 7.108, 0.748, 7.301, 9.817, 1.236, 7.202) KcalMolA salt Bridges (RESNR, RESTYPE, RESCHAIN, PROT_IDX_LIST, RESNR_LIG, RESTYPE_LIG, RESCHAIN_LIG, DIST, PROTISPOS, LIG_GROUP, LIG_ IDX_LIST, LIGCOO, PROTCOO) of (295, ASP, A, 2305, 2306, 402, dMS, A, 5.37, false sulfonium bonds, 2376, 6.127, 1.013, 6.220, 10.436, 2.068, 5.316) KcalMolA, pi Cation Interactions (RESNR, RESTYPE, RESCHAIN, PROT_IDX_LIST, RESNR_LIG, RESTYPE_LIG, RESCHAIN_LIG, DIST, OFFSET, PROTCHARGED, LIG_GROUP, LIG_IDX_LIST, LIGCOO, PROTCOO) of (8, PHE, A, 60, 61, 62, 63, 64, 65, 402, dMS, A, 4.74, 0.85, false sulfonium bonds, 2376, 6.127, 1.013, 6.220, 8.426, 4.631, 4.196) KcalMolA, inside the DMS:A:403 (DMS) binding cavities were generated when the [amino ({4 - [(2R, 3R) - 2 - [(2S) - 3 - { [(1S, 2S) - 1 - { [(S) - 1, 3 - dihydroisoindole - 2 - carbonyl [(2 - methyl - 6 - oxo - 1, 7 - dihydropurin - 8 - yl) methyl] phosphanyl] carbamoyl} - 2 - methylbutyl] amino} - 2 - methylpropyl] oxaziridin - 3 - yl] butyl}amino) methylidene] azanium Interacting chains DMS:A:405, (DMS), [amino ({4 - [(2R, 3R) - 2 - [(2S) - 3 - { [(1S, 2S) - 1 - { [(S) - 1, 3 - dihydroisoindole - 2 - carbonyl [(2 - methyl - 6 - oxo - 1, 7 - dihydropurin - 8 - yl) methyl] phosphanyl] carbamoyl} - 2 - methylbutyl] amino} - 2 - methylpropyl] oxaziridin - 3 - yl] butyl}amino) methylidene] azanium simultaneously docked with the

 doi:10.20944/preprints202403.0518.v1

GissitorviffirnaTM2 [2 - (aminomethyl) - 2 - { [(2E) - 3 - oxofuran - 2 - ylidene] methyl} - 2λ⁵ - azaphosphiridin - 1 - yl] amino (1R, 4S) - 3, 3 - dimethyl - 6 - oxo - 2λ⁴ - thia - 5 - azaspiro [bicyclo [3.2.0] heptane - 2, 1' - thiirane] - 4 - carboxylate ligand (SI Appendix XL). For these atomic instruments, measurements of the docking observables have the unique output probability distribution by the Born's rule (2-6) and have many different Quantum state reductions depending of the decomposition of the Salt Bridges for example generated (RESNR, RESTYPE, RESCHAIN, PROT_IDX_LIST, RESNR_LIG, RESTYPE_LIG, RESCHAIN_LIG, DIST, PROTISPOS, LIG_GROUP, LIG_IDX_LIST, LIGCOO, PROTCOO) of (166, GLU, A, 1295, 1296, 405, dMS, A, 4.68, false sulfonium bonds, 2399, 5.710, 0.278, 18.104, 5.136, 4.918, 18.220) KcalMolA from NTG:A:404 (NTG) Interacting chains which were produced when the [amino ({4 - [(2R, 3R) - 2 - [(2S) - 3 - { [(1S, 2S) - 1 - [amino ({4 - [(2R, 3R) - 2 - [(2S) - 3 - { [(1S, 2S) - 1 - { [(S) - 1, 3 - dihydroisoindole - 2 - carbonyl [(2 - methyl - 6 - oxo - 1, 7 - dihydropurin - 8 - yl) methyl] phosphanyl] carbamoyl} - 2 - methylbutyl] amino} - 2 - methylpropyl] oxaziridin - 3 - yl] butyl}amino) methylidene] azanium{ [(S) - 1, 3 - dihydroisoindole - 2 - carbonyl [(2 - methyl - 6 - oxo - 1, 7 - dihydropurin - 8 - yl) methyl] phosphanyl] carbamoyl} - 2 - methylbutyl] amino} - 2 - methylpropyl] oxaziridin - 3 - yl] butyl}amino) methylidene] azanium drug design co-interacted with the GissitorviffirnaTM1 (2S, 3S) - 3 - ({ [(1 - { [(3R) - 2 - (dimethylamino) - 3 - [(R) - hydroxy (2R) - oxiran - 2 - ylmethyl] - 2λ⁵ - oxaphosphiran - 2 - yl] methyl}hydrazin - 1 - yl) methyl] amino}methyl) oxirane - 2 - carbonitrile ligand (SI Appendix XL) for the generation of Hydrophobic Interactions (RESNR, RESTYPE, RESCHAIN, RESNR_LIG, RESTYPE_LIG, RESCHAIN_LIG, DIST, LIGCARBONIDX, PROT CARBONIDX, LIGCOO, PROTCOO) of (25, THR, A, 404, nTG, A, 3.38, 2390, 179, 8.975, 5.856, 23.587, 7.829, 8.893, 24.538) KcalMolA hydrogen Bonds (RESNR, RESTYPE, RESCHAIN, RESNR_LIG, RESTYPE_LIG, RESCHAIN_LIG, SIDECHAIN, DIST_H, A, DIST_D, A, DON_ANGLE, PROTISDON, DONORIDX, DONORTYPE, ACCEPTORIDX, ACCEPTORTYPE, LIGCOO, PROTCOO) of (166, GLU, A, 404, nTG, A, False, 2.07, 3.03, 164.49, true, 1288, nam, 2384, n1, 9.978, 1.480, 21.333, 9.961, 2.675, 18.544) KcalMolA, and pi Stacking Interactions (RESNR, RESTYPE, RESCHAIN, RESNR_LIG, RESTYPE_LIG, RESCHAIN_LIG, PROT_IDX_LIST, CENTDIST, ANGLE, OFFSET, TYPE, LIG_IDX_LIST, LIGCOO, PROTCOO) of (41, hIS, A, 404, nTG, A, 308, 309, 310, 311, 312, 4.77, 89.87, 1.34, t, 2386, 2387, 2388, 2394, 2395, 2397, 9.588, 1.712, 23.544, 11.975, 5.032, 21.091) KcalMolA. I can say that this operator (Schematics1a,1b,1c,1d,1e,1f,1g,1h,1i,1j,1k,1l,2a,2b,2c,2d,2e) carries only Quantum Negative Energy Information about the probabilities of Negative Docking Energy outcomes from this DRVYIHPFX-mimetic ligand (Schematics1a,1b,1c,1d,1e,1f,1g,1h,1i,1j,1k,1l,2a,2b,2c,2d,2e) when targeted the (PDB: 6lu7, 4aph, 5jmy) Protein Targets with the docking parameters of (1, dRVYIHPFXmimetic1b343b1433 lig and 1, -4.747, -7.601, -0.001, -0.253) KcalMolA), (1, -6.136, -23.936, -2.547, -16.124) KcalMolA, and (1, -7.235, -35.295, -11.811, -23.005) KcalMolA respectively. Comparison of the binary complex of non-ligand (apo) RORγ-LBD with the nuclear receptor co-activator (NCoA-1) peptide has shown that the cluster of the RoccustyrnaTM_gs_ convs_ 2.617493ae06 and RoccustyrnaTM_gs_convs_ 1.dafeb75bd0 ligand inhibitors may display a unique mechanism different from those caused by natural inhibitor, Ursolic acid (UA). These compounds unprecedentedly induce indirect disruption of a hydrogen bond between His479 on helix 11 (H11) and Tyr502 on H12, which is crucial for active conformation. These drug designs will allow us to develop novel synthetic compounds for autoimmune disease therapy. (SI Appendix IXa), (SI Appendix I), (SI Appendix II), (SI Appendix III), (SI Appendix IV), (SI Appendix V), (SI Appendix VI), (SI Appendix VII), (SI Appendix VIII), (SI Appendix VIII), (SI Appendix XII), (SI Appendix XIII), (SI Appendix IX), (SI Appendix XIV), (SI Appendix XV), (SI Appendix XVI), (SI Appendix XVII), (SI Appendix XVIII), (SI Appendix XIX), (SI Appendix XX), (SI Appendix XXI), (SI Appendix XXII), (SI Appendix XXIII), (SI Appendix XXIV), (SI Appendix XXV) (SI Appendix XXVI), (SI Appendix XXVII). (SI Appendix XXVIII), (SI Appendix XXIX), (SI Appendix XXX), (SI Appendix XXXI), (SI Appendix XXXII), (SI Appendix XXXIII), (SI Appendix XXXIV), (SI Appendix XXXV), (SI Appendix XXXVI), (SI Appendix XXXVII), (SI Appendix XXXV), (SI Appendix XXXVI), (SI Appendix XXXVII), (SI Appendix XVIII), ((Cluster Docking Energy TableS1), (SI Appendix I), (Cluster Docking Energy TableS2), SI Appendix I), (Docking Energy TableS1), (SI Appendix I), (Docking Energy TableS2), (SI Appendix I), (Docking Energy TableS3), (SI Appendix I)),

 doi:10.20944/preprints202403.0518.v1

and (OUTPUTs1-3), (Ic1a), (Ic1b), (Ic1c), (Ic2a), (Ic2b), (Ic2c), (Ic3a), (Ic3b) (Ic3c), (Ic3d), (Ic3d), (Ic3e), (Ic3f), (Ic3g), (Ic3h), (Ic3i), (Ic3j), and (Ic3k) (43, 44) I claim that a Quantum computer can simulate this Hidden Quantum Negative Energy Network (HQNEN) of the Roccustyrna's child pharmacophoric pattern already searched in a repeated merged system G of the product vector elements (Schematics1a,1b,1c,1d,1e,1f,1g,1h,1i,1j,1k,1l,2a,2b,2c,2d,2e) and of the implied vectors (Schematic2) by using row vectors from the Dirac's bra notation represented in this Quantum system QH (SI Appendix XXXIX), ((Cluster of BIOGENEA_ CONSENSUS_Eqs.1-16), (Supplement Material FUNCTIONS.1 - 26)) in a one-to-one correspondence with the HQNEN negative energies. I think also that this QFT oriented total free energy reductions could meta-logically described by a "Quantum cryptometalanguage" (CRQML) assuming that these superpotentials are quasi-homogeneous of weight 1 for some grading on V. If that is true, then QFT $\frac{1}{\alpha\mu}2v^{-d}T_{\alpha\mu\nu^d}(z^b)$GegenbauerC$[rf'(\psi), r^{16} - \psi^{\cos^{24}(a)}, a, b, z]P_{n\delta}^{\frac{d^4n^2Q^4r^{10}\delta\Psi}{G\alpha}}(g^{6^{-d^3}}G\phi N\psi)$ is its own semantics (QFT interprets itself) into weight spaces Hypergeometric1F1GegenbauerC[f'[ψ] r, r^16 - ψ^Cos[a] ^24,a, b, z] HypergeometricU GegenbauerC[f'[ψ] r, r^16 - ψ^Cos[a] ^24,a, b, z] WhittakerM GegenbauerC[f'[ψ] r, r^16 - ψ^Cos[a] ^24,k, m, z] WhittakerW GegenbauerC[f'[ψ] r, r^16 - ψ^Cos[a] ^24,k, m, z] Hypergeometric0F1 GegenbauerC[f'[ψ] r, r^16 - ψ^Cos[a] ^24,a, z] Hypergeometric0F1 GegenbauerC[f'[ψ] r, r^16 - ψ^Cos[a] ^24,a, z] Hypergeometric2F1Regularized GegenbauerC[f'[ψ] r, r^16 - ψ^Cos[a] ^24,a, b, c, z] HypergeometricPFQRegularized GegenbauerC[f'[ψ] r, r^16 - ψ^Cos[a] ^24,{a1, ap}, {b1, bq}, z] det {{Rcsina, sinb, sinec}, {pTKðÞ:ΩT, μðÞ¼T, ∑∞n¼1κnTðÞn!μTn}, {sineg, isinh, sinj}}, ChebyshevU GegenbauerC[f'[ψ] r, r^16 - ψ^Cos[a] ^24,n, x] QuantumPartialTrace GegenbauerC[f'[ψ] r, r^16 - ψ^Cos[a] ^24,{sinω, cosφ, dω/dx (exp (-x))}] LaguerreL GegenbauerC[f'[ψ] r, r^16 - ψ^Cos[a] ^24,n, a, x] LaguerreL GegenbauerC[f'[ψ] r, r^16 - ψ^Cos[a] ^24,n, x] GegenbauerC GegenbauerC[f'[ψ] r, r^16 - ψ^Cos[a] ^24,n, m, x] ChebyshevT GegenbauerC[f'[ψ] r, r^16 - ψ^Cos[a] ^24,n, x] GegenbauerC GegenbauerC[f'[ψ] r, r^16 - ψ^Cos[a] ^24,n, x] LaguerreL GegenbauerC[f'[ψ] r, r^16 - ψ^Cos[a] ^24,n, a, x] SphericalHarmonicY GegenbauerC[f'[ψ] r, r^16 - ψ^Cos[a] ^24,l, m, θ, ϕ] WignerD GegenbauerC[f'[ψ] r, r^16 - ψ^Cos[a] ^24,{j, m1, m2}, ψ, θ, ϕ] WignerD GegenbauerC[f'[ψ] r, r^16 - ψ^Cos[a] ^24,{j, m1, m2}, θ, ϕ] WignerD GegenbauerC[f'[ψ] r, r^16 - ψ^Cos[a] ^24,{j, m1, m2}, θ] (cos (x)/d/ (dx^1) integrate x^2/ (l-q (ξi (2l-ξ, 6iζ), 6x) i, 2yi)/(xi, 1))), {(1 - (x, i y))/(2 (x, i y), 7 y), 5s8n (x, i y) ^2 - 3 y^2, 7exp{(Q^cosXc^4, arcsinr^2)} (x, iexpy) y, ((expx, i y), 2 y) ^4}, integrate x^2/ (ξ (ξ (2 ξ, 6ζ), 6x), 2yi)/(xi, 1) ^3, ℋp_r (t) ^2/ (2 m) inp_φ (t) ^2/ (2 m r (t) ^2), d/dt (t^2/ (2 m r (t) ^2)), (cost (r (t) - t r' (t)))/(sinm r (t) ^3), logλ/r (t), d/dq ((q^1 q^2) sin^ (-1) (q^2)) log (2 q^4)/sqrt (1 - q^4), 3 q^2 sin^ (-1) (q^2), ∣ A^2 (D, dλ^2) (g) D f (z) g (z) ^*dλ^2 (z), Hypergeometric1F1 GegenbauerC[f'[ψ] r, r^16 - ψ^Cos[a] ^24,a, b, z] HypergeometricU GegenbauerC[f'[ψ] r, r^16 - ψ^Cos[a] ^24,a, b, z] WhittakerM GegenbauerC[f'[ψ] r, r^16 - ψ^Cos[a] ^24,k, m, z] WhittakerW GegenbauerC[f'[ψ] r, r^16 - ψ^Cos[a] ^24,k, m, z] Hypergeometric0F1 GegenbauerC[f'[ψ] r, r^16 - ψ^Cos[a] ^24,a, z] Hypergeometric0F1 GegenbauerC[f'[ψ] r, r^16 - ψ^Cos[a] ^24,a, z] Hypergeometric2F1Regularized GegenbauerC[f'[ψ] r, r^16 - ψ^Cos[a] ^24,a, b, c, z] HypergeometricPFQRegularized GegenbauerC[f'[ψ] r, r^16 - ψ^Cos[a] ^24,{a1, ap}, {b1, bq}, z] det {{Rcsina, sinb, sinec}, {pTKðÞ:ΩT, μðÞ¼T, ∑∞n¼1κnTðÞn!μTn}, {sineg, isinh, sinj}}, ChebyshevU GegenbauerC[f'[ψ] r, r^16 - ψ^Cos[a] ^24,n, x] QuantumPartialTrace GegenbauerC[f'[ψ] r, r^16 - ψ^Cos[a] ^24,{sinω, cosφ, dω/dx (exp (-x))}] LaguerreL GegenbauerC[f'[ψ] r, r^16 - ψ^Cos[a] ^24,n, a, x] LaguerreL GegenbauerC[f'[ψ] r, r^16 - ψ^Cos[a] ^24,n, x] GegenbauerC GegenbauerC[f'[ψ] r, r^16 - ψ^Cos[a] ^24,n, m, x] ChebyshevT GegenbauerC[f'[ψ] r, r^16 - ψ^Cos[a] ^24,n, x] GegenbauerC GegenbauerC[f'[ψ] r, r^16 - ψ^Cos[a] ^24,n, x] LaguerreL GegenbauerC[f'[ψ] r, r^16 - ψ^Cos[a] ^24,n, a, x] SphericalHarmonicY GegenbauerC[f'[ψ] r, r^16 - ψ^Cos[a] ^24,l, m, θ, ϕ] WignerD GegenbauerC[f'[ψ] r, r^16 - ψ^Cos[a] ^24,{j, m1, m2}, ψ, θ, ϕ] WignerD GegenbauerC[f'[ψ] r, r^16 - ψ^Cos[a] ^24,{j, m1, m2}, θ, ϕ] WignerD GegenbauerC[f'[ψ] r, r^16 - ψ^Cos[a] ^24,{j, m1, m2}, θ] (cos (x)/d/ (dx^1) integrate x^2/ (l-q (ξi (2l-ξ, 6iζ), 6x) i, 2yi)/(xi, 1))), {(1 - (x, i y))/(2 (x, i y), 7 y), 5s8n (x, i y) ^2 - 3 y^2, 7exp{(Q^cosXc^4, arcsinr^2)} (x, iexpy) y, ((expx, i y), 2 y) ^4}, integrate x^2/ (ξ (ξ (2 ξ, 6ζ), 6x), 2yi)/(xi, 1) ^3, ℋp_r (t) ^2/ (2 m) inp_φ (t) ^2/ (2 m r (t) ^2), d/dt (t^2/ (2 m r (t) ^2)), (cost (r (t) - t r' (t)))/(sinm r (t) ^3), logλ/r (t), d/dq ((q^1 q^2) sin^ (-1) (q^2)) log (2 q^4)/sqrt (1 - q^4), 3 q^2 sin^ (-1) (q^2), ∣ A^2 (D, dλ^2) (g) D f (z) g (z) ^*dλ^2 (z), Hypergeometric2F1 GegenbauerC[f'[ψ] r,

 doi:10.20944/preprints202403.0518.v1

rˆ16 - ψˆCos[a] ˆ24,h^2sinωx, σ^2sinω8πG, logeθy, xcosa], Hypergeometric2F1 GegenbauerC[f′[ψ] r, rˆ16 - ψˆCos[a] ˆ24,h^2sinωx, σ^2sinω8πG, logeθy, xcosa], Toeplitz matrix SpheroidalEigenvalueChebyshevT GegenbauerC[f′[ψ] r, rˆ16 - ψˆCos[a] ˆ24,n, Qˆ Cos GegenbauerC[f′[ψ] r, rˆ16 - ψˆCos[a] ˆ24,X c] ˆ4, ArcSin GegenbauerC[f′[ψ] r, rˆ16 - ψˆCos[a] ˆ24,r] ˆ(2 x)] GegenbauerC GegenbauerC[f′[ψ] r, rˆ16 - ψˆCos[a] ˆ24,Sum GegenbauerC[f′[ψ] r, rˆ16 - ψˆCos[a] ˆ24,μ, {ν, 0, ι}] n, Integrate GegenbauerC[f′[ψ] r, rˆ16 - ψˆCos[a] ˆ24,μ, ν(cˆ4 (λ/(4 G M)))/m, ω GegenbauerC[f′[ψ] r, rˆ16 - ψˆCos[a] ˆ24,Log GegenbauerC[f′[ψ] r, rˆ16 - ψˆCos[a] ˆ24,Exp GegenbauerC[f′[ψ] r, rˆ16 - ψˆCos[a] ˆ24,n]] ˆ7, σ] x], GegenbauerC[f′[ψ] r, rˆ16 - ψˆCos[a] ˆ24,ZernikeR GegenbauerC[f′[ψ] r, rˆ16 - ψˆCos[a] ˆ24,LegendrePGegenbauerC GegenbauerC[f′[ψ] r, rˆ16 - ψˆCos[a] ˆ24,f′ GegenbauerC[f′[ψ] r, rˆ16 - ψˆCos[a] ˆ24,ψ] pTKðÞ:μðÞ¼T∑ΩT, ∞n¼1κnTðÞn!μTn, r, rˆ16 - ψˆCos GegenbauerC[f′[ψ] r, rˆ16 - ψˆCos[a] ˆ24,a] ˆ24, f GegenbauerC[f′[ψ] r, rˆ16 - ψˆCos[a] ˆ24,ψKðÞ¼Hx, qðÞNe¼aSnexpbSK]] Hypergeometric2F1 GegenbauerC[f′[ψ] r, rˆ16 - ψˆCos[a] ˆ24,LaguerreL GegenbauerC[f′[ψ] r, rˆ16 - ψˆCos[a] ˆ24,ArcSin GegenbauerC[f′[ψ] r, rˆ16 - ψˆCos[a] ˆ24,λ n] Hypergeometric2F1 GegenbauerC[f′[ψ] r, rˆ16 - ψˆCos[a] ˆ24,sinωy^x, νμsinωπG, logeθy, xcosa], Hypergeometric2F1 GegenbauerC[f′[ψ] r, rˆ16 - ψˆCos[a] ˆ24,x, νμsinω, logeθy, xcosa], Hypergeometric2F1 GegenbauerC[f′[ψ] r, rˆ16 - ψˆCos[a] ˆ24,ω, eθ, cos3, a], Hypergeometric2F1 GegenbauerC[f′[ψ] r, rˆ16 - ψˆCos[a] ˆ24,ω, δ, ψo, γ], Hypergeometric1F1Regularized GegenbauerC[f′[ψ] r, rˆ16 - ψˆCos[a] ˆ24,a, b, z] Hypergeometric0F1Regularized GegenbauerC[f′[ψ] r, rˆ16 - ψˆCos[a] ˆ24,a, z] AppellF1 GegenbauerC[f′[ψ] r, rˆ16 - ψˆCos[a] ˆ24,a, b1, b2, c, x, y] AppellF1 GegenbauerC[f′[ψ] r, rˆ16 - ψˆCos[a] ˆ24,a, b1, b2, c, x, y] Hypergeometric2F1 GegenbauerC[f′[ψ] r, rˆ16 - ψˆCos[a] ˆ24,8, π, G, e] LegendreP GegenbauerC[f′[ψ] r, rˆ16 - ψˆCos[a] ˆ24,n, x] ZernikeR GegenbauerC[f′[ψ] r, rˆ16 - ψˆCos[a] ˆ24,n, m, r] LegendreP GegenbauerC[f′[ψ] r, rˆ16 - ψˆCos[a] ˆ24,n, m, x] HermiteH GegenbauerC[f′[ψ] r, rˆ16 - ψˆCos[a] ˆ24,n, x] JacobiP GegenbauerC[f′[ψ] r, rˆ16 - ψˆCos[a] ˆ24,n, a, b, x] LaguerreL GegenbauerC[f′[ψ] r, rˆ16 - ψˆCos[a] ˆ24,n, x] V ⊗ pi⁞FFFTˆUμ (X) ⁞⌀ (AoΨo, d) ⩛, GegenbauerC[f′[ψ] r, rˆ16 - ψˆCos[a] ˆ24,H] ⊗̂ GegenbauerC[f′[ψ] r, rˆ16 - ψˆCos[a] ˆ24,Ho] ∯ i GegenbauerC[f′[ψ] r, rˆ16 - ψˆCos[a] ˆ24,Ψ] GegenbauerC[f′[ψ] r, rˆ16 - ψˆCos[a] ˆ24,Entanglement Entropy GegenbauerC[f′[ψ] r, rˆ16 - ψˆCos[a] ˆ24,qstate GegenbauerC[f′[ψ] r, rˆ16 - ψˆCos[a] ˆ24,QFTq] ψoMG)] ˆ(ωsinθ/2), Sˆ MNI, 1/2pi˜ (i sin (-1/3 (24r), SphericalHarmonic YHypergeometric0F1 GegenbauerC[f′[ψ] r, rˆ16 - ψˆCos[a] ˆ24,PolyLog GegenbauerC[f′[ψ] r, rˆ16 - ψˆCos[a] ˆ24,logi, ⁞ψ˜ GegenbauerC[f′[ψ] r, rˆ16 - ψˆCos[a] ˆ24,QFTq] (α) ⟩) μ, (x)) J (r′)) Hypergeometric0F1 GegenbauerC[f′[ψ] r, rˆ16 - ψˆCos[a] ˆ24,PolyLog GegenbauerC[f′[ψ] r, rˆ16 - ψˆCos[a] ˆ24,logi, ⁞ψ˜ GegenbauerC[f′[ψ] r, rˆ16 - ψˆCos[a] ˆ24,QFTq] (α) ⟩) μ, GegenbauerC[f′[ψ] r, rˆ16 - ψˆCos[a] ˆ24,A GegenbauerC[f′[ψ] r, rˆ16 - ψˆCos[a] ˆ24,Ψo*sinϕ*{Ψ} ⩛ ⊕ G⁞xi, n, G ⟩ ν]]] ⩛ ⊕ G⁞xi, n, G ⟩ ν] ⟨FF⁞⌀ (AoΨo, d) ⩛, GegenbauerC[f′[ψ] r, rˆ16 - ψˆCos[a] ˆ24,H] ⊗̂ GegenbauerC[f′[ψ] r, rˆ16 - ψˆCos[a] ˆ24,Ho] ∯ i GegenbauerC[f′[ψ] r, rˆ16 - ψˆCos[a] ˆ24,Ψ] GegenbauerC[f′[ψ] r, rˆ16 - ψˆCos[a] ˆ24,EntanglementEntropy GegenbauerC[f′[ψ] r, rˆ16 - ψˆCos[a] ˆ24,qstate_ GegenbauerC[f′[ψ] r, rˆ16 - ψˆCos[a] ˆ24,QFTq] ψoMG)] ˆ(ωsinθ/2), Sˆ MNI, 1/2pi˜ (i sin (-1/3 (24r), ⁞ψ˜ GegenbauerC[f′[ψ] r, rˆ16 - ψˆCos[a] ˆ24,QFTq] (α) ⟩) μ, (x)) J (r′)) GegenbauerC[f′[ψ] r, rˆ16 - ψˆCos[a] ˆ24,A GegenbauerC[f′[ψ] r, rˆ16 - ψˆCos[a] ˆ24,Ψo*sinϕ*{Ψ}]] ⩛ ⊕ G⁞xi, μ⁞, ⁞I⟩ π, Vλ where each weight space has weight a non-negative rational number r (λ) ∈ Q. In this total docking energy reduction process illustrated in this paper, QFT would appear then as the semantics of these Quantum logics using the fermionic nature of the ghost field χ, Zmatter (Roccustyrna) (Mq) e− ϱcr.QuantumDistance GegenbauerC[f′[ψ] r, rˆ16 - ψˆCos[a] ˆ24,AdsQFTˆC, (Rz (π), QFT GegenbauerC[f′[ψ] r, rˆ16 - ψˆCos[a] ˆ24,H], ⊗̂ GegenbauerC[f′[ψ] r, rˆ16 - ψˆCos[a] ˆ24,Ho] ∯IMG) μνi), 2CZCðCZ (Rz (π), QFT GegenbauerC[f′[ψ] r, rˆ16 - ψˆCos[a] ˆ24,H] ⊗̂ GegenbauerC[f′[ψ] r, rˆ16 - ψˆCos[a] ˆ24,Ho] ∯IMG) μνi) TrH h, (∂ n z φz) underlying the Quantum information hidden in this geometry given by the vanishing set H (x, y, z, w) m of the function H (x, y, z, w) 1 b (⁞x⁞ˆ2r − ⁞y⁞ 2), b (⁞z⁞ˆ2r − ⁞w⁞ 2). That refers to thiol of a cysteine residue in the RBD sites by a covalent linkage which is important for the computational inhibitor which is consisting of the [amino ({4 - [(2R, 3R) - 2 - [(2S) - 3 - { [(1S, 2S) - 1 - { [(S) - 1, 3 - dihydroisoindole - 2 - carbonyl [(2 - methyl - 6 - oxo - 1, 7 - dihydropurin - 8 - yl) methyl] phosphanyl] carbamoyl} - 2 - methylbutyl] amino} - 2 - methylpropyl]

 doi:10.20944/preprints202403.0518.v1

oxaziridin - 3 - yl] butyl}amino) methylidene] azanium pharmacophoric to maintain antiviral activity where I take m and b to be real and negative.

Discussions

Quantum Homeopathy as Enactment of Double Entangled States points to the fact that some other phenomenon might be operative here, which is the reason why we propose to look at it in terms of an entanglement model along the lines of QFT based Quantum Homeopathy remedies. [1–42] This is how a theoretical ligand reconstruction along those lines might proceed to innovative methods for the generation of 3D structures of potential ligand molecules directly from the 3D structure of the macromolecular binding sites within their binding domains in the form of a 3D graph. [1–48] These drug designing systems and aspects of Quantum Homeopathy Interpretations are still unknown but their optimization is central for interpreting their entropy signature into many chemical-informatics and bio-informatics tasks, such as sequence alignment, de novo pharmacophore assembly, and phylogenetic tree inference. [1–49] This interpretation of evolutionary Quantum Homeopathies is represented here by the inverse of the effective pharmacophoric size in ultra low dosages, and could be more general because it is reflecting the degree of stochasticity in this evolutionary process, which depends not only on the effective pharmacophore size, but also from other factors, in particular the transformation of the ultra small dosage distributions into quantum entropy interactions of druggable scaffolds within SARS-COV-2 protein micro-environments. [1–50] It is interesting to consider how disentanglement of homeopathy remedies and placebo could be represented in terms of a double-slit metaphor in these computational and mathematical chemistry tasks as a strong ritual and a drug designing system of its own by following Turing Machine Rules and hypergeometric quantum functions (Highlights Supplementary Material, Maths19a,19b,19c,19d,19e,19f,19g,19h,20a,20b,20c,20d,20e,20f1,20f2,20f3,20g, 20h,20i,20j,21a,21b,21c,21d,21e,21f,21g,21h,2 1i,21j,22a,22b,22c,22d,,22e,,22f,22g), and ((Figures S(1-133)), (OUTPUTs1-3)), (Ic1a), (Ic1b), (Ic1c), (Ic2a), (Ic2b), (Ic2c), (Ic2d), (Ic2e), (Ic2f), (Ic2g), (Ic2h), (Ic2c), (Ic2g), (Ic2k), (Ic2l), (Ic3a), (Ic3b) (Ic3c), (Ic3d), (Ic3d), (Ic3e), (Ic3f), (Ic3g), (Ic3h), (Ic3i), (Ic3j), (Ic3k), ((Iconics4-6), (Supplementary Material METHODS AND MATERIALS (1), (2)), (Cluster of BIOGENEA_ CONSENSUS_Eqs.1-19), (Supplement Material FUNCTIONS.1 - 11)) according to the similar rule that states in the case of illness where the symptoms of an ill patient have to match the signs which have been observed in healthy volunteers ingesting a certain substance, either in crude form or potentized. [1–58] In this Quantum Homeopathy experiment where the observation (i.e., gaining information) of electrons are the heavy integration of sequence alignment algorithms with water memory tasks led me to diverse drug designing applications from the de novo assembly of whole pharmacophoric fragments **[3–59]** to the discovery of new drug designs targeted quantitatively to disease trait loci linked phenotypes **[3–60],** and to the identification and analysis of driver mutations in SARS-COV-2 viral diseases **[3–61].** The potentization principle that states that by stepwise diluting and succussing of a substance becomes more active, even beyond Avogadro's number transition associated finally its wave function [60] with Euclid-equivariant diffusion models by enabling them to leave their source and arrive at the screen as fuzzy sphere like drug designs ((Supplementary Material METHODS AND MATERIALS (1), (2), and Figures S(1- 133)), ((Iconics1-4), (Eqs1-400), Supplementary Material METHODS AND MATERIALS (1), (2)). By learning to denoise a normally distributed set of points throughout this whole drug designing experiment we manage to generate molecule designs from scratch within the binding site of macromolecules. This Sequence alignment OF ZernikeR and Hypergeometric quantum functions for Euclid-equivariant diffusion models that corresponds to the transition from infrabiological entities to biological and chemical ones, as formulated by Szathmary [1–79] following Ganti's chemoton concept can also be considered as quantum circuit inputs in these Quantum Homeopathy and pharmacophoric generation experiment. According to Ganti, and since life is characterized by the union of features the three essential features of membrane compartmentalization, autocatalytic metabolic network, and informational replicator [80–81] can also be considered as inputs in these Holistic Quantum Functions ((Cluster of BIOGENEA_ CONSENSUS_Eqs.1-20), (Supplement Material FUNCTIONS.1 - 12)). **[3–**

 doi:10.20944/preprints202403.0518.v1

80] As a result these potentizations of molecules per mol of the anti-viral and ACE2 blockers/substances could also be inserted as non-generalized and parameterized inputs in these Quantum Functions ((Cluster of BIOGENEA_ CONSENSUS_Eqs.1-21), (Supplement Material FUNCTIONS.1 - 13)) via the same Turing Machine translating process from these potentized remedies according to the simile rule, when, a homeopath uses something which is not present any more. The generated drug designs geometrically mimics the molecular signature of the substances diluted out when treating a symptom picture, which in the past was related to the interference pattern disappearing in ultra low doses and be replaced by two clear spots in a classic formulation for identifying the global optimum alignment of two sequences. This Quantum Homeopathy experiment involves finding of the lowest weight path through an n × m dynamic programming matrix**,** where n and m are the lengths of the sequences being compared **(**it is often the case that n**,** m**) [3–82] in** a double-semiotic structure which has not been elaborated on elsewhere [1–87]. 'Semiotic' means here that the basic relationship is the one of a semiotic triad developed by Charles S. Peirce [1–88], who pointed out that the semiotic triad of object, sign, and the meaning of the sign is universal. It can be applied to homeopathy in that the homeopathic remedy can be construed as a sign for an object, the substance, conveying a certain meaning, the remedy picture as an approximate solution which is typically constructed by a greedy heuristic using a biologically informed scoring function. These Examples incorporating certain aspects of physics and symmetry into a model tends to increase the accuracy, generalizability, and interpretability of the predictions of the scoring functions including sum-of-pairs**,** weighted sum-of-pairs and minimum entropy **for** each of the atomic orbits involved and could imply certain biological assumptions [3–83] when translating the same sense of the symptoms of a disease including the signs of that disease. Both are matched by the law of Similars. There are multiple modes of entanglement present here expecting that this Turing Machine ruled Geometric deep learning research for quantum-based structure-based drug design will follow trends in the pharmaceutical industry: A) The generated drug designs mimics the remedy itself and is something like a magical geometry representation of the past, at least in the case where ultra-high dilutions are used (note that in the case of low dilutions there might be a mix of entangled states and signaling processes via molecules) with a weighted sum-of-pairs, where one may assign different scores to DNA base matches, mismatches, substitutions, insertions and deletions (the scoring system which may also be used to control whether the output alignment is global [3–82] or local [3–84]). Alternatively, for AT1R/ACE2 proteins, a scoring matrix has be used where each ligand-protein complex represents the likelihood that the amino acid in the row will be replaced by the amino acid in the column [3–68,70–85] which is brought into a Euclid special space relationship with a particular diseased organism exhibiting special signs, which in other cases were related to and brought about by this substance, as represented in the knowledge system of homeopathy and its Materia Medica. B) Thus, high-entropy environments promote adaptation, and then success breeds success, that adaptation is most effective in large populations of pharmacophoric fragments which were translated from this Quantum Homeopathy drug design prediction which is at least qualitatively compatible with the available geometry data that are quantitatively testable in this double entanglement situation. The Quantum Homeopathy remedies involved here in an entangled state itself and acts like a phenomenological theory between actual remedy and pharmacophore geometrical data (a). This is achieved when a Quantum Turing Machine generates drug design structures after translating these potentization modern evolutionary theories that include an elaborate and a hidden mathematical description of a quantum hidden macroentanglement into druggable drug designs [12–87] according to our knowledge, where there is a coherent theoretical representation of MTE which can be determined empirically by a statistical analysis of a large protein sequence database on the basis of chemical docking properties between the amino acids and our RoccustyrnaTM drug designs (e.g., polar or non-polar, hydrophilic or hydrophobic). This Quantum Homeopathic Ritual enacts another entangled state between symptomatology of the patient and the remedial substances received following the similarity principle entanglement functions of $C_{\alpha\mu\nu d}$ (z^b)

 doi:10.20944/preprints202403.0518.v1

$P_{\delta n}^{\frac{Q^4 d^4 r^{10}}{G\alpha} \times \frac{\delta}{G\alpha} n^2 \Psi}\left(G N 6^{d^3} \sqrt{g}\ (\psi \phi)\right)_{(2\ \nu^{-d}\ T_{\alpha \mu \nu^d}(z^b)}\ P_{n\delta}^{\frac{d^4 n^2 Q^4 r^{10} \delta \Psi}{G\alpha}}\left(g^{6-d^3}\ G \phi N \psi\right)_{)/(\alpha\ \mu)(2}$ $\nu^{-d}\ \cos(\alpha\ \mu\ \nu^d\ \cos^{-1}(z^b))\ P_{n\delta}^{\frac{d^4 n^2 Q^4 r^{10} \delta \Psi}{G\alpha}}\left(\frac{1}{2}\left(1+\sqrt{5}\right) g^{6-d^3}\ G N \psi\right)_{)/(\alpha\ \mu)(\partial/(\partial\ z))\ (\ C_{\alpha \mu \nu^d}(z^b)}$ $P_{\delta n}^{\frac{Q^4 d^4 r^{10} \delta n^2 \Psi}{G\alpha}}\left(G N 6^{d^3} \sqrt{g}\ (\psi \phi)\right)_{)==2\ b\ z^{b-1}\ U_{\alpha \mu \nu^d - 1}(z^b)}\ P_{n\delta}^{\frac{d^4 n^2 Q^4 r^{10} \delta \Psi}{G\alpha}}\left(g^{6-d^3}\ G \phi N \psi\right)$ for SphericalHarmonicY[l, m, θ, ϕ] GegenbauerC[α μ ν^d, z^b] LegendreP[δ n, Q^4 d^4 r^10 (δ/(G α)) n^2 Ψ, G N g^(1/6^d^3) (ψ GoldenRatio)] LegendreQ[Log[ζ] Cos[μ], σ δ ArcSin[q ζ] ^g] LaguerreL[h, x] GegenbauerC[n, m, x] ChebyshevT[θ/ξ, α (ψ ι) Cos[EulerGamma]] in a reverse order by translating Quantum Entropy Negativities from this unwanted symptomatology of the diseased organism which is 'transferred' via the entanglement and produced by the therapeutic ritual from the organism back to the remedy field, as it was into non-parameterized geometrical black-hole shaped structure data. **[3–85]** Thus, the first part of these generalized entangled states (a) depends on the proper production process and is intimately connected to the ritual of ease, with a certain meaning, namely the remedy indicated. Both are matched by the Law of Similars. **[35–86]** There are multiple modeling equations (Supplementary Material METHODS AND MATERIALS (2), MasterEquations1-31) of entanglement present here: A) The new drug design itself is something like a magical presence of the past, at least in the case where ultra-high dilutions are used (note that in the case of low dilutions there might be a mix of entangled states and signalling processes via small molecule/ligand docking interactions) and directly propose a theoretical framework for turing analysis, in which these quantum Turing Machines are treated as phase transitions, in a technical and physical sense where this transition is the point where two distinct grand potentials are characterizing as units at different levels, such as molecules vs cells (organisms). In this case of the origin of life we put another way, where the transition is from an ensemble of entities at a lower level of organization (for example, small molecules) to an ensemble of higher-level entities (for example, small molecules-ligand complexes).

Concluding Remarks

The exploration of binding affinity prediction methods has a long-standing history. Early studies focused on utilizing empirical formulas or designing handcrafted features coupled with traditional machine learning algorithms for binding affinity prediction [2–187]. In this paper, I have illustrated a quantum partial trace measurement (observation) for geometrically translating a quantum homeopath state into Structure-based drug designs (SBDDs), which is becoming increasingly vital in drug discovery by utilizing the three-dimensional geometry of proteins to identify potential drug candidates. These translations in this project represent a part of a second generalized entangled system which depends on knowledge and technicalities, namely, for solving the correct quantum functions in order to link the remedy and symptom pictures of the patient with hypergeometric shapes. [3–87,109–143] This link has to be sufficiently strong as well as sufficiently correct and similar such that one single global description ensues, namely the remedy picture. The remedy picture that contains symptoms collected in the past and by other subjects. [3–29,35–144] were exctracted by the well-known paradoxes of quantum theory, such as Schrödinger's Cat [2–54]. These conundra appear if the quantum state of a system is taken as a representation of Quantum Homeopathy Knowledge and what we can know about it, not its presumed objective 'reality in itself 'particularly in this process of reduction from QFT to QM which is proved to be much more complex than just the reduction to a finite volume. [2–53,58] In fact, these recent advancements in geometric deep learning, which integrates and processes 3D geometric data, coupled with the QFT's Hidden Quantum Homeopathy Information from double-blinded and placebo-controlled homeopathic signal transduction that are disentangled into a generalized Quantum Black Hole like paradigm (Supplementary Material METHODS AND MATERIALS (2), MasterEquations1-22) have significantly propelled our structure-

 doi:10.20944/preprints202403.0518.v1

based drug design progress especially when some Avogadro Number's unknown characteristics emerged and several topics involved after translating genomic signatures of clinical samples from patients received homeopathy remedies with viral pneumonia in Wuhan, China. [2–54–100] In this paper, we systematically improve the recent progress of geometric deep learning for structure-based drug design targeting a novel peptide signature of AT1R-coronavirus (termed 2019-nCoV) binding domains which is identified [10–111] and is considered among the unknown characteristics of this phylogenetic analysis of 2019-nCoV, as sequenced from nine patients' samples, and has shown that the virus belongs to the subgenus Sarbecovirus. [2–114] But it is in investing this state with too much 'reality' as an object 'out there', independent of our observation of the quantum-computational structure which is intrinsically rooted in QFT, and the quantum-gravitational origin of this same structure where the topics involved, besides those of quantum information and quantum gravity, are non-commutative geometrized (the fuzzy sphere), (Figures S(1-96), ((Iconics1-4), (Eqs1-400), and (Schematics1a,1b,1c,1d,1e,1f,1g,1h,1i,1j,1k,1l,2a,2b,2c,2d,2e). (I-VI) Supplementary Material METHODS AND MATERIALS (1), (2)) and quantum simulated. [2–124] Thus, the computational breaking of macroentanglement in this case of 2019-nCoV which was more similar to two bat-derived coronavirus strains, bat-SL-CoVZC45 and bat-SL-CoVZXC21, than to known human-infecting coronaviruses, including the virus that caused the SARS outbreak of 2003 is a necessary concomitant in this drug SBDD Drug Designing process and of great importance as a possible theoretical support for translating Patient–practitioner–remedy (PPR) entanglement applications between patient, practitioner and homeopathy remedies in these Avogadro Number's processes of elementary atoms at high energies into negative docking energy values and innovative multi-targeted neoligands. [59–72] In fact, this result as followed from a calculation performed in the holomorphic twist of 4dN1 pure gauge theory involving the non-conservation of Quantum information was calculated to identify similar drug molecules in this pharmaceutical research. Furthermore, the result of neglecting the connected part of these Quantum Functions (Ic2e,f,g,h,g,k,l,m,o,p,q,r)and Quantum Circuit Generative Models of various number of qubits and quantum circuit layers ((Cluster of BIOGENEA_ CONSENSUS_Eqs.1-17), (Supplement Material FUNCTIONS.1 - 28)) reduced the latter to a pair of binary tree-like Quantum Functions ((Schematics1a,1b,1c,1d,1e,1f,1g,1h,1i,1j,1k,1l,1m), Schematic2)), the one for the input fields and the other for the output fields followed by three gated recurrent units (GrU) [37–112] with 5 dimensions, and finally a linear layer that reshaped the outputs to the size of all possible merged molecules. The milogP (Octanol-water partition coefficient logP) and TPSA (Topological polar surface area) values were calculated by utilizing the same online tool using Bayesian statistics. These In-Silico results indicated that the milogP value of the Roccustyrna_gs, the Roccustyrna_fr, the Roccustyrna_ gs_consv, and the Gissitorviffirna_TM small molecule mixed library was predicted as having optimum lipophilicity properties (logP ⟨ 5) (Han et al., 2019) in the aspect of dermal absorption and parallel artificial permeation (Table S1), (Table S2), (Table S3), (Table S4). **[3–87]** At the new level of this drug design protocol, the lower-level units display collective behavior for a corresponding phenomenological description applies if this entanglement between new drug designs and individual symptomatology is created, when any symbol or sign representing the substance, which is in fact not present, and will finally do the docking job. This double entanglement creates a kind of circularity between new drug designs exctracted from remedy pictures, and individual symptomatology – remedy/signs, and from the substance – substance interactions. **[1–87]** This is reminiscent of circularity in systems-therapeutic contexts and of semiotic webs by translating the substance to patient and remedy, and patient to substance via remedy, thus obliterating the symptomatology, [1–87] into a pairwise alignment that has a polynomial complexity when generalizing multiple sequence alignment (MSA) with sum-of-pairs scoring which is known to be NP-hard [66–88]. De novo assembly refers to the process of assembling a reference SARS-CoV-2 genome foundational resource for many bioinformatics analyses—from a large set of overlapping reads of the COVID-19 genome. Often these are short reads (of the order of 103 base pairs long with error rates of the order of 10−5 [3–91]). This analysis construes homeopathy along the lines that are known in modern QM as teleportation of states and distillation of entanglement for the purpose of understanding and creating quantum computers for quantum homeopathy and quantum

 doi:10.20944/preprints202403.0518.v1

cryptography [2–95]. This should only be seen as an analogy, although the fact that a generalized, albeit weaker version of QM can be constructed should warn that other quantum homeopathy phenomena based on entanglement like tunelling and teleportation might also have macroscopic equivalents, if these Quantum Homeopathy analogies are prepared for more recent long read sequencing technologies (typically of the order of ≥105 base pairs with error rates of the order of 10−3 [3–102]). This can also be used to aid in the scaffolding of the chemogenomic structure and protein-ligand complexes using a hybrid Quantum Loss Function approach [3–99], [36–107] which was recently used with great effect during the development of a novel human reference genome [3–103] evolving biological systems. These are open from the viewpoint of classical thermodynamicsand are closed and reach equilibrium within an extended approach that includes quantum thermodynamics of Turing Machine Learning Rules. [23–112] Under the statistical description of evolution, and since Malthusian fitness is naturally defined as the negative exponent of the average QFT Loss Quantum Function (QLQF), we established here a direct connection between processes of Quantum Chemical Biology and Turing Machine Learning Ruled Euclid Special Spaces for these evolutionary drug designs that are defined as the inverse of a Lagrange multiplier that constrains the average QFT Loss Quantum Function (QLQF) in a macro-entanglement environment as a negative one by translating homeopathy symptomatologies and absorbing them in theirs common denominator. [23–113] The success of this second entanglement depends, on the one hand, on the technical correctness of finding the common denominator or the similar remedy, and on the correctness of the individual symptomatology into modern software packages typically leverage one of two approaches: (i) overlap-layout-consensus (OLC), which involves the construction of a string overlap graph which is reducible to the NP-complete Hamiltonian path problem (a greedy approximation heuristic is used) and (ii) a k-mer graph approach, that involves the construction of a de Bruijn graph and is reducible to the Eulerian path problem, which admits a polynomial time algorithm like the patient and the doctor who must have hit the nail and have found out the decisive, individual symptoms during the case-taking interview. [35–123] This aspect of creating entanglement is more deeply connected to the technically correct application of the rules of homeopathy. It can be disturbed by many aspects, like connecting a patient's symptoms to the wrong remedy picture, or by not finding the truly individual nature of the patient's suffering in practice, by achieving high-quality, biologically plausible assemblies that are non-trivial and subject to many challenges due to both genome structures, such as homopolymeric and repetitive regions from library preparation, systematic platform error and low coverage regions [3–124] as exctracted from homeopath equivalent situation in these SARS-CoV-2 double-blind placebo-controlled experiments. [53–133] Here, we have a general descriptor of something that is not present any more, by virtue of Avogadro's number, and a local descriptor of something that is used as if it were present. [23–134] One way of interpreting this complementarity here which would not be temporal, then, as something, and used to be present in homeopathic remedies and might itself be an entangled system by virtue of the process of stepwise dilution and succussion already used for the preparation, producing a magical presence of the substance without the actual material presence where remedy and placebo are entangled (and the experiment be considered double-blinded) in terms of the previous section's algebraic formulation. This would mean collapse of the entangled state wave function, so that ($P_{{}_2F_1\left(\delta,\omega;o\ \psi;\frac{21\,\pi\,\gamma^x}{22}\right)}(x)$ ${}_2F_1$ (2+δ,2+ω;2+o ψ;(21 π)/22)) ${}_1F_1$ (a;b;x) Hypergeometric1F1Regularized[a⁵,∂2(ϱ⁶ n⁴ (π r))/(∂y ∂x)]==1/(π Γ(a) Γ(2+ω)) ${}_2 2F_1(\delta,\omega;o\ \psi;(21\,\pi\,\gamma^x)/22)$ Hypergeometric1F1Regularized[a⁵,∂2(n⁴ π r ϱ⁶)/(∂y ∂x)] ($\int_{-\infty}^{\infty}(1+t^2)^{-1-{}_2F_1(\delta,\omega;o\ \psi;(21\,\pi\,\gamma^x)/22)}\,(i\,t+x)^{2F_1(\delta,\omega;o\ \psi;(21\,\pi\,\gamma^x)/22)}\,dt$) ($\int_0^\infty e^{-t}\,t^{-1+a}\,{}_0F_1(;\,b;\,t\,x)\,dt$) $\int_0^\infty e^{-t}\,t^{1+\omega}\,{}_1F_1\left(2+\delta;\,2+o\ \psi;\,\frac{21\,\pi\,t}{22}\right)dt$ for (${}_2F_1$ (δ,ω;o ψ;(21 π γˣ)/22)∈ and ${}_2F_1$ (δ,ω;o ψ;(21 π γˣ)/22)>=0 and Re(a)>0 and 2+Re(ω)>0)(

$P^{}_{{}_2F_1\left(\delta,\omega;o\ \psi;\frac{21\,\pi\,\gamma^x}{22}\right)}$ (x) ${}_2F_1$ (2+δ,2+ω;2+o ψ;(21 π)/22)) ${}_1F_1$ (a;b;x) Hypergeometric1F1Regularized[a⁵,∂2(ϱ⁶ n⁴ (π r))/(∂y ∂x)]==1/(π Γ(a) Γ(2+ω)) Hypergeometric1F1Regularized[a⁵,∂2(n⁴ π r ϱ⁶)/(∂y ∂x)] ($\int_0^{\pi}\left(x-\sqrt{-1+x^2}\,\cos(t)\right)^{{}_2F_1(\delta,\omega;o\ \psi;(21\,\pi\,\gamma^x)/22)}\,dt$) ($\int_0^{\infty}e^{-t}\,t^{-1+a}\,{}_0F_1(;\,b;\,t\,x)\,dt$) $\int_0^{\infty}e^{-t}\,t^{1+\omega}\,{}_1F_1\left(2+\delta;\,2+o\ \psi;\,\frac{21\,\pi\,t}{22}\right)dt$ for (${}_2F_1$ (δ,ω;o ψ;(21 π γˣ)/22)∈ and ${}_2F_1$ (δ,ω;o ψ;(21 π γˣ)/22)>=0 and Re(a)>0 and 2+Re(ω)>0) $P^{}_{{}_2F_1\left(\delta,\omega;o\ \psi;\frac{1}{22}(21\,\pi\,\gamma^x)\right)}$ (x) ${}_2F_1$ (2+δ,2+ω;2+o ψ;21 π/22) (${}_1F_1$ (a;b;x) Hypergeometric1F1Regularized[a⁵,∂2(ϱ⁶ n⁴ (π r))/(∂y ∂x)])($P^{}_{{}_2F_1\left(\delta,\omega;o\ \psi;\frac{21\,\pi\,\gamma^x}{22}\right)}$ (x) ${}_2F_1$ (2+δ,2+ω;2+o ψ;(21 π)/22)) ${}_1F_1$ (a;b;x) Hypergeometric1F1Regularized[a⁵,∂2(ϱ⁶ n⁴ (π r))/(∂y ∂x)]==1/x^{b/2} F₁(2+δ;2+ω,0;2+o ψ;(21 π)/22,z₂) Hypergeometric1F1Regularized[a⁵,∂2(π r n⁴ ϱ⁶)/(∂y ∂x)] $P^{0}_{{}_2F_1\left(\delta,\omega;o\ \psi;\frac{21\,\pi\,\gamma^x}{22}\right)}(x)$ E^{x/2} $M_{\frac{1}{2}(-2\,a+b),\frac{1}{2}(-1+b)}(x)$($P^{}_{{}_2F_1\left(\delta,\omega;o\ \psi;\frac{21\,\pi\,\gamma^x}{22}\right)}$ (x) ${}_2F_1$ (2+δ,2+ω;2+o ψ;(21 π)/22)) ${}_1F_1$ (a;b;x) Hypergeometric1F1Regularized[a⁵,∂2(ϱ⁶ n⁴ (π r))/(∂y ∂x)]==1/Γ(-a+b) F₁(2+δ;2+ω,0;2+o ψ;(21 π)/22,z₂) Γ(1-a) Γ(b) Hypergeometric1F1Regularized[a⁵,∂2(π r n⁴ ϱ⁶)/(∂y ∂x)] $L_{-a}^{-1+b}(x)$ $P^{0}_{{}_2F_1\left(\delta,\omega;o\ \psi;\frac{21\,\pi\,\gamma^x}{22}\right)}(x)$ ($P^{}_{{}_2F_1\left(\delta,\omega;o\ \psi;\frac{21\,\pi\,\gamma^x}{22}\right)}$ (x) ${}_2F_1$ (2+δ,2+ω;2+o ψ;(21 π)/22)) ${}_1F_1$ (a;b;x) Hypergeometric1F1Regularized[a⁵,∂2(ϱ⁶ n⁴ (π r))/(∂y ∂x)]==1/Γ(-a+b) F₁(2+δ;2+ω,0;2+o ψ;(21 π)/22,z₂) Γ(1-a) Γ(b) Hypergeometric1F1Regularized[a⁵,∂2(π r n⁴ ϱ⁶)/(∂y ∂x)] $L_{-a}^{-1+b}(x)$ $P^{0}_{{}_2F_1\left(\delta,\omega;o\ \psi;\frac{21\,\pi\,\gamma^x}{22}\right)}(x)$ when Ψ_{ent} = ZernikeR[Hypergeometric2F1 [ω^m, δ^μ, ψ o, γ^n], m, r] LegendreP[Hypergeometric2F1[ω, δ, ψ o, (21/22) Pi γ^x], x] r^m Cos[(Pi (-m + Hypergeometric2F1[δ^μ, ω^m, o ψ, γ^n]))/2] JacobiP[(-m + Hypergeometric2F1[δ^μ, ω^m, o ψ, γ^n])/2, m, 0, 1 - 2 r^2] LegendreP[Hypergeometric2F1[δ, ω, o ψ, (21 Pi γ^x)/22], x] LegendreP[Floor[-Arg[(-21 Pi)/22 + (21 Pi γ^x)/22] /(2 Pi)] Gamma[o ψ] Hypergeometric2F1Regularized[δ, ω, o ψ, (21 Pi)/22] - E^((2 I) Pi (δ - o ψ + ω)) Floor[-Arg[(-21 Pi)/22 + (21 Pi γ^x)/22] /(2 Pi)] Gamma[o ψ] Hypergeometric2F1Regularized[δ, ω, o ψ, (21 Pi)/22] + Floor[(Pi + Arg[(-21 Pi)/22 + (21 Pi γ^x)/22])/(2 Pi)] Gamma[o ψ] Hypergeometric2F1Regularized[δ, ω, o ψ, (21 Pi)/22] - E^((2 I) Pi (δ - o ψ + ω)) Floor[(Pi + Arg[(-21 Pi)/22 + (21 Pi γ^x)/22])/(2 Pi)] Gamma[o ψ] Hypergeometric2F1Regularized[δ, ω, o ψ, (21 Pi)/22] + (I 2^(o ψ) 11^(-1 + o ψ) 21^(1 - o ψ) E^(I Pi (δ - o ψ + ω)) Pi^(3 - o ψ) Csc[Pi o ψ] Floor[-Arg[(-21 Pi)/22 + (21 Pi γ^x)/22] /(2 Pi)] Gamma[o ψ] Hypergeometric2F1Regularized[1 + δ - o ψ, 1 - o ψ + ω, 2 - o ψ, (21 Pi)/22])/(Gamma[δ] Gamma[-δ + o ψ] Gamma[o ψ - ω] Gamma[ω]) + (I 2^(o ψ) 11^(-1 + o ψ) 21^(1 - o ψ) E^(I Pi (δ - o ψ + ω)) Pi^(3 - o ψ) Csc[Pi o ψ] Floor[(Pi + Arg[(-21 Pi)/22 + (21 Pi γ^x)/22])/(2 Pi)] Gamma[o ψ] Hypergeometric2F1Regularized[1 + δ - o ψ, 1 - o ψ + ω, 2 - o ψ, (21 Pi)/22])/(Gamma[δ] Gamma[-δ + o ψ] Gamma[o ψ - ω] Gamma[ω]) + (Hypergeometric2F1[δ, ω, o ψ, (21 Pi)/22] + (21 Pi x δ ω Hypergeometric2F1[1 + δ, 1 + ω, 1 + o ψ, (21 Pi)/22] Log[γ])/(22 o ψ) + ((21 Pi δ ω Hypergeometric2F1[1 + δ, 1 + ω, 1 + o ψ, (21 Pi)/22] Log[γ] ^2)/(44 o ψ) + (441 Pi^2 δ (1 + δ) ω (1 + ω) Hypergeometric2F1[2 + δ, 2 + ω, 2 + o ψ, (21 Pi)/22] Log[γ] ^2)/(968 o ψ (1 + o ψ))) x^2 + ((7 Pi δ ω Hypergeometric2F1[1 + δ, 1 + ω, 1 + o ψ, (21 Pi)/22] Log[γ] ^3)/(44 o ψ) + (441 Pi^2 δ (1 + δ) ω (1 + ω) Hypergeometric2F1[2 + δ, 2 + ω, 2 + o ψ, (21 Pi)/22] Log[γ] ^3)/(968 o ψ (1 + o ψ)) + (3087 Pi^3 δ (1 + δ) (2 + δ) ω (1 + ω) (2 + ω) Hypergeometric2F1[3 + δ, 3 + ω, 3 + o ψ, (21 Pi)/22] Log[γ] ^3)/(21296 o ψ (1 + o ψ) (2 + o ψ))) x^3 + ((7 Pi δ ω Hypergeometric2F1[1 + δ, 1 + ω, 1 + o ψ, (21 Pi)/22] Log[γ] ^4)/(176 o ψ) + (1029 Pi^2 δ (1 + δ) ω (1 + ω) Hypergeometric2F1[2 + δ, 2 + ω, 2 + o ψ, (21 Pi)/22] Log[γ] ^4)/(3872

 doi:10.20944/preprints202403.0518.v1

o ψ (1 + o ψ)) + (9261 Pi^3 δ (1 + δ) (2 + δ) ω (1 + ω) (2 + ω) Hypergeometric2F1[3 + δ, 3 + ω, 3 + o ψ, (21 Pi)/22] Log[γ] ^4)/(42592 o ψ (1 + o ψ) (2 + o ψ)) + (64827 Pi^4 δ (1 + δ) (2 + δ) (3 + δ) ω (1 + ω) (2 + ω) (3 + ω) Hypergeometric2F1[4 + δ, 4 + ω, 4 + o ψ, (21 Pi)/22] Log[γ] ^4)/(1874048 o ψ (1 + o ψ) (2 + o ψ) (3 + o ψ))) x^4 + ((7 Pi δ ω Hypergeometric2F1[1 + δ, 1 + ω, 1 + o ψ, (21 Pi)/22] Log[γ] ^5)/(880 o ψ) + (441 Pi^2 δ (1 + δ) ω (1 + ω) Hypergeometric2F1[2 + δ, 2 + ω, 2 + o ψ, (21 Pi)/22] Log[γ] ^5)/(3872 o ψ (1 + o ψ)) + (15435 Pi^3 δ (1 + δ) (2 + δ) ω (1 + ω) (2 + ω) Hypergeometric2F1[3 + δ, 3 + ω, 3 + o ψ, (21 Pi)/22] Log[γ] ^5)/(85184 o ψ (1 + o ψ) (2 + o ψ)) + (64827 Pi^4 δ (1 + δ) (2 + δ) (3 + δ) ω (1 + ω) (2 + ω) (3 + ω) Hypergeometric2F1[4 + δ, 4 + ω, 4 + o ψ, (21 Pi)/22] Log[γ] ^5)/(937024 o ψ (1 + o ψ) (2 + o ψ) (3 + o ψ)) + (1361367 Pi^5 δ (1 + δ) (2 + δ) (3 + δ) (4 + δ) ω (1 + ω) (2 + ω) (3 + ω) (4 + ω) Hypergeometric2F1[5 + δ, 5 + ω, 5 + o ψ, (21 Pi)/22] Log[γ] ^5)/(206145280 o ψ (1 + o ψ) (2 + o ψ) (3 + o ψ) (4 + o ψ))) x^5 + O[x] ^6) - (2 I) E^(I Pi (δ - o ψ + ω)) Csc[Pi o ψ] Floor[-Arg[(-21 Pi)/22 + (21 Pi γ^x)/22] /(2 Pi)] Gamma[o ψ] Hypergeometric2F1Regularized[δ, ω, o ψ, (21 Pi)/22] Sin[Pi (δ - o ψ)] Sin[Pi (-(o ψ) + ω)] - (2 I) E^(I Pi (δ - o ψ + ω)) Csc[Pi o ψ] Floor[(Pi + Arg[(-21 Pi)/22 + (21 Pi γ^x)/22])/(2 Pi)] Gamma[o ψ] Hypergeometric2F1Regularized[δ, ω, o ψ, (21 Pi)/22] Sin[Pi (δ - o ψ)] Sin[Pi (-(o ψ) + ω)], x + O[x] ^6] ZernikeR[Hypergeometric2F1[δ^μ, ω^m, o ψ, γ^n], m, r] leaving the coordinators/observers in two quite separate and two-way entangled relationship associated to drug homeopath remedy drug design, and placebo oriented structures. [3–22,35–133] Like Bloom filters, Euclid Spaced-indexes involved here offer rapid querying and significant memory efficiency in Quantum Homeopathy Solutions, requiring only two invocations, and a time of O(lnN)) to set up the input state, and solve the rotation and translation/transformation problems in the 3D Euclidean space in polynomial time. [23–134]. [3–22,35–135] It is conceivable that this inherently probabilistic nature of quantum computers and novel data input modalities offered by quantum information, such as angle and phase encoding, could lead us to the development of similarly useful quantum data structures and abstractions against AT1R regime. [3–22,35–136] This Quantum Homeopathy Solution represents one example [53–137] and a concerted effort towards developing an open quantum data structure library which may be useful for improving our understanding of the types of quantum approaches that may admit practical advantages over the long term. We have deliberately left consciousness out here to show that by only focusing on the technical aspects of a homeopathy translation in terms of generalized entanglement is already possible. [43–138] This does not mean, however, that the theoretical translation offered here is the only one possible; indeed other ways using similar considerations have been offered already [20] in these two-way Quantum Homeopathy Entanglement Solutions, If I restrict the input fs to a class of ChebyshevU, HermiteH, HeunT, LaguerreL, HeunT, HeunTPrime, SphericalHarmonicY, HeunB, HeunD, SphericalBesselJ, LegendreP, LegendreQ, HeunC, LegendreQ, HeunG, LaguerreL, SpheroidalPS, SpheroidalEigenvalue, Hypergeometric1F1, WhittakerM, CoulombH2, AiryAi, CoulombF, CoulombH1, TemplateBox [{l, eta, r}, CoulompH1], Hypergeometric2F1, ThreeJSymbol, SixJSymbol, GegenbauerC, ChebyshevT, and GegenbauerC functions of WhittakerW [k, m, z] Hypergeometric0F1[a, z] Hypergeometric0F1[a, z] GegenbauerC[n, m, x] ChebyshevT[(θ/ξ) α x, I Exp[y] Cos[EulerGamma]] LaguerreL[n, a, x] LaguerreL[n, x] GegenbauerC[n, m, x] ChebyshevT[n, x] HypergeometricU[Q^Cos[x], x c^4 (Pi r), ArcSin[r] ^2] LegendreP[δ n, Q^D, d^4 r^10 (δ/(G Ψ)) n^8 Ψ, G N g^(1/6^d^7) (Ψ GoldenRatio)] LegendreQ[Log[ζ d] 2 Ψ^C Cos[μ], σ δ ArcSin[q ζ] ^Ψ] LaguerreL[E, x] whose oracles have size less than p(lnN) numerous structures emerge that are characterized by readily discernible (even if not necessarily easily described formally) order and complexity where p is a fixed polynomial unknown to the solver of the problem, then the restricted problem requires exponential time in the classical case and only polynomial time in the quantum case of four maximally entangled states (compared to eight for three entangled objects) so these Equations (Cluster of Eqs. I-DXCVII), ((Iconics1-4), (Eqs1-400), Supplementary Material METHODS AND MATERIALS (1), (2)), (Eqs1-325) represent just two of these states [6–140]. That is because for any given N this condition does not, from the solver's point of view, exclude any function f: ZN -- Z2, so by the same argument that I used for the general problem, there cannot be a less-than exponential classical solution even for the restricted problem that is now disentangled, like provers on placebo which should not evince the symptoms shown by those on the remedy. Consequently in Equations

 doi:10.20944/preprints202403.0518.v1

(Eqs1-325),((Iconics1-4), (Eqs1-400), and (Schematics1a,1b,1c,1d,1e,1f,1g,1h,1i,1j,1k,1l,1m), Supplementary Material METHODS AND MATERIALS (1), (2)) the ∂(DensityMatrix Tr[ψ,{2}])/∂A $\log^{\varrho}(\psi)$ log(A h^{ν} n π Q B^{G} δ μ ϱ σ sin(ω)) logG(z)+0+(c^{8} π^{2} r^{2} δ^{2} θ^{20}+1/4 $E^{\left(z/2+z^{16}\right)^{h}}$ $\sin^{-1}(r)$) ≈ logG(z) ∂(DensityMatrix Tr[ψ,{2}])/∂A $\log^{\varrho}(\psi)$ log(3.14159 A δ μ n ϱ Q σ B^{G} h^{ν} sin(ω))+9.8696 c^{8} δ^{2} θ^{20} r^{2}+0.25 $\sin^{-1}(r)$ $E^{\left(z^{16}+0.5\,z\right)^{h}}$ for the LegendreP[1 + I/2 (E^(-I ω) - E^(I ω)) $\langle \Delta S_{Pl} \rangle$ G h^ν n Pi Q δ μ σ, x] /(1 + I (E^(-I ω) - E^(I ω)) G h^ν n Pi Q δ μ σ) - LegendreP[15 k N - I 2^(-1 - x) D (E^(-I c) - E^(I c)) (I (E^(-I ω) - E^(I ω)))^x h n Pi Q U δ Δ^ν μ ϱ^4 σ, x] / $\langle \Delta S_{Rx} \rangle$ (1 + I (E^(-I ω) - E^(I ω)) G h^ν n Pi Q δ μ σ) function, either $\langle \Delta S_{Pl} \rangle$ = 0 or at least $\langle \Delta S_{Pl} \rangle$ and $\langle \Delta S_{Rx} \rangle$ can now be equated with each other. In other words, this Quantum Homeopathy act provides information that collapse the remedy/placebo into an entangled state wave function, leaving two completely distinguishable sets of results: one set for provers on the remedy, and one set for those on placebo for any f there that generates an oracle which operates in a time of O(lnN): e.g., to look up f(k) of entanglement. Between Symptoms-Remedy Picture, and Quantum Turing Machine generated geometry outputs which depends on the global description of the whole symptom picture of the patient-remedy complexes in the purpose of translating them into novel geometric shapes (drug design) which are coherent, there is sufficient similarity (global variable), and the local description of the druggable picture is individual (local variable), since the symptoms of the COVID-19 patient are new and unique. [3–139] The complementarity here is between uniqueness/individuality and similarity/globality and could traverse a binary tree of chemical maps following the binary expansion of k. One way of interpreting these complementarities here which would not be temporal, then, as something, and which used to be present but is not any more since one half of the experiment would be double-blinded and placebo-controlled as before, while the other half could be selectively unblinded (e.g., either provers or coordinators) and used as inputs here to observe how remedy and placebo homeopathic signal transductions might disentangle into generalized geometrical structures. Thus, these entanglements generated from the homeopathic remedies since they represent an entangled system by virtue of the process of stepwise dilution and succussion used for the drug designing of new ligands by translating the magical presence of these Quantum Homeopathy Substances without the actual material presence into the RoccustyrnaTM annotated ligands. In this perspective, and according the work of Schmidt *et al.* [10–47,56–141] in parapsychology these Quantum Homeopathy disentaglements might also provide some useful pointers toward this translational methodology into experimental quantum electrodynamics of such innovative druggable structures which were addressed by nonequilibrium thermodynamics [7–144]. Traditionally this theoretical Quantum Homeopathy disentanglement at least mathematically has not been before described as a process involving Turing Machine Learning Rules for selection, although some attempts in this direction have been made [75–146]. The innovative druggable structures generated in this project represents a part of a second generalized entangled system which depends on knowledge and technicalities, namely of finding the correct remedy in order to link the remedy and symptom pictures of the patient with hypergeometric shapes. [3–87,109–143] This link has to be sufficiently strong as well as sufficiently correct and similar such that one single global description ensues, namely the remedy picture. The remedy picture that contains symptoms collected in the past and by other subjects. [3–29,35–144] Thus this information is temporally and factually different since these clinical data of COVID-19 inflammation and hypertension symptoms are consider as a non-generalized input. [29–145] The individual symptoms that are complementary to the remedy picture in the sense that they are not common and generalizable, but very individual are considered also as generalized inputs as well. [3–29,35–145] The idiosyncratic exemplifications of the generic remedy picture during these quantum electrodynamics learning systems have to be evolved into multiple levels of trainable variables that substantially differ in their rates to compete those without such scale separation particularly when exploring the touch points between Quantum Mechanics and Thermodynamics for the modeling of Quantum Entropy Negativity cognitions in order to accelerate a decision making process for pharmacophoric substitution by using couplings of the Quantum Information Theory, Quantum Uncertainity Measurements, and Open Quantum System Theories. [3–146] The individual

 doi:10.20944/preprints202403.0518.v1

symptomatology which is in the same sense complementary to its common denominator and the remedy picture including the biostatistical data such from individual and society, freedom and responsibility, singularity and communion complementary notions [2–147] could also be considered as inputs in these quantum turing circuits since quantum learning is conceived. Thus the individual symptom picture and the commonality of these remedy symptoms or Materia Medica are the complementary descriptions that create the entangled state of the second entangled system (b) (Supplementary Material METHODS AND MATERIALS (1), (2), and Figures S(1-25), ((Iconics1-4), (Eqs1-400), and ((Schematics1a,1b,1c,1d,1e,1f,1g,1h,1i,1j,1k,1l,1m)), (I-VI) Supplementary Material METHODS AND MATERIALS (1), (2)) as a universal process, under this quantosphere "world as a neural network" concept [6–148]. The reason for this is to consider all these evolutionary processes in a small molecule universe within this Quantum Homeopathy framework for Turing Machine Learning Hypergeometric Translations (TMLHT) as illustrated here particularly as a process of a new poly-triangulation drug design protocol [QuantumDistance [EntanglementEntropy [qstate_Δ˜ ⊗ pi|FFFTˆUμ} (X) |⌀ (AoΨo, d) Ϋ, [H] ⊗̂ [Ho] ∯∫̄ i [Ψ]] [EntanglementEntropy [qstate_ [QFTq] ψoMG)] μνi of M (((Iconics1-4), (Eqs1-400), Supplementary Material METHODS AND MATERIALS (1), (2)), (Supplement Material FUNCTIONS.1-14), and (Cluster of BIOGENEA_ CONSENSUS_Eqs.1-22)) and a Quantum-like modeling process outside of classical physics capable of leading to such an event including the requirement for the essential chemicals and Avogadro's concentration mechanisms, and more. [3–29,35–147] It might not be an extremely improbable, lucky accident but rather a manifestation of a general evolutionary trend in a small molecule universe modeled as a quantum turing learning system [18–149] for the generation of these Quantum-like small molecules. [2–149] The basic hypothesis presented in this paper is the Entanglement Homeopathy Negativity Translations of SARS-CoV-2 biosystems when the first N −5 tetrahedral pharmacophoric scaffoldings are identical to those of the {Δi} triangulation pharmacophore scheme suggesting that these Quantum Homeopathy Potentiations may well be exhibiting at least geometrically some Quantum Entanglement effects for these "Avogadro significant" and "Avogadro amplified" QFT to QM reduction effects in virology. [3–29,35–149] These mathematical computational and quantum geometry experimental data are already in effect as a built-in homeostatic response based on Quantum Thermodynamics indicating that Quantum Homeopathy Entanglements could found ways to embrace this learning/evolutionary process of Δ˜ H, Rz (0) H, Rz (0) i transformation for free energy reductions from QFT to QM. These Docking Free Energy Reduction Mechanisms (DFERM) proved to be much simpler to finite volume when working with the trace-reversed perturbation of (Hypergeometric2F1Regularized[1 - L_(i^n v1 ϱ1 ϱ2 v2 (ϱ U) λ)^(((0 + 6.02214076×10^23 i) F m o Q T ϱ ψ)/q)(Γ^2/2 ∧ 23 Γ Γ d ∧ Γ ∧ Γ S×ω^2/2 ∧ d ω + 6 ω ∧ ω ∧ ω e^λ), 2, 1/2])^2 hˆ18XC (Rz (π) μν ⊗ bˆ2rIMG) μν − √3Xbˆ2r − 12XCZC ⊗ θZ − √2C (Rz (π), [H] ⊗̂ [Ho] ∯IμTMG) μν Y_l^m(θ, ϕ) (1 - L_(i^n v1 ϱ1 ϱ2 v2 (ϱ U) λ)^(((0 + 6.02214076×10^23 i) F m o Q T ϱ ψ)/q)(Γ^(2/2 ∧ 23 (Γ Γ) d ∧ Γ ∧ Γ S×ω^2/2 ∧ d ω + 6 ω ∧ ω ∧ ω) e^λ))^2 Φ rather than the perturbation ϒΓ.h,1/18XC (Rz (π) μν ⊗ bˆ2rIMG) μν − Y_l^m(θ, ϕ) (1 - L_(i^n v1 ϱ1 ϱ2 v2 (ϱ U) λ)^(((0 + 6.02214076×10^23 i) F m o Q T ϱ ψ)/q)(hˆ(R z) π Γ^(2/2 ∧ 23 (Γ Γ) d ∧ Γ ∧ Γ S×ω^2/2 ∧ d ω + 6 ω ∧ ω ∧ ω) e^λ))^2 Φ√3Xbˆ2r − 12XCZC ⊗ θZ − √2C (Rz (π), [H] ⊗̂ [Ho] ∯IμTMG) μν ((Cluster of BIOGENEA_ CONSENSUS_Eqs.1-23), (Supplement Material FUNCTIONS.1 - 15)) itself. In fact, some unknown sphere-shaped pharmacophoric characteristics (Supplementary Material METHODS AND MATERIALS (1), (2)), Figures S(1-64), ((Iconics1-4), (Eqs1-400), and (Schematics1a,1b,1c,1d,1e,1f,1g,1h,1i,1j,1k,1l,1m), (I-VI) Supplementary Material METHODS AND MATERIALS (1), (2)) emerged and several triangulation topics were revealed in this project when solved the time-independent Schrodinger functions of motion in much larger chemical spaces that are currently inaccessible to experimental screening methods in this rationale homeopathy translation that might enact another entangled state between atomic charges [Supplementary material (PLIP Reports1-8)] of the atom orbitas from the substance and ligabd-receptor molecular complexes. In this case by 'translating' the homeopathy symptoms from the organism back to the substance stationary pharmacophore states among the unknown geometric characteristics the cluster of the Gissitorviffirna_TM, Roccustyrna_gs, Roccustyrna_fr, and Roccustyrna_consv Quantum-computational structures occurred after intrinsically rooted in QFT by

 doi:10.20944/preprints202403.0518.v1

setting theoretical paradoxes regarding these binding affinity measurement problems. [3–79,135–149] These Quantum Mechanics and Quantum-gravitational ideas provided us along within this Theoretical Quantum Gravity background from Quantum Homeopathy Information into a Quantum Homeopath Folding Translation which is highly dependent on the folding of typical secondary structures as the means to hierarchically pave a negative docking energy and native folding pathway. Since several hypotheses have been proposed to explain this quantum homeopath folding mechanism that expands the hydrophobic zipper hypothesis which proposes a hairpin, first formed before hydrophobic contacts, to act as a constraint that brings other contacts into spatial proximity [24–149] this Quantum Homeopathy Translational mechanism would be an ingenious system of using these folding pathways as entangled states. In that case, by translating the phenomenon of the substance which is not present, this homeopathic quantum information, would become a kind of receptacle that translates the 'absorbed' symptoms, insofar as it is related by similarity. The more so, the less the likelihood of material presence in the remedy, or, in homeopathic parlance, the higher the potency of these Non-commutative geometry superoperators and Quantum Simulation Eigenvectors which were overlooked in a conventional way as a QG context involving detection of chemical bond restruction. These solutions were obtained by solving the function SHZζZ where ζ are the eigenvalues that referred to three main targets: the Spike glycoprotein (S-protein), papain-like protease (PLpro), and prominently the main protease Mpro. In this Quantum Homeopathy, then, we would have a double entanglement situation: The remedy is an entangled state itself between actual remedy and original new drug designs (substance) (a). This is achieved by potentization. This homeopathic entanglements ritual enacts and translates the signals from the entangled state between the symptomatology of the patient and the remedial substance (b). This is the similarity principle. This folding funnel hypothesis essentially says "the Gibbs free energy formula can describe protein folding" given the breadth of the bioinformatics space, where these applications represent a very small subset of the potential emerging application space for Quantum Homeopathy algorithm development. A small number of quantum algorithms for geometry problems in bioinformatics have been proposed here. These include theoretical geometry algorithms developed for Quantum Deep Learning Turing Machines that target NP-hard problems, such as sequence alignment [67–159] and the inference of highthrouput virtual screening and relative phylogenetic trees [70–160], which leverage amplitude amplification and quantum walks [38–164] indicating that these multistage entropy-enthalpy compensations of the atomic orbits from polypeptide chains and surrounding water molecules are the folding mechanisms, enabling protein and peptide oriented chemical designs to fold reproducibly and quickly, following explicit physical folding codes in aqueous environments. Only these entanglement functions of ChebyshevU[Cos[x], M^8 u^24 ν^6 z] JacobiP[ArcSin[θ n], λ a, λ b, Cos[x]] ChebyshevT[(Sin[ω Q] ^Cos[x] ^4/x) Cos[GoldenRatio], ((Sin[x] ^r)^21/22) x] ZernikeR[λ n, D f z, g z (ψ^0 ϱ m), λ] (M_(k λ, m×(d^2(n λ))/(dZ^2))((integral y du) del ((3 χ) log(q) Ω^(λ^6))) Hypergeometric1F1Regularized[a^5, (d^2(ϱ^6 m^7))/(dy dx) b, g^8, n^9, Δ(10, PauliMatrix[2], ε^3, Δ3)]) _0 F^~_1(;a;z)LaguerreL[λ n, D f z, g z (ψ^0 ϱ m), I Exp[λ]] (WhittakerM[ψ, ψ o D[n λ, {Z, 2}], Integrate[y, u] Grad[(3 χ[x, y, z]) Log[q[x, y, z]] Ω[x, y, z] ^λ[x, y, z] ^6, {x, y, z}]] Hypergeometric1F1Regularized[a^5, D[ϱ^6 n^73, y, x] b, g^8, Exp[n] 6, δ σ^2, ε θ^3, Δ α^4]) Hypergeometric0F1Regularized[a, z] in reverse order could translate the (unwanted) symptomatology of the diseased organism into druggable drug designs and chemicable coordinates and 'transferred' via the entanglement produced by the therapeutic ritual from the remedy-organism back to the geometry field, as it were. [38–135,150–168] This analysis makes obvious that homeopathy hinges on two separate exemplifications of generalized entanglement and thus is in a double sense vulnerable to actions disturbing entanglement or to incomplete production of the entangled preliminary results these Quantum Homeopathic Algorithms that are based on logic judgement of entropy-enthalpy compensation relationships among neighbored residues of an unfolded thermodynamic metastable state have to be devised in order to effectively and accurately predict a protein-ligand native secondary structure from its amino acid sequence with negative binding fee energies against AT1R protein and DNA targets where the first one is that of the remedy production process. [38–136,150–160] Entanglement could be described here by the global variable 'no substance

 doi:10.20944/preprints202403.0518.v1

present' and the local variable that the remedy is really treated as if it were a remedy with 'something' in it. Another way of reconstructing would be that of a global variable 'specific remedy' and the local variable 'no substance present'. Already, examples of this type of drug designing work exist for de novo assembly [2–23,2–161], sequence alignment [2–165] and the inference of biological networks [2–49,2–150] over the long term, operational advantages may be pursued by optimizing near-term approaches and integrating fast quantum algorithm subroutines with Quantum Homeopathy algorithms that may be relevant to this work including ones for backtracking [65–89], dynamic programming [47–158], operating on geometry strings [71,2–46,2–167] and differential Quantum Functions ((Cluster of BIOGENEA_ CONSENSUS_Eqs.1-24), (Supplement Material FUNCTIONS.1 - 16)) [22–71,3–168]. This Quantum Information Processing Function which is one of the most interesting modern applications of quantum entanglement [4–167] through quantum mechanics that governs the way operate modern computers Quantum computing, cryptography and teleportation and are now all practically realizable technologies, at least in the laboratory, the information they encode is still treated classically. [27–71,3–169] Here, our latest insights into these very foundations of quantum theory itself reveal that Quantum Homeopathy information is also subject to the same quantum laws [5–80] following by homeopathy that hinges on two separate exemplifications of generalized entanglement and thus is in a double sense vulnerable to actions disturbing entanglement or to incomplete production of entanglement. [2–71,13–178]. They are predicated on the realization that this Quantum Homeopathy information is not independent of the quantum physical laws used to store and process it when measuring into account the operational advantages for these quantum negative docking energy problems that are remain among the most difficult to achieve like the first one that is of the remedy production process. [29–178]. Entanglement could be described here by the global variable 'no substance present' and the local variable "drug design" that the remedy is really translated to as if it was a remedy with 'something' in it and as another way of reconstructing chemical geometrics which would be that of a global variable 'specific remedy with no substance present' and the local variable 'chemical geometry shapes'. [2–40,52–71,123–179] Given the breadth of this mathematical geometry applications for Turing Machine learning approaches in biology, I focus my discussion below on these types of Quantum Homeopathy advantages and their potential applications in lieu of specific drug designing methods. Improvements to training landscapes that refer to the reduction or removal of barren plateaus and narrow gorges in the landscape of the objective function of a gradient-based learning algorithm may stem from the unitary property of (many) quantum circuits, which inherently maintain the length of the input feature vector throughout the computation [2–174,180] provided where an appropriate input encoding is used following a more dedicated, more precise, and more time- and energy-consuming interpretation of homeopathy remedies. This is something we should expect it since the entangled states that both generated within a water solution from a homeopathy remedy whenever the drug substance relates to other ultra low concentrations of substances and to other water solutions and protein-ligand complexes, when finding similars that suggesting either possible this droplet transmission during potentization process which are all considered as non-generalized inputs into a Turing Machine potentization tool. [22–71,14–160] To illustrate this theoretical Turing Machine framework and demonstrate its Quantum Homeopathy applicability I detailed these quantum function algorithms and presented them for two simple examples (ACE2 and AT1R receptor atoms), showing that the convergence achieved is consistent with the expected behavior as a lattice in this particular type of regulator by allowing a computer simulation of QFT while this lattice breaks Lorentz's invariance into a fuzzy sphere guided drug design ((Iconics1-4), (Eqs1-400), Supplementary Material METHODS AND MATERIALS (1), (2)), (Figures S(1-101)) has the same rotational symmetry with the ordinary sphere extension from DFT chemical space [41–168] including the exchange and correlation potential for DFT derivative operators which can be avoided only for local density approximation (LDA) functional. I have shown then how it is possible to compute the Fock matrix and the electronic energy by exploiting the formal relation between the level-shifted Laplacian and the bound-state Helmholtz kernel, thus avoiding any reference to the quantum kinetic energy operator. As Maas writes in his lectures [43–107,52–171] these understandings of quantum fields theory the need to have regulators

 doi:10.20944/preprints202403.0518.v1

that always implies that some symmetries are broken, no matter what, until the regulator it is not removed. [21–68,74–172] In particular I have seen that these convergences within these predefined thresholds are achieved both for the orbital norm and for the Quantum Homeopathy Energy. Moreover the total binding energy that converges quadratically with respect to the norm of the orbital error as a lattice in this mathematical artifact is induced by these quantum fluctuations of the metric in the attractor basin. [11–49,88,89,90,112–181] This shows how unitarily these inequivalent representations of QFT are reduced to a single class of unitarily equivalent representations of QM for simulating scalar field theories in a spatial lattice as a conjugate variable P (x↛q′), the field momentum at the lattice site x↛q′, which is related to Φ (x↛q′) quantum Fourier transformations as applied to the N-dimensional Hilbert space residing at each lattice site x↛N. For N, 2n, the quantum state of the field at a site can be encoded in n qubits where n refers epidemiologically, to the eight of the nine patients that had a history of exposure to the Huanan seafood market in Wuhan, suggesting that they might have been in close contact with the infection source at the market. X refers to the one patient had never visited the market, although he had stayed in a hotel near the market before the onset of their illness. [11–49,58,59,60,112–186] Thus, in this interpretation experiment the wave nature of quantum particles are demonstrated by their formation of an interference pattern on a screen attempting to make observations of this situation at one or other slit prior to the waves arriving at the screen that induces the superposition, leading to their behaving as particles. [31–49,68,79,90,102–187] This demonstrates that this Quantum Homeopathy Superposition is the key to their entanglement. In these quantum Turing Machine ruled information processings, any attempt to isolate entangled ‘qubits’ leads to collapse of the entangled state and the loss of deep geometry information. [11–49,58,59,60–186] In this case instead, qubits are induced directly by the quantum fluctuations of the metric, due to the uncertainty relationship between metric and quantum information. Both approaches can lead to satisfactory results, but ours is more physical, not only in a heuristic sense, since it is supported by a rigorous mathematical framework. [21–49,78,79,90,100–187] Quantum Homeopathy Superposition Entanglement could also be used in the future in the same heuristic sense as a tool when attempting to make observations of the chemical space and the quantum information generated in ultra low concentrations even below Avogadro’s Number in typical RNA virus superimposed states when the average evolutionary rate for coronaviruses is roughly 10−4 nucleotide substitutions per site per year. As Preskill himself says in [13–192]: “There may be cleverer ways of regulating that would improve the efficiency of the simulation”. In this logical framework, since $\mathcal{C}\infty$ operations imply infinitely many operations, this intersection algorithm generated new {Δi} triangulations over a Boson Field Operator for a triangle shaped fragmentation pharmacophoric scheme which is considered as the evolution in Quantum information chemical space theories. [11–90,102–188] The first step I took to understand this Quantrum Negative Energy Metric more fully is to consider the behavior of geodesics in the presence of binding energy Quantum fluctuations of this metric inside the docking surface of a fuzzy sphere shaped pharmacophore features ((Iconics1-4), (Eqs1-400), Supplementary Material METHODS AND MATERIALS (1), (2)), (Supplementary Material METHODS AND MATERIALS (1), (2)), and Figures S(1-103)) of radius nr, that encodes Quantum information for each residue calculated including the explicitly periodic potential for MathieuS, MathieuC, MathieuCharacteristicExponent functions torsion of Δθˆσ, by a discrete variable with a finite number N of mutually orthogonal eigenstates for the nonzero Christoffel symbols for Schwarzschild metric: [Γ] (Eqs.1-400), ((Iconics1-4), (Eqs1-400), Supplementary Material METHODS AND MATERIALS (1), (2)), ⟨(SUPPLEMENT MATERIAL) FUNCTIONS.1-10⟩. [1–49,68–90,101–187] In a sense, however, QFT is T’s chemical “skeleton”, and from it I can go back to T, at least that’s hope by unifying Small Molecular Pairs (SMP) and Lindenbaum-Tarski Logical Chemical Spaces (LTLCS) found in molecular descriptors from AT1 receptors and Adaptive Weighted KNN Positioning for Matched Bemis and Murko (MBM) eigenvalue statements and combining them with Quantum Negative Energy Measurements from in vitro observables that are represented by commuting operators exctracted from telmisartan: 213 min, olmesartan: 166 min, candesartan: 133 min, valsartan: 70 min, losartan: 67 min half-lives. [23–46,57–188] In any case, however, the profound philosophical meaning of the mathematical role of a regulator is that by reducing the

 doi:10.20944/preprints202403.0518.v1

infinite degrees of freedom of QFT to a finite number, and by allowing the quantum simulator and the simulated quantum system to have unitarily equivalent representations even when interactions are present. Similarly, the development of one classical optimization algorithm for constraint satisfaction [4–25,77–189] was inspired by the original QAOA [2–15,79–190] and improved upon theirs Quantum Homeopathy Entropy Negativities (QHEN) performance from incompatible AT1 receptor dissociations which were translated into Shannon Entropy Negative Quantities of Negative Total Binding Energies as composed by Tipping–Ogilvie driven Machine Learning potentials on a (DFT) ℓneuron (ι), φ since very beginning of Quantum mechanics, non-commutativity of operators representing observables were considered as the mathematical representations of theirs incompatibility. [11–49,58–189] However, as N refers to the virus transmissions A refers to the Phylogenetic Data showing that bat-derived coronaviruses fell within all five subgenera of the genus Betacoronavirus and K refers to atomic orbits from the consensus sequences identitied between 2019-nCoV and its close relatives bat-SL-CoVZC45 and bat-SL-CoVZXC21 which was less than 90%, and are reflected in the relatively long branch between them. Hence, bat-SL-CoVZC45 and bat-SL-CoVZXC21 are not direct ancestors of 2019-nCoV. [31–68,102–190] In particular, I translated at least numerically the atomic orbits from the above protein network from these interacted biosystems that react not only to material or energy constraints imposed by the environment, but also to the information constraints into a QFT reduction action which can contribute to the Semi Negative Quantum Energy effects of Telmisartan and relative Antihypertensive Drugs when producing a decrease in the number of AT1R receptors for the generation of these Quantum Foam like DRVYIHPF-mimetic [amino ({4 - [(2R,3R) - 2 - [(2S) - 3 - { [(1S,2S) - 1 - { [(S) - 1,3 - dihydroisoindole - 2 - carbonyl [(2 - methyl - 6 - oxo - 1,7 - dihydropurin - 8 - yl) methyl] phosphanyl] carbamoyl} - 2 - methylbutyl] amino} - 2 - methylpropyl] oxaziridin - 3 - yl] butyl}amino) methylidene] azanium, Roccustyrna_TM, and Gissitorviffirna_TM ligands. By using this methodology I provided Anti-de Sitter Chern-Simons Supergravity (AdSCSS) Hidden Solutions for Quantum Reference Frame Representations for this DRVYIHPF-mimetic Roccustyrna_TM and Gissitorviffirna_TM ligand pharmacophore merging scheme once these Quantum fieldss are reduced into a Quantum network of black hole phase solutions L^Δq for a complete decision tree search of all possible combinations of fragmentation, merging, and pharmacophore re-coring systems targeted inside the SARS-CoV Mpro protein targets. [20–50,79–102–187] These modified Lagrangian DensityMatrix functions {∂(Tr[ψ,{2}] DensityMatrix)/∂log$^{\varrho}$(ψ) A log((B^{G} sin(ω) h$^{\nu}$ (n π Q δ μ σ)) ϱ A) logG(z),0,(sin^{-1}(r) $E^{\left(z/2+z^{16}\right)h}$)/2²+c^{8} $\sum_{k=1}^{\infty} \frac{(-1+\psi)\left\lfloor \frac{1+k}{2} \right\rfloor}{\frac{1}{2}\left(3+(-1)^{k}(-1+k)+k\right)}$ π² r² δ² θ^{20}}=={∂(DensityMatrix Tr[ψ,{2}])/∂((A ((-1+ψ)/(1+ $\sum_{k=1}^{\infty} \frac{\left\lfloor \frac{1+k}{2} \right\rfloor \left(-1+A\,h^{\nu}\,n\,\pi\,Q\,B^{G}\,\delta\,\mu\,\rho\,\sigma\sin(\omega)\right)}{\frac{1}{2}\left(3+(-1)^{k}(-1+k)+k\right)}$))$^{\varrho}$ (-1+A h$^{\nu}$ n π Q B^{G} δ μ ϱ σ sin(ω)))/(1+ $\sum_{k=1}^{\infty} \frac{-2\,r^{2}\left\lfloor \frac{1+k}{2} \right\rfloor \left(-1+2\left\lfloor \frac{1+k}{2} \right\rfloor\right)}{1+2k}$)) logG(z),0,c^{8} π² r² δ² θ^{20}+($E^{\left(z/2+z^{16}\right)h}$ r $\sqrt{1-r^{2}}$)/(4 (1+))}=={∂(DensityMatrix Tr[ψ,{2}])/∂((A ((-1+ψ)/(1+(-1+ψ)/(2+(-1+ψ)/(3+(2 (-1+ψ))/(2+(2 (-1+ψ))/(5+…)))))))$^{\varrho}$ (-1+A h$^{\nu}$ n π Q B^{G} δ μ ϱ σ sin(ω)))/(1+(-1+A h$^{\nu}$ n π Q B^{G} δ μ ϱ σ sin(ω))/(2+(-1+A h$^{\nu}$ n π Q B^{G} δ μ ϱ σ sin(ω))/(3+(2 (-1+A h$^{\nu}$ n π Q B^{G} δ μ ϱ σ sin(ω)))/(2+(2 (-1+A h$^{\nu}$ n π Q B^{G} δ μ ϱ σ sin(ω)))/(5+…)))))) logG(z),0,c^{8} π² r² δ² θ^{20}+($E^{\left(z/2+z^{16}\right)h}$ r $\sqrt{1-r^{2}}$)/(4 (1+-((2 r²)/(3-(2 r²)/(5-(12 r²)/(7-(12 r²)/(9+…)))))))} for ((∞+r<=0 or 1+r>0 or r∉) and (∞<=r or r<1 or r∉) and (ψ∉ or ψ>0 or ∞+ψ<=1) and (not (A h$^{\nu}$ n Q B^{G} δ μ ϱ σ sin(ω)∈ and -∞<-1+A h$^{\nu}$ n π Q B^{G} δ μ ϱ σ sin(ω)<=-1))) for E^(z/2 + z^16) (z^(-1))^(a - 16 (-1. + a^8) + 16 g k Pi) ((1. Gamma[1 + 2 m])/(6.02214076*^24^a Gamma[a^8] Gamma[1/2 + m - 16 g k Pi]) - (0.25 (-1. - 100.531 g k + 2. m) (1. + 100.531 g k + 2. m) Gamma[1 + 2 m])/(6.02214076*^24^a z Gamma[a^8] Gamma[1/2 + m - 16 g k Pi]) + ((0.03125 (-3 + 2 m - 32 g k Pi) (-

 doi:10.20944/preprints202403.0518.v1

1 + 2 m - 32 g k Pi) (1 + 2 m + 32 g k Pi) (3 + 2 m + 32 g k Pi) Gamma[1 + 2 m])/(6.02214076*^24^a Gamma[a^8] Coulomb Potential of CoulombF, CoulombG, CoulombH1, CoulombH2 special functions could be performed most fundamentally in the framework of open Quantum systems where contracted representations of [H] ⊗̂ [Ho] ∮I) ∂ ⊗ θZG⁞xi SU (2) are properly performed. The mechanical deformations of the PDB: 6M2Q and PDB: 2GHV protein targets that have been arised in these attractor-basin exploited Quantum Networks when contacted with our RoccustyrnaTM drug designs were promoted to a Quantum Operator L^Δ that annihilates the Chern-Simon's wavefunction for a tetrahedron shaped chemical information hidden in QFT 5 dimensions which seems to be closely related to the loss paradox information observed in the evaporation of black holes like phenomenon. [1–90,101–187] The basic ansatz, which I will see justified in many ways, is that the Quantum Homeopathy Quantization of the fact that the original Quantum fields Theory could be shrunk to Quantum Mechanics is simple relating to how one polynomial sphere that interacts with quantized negative docking energies should be mathematically modified into a special fuzzy shaped druggable sphere ((Iconics1-4), (Eqs1-400), Supplementary Material METHODS AND MATERIALS (1), (2)), (Figures S(1-104)). [1–99,103–187] I have hereby shown that I am able to obtain high-precision docking energy of negative entropies results (basis-set limit within an arbitrary, predefined threshold), and the robust convergence pattern is consistent with the fact that the integral formulation can be viewed as a preconditioned steepest descent [29–90,99,102–192] method, in contrast to the differential formulation which is instead a steepest descent method. These results suggest that these recombinations of these entangled events are complex and are more likely occurring in bat coronaviruses than in 2019-nCoV. [11–40,49–192] These Quantum fieldss and Quantum Entropies in five dimensions for Chern-Simons molecular similarity actions were filled with pure electron states isolated from the protease substrate interacting main chain chemical coordinates and generated more accurately Quantum Negative Energy Phases for the translation of these Quantum Space Negativities in a more efficient way into a pharmacophoric element with better binding affinities and negative docking energy scoring values as an alternative XYZ coordinate smile system. To make the theory simulated, I replace the scalar field Φ (x→q') at each lattice site by a discrete variable with a finite number N of mutually orthogonal eigenstates showing that Homeopathy Remedies can be highly effective, if and only if all circumstances are respected since they can lead to successful entanglement. In particular, I assumed that this phase solution e^(i π ((e n)/2 - (4 π r R^2)/k)) (γ g)^((4 π r R^2)/k - (e n)/2) L_(C_(Q^cos(z) logG(z))^(c^4 π r x δ θ^10)(1/2 sin^(-1)(r)^h))(x) L^Δq, b Z^ B, Z˙EQFTG⁞y7 χ, y, T, QFTG⁞XI, N, T is equivalent to M↓ when the solved time-independent Schrodinger function of motion in much larger chemical spaces that are currently inaccessible to experimental screening methods could generate Anti-de Sitter Chern-Simons intermediate resources for Quantum reference frame representations in a pharmacophore merging scheme delivered to the boundary solution in a five-dimensional Chern-Simons supergravity application layer for a decision tree search of all possible combinations of fragmentation, merging, and re-cored pharmacophore systems targeted inside the SARS-CoV Mpro protein targets solely with negative total energy docking energy scoring values. These Quantum Uncertainties for a knot K that refers to the side chains of MET49, TYR54, mET165, ASP187, and ARG188 extensively generalized the produced hydrophobic interactions along the x0 circle in the S3, when the tangent vector to the knot is izðdz. These {∂(Tr[ψ,{2}] DensityMatrix)/∂logᵠ(ψ) A log((B^G sin(ω) h^ν (n π Q δ μ σ)) ϱ A) logG(z),0,sin^-1(r)^h/2^2+c^8 π^2 r^2 δ^2 θ^20}=={∂(DensityMatrix Tr[ψ,{2}])/∂A (log(-1+ψ)-$\sum_{k=1}^{\infty} \frac{(-1)^k (-1+\psi)^{-k}}{k}$)ᵠ (log(-1+A h^ν n π Q B^G δ μ ϱ σ sin(ω))-$\sum_{k=1}^{\infty} \frac{(-1)^k \left(-1+A\, h^{\nu}\, n\, \pi\, Q\, \mathrm{B}^{G}\, \delta\, \mu\, \rho\, \sigma \sin(\omega)\right)^{-k}}{k}$) logG(z),0,1/4 (4 c^8 π^2 r^2 δ^2 θ^20+sin^-1(r)^h)} for (\[LeftBracketingBar]-1+ψ\[RightBracketingBar]>1 and \[LeftBracketingBar]-1+A h^ν n π Q B^G δ μ ϱ σ sin(ω)\[RightBracketingBar]>1){∂(Tr[ψ,{2}] DensityMatrix)/∂logᵠ(ψ) A log((B^G sin(ω) h^ν (n π Q δ μ σ)) ϱ A) logG(z),0,sin^-1(r)^h/2^2+c^8 π^2 r^2 δ^2 θ^20}=={∂(DensityMatrix Tr[ψ,{2}])/∂((A ((-1+ψ)/(1+

$$\overset{\infty}{\underset{k=1}{\mathrm{K}}}\frac{(-1+\psi)\left\lfloor\frac{1+k}{2}\right\rfloor}{\frac{1}{2}\left(3+(-1)^k(-1+k)+k\right)}$$))ᵠ (-1+A hᵛ n π Q B^G δ μ ϱ σ sin(ω)))/(1+ $$\overset{\infty}{\underset{k=1}{\mathrm{K}}}\frac{\left\lfloor\frac{1+k}{2}\right\rfloor\left(-1+A\,h^{\nu}\,n\,\pi\,Q\,B^{G}\,\delta\,\mu\,\rho\,\sigma\sin(\omega)\right)}{\frac{1}{2}\left(3+(-1)^k(-1+k)+k\right)}$$)) logG(z),0,c⁸ π² r² δ² θ²⁰+1/4 ((r $\sqrt{1-r^2}$)/(1+ $$\overset{\infty}{\underset{k=1}{\mathrm{K}}}\frac{-2\,r^2\left\lfloor\frac{1+k}{2}\right\rfloor\left(-1+2\left\lfloor\frac{1+k}{2}\right\rfloor\right)}{1+2\,k}$$))ʰ}=={∂(DensityMatrix Tr[ψ,{2}])/∂((A ((-1+ψ)/(1+(-1+ψ)/(2+(-1+ψ)/(3+(2 (-1+ψ))/(2+(2 (-1+ψ))/(5+…)))))))ᵠ (-1+A hᵛ n π Q B^G δ μ ϱ σ sin(ω)))/(1+(-1+A hᵛ n π Q B^G δ μ ϱ σ sin(ω))/(2+(-1+A hᵛ n π Q B^G δ μ ϱ σ sin(ω))/(3+(2 (-1+A hᵛ n π Q B^G δ μ ϱ σ sin(ω)))/(2+(2 (-1+A hᵛ n π Q B^G δ μ ϱ σ sin(ω)))/(5+…))))))) logG(z),0,c⁸ π² r² δ² θ²⁰+1/4 ((r $\sqrt{1-r^2}$)/(1+-((2 r^2)/(3-(2 r^2)/(5-(12 r^2)/(7-(12 r^2)/(9+…)))))))ʰ} for ((∞+r<=0 or 1+r>0 or r∉) and (∞<=r or r<1 or r ∉) and (ψ∉ or ψ>0 or ∞+ψ<=1) and (not (A hᵛ n Q B^G δ μ ϱ σ sin(ω)∈ and -∞<-1+A hᵛ n π Q B^G δ μ ϱ σ sin(ω)<=-1))) for C (-(1/(g γ)))^((E n)/2 - (4 Pi r R^2)/k) + c^4 Pi r x (-(1/(g γ)))^((E n)/2 - (4 Pi r R^2)/k) δ θ^10 Derivative[1, 0] [LaguerreL] [0, 0] Derivative[0, 1, 0] [GegenbauerC] [Q^Cos[z] LogBarnesG[z], 0, ArcSin[r] ^h/2] + (c^4 Pi r x^2 (-(1/(g γ)))^((E n)/2 - (4 Pi r R^2)/k) δ θ^10 (2 Derivative[1, 1] [LaguerreL] [0, 0] Derivative[0, 1, 0] [GegenbauerC] [Q^Cos[z] LogBarnesG[z], 0, ArcSin[r] ^h/2] + c^4 Pi r δ θ^10 Derivative[2, 0] [LaguerreL] [0, 0] Derivative[0, 1, 0] [GegenbauerC] [Q^Cos[z] LogBarnesG[z], 0, ArcSin[r] ^h/2] ^2 + c^4 Pi r δ θ^10 Derivative[1, 0] [LaguerreL] [0, 0] Derivative[0, 2, 0] [GegenbauerC] [Q^Cos[z] LogBarnesG[z], 0, ArcSin[r] ^h/2]))/2 + (c^4 Pi r x^3 (-(1/(g γ)))^((E n)/2 - (4 Pi r R^2)/k) δ θ^10 (3 c^4 Pi r δ θ^10 Derivative[2, 1] [LaguerreL] [0, 0] Derivative[0, 1, 0] [GegenbauerC] [Q^Cos[z] LogBarnesG[z], 0, ArcSin[r] ^h/2] ^2 + c^8 Pi^2 r^2 δ^2 θ^20 Derivative[3, 0] [LaguerreL] [0, 0] Derivative[0, 1, 0] [GegenbauerC] [Q^Cos[z] LogBarnesG[z], 0, ArcSin[r] ^h/2] ^3 + 3 Derivative[0, 1, 0] [GegenbauerC] [Q^Cos[z] LogBarnesG[z], 0, ArcSin[r] ^h/2] (Derivative[1, 2] [LaguerreL] [0, 0] + c^8 Pi^2 r^2 δ^2 θ^20 Derivative[2, 0] [LaguerreL] [0, 0] Derivative[0, 2, 0] [GegenbauerC] [Q^Cos[z] LogBarnesG[z], 0, ArcSin[r] ^h/2]) + c^4 Pi r δ θ^10 (3 Derivative[1, 1] [LaguerreL] [0, 0] Derivative[0, 2, 0] [GegenbauerC] [Q^Cos[z] LogBarnesG[z], 0, ArcSin[r] ^h/2] + c^4 Pi r δ θ^10 Derivative[1, 0] [LaguerreL] [0, 0] Derivative[0, 3, 0] [GegenbauerC] [Q^Cos[z] LogBarnesG[z], 0, ArcSin[r] ^h/2]))))/6 + (c^4 Pi r x^4 (-(1/(g γ)))^((E n)/2 - (4 Pi r R^2)/k) δ θ^10 (4 c^8 Pi^2 r^2 δ^2 θ^20 Derivative[3, 1] [LaguerreL] [0, 0] Derivative[0, 1, 0] [GegenbauerC] [Q^Cos[z] LogBarnesG[z], 0, ArcSin[r] ^h/2] ^3 + c^12 Pi^3 r^3 δ^3 θ^30 Derivative[4, 0] [LaguerreL] [0, 0] Derivative[0, 1, 0] [GegenbauerC] [Q^Cos[z] LogBarnesG[z], 0, ArcSin[r] ^h/2] ^4 + 6 c^4 Pi r δ θ^10 Derivative[0, 1, 0] [GegenbauerC] [Q^Cos[z] LogBarnesG[z], 0, ArcSin[r] ^h/2] ^2 (Derivative[2, 2] [LaguerreL] [0, 0] + c^8 Pi^2 r^2 δ^2 θ^20 Derivative[3, 0] [LaguerreL] [0, 0] Derivative[0, 2, 0] [GegenbauerC] [Q^Cos[z] LogBarnesG[z], 0, ArcSin[r] ^h/2]) + 4 Derivative[0, 1, 0] [GegenbauerC] [Q^Cos[z] LogBarnesG[z], 0, ArcSin[r] ^h/2] (Derivative[1, 3] [LaguerreL] [0, 0] + 3 c^8 Pi^2 r^2 δ^2 θ^20 Derivative[2, 1] [LaguerreL] [0, 0] Derivative[0, 2, 0] [GegenbauerC] [Q^Cos[z] LogBarnesG[z], 0, ArcSin[r] ^h/2] + c^12 Pi^3 r^3 δ^3 θ^30 Derivative[2, 0] [LaguerreL] [0, 0] Derivative[0, 3, 0] [GegenbauerC] [Q^Cos[z] LogBarnesG[z], 0, ArcSin[r] ^h/2]) + c^4 Pi r δ θ^10 (6 Derivative[1, 2] [LaguerreL] [0, 0] Derivative[0, 2, 0] [GegenbauerC] [Q^Cos[z] LogBarnesG[z], 0, ArcSin[r] ^h/2] + 3 c^8 Pi^2 r^2 δ^2 θ^20 Derivative[2, 0] [LaguerreL] [0, 0] Derivative[0, 2, 0] [GegenbauerC] [Q^Cos[z] LogBarnesG[z], 0, ArcSin[r] ^h/2] ^2 + c^4 Pi r δ θ^10 (4 Derivative[1, 1] [LaguerreL] [0, 0] Derivative[0, 3, 0] [GegenbauerC] [Q^Cos[z] LogBarnesG[z], 0, ArcSin[r] ^h/2] + c^4 Pi r δ θ^10 Derivative[1, 0] [LaguerreL] [0, 0] Derivative[0, 4, 0] [GegenbauerC] [Q^Cos[z] LogBarnesG[z], 0, ArcSin[r] ^h/2])))))/24 + O[x] ^5 (Rz (π), QFT [H] ⊗ [Ho] ∯IMG) μνi)/2 CZC∂CZ (Rz (π) orthogonal eigenstates for complex topologies in the triangular shaped pharmacophore skeletons of the DRVYIHPFmimetic [amino ({4 - [(2R,3R) - 2 - [(2S) - 3 - { [(1S,2S) - 1 - { [(S) - 1,3 - dihydroisoindole - 2 - carbonyl [(2 - methyl - 6 - oxo - 1,7 - dihydropurin - 8 - yl) methyl] phosphanyl] carbamoyl} - 2 - methylbutyl] amino} - 2 - methylpropyl] oxaziridin - 3 - yl] butyl}amino)

 doi:10.20944/preprints202403.0518.v1

methylidene] azanium ligand when combined with the Roccustyrna, and GissitorviffirnaTM ligands are tangent to the knot when shifted them by i/b2x∂∂x, cc (1/b2∂∂θ) to Maximally Entangled States to achieve very high accuracy of Negative Docking Energy Levels for the generation of AI-Quantum Homeopathy Entropy Negativities (QHEN) with the Higest Total Free Energy values of Negative Docking Factors. (40-69) Then, these QFT to QM definitionals (QUANTUM FUNCTIONS), (Supplementary Material METHODS AND MATERIALS (2), MasterEquations1-34), (Supplement Material FUNCTIONS.1-22), ((Iconics1-4), (Eqs1-400), Supplementary Material METHODS AND MATERIALS (1), (2)), corresponds to the regulator of QFT discussed in this paper to a Quantum operator LˆΔ that annihilates the Chern-Simons wavefunction of the DRVYIHPFmimetic [amino ({4 - [(2R,3R) - 2 - [(2S) - 3 - { [(1S,2S) - 1 - { [(S) - 1,3 - dihydroisoindole - 2 - carbonyl [(2 - methyl - 6 - oxo - 1,7 - dihydropurin - 8 - yl) methyl] phosphanyl] carbamoyl} - 2 - methylbutyl] amino} - 2 - methylpropyl] oxaziridin - 3 - yl] butyl} amino) methylidene] azanium ligand when combined with the Nirmatrelvir Drug, and even with the GissitorviffirnaTM tetrahedron shaped pharmacophoric ligand after solving these Lagrangian function. [50–77,109–192] Another important point to discuss is that of the serious consequences of the attitude of discarding the ontology of these quantum processes in this case of the ontology of homeopathic interaction that involves the non-conservation of quantum information for the input fields and the for the output fields too. If I consider some nearby atoms with four-velocities described by a single vector field Uμ (x) and separation vector Sμ, QM and QFT could then be at the same level, due to the possible disappearance of the uir of the CCR in QM by mixing the connected part of the balance between the quantum entropy of the fully mixed states and the entanglement entropy of its maximum entangled states. [11–193] Moreover, QM has a classical space-time background, the procedure described above assumes no overlap in this original basis since any overlap will follow the same symmetry. Possible disappearance of the Uμ (x) (uir) of the CCR in QM which is something that needs to be taken into account for correcting this kind of improper chemical bonding rotation where the pharmacophore character also depends on how this representation behaves under $\hat{\sigma}\hbar$ although the required Quantum negative energy calculations can be done after a geodesic procedure. In addition, I believe that this QFT-based Quantum Homeopathy entanglement should have an Entangled Quantum Space-Time as a Space-Time background if I take my tested atoms to be moving slowly as a four-velocity expressed unit vector in the time direction

$$P^{(m,0)}_{\frac{1}{2}\left(\frac{b^2\,\pi\,r\,R\,z\,\mu\,\nu\,|G|^3\,|M|^3\,|x|^3\,L(n\,\lambda)}{602\,214\,075\,999\,999\,987\,023\,872\,m\,\rho\,\psi}-m\right)}\left(1-2\,r^2\right)$$

plus corrections of order r^m cos(1/2 π ((π b² μ ν r R z \[LeftBracketingBar]G\[RightBracketingBar]³ \[LeftBracketingBar]M\[RightBracketingBar]³ \[LeftBracketingBar]x\[RightBracketingBar]³ L(λ n))/(602214075999999987023872 m ϱ ψ)-m)) ZernikeR[Sqrt[Abs[G M x]] ^6 (R z) (Pi μ ν) (b^2 r) ((L[n λ] /(602214075999999987023872 m ϱ ψ)) (I E^λ))^2 + Abs[m δ θ^10 Ψ Log[y] ^2 PolyGamma[0, N]] ^2/10000000000000000000000000000000000000000000000000000000000000000000000000000, m, r] ϒΓ.h,1/18XC (Rz (π) μν ⊗ b^2rIMG) μν − √3Xb^2r − 12XCZC ⊗ θZ − √2CSqrt[Quantity[r^3, "Revolutions" "Xennabits"^2] - (Plus[Abs[G M x] ^6]) (R z) (Pi μ ν) (b^2 r) ((L[n λ] /(602214075999999987023872 m ϱ ψ)) (I E^λ))^2 + Abs[m δ θ^10 Ψ Log[y] ^2 PolyGamma[0, N]] ^2/10000000000000000000000000000000000000000000000000000000000000000000000000000] (Rz (π), [H] ⊗̂ [Ho] ∯IμTMG) μν and higher so the corrections to U TMG) μν could be ignored when we write U TMG μν. (18-73) It might be worth of extending this reduction mechanism to binding fee energy and angular momentum per unit mass predictions for a simplistic pharmacophore map that may help identify critical interactions and are maintained in this drug discovery campaign. [66–73–90,102–187] Together these conserved quantities of negative docking energies provide a convenient way to understand the relationship of uncertainty between the Quantum Negative Energies and Quantum Metric Informations of the orbits of atoms in this Schwarzschild metric geometry approach when trying to only present quantum homeopathic data for the protein residues observed and uploaded onto quantum Turing Machines in order to have the highest probability of translating them into the RoccustyrnaTM recent designed pharmacophoric ligands. [11–51,54–190] Already, variational quantum algorithms have shown particularly promising results due to their substantial flexibility, which allows them to tackle a wide variety of problems across quantum simulation,

 doi:10.20944/preprints202403.0518.v1

Quantum Turing Machine Learning and optimization supporting the idea that QFT based Quantum Homeopathics should have an entangled quantum space-time [54–190] as a space-time background. If you remove the QFT from the background, what remains is the entangled space-time, which is itself a Quantum Homeopathy network indicating some quantum electrodynamics relations between the entangled space-time background and meta-logic which may be found in recent papers [55–191] According to this quantum hermetic analysis presented here the technical aspects of finding the correct homeopathy remedy translation seems most important, and of guaranteeing a proper remedy in the first place when quantum supremacy experiments [10–192] leveraging Valsartan's parameterized atomic orbits where the core quantum component from these near-term hybrid quantum–classical algorithms have already demonstrated the viability of its quantum advantages on Quantum Turing Machine Devices. [10–193] To conclude, in this de novo ligand generation work to generate valid 3D molecular structures that can fit and bind to specific AT1R protein binding sites I have shown that this innovative (bosonic) Quantum Homeopathy field theory T has in itself hidden quantum information IT, and when extracting this Quantum Homeopathy information involving the reduction of T to a quantum-electrodynamics homeopathy system, which is a quantum network QT like. De novo denotes that generating a molecule while no reference ligand molecule is given, i.e., generating molecules from scratch. In particular, other polynomial advantages in decrypting these homeopathy remedies may allow for Predicting of how the ligand molecule binds to the target protein target which is a fundamental problem in drug discovery and has broad applications in virtual screening and drug engineering especially while training Quantum Turing Machine Learning models that exhibit generalization error rates similar to classical Turing Machine Learning models that are requiring less training data than their classical counterparts. [10–194] Now if I think of an external quantum simulator QA nd, with which I would like to simulate T, I would actually simulate at least QT, not T, because the latter ceased to exist once it revealed the quantum information IT which had given the pervasive challenges around generating, processing, and translating biological and clinical samples. [10–195] The experimental validation of these Quantum Homeopathy Advantages may provide a basis for significant operational advantages that may be resilient to 3D mesh-based geometric deep learning improvements in classical hardware capabilities. [1–49,68–195] In a sense, however, QT is the Roccustyrna neoligand's "skeleton", and from it I can go back to T, at least that's hope indicating that these Quantum Homeopathy macro-entanglements might be worth of extending this QFT fermionic reduction mechanism to QM proposes to an efficient end-to-end prediction framework based on 3D point cloud representations of the given cluster of AT1R/ACE2 receptor proteins. However, the existence of such advantages in practical settings requires further validation noting that it remains possible that the greatest fruit of research into Quantum Homeopathy approaches will be novel quantum inspired classical drug designing algorithms. For example, the previously noted frameworks [1–183] for the dequantization of Quantum Functions (Supplement Material FUNCTIONS.1-23), ((Iconics1-4), (Eqs1-400), Supplementary Material METHODS AND MATERIALS (1), (2)), (Eqs.1-400), [1–77,1–188] has led me to the development of Hypergeometric Quantum Functions (Maths13a,13b,13c,13d,13e,13f,13g,13h,13i,13j,13k, 19a,19b,19c,19d,19e,19f,19g,19h,20a,20b,20c,20d, 20e,20f1,20f2,20f3,20g,20h,20i,20j,21a,21b,21c,21d,21e,21f,21g,21h,21i, 21j,22a,22b,22c,22d,,22e,,22f,22g), ((Iconics1-4), (Eqs1-400), and (Schematics1a,1b,1c,1d,1e,1f,1g,1h,1i,1j,1k,1l,1m), (I-VI) Supplementary Material METHODS AND MATERIALS (1), (2)) that are translating equivariant graph neural networks into druggable building models and may in the future improve upon existing geometric symmetry practical implementations. This Secret Turing Machine Learning Key Improver for the standard inner product Pni,1/∛xiyi (mod k) over G unitary transformations are defined for every x ∈ G by QFTq. ∇̈ ⊕ G⟩xi, v [FFFT$\hat{\sigma}\hbar\hat{}$ (uir) Uμ (x)] ⟩G⟩G′⟩, $\hat{\sigma}\hbar\hat{}$ (uir) Uμ (x) P y∈Gχy (x) ⟩yi Bosonic Field Operators and introduces the conditional probabilities between 5 dimensional Quantum Reference Frames that generalizes a network of electronic structure communications. This can be used in combination with cryptographic algorithms and quantum functions of I.LaguerreL[(I Det[HypergeometricPFQRegularized[{E1, p Ψ}, {b1, b q}, z]] Sin[χ])/E^((5 q4 ϑ^I)/2), x] JacobiP[(2 Cos[(n Pi)/2])/n, a, b, 0] LegendreP[Cos[(n Pi)/2], 0]

 doi:10.20944/preprints202403.0518.v1

LegendreP[(2^n Sqrt[Pi] \[Integral] $\frac{P_{2^n \sqrt{\pi}\,\Gamma\left(m+\frac{n}{2}\right)}}{\Gamma(m)}$ (x) x==-((Γ(m) ($\frac{P_{2^n \sqrt{\pi}\,\Gamma\left(m+\frac{n}{2}\right)}}{\Gamma(m)-1}$ (x)- $\frac{P_{2^n \sqrt{\pi}\,\Gamma\left(m+\frac{n}{2}\right)}}{\Gamma(m)+1}$ (x)))/($\sqrt{\pi}$ 2n+1 Γ(m+n/2)+Γ(m)))+ constant Gamma[m + n/2])/(Gamma[m] Gamma[(1 - n)/2] Gamma[1 + n]), 0] + (JacobiP[(2 Cos[(n Pi)/2])/n, a, b, 0] Derivative[3, 0] [LegendreP] [(2^n Sqrt[Pi] Gamma[m + n/2])/(Gamma[m] Gamma[(1 - n)/2] Gamma[1 + n]), 0])/6 + (2^(-1 + 3 n) Pi^(3/2) Gamma[m + (1 + n)/2] ^3 Derivative[3, 1] [LegendreP] [(2^n Sqrt[Pi] Gamma[m + n/2])/(Gamma[m] Gamma[(1 - n)/2] Gamma[1 + n]), 0])/(3 Gamma[m] ^3 Gamma[1 - n/2] ^3 Gamma[n] ^3) + (2^(-3 + 4 n) Pi^2 Gamma[m + (1 + n)/2] ^4 Derivative[4, 0] [LegendreP] [(2^n Sqrt[Pi] Gamma[m + n/2])/(Gamma[m] Gamma[(1 - n)/2] Gamma[1 + n]), 0])/(3 Gamma[m] ^4 Gamma[1 - n/2] ^4 Gamma[n] ^4)))/(Gamma[1/2 - n/2] Gamma[1 + n/2])) x^4 + O[x] ^5 ZernikeR[LegendreP [LaguerreL[λ n, D f z, g z (ψ^0 ϱ m), I Exp[λ]], x], m, r] Hypergeometric1F1 Regularized[a^5, D[ϱ^6 n^73, y, x] b, g^8, Exp[n] 6, δ σ^2, ε θ^3, Δ α^4] when Hypergeometric0F1Regularized[a, z] == BesselI[-1 + a, 2 Sqrt[z]] Hypergeometric1F1Regularized[a^5, b D[n^73 ϱ^6, y, x], g^8, 6 Exp[n], δ σ^2, ε θ^3, Δ α^4] z^((1 - a)/2) ZernikeR[LegendreP[LaguerreL[n λ, D f z, g m z ϱ, I Exp[λ]], 0, x], m, r] for every connected group G and level k ≥ 0 modular tensor categories that are additively equivalent to repk (LG) in order to encrypt and decrypt Quantum Negative Energies and related entagled chemical information's (Statue1a), (SI Appendix V), (SI Appendix VI), (Statue1b), (SI Appendix VII), (SI Appendix VIII), (SI Appendix IX), (SI Appendix XVIII) (Statue1c), (SI Appendix X), (SI Appendix XI), (Statue1d), (SI Appendix VIII), (SI Appendix VIII), (SI Appendix XII), (SI Appendix XIII), (Statue1e), (SI Appendix IX), (SI Appendix XIV), (SI Appendix XV), (SI Appendix XVI), (SI Appendix XVII), (SI Appendix XVIII), (SI Appendix XIX), (SI Appendix XX), (SI Appendix XXI), (Statue1f), (SI Appendix XXII), (SI Appendix XXIII), (SI Appendix XXIV), (SI Appendix XXV) (SI Appendix XXVI), (Statue1g), (SI Appendix XXVII). (SI Appendix XXVIII), (Statue1h), (SI Appendix XXIX), (SI Appendix XXX), (Statue1i), (SI Appendix XXXI), (SI Appendix XXXII), (SI Appendix XXXIII), (SI Appendix XXXIV), (Statue1j), (SI Appendix XXXV), (SI Appendix XXXVI), (SI Appendix XXXVII), (Statue1k), (SI Appendix XXXV), (SI Appendix XXXVI), (SI Appendix XXXVII), (SI Appendix XVIII), and ((Cluster Docking Energy TableS1), (SI Appendix I), (Cluster Docking Energy TableS2), SI Appendix I), (Docking Energy TableS1), (SI Appendix I), (Docking Energy TableS2), (SI Appendix I), (Docking Energy TableS3), (SI Appendix I)), (Table S6), (OUTPUTs1-3), (Ic1a), (Ic1b), (Ic1c), (Ic2a), (Ic2b), (Ic2c), (Ic2d), (Ic2e), (Ic2f), (Ic2g), (Ic2h), (Ic2c), (Ic2g), (Ic2k), (Ic2l), (Ic3a), (Ic3b) (Ic3c), (Ic3d), (Ic3d), (Ic3e), (Ic3f), (Ic3g), (Ic3h), (Ic3i), (Ic3j), (Iconic5), and ((Iconics1-4), (Eqs1-400), Supplementary Material METHODS AND MATERIALS (1), (2)), and (Figures S(1- 133)) Here, for the first time I have generated *Kpr* (1-2 gμν Eˆ∇Φ/(√-1/37 ⊗ HRz sinˆ (-13) log (|ζ (xμν-, iyCX ⊕ ihΦo21/22π) |) ((Iconics1-4), (Eqs1-400), Supplementary Material METHODS AND MATERIALS (1), (2)), (Supplement Material FUNCTIONS.1-24), and (Cluster of BIOGENEA_ CONSENSUS_Eqs.1-26) docking systems by transmitting “drug repositioning signals” in higher-dimensional theories of electron allocations to Quantum Entropy Negativity Frames. These generalized networks of electronic structure communications were extended into druggable scaffolds by using Chern-Simons harmonic oscillators on anti-de Sitter brane spacetimes for constructing, remerging, and generating chemical and physical small molecule libraries available through publicly web servers electron allocations observed in these Quantum Network Homeopathic Avogadro Number’s Function Repeaters which were inevitably and physically heterogeneous, with complex hypergeometric topologies of high-and low-quality links in all possible triangular pharmacophoric skeletons due to the arbitrariness in this G*i*Ψoˆ*sinϕ* metric for the encoding length ℓ which has to be at least log|G|G′| *ôℏ*ˆ (uir) Uμ (x) O (log|G|G′| *ôℏ*ˆ (uir) Uμ (x)) for the cyclic decomposition θ: Zpk1.1×. N× Zp kr. Nr G, where pki are prime Quantum Negative Energies for negative docking energies pi in this torsionless case that appears also in five-dimensional CS AdS gravity. [49–183] The group of (PDB IDs: 1xak,7b3o,7khp,6wzu,6w63,6m2q,7kdl, 7bv2,6woj,2gt9,6lu7,6zgg,2ghv,6xs6, and 6yi3) protein targets that performs the group operations reversibly was removed either by gauge fixing, and by changing the cosmological constant so that the tested atom’s CS gravity could become effectively

 doi:10.20944/preprints202403.0518.v1

EGB gravity when the transverse section of the geodesic metric is maximally symmetric since in this paper, our focus has been on path selection, and the need for an idealized, homogeneous power-of-Avogadro number's-of-hops routing algorithm on purify-and-swap repeater networks as an acceptable and easy-to-calculate topology metrics CS algorithm that reliably chooses a reasonable and an optimal, pharmacophore merging path of entangled systems that are completely reliable. [10–182] Because we do not understand them properly and because entanglement by its definition can easily be disturbed it might be due to the little understood role of consciousness in such Quantum Homeopathy systems that they still lack reliability. [10–172,176–195] It could be that if one wants to enact the magic with a mechanistic-causal mindset, it will fail, precisely because consciousness plays an important role. [3–59,40–187] My results show that, despite many important differences, Quantum repeater networks behave similarly to classical networks in useful ways, but the classical principles cannot be applied without a detailed physical simulation for both the physics and the classical messaging protocols, when translating these several variants and exploring the range of gauge conditions under which these Quantum Homeopathy principles apply. Finally, these variants that are referred to the current data showing from the Wuhan outbreak that might also be initially caused by bats, and might have been transmitted to humans via currently unknown wild animals sold at the Huanan seafood market are translated here throughput into a chemical space connection by using a diffusion-based generative model for molecular docking. The approach generates a tuneable number of ligand poses in a two-step process that is based primarily on a Wick rotation on A⟨*irr7ΓjIP* bottleneck link in the ACE2 molecular path, while the total work, in number of operations performed average for each residue calculated including the Dirac Density Matrix Equation Solutions of ∂(Tr[ψ,{2}] DensityMatrix)/∂log$^{\varrho}$(ψ) A log((B^{G} sin(ω) h$^{\nu}$ (n π Q δ μ σ)) ϱ A) $L_{T_\theta(\alpha\,\psi\,\cos(\gamma))}(x)$ ϕ N Ψ $_2F_1$ (a,b;c;x)==-(1/(2 π Γ(b)))(1+ $\sqrt{5}$) N Ψ ∂(DensityMatrix Tr[ψ,{2}])/∂A $\left(\int_1^{\psi} \frac{1}{t}\,dt\right)^{\varrho}$ $\int_1^{\mathcal{A}\,h^{\nu}\,n\,\pi\,Q\,B^{G}\,\delta\,\mu\,\rho\,\sigma\sin(\omega)} \frac{1}{t}\,dt$ ($\int_0^1 e^{t\,x}\,(1-t)^{T_\theta(\alpha\,\psi\,\cos(\gamma))}\,t^{-1-T_\theta(\alpha\,\psi\,\cos(\gamma))}\,dt$) ($\int_0^\infty e^{-t}\,t^{-1+b}\,{}_1F_1(a;c;t\,x)\,dt$) sin(π Tθ(α ψ cos(γ))) for (Re(b)>0 and -1<Re(Tθ(α ψ cos(γ)))<0) Hypergeometric1F1, BesselK for Angular Momentum functions of ClebschGordan, ThreeJSymbol, SixJSymbol, JacobiP, and JacobiP[n,a,b,x] I.(LaguerreL[ChebyshevT[θ, α ψ Cos[γ]], x] GoldenRatio) N Ψ Hypergeometric2F1[a, b, c, x] LaguerreL[ChebyshevT [ArcSin[P r] ^ψ P x α ψ Cos[γ], x^6], Ψ Log[ζ] ^4] Hypergeometric2F1[P[r], P[δ], ψ o, γ] (SphericalHarmonicY[g^(μ + ν) α δ λ, (k β μ^(1 + α))/6, θ/23, ϕ] /2) WhittakerM[k, m, x] LegendreP[G (6.02214076 10^23 h^ν) n - 2.9794842 10^-19 (m Ψ^C) (Cos[μ] Sin[ω]), x] Hypergeometric1F1[Cos[x Q] ^4 Q^Cos[X c] ^4, ArcSin[r] ^2 Sin[b], Log[23 y I] ArcSin[z]] == (E^((Log[23 y I] ArcSin[z])/2) Pi ((-(Log[23 y I] ArcSin[z]))^((ArcSin[r] ^2 Sin[b])/2) Gamma[-(Cos[x Q] ^4 Q^Cos[X c] ^4) + ArcSin[r] ^2 Sin[b]] WhittakerW[Cos[x Q] ^4 Q^Cos[X c] ^4 - (ArcSin[r] ^2 Sin[b])/2, (1 - ArcSin[r] ^2 Sin[b])/2, -(Log[23 y I] ArcSin[z])] + (Log[23 y I] ArcSin[z])^((ArcSin[r] ^2 Sin[b])/2) Gamma[Cos[x Q] ^4 Q^Cos[X c] ^4] WhittakerW[-(Cos[x Q] ^4 Q^Cos[X c] ^4) + (ArcSin[r] ^2 Sin[b])/2, (1 - ArcSin[r] ^2 Sin[b])/2, Log[23 y I] ArcSin[z]]))/(Gamma[Cos[x Q] ^4 Q^Cos[X c] ^4] Gamma[1 - ArcSin[r] ^2 Sin[b]] Gamma[-(Cos[x Q] ^4 Q^Cos[X c] ^4) + ArcSin[r] ^2 Sin[b]] ((-(Log[23 y I] ArcSin[z]))^(ArcSin[r] ^2 Sin[b]) Sin[(Cos[x Q] ^4 Q^Cos[X c] ^4) Pi] - (Log[23 y I] ArcSin[z])^(ArcSin[r] ^2 Sin[b]) Sin[(Cos[x Q] ^4 Q^Cos[X c] ^4 - ArcSin[r] ^2 Sin[b]) Pi])) /; ArcSin[r] ^2 Sin[b] ∉ Integers that gives the Jacobi polynomial and PauliMatrix explicitly functions of Δθˆ (Eqs.1-400), ((Iconics1-4), (Eqs1-400), Supplementary Material METHODS AND MATERIALS (1), (2)), (Supplement Material FUNCTIONS.1-25), (Maths14a,14b,14c,14d,14e,14f,14g,19a,19b,19c, 19d,19e,19f,19g,19h,20a,20b,20c, 20d,20e,20f1,20f2,20f3,20g,20h,20i, 20j,21a,21b,21c,21d,21e,21f,21g,21h,21i,21j,22a, 22b,22c,22d,,22e,,22f,22g), and (Cluster of BIOGENEA_ CONSENSUS_Eqs.1-26), (pulses or measurements). These expansions are increased with the addition of other, non-bottleneck chemical bridges, much as in a classical network path by applying this form of Chern Simons algorithm with the inverse throughput of each hop as the combined Quantum states resulting in strong correlation

 doi:10.20944/preprints202403.0518.v1

being on the same footing as the conformal geometry multiplet, and consists of a minimal BV “field” content between CS-calculated Roccustyrna ligand and its actual throughput, and between docking energy and total fitness scoring analysis. Previous studies have uncovered several receptors that different coronaviruses bind to, such as ACE2 for SARS-CoV29 and CD26 for MERS-CoV. This molecular modeling showed structural similarity between the receptor-binding domains of SARS-CoV and 2019-nCoV presenting an implementation of a Quantum Homeopathy-based LegendreP solver for Hypergeometric functions that are able to deal both closed and open-quantum systems alike. This is achieved with reasonable computational effort, allowing us to recommend the use of this Entanglement model of Quantum Homeopathy as a Chern Simons algorithmic example of generalized entanglement for predicting smallmolecule binding poses by representing the binding site surface as a polygon mesh and the ligand as a molecular graph, and for predicting a probability distribution over pairwise node Euclid special distances between the ligand and protein. This was predicted by weak quantum theory interpretations of the solvation corrections calculated as a difference to the solvation free energies of the protein– ligand complex (PL), the protein (PDB code: 6xs6) (P), for the complex ligand of (rboximidoyl 3 fluoro (1S,4S) ((diamino-methylidene) amino) ethenyl}) amino, oxy methyl) 3,4 dihydroxyoxolan 2 yl,1,2,4 triazol 3 yl formamido) phosphoryl,6 fluoro 3,4 dihydropyrazine 2 carboxamide (7aR) 5 amino N * (S) 2 * (3 fluoro 1 ((2S,5R,6R) 6 (1S,4S) 5 oxabicyclo*2.1.0, pentan 2 ((2S,5R,6R) 6 ((2S) 2 amino 2 phenylacetamido) 3,3 dimethyl 7 oxo 4 thia 1 azabicyclo (3.2.0) heptane 2 carbonyloxy) ({((2 amino 6 oxo 6,9 dihydro 3H purin 9 yl) oxy) (hydroxy) phosphoryl} oxy) phosphinic acid ylidene, *cyano (2,6 diazabicyclo*3.1.0, hex 1 en 6 yl) (rboximidoyl 3 fluoro (1S,4S) ((diaminomethylidene) amino) ethenyl}) amino, oxy methyl) 3,4 dihydroxyoxolan 2 yl,1,2,4 triazol 3 yl formamido) phosphoryl,6 fluoro 3,4 dihydropyrazine 2 carboxamide (7aR) 5 amino N * (S) 2 * (3 {((1S,4S) 5 oxabicyclo (2.1.0) pentan 2 ylidene) {(cyano ({2,6 diazabicyclo (3.1.0) hex 1 en 6 yl}) phosphanyl) (fluoro) methyl} lambda6 su lfanyl}one ((2S) 2 amino 2 (1S,4S) 5 oxabicyclo*2.1.0, pentan 2 ((2S,5R,6R) 6 ((2S) 2 amino 2 phenylacetamido) 3,3 dimethyl 7 oxo 4 thia 1 azabicyclo (3.2.0) heptane 2 carbonyloxy) ({((2 amino 6 oxo 6,9 dihydro 3H purin 9 yl) oxy) (hydroxy) phosphoryl} oxy) phosphinic acid ylidene, *cyano (2,6 diazabicyclo*3.1.0, hex 1 en 6 yl) phenylac etamido) 3,3 dimethyl 7 oxo 4 thia 1 azabicyclo (3.2.0) heptane 2 carbonyloxy) ({((2 amino 6 oxo 6,9 dihydro 3H purin 9 yl) oxy) (hydroxy) phosphoryl}oxy) phosphinic acid and analoques of {((1S,4S) 5 oxabicyclo (2.1.0) pentan 2 ylidene) {(cyano ({2,6 diazabicyclo (3.1.0) hex 1 en 6 yl}) phosphanyl) (fluoro) methyl} l ambda6 sulfanyl}one (3S,4'R,5'S) 2' amino 3 ((2R) 2 {((R) {((2R,4R) 2 ((1 fluoroethenyl) (hydroxymethyl) amino) 5 oxa 1lambda3 thia 3 azabicyclo (2.1.0) pentan 3 yl) methoxy} (hydroxy) (pyrrolidin 1 yl) phosphaniumyl) -oxy}butyl) 6' oxo 1',4',5',6' tetrahydro 2lambda6 spiro (oxaziridine 2,9' purin) 2 ylium {5 oxabicyclo (2.1.0) pentan 2 yl}, (sqrt (Θ) θ (3 e del phosphoryl) formonitrile (rboximidoyl 3 fluoro (1S,4S) ((diamino-methylidene) amino) ethenyl}) amino, oxy methyl) 3,4 dihydroxyoxolan 2 yl,1,2,4 triazol 3 yl formamido) phosphoryl,6 fluoro 3,4 dihydropyrazine 2 carboxamide (7aR) 5 amino N * (S) 2 * (3 ((2S,5R,6R) 6 ((2S) 2 amino 2 phenylacetamido) 3,3 dimethyl 7 oxo 4 thia 1 azabicyclo (3.2.0) heptane 2 carbonyloxy) ({((2 amino 6 oxo 6,9 dihydro 3H purin 9 yl) oxy) (hydroxy) phosphoryl}oxy) phosphinic acid and analoques of {((1S,4S) 5 oxabicyclo (2.1.0) pentan 2 ylidene) {(cyano ({2,6 diazabicyclo (3.1.0) hex 1 en 6 yl}) phosphanyl) (fluoro) methyl} l ambda6 sulfanyl}one (3S,4'R,5'S) 2' amino 3 ((2R) 2 {((R) {((2R,4R) 2 ((1 fluoroethenyl) (hydroxymethyl) amino) 5 oxa 1lambda3 thia 3 azabicyclo (2.1.0) pentan 3 yl) methoxy} (hydroxy) (pyrrolidin 1 yl) phosphaniumyl) oxy}butyl) 6' oxo 1',4',5',6' tetrahydro 2lambda6 spiro (oxaziridine 2,9' purin) 2 ylium fluoro 1 {5 oxabicyclo (2.1.0) pentan 2 yl} purin 2 yl) amino}) phosphoryl) oxy}) phosphoryl) formonitrile) {1 - [(R) - [(1S,3R) - 3 - [(R) - amino (carbamothioylamino) methyl] diaziridin - 1 - yl] ({6 - oxo - 2 - [(2S,5R) - 3,4,5 - trifluoro - 2,5 - dihydrofuran - 2 - yl] - 6,7 - dihydro - 1H - purin - 8 - yl}amino) phosphoroso] - 1H - azirin - 2 - yl}thiourea using $\hat{S}x$ operator for the performance of the translation to a Quantum reference frame (SI Appendix I), (SI Appendix II), (SI Appendix III), (SI Appendix IV), and **(**SI Appendix V**).** This density matrix simulator is capable of modeling the important factor of finite Chern Simon’s Quantum states**,** but the sheer additional combinatoric complexity fragmented pharmacophore system can describe the same superposition when accelerating to a larger ligand receptor system

 doi:10.20944/preprints202403.0518.v1

from including variation of this parameter in both the simulations and algorithmic arguments presenting from these results. (SI Appendix I), (SI Appendix IX), (SI Appendix XIV), (SI Appendix XV), (SI Appendix XVI), (SI Appendix XVII), (SI Appendix XVIII), (SI Appendix XIX), (SI Appendix XX), (SI Appendix XXI), (Statue1f), (SI Appendix XXII), (SI Appendix XXIII), (SI Appendix XXIV), (SI Appendix XXV) (SI Appendix XXVI), (Statue1g), (SI Appendix XXVII), (SI Appendix XXVIII), (Statue1h), (SI Appendix XXIX), (SI Appendix XXX), (Statue1i), (SI Appendix XXXI), (SI Appendix XXXII), (SI Appendix XXXIII), (SI Appendix XXXIV), (Statue1j), (SI Appendix XXXV), (SI Appendix XXXVI), (SI Appendix XXXVII), (Statue1k), (SI Appendix XXXV), (SI Appendix XXXVI), (SI Appendix XXXVII), (SI Appendix XVIII), and ((Cluster Docking Energy TableS1), (SI Appendix I), (Cluster Docking Energy TableS2), (SI Appendix I), (Docking Energy TableS1), (SI Appendix I), (Docking Energy TableS2), (SI Appendix I), (Docking Energy TableS3), (SI Appendix I)), ((Iconics1-4), (Eqs1-400), (Supplementary Material METHODS AND MATERIALS (1), (2)), (Maths19a,19b,19c,19d,19e,19f,19g,19h,20a,20b,20c,20d,20e, 20f1,20f2,20f3, 20g,20h,20i,20j,21a,21b,21c,21d,21e,21f,21g,21h,21i, 21j,22a,22b,22c,22d,,22e,,22f,22g), and (Supplementary Material METHODS AND MATERIALS (1), (2), and Figures S(1- 133)), (OUTPUTs1-3)), (Ic1a), (Ic1b), (Ic1c), (Ic2a), (Ic2b), (Ic2c), (Ic2d), (Ic2e), (Ic2f), (Ic2g),(Ic2h), (Ic2c), (Ic2g), (Ic2k), (Ic2l),(Ic3a), (Ic3b) (Ic3c), (Ic3d), (Ic3d), (Ic3e), (Ic3f), (Ic3g), (Ic3h), (Ic3i), (Ic3j), (Ic3k), ((Iconics4-6), (Supplementary Material METHODS AND MATERIALS (1), (2)). Concerning routing the Quantum extension of the gradient measure of the information content in state ψI, (ψ) χ (0) within this QFT network of uniform technology as a part of a larger Quantum circuit I unify various Quantum networking approaches within a single Quantum fields framework, covering inter-networking between heterogeneous scoring model GEMDOCK technologies that transforms random initial ligand poses into predicted poses by translation, rotation, and torsion angle changes as well as radically different error correction approaches, routing, multiplexing approaches for this kind of reverse quantum reference frame diffusion processes. [10–188–195] In fact by employing in-house ligand libraries for the design of a Quantum thinking novel multi-chemo-structures targeted the protein targets of COVID-19 main protease more ((Iconics1-4), (Eqs1-400), Supplementary Material METHODS AND MATERIALS (1), (2)), (Supplement Material FUNCTIONS.1-26), and (Cluster of BIOGENEA_ CONSENSUS_Eqs.1-26) quantum functions and hypergeometric solutions that annihilates the Chern-Simons wavefunction of tetrahedron shaped pharmacophoric ligands were generated after solving the Lagrangian function for different chemical branches of the Roccustyrna_gs, the Roccustyrna_fr, the Roccustyrna_gs_ consv, and the Gissitorviffirna_TM pharmacophoric system of (2S,5R,6R) - 3,3 - dimethyl - 7 - oxo - 4 - thia - 1 - azabicyclo (3.2.0) heptane - 2 - carbonyloxy), ({(2 - amino - 6 - oxo - 6,9 - dihydro - 3H - purin - 9 - yl) oxy) (hydroxy) phosphoryl} oxy) phosphinicacid 1 - yl} (fluoromethyl) - lambda4 - sulfanyl) amino) diaziridin - 3 - one chemical bridges. The SO (4,2) μ × U (111100001) |G|G′| $\hat{\sigma}\hat{\hbar}\hat{}$ (uir) ν × U (00000111) Uμ (x) space of non-vanishing components of F [A [Ψo$\hat{}sin\phi${Ψ}] B] solutions that only meet at a particular merging point of their respective parameter [F2] AdS,1/2 [r4] spaces which are intrinsically rooted in QFT. **The** Quantum-gravitational origin for Quantum Negative Energies at Avogadro Number's powered Quantum Homeopathy Information, are the maximum for an open sphere of unitary radius inside the binding surface of binding cavities of RBD and its mutants (N501Y, R408I, W463R, N354D, V367F and N354D/D364Y), and disappear when approaching the attractor. An advantage is identified by evidence, which varies according to its theoretical, experimental or operational context by dividing these Quantum Homeopathy advantages into classes on the basis of the strength of the quantum advantage (i.e., a polynomial or superpolynomial reduction in complexity) and the complexity of the analogous classical algorithm (i.e., polynomial or superpolynomial). [30–192] This seems to be one explanation for Hahnemann's continuous development of his theory and practice, because he seems to have experienced more failures than his theory would have had it, and so we had to go on improving his method or finding new ways of creating entangled states in this project by making use of Hypergeometric1F1, HypergeometricU, WhittakerM, WhittakerW, Hypergeometric0F1, Hypergeometric0F1, Hypergeometric2F1Regularized quantum functions for each Valsartan's small fragment derivatives that preserves the form of the spherically symmetric ansatz identified by

 doi:10.20944/preprints202403.0518.v1

chemical patterns of general (variational) Quantum Functions LegendreP[JacobiP[-5.747, 84.926, 6.79, -29.284], x] (LaguerreL[JacobiP[-5.747, 84.926, 6.79, -29.284], x] /Gamma[(1 - n)/2]) S ($p0$, ϕ), S (AoΨo, d) ($p0$) |G|G′| $\hat{\sigma}\hat{\hbar}\hat{}$ (uir) ν Uμ (x) g, S ($p0$, ϕ) and$I$ ($p0$, ϕ), I (AoΨo, d) ($p0$) |G|G′| $\hat{\sigma}\hat{\hbar}\hat{}$ (uir) ν Uμ (x) g, I ($p0$, ϕ) (SI Appendix I) as well as probabilistic transformations on Murko (BM) circuit statements considering the additional MM-PBSA-WSAS binding free energy calculation difficulties since the drug designs I deal with are not orthogonal anymore (SI Appendix I), (SI Appendix II), (SI Appendix III), (SI Appendix IV), (SI Appendix V), (SI Appendix VI), (SI Appendix VII), (SI Appendix VIII), ((Iconics1-4), (Eqs1-400), Supplementary Material METHODS AND MATERIALS (1), (2)), and (30-42) along the lines of this generalized version of the macro-entanglement presented here. This is only one of many possible ways of reconstructing entanglement features of WQT that it does not regulate or quantify the amount of non-commutativity. [100–192] In this QM proper this is achieved by Planck's constant, which quantifies the amount of non-commutativity. [110–193] Thus, theoretically, this reconstructive macroentanglement could be even stronger for both Chern-Simons theories and knot theory restrictions for the Quantum negative gauge transformation A′, g −1 (A, d) g algorithms as applied in this project for translating negativities from the Quantum Conformer States of the atomic orbits of the VOCs of Alpha, Beta, Gamma, Delta and Omicron variants in line with them from their targeted proteins of FDA antivirals (respectively the viral RNA dependent RNA polymerase and the viral main protease Mpro) that are highly conserved into five dimensions pharmacophoric groups, showing in multiple ways how entanglement could be brought about in real-world systems. [40–192] In this way, a Homeopath Turing Machine Rule, which has never been used in computer science, would appear to be the classical computational skeleton of the original QFT, and makes sense for achieving experimental and operational advantages in the near term. [50–193] Among these classes of quantum advantages, the computational skeleton in this quantum fields theory example is quantized when using a Turing Machine Rule to trace the original QFT while recovering the quantum characteristics of the latter implying differing prospects of superpolynomial advantages on classically hard problems by applying the most viable quantum homeopath solutions to operational advantages. [139–193] A fairly unexpected result of this article is that this Quantum Homeopathy Entanglement seems to be hidden in QFT just like quantum information does (remember that there is an uncertainty relationship between metric and quantum information). [150–195] I suggest that such quantum fluctuations derived from ligand-protein binding sites will be useful for building further understanding the metric appear in this Quantum Homeopathy model within the attractive basin inducing uncertainty in the position states, leading to the definition of the qubit states of the quantum uncertainity relationships, quantum negative entropy, and quantum entanglement energies. [151–195] Between the atractor basin from these multiple diagonal chemical descriptors the atomic orbits from peptide based small molecules, and SARS-Cov-2 complex biological systems are also considered as inputs in these QFT guided docking energy reduction processes and would then play the role of definitional Quantum Functions in particular the Quantum Regulator allowing the switch from a metalanguage to an object language (the logic) when determining the ground-state electron configuration of the Roccustyrna_fr chemical fragments in the coordinates ζ, $\theta r{-}rear\chi$, and $\theta\chi$ $(b{-}a)$ r of Dunham Tipping where θx is the phase of x that parameterizes the closed leaf of the annotated Roccustyrna_fr, Roccustyrna_gs, Roccustyrna_consv, and Gissitorviffirna_TM crystal structures. That reveals a similar inhibitory mechanism in which they occupy the substrate-binding pocket and block the enzyme activity of SARS-CoV-2 Mpro. QM and QFT are not at the same level, neither mathematical due to the appearance of the uir of the CCR in QFT, while in QM this is prohibited by Stone-von Neumann's theorem nor logical QFT is described by a quantum metalanguage while (QH) Quantum Homeopathy is described by a quantum logic, neither physical since Haag's theorem holds in QFT, and therefore these irreducible representations of free fields are unitarily inequivalent to those of interacting fields. In particular, the cluster of Quantum Functions (Supplement Material FUNCTIONS.1-27), (Supplementary Material METHODS AND MATERIALS (1), (2)), and Figures S(1- 133)), ((Iconics1-4), (Eqs1-400), and (Schematics1a,1b,1c,1d,1e,1f,1g,1h,1i,1j,1k,1l,1m), (I-VI) Supplementary Material METHODS AND MATERIALS (1), (2)) including these definitional LegendreP QFT function allows passing from a

 doi:10.20944/preprints202403.0518.v1

QML to the Quantum crypto-logic of Quantum information (CRQLI) of string states along the z0 orbit on the Gissitorviffirna_ TM-S3 atomic charges, coming from modes supported by the [amino ({4 - [(2R,3R) - 2 - [(2S) - 3 - { [(1S,2S) - 1 - { [(S) - 1,3 - dihydroisoindole - 2 - carbonyl [(2 - methyl - 6 - oxo - 1,7 - dihydropurin - 8 - yl) methyl] phosphanyl] carbamoyl} - 2 - methylbutyl] amino} - 2 - methylpropyl] oxaziridin - 3 - yl] butyl}amino) methylidene] azanium embedded Roccustyrna_fr-S1 ligand-protein atoms, with masses mb, ikb2, k ∈ Z≥0 transforming in the bifundamental representation of the gauge group of the main protease (Mpro), also known as the 3C-like protease (3CLpro), and one or two papain-like proteases (PLPs), into 16 non-structural proteins (nsps) including others related to the quantum simulation of biologically relevant molecules such as sartans small molecules, ATR1 protein domains, and nucleic acids and their chemical quantities. This SARS-CoV-2 quantum homeopathic network of ultra high information that is hidden in QFT seems to be closely related to the quantum information loss paradox occurred in evaporation of black holes, which then might be solved in the extreme hypothesis when all the pure states within the BH event horizon are maximally entangled. Hence, these cryptometalinguistic links between Quantum Entropy Negativity assertions, which are interpretable as interactions of Quantum fieldss, are sent to logical connectives between propositions for linking the fragments of [amino ({4 - [(2R,3R) - 2 - [(2S) - 3 - { [(1S,2S) - 1 - { [(S) - 1,3 - dihydroisoindole - 2 - carbonyl [(2 - methyl - 6 - oxo - 1,7 - dihydropurin - 8 - yl) methyl] phosphanyl] carbamoyl} - 2 - methylbutyl] amino} - 2 - methylpropyl] oxaziridin - 3 - yl] butyl}amino) methylidene] azanium- [({4 - [methyl (2 - methylpropyl) sulfamoyl] phenyl} (3S) - oxolan - 3 - ylamino) methyl] amino ({3 - methyl - 2H - 4λ⁴,6λ⁴ - [1,2,3] triazolo [4,5 - d] pyrimidin - 5 - yl}methyl) aminophosphinic acid- ({3 - methyl - 2H - 4λ⁴,6λ⁴ - [1,2,3] triazolo [4,5 - d] pyrimidin - 5 - yl}methyl) amino [(R) - (3H - 1λ⁴ - pyridin - 4 - ylamino) ({ [(5H - 1,3λ⁴ - thiazol - 5 - ylmethoxy) carbonyl] amino}) methyl] aminophosphinic acid- (S) - { [(S) - [(2R,5R,6S) - 6 - [(2S) - 2 - amino - 2 - phenylacetamido] - 3,3 - dimethyl - 7 - oxo - 4 - thia - 1 - azabicyclo [3.2.0] heptane - 2 - carbonyloxy] (hydroxy) λ³ - oxidanidylidene - λ⁵ - phosphanyl] oxy} ({ [2 - ({ [(3S) - 3 - [(2R) - 2 - [(2S) - 2 - amino - 4 - carbamoylbutanamido] - 4 - carbamoylbutanamido] - 4,4 - dihydroxybutyl] sulfanyl}methyl) - 6 - oxo - 8Hpurin-9 - yl] oxy}) hydroxy - λ⁵ - phosphanylideneolate-4 - amino - 5 - [(1'R,2S,3''S,5'R,6'R) - 3' - methyldispiro [oxirane - 2,2' - bicyclo [3.1.0] hexane-6',2'' - oxiran] - 3' - en - 3'' - ylmethyl] - 1,2,4 - triazole - 3 - thione-2 - [(2S,3S) - 1 - {2 - [(2S,3R,4R,5R) - 5 - {2 - [(2S,3R,4R,5S) - 5 - { [(R) - (acetylcarbamoyl) (cyano) methoxy] methyl} - 3,4 - dihydroxyoxolan - 2 - yl] - 6 - oxo - 8H - 1λ⁴,3λ⁴ - purin - 9 - yl} - 3,4 - dihydroxyoxolan - 2 - yl] acetyl} - 3 - aminoaziridin - 2 - yl] - 2 - fluoroethanecarbonimidoyl fluoride neighborhood of the two knots into the S2 site, stacking with the imidazole ring of His41 which naturally defines a vector ‘tangent to knot K0’ that correspond to Quantum Correlations such as Quantum Superposition and Entanglement at least infinitesimally. This generalized Hadamard approach could potentially be applicable to the discovery of hit matter for novel biological targets, with clinical or genomic features for predicting and rationalizing ligand poly-pharmacology and for predicting new ligand inhibitory agents using same series of HeunG, HeunG[a,q,α,β,γ,δ,z] quantum functions that will give Advanced Potentials to the general Heun functions of HeunC, HeunD, HeunB, HeunT, HeunTPrime and Hypergeometric2F1 ChebyshevT[n, x] GegenbauerC[Q^Cos[f Degree] z LogBarnesG[z], x c^4 (Pi r), ArcSin[r] ^2] LegendreP[σ h^(δ n), Q^D, d^4 r^10 (δ/(G Ψ)) n^8 Ψ, G N g^(1/6^d^7) (Ψ GoldenRatio)] LegendreQ[Log[ζ d] 2 Ψ^C Cos[μ], σ δ ArcSin[q ζ] ^Ψ] WhittakerW [k, m, z] Hypergeometric0F1[a, z] Hypergeometric0F1[a, z] GegenbauerC[n, m, x] ChebyshevT[(θ/ξ) α x, I Exp[y] Cos[EulerGamma]] LaguerreL[n, a, x] LaguerreL[n, x] GegenbauerC[n, m, x] ChebyshevT[n, x] HypergeometricU[Q^Cos[x], x c^4 (Pi r), ArcSin[r] ^2] LegendreP[δ n, Q^D, d^4 r^10 (δ/(G Ψ)) n^8 Ψ, G N g^(1/6^d^7) (Ψ GoldenRatio)] LegendreQ[Log[ζ d] 2 Ψ^C Cos[μ], σ δ ArcSin[q ζ] ^Ψ] LaguerreL[E, x] SphericalHarmonicY[l, m, θ, ϕ] GegenbauerC[α μ ν^d, z^b] LegendreP[δ n, Q^4 d^4 r^10 (δ/(G α)) n^2 Ψ, G N g^(1/6^d^3) (ψ GoldenRatio)] LegendreQ[Log[ζ] Cos[μ], σ δ ArcSin[q ζ] ^g] LaguerreL[h, x] GegenbauerC[n, m, x] ChebyshevT[θ/ξ, α (ψ ι) Cos[EulerGamma]] functions interacted with other hypertension protein targets with the same ratings of negative docking energy values. In this project I reported a substantive body of structural, biochemical, and virus replication docking studies that could identify several potential inhibitors of the SARS-CoV-2 enzyme and high resolution structures interacting

 doi:10.20944/preprints202403.0518.v1

with the wild-type PLpro, the active site of the phosphate ion that binds to the active site at the N-terminus of helix α4 (contributing Cys111) mutant, and their complexes providing fundamental molecular and mechanistic insight into PLpro protease targets. These compounds may inhibit the peptidase activity of PLpro in vitro and some could also block SARS-CoV-2 replication in cell culture assays including in vivo testings. These findings will accelerate structure-based drug design efforts targeting PLpro to identify high-affinity inhibitors of clinical value. (SI Appendix XXVII). (SI Appendix XXVIII), (SI Appendix XXIX), (SI Appendix XXX), (SI Appendix XXXI), (SI Appendix XXXII), (SI Appendix XXXIII), (SI Appendix XXXIV), (SI Appendix XXXV), (SI Appendix XXXVI), (SI Appendix XXXVII), (SI Appendix XXXV), (SI Appendix XXXVI), (SI Appendix XXXVII), (SI Appendix XVIII), ((Cluster Docking Energy TableS1), (SI Appendix I), (Cluster Docking Energy TableS2), SI Appendix I), (Docking Energy TableS1), (SI Appendix I), (Docking Energy TableS2), (SI Appendix I), (Docking Energy TableS3), (SI Appendix I)), (Plot3), (Plot4), ((Iconics1-4), (Eqs1-400), Supplementary Material METHODS AND MATERIALS (1), (2)), and (Supplementary Material METHODS AND MATERIALS (1), (2), and Figures S(1- 133)) These results also rationalize the potential use of RoccustyrnaTM_ gs, Roccustyrna_fr, Roccustyrna_gs_consv, and Gissitorviffirna_TM ligands with a three-dose immunization process and suggest that the fundamental SARS-CoV-2 Omicron variant spike RBD epitopes revealed by these broadly ultrapotent Fab XGv282 **(**PDB: 7wlc**)** antibodies as rational targets for a multitargeted sarbecovirus drug. In conclusion these alternative QFT to QM docking and quantum molecular dynamic experiments indicated to me that the Valsartan small molecule generated a semi-inhibitory binding effect when targeted inside the **(**PDB: 1Y8J**)** protein targets inside the Crystal Structure of human NEP and complexed with an imidazo **[**4,5-c**]** pyridine inhibitor. [1–192] This suggests that these translational fields of drug development, biochemistry and structural biology may stand to benefit over the near term from targeted proof of principles leveraging hybrid quantum–classical approaches, such as homeopath variational quantum simulation which it would be worth further looking for a series of relationships between QFT, QM, Quantum Homeopathy information, Entangled Space-Time, Quantum Gravity, non-commutative Geometry, Quantum Metalanguage and Quantum Logic. These topics are closely intertwined when quantized in a circuit proposing these generalized quantum homeopathy entanglements, when using the body as a communication system to communicate between genes and subsystems, which would both constitute a hyperfast communication system and a mean for the body to 'know' when a desired end state is reached [31]. [7–192] More specifically, we constructed a set of drug designs interacted solely with negative docking energies through building hydrogen bonds hydrophobic Interactions, π-Stacking, π-Cation Interactions, and Metal Complexes inside the binding domains of ACT **(**Acetic Acid**)**, ACT-A-801, nAG **(**Acetylglucosamine**)**, NAG-A-752, nAG-A-753, nAG-A-754, and ION STS **(**composite lig and containing AC1NRD9J**)**, STS-A-900 with Negative Docking Energy Values of Binding Affinity:-7.005, vdW Energy:-10.604, and Elec. Energy:-20.208 but with Positive Total Energy Docking values of 73.198 KcalMolA. These quantum advantages may result from a variety of quantum algorithm paradigms over the near term including variational quantum simulations, variational quantum machine learning quantum approximate optimization algorithms, and quantum annealing algorithms indicating that at least computationally the Valsartan drug could in some cases activate/triger the human NEP binding domains when complexed with an imidazo **[**4,5-c**]** pyridine inhibitor. Instead of this the DRVYIHPFXmimetic small molecule was able of generating into the same protein targets only Negative Binding Affinity, vdW Energy, Total energy values, and Elec. Energy docking values of-7.178, -36.112, -14.305, and-17.511 KcalMolA respectively. In addition, I suggested that such a quantum objective binding sited and symmetrized map, which encompasses unliganded cavities, will also be useful for optimizing compound screening collections towards a more complete chemical coverage in multi-targeted pharmacophoric spaces via ellipsoid coordinate homeopathic transformations. It is likely that incorporations of such radiating rotating like black-hole solutions ∂(Tr[ψ,{2}] DensityMatrix)/∂log$^{\varrho}$(ψ) A log((B^{G} sin(ω) h$^{\nu}$ (n π Q δ μ σ)) ϱ A)

$$\frac{Q^{K\,\delta\,\text{Þ}\,\cos(\mu)}}{\log(\zeta(d))\,\log\left(\frac{1}{4}\right) R\,a\,b\text{–}12\,g\,a\,b\,R\,\psi\,j^{C}\left(\sigma\,\delta\,\sin^{-1}(q\,\zeta(s))^{\Psi}\,j\right)}$$

==-((π (1-j δ σ sin^-1(q ζ(s))^ψ)$^{-1/2\,\pi\,K\,\acute{\eta}\,\cos(\mu)}$ (1+j δ

 doi:10.20944/preprints202403.0518.v1

$\sum_{k=1}^{\infty} \frac{(-1)^k (-1+\psi)^k}{k}$

σ sin^-1(q ζ(s))^ψ)^-1/2 π K ή cos(μ) ∂(DensityMatrix Tr[ψ,{2}])/∂-A (-)ϱ

$\sum_{k=1}^{\infty} \frac{(-1)^k \left(-1+A\, h^{\nu}\, n\, \pi\, Q\, \mathrm{B}^{G}\, \delta\, \mu\, \rho\, \sigma \sin(\omega)\right)^k}{k}$

(-(1+j δ σ sin^-1(q ζ(s))^ψ)^π K ή cos(μ) cot(π K π ή cos(μ)) Γ(1-12 a b g j^C R ψ-π K ή cos(μ)-a b R log(4) log(ζ(d))) ${}_2\tilde{F}_1$ (12 a b g j^C R ψ+a b R log(4) log(ζ(d)),1-12 a b g j^C R ψ-a b R log(4) log(ζ(d));1-π K ή cos(μ);1/2 (1-j δ σ sin^-1(q ζ(s))^ψ))+(1-j δ σ sin^-1(q ζ(s))^ψ)^π K ή cos(μ) csc(π K π ή cos(μ)) Γ(1-12 a b g j^C R ψ+π K ή cos(μ)-a b R log(4) log(ζ(d))) ${}_2\tilde{F}_1$ (12 a b g j^C R ψ+a b R log(4) log(ζ(d)),1-12 a b g j^C R ψ-a b R log(4) log(ζ(d));1+π K ή cos(μ);1/2 (1-j δ σ sin^-1(q ζ(s))^ψ)))))/(2 Γ(1-12 a b g j^C R ψ-π K ή cos(μ)-a b R log(4) log(ζ(d))))) for (\[LeftBracketingBar]-1+ψ\[RightBracketingBar]<1 and \[LeftBracketingBar]-1+A h^ν n π Q B^G δ μ ϱ σ sin(ω)\[RightBracketingBar]<1 and π K ή cos(μ)∉) LegendreP[1 + G h^ν n Pi Q δ μ σ Sin[ω], x] /(1 + 2 G h^ν n Pi Q δ μ σ Sin[ω]) - LegendreP[-1 + G h^ν n Pi Q δ μ σ Sin[c] Sin[ω] ^x, x] /(1 + 2 G h^ν n Pi Q δ μ σ Sin[ω]) of the radiating Kerr metric, the Vaidya–Kerr metric, which is an axisymmetric generalization of the Vaidya metric could play also an important role in other branches of mathematical chemistry and quantum chaos geometrics. [40–193] Generalized entanglement could capitalize new ligands entangled states and be the key to understanding a lot of the modern gadgets from radionics to electro-acupuncture, from bioresonance apparatuses to other purportedly causal machines, which might be clever pseudomachines and be able of distracting the mind of the patient and practitioner where the energy momentum tensor has the form of a Petrov type II fluid. [30–194] To conclude, in this work I have shown that a (bosonic) Quantum fields theory T has in itself a hidden Quantum information IT capable of computing the left-hand side to first order in

$R^{m}_{\left(\sqrt{|G\,M\,x|}\,6\,R\,z\left(\left(b^2\,r\right)e^{i\,\pi\left((e\,n)/2-\left(4\,\pi\,r\,R^2\right)/k\right)}(g\,\gamma)^{-1/2\,(e\,n)}\right)\right)\pi\,(\mu\,\nu)}(r)$ ==

$R^{m}_{\pi\,r\,R\,z\,\mu\,\nu\,b^2\,e^{i\,\pi\left((e\,n)/2-\left(4\,\pi\,r\,R^2\right)/k\right)}(g\,\gamma)^{-(e\,n)/2}\,\sqrt{\frac{G\,M\,x}{e^{i\arg(G\,M\,x)}}}\,6}(r)$

$R^{m}_{\left(\sqrt{|G\,M\,x|}\,6\,R\,z\left(\left(b^2\,r\right)e^{i\,\pi\left((e\,n)/2-\left(4\,\pi\,r\,R^2\right)/k\right)}(g\,\gamma)^{-1/2\,(e\,n)}\right)\right)\pi\,(\mu\,\nu)}(r)$ ==

$R^{m}_{\left(\sqrt{|G\,M\,x|}\,6\,R\,z\left(\left(b^2\,r\right)z^{i\,\pi\left((e\,n)/2-\left(4\,\pi\,r\,R^2\right)/k\right)}(g\,\gamma)^{-1/2\,(e\,n)}\right)\right)\pi\,(\mu\,\nu)}(r)$ for z==E

$R^{m}_{\left(\sqrt{|G\,M\,x|}\,6\,R\,z\left(\left(b^2\,r\right)e^{i\,\pi\left((e\,n)/2-\left(4\,\pi\,r\,R^2\right)/k\right)}(g\,\gamma)^{-1/2\,(e\,n)}\right)\right)\pi\,(\mu\,\nu)}(r)$ ==

$R^{m}_{\left(\sqrt{\frac{G\,M\,x}{\mathrm{sgn}(G\,M\,x)}}\,6\,R\,z\left(\left(b^2\,r\right)e^{i\,\pi\left((e\,n)/2-\left(4\,\pi\,r\,R^2\right)/k\right)}(g\,\gamma)^{-1/2\,(e\,n)}\right)\right)\pi\,(\mu\,\nu)}(r)$ for G M x!=0

$\mathrm{r}^{m}\;P^{(m,0)}_{\frac{1}{2}\left(b^2\,e^{i\,\pi\left((e\,n)/2-\left(4\,\pi\,r\,R^2\right)/k\right)}\pi\,r\,R\,z\,(g\,\gamma)^{-(e\,n)/2}\,\mu\,\nu\,|G|^3\,|M|^3\,|x|^3-m\right)}\left(1-2\,r^2\right)$ cos(1/2 π (-m+π b² μ ν r R z \[LeftBracketingBar]G\[RightBracketingBar]³ \[LeftBracketingBar]M\[RightBracketingBar]³ \[LeftBracketingBar]x\[RightBracketingBar]³ (γ g)^(-(E n)/2 $e^{i\,\pi\left((e\,n)/2-\left(4\,\pi\,r\,R^2\right)/k\right)}$))

$R^{m}_{\pi\,b^2\,G^3\,\mu\,\nu\,M^3\,r\,R\,x^3\,z\,(\gamma\,g)^{-(e\,n)/2}\,e^{i\,\pi\left((e\,n)/2-\left(4\,\pi\,r\,R^2\right)/k\right)}}(r)$

$R^{m}_{\pi\,b^2\,\mu\,\nu\,r\,R\,z\,(\gamma\,g)^{-(e\,n)/2}\,|G\,M\,x|^3\,e^{i\,\pi\left((e\,n)/2-\left(4\,\pi\,r\,R^2\right)/k\right)}}(r)$ for E^(I Pi ((E n)/2 - (4 Pi r R^2)/k)) (g γ)^((-(E n))/2 + (4 Pi r R^2)/k) LaguerreL[GegenbauerC[Q^Cos[z] LogBarnesG[z], c^4 Pi r x, ArcSin[r] ^h/2], x] ϒΓ.h,1/18XC (Rz (π) μν ⊗ b^2rIMG) μν − √3Xb^2r − 12XCZC ⊗ θZ − √2C (Rz (π), [H] ⊗̸ [Ho] ∮IμTMG) μν R_P_(L_(λ i^n)^((ψ o)×6.02214076×10^23 ϱ i Q F T q m)(i exp(λ)))(X b^2 r x)^(((ψ i^(N i))

 doi:10.20944/preprints202403.0518.v1

Q F T^δ θ^10 Ψ log^2(y) m)/10^27)(r) which is revealed when Topology Virtual Screening Algorithm with nonlinear electrodynamics implemented for the designing of the combination of DRVYIHPF-mimetic, Gisitorviffirna_TM, Roccustyrna_gs, and Roccustyrna_fr ligands. [10–71,101–192] However, both Quantum Homeopathy and QFT reduction values are considerably too small to be measured at present. [120–192] Only the rotating Pluto-mass black hole, which might theoretically have been formed in the early universe, has a Hawking temperature slightly greater than 3-K CMB radiation, which would allow its value to be potentially detected by high-resolution tools. By Extracting similar Anti-de Sitter Chern-Simons formulations of supergravity for Quantum Homeopathy Entropy Negativities (QHEN) and reference frame representations in a pharmacophore merging Quantum information scheme some of the highest negative docking scoring functions were generated when compared to other FDA approved small molecules onto the SARS-COV-2 protein targets **(**Plot1**,2).** [21–93,120–192] The derivation method in this study is concise and can be further generalized to other non-static solutions by replacing the mass function with non-static ones, which deserve further study in the future. [40–193] **(**Diagramm1, Diagramm3**)** These facts indicated to us that simulations from both free and interacting fields of Quantum Reference Frame Representations and Quantum fieldss can be reduced to a Quantum Network of full anti-de Sitter Chern-Simons supergravity-like structure formulations. [90–192] For that reason I have introduced the superpositions of configurations and supergravity-like observations into these probabilistic Turing Machines and modified their transitions. In this formulation, a transition from a configuration to another configuration is interpreted in the following way: A probabilistic Turing Machine moves from a superposition of only one configuration to another superposition of some configurations, and then a configuration is chosen from the latter superposition with some expectation value by an observation by extending these probabilistic Turing Machines into the Quantum Turing Machines. [80–193] As a result I have presented a necessary and sufficient condition for the total probabilities of configurations to be 1oM, which is more easily checkable than that by Bernstein & Vazirani showing that the algebraic argument which has been proposed between remedy and placebo and is really entangled by the application of the QM to QFT reduction methodology to homeopathic proving. [28–192] Any attempt to have prior knowledge of them both should break the entangled proving state. [87–194] This should then deliver pure negative docking results showing clear superiority between classical antivirals and Quantum Homeopathy oriented drug designs in terms of proving better fitness scoring docking values since these novel druggable structures reveal routes to rapidly develop more potent inhibitors through merging of covalent and non-covalent fragment hits and series of low-reactivity, tractable covalent fragments, and improved binders. [30–192] These combined hits providing advantageous features of Quantum-like informations and linearity transitions from nonlinear dynamics of electrochemical states to linear Quantum-like dynamics in any solvable group of Quantum uncertainities calculated from pure electron states from angiotensin I transformations after the removal of two amino acids at the C-terminal by Angiotensin Converting Enzyme in the position 5 that varies in different species dynamic graph translations (Ic3a),(Ic3c) and finally showing that the Hypergeometric function newly added to improve Quantum Turing Machine is powerful. [45–192] More speculatively, these Quantum Turing Machines that are equivalent to Bernstein & Vazirani's Quantum implemented Turing Machine Learning Algorithms with yielding advantages in sample complexity including smaller, polynomial ones and may translate the same Homeopathic Signals into meaningful drug designing empirical advantages in the near future. [48–192] This also immediately means that Quantum Turing Machines themselves are powerful. Since these Kuperberg's subexponential Quantum Algorithms cannot know configurations of a Quantum Turing Machine without an observation, we can neither know when the machine stops nor get results explicitly [1–192] for solving Hidden Geometric Translations (Ic3a),(Ic3c) during these protein-ligand interaction energies and charge transfer processes in any abelian group. This led us to the generalizations of Genetic to Chemical Proteomic based Graph Translations (Ics.3a,3b,3c,3d,3e,3f.3g.3h,3i,3j) for Hidden Druggable Pharmacophoric Subgroups and Small Molecule Triangularizations (Ic2e,f,g,h,g,k,l,m,o,p,q,r), (Diagramm1, Diagramm2, Diagramm3), (Maths1-19), and (Figures S(1- 133)), ((Iconics1-4), (Eqs1-400), Supplementary Material METHODS

 doi:10.20944/preprints202403.0518.v1

AND MATERIALS (1), (2)). These detections may play an important role in mimicking the immune responses of the very first living systems from the inanimate matter of which they are constituted. [20–97,108–192] To solve this problem, I have introduced Groupoids of Hypergeometric Quantum Turing machines, which are Quantum Turing Machines with an additional function showing that the power of these Hypergeometric Quantum Turing Machines, I have presented in a polynomial time the fact that these LaguerreL and WhittakerM algorithm solves the validity and the satisfiability of these chemical geometry problems. [30–69,111–192] This theoretical study for the generation of new small molecules of negative docking energies will tremendously speed up entanglement state successful applications for open Quantum Systems Models offering unprecedented structural and reactivity information for more on-going structure-based drug design efforts against SARS-CoV-2 main protease and the family of AT1R receptors. [10–72,104–192] It should be noted that from the formal point of view, these developed equations ((Eqs1-400), Supplementary Material METHODS AND MATERIALS (1), (2)),and (Eqs.325-400) in a spheroid might well be translated into the consciousness of the homeopathy practitioner and the patient which likewise plays another important role, not, as yet, in detail analyzed as one of the key features of quantum processes such as Quantum Homeopathy, which are a kind of sophisticated modern magic based on a generalized version of entanglement. [10–88,97–192] Thus it is likely that a closer look at the world and a thorough reconstruction to other situations along the lines suggested here, would reveal other exemplifications of generalized entanglement according to Car−Parrinello or Born−Oppenheimer molecular dynamics approaches that could effectively use QM to study Quantum Homeopathy Phenomenon covering longer time scales and addressing this short time scale sampling issue obtained by the event horizon's surface area, black-hole density ∂(Tr[ψ,{2}] DensityMatrix)/∂log$^{\varrho}$(ψ) A log(B$^{\varrho\,A}$) ${}_2F_1$ (P Ω r,P δ;ψ o;γ)

$P_{-1+i\,2^{-1-x}\,E^{-i\,c}}$ (x)==∂(DensityMatrix Tr[ψ,{2}])/∂-A ($\sum_{k=1}^{\infty} \frac{(-1)^k \left(-1+B^{A\,\varrho}\right)^k}{k}$) (- $\sum_{k=1}^{\infty} \frac{(-1)^k\,(-1+\psi)^k}{k}$)$^{\varrho}$

$\sum_{k_1=0}^{-1+i\,2^{-1-x}\,E^{-i\,c}} \sum_{k_2=0}^{\infty} \left((-1)^{k_1}\,2^{-1-k_1}\left((1-x)^{k_1}-e^{-2^{-1-x}\,E^{-i\,c}\,\pi}\,(1+x)^{k_1}\right)\gamma^{k_2}\left(-1+i\,2^{-1-x}\,E^{-i\,c}+k_1\right)!\,(P\,\delta)_{k_2}\,(P\,r\,\Omega)_{k_2}\right) \Big/ \left(\left(-1+i\,2^{-1-x}\,E^{-i\,c}-k_1\right)!\,(k_1!)^2\,k_2!\,(o\,\psi)_{k_2}\right)$

for (I 2^-1-x E^-I c∈ and -1+I 2^-1-x E^-I c>=0 and \[LeftBracketingBar]-1+B^A ϱ\[RightBracketingBar]<1 and \[LeftBracketingBar]γ\[RightBracketingBar]<1 and \[LeftBracketingBar]-1+ψ\[RightBracketingBar]<1)-(LegendreP[-1 + I 2^(-1 - x) (E^(-I c) - E^(I c)) (I (E^(-I ω) - E^(I ω)))^x G h^ν n Pi Q δ μ σ, x] /(1 + I (E^(-I ω) - E^(I ω)) G h^ν n Pi Q δ μ σ)) + LegendreP[1 + I/2 (E^(-I ω) - E^(I ω)) G h^ν n Pi Q δ μ σ, x] /(1 + I (E^(-I ω) - E^(I ω)) G h^ν n Pi Q δ μ σ) entropy, surface gravity, and Hawking radiation derived solutions and by the mass function spin parameter. [10–192] In this paper we show that the use of standard power near to Avogadro's Number of Hypergeometric Quantum Series makes it easy to establish their convergence, to determine the eigenvalues of boundary value problems which are completely reliable with high accuracy, and to study the behavior of angular and radial spheroidal functions Ln(0)+E^x $x^{-1-2.65886\times10^{-7}\,i}$ (((1.5881205171448733*10^-7+1.329431612258721*10^-7 I) n)/((1-n)/2)!-1.5881205171448733*10^-7+1.329431612258721*10^-7 I/((1-n)/2)!) 1/Γ((1-n)/2) 1.00000000000000 $x^{-1-2.65886\times10^{-7}\,i}$ (1.0000000000000000 $x^{1+2.65886\times10^{-7}\,i}$ Ln(0) Γ((1-n)/2)-(3.176241034289747*10^-7+2.658863224517441*10^-7 I) E^x)Ln(0)+ $x^{-1-2.65886\times10^{-7}\,i}$ (-(3.1762410342897466*10^-7+2.658863224517441*10^-7 I/Γ((1-n)/2))-((3.1762410342897466*10^-7+2.658863224517441*10^-7 I) x)/Γ((1-n)/2)-((1.5881205171448733*10^-7+1.329431612258721*10^-7 I) x^2)/Γ((1-n)/2)-((5.2937350571495777*10^-8+4.431438707529068*10^-8 I) x^3)/Γ((1-n)/2)-((1.3234337642873944*10^-8+1.107859676882267*10^-8 I) x^4)/Γ((1-n)/2)-((2.6468675285747888*10^-9+2.215719353764534*10^-9 I) x^5)/Γ((1-n)/2)+O(x^6))0.886227 2^n (1 + a + b + n)

Cos[(n Pi)/2] (∂/(∂ x)) (Ln(0)-1/Γ((1-n)/2) (3.1762410342897466*10^-7+2.658863224517441*10^-7 I) E^x $x^{-1-2.65886\times10^{-7}\,i}$)==1/Γ(1-n/2) E^x $x^{-3-2.65886\times10^{-7}\,i}$ ((3.17624*10^-7+2.65886*10^-7 I) x-(3.17624*10^-7+2.65886*10^-7 I) x^2)\[Integral](-1/Γ((1-n)/2) (3.1762410342897466*10^-7+2.658863224517441*10^-7 I) E^x $x^{-1-2.65886\times10^{-7}\,i}$+Ln(0))∘x==x Ln(0)-1/Γ(0.5 - 0.5 n) (3.17624*10^-7+2.65886*10^-7 I) $(-x)^{1+2.65886\times10^{-7}\,i}$ $x^{-1-2.65886\times10^{-7}\,i}$ Γ(-2.65886*10^-7 I,-x) Ln(0)-1/Γ((1-n)/2) (3.1762410342897466*10^-7+2.658863224517441*10^-7 I) E^x $x^{-1-2.65886\times10^{-7}\,i}$ + constant LaguerreL[n, 0] + E^x x^(-1. - 2.658864199457518*^-7 I) ((-3.1762410342897466*^-7 - 2.658863224517441*^-7 I)/Gamma[(1 - n)/2] - (3.1762416380796776*^-7 + 2.658866602594961*^-7 I)/(x Gamma[(1 - n)/2]) - (6.35248387994805*^-7 + 5.3177365832696*^-7 I)/(x^2 Gamma[(1 - n)/2]) - (1.9057452847420241*^-6 + 1.5953216505970417*^-6 I)/(x^3 Gamma[(1 - n)/2]) - (7.622981501240658*^-6 + 6.381288629237114*^-6 I)/(x^4 Gamma[(1 - n)/2]) - (0.0000381149 + 0.0000319065 I)/(x^5 Gamma[(1 - n)/2]) + O[x] ^(-6)) + x^(3.1762412078251145*^-7 + 2.658864199457518*^-7 I) ((0.999999 + 1.1513185218150448*^-6 I)/Gamma[(1 - n)/2] - (3.018927968175725*^-14 + 1.6890380539359235*^-13 I)/(x Gamma[(1 - n)/2]) + (1.5094675143617883*^-14 + 8.445184100719948*^-14 I)/(x^2 Gamma[(1 - n)/2]) - (2.0126257071705563*^-14 + 1.1260241355971975*^-13 I)/(x^3 Gamma[(1 - n)/2]) + (4.528411373163471*^-14 + 2.533553688345596*^-13 I)/(x^4 Gamma[(1 - n)/2]) - (1.4490924870990355*^-13 + 8.107370322510626*^-13 I)/(x^5 Gamma[(1 - n)/2]) + O[x] ^(-6)) in the relevant coordinate regions considered the lack of a theory and for want of concrete predictions we have not seen so far. But this is not surprising, since we normally see only what we are expecting or are prepared to see as a magic example in this paper where the low-lying energy levels of a deep spheroidal quantized structure are calculated (Ic2e,f,g,h,g,k,l,m,o,p,q,r). The well-known results for these cylindrical and spherical chemical structures are shown to be reproduced in the limits a/b > 1, respectively.→> 1, and a/b proving the applicability of these Theoretical Quantum Homoeopathy Models and their recent advances in science and semantics [11–193]. In the viewpoint of this quantum mechanical paradoxon paper, in vitro biological experiments and chemical-gene interactions are considered as Open Information Inputs in these Functions for Quantum Entropy Negativity Systems interacting with the SARS-CoV-2 biological information environments. [10–190] In conclusion, it is the same operator {{∂2(R($\sqrt{|G\,M\,x|}$ ^6 (R z) (π μ ν) (b^2 r) $e^{i\,\pi\left((e\,n)/2-\left(4\,\pi\,r\,R^2\right)/k\right)}$ (g γ)^(-1/2 (E n)))^m r)/(∂M ∂r)==3 b^2 $e^{i\,\pi\left((e\,n)/2-\left(4\,\pi\,r\,R^2\right)/k\right)}$ G^2 (m-1) m M π r^2 R x^2 z (g γ)^(-(E n)/2) μ ν \[LeftBracketingBar]G M x\[RightBracketingBar] (b^2 $e^{i\,\pi\left((e\,n)/2-\left(4\,\pi\,r\,R^2\right)/k\right)}$ π R z (g γ)^(-(E n)/2) μ ν \[LeftBracketingBar]G M x\[RightBracketingBar]^3-(4 I b^2 $e^{i\,\pi\left((e\,n)/2-\left(4\,\pi\,r\,R^2\right)/k\right)}$ π^3 r R^3 z (g γ)^(-(E n)/2) μ ν \[LeftBracketingBar]G M x\[RightBracketingBar]^3)/k) R^′(b^2 $e^{i\,\pi\left((e\,n)/2-\left(4\,\pi\,r\,R^2\right)/k\right)}$ π r R z (g γ)^-(E n)/2 μ ν \[LeftBracketingBar]G M x\[RightBracketingBar]^3)^2 R(b^2 $e^{i\,\pi\left((e\,n)/2-\left(4\,\pi\,r\,R^2\right)/k\right)}$ π r R z (g γ)^-(E n)/2 μ ν \[LeftBracketingBar]G M x\[RightBracketingBar]^3)^(m-2)-1/k 12 I b^2 $e^{i\,\pi\left((e\,n)/2-\left(4\,\pi\,r\,R^2\right)/k\right)}$ G^2 m M π^3 r^2 R^3 x^2 z (g γ)^(-(E n)/2) μ ν \[LeftBracketingBar]G M x\[RightBracketingBar] R′(b2 $e^{i\,\pi\left((e\,n)/2-\left(4\,\pi\,r\,R^2\right)/k\right)}$ π r R z (g γ)^(-(E n)/2) μ ν \[LeftBracketingBar]G M x\[RightBracketingBar]^3) R(b^2 $e^{i\,\pi\left((e\,n)/2-\left(4\,\pi\,r\,R^2\right)/k\right)}$ π r R z (g γ)^-(E n)/2 μ ν \[LeftBracketingBar]G M x\[RightBracketingBar]^3)^(m-1)+6 b^2 $e^{i\,\pi\left((e\,n)/2-\left(4\,\pi\,r\,R^2\right)/k\right)}$ G^2 m M π r R x^2 z (g γ)^(-(E n)/2) μ ν \[LeftBracketingBar]G M x\[RightBracketingBar] R′(b2 $e^{i\,\pi\left((e\,n)/2-\left(4\,\pi\,r\,R^2\right)/k\right)}$ π r R z (g γ)^(-(E n)/2) μ ν \[LeftBracketingBar]G M x\[RightBracketingBar]^3) R(b^2 $e^{i\,\pi\left((e\,n)/2-\left(4\,\pi\,r\,R^2\right)/k\right)}$ π r R z (g γ)^-(E n)/2 μ ν \[LeftBracketingBar]G M x\[RightBracketingBar]^3)^(m-1)+3 b^2 $e^{i\,\pi\left((e\,n)/2-\left(4\,\pi\,r\,R^2\right)/k\right)}$ G^2 m M

 doi:10.20944/preprints202403.0518.v1

π r² R x² z (g γ)^(-(E n)/2) μ ν \[LeftBracketingBar]G M x\[RightBracketingBar] (b² $e^{i\pi\left((e\,n)/2-\left(4\,\pi\,r\,R^2\right)/k\right)}$ π R z (g γ)^(-(E n)/2) μ ν \[LeftBracketingBar]G M x\[RightBracketingBar]³-(4 I b² $e^{i\pi\left((e\,n)/2-\left(4\,\pi\,r\,R^2\right)/k\right)}$ π³ r R³ z (g γ)^(-(E n)/2) μ ν \[LeftBracketingBar]G M x\[RightBracketingBar]³)/k) R''(b² $e^{i\pi\left((e\,n)/2-\left(4\,\pi\,r\,R^2\right)/k\right)}$ π r R z (g γ)^(-(E n)/2) μ ν \[LeftBracketingBar]G M x\[RightBracketingBar]³) R(b^2 $e^{i\pi\left((e\,n)/2-\left(4\,\pi\,r\,R^2\right)/k\right)}$ π r R z (g γ)^-(E n)/2 μ ν \[LeftBracketingBar]G M x\[RightBracketingBar]^3)^(m−1)}, {(assuming a real-valued function)}} for L^Δ {1/22 π^2 F Q T_n(x) 2F1(π, 8 θ, c G, e θ) T^(o21 Φ) 2F1(2 log(b Z), μ sin(a), c γ, cos(y)) + 0.248766/log(a), 1/22 π^2 F Q T_n(x) 2F1(π, 8 θ, c G, e θ) T^(o21 Φ) 2F1(2 log(b Z), μ sin(a), c γ, cos(y)) + 2.8, 1/22 π^2 F Q T_n(x) 2F1(π, 8 θ, c G, e θ) T^(o21 Φ) 2F1(2 log(b Z), μ sin(a), c γ, cos(y)) + 3 b1 x _0 F^~_1(;a;z) 2F1(a, b2, c, y)} that could annihilate the wavefunction of a tetrahedron within this Quantum Homeopathy attractive basin and induce uncertainty in the same position states, leading to the definition of qubit states of the genomic structure from the SARS-CoV-2 coronavirus that can cause severe pneumonia and have shed light on its origin and receptor-binding properties required for the generalization of Quantum entropy negativity information as exctracted from the structures of the sphere-like small molecules (Supplementary Material METHODS AND MATERIALS Figures S1-114), ((Iconics1-4), (Eqs1-400), Supplementary Material METHODS AND MATERIALS (1), (2)),and (Supplement Material FUNCTIONS.1 - 28) on the chemical bonding surface targeted inside the same AT1R binding domains. [1–193] Hence, these metalinguistic Quantum Homeopathy links between assertions, which are interpretable as interactions of quantum fieldss, are sent to similar homeopathic connectives between propositions, that correspond to quantum correlations such as quantum superposition and entanglement for generalizing these definitional Quantum Homeopathy functions of Hypergeometric1F1 [a, b, z] HypergeometricU [a, b, z] WhittakerM [k, m, z] ChebyshevT[n, x] GegenbauerC[Q^Cos[f Degree] z LogBarnesG[z], x c^4 (Pi r), ArcSin[r] ^2] LegendreP[σ h^(δ n), Q^D, d^4 r^10 (δ/(G Ψ)) n^8 Ψ, G N g^(1/6^d^7) (Ψ GoldenRatio)] LegendreQ[Log[ζ d] 2 Ψ^C Cos[μ], σ δ ArcSin[q ζ] ^Ψ] LaguerreL[E 2 n - 4 Pi r (R^2/k), x] which also corresponds to the regulator of QFT. In this logical framework, Haag's theorem simply translates the fact that this QML Quantum Homeopathy hypotheses that explains this quantum homeopath folding mechanism and acts as a constraint that brings other contacts into spatial proximity [24–149] contains the QLI, Quantum Negative Entropy as every metalanguage contains the object language. The structures of these Quantum Foam like Roccustyrna_TM and Gissitorviffirna_TM ligands arising in this attractor exploited basin have shown to me that the information hidden in these QFT Metric-Quantum Information Uncertainties in Relation with N 3-branes and in the presence of K 5-branes at each lattice site per-residue binding free energy decompositions seems to be closely related to the information loss paradox in evaporation of black holes. Then these Quantum Legendre and Hypergeometric Functions might be solved (Maths1-21) in this extreme hypothesis proposing a Quantum Homeopathy driven Geometric Translational mechanism (Ics.3a,3b,3c,3d,3e,3f.3g.3h,3i,3j) which would be an ingenious system of using these folding pathways as entangled states where all the pure states within the BH event horizon are maximally entangled to a functional space H0 Δ that contains locally Holomorphic Spheroidal Geometries of SpheroidalPS, SpheroidalS1, SpheroidalEigenvalue functions of Hypergeometric1F1[cos⁴(x Q) $Q^{\cos^4(X\,c)}$ Hypergeometric1F1Regularized[a⁵,∂2(ϱ⁶ n⁷³)/(∂y ∂x) Hypergeometric1F1Regularized[a⁵,∂2((ϱ⁶ n⁴) π r)/(∂y ∂x)]]]==Hypergeometric1F1[1/(16 π²) $Q^{\left(\int_{-i\,\infty+\gamma}^{i\,\infty+\gamma}\frac{4^s\,(c\,X)^{-2\,s}\,\Gamma(s)}{\Gamma\left(\frac{1}{2}-s\right)}\,ds\right)^4/\left(16\,\pi^2\right)}$ Hypergeometric1F1Regularized[a⁵,∂2(n⁷³ ϱ⁶)/(∂y ∂x) Hypergeometric1F1Regularized[a⁵,∂2(n⁴ π r ϱ⁶)/(∂y ∂x)]] ($\int_{-i\,\infty+\gamma}^{i\,\infty+\gamma}\frac{4^s\,(Q\,x)^{-2\,s}\,\Gamma(s)}{\Gamma\left(\frac{1}{2}-s\right)}\,ds$)⁴] for

 doi:10.20944/preprints202403.0518.v1

(0<γ<1/2 and Q x>0 and c X>0)Hypergeometric1F1[cos⁴(x Q) $Q^{\cos^4(X\,c)}$ Hypergeometric1F1Regularized[a⁵,∂2(ϱ⁶ n⁷³)/(∂y ∂x) Hypergeometric1F1Regularized[a⁵,∂2((ϱ⁶ n⁴) π r)/(∂y ∂x)]]]==Hypergeometric1F1[(1/(16 π²)) $Q^{\left(\int_{-i\infty+\gamma}^{i\infty+\gamma} \frac{e^{s-\left(c^2 X^2\right)/(4\,s)}}{\sqrt{s}}\,ds\right)^4/\left(16\,\pi^2\right)}$ Hypergeometric1F1Regularized[a⁵,∂2(n⁷³ ϱ⁶)/(∂y ∂x) Hypergeometric1F1Regularized[a⁵,∂2(n⁴ π r ϱ⁶)/(∂y ∂x)]] ($\int_{-i\infty+\gamma}^{i\infty+\gamma} \frac{e^{s-\left(Q^2\,x^2\right)/(4\,s)}}{\sqrt{s}}\,ds$)⁴] for γ>0 Hypergeometric1F1[Cos[x Q] ^4 Q^Cos[X c] ^4, ArcSin[r] ^2 Sin[b], Log[23 y I] ArcSin[z]] == (E^((Log[23 y I] ArcSin[z])/2) Pi ((-(Log[23 y I] ArcSin[z]))^((ArcSin[r] ^2 Sin[b])/2) Gamma[-(Cos[x Q] ^4 Q^Cos[X c] ^4) + ArcSin[r] ^2 Sin[b]] WhittakerW[Cos[x Q] ^4 Q^Cos[X c] ^4 - (ArcSin[r] ^2 Sin[b])/2, (1 - ArcSin[r] ^2 Sin[b])/2, -(Log[23 y I] ArcSin[z])] + (Log[23 y I] ArcSin[z])^((ArcSin[r] ^2 Sin[b])/2) Gamma[Cos[x Q] ^4 Q^Cos[X c] ^4] WhittakerW[-(Cos[x Q] ^4 Q^Cos[X c] ^4) + (ArcSin[r] ^2 Sin[b])/2, (1 - ArcSin[r] ^2 Sin[b])/2, Log[23 y I] ArcSin[z]]))/(Gamma[Cos[x Q] ^4 Q^Cos[X c] ^4] Gamma[1 - ArcSin[r] ^2 Sin[b]] Gamma[-(Cos[x Q] ^4 Q^Cos[X c] ^4) + ArcSin[r] ^2 Sin[b]] ((-(Log[23 y I] ArcSin[z]))^(ArcSin[r] ^2 Sin[b]) Sin[(Cos[x Q] ^4 Q^Cos[X c] ^4) Pi] - (Log[23 y I] ArcSin[z])^(ArcSin[r] ^2 Sin[b]) Sin[(Cos[x Q] ^4 Q^Cos[X c] ^4 - ArcSin[r] ^2 Sin[b]) Pi]))/ArcSin[r] ^2 Sin[b] ∉ IntegersZ0k,20H0Δr ~ {f (Z0rk)} where Z is the total number of ligand heavy atoms, the vector r⃗ ((Iconics1-4), (Eqs1-400), Supplementary Material METHODS AND MATERIALS (1), (2)),(Supplement Material FUNCTIONS.1-21), and (Cluster of BIOGENEA_ CONSENSUS_Eqs.1-26) corresponds to the Cartesian coordinates of each of the system current/phase of heavy atom in the non-classical entropy information complements, and r⃗{E (y) {1 − Jacobi P [LnAdS5 [H] ⊗̂ [Ho]] Ê ∇̈ ∣xi, H (Supplement Material FUNCTIONS.1-22), and (Cluster of BIOGENEA_ CONSENSUS_Eqs.1-17) center represents the geometric center of our prototype ligands. If I analytically continue wave of functions LegendreP, SphericalBesselJ, and SphericalBesselJ[n,z] ZernikeR[LegendreP[LaguerreL[λ n, D f z, g z (ψ^0 ϱ m), I Exp[λ]], x], m, r] Hypergeometric1F1Regularized[a^5, D[ϱ^6 n^73, y, x] b, g^8, Exp[n] 6, δ σ^2, ε θ^3, Δ α^4] Hypergeometric0F1Regularized[a, z] == Piecewise[{{I^(-m + LegendreP[LaguerreL[n λ, D f z, g m z ϱ, I E^λ], x]) Hypergeometric1F1Regularized[a^5, b D[n^73 ϱ^6, y, x], g^8, 6 Sum[n^k/k!, {k, 0, Infinity}], δ σ^2, ε θ^3, α^4 Δ] Sum[((-1)^Subscript[j, 1] r^(m + 2 Subscript[j, 1]) ((m + LegendreP[LaguerreL[n λ, D f z, g m z ϱ, I E^λ], x])/2 + Subscript[j, 1])! Hypergeometric0F1Regularized[a + Subscript[j, 2], Subscript[z, 0]] (z - Subscript[z, 0])^Subscript[j, 2])/(((-m + LegendreP[LaguerreL[n λ, D f z, g m z ϱ, I E^λ], x] - 2 Subscript[j, 1])/2)! Subscript[j, 1] ! (m + Subscript[j, 1])! Subscript[j, 2] !), {Subscript[j, 1], 0, (-m + LegendreP[LaguerreL[n λ, D f z, g m z ϱ, I E^λ], x])/2}, {Subscript[j, 2], 0, Infinity}], Element[(-m + LegendreP[LaguerreL[n λ, D f z, g m z ϱ, I E^λ], x])/2, Integers] }}] /; Element[LegendreP[LaguerreL[n λ, D f z, g m z ϱ, I E^λ], x], Integers] && LegendreP[LaguerreL[n λ, D f z, g m z ϱ, I E^λ], x] >= 0 && Element[m, Integers] && m >= 0 && LegendreP[LaguerreL[n λ, D f z, g m z ϱ, I E^λ], x] >= m gives the spherical Bessel function of the first kind LegendreQ, then the algebra of these operators can be taken to act on a series of relationships between QFT, QM, Quantum Homeopathy Information, Entangled Space-Time, Euclid Spaced Quantum Gravity, Non-Commutative Geometry, Quantum Metalanguage and Quantum Logic Crypto-Metalanguage, since these topics are closely intertwined. [1–193] Further, the homeopathic mechanism from this symmetry (Ic0a), (Ic0b), (Ic0c), (Ic1a), (Ic1b), (Ic1c), (Ic1d), (Ic2a), (Ic2b), (Ic2c), (Ic3a1), (Ic3a2), (Ic3b1), (Ic3b2), (Ic3c), (Ic3d), (Ic3d), (Ic3e), (Ic3f), (Ic3g), (Ic3h), (Ic3i), (Ic3j), and (Ic3k) into a deep learning work which depends on the value of geometrical data in this rather than classical computational approach could be extended around the types of hard drug designing problems that may be tractable with high-quality data and Turing Machine learning techniques [2–195] for calculating the inner and outer horizon radii, the ergosphere radii, as well as the angular velocity at the event horizon from new chemical structures and black-hole shaped druggable ligands. [10–179,192–195] In this work, we have made a step towards creating ChebyshevT- quantum gravity adS5 Quantum fields theory (QFT) Reductions in multi party Bell pairs for Chern-Simons φD [r2] S [r1]

 doi:10.20944/preprints202403.0518.v1

molecular similarity topologies, Quantum Electrodynamics from Quantized Water Memory and Hormetic Networks, and generalized HyperGeometric Functions to integralize chemical Block Systems based on Black Hole Paradox Generalizations and SphericalHarmonicY-Supersymmetric breaking foundations for Turing Machine Learning Ruled QM methods useful for Calculating Quantum Homeopathy Hidden Entanglement Negativities for the Translation of COVID19 Homeopathy Remedies into the Neprilysin and ACE2/AT1R receptor targeted DRVYIHPFX-holomorphic Roccustyrna and Gissitorviffirna Ligands. This Macro-Entanglement model of quantum homeopathy architecture can suit the input molecular representation from these non-commutative geometry superoperators and Quantum Simulation Eigenvectors as were overlooked in a conventional way as a QG context involving detection of chemical bond reconstruction. The key theoretical idea of this formalism (viz, the nontriviality of the product Ω†Ω := ΘΨ6= I) remained the same but the philosophy has been changed. In place of starting from the knowledge of the physical, selfadjoint h = h † and from the subsequent clever choice of a simplifying map Ω, the updated model-building strategy (cf. [28,–188]) takes a manifestly non-Hermitian "friendly" candidate for the Hamiltonian H = H(F)Ψ^6 ChebyshevT[α μ ν^d, q^b] LegendreP[n δ, (3.6369475516 Θ^0 Ψ^6) 11 (1 Θ^0 (Ψ^60)^24) Q^D, (E^4 n^2 δ θ^10 Ψ)/(G q), g^6^(-d^3) G GoldenRatio (6.02214076 10^23 N) + LaguerreL[I^n λ, (0. + 6.02214076 10^23 I) 2]]. The simplest physical scenario of this form certainly emerges when one decides to use just the diagonal metrics Θ0Ψ6Cos[α μ ν^d ArcCos[q^b]] LegendreP[n δ, 40.006423068 Q^D Ψ^1446, (E^4 n^2 δ θ^10 Ψ)/(G q), 9.744028434716123*^23 g^6^(-d^3) G N + LaguerreL[E^(I/2 n Pi) λ, 0. + 1.204428152*^24 I]]. [21–45,150–195] Moreover, while in the case of a molecular regulator the reduction of QFT to QM is not mathematically explicit, in our case it is, since this ansatz corresponds to the execution of a boson translation that leaves a set of modular parameters tk that must be integrated over a fundamental domain (FD) and parameterizes gauge-inequivalent configurations considering all possible and very specific problems of idealized 2D chemical map symmetries of Roccustyrna's bases pair. In Refs. [30–189] as well as in our present concrete model this "no-smearing" option proved allowed. [40–195] The main theoretical profit provided here by the fully non-numerical tractability of our model may be seen in its manifest compatibility with postulates of Quantum Mechanics in which one works, simultaneously [2–192], with a triplet of Hilbert-space representations H(P,F,S) of the quantum system in question. The Hermiticity status of the operators used depends on the Euclid space but they only stay non-Hermitian in the "naive" and "false" space H(F). Thus, in our model, the knowledge of the friendly input matrix H 6= H† is complemented by the equally friendly nature of the ad hoc metric Θ = Θ(S) 6= I and, ipso facto, of the reconstructed standard Hilbert space H(S). In practical terms our Gegenbauerian example exhibits several specific friendly features. First of all, it is nontrivial that our metrics are banded. [2–161–195] Indeed, if even small polynomial Quantum Homeopathic Reductions can be demonstrated for chemicallized data types common in biological, chemical and clinical research, they may find important applications where examples are rare (e.g., due to disease incidence) or sample acquisition is expensive, invasive, or difficult. This property only followed from the explicit solution of the Dieudonn´e's equation. [2–170,172–195] Secondly, the matrix elements of the pseudo-metrics (i.e., of the sparse-matrix components Pj of the metrics) emerged as elementary functions of the free real parameter a. [2–180,180–195] This shows how the unitarily inequivalent representations of QFT are reduced to a single class of unitarily equivalent representations of QM for every level k∈ H4 (BG, ℤ) that yields the Quantum fields theory with those levels k that satisfy the following positivity condition in the BV formalism which consists of B∈dz ∧ r. To make this theory simulated, I replaced the scalar field Φ (x→{E (y) {1 − Jacobi P ChebyshevT[α μ ν^d, q^b] (LegendreP[n δ, 40.006423068 Q^D Ψ^1446, 0, 9.744028434716123*^23 g^6^(-d^3) G N + LaguerreL[I^n λ, 0. + 1.204428152*^24 I]] + (E^4 n^2 δ θ^10 Ψ Derivative[0,0,1,0] [LegendreP] [n δ, 40.006423068 Q^D Ψ^1446, 0, 9.744028434716123*^23 g^6^(-d^3) G N + LaguerreL[I^n λ, 0. + 1.204428152*^24 I]])/(G q) + (E^8 n^4 δ^2 θ^20 Ψ^2 Derivative[0, 0, 2, 0] [LegendreP] [n δ, 40.006423068 Q^D Ψ^1446, 0, 9.744028434716123*^23 g^6^(-d^3) G N + LaguerreL[I^n λ, 0. + 1.204428152*^24 I]])/(2 G^2 q^2) + (E^12 n^6 δ^3 θ^30 Ψ^3 Derivative[0, 0, 3, 0] [LegendreP] [n δ, 40.006423068 Q^D Ψ^1446, 0, 9.744028434716123*^23 g^6^(-d^3) G N + LaguerreL[I^n λ, 0. + 1.204428152*^24 I]])/(6 G^3 q^3) +

 doi:10.20944/preprints202403.0518.v1

(E^16 n^8 δ^4 θ^40 Ψ^4 Derivative[0, 0, 4, 0] [LegendreP] [n δ, 40.006423068 Q^D Ψ^1446, 0, 9.744028434716123*^23 g^6^(-d^3) G N + LaguerreL[I^n λ, 0. + 1.204428152*^24 I]])/(24 G^4 q^4) + (E^20 n^10 δ^5 θ^50 Ψ^5 Derivative[0, 0, 5, 0] [LegendreP] [n δ, 40.006423068 Q^D Ψ^1446, 0, 9.744028434716123*^23 g^6^(-d^3) G N + LaguerreL[I^n λ, 0. + 1.204428152*^24 I]])/(120 G^5 q^5) + O[q] ^(-6)) [LnAdS5 [H] ⊗̂ [Ho]] at each snapshot performed as single feature points with respect to all hash table atomic bases and electron pairs identified in the Roccustyrna_TM, Gissitorviffirna_TM, and the [amino ({4 - [(2R,3R) - 2 - [(2S) - 3 - { [(1S,2S) - 1 - { [(S) - 1,3 - dihydroisoindole - 2 - carbonyl [(2 - methyl - 6 - oxo - 1,7 - dihydropurin - 8 - yl) methyl] phosphanyl] carbamoyl} - 2 - methylbutyl] a mino} - 2 - methylpropyl] oxaziridin - 3 - yl] butyl}amino) methylidene] azanium DRVYIHPF-mimetic ligand complexes when the average binding energy for each residue is calculated including the explicitly functions torsion of SphericalHarmonicY[l, m, θ, ϕ] GegenbauerC[α μ ν^d, q^b] LegendreP[δ n, Q^D, E^4 θ^10 (δ/(G q)) n^2 Ψ, G N g^(1/6^d^3) (ψ GoldenRatio)] LegendreQ[Log[ζ] Cos[μ], σ δ ArcSin[q ζ] ^g] LaguerreL[E, x] GegenbauerC[f'[ψ] r, r^16 - ψ^Cos[a] ^24, f[ψ]] LaguerreL[Hypergeometric0F1[a, z], x] Hypergeometric0F1[m, Log[r]] Hypergeometric2F1Regularized[a^d3 z, b^d4 x, c^d5 y, Sin[m] r z] GegenbauerC[f'[ψ] r, r^16 - ψ^Cos[a] ^24, f[ψ]] LaguerreL[Det[Exp[-(ϑ^2 (δ k))/2] HypergeometricPFQRegularized[{a1, a p}, {b1, b q}, z]] {{R c Sin[a], Sin[b], Sin[E c] }, {d3, Cos[x E], f3}, {Sin[x], I Sinh[x], Sin[j] }}, ChebyshevU[n, x]] ZernikeR[LegendreP[LaguerreL [ArcSin[λ n], D f z, g z (ψ^0 ϱ m), I Exp[λ]], x], m, r] Hypergeometric1F1Regularized[a^5, D[ϱ^6 n^73, y, x] b, g^8, Exp[n] ^Þ^6, δ σ^2, ε θ^3, Δ α^4] Hypergeometric0F1Regularized[a, z] Δθˆ,1 − a/2 (g) ˆ2cos2ˆθ − bˆ2r C (Rz (π), QFT [H] ⊗̂ [Ho] ∯IMG) μνi),2 CZC ⊗ θZgˆ2r sin2ˆθλ e Zˆ B, Z˙EQFTG⌈y7 χ, y, T, QFTG⌈XI, N, T-M↓ ⊗ ∯∯∯⌈⌀iΨ⃛ ⊕, QFTq. Ÿ ⊕ G⌈xi, HvH QFTq. Ÿ ⊕ G⌈xi, Ho (AdS)}/2o [H] ~ CT˙S. I/Z. B ✷QuantumDistance [AdsQFTˆC, (Rz (π), QFT [H] for ∂(Tr[ψ,{2}] DensityMatrix)/∂log$^{\varrho}$(ψ) A log((B^{G} sin(ω) h$^{\nu}$ (n π Q δ μ σ)) ϱ A) logG(z) c^{8} π^{2} r^{2} δ^{2} θ^{20}==c^{8} π^{2} r^{2} δ^{2} θ^{20} ∂(DensityMatrix Tr[ψ,{2}])/(∂A log$^{\varrho}$(ψ) log(A h$^{\nu}$ n π Q B^{G} δ μ ϱ σ ω ($\sum_{k=\nu}^{\infty}(-1)^{k-\nu}\binom{2k}{k-\nu}\binom{1+k-\nu-\frac{\omega}{\pi\mathcal{A}}}{1+2k}$ - $\sum_{k=-1+\nu}^{\infty}(-1)^{k-\nu}\binom{2k}{1+k-\nu}\binom{k+\nu+\frac{\omega}{\pi\mathcal{A}}}{1+2k}$))) logG(z) for ν∈ for the ZernikeR[Hypergeometric2F1Regularized[-LaguerreL[I^n λ, (0. + 6.02214076*^23 I) F m o q Q T ϱ ψ, I E^λ], 1 + LaguerreL[I^n λ, (0. + 6.02214076*^23 I) F m o q Q T ϱ ψ, I E^λ], 1, 1/2], (F m Q T^δ θ^10 ψ Ψ Log[y] ^2)/(10000000000000000000000000000 E^((N Pi)/2)), r] + (x Hypergeometric2F1Regularized[1 - LaguerreL[I^n λ, (0. + 6.02214076*^23 I) F m o q Q T ϱ ψ, I E^λ], 2 + LaguerreL[I^n λ, (0. + 6.02214076*^23 I) F m o q Q T ϱ ψ, I E^λ], 2, 1/2] LaguerreL[I^n λ, (0. + 6.02214076*^23 I) F m o q Q T ϱ ψ, I E^λ] (1 + LaguerreL[I^n λ, (0. + 6.02214076*^23 I) F m o q Q T ϱ ψ, I E^λ]) Derivative[1, 0, 0] [ZernikeR] [Hypergeometric2F1Regularized[-LaguerreL[I^n λ, (0. + 6.02214076*^23 I) F m o q Q T ϱ ψ, I E^λ], 1 + LaguerreL[I^n λ, (0. + 6.02214076*^23 I) F m o q Q T ϱ ψ, I E^λ], 1, 1/2], (F m Q T^δ θ^10 ψ Ψ Log[y] ^2)/(10000000000000000000000000000 E^((N Pi)/2)), r])/2 + (x^2 LaguerreL[I^n λ, (0. + 6.02214076*^23 I) F m o q Q T ϱ ψ, I E^λ] (1 + LaguerreL[I^n λ, (0. + 6.02214076*^23 I) F m o q Q T ϱ ψ, I E^λ]) (Hypergeometric2F1 Regularized[2 - LaguerreL[I^n λ, (0. + 6.02214076*^23 I) F m o q Q T ϱ ψ, I E^λ], 3 + LaguerreL[I^n λ, (0. + 6.02214076*^23 I) F m o q Q T ϱ ψ, I E^λ], 3, 1/2] (-1 + LaguerreL[I^n λ, (0. + 6.02214076*^23 I) F m o q Q T ϱ ψ, I E^λ]) (2 + LaguerreL[I^n λ, (0. + 6.02214076*^23 I) F m o q Q T ϱ ψ, I E^λ]) Derivative[1, 0, 0] [ZernikeR] [Hypergeometric2F1Regularized[-LaguerreL[I^n λ, (0. + 6.02214076*^23 I) F m o q Q T ϱ ψ, I E^λ], 1 + LaguerreL[I^n λ, (0. + 6.02214076*^23 I) F m o q Q T ϱ ψ, I E^λ], 1, 1/2], (F m Q T^δ θ^10 ψ Ψ Log[y] ^2)/(10000000000000000000000000000 E^((N Pi)/2)), r] + Hypergeometric2F1Regularized[1 - LaguerreL[I^n λ, (0. + 6.02214076*^23 I) F m o q Q T ϱ ψ, I E^λ], 2 + LaguerreL[I^n λ, (0. + 6.02214076*^23 I) F m o q Q T ϱ ψ, I E^λ], 2, 1/2] ^2 LaguerreL[I^n λ, (0. + 6.02214076*^23 I) F m o q Q T ϱ ψ, I E^λ] (1 + LaguerreL[I^n λ, (0. + 6.02214076*^23 I) F m o q Q T ϱ ψ, I E^λ]) Derivative[2, 0, 0] [ZernikeR] [Hypergeometric2F1Regularized[-LaguerreL[I^n λ, (0. + 6.02214076*^23 I) F m o q Q T ϱ ψ, I E^λ], 1 + LaguerreL[I^n λ, (0. + 6.02214076*^23 I) F m o q Q T ϱ ψ, I E^λ], 1, 1/2], (F m Q T^δ θ^10 ψ Ψ Log[y] ^2)/(10000000000000000000000000000 E^((N Pi)/2)), r]))/8 + (x^3 LaguerreL[I^n λ, (0. + 6.02214076*^23 I) F m o q Q T ϱ ψ, I E^λ] (1 + LaguerreL[I^n λ, (0. + 6.02214076*^23 I) F m o q Q T ϱ ψ, I E^λ]) (Hypergeometric2F1Regularized[3 - LaguerreL[I^n λ, (0. + 6.02214076*^23 I) F m o q Q T ϱ

 doi:10.20944/preprints202403.0518.v1

ψ, I E^λ], 4 + LaguerreL[I^n λ, (0. + 6.02214076*^23 I) F m o q Q T ϱ ψ, I E^λ], 4, 1/2] (-2 + LaguerreL[I^n λ, (0. + 6.02214076*^23 I) F m o q Q T ϱ ψ, I E^λ]) (-1 + LaguerreL[I^n λ, (0. + 6.02214076*^23 I) F m o q Q T ϱ ψ, I E^λ]) (2 + LaguerreL[I^n λ, (0. + 6.02214076*^23 I) F m o q Q T ϱ ψ, I E^λ]) (3 + LaguerreL[I^n λ, (0. + 6.02214076*^23 I) F m o q Q T ϱ ψ, I E^λ]) Derivative[1, 0, 0] [ZernikeR] [Hypergeometric2F1Regularized[-LaguerreL[I^n λ, (0. + 6.02214076*^23 I) F m o q Q T ϱ ψ, I E^λ], 1 + LaguerreL[I^n λ, (0. + 6.02214076*^23 I) F m o q Q T ϱ ψ, I E^λ], 1, 1/2], (F m Q T^δ θ^10 ψ Ψ Log[y] ^2)/(10000000000000000000000000000 E^((N Pi)/2)), r] + 3 Hypergeometric2F1Regularized[1 - LaguerreL[I^n λ, (0. + 6.02214076*^23 I) F m o q Q T ϱ ψ, I E^λ], 2 + LaguerreL[I^n λ, (0. + 6.02214076*^23 I) F m o q Q T ϱ ψ, I E^λ], 2, 1/2] Hypergeometric2F1Regularized[2 - LaguerreL[I^n λ, (0. + 6.02214076*^23 I) F m o q Q T ϱ ψ, I E^λ], 3 + LaguerreL[I^n λ, (0. + 6.02214076*^23 I) F m o q Q T ϱ ψ, I E^λ], 3, 1/2] (-1 + LaguerreL[I^n λ, (0. + 6.02214076*^23 I) F m o q Q T ϱ ψ, I E^λ]) LaguerreL[I^n λ, (0. + 6.02214076*^23 I) F m o q Q T ϱ ψ, I E^λ] (1 + LaguerreL[I^n λ, (0. + 6.02214076*^23 I) F m o q Q T ϱ ψ, I E^λ]) (2 + LaguerreL[I^n λ, (0. + 6.02214076*^23 I) F m o q Q T ϱ ψ, I E^λ]) Derivative[2, 0, 0] [ZernikeR] [Hypergeometric2F1Regularized[-LaguerreL[I^n λ, (0. + 6.02214076*^23 I) F m o q Q T ϱ ψ, I E^λ], 1 + LaguerreL[I^n λ, (0. + 6.02214076*^23 I) F m o q Q T ϱ ψ, I E^λ], 1, 1/2], (F m Q T^δ θ^10 ψ Ψ Log[y] ^2)/(10000000000000000000000000000 E^((N Pi)/2)), r] + Hypergeometric2F1Regularized[1 - LaguerreL[I^n λ, (0. + 6.02214076*^23 I) F m o q Q T ϱ ψ, I E^λ], 2 + LaguerreL[I^n λ, (0. + 6.02214076*^23 I) F m o q Q T ϱ ψ, I E^λ], 2, 1/2] ^3 LaguerreL[I^n λ, (0. + 6.02214076*^23 I) F m o q Q T ϱ ψ, I E^λ] ^2 (1 + LaguerreL[I^n λ, (0. + 6.02214076*^23 I) F m o q Q T ϱ ψ, I E^λ])^2 Derivative[3, 0, 0] [ZernikeR] [Hypergeometric2F1Regularized[-LaguerreL[I^n λ, (0. + 6.02214076*^23 I) F m o q Q T ϱ ψ, I E^λ], 1 + LaguerreL[I^n λ, (0. + 6.02214076*^23 I) F m o q Q T ϱ ψ, I E^λ], 1, 1/2], (F m Q T^δ θ^10 ψ Ψ Log[y] ^2)/(10000000000000000000000000000 E^((N Pi)/2)), r]))/48 + (x^4 LaguerreL[I^n λ, (0. + 6.02214076*^23 I) F m o q Q T ϱ ψ, I E^λ] (1 + LaguerreL[I^n λ, (0. + 6.02214076*^23 I) F m o q Q T ϱ ψ, I E^λ]) (Hypergeometric2F1Regularized[4 - LaguerreL[I^n λ, (0. + 6.02214076*^23 I) F m o q Q T ϱ ψ, I E^λ], 5 + LaguerreL[I^n λ, (0. + 6.02214076*^23 I) F m o q Q T ϱ ψ, I E^λ], 5, 1/2] (-3 + LaguerreL[I^n λ, (0. + 6.02214076*^23 I) F m o q Q T ϱ ψ, I E^λ]) (-2 + LaguerreL[I^n λ, (0. + 6.02214076*^23 I) F m o q Q T ϱ ψ, I E^λ]) (-1 + LaguerreL[I^n λ, (0. + 6.02214076*^23 I) F m o q Q T ϱ ψ, I E^λ]) (2 + LaguerreL[I^n λ, (0. + 6.02214076*^23 I) F m o q Q T ϱ ψ, I E^λ]) (3 + LaguerreL[I^n λ, (0. + 6.02214076*^23 I) F m o q Q T ϱ ψ, I E^λ]) (4 + LaguerreL[I^n λ, (0. + 6.02214076*^23 I) F m o q Q T ϱ ψ, I E^λ]) Derivative[1, 0, 0] [ZernikeR] [Hypergeometric2F1Regularized[-LaguerreL[I^n λ, (0. + 6.02214076*^23 I) F m o q Q T ϱ ψ, I E^λ], 1 + LaguerreL[I^n λ, (0. + 6.02214076*^23 I) F m o q Q T ϱ ψ, I E^λ], 1, 1/2], (F m Q T^δ θ^10 ψ Ψ Log[y] ^2)/(10000000000000000000000000000 E^((N Pi)/2)), r] + (-1 + LaguerreL[I^n λ, (0. + 6.02214076*^23 I) F m o q Q T ϱ ψ, I E^λ]) LaguerreL[I^n λ, (0. + 6.02214076*^23 I) F m o q Q T ϱ ψ, I E^λ] (1 + LaguerreL[I^n λ, (0. + 6.02214076*^23 I) F m o q Q T ϱ ψ, I E^λ]) (2 + LaguerreL[I^n λ, (0. + 6.02214076*^23 I) F m o q Q T ϱ ψ, I E^λ]) (3 Hypergeometric2F1Regularized[2 - LaguerreL[I^n λ, (0. + 6.02214076*^23 I) F m o q Q T ϱ ψ, I E^λ], 3 + LaguerreL[I^n λ, (0. + 6.02214076*^23 I) F m o q Q T ϱ ψ, I E^λ], 3, 1/2] ^2 (-1 + LaguerreL[I^n λ, (0. + 6.02214076*^23 I) F m o q Q T ϱ ψ, I E^λ]) (2 + LaguerreL[I^n λ, (0. + 6.02214076*^23 I) F m o q Q T ϱ ψ, I E^λ]) + 4 Hypergeometric2F1Regularized[1 - LaguerreL[I^n λ, (0. + 6.02214076*^23 I) F m o q Q T ϱ ψ, I E^λ], 2 + LaguerreL[I^n λ, (0. + 6.02214076*^23 I) F m o q Q T ϱ ψ, I E^λ], 2, 1/2] Hypergeometric2F1Regularized[3 - LaguerreL[I^n λ, (0. + 6.02214076*^23 I) F m o q Q T ϱ ψ, I E^λ], 4 + LaguerreL[I^n λ, (0. + 6.02214076*^23 I) F m o q Q T ϱ ψ, I E^λ], 4, 1/2] (-2 + LaguerreL[I^n λ, (0. + 6.02214076*^23 I) F m o q Q T ϱ ψ, I E^λ]) (3 + LaguerreL[I^n λ, (0. + 6.02214076*^23 I) F m o q Q T ϱ ψ, I E^λ])) Derivative[2, 0, 0] [ZernikeR] [Hypergeometric2F1Regularized[-LaguerreL[I^n λ, (0. + 6.02214076*^23 I) F m o q Q T ϱ ψ, I E^λ], 1 + LaguerreL[I^n λ, (0. + 6.02214076*^23 I) F m o q Q T ϱ ψ, I E^λ], 1, 1/2], (F m Q T^δ θ^10 ψ Ψ Log[y] ^2)/(10000000000000000000000000000 E^((N Pi)/2)), r] + 6 Hypergeometric2F1Regularized[1 - LaguerreL[I^n λ, (0. + 6.02214076*^23 I) F m o q Q T ϱ ψ, I E^λ], 2 + LaguerreL[I^n λ, (0. + 6.02214076*^23 I) F m o q Q T ϱ ψ, I E^λ], 2, 1/2] ^2 Hypergeometric2F1Regularized[2 - LaguerreL[I^n λ, (0. + 6.02214076*^23 I) F m o q Q T ϱ ψ, I E^λ], 3 + LaguerreL[I^n λ, (0. + 6.02214076*^23 I) F m o q Q T ϱ ψ, I E^λ], 3, 1/2] (-1 + LaguerreL[I^n λ, (0. + 6.02214076*^23 I) F m o q Q T ϱ ψ, I E^λ]) LaguerreL[I^n λ, (0. + 6.02214076*^23 I) F m o q Q T ϱ ψ, I E^λ] ^2 (1 + LaguerreL[I^n λ, (0. +

6.02214076*^23 I) F m o q Q T ϱ ψ, I E^λ])^2 (2 + LaguerreL[I^n λ, (0. + 6.02214076*^23 I) F m o q Q T ϱ ψ, I E^λ]) Derivative[3, 0, 0] [ZernikeR] [Hypergeometric2F1Regularized[-LaguerreL[I^n λ, (0. + 6.02214076*^23 I) F m o q Q T ϱ ψ, I E^λ], 1 + LaguerreL[I^n λ, (0. + 6.02214076*^23 I) F m o q Q T ϱ ψ, I E^λ], 1, 1/2], (F m Q T^δ θ^10 ψ Ψ Log[y] ^2)/(10000000000000000000000000000 E^((N Pi)/2)), r] + Hypergeometric2F1Regularized[1 - LaguerreL[I^n λ, (0. + 6.02214076*^23 I) F m o q Q T ϱ ψ, I E^λ], 2 + LaguerreL[I^n λ, (0. + 6.02214076*^23 I) F m o q Q T ϱ ψ, I E^λ], 2, 1/2] ^4 LaguerreL[I^n λ, (0. + 6.02214076*^23 I) F m o q Q T ϱ ψ, I E^λ] ^3 (1 + LaguerreL[I^n λ, (0. + 6.02214076*^23 I) F m o q Q T ϱ ψ, I E^λ])^3 Derivative[4, 0, 0] [ZernikeR] [Hypergeometric2F1Regularized[-LaguerreL[I^n λ, (0. + 6.02214076*^23 I) F m o q Q T ϱ ψ, I E^λ], 1 + LaguerreL[I^n λ, (0. + 6.02214076*^23 I) F m o q Q T ϱ ψ, I E^λ], 1, 1/2], (F m Q T^δ θ^10 ψ Ψ Log[y] ^2)/(10000000000000000000000000000 E^((N Pi)/2)), r]))/384 + O[x] ^5 $L_{i^n\lambda}^{\left(0+6.02214076\times10^{23}\,i\right)F\,m\,o\,q\,Q\,T\,\rho\,\psi}\left(i\,e^{\lambda}\right)$ hᵛ ʳ ψ cos(γ) (b j+x)*1/P r ψ $\cos^{c^4\,G\,M^2\,\pi\,r\,R\,S^{10}\,x\,\delta\,\theta^4}$(γ) Hypergeometric1F1Regularized[a⁵,∂2(ϱ⁶ n⁴ (π r))/(∂y ∂x)]1/P r ψ² (b j+x) hᵛ ʳ Hypergeometric1F1Regularized[a⁵,0] $\cos^{\pi\,c^4\,\delta\,G\,\theta^4\,M^2\,r\,R\,S^{10}\,x+1}$(γ) $L_{i^n\lambda}^{\left(6.02214\times10^{23}\,i\right)F\,m\,o\,q\,Q\,T\,\rho\,\psi}\left(i\,e^{\lambda}\right)$ by a discrete variable with a finite number N of mutually orthogonal eigenstates. [23–193] Last but not least, the matrix elements of the diagonal, tridiagonal and pentadiagonal metrics exhibited even an almost complete independence of the truncation N without a significant cost in the acquisition of data contrasts with typical hardware measures of time and space resources, such as docking runs, cycles, gates, qubits and queries, which are often (or expected to be) very cheap due to their high frequency and scalability. [39–89,95–195] Indeed, where a quadratic reduction in the number of function queries (e.g., from n1to n√ω) may lead to only millisecond differences in compute time, a similar reduction in the numbers of samples could save months or years in biological sample collection and processing time (to say nothing of the economic considerations). [9–59,95–195] There is a conjugate variable π (x÷{E (y) {1 − Jacobi P [LnAdS5 [H] ⊗ [Ho]] Ê Ÿ ⊕ (Sqrt[Pi] /(Gamma[(-(G h^ν n Pi Q δ μ σ Sin[ω]))/2] Gamma[3/2 + (G h^ν n Pi Q δ μ σ Sin[ω])/2]) - LegendreP[-1 + A D^5 r ν + G h^ν n Pi Q δ μ σ Sin[c], 0])/(1 + 2 G h^ν n Pi Q δ μ σ Sin[ω]) + (x (LegendreP[A D^5 r ν + G h^ν n Pi Q δ μ σ Sin[c], 0] (A D^5 r ν + G h^ν n Pi Q δ μ σ Sin[c]) + (Sqrt[Pi] (1 + G h^ν n Pi Q δ μ σ Sin[ω]) (2 + G h^ν n Pi Q δ μ σ Sin[ω]))/(2 Gamma[1/2 - (G h^ν n Pi Q δ μ σ Sin[ω])/2] Gamma[2 + (G h^ν n Pi Q δ μ σ Sin[ω])/2]) - G h^ν n Pi Q δ μ σ Log[Sin[ω]] Sin[c] Derivative[1, 0] [LegendreP] [-1 + A D^5 r ν + G h^ν n Pi Q δ μ σ Sin[c], 0]))/(1 + 2 G h^ν n Pi Q δ μ σ Sin[ω]) + (x^2 ((LegendreP[-1 + A D^5 r ν + G h^ν n Pi Q δ μ σ Sin[c], 0] (-(A D^5 r ν) - G h^ν n Pi Q δ μ σ Sin[c]) - LegendreP[1 + A D^5 r ν + G h^ν n Pi Q δ μ σ Sin[c], 0] (A D^5 r ν + G h^ν n Pi Q δ μ σ Sin[c]) (1 + A D^5 r ν + G h^ν n Pi Q δ μ σ Sin[c]))/2 + (G h^ν n Pi^(3/2) Q δ μ σ Sin[ω] (1 + G h^ν n Pi Q δ μ σ Sin[ω]) (2 + G h^ν n Pi Q δ μ σ Sin[ω]) (3 + G h^ν n Pi Q δ μ σ Sin[ω]))/(8 Gamma[1 - (G h^ν n Pi Q δ μ σ Sin[ω])/2] Gamma[5/2 + (G h^ν n Pi Q δ μ σ Sin[ω])/2]) - (G h^ν n Pi Q δ μ σ Log[Sin[ω]] ^2 Sin[c] Derivative[1, 0] [LegendreP] [-1 + A D^5 r ν + G h^ν n Pi Q δ μ σ Sin[c], 0])/2 - G h^ν n Pi Q δ μ σ Log[Sin[ω]] Sin[c] Derivative[1, 1] [LegendreP] [-1 + A D^5 r ν + G h^ν n Pi Q δ μ σ Sin[c], 0] - (G^2 h^(2 ν) n^2 Pi^2 Q^2 δ^2 μ^2 σ^2 Log[Sin[ω]] ^2 Sin[c] ^2 Derivative[2, 0] [LegendreP] [-1 + A D^5 r ν + G h^ν n Pi Q δ μ σ Sin[c], 0])/2))/(1 + 2 G h^ν n Pi Q δ μ σ Sin[ω]) + (x^3 ((2 LegendreP[A D^5 r ν + G h^ν n Pi Q δ μ σ Sin[c], 0] (A D^5 r ν + G h^ν n Pi Q δ μ σ Sin[c]) - 2 LegendreP[A D^5 r ν + G h^ν n Pi Q δ μ σ Sin[c], 0] (-(A D^5 r ν) - G h^ν n Pi Q δ μ σ Sin[c]) (A D^5 r ν + G h^ν n Pi Q δ μ σ Sin[c]) - (A D^5 r ν + G h^ν n Pi Q δ μ σ Sin[c]) (LegendreP[A D^5 r ν + G h^ν n Pi Q δ μ σ Sin[c], 0] (-1 - A D^5 r ν - G h^ν n Pi Q δ μ σ Sin[c]) - LegendreP[2 + A D^5 r ν + G h^ν n Pi Q δ μ σ Sin[c], 0] (1 + A D^5 r ν + G h^ν n Pi Q δ μ σ Sin[c]) (2 + A D^5 r ν + G h^ν n Pi Q δ μ σ Sin[c])))/6 + (G h^ν n Pi^(3/2) Q δ μ σ Sin[ω] (-1 + G h^ν n Pi Q δ μ σ Sin[ω]) (1 + G h^ν n Pi Q δ μ σ Sin[ω]) (2 + G h^ν n Pi Q δ μ σ Sin[ω]) (3 + G h^ν n Pi Q δ μ σ Sin[ω]) (4 + G h^ν n Pi Q δ μ σ Sin[ω]))/(48 Gamma[3/2 - (G h^ν n Pi Q δ μ σ Sin[ω])/2] Gamma[3 + (G h^ν n Pi Q δ μ σ Sin[ω])/2]) - (G h^ν n Pi Q δ μ σ Log[Sin[ω]] ^3 Sin[c] Derivative[1, 0] [LegendreP] [-1 + A D^5 r ν + G h^ν n Pi Q δ μ σ Sin[c], 0])/6 - (G h^ν n Pi Q δ μ σ Log[Sin[ω]] ^2 Sin[c] Derivative[1, 1] [LegendreP] [-1 + A D^5 r ν + G h^ν n Pi Q δ μ σ Sin[c], 0])/2 - (G h^ν n Pi Q δ μ σ Log[Sin[ω]] Sin[c] Derivative[1, 2] [LegendreP] [-1 + A D^5 r ν + G h^ν n

 doi:10.20944/preprints202403.0518.v1

Pi Q δ μ σ Sin[c], 0])/2 - (G^2 h^(2 ν) n^2 Pi^2 Q^2 δ^2 μ^2 σ^2 Log[Sin[ω]] ^3 Sin[c] ^2 Derivative[2, 0] [LegendreP] [-1 + A D^5 r ν + G h^ν n Pi Q δ μ σ Sin[c], 0])/2 - (G^2 h^(2 ν) n^2 Pi^2 Q^2 δ^2 μ^2 σ^2 Log[Sin[ω]] ^2 Sin[c] ^2 Derivative[2, 1] [LegendreP] [-1 + A D^5 r ν + G h^ν n Pi Q δ μ σ Sin[c], 0])/2 - (G^3 h^(3 ν) n^3 Pi^3 Q^3 δ^3 μ^3 σ^3 Log[Sin[ω]] ^3 Sin[c] ^3 Derivative[3, 0] [LegendreP] [-1 + A D^5 r ν + G h^ν n Pi Q δ μ σ Sin[c], 0])/6))/(1 + 2 G h^ν n Pi Q δ μ σ Sin[ω]) + (x^4 ((-2 LegendreP[1 + A D^5 r ν + G h^ν n Pi Q δ μ σ Sin[c], 0] (A D^5 r ν + G h^ν n Pi Q δ μ σ Sin[c]) (1 + A D^5 r ν + G h^ν n Pi Q δ μ σ Sin[c]) + 6 (LegendreP[-1 + A D^5 r ν + G h^ν n Pi Q δ μ σ Sin[c], 0] (-(A D^5 r ν) - G h^ν n Pi Q δ μ σ Sin[c]) - LegendreP[1 + A D^5 r ν + G h^ν n Pi Q δ μ σ Sin[c], 0] (A D^5 r ν + G h^ν n Pi Q δ μ σ Sin[c]) (1 + A D^5 r ν + G h^ν n Pi Q δ μ σ Sin[c])) - 3 (-(A D^5 r ν) - G h^ν n Pi Q δ μ σ Sin[c]) (LegendreP[-1 + A D^5 r ν + G h^ν n Pi Q δ μ σ Sin[c], 0] (-(A D^5 r ν) - G h^ν n Pi Q δ μ σ Sin[c]) - LegendreP[1 + A D^5 r ν + G h^ν n Pi Q δ μ σ Sin[c], 0] (A D^5 r ν + G h^ν n Pi Q δ μ σ Sin[c]) (1 + A D^5 r ν + G h^ν n Pi Q δ μ σ Sin[c])) - (A D^5 r ν + G h^ν n Pi Q δ μ σ Sin[c]) (-2 LegendreP[1 + A D^5 r ν + G h^ν n Pi Q δ μ σ Sin[c], 0] (-1 - A D^5 r ν - G h^ν n Pi Q δ μ σ Sin[c]) (1 + A D^5 r ν + G h^ν n Pi Q δ μ σ Sin[c]) - (1 + A D^5 r ν + G h^ν n Pi Q δ μ σ Sin[c]) (LegendreP[1 + A D^5 r ν + G h^ν n Pi Q δ μ σ Sin[c], 0] (-2 - A D^5 r ν - G h^ν n Pi Q δ μ σ Sin[c]) - LegendreP[3 + A D^5 r ν + G h^ν n Pi Q δ μ σ Sin[c], 0] (2 + A D^5 r ν + G h^ν n Pi Q δ μ σ Sin[c]) (3 + A D^5 r ν + G h^ν n Pi Q δ μ σ Sin[c])))))/24 + (G h^ν n Pi^(3/2) Q δ μ σ Sin[ω] (-2 + G h^ν n Pi Q δ μ σ Sin[ω]) (-1 + G h^ν n Pi Q δ μ σ Sin[ω]) (1 + G h^ν n Pi Q δ μ σ Sin[ω]) (2 + G h^ν n Pi Q δ μ σ Sin[ω]) (3 + G h^ν n Pi Q δ μ σ Sin[ω]) (4 + G h^ν n Pi Q δ μ σ Sin[ω]) (5 + G h^ν n Pi Q δ μ σ Sin[ω]))/(384 Gamma[2 - (G h^ν n Pi Q δ μ σ Sin[ω])/2] Gamma[7/2 + (G h^ν n Pi Q δ μ σ Sin[ω])/2]) - (G h^ν n Pi Q δ μ σ Log[Sin[ω]] ^4 Sin[c] Derivative[1, 0] [LegendreP] [-1 + A D^5 r ν + G h^ν n Pi Q δ μ σ Sin[c], 0])/24 - (G h^ν n Pi Q δ μ σ Log[Sin[ω]] ^3 Sin[c] Derivative[1, 1] [LegendreP] [-1 + A D^5 r ν + G h^ν n Pi Q δ μ σ Sin[c], 0])/6 - (G h^ν n Pi Q δ μ σ Log[Sin[ω]] ^2 Sin[c] Derivative[1, 2] [LegendreP] [-1 + A D^5 r ν + G h^ν n Pi Q δ μ σ Sin[c], 0])/4 - (G h^ν n Pi Q δ μ σ Log[Sin[ω]] Sin[c] Derivative[1, 3] [LegendreP] [-1 + A D^5 r ν + G h^ν n Pi Q δ μ σ Sin[c], 0])/6 - (7 G^2 h^(2 ν) n^2 Pi^2 Q^2 δ^2 μ^2 σ^2 Log[Sin[ω]] ^4 Sin[c] ^2 Derivative[2, 0] [LegendreP] [-1 + A D^5 r ν + G h^ν n Pi Q δ μ σ Sin[c], 0])/24 - (G^2 h^(2 ν) n^2 Pi^2 Q^2 δ^2 μ^2 σ^2 Log[Sin[ω]] ^3 Sin[c] ^2 Derivative[2, 1] [LegendreP] [-1 + A D^5 r ν + G h^ν n Pi Q δ μ σ Sin[c], 0])/2 - (G^2 h^(2 ν) n^2 Pi^2 Q^2 δ^2 μ^2 σ^2 Log[Sin[ω]] ^2 Sin[c] ^2 Derivative[2, 2] [LegendreP] [-1 + A D^5 r ν + G h^ν n Pi Q δ μ σ Sin[c], 0])/4 - (G^3 h^(3 ν) n^3 Pi^3 Q^3 δ^3 μ^3 σ^3 Log[Sin[ω]] ^4 Sin[c] ^3 Derivative[3, 0] [LegendreP] [-1 + A D^5 r ν + G h^ν n Pi Q δ μ σ Sin[c], 0])/4 - (G^3 h^(3 ν) n^3 Pi^3 Q^3 δ^3 μ^3 σ^3 Log[Sin[ω]] ^3 Sin[c] ^3 Derivative[3, 1] [LegendreP] [-1 + A D^5 r ν + G h^ν n Pi Q δ μ σ Sin[c], 0])/6 - (G^4 h^(4 ν) n^4 Pi^4 Q^4 δ^4 μ^4 σ^4 Log[Sin[ω]] ^4 Sin[c] ^4 Derivative[4, 0] [LegendreP] [-1 + A D^5 r ν + G h^ν n Pi Q δ μ σ Sin[c], 0])/24))/(1 + 2 G h^ν n Pi Q δ μ σ Sin[ω]) + O[x] ^5, otherwise ׀xi, H A ∧ G0 ∧ G1 ∧. ∧ GMa ׀ the field momentum at the lattice site x⫤{E (y) {1 − Jacobi P [LnAdS5 [H], RamanujanTauZ (-LegendreP[A^5 ν r - 1 + G h^ν n Pi Q δ μ σ (Sin[1 c] Sin[ω] ^x), x] + LegendreP[1 + G h^ν n Pi Q δ μ σ Sin[ω], x])/(1 + 2 G h^ν n Pi Q δ μ σ Sin[ω]) [cosQFTq. [H] ⊗̂ [Ho] ∯ (AdS5νr))] otherwise ׀xi, H C, T˙, S. I, which is related to Quantum Uncertainties in ˆ ∞ operations for QuantumDistance [AdsQFTˆC, (Rz (π), QFT [H], orthogonal eigenstates for complex topologies in triangular skeletons where Φ when the Quantum Fourier transform applied to the N-dimensional Hilbert space residing at each lattice site x⫤ and at each lattice site per-residue binding free energy decomposition [3-109,135-195]. The Variational Quantum Homeopathy Machine Learning (QML) is expected to provide a methodological toolbox with significant relevance to a wide range of biological research and clinical applications since its substantial numerical and theoretical evidence now points towards a variety of strengths related to variational quantum homeopath interpretation algorithms, and for generative and predictive modeling which is now widely used in this global drug designing field [40–187,189–195]. The theory on N 3-branes in the presence of K 5-branes provided me with fields for N, Quantum states at each field site that can be encoded in n qubits in the presence of binding energy Quantum Fluctuations of the Euclid metric where the docking surface of a sphere oriented druggable drug design (Supplementary Material METHODS AND MATERIALS Figures S(1-86)), ((Iconics1-4), (Eqs1-400), and (Schematics1a,1b,1c,1d,1e,1f,1g,1h,1i,1j,1k,1l,1m), (I-VI) Supplementary Material METHODS AND MATERIALS)) of radius nr incorporates the attractor basin and encodes Quantum

 doi:10.20944/preprints202403.0518.v1

Potentization Information for each binding residue calculated including the explicitly functions torsion of (∂(Tr[ψ,{2}] DensityMatrix)/∂log$^{\varrho}$(ψ) A log(B^{G} sin(ω) (ϱ A) h$^{\nu}$ (n π Q δ μ σ)) 3) logG(z) (2+G h$^{\nu}$ n π Q δ μ σ sin(ω))+G h$^{\nu}$ n π Q δ μ σ sin(ω)+c^{8} π^{2} r^{2} δ^{2} θ^{20}==G n π Q δ μ σ cos(π/2-ω) h$^{\nu}$+3 ∂(DensityMatrix Tr[ψ,{2}])/(∂A log$_{E}$(A n π Q δ μ ϱ σ h$^{\nu}$ B^{G} sin(ω)) $\log_{\varepsilon}^{\rho}(\psi)$) logG(z) (2+G n π Q δ μ σ cos(π/2-ω) h$^{\nu}$)+c^{8} π^{2} r^{2} δ^{2} θ^{20} for Δθ^ (Sqrt[Pi] /(Gamma[(-(G h^ν n Pi Q δ μ σ Sin[ω]))/2] Gamma[3/2 + (G h^ν n Pi Q δ μ σ Sin[ω])/2]) - LegendreP[-1 + 15 k N + G h^ν n Pi Q δ μ σ Sin[c], 0])/(1 + 2 G h^ν n Pi Q δ μ σ Sin[ω]) + (x (LegendreP[15 k N + G h^ν n Pi Q δ μ σ Sin[c], 0] (15 k N + G h^ν n Pi Q δ μ σ Sin[c]) + (Sqrt[Pi] (1 + G h^ν n Pi Q δ μ σ Sin[ω]) (2 + G h^ν n Pi Q δ μ σ Sin[ω]))/(2 Gamma[1/2 - (G h^ν n Pi Q δ μ σ Sin[ω])/2] Gamma[2 + (G h^ν n Pi Q δ μ σ Sin[ω])/2]) - G h^ν n Pi Q δ μ σ Log[Sin[ω]] Sin[c] Derivative[1, 0] [LegendreP] [-1 + 15 k N + G h^ν n Pi Q δ μ σ Sin[c], 0]))/(1 + 2 G h^ν n Pi Q δ μ σ Sin[ω]) + (x^2 ((LegendreP[-1 + 15 k N + G h^ν n Pi Q δ μ σ Sin[c], 0] (-15 k N - G h^ν n Pi Q δ μ σ Sin[c]) - LegendreP[1 + 15 k N + G h^ν n Pi Q δ μ σ Sin[c], 0] (15 k N + G h^ν n Pi Q δ μ σ Sin[c]) (1 + 15 k N + G h^ν n Pi Q δ μ σ Sin[c]))/2 + (G h^ν n Pi^(3/2) Q δ μ σ Sin[ω] (1 + G h^ν n Pi Q δ μ σ Sin[ω]) (2 + G h^ν n Pi Q δ μ σ Sin[ω]) (3 + G h^ν n Pi Q δ μ σ Sin[ω]))/(8 Gamma[1 - (G h^ν n Pi Q δ μ σ Sin[ω])/2] Gamma[5/2 + (G h^ν n Pi Q δ μ σ Sin[ω])/2]) - (G h^ν n Pi Q δ μ σ Log[Sin[ω]] ^2 Sin[c] Derivative[1, 0] [LegendreP] [-1 + 15 k N + G h^ν n Pi Q δ μ σ Sin[c], 0])/2 - G h^ν n Pi Q δ μ σ Log[Sin[ω]] Sin[c] Derivative[1, 1] [LegendreP] [-1 + 15 k N + G h^ν n Pi Q δ μ σ Sin[c], 0] - (G^2 h^(2 ν) n^2 Pi^2 Q^2 δ^2 μ^2 σ^2 Log[Sin[ω]] ^2 Sin[c] ^2 Derivative[2, 0] [LegendreP] [-1 + 15 k N + G h^ν n Pi Q δ μ σ Sin[c], 0])/2))/(1 + 2 G h^ν n Pi Q δ μ σ Sin[ω]) + (x^3 ((2 LegendreP[15 k N + G h^ν n Pi Q δ μ σ Sin[c], 0] (15 k N + G h^ν n Pi Q δ μ σ Sin[c]) - 2 LegendreP[15 k N + G h^ν n Pi Q δ μ σ Sin[c], 0] (-15 k N - G h^ν n Pi Q δ μ σ Sin[c]) (15 k N + G h^ν n Pi Q δ μ σ Sin[c]) - (15 k N + G h^ν n Pi Q δ μ σ Sin[c]) (LegendreP[15 k N + G h^ν n Pi Q δ μ σ Sin[c], 0] (-1 - 15 k N - G h^ν n Pi Q δ μ σ Sin[c]) - LegendreP[2 + 15 k N + G h^ν n Pi Q δ μ σ Sin[c], 0] (1 + 15 k N + G h^ν n Pi Q δ μ σ Sin[c]) (2 + 15 k N + G h^ν n Pi Q δ μ σ Sin[c])))/6 + (G h^ν n Pi^(3/2) Q δ μ σ Sin[ω] (-1 + G h^ν n Pi Q δ μ σ Sin[ω]) (1 + G h^ν n Pi Q δ μ σ Sin[ω]) (2 + G h^ν n Pi Q δ μ σ Sin[ω]) (3 + G h^ν n Pi Q δ μ σ Sin[ω]) (4 + G h^ν n Pi Q δ μ σ Sin[ω]))/(48 Gamma[3/2 - (G h^ν n Pi Q δ μ σ Sin[ω])/2] Gamma[3 + (G h^ν n Pi Q δ μ σ Sin[ω])/2]) - (G h^ν n Pi Q δ μ σ Log[Sin[ω]] ^3 Sin[c] Derivative[1, 0] [LegendreP] [-1 + 15 k N + G h^ν n Pi Q δ μ σ Sin[c], 0])/6 - (G h^ν n Pi Q δ μ σ Log[Sin[ω]] ^2 Sin[c] Derivative[1, 1] [LegendreP] [-1 + 15 k N + G h^ν n Pi Q δ μ σ Sin[c], 0])/2 - (G h^ν n Pi Q δ μ σ Log[Sin[ω]] Sin[c] Derivative[1, 2] [LegendreP] [-1 + 15 k N + G h^ν n Pi Q δ μ σ Sin[c], 0])/2 - (G^2 h^(2 ν) n^2 Pi^2 Q^2 δ^2 μ^2 σ^2 Log[Sin[ω]] ^3 Sin[c] ^2 Derivative[2, 0] [LegendreP] [-1 + 15 k N + G h^ν n Pi Q δ μ σ Sin[c], 0])/2 - (G^2 h^(2 ν) n^2 Pi^2 Q^2 δ^2 μ^2 σ^2 Log[Sin[ω]] ^2 Sin[c] ^2 Derivative[2, 1] [LegendreP] [-1 + 15 k N + G h^ν n Pi Q δ μ σ Sin[c], 0])/2 - (G^3 h^(3 ν) n^3 Pi^3 Q^3 δ^3 μ^3 σ^3 Log[Sin[ω]] ^3 Sin[c] ^3 Derivative[3, 0] [LegendreP] [-1 + 15 k N + G h^ν n Pi Q δ μ σ Sin[c], 0])/6))/(1 + 2 G h^ν n Pi Q δ μ σ Sin[ω]) + (x^4 ((-2 LegendreP[1 + 15 k N + G h^ν n Pi Q δ μ σ Sin[c], 0] (15 k N + G h^ν n Pi Q δ μ σ Sin[c]) (1 + 15 k N + G h^ν n Pi Q δ μ σ Sin[c]) + 6 (LegendreP[-1 + 15 k N + G h^ν n Pi Q δ μ σ Sin[c], 0] (-15 k N - G h^ν n Pi Q δ μ σ Sin[c]) - LegendreP[1 + 15 k N + G h^ν n Pi Q δ μ σ Sin[c], 0] (15 k N + G h^ν n Pi Q δ μ σ Sin[c]) (1 + 15 k N + G h^ν n Pi Q δ μ σ Sin[c])) - 3 (-15 k N - G h^ν n Pi Q δ μ σ Sin[c]) (LegendreP[-1 + 15 k N + G h^ν n Pi Q δ μ σ Sin[c], 0] (-15 k N - G h^ν n Pi Q δ μ σ Sin[c]) - LegendreP[1 + 15 k N + G h^ν n Pi Q δ μ σ Sin[c], 0] (15 k N + G h^ν n Pi Q δ μ σ Sin[c]) (1 + 15 k N + G h^ν n Pi Q δ μ σ Sin[c])) - (15 k N + G h^ν n Pi Q δ μ σ Sin[c]) (-2 LegendreP[1 + 15 k N + G h^ν n Pi Q δ μ σ Sin[c], 0] (-1 - 15 k N - G h^ν n Pi Q δ μ σ Sin[c]) (1 + 15 k N + G h^ν n Pi Q δ μ σ Sin[c]) - (1 + 15 k N + G h^ν n Pi Q δ μ σ Sin[c]) (LegendreP[1 + 15 k N + G h^ν n Pi Q δ μ σ Sin[c], 0] (-2 - 15 k N - G h^ν n Pi Q δ μ σ Sin[c]) - LegendreP[3 + 15 k N + G h^ν n Pi Q δ μ σ Sin[c], 0] (2 + 15 k N + G h^ν n Pi Q δ μ σ Sin[c]) (3 + 15 k N + G h^ν n Pi Q δ μ σ Sin[c])))))/24 + (G h^ν n Pi^(3/2) Q δ μ σ Sin[ω] (-2 + G h^ν n Pi Q δ μ σ Sin[ω]) (-1 + G h^ν n Pi Q δ μ σ Sin[ω]) (1 + G h^ν n Pi Q δ μ σ Sin[ω]) (2 + G h^ν n Pi Q δ μ σ Sin[ω]) (3 + G h^ν n Pi Q δ μ σ Sin[ω]) (4 + G h^ν n Pi Q δ μ σ Sin[ω]) (5 + G h^ν n Pi Q δ μ σ Sin[ω]))/(384 Gamma[2 - (G h^ν n Pi Q δ μ σ Sin[ω])/2] Gamma[7/2 + (G h^ν n Pi Q δ μ σ Sin[ω])/2]) - (G h^ν n Pi Q δ μ σ Log[Sin[ω]] ^4 Sin[c] Derivative[1, 0] [LegendreP] [-1 + 15 k N + G h^ν n Pi Q δ μ σ Sin[c], 0])/24 - (G h^ν n Pi Q δ μ σ Log[Sin[ω]] ^3 Sin[c] Derivative[1, 1] [LegendreP] [-1 + 15 k N + G h^ν n Pi Q δ μ σ Sin[c], 0])/6 - (G h^ν n Pi Q δ μ σ Log[Sin[ω]] ^2 Sin[c] Derivative[1, 2] [LegendreP] [-1 + 15 k N + G h^ν n Pi Q δ μ σ Sin[c], 0])/4 - (G

 doi:10.20944/preprints202403.0518.v1

h^ν n Pi Q δ μ σ Log[Sin[ω]] Sin[c] Derivative[1, 3] [LegendreP] [-1 + 15 k N + G h^ν n Pi Q δ μ σ Sin[c], 0])/6 - (7 G^2 h^(2 ν) n^2 Pi^2 Q^2 δ^2 μ^2 σ^2 Log[Sin[ω]] ^4 Sin[c] ^2 Derivative[2, 0] [LegendreP] [-1 + 15 k N + G h^ν n Pi Q δ μ σ Sin[c], 0])/24 - (G^2 h^(2 ν) n^2 Pi^2 Q^2 δ^2 μ^2 σ^2 Log[Sin[ω]] ^3 Sin[c] ^2 Derivative[2, 1] [LegendreP] [-1 + 15 k N + G h^ν n Pi Q δ μ σ Sin[c], 0])/2 - (G^2 h^(2 ν) n^2 Pi^2 Q^2 δ^2 μ^2 σ^2 Log[Sin[ω]] ^2 Sin[c] ^2 Derivative[2, 2] [LegendreP] [-1 + 15 k N + G h^ν n Pi Q δ μ σ Sin[c], 0])/4 - (G^3 h^(3 ν) n^3 Pi^3 Q^3 δ^3 μ^3 σ^3 Log[Sin[ω]] ^4 Sin[c] ^3 Derivative[3, 0] [LegendreP] [-1 + 15 k N + G h^ν n Pi Q δ μ σ Sin[c], 0])/4 - (G^3 h^(3 ν) n^3 Pi^3 Q^3 δ^3 μ^3 σ^3 Log[Sin[ω]] ^3 Sin[c] ^3 Derivative[3, 1] [LegendreP] [-1 + 15 k N + G h^ν n Pi Q δ μ σ Sin[c], 0])/6 - (G^4 h^(4 ν) n^4 Pi^4 Q^4 δ^4 μ^4 σ^4 Log[Sin[ω]] ^4 Sin[c] ^4 Derivative[4, 0] [LegendreP] [-1 + 15 k N + G h^ν n Pi Q δ μ σ Sin[c], 0])/24))/(1 + 2 G h^ν n Pi Q δ μ σ Sin[ω]) + O[x] ^5] [ChebyshevT[α μ ν^d, q^b] LegendreP[n δ, Q^D, (3.2879774473519326*^25 n δ θ^10 Ψ)/(G q), g^6^(-d^3) G GoldenRatio N ψ] - 2 E x ChebyshevT[α μ ν^d, q^b] LegendreP[n δ, Q^D, (3.2879774473519326*^25 n δ θ^10 Ψ)/(G q), g^6^(-d^3) G GoldenRatio N ψ] + ((-1 + E) E x^2 ChebyshevT[α μ ν^d, q^b] 0.5 ((-1. ChebyshevT[-1. + Hypergeometric2F1[2.71828 Δ θ Θ K Ψ, γ ω, 6.02214076*^23 Cos[69.9827 K], Δ Θ Ψ], x])/(-1. + Hypergeometric2F1[2.71828 Δ θ Θ K Ψ, γ ω, 6.02214076*^23 Cos[69.9827 K], Δ Θ Ψ]) + ChebyshevT[1. + Hypergeometric2F1[2.71828 Δ θ Θ K Ψ, γ ω, 6.02214076*^23 Cos[69.9827 K], Δ Θ Ψ], x] /(1. + Hypergeometric2F1[2.71828 Δ θ Θ K Ψ, γ ω, 6.02214076*^23 Cos[69.9827 K], Δ Θ Ψ])) LaguerreL[0.954545 r μ^24 ω, (1.126802747217019*^-13 c^4 m λ Csc[Q])/(G M q^(1. μ) ν), z Δ] ((16. a^8 z^16 Hypergeometric1F1[1 + a^8, 2., z^16] HypergeometricU[a, Cos[b], 6.02214076*^24 z] + Hypergeometric1F1[a^8, 1., z^16] ((-50.2655 g k + 0.5 z) HypergeometricU[a, Cos[b], 6.02214076*^24 z] - 6.02214076*^24 a z HypergeometricU[1 + a, 1 + Cos[b], 6.02214076*^24 z])) WhittakerM[16 g k Pi, m, z] + (0.5 + 50.2655 g k + 1. m) Hypergeometric1F1[a^8, 1., z^16] HypergeometricU[a, Cos[b], 6.02214076*^24 z] WhittakerM[1 + 16 g k Pi, m, z])/z JacobiP[-5.747, 84.926, 6.79, -29.284] JacobiP[-6.57, 88.260, -6.692, -18.765] (LaguerreL[-1 + 10^23, 1, 0] /Gamma[(1 - 10^23)/2]) + LaguerreL[n, 0] (2^(-1 + n) (1 + a + b + 1) Sqrt[Pi] Cos[(n Pi)/2]) (-8.975790805766743*^-11 + 1.3853244171495244*^-10 I)/Gamma[-9999999999999999999999/2] + 2^(-1 + n) (2 + a + b) Sqrt[Pi] Cos[(n Pi)/2] LaguerreL[n, 0] 2^n Sqrt[Pi] Cos[(n Pi)/2] LaguerreL[n, 0] + 2^(-1 + n) a Sqrt[Pi] Cos[(n Pi)/2] LaguerreL[n, 0] + 2^(-1 + n) b Sqrt[Pi] Cos[(n Pi)/2] LaguerreL[n, 0], by a discrete variable with a finite number N of mutually orthogonal eigenstates. In my case, qubits are induced directly on 5-brane solvation free energy calculations using a Poisson–Boltzmann (PB) based self-consistent reaction field (PB/SCRF) method and on the Quantum fluctuations of the Euclid metric, due to the uncertainty relationship between Euclid special metrics and Quantum information. [31-119,125-195] The first component of this pair is the N−dimensional Gegenbauerian Hamiltonian H which has been chosen tridiagonal for reshaping and re-encoding of the node distances (atom-atom distance or residue-residue distance) as edge features of different edge types (e.g., intra-and intermolecular edges to differentiate between ligand and protein subgraphs), and for constructing edges in the molecular graph if the node distance falls below a pre-defined threshold. [3-23,109-195] The second component Θ of this pair is the reconstructed (and non-unique) metric that represents a protein-ligand complexes using a regular 3D grid with voxels characterized by pharmacophoric features of nearby atom types. While there is substantial evidence supporting reductions in docking energy and binding affinity scoring values [1-37,23–195], evidence of generalization performance under certain constructions of edges also exists (e.g., [92-186,195]) which may be partly attributable to shallower quantum circuits providing better utility bounds than deeper circuits [93-195], and constraints with classical neural network intuition with increased layer depth and with an exponential increase in model expressiveness [94-108,121-194]. This historical detour let us remind the readers that nuclear physicists opened this Pandora's box twenty years ago [18-195] when considering fermionic Hamiltonians h (acting in complicated Fock's space H(P) of "physical" states |ψ (P) i) as transformed into isospectral operators H (acting in another "friendly" space H(F)) which can be easily be combined with a topological string field theory analysis similar to the one given earlier in a heuristic sense, since it is supported by a rigorous mathematical framework due to the uncertainty relation, between two spheres of radius nr and n✷ respectively, since also $\mathcal{C}\hat{}\ \infty$ operations imply infinitely many operations. [3–80,105–195] This intersection algorithm outputs the

 doi:10.20944/preprints202403.0518.v1

probability that this sub-grid is close to a druggable binding site and generates new docking operations using this sliding subgrid network approach by extending this approach to ligand-binding sites of the AT1R/ACE2 complex structures. [7–59,115–195] This surface-based approach describes individual points on the protein surface in geodesic space, such that distances between points correspond to the reduction of the docking energy scoring values. [13–79,103–195] Our quantum Hamiltonians then became tractable as a living finite set of Haag's theorem that simply translates the fact that the CRQML contains the CRQLI, cryptometalanguage object language on deformed but still local one-dimensional discrete N−site lattices. Once we turn attention to our present model and to its generic bandmatrix metrics Θk(a) with $1 \leq k \ll N$, the picture is changed and the coordinates prove quantized polarizations [41–195] in this project, showing that a successful docking method has to be used in seven (7) dimensions when constructing supersymmetric chemical bridge extensions of general relativity which can be generalized to any odd-dimensional Spacetime Quantum fieldss and Quantum Entropy in five (5) dimensions for Chern-Simons molecular similarity actions when chemical reactions do not need to be considered in a simulation. [3-109,135-195] Accordingly, I have restricted myself, however, to Poincar´e supergravity in terms of "bonded atoms" as should be modified into a special fuzzy shaped sphere (Supplementary Material METHODS AND MATERIALS Figures S(1-89), ((Iconics1-4), (Eqs1-400), and (Schematics1a,1b,1c,1d,1e,1f,1g,1h,1i,1j,1k,1l,1m), (I-VI) Supplementary Material METHODS AND MATERIALS)) with rational radius r for mechanical deformation of (AT1R) DNA, RNA, and proteins, and changes in SARS-CoV-2 function which have been distorted from [amino ({4 - [(2R,3R) - 2 - [(2S) - 3 - { [(1S,2S) - 1 - { [(S) - 1,3 - dihydroisoindole - 2 - carbonyl [(2 - methyl - 6 - oxo - 1,7 - dihydropurin - 8 - yl) methyl] phosphanyl] carbamoyl} - 2 - methylbutyl] amino} - 2 - methylpropyl] oxaziridin - 3 - yl] butyl}amino) methylidene] azanium idealized geometrics due to unbound van der Waals and Columbic interactions. This full anti de Sitter Homeopathic extension at its core classical algorithms for these hypergeometric problems use subroutines of Matching Substring and Turing Machine constructing by traversing subcomponents in images, nodes, edges in graphs, string graphs and Turing Machine Rule sampling for counting k-mers (i.e., substrings of biological sequences) in a fundamental representation of SU (20) with twenty elementary potentzization steps after a proper contraction is partially performed since it still remains an open problem when solving the Schrödinger and Chern-Simons function for electron motions. [3-79,125-195] This requires an explicit description of chemical bonding and lots of information about the structures of molecules which were generated by analogy with Quantum Homeopathy Teleportation and Quantum Encryption functions from COVID-19 clinical trials that are by their very nature considered as classical 'detectors' of causality when tending to regard treatment groups as similar to causal signals, especially after considering as inputs the atomic orbitals of the sequences from the Homeopathy Clinical Remedies of the Bryonia alba, Phosphorus, Arsenic album, Gelsemium sempervirens, and Carboneum oxygenisatum or Pulsatilla nigricans. [3-89,109-195] This, it has been in part argued, is one of the reasons why clinical trials cannot be used for a detection of homeopathy effects that are based on non-quantum mechanisms. [15-195] They lead to loss of information of entangled states when 'intercepted' as causal signals [62,63] without taking into account the five dimensions of this Chern-Simons action for anti-de Sitter supergravity based electron motions that can rely on force fields with fixed parameters and it is possible to provide better understanding of conformational analysis between superimposed chemical conformers. [37-195] This Turing Machine action, which is considered here a Quantum Encrypted Hypergeometric function after a proper contraction is performed for quantum mechanical deformation, converts the complex structure of ACE2 and AT1R DNA, RNA, and proteins, and changes in their cellular structure into a complex 3D graph and designs a structure-aware interactive graph neural network to capture 3D spatial information and global long-range interactions using polar-inspired graph attention layers in a semisupervised manner via this full anti-de Sitter Chern-Simons formulation of Vaidya Supergravity Functions [EqsA-K]. First, the bosonic Lagrangian in the Poincar´e case does not contain the Hilbert term thus making the contact with four dimensional theories rather obscure [6-192]. Secondly, the Poincar´e theory in odd dimensions, which does not possess black hole solutions while the anti-de Sitter theory does,

 doi:10.20944/preprints202403.0518.v1

combined the electron motions and atomic orbits from the ACE2 and AT1R DNA-Protein-Ligand signatures. [43-195] In more general spacetimes enhanced by ZK-based proofs of nonlinear dynamics in this extended quantum cryptography model encrypt and decrypt homeopathy chemical data which may be extended to hyper-symmetric SphericalHarmonicY, LaguerreL, Hypergeometric1F1, WhittakerM functions of SphericalBesselJ[n, z] LegendreP[n, m, x] LegendreQ[n, z] LaguerreL[ChebyshevT[Log[x], α ψ Cos[γ]], x] Hypergeometric1F1[Cos[x Q] ^4 Q^Cos[X c] ^4, ArcSin[r] ^2 Sin[b], Log[23 y I] ArcSin[z]] Hypergeometric1F1[a^8, G^24, z^16] HypergeometricU[a, Cos[b], z] WhittakerM[16 k Pi g, m, z] Hypergeometric0F1[μ a, η z] Hypergeometric0F1[EulerGamma a, z] Hypergeometric2F1[-(ϑ^2 (δ x))/23, ν μ Sin[ω], Log[E a], (Cosh[21] /22) a] Hypergeometric0F1Regularized[a, z] AppellF1[a, b1, b2, c, x, y] AppellF1[a, b1, b2, c, x, y] Hypergeometric2F1[8, Pi, G, E] for {F_1(a;b1, b2;c;x, y) C_(α μ ν^d)(z^b) (P_(δ n)^(Q^4 d^4 r^10×δ/(G α) n^2 Ψ)(G N g^(1/(6^(d^3))) (ψ ϕ))×1/24)×Γ^2/2 ∧ 23 (Γ Γ) d ∧ Γ ∧ Γ S×ω^2/2 ∧ d ω, ω^6 ω ∧ ω ∧ ω}Chern-Simons Topology driven functions for a collection of nonlinearly coupled remerging harmonic oscillators. [87-195] Although quantum teleportation works via entangled states over a distance, it is also necessary to access a completely separate and classical code in order to make any sense of the encoding of information from these entangled states of special interest for the fusion of pharmacophoric product of Quantum Homeopathy Frame representations from the Hopf algebra structure on Uqg, when the universal r matrix may provide more drug designing applications, including medicinal products, gene therapy for biological macromolecules (Farraha et al.,2018), and for the nervous system (Bowers et al.,2011) that are capable of interacting within protein and gene targets absolutely with negative docking energy values. [4-59,109-195] This is an additional requirement for the usage of homeopathy remedy information transferred via entangled states, explaining the difference between quantum information and the classical information. [35-195] The clarification of the paradox dates back to Scholtz et al. [18-187] and Bender et al. [32-189] could make our elementary solvable model tractable, e.g., as a controllably non-local alternative to a deformed local k = 0 lattice [30, 42-191]. However, this raises the problem that entangled states in themselves cannot be treated as if they could be the source of causal signals in the classical sense: if treated as such, the entangled state is broken and the information lost. [The explanation of this state of affairs is a sophisticated argument which rests on the assumption that the standard linear formalism of quantum mechanics forbids the use of entanglement for superluminal (i.e., faster than light or backwards in time) communication] [57-194]. Nonetheless, polynomial [2-187] or even sub-linear QFT reductions in the number of Quantum Homeopathic Algorithms required to build a classifier which could provide significant operational advantages in this drug designing and mathematical chemistry field. [23-195] The latter is of great importance as a possible theoretical support for practical applications of these diffraction and interference states which deviate even more from this classical expectations when observing them with massive particles, such as electrons, neutrons, or atoms in these molecular merging processes for mimicking localized signals in homeopathic remedies which might in the end be important in that a classical channel and could be established by that Avogadro Number's route enabling the teleportation element stemming from generalized entanglement to become effective in the first place. As noted above, it might be possible to reconstruct an entanglement version of homeopathy along different lines, and it might be possible that for different versions of homeopathy different processes that are active and could even be conceived as operating in parallel with these Quantum Homeopathy-like thermodynamically metastable states which were able of shaping unfolded proteins/polypeptides/small ligands that most likely can be experimentally observed by using solution nuclear magnetic resonance (NMR) method. [10-195] These practical applications of QM Homeopathy advantages still remaining largely theoretical, but their potential to address existing domain constraints by providing ample motivation for further research into variational QM approaches is limited. [21-195] The purpose of this analysis was to show that such a drug design reconstruction along the lines of QFT is possible and yields a plausible explanatory and translational model of homeopathy, which is able to transcript the paradoxes from the two basic rules of homeopathy into a bioinformatics and computational biology project, for the generation of non-traditional data structures. [11-195] Since similar approaches have not been able of being leveraged

 doi:10.20944/preprints202403.0518.v1

by classical algorithms they may great effect future drug designing protocols even while electrons and neutrons are still rather small and elementary particles. In principle, this Chern-Simons anti-de Sitter supergravity function of the N pharmacophoric elements encodes a string of n bits, and such geometrical representation would be that of a separable n-qubits state for anti-de Sitter supergravity since it can rely on translational model from homeopathy force fields with negative docking energy fixed parameters. [11-90,122-191] It is possible to provide better understanding of conformational analysis between ligand conformers which can be constructed from the knowledge of these associated supergroups and invariant tensors only when finding an invariant tensor in future non-trivial task. In five dimensions, the relevant supergroup is SU [2,21-191] while in the important example of eleven dimensions the supergroup is OSp [32-,89,90,142-186]. On the experimental level one expects that such a weakly nonlocal scenario and its consequences (including, e.g., phase transitions) might find simulations in classical systems. A decisive theoretical as well as experimental progress in this direction has already been reported in optics [43, 44-81,117-193] as the spacetime dimension increases, one faces a growing multiplicity of choices for the invariant tensor of n-maximally entangled states that are proven to be also accommodated here in two generalized chemical structures, the GissitorviffirnaTM and the RoccustyrnaTM chemical structures each one encoding either a string QuantumDistance [AdsQFTˆC, (Rz (π), QFT [H], ⊗̂ [Ho] ∯IMG) μνi),2r^((F m Q T^δ θ^10 ψ Ψ Log[y] ^2)/(10000000000000000000000000000 E^((N Pi)/2))) Cos[(Pi (LegendreP[LaguerreL[E^(I/2 n Pi) λ, (0. + 6.02214076*^23 I) F m o q Q T ϱ ψ, I E^λ], x] - (F m Q T^δ θ^10 ψ Ψ Log[y] ^2)/(10000000000000000000000000000 E^((N Pi)/2))))/2] JacobiP[(LegendreP[LaguerreL[E^(I/2 n Pi) λ, (0. + 6.02214076*^23 I) F m o q Q T ϱ ψ, I E^λ], x] - (F m Q T^δ θ^10 ψ Ψ Log[y] ^2)/(10000000000000000000000000000 E^((N Pi)/2)))/2, (F m Q T^δ θ^10 ψ Ψ Log[y] ^2)/(10000000000000000000000000000 E^((N Pi)/2)), 0, 1 - 2 r^2] ((Iconics1-4), (Eqs1-400), Supplementary Material METHODS AND MATERIALS (1), (2)),((Cluster of BIOGENEA_ CONSENSUS_Eqs.1-26), (Supplement Material FUNCTIONS.1 - 19)). These QFT to QM Maximally Entangled States for the Special Fuzzy Shaped Sphere based Drug Designs (Supplementary Material METHODS AND MATERIALS Figures S(1-90)), ((Iconics1-4), (Eqs1-400), and (Schematics1a,1b,1c,1d,1e,1f,1g,1h,1i,1j,1k,1l,1m), (I-VI) Supplementary Material METHODS AND MATERIALS)) are considered to be a natural basis for the Lie algebra of Sp (32) as given by the Dirac matrices Γa, Γab, Γabcde. This basis is easily extended to expand the superalgebra of OSp (32) under appropriate conditions to preserve the topological nature of the CS theory. [35-195] These Quantum Homeopathy Molecular Pairs (QHMMP), Lindenbaum-Tarski logical spaces and Adaptive Weighted KNN Positioning for Matched Bemis and Murko (BM) driven eigenvalue statements were quantified into measurable Shannon Entropy quantities while coupling the chemical spaces between the atomic orbits from the COVID-19-SARS-COV-2 SPIKE D614G mutation as infinitely massive sources at the expense of requiring the underlying 3 - manifolds for the generation of the DRVYIHPF-mimetic, Gisitorviffirna_TM, Roccustyrna_gs, Gissitorviffirna_TM, Roccostyrna_ gs_consv, and Roccustyrna _fr ligands. In this respect, the idea of ‘macro-quantum teleportation’ would have certain similarities to Walach's notion of generalized entanglement, based on semiotics [58,63,64-195]. However, it is only the entangled state which contains information about the whole experimental situation and, therefore, by implication, this homeopathic process might be considered to involve macro-quantum ‘teleportation’ of geometric deep-learning methods for structure-based drug design from the perspective of machine learning/deep learning where the corresponding representative works, benchmark datasets, and evaluation metrics are clearly stated. [42,43,47,49-195] Since the practical implementation of these parallel experimentings in quantum world is hindered by several mutually interrelated obstacles, the most serious one may be identified with a certain conflict between the simplicity of the matrix H and the complicated guarantee of its Hermiticity via metric Θ. For that reason our SBDD task-oriented sections are organized and based on the task categories where each SBDD task is formulated as a Turing Machine learning/deep learning problem and based on the simultaneous simplicity of both the operators H and Θ by using notions of Quantum Homeopathy Macro-Entanglement Equations (I-DXCVII), ((Iconics1-4), (Eqs1-400), Supplementary Material METHODS AND MATERIALS (1), (2)),(Eqs.1-400) and hidden Quantum Homeopathy Information

 doi:10.20944/preprints202403.0518.v1

processors for the illustrated certain features in this quantum homotherapeutic process in order to topologically generate a complex of networks of chemical Quantum Homeopathy Repeaters that are composed of heterogeneous mathematical and chemical nano-links. [2-95,100-195] These Quantum Homeopathy Functions breaks the entangled state that necessarily leads to loss of quantum hidden information about the integration of function of the chemical systems as a whole 3D-aware pharmacophoric system at the forefront of future generative modeling studies. Clearly, this could happen when translating the homeopathic efficacy of a remedy as removed from their entangled therapeutic context by using Quantum Turing Machine Rule without having fundamental behavioral differences from classical networks. These solutions were obtained by solving the functions ((Supplementary Material) FUNCTIONS1-28) where ζ are the eigenvalues that referred to three main targets: the Spike glycoprotein (S-protein), papain-like protease (PLpro), and prominently the main protease Mpro for enabling effective Turing Machine Geometric Learning Rules to act as an example of generalized entanglement predicted by weak quantum theory when superimposing the most relevant symmetry groups of these RoccustyrnaTM-AT1R molecular systems. Our out-of-the-box approach synergistically combines the best of two worlds transferability of QM and high accuracy of AI approaches including the Euclidean group, the special Euclidean group, and the permutation group in a 3D coordinate system into the aforementioned QFTT molecular systems for these Quantum-mechanical-mimicking structured chemical biosystems following the nature of the active ingredient in ultramolecular dilutions that correspond to QFFFT Quantum network-like Functions ((Supplement Material) FUNCTIONS1, (Supplement Material) FUNCTIONS2), (⟨(SUPPLEMENT MATERIAL) FUNCTIONS.1-26⟩) of r that goes to zero faster than r itself. [10-195] So for these rotations and graph translations (Ics.3a,3b,3c) that covers reflections from the Roccustyrna's ligand total free energy negative reductions there are no singularities to deal with at all especially when designing these "Stealth Fuzzy Shaped Drug Designs" that are interacting with negative binding free energies, less serious side effects (SI Appendix II SwissADME), and microblack hole negative docking energy properties. More specifically, as argued in the accompanying paper, scale separation is considered to be a prerequisite for the origin of Quantum Homeopathy Fields when [18-151] combined with quantum thermodynamics of learning [17-152], and with the theory of similar [18-153], in an attempt to construct a formal framework for a phenomenological description of an revolutionized druggable scaffold that is capable of interacting solely with negative docking energies against AT1R binding domains. These new annotated substances (Ic3a1), (Ic3a2), (Ic3b1), (Ic3b2), (Ic3c), (Ic3d), (Ic3d), (Ic3e), (Ic3f), (Ic3g), (Ic3h), (Ic3i), and (Ic3j) are brought into a relationship with a particular diseased organism exhibiting special signs, which in other cases were related to and brought about by this substance, as represented in the knowledge system of homeopathy and its materia medica. B) By taking advantage this therapeutic rationale of Quantum Homeopathy that enacts another entangled state between substance and diseased organism in this case and also by 'Turing Machine transferring' the Quantum Information from these symptoms from the organism back to innovative drug designs I continue along the lines of the previous efforts on establishing the correspondence between quantum thermodynamics and quantum entropy evolutions for transcripting Quantum Homeopathy solutions in a set of framework of ChebyshevU, HermiteH, HeunT, LaguerreL, HeunT, HeunTPrime, SphericalHarmonicY, HeunB, HeunD, SphericalBesselJ, LegendreP, LegendreQ, HeunC, LegendreQ, HeunG, LaguerreL, SpheroidalPS, SpheroidalEigenvalue, Hypergeometric1F1, WhittakerM, CoulombH2, AiryAi, CoulombF, CoulombH1, TemplateBox [{l, eta, r}, CoulompH1], Hypergeometric2F1, ThreeJSymbol, SixJSymbol, GegenbauerC, ChebyshevT, and GegenbauerC quantum functions of ChebyshevT[n, x] GegenbauerC[Q^Cos[f Degree] z LogBarnesG[z], x c^4 (Pi r), ArcSin[r] ^2] LegendreP[σ h^(δ n), Q^D, d^4 r^10 (δ/(G Ψ)) n^8 Ψ, G N g^(1/6^d^7) (Ψ GoldenRatio)] LegendreQ[Log[ζ d] 2 Ψ^C Cos[μ], σ δ ArcSin[q ζ] ^Ψ] LaguerreL[E 2 n - 4 Pi r (R^2/k), x] Cos[x/(d/ξ[r[x]])] Integrate[1, x] (x/WeierstrassZeta[u, {Subscript[g, 2], Subscript[g, 3] }]) (({l - q {ξ I {2 l - ξ, 6 I ζ}, 6 x} I, C0[G^(l c)], 2 y I}/{ξ, 1}) (L/(G l c))) WhittakerM[(21/22) c^24 (G Pi k), (c^4/(4 G M)) m d λ^2, z] [13,14-113]. [29-174,182] Predictions and Quantum functions in this project were used as inputs homeopathy substances and remedies produced by hand, by trituration or other complicated procedures which

 doi:10.20944/preprints202403.0518.v1

are more effective than those coming from industrial production with succusion machines or sonicated production since the first part of the entangled state which depends on a correct production process that is possibly helped by a pseudo-causal theory, which Walter von Lucadou has called already a pseudo-machine [19-183]. In these quantum teleportation for homeopathy driven drug designing experiments the interpreted quantum information can *completely and directly* be transferred from one system to another, *without that information traveling down any physically identifiable signaling pathway*. [2-50,62-71,103-184] This quantum interpretation 'mechanism' which permits this direct transfer of information is a Quantum Homeopathy Entanglement and is completely different to any drug designing system developed so far. [2-60,62-81,113-184] These quantum entangled drug designing systems are more strongly coupled than classical drug designing systems, and together have well-defined informational characteristics. However, these individual Quantum Homeopathy Systems may be completely random without any information content. [2-50,62-184] Successful quantum teleportation means that this new teleported system becomes completely identical with the original, which by necessity has to disappear emphasizing to the entropy and enthalpy change in the process of protein folding which are the key factors that drive protein folding. In 'classical' information theory, the elementary quantity of information is the bit that can have one of two values, e.g., 0 or 1. Physical realization of a bit requires any system which can exist in two well-defined separate states where quantum information technology differs from previous 'classical' information technologies, is that a quantum system can be in a superposition of both the 0 and 1 states (called a qubit). [50-185] There is no parallel in classical information theory. [45-186] Far from superposition that leading to a loss of information, these Quantum Homeopathy Technologies offers a completely different way of encoding information onto two or more qubits which actually uses the entangled superposition of states. [45-187] In particular, I found quantum function solutions that stabilization through hydrophobic contacts between residues and hydrogen bonding interactions which are important for the formation of the β-hairpin. [29-194] With respect to applications, much like improvements in training landscapes, QFT to QM reductions in quantum potentization generalization error (despite having broad relevance) may alone be insufficient to provide a practical quantum advantage in the near term. [28-194] These reductions in sample complexity may allow these Turing Learning Machine of robust Turing Machine learning models from fewer examples noting that it is possible to use different modes of reconstructing entanglement in a Turing Machine Learning Quantum Homeopathy System (TMLQHS) where it might also be possible by translating the consciousness of the persons active during the homeopathy production and application process into druggable and hypergeometric scaffoldings. [23–70-194] However, we still lack a "Folding Turing Machine for an applied Quantum Homeopathy Mechanism" to explain how the time evolution of a Turing Learning Machine for Quantum Homeopathy Folding Development could lead us to Quantum Chaos Solution conditions. [2-70,92-194] The core of this Turing Machine Learning Quantum Homeopathy protein-ligand folding problem is to crack the folding mechanism demonstrating the detail steps in the protein folding processes of secondary, tertiary and quaternary structures which strictly conforms to the Negative Gibbs free energy equation in the local space of the Quantum Homeopathy solution conditions where the formation of H-bonds in the protein-folding processes satisfies the entropy-enthalpy compensation requirements for the spontaneous reaction in the local space of the ultra low homeopathy conditions. [2-100,62-195] The information encoded here in such a way that neither of the two qubits carries any well-defined information on its own: all of the information is encoded in the joint properties of their entangled state since any attempt to 'get at' the presumed information content of the individual qubits is doomed because it means breaking the entanglement between them, leading to the loss of information from the methods of energetically while searching for the global minimum in a given protein's energy landscape that employed by these successful artificial intelligence algorithms [10-163,169-195] for quantum teleportation applications that always use double-entangled states plus a weak classical channel of communication. [22-70,82-195] The latter is needed to actually decode the original signal, while also the entangled states are used to get the code across in this Quantum Homeopathy Translational Experiment as an analogous situation for tracing and designing novel substance as a classically conceived information channel which could either be

 doi:10.20944/preprints202403.0518.v1

materially left over in terms of single molecules, or as imprints of those molecules. [2-150,162-195] This will guarantee that the protein-folding problem can be solved using second law of thermodynamics, even without using any artificial intelligence algorithm inside this hydrophobic environment of a guanidine that may contribute to initiate some critical entropy-enthalpy compensations encoded in the amino acid sequence, and enable proteins folding into different stabilized conformations in different environments. [2-162,170-195] This experiment was able to demonstrate the delocalization of entire small molecules by combining Metal Complexes, Water Bridges, Salt Bridges, and Hydrophobic Interactions at high energies together after solving the vertex functions $T_{2\,c^2\,Q^{\cos^4(c\,X)}\cos^2(c\,X)\log(Q)}(x)$ $x^{-2\,c^2\log(Q)\cos^2(c\,X)\,Q^{\cos^4(c\,X)}}$ ($2^{-2\,c^2\cos^2(c\,X)\log(Q)\,Q^{\cos^4(c\,X)}-1}$ +($2^{-2\,c^2\cos^2(c\,X)\log(Q)\,Q^{\cos^4(c\,X)}-2}$ c^2 $Q^{\cos^4(c\,X)}$ $\cos^2(c\ X)$ $\log(Q))/x^2+(1/x^4)$ $2^{-2\,c^2\cos^2(c\,X)\log(Q)\,Q^{\cos^4(c\,X)}-5}$ c^2 $Q^{\cos^4(c\,X)}$ $\cos^2(c\ X)\log(Q)$ (2 $c^2\cos^2(c\ X)\log(Q)$ $Q^{\cos^4(c\,X)}$ +3)+O((1/x)⁶))+ $x^{2\,c^2\log(Q)\cos^2(c\,X)\,Q^{\cos^4(c\,X)}}$ ($2^{2\,c^2\,Q^{\cos^4(c\,X)}\cos^2(c\,X)\log(Q)-1}$ -($2^{2\,c^2\,Q^{\cos^4(c\,X)}\cos^2(c\,X)\log(Q)-2}$ c^2 $Q^{\cos^4(c\,X)}$ $\cos^2(c\ X)$ $\log(Q))/x^2+(1/x^4)$ $2^{2\,c^2\,Q^{\cos^4(c\,X)}\cos^2(c\,X)\log(Q)-5}$ c^2 $Q^{\cos^4(c\,X)}$ $\cos^2(c\ X)$ log(Q) (2 c^2 $Q^{\cos^4(c\,X)}$ $\cos^2(c\ X)\log(Q)$-3)+O((1/x)⁶)) \[Integral] $T_{2\,c^2\,Q^{\cos^4(c\,X)}\cos^2(c\,X)\log(Q)}(x)$ x==1/2 ($T_{2\,c^2\cos^2(c\,X)\log(Q)\,Q^{\cos^4(c\,X)}+1}$ (x)/(2 c^2 log(Q) $\cos^2(c\ X)$ $Q^{\cos^4(c\,X)}$ +1)- $T_{2\,c^2\,Q^{\cos^4(c\,X)}\cos^2(c\,X)\log(Q)-1}$ (x)/(2 c^2 log(Q) $\cos^2(c\ X)$ $Q^{\cos^4(c\,X)}$ -1)) cos(π c^2 log(Q) $\cos^2(c\ X)$ $Q^{\cos^4(c\,X)}$)+2 c^2 x log(Q) $\cos^2(c\ X)$ $Q^{\cos^4(c\,X)}$ sin(π c^2 log(Q) $\cos^2(c\ X)$ $Q^{\cos^4(c\,X)}$)-2 x^2 (c^4 $\log^2(Q)$ $\cos^4(c\ X)$ $Q^{2\cos^4(c\,X)}$ cos(π c^2 log(Q) $\cos^2(c\ X)$ $Q^{\cos^4(c\,X)}$))+1/3 c^2 x^3 log(Q) $\cos^2(c\ X)$ $Q^{\cos^4(c\,X)}$ (1-2 c^2 log(Q) $\cos^2(c\ X)$ $Q^{\cos^4(c\,X)}$) (2 c^2 log(Q) $\cos^2(c\ X)$ $Q^{\cos^4(c\,X)}$ +1) sin(π c^2 log(Q) $\cos^2(c\ X)$ $Q^{\cos^4(c\,X)}$)+2/3 c^4 x^4 $\log^2(Q)$ $\cos^4(c\ X)$ $Q^{2\cos^4(c\,X)}$ cos(π c^2 log(Q) $\cos^2(c$ X) $Q^{\cos^4(c\,X)}$) (c^2 log(Q) $\cos^2(c\ X)$ $Q^{\cos^4(c\,X)}$ -1) (c^2 log(Q) $\cos^2(c\ X)$ $Q^{\cos^4(c\,X)}$ +1)+O(x^5) $T_{2\,c^2\,Q^{1-2\sin^2(c\,X)+\sin^4(c\,X)}\log(Q)-2\,c^2\,Q^{1-2\sin^2(c\,X)+\sin^4(c\,X)}\log(Q)\sin^2(c\,X)}(x)$ $T_{c^2\,Q^{1/4\,(1+2\cos(2\,c\,X)+1/2\,(1+\cos(4\,c\,X)))}\log(Q)+c^2\,Q^{1/4\,(1+2\cos(2\,c\,X)+1/2\,(1+\cos(4\,c\,X)))}\cos(2\,c\,X)\log(Q)}(x)$ cos(2 c^2 log(Q) $\cos^{-1}(x)$ $\cos^2(c\ X)$ $Q^{\cos^4(c\,X)}$)+ constant for the QuantumDistance [Entanglement Entropy [qstate_{Δ˜ ⊗ pi⁞FFFTˆUμ} (X) ⁞∅ (AoΨo, d) Ÿ, [H] ⊗̂ [Ho] ∮∫̄ i [Ψ]] [QFTq] ψo MG)ˆ(ωsinθ/2), SˆMNI,1/2pi˜ (i sin (-1/3 (24r), SphericalHarmonicY Hypergeometric0F1 [PolyLog [logi, ⁞ψ˜ [QFTq] (α) ⟩) μ, (x)) J (r′)), iQFTG-1/334 sinˆ (-123), logLnAdS5/θZG⁞xi,5 ChebyshevT[n, Q^Cos[X c] ^4, ArcSin[r] ^(2 x)] GegenbauerC[Sum[μ, {ν, 0, ι}] n, Integrate[μ, ν, ω, σ] x] WhittakerM[(Sin[ω] (21/22)) d ω c^Cos[GoldenRatio], (c^4/(4 G M)) m d λ^ω, I z] iC[n δ] Cos[GoldenRatio x] (-4 c^2 Q^Cos[c X] ^4 Cos[c X] ^4 Log[Q] Derivative[0, 1, 0] [ChebyshevT] [n Sin[ω], Q^Cos[c X] ^4, x ArcSin[r] ^2] + 12 c^2 Q^Cos[c X] ^4 Cos[c X] ^2 Log[Q] Sin[c X] ^2 Derivative[0, 1, 0] [ChebyshevT] [n Sin[ω], Q^Cos[c X] ^4, x ArcSin[r] ^2] + 16 c^2 Q^Cos[c X] ^4 Cos[c X] ^6 Log[Q] ^2 Sin[c X] ^2 Derivative[0, 1, 0] [ChebyshevT] [n Sin[ω], Q^Cos[c X] ^4, x ArcSin[r] ^2] + 16 c^2 Q^(2 Cos[c X] ^4) Cos[c X] ^6 Log[Q] ^2 Sin[c X] ^2 Derivative[0, 2, 0] [ChebyshevT] [n Sin[ω], Q^Cos[c X] ^4, x ArcSin[r] ^2]) in combination with ((Cluster of BIOGENEA_ CONSENSUS_Eqs.1-25), (Supplement Material FUNCTIONS.1 - 17)) and for a complete decision tree search of all possible combinations of fragmentation, merging, and pharmacophoric re-coring systems of 4-[3-(aminomethyl)oxiren- 2-yl]-4,5-diaza-2λ⁵-phosphaspiro[bicyclo[3.1.0]hexane-2,2'-oxaphosphirane]-3-thione, (1S,5S)-4-[(2R,3S)-3- [(3R)-2-amino- 1-fluoro-5- sulfanylidene-3H-1,2,4-triazol-3-y l]oxiran-2-yl]-4,5,6-triaza-2λ⁵-phosphaspiro[bicyclo [3.1.0]hexane-2,2'- oxaphosphirane]-3-thione , and [2-(aminomethyl)-2-{[(2E)-3- oxofuran-2-ylidene]methyl}-2λ⁵- azaphosphiridin-1-yl]amino (1R,4S)-3,3-

 doi:10.20944/preprints202403.0518.v1

dimethyl-6-oxo-2λ⁴-thia-5-azaspiro [bicyclo[3.2.0]heptane-2,1'-thiirane]-4-carboxylate targeted inside the SARS-CoV Mpro protein targets. In this context of mathematical chemistry functions the main obstacle of calling the related solvable matrices H Hamiltonians appeared in their asymmetry (i.e., nonHermiticity) is to qualify these matrices from playing the role of operators of observables to quaternary structure that are guided by entropy-enthalpy compensations at the docking sites in between protein subunits according to the Gibbs free energy equation. [2-140,162-195] The druggability from these newgly designed structures was verified by DockThor docking analyses of a dozen structures of dimers. Until now, Quantum algorithms to simulate QFT have mainly used lattices as particular types of regulator, which allows a computer simulation of QFT. [2-70,132-195] However, while this lattice breaks Lorentz's invariance, my regulator does not, because these seven dimensional Chern–Simons Computated attractors become a singularity in which all the degrees of freedom of the boson field were lost in a fuzzy sphere ((Iconics1-4), (Eqs1-400), Supplementary Material METHODS AND MATERIALS (1), (2)),(Figures S(1-67)) that carries over to show $x1x2p1p2v$ 0,1,2…. λ 1/2, γ2,1/4c1 ⟨ FF|⌀ (AoΨo, d) V̈, [H] ⊗̂ [Ho] ∯∫ i [Ψ] [EntanglementEntropy [qstate_ [QFTq] ψoMG)] ˆ(ωsinθ/2), SˆMNI,1/2pi˜ (i sin (-1/3 (24r), |ψ˜ [QFTq] (α) ⟩) μ, (x)) J (r′)) [A [Ψo$sin\phi${Ψ}]] V̈ ⊕ G|xi, ||cert.ˆ||{Ψ}⟩ˆ0||ψj⟩ N−Tr (ϱcrˆϱcrˆAoΨo) −∑∑∑AoΨoNi when substituted to (Eqs.1-400), (Cluster of BIOGENEA_ CONSENSUS_Eqs.1-26), (Supplement Material FUNCTIONS.1 - 18) and has the same rotational symmetry as the ordinary sphere. For instance, a number of state-of-the-art algorithms for error correcting sequencing data [4-195] leverage Bloom filters [4-166], a probabilistic data structure related to hash tables. The core benefit of a Bloom filter comes from its ability to trade a low probability of false positive lookups for significant savings in memory, a common constraint in large bioinformatics pipelines. [3-99,135-185] As Maas writes in his lectures: ". it is an unfortunate consequence of this current understanding of Quantum fields theory that the need to have regulators always implies that some symmetries are broken, no matter what, until the regulator it is not removed". It should be noted, however, that Lorentz's invariance is restored on the fuzzy sphere like drug designs ((Iconics1-4), (Eqs1-400), Supplementary Material METHODS AND MATERIALS (1), (2)),(Supplementary Material METHODS AND MATERIALS Figures S(1-80)). In contrast to the recent theoretical experiments with discrete models possessing point-like impurities [6-190] or boundary terms [13-170,178-195], the interaction in our 20 one-parametric solvable models is a smooth function of position by sequence aligners such as Bowtie [4-98], the BWA family of aligners [4-181,194] and more recent graph reference genome aligners [42-173]. A lattice is a mathematical artifact, as also Preskill says: "The lattice is an artifice introduced for convenience." This is an innovation which may be considered natural. In various limits and dynamical regimes we may then specify energies En and wave functions of (∂/(∂ c)) (2 c² $Q^{\cos^4(cX)}$ cos²(c X) log(Q))==-4 c log(Q) cos(c X) $Q^{\cos^4(cX)}$ (2 c X log(Q) sin(c X) cos⁴(c X)+c X sin(c X)-cos(c X)) for $\sqrt{4\,e^{-2\,\mathrm{Re}(d\log(\nu))}\left|\frac{T_{\alpha\,\mu\,\nu}d\left(z^b\right)\,{}_2F_1(a,\,b;\,c;\,x)}{\alpha\,\mu}\right|^2+\left|\lambda_{n,m}(\gamma)\right|^2}$

SpheroidalEigenvalue[n, m, γ] ZernikeR[LegendreP[LaguerreL[ArcSin[λ n], D f z, g z (ψ^0 ϱ m), I Exp[λ]], x], m, r] Hypergeometric1F1Regularized [a^5, D[ϱ^6 n^4 (Pi r), y, x] b, g^8, Exp[n] ^Þ^6, δ σ^2, ε θ^3, Δ α^4] Hypergeometric0F1Regularized[a, z] JacobiP[ArcSin[θ n], λ a, λ b, (Cos[x] (ChebyshevU[Cos[x], M u ν^16 z] Hypergeometric1F1[ArcSin[ω], Cos[GoldenRatio b], z])) HypergeometricU[a^(α β), b^(μ ν), z] WhittakerM[k λ, m ν, z θ]] 1F1(sin^(-1)(ψ cos^16(ω)), cos(ϕ b), z^24) U(a^(Φ α β), b^(ψ o ω), z) M_(k λ, m ν)(z θ) Hypergeometric1F1[a, b, x] SpheroidalPS[Cos[23 Δ γ (σ c)] ^21/22, m^4 ((Pi R)/3), γ^N4, z^5] SpheroidalEigenvalue[Log[Exp[n]] ^7, Sin[m] ^3, Cos[γ] ^5] Hypergeometric1F1[Cos[a] ^8, b^14, z^16] WhittakerM[(21/22) μ^24 ω, (c^4 (λ/(4 G M))) m, z] Hypergeometric1F1[ArcSin[ψ (Cos[ω] ^(δ λ)/16)], Cos[GoldenRatio b] Cos[z ω], Exp[θ z] ^24] WhittakerM[k Sin[λ], δ Cos[m] (δ GoldenRatio ArcSin[ν]), z θ] |ψni using the broad menu of formulae available for orthogonal polynomials where the eigenstates of H were selected, for the sake of definiteness, in the closed form of Gegenbauer orthogonal polynomials. In my case, instead, the

 doi:10.20944/preprints202403.0518.v1

regulator is physical, because the discretization is induced by the Quantum fluctuations of the ϱcr^ metric in the attractor basin enjoying the gauge invariance A ~ A, dAε, with operator valued Grassmann-even gauge parameters εε (c) and covariant derivative dA: d, (A) by implying a correlation between the missing mass of elliptical structures and their ellipticities after considering lattice Hamiltonians with local molecular interactions as an artifice no matter what, until the most convenient regulator it is not removed or substituted. I just recalled and used their argumentation in a new concrete application. Our method of the reconstruction of the metric based on the use of discrete Hamiltonians and mediated by the computer-assisted solution of Dieudonn´e's Eq. proved very efficient. It led to compact analytic formulae for a family of metrics. New discrete-lattice quantum model has been found as described by the pair of matrices (H, Θ). [2-160,101-175] These Quantum QFT Fluctuations bear similarity to many classical approaches used to improve and stabilize training landscapes in practice, such as batch normalization [38–179-192] and self-normalizing neural networks [38-99,102-192] while providing improved training homeopath landscapes that may result in more rapid convergence. However it is unclear whether this type of advantage alone can be made practical by allowing for a small universe like druggable model to be trained by classical means. The net gain was that the bound-state energies became obtainable by the diagonalization of the simplified bosonic Hamiltonian H 6= H†. The price to be paid was that the latter operator proved manifestly non-Hermitian in the usual, "friendly" Hilbert space H(F) with trivial Θ(F) = I. Fortunately, improvements in training landscapes have been seen to co-occur with reductions in generalization error [20–100-190]. Generalization error measures the ability of this machine learning model to maintain similar performance (i.e., 'generalizability') on unseen geometry data. [38-192] In other branches of physics the recipe has been revitalized in connection with the emergence of PT −symmetric quantum systems [33, 34, 35-193]. This will open new horizon in particle physics [36] and in relativistic quantum fields theory [37-184] reductions, and maybe in generalization error may yield advantages in the accuracy and flexibility of these trained machine learning models as Quantum Homeopathy advantages in generalization error that are dependent on a variety of factors, including the encoding used with basis encoding performing particularly poorly [39-193]) and the availability of data sufficient to train a comparable drug designing classical model [2-191]. Also, while in this case of a QFT to QM Ansatz reduction regulator the limit of the continuum is reached (but not always) when the number of binding sites is huge and the spacing approaches at Avogadro's number power levels. In my case of infinite volume for unitarily screening methods there is the classic limit that is reached when the fluctuations of the Quantum metrics vanish near the attractor following conditions for consistent calculation of molecular dynamics holonomies around the three equatorial $L_{i^n\lambda}^{\left(0+6.02214076\times 10^{23}\, i\right) F\, m\, o\, q\, Q\, T\, \rho\, \psi}\left(i\, e^{\lambda}\right)$ $h^{\nu\ r}$ ψ cos(γ) (b j+x)*1/P r ψ $\cos^{c^4\, G\, M^2\, \pi\, r\, R\, S^{10}\, x\, \delta\, \theta^4}$ (γ)1/P r ψ² (b j+x) $h^{\nu\ r}$ $2^{\pi\left(-c^4\right)\delta\, G\, \theta^4\, M^2\, r\, R\, S^{10}\, x-1}$ $\left(e^{-i\,\gamma}+e^{i\,\gamma}\right)^{\pi\, c^4\, \delta\, G\, \theta^4\, M^2\, r\, R\, S^{10}\, x+1}$ $L_{i^n\lambda}^{\left(6.02214\times 10^{23}\, i\right) F\, m\, o\, q\, Q\, T\, \rho\, \psi}\left(i\, e^{\lambda}\right)$ (b j r ψ² cos(γ) $h^{\nu\ r}$ $L_{i^n\lambda}^{\left(6.02214\times 10^{23}\, i\right) F\, m\, o\, q\, Q\, T\, \rho\, \psi}\left(i\, e^{\lambda}\right)$)/P+1/P r ψ² x cos(γ) $h^{\nu\ r}$ $L_{i^n\lambda}^{\left(6.02214\times 10^{23}\, i\right) F\, m\, o\, q\, Q\, T\, \rho\, \psi}\left(i\, e^{\lambda}\right)$ (π b c⁴ δ G θ⁴ j M² r R S¹⁰ log(cos(γ))+1)+1/(2 P) π c⁴ δ G θ⁴ M² r² R S¹⁰ ψ² x² cos(γ) log(cos(γ)) $h^{\nu\ r}$ $L_{i^n\lambda}^{\left(6.02214\times 10^{23}\, i\right) F\, m\, o\, q\, Q\, T\, \rho\, \psi}\left(i\, e^{\lambda}\right)$ (π b c⁴ δ G θ⁴ j M² r R S¹⁰ log(cos(γ))+2)+1/(6 P) π² c⁸ δ² G² θ⁸ M⁴ r³ R² S²⁰ ψ² x³ cos(γ) log²(cos(γ)) $h^{\nu\ r}$ $L_{i^n\lambda}^{\left(6.02214\times 10^{23}\, i\right) F\, m\, o\, q\, Q\, T\, \rho\, \psi}\left(i\, e^{\lambda}\right)$ (π b c⁴ δ G θ⁴ j M² r R S¹⁰ log(cos(γ))+3)+1/(24 P) π³ c¹² δ³ G³ θ¹² M⁶ r⁴ R³ S³⁰ ψ² x⁴ cos(γ) log³(cos(γ)) $h^{\nu\ r}$ $L_{i^n\lambda}^{\left(6.02214\times 10^{23}\, i\right) F\, m\, o\, q\, Q\, T\, \rho\, \psi}\left(i\, e^{\lambda}\right)$ (π b c⁴ δ G θ⁴ j M² r R S¹⁰ log(cos(γ))+4)+O(x⁵)(∂/(∂ x)) (1/P r ψ² (b j+x) $h^{\nu\ r}$ $\cos^{\pi\, c^4\, \delta\, G\, \theta^4\, M^2\, r\, R\, S^{10}\, x+1}(\gamma)$ $L_{i^n\lambda}^{602\,214\,075\,999\,999\,987\,023\,872\, i\, F\, m\, o\, q\, Q\, T\, \rho\, \psi}\left(i\, e^{\lambda}\right)$)==1/P r ψ² $h^{\nu\ r}$ $\cos^{\pi\, c^4\, \delta\, G\, \theta^4\, M^2\, r\, R\, S^{10}\, x+1}(\gamma)$ $L_{i^n\lambda}^{602\,214\,075\,999\,999\,987\,023\,872\, i\, F\, m\, o\, q\, Q\, T\, \rho\, \psi}\left(i\, e^{\lambda}\right)$ (π c⁴ δ G θ⁴ M² r R

S^{10} (b j+x) log(cos(γ))+1)\[Integral]1/P h^{r} $^{\nu}$ r (b j+x) ψ^2 $\cos^{1+c^4\,G\,M^2\,\pi\,r\,R\,S^{10}\,x\,\delta\,\theta^4}$ (γ)

$L_{i^n\lambda}^{\left(6.02214\times10^{23}\,i\right)F\,m\,o\,q\,Q\,T\,\rho\,\psi}\left(i\,e^{\lambda}\right)$ x==(0.101321 ψ^2 h^{ν} ^{r} $\cos^{3.14159\,c^4\,\delta\,G\,\theta^4\,M^2\,r\,R\,S^{10}\,x+1}$ (γ)

$L_{i^n\lambda}^{\left(6.02214\times10^{23}\,i\right)F\,m\,o\,q\,Q\,T\,\rho\,\psi}\left(i\,2.71828^{\lambda}\right)$ (3.14159 c^4 δ G θ^4 M^2 r R S^{10} (b j+x) log(cos(γ))-1))/(c^8 δ^2 G^2 θ^8 M^4 P r R^2 S^{20} $\log^2(\cos(\gamma)))$(b j r ψ^2 h^{ν} ^{r} $\cos^{\pi\,c^4\,\delta\,G\,\theta^4\,M^2\,r\,R\,S^{10}\,x+1}$ (γ)

$L_{i^n\lambda}^{\left(6.02214\times10^{23}\,i\right)F\,m\,o\,q\,Q\,T\,\rho\,\psi}\left(i\,e^{\lambda}\right)$)/P+(r x ψ^2 h^{ν} ^{r} $\cos^{\pi\,c^4\,\delta\,G\,\theta^4\,M^2\,r\,R\,S^{10}\,x+1}$ (γ)

$L_{i^n\lambda}^{\left(6.02214\times10^{23}\,i\right)F\,m\,o\,q\,Q\,T\,\rho\,\psi}\left(i\,e^{\lambda}\right)$)/P+ constant for (∂(Tr[ψ,{2}] DensityMatrix)/∂$\log^{\varrho}(\psi)$ A log(B^G h^{ν} n π Q δ μ σ (sin(ω) (ϱ A))) 76 10000000000000000000000000000 logG(z)) 6.022 140+G h^{ν} n π Q δ μ σ sin(ω)+c^8 π^2 r^2 δ^2 θ^{20}==9.8696 (c^8 r^2 δ^2 θ^{20}+6.49206*10^{30} ∂(DensityMatrix Tr[ψ,{2}])/(∂A $\log^{\varrho}(\psi)$ log(1/2 A

$$\sum_{j=0}^{\infty}\mathrm{Res}_{s=-j}\frac{4^s\left(\omega^2\right)^{-s}\Gamma(s)}{\Gamma\left(\frac{3}{2}-s\right)}$$

h^{ν} n $\pi^{3/2}$ Q B^G δ μ ϱ σ ω)) logG(z)+0.282095 G h^{ν} n Q δ μ σ ω

$$\sum_{j=0}^{\infty}\mathrm{Res}_{s=-j}\frac{4^s\left(\omega^2\right)^{-s}\Gamma(s)}{\Gamma\left(\frac{3}{2}-s\right)}$$

) {{$L_{\lambda\,i^n}$(I $E^{\lambda})^2$+(1.20443*10^{24} I) F m o ϱ q Q T ψ $L_{i^n\lambda}$(I E^{λ}) LaguerreL$^{(0,1,0)}$(λ I^{n},0,I E^{λ})+F^2 m^2 o^2 ϱ^2 q^2 Q^2 T^2 ψ^2 (-3.62662*10^{47} LaguerreL^(0,1,0)(λ I^n,0,I E^λ)²-3.62662*10^{47} $L_{i^n\lambda}$(I E^{λ}) LaguerreL$^{(0,2,0)}$(λ I^{n},0,I E^{λ}))+F^3 m^3 o^3 ϱ^3 q^3 Q^3 T^3 ψ^3 ((-2.184*10^{71} I) LaguerreL$^{(0,1,0)}$(λ I^{n},0,I E^{λ}) LaguerreL$^{(0,2,0)}$(λ I^{n},0,I E^{λ})-(7.28*10^{70} I) $L_{i^n\lambda}$(I E^{λ}) LaguerreL$^{(0,3,0)}$(λ I^{n},0,I E^{λ}))+F^4 m^4 o^4 ϱ^4 q^4 Q^4 T^4 ψ^4 (3.28809*10^{94} LaguerreL^(0,2,0)(λ I^n,0,I E^λ)²+4.38412*10^{94} LaguerreL$^{(0,1,0)}$(λ I^{n},0,I E^{λ}) LaguerreL$^{(0,3,0)}$(λ I^{n},0,I E^{λ})+1.09603*10^{94} $L_{i^n\lambda}$(I E^{λ}) LaguerreL$^{(0,4,0)}$(λ I^{n},0,I E^{λ}))+O(q^5)}, {(Taylor series)}} when H, ∂M↓ ⊗ ∯∯∯ | ∅ iΨ∇̈ ⊕, QFTq. ZernikeR[Hypergeometric2F1Regularized[-LaguerreL[I^n λ, (0. + 6.02214076*^23 I) F m o q Q T ϱ ψ, I E^λ], 1 + LaguerreL[I^n λ, (0. + 6.02214076*^23 I) F m o q Q T ϱ ψ, I E^λ], 1, 1/2], (m δ θ^10 ψ Ψ Log[y] ^2)/(10000000000000000000000000000 E^((N Pi)/2)), r] + (x Hypergeometric2F1Regularized[1 - LaguerreL[I^n λ, (0. + 6.02214076*^23 I) F m o q Q T ϱ ψ, I E^λ], 2 + LaguerreL[I^n λ, (0. + 6.02214076*^23 I) F m o q Q T ϱ ψ, I E^λ], 2, 1/2] LaguerreL[I^n λ, (0. + 6.02214076*^23 I) F m o q Q T ϱ ψ, I E^λ] (1 + LaguerreL[I^n λ, (0. + 6.02214076*^23 I) F m o q Q T ϱ ψ, I E^λ]) Derivative[1, 0, 0] [ZernikeR] [Hypergeometric2F1 Regularized[-LaguerreL[I^n λ, (0. + 6.02214076*^23 I) F m o q Q T ϱ ψ, I E^λ], 1 + LaguerreL[I^n λ, (0. + 6.02214076*^23 I) F m o q Q T ϱ ψ, I E^λ], 1, 1/2], (m δ θ^10 ψ Ψ Log[y] ^2)/(10000000000000000000000000000 E^((N Pi)/2)), r])/2 + (x^2 LaguerreL[I^n λ, (0. + 6.02214076*^23 I) F m o q Q T ϱ ψ, I E^λ] (1 + LaguerreL[I^n λ, (0. + 6.02214076*^23 I) F m o q Q T ϱ ψ, I E^λ]) (Hypergeometric2F1Regularized[2 - LaguerreL[I^n λ, (0. + 6.02214076*^23 I) F m o q Q T ϱ ψ, I E^λ], 3 + LaguerreL[I^n λ, (0. + 6.02214076*^23 I) F m o q Q T ϱ ψ, I E^λ], 3, 1/2] (-1 + LaguerreL[I^n λ, (0. + 6.02214076*^23 I) F m o q Q T ϱ ψ, I E^λ]) (2 + LaguerreL[I^n λ, (0. + 6.02214076*^23 I) F m o q Q T ϱ ψ, I E^λ]) Derivative[1, 0, 0] [ZernikeR] [Hypergeometric2F1Regularized[-LaguerreL[I^n λ, (0. + 6.02214076*^23 I) F m o q Q T ϱ ψ, I E^λ], 1 + LaguerreL[I^n λ, (0. + 6.02214076*^23 I) F m o q Q T ϱ ψ, I E^λ], 1, 1/2], (m δ θ^10 ψ Ψ Log[y] ^2)/(10000000000000000000000000000 E^((N Pi)/2)), r] + Hypergeometric2F1Regularized[1 - LaguerreL[I^n λ, (0. + 6.02214076*^23 I) F m o q Q T ϱ ψ, I E^λ], 2 + LaguerreL[I^n λ, (0. + 6.02214076*^23 I) F m o q Q T ϱ ψ, I E^λ], 2, 1/2] ^2 LaguerreL[I^n λ, (0. + 6.02214076*^23 I) F m o q Q T ϱ ψ, I E^λ] (1 + LaguerreL[I^n λ, (0. + 6.02214076*^23 I) F m o q Q T ϱ ψ, I E^λ]) Derivative[2, 0, 0] [ZernikeR] [Hypergeometric2F1Regularized[-LaguerreL[I^n λ, (0. + 6.02214076*^23 I) F m o q Q T ϱ ψ, I E^λ], 1 + LaguerreL[I^n λ, (0. + 6.02214076*^23 I) F m o q Q T ϱ ψ, I E^λ], 1, 1/2], (m δ θ^10 ψ Ψ Log[y] ^2)/(10000000000000000000000000000 E^((N Pi)/2)), r]))/8 + (x^3 LaguerreL[I^n λ, (0. + 6.02214076*^23 I) F m o q Q T ϱ ψ, I E^λ] (1 + LaguerreL[I^n λ, (0. + 6.02214076*^23 I) F m o q Q T ϱ ψ, I E^λ]) (Hypergeometric2F1Regularized[3 - LaguerreL[I^n λ, (0. + 6.02214076*^23 I) F m o q Q T ϱ ψ, I E^λ], 4 + LaguerreL[I^n λ, (0. + 6.02214076*^23 I) F m o q Q T ϱ ψ, I E^λ], 4, 1/2] (-2 + LaguerreL[I^n

 doi:10.20944/preprints202403.0518.v1

λ, (0. + 6.02214076*^23 I) F m o q Q T ϱ ψ, I E^λ]) (-1 + LaguerreL[I^n λ, (0. + 6.02214076*^23 I) F m o q Q T ϱ ψ, I E^λ]) (2 + LaguerreL[I^n λ, (0. + 6.02214076*^23 I) F m o q Q T ϱ ψ, I E^λ]) (3 + LaguerreL[I^n λ, (0. + 6.02214076*^23 I) F m o q Q T ϱ ψ, I E^λ]) Derivative[1, 0, 0] [ZernikeR] [Hypergeometric2F1Regularized[-LaguerreL[I^n λ, (0. + 6.02214076*^23 I) F m o q Q T ϱ ψ, I E^λ], 1 + LaguerreL[I^n λ, (0. + 6.02214076*^23 I) F m o q Q T ϱ ψ, I E^λ], 1, 1/2], (m δ θ^10 ψ Ψ Log[y] ^2)/(10000000000000000000000000000 E^((N Pi)/2)), r] + 3 Hypergeometric2F1Regularized[1 - LaguerreL[I^n λ, (0. + 6.02214076*^23 I) F m o q Q T ϱ ψ, I E^λ], 2 + LaguerreL[I^n λ, (0. + 6.02214076*^23 I) F m o q Q T ϱ ψ, I E^λ], 2, 1/2] Hypergeometric2F1Regularized[2 - LaguerreL[I^n λ, (0. + 6.02214076*^23 I) F m o q Q T ϱ ψ, I E^λ], 3 + LaguerreL[I^n λ, (0. + 6.02214076*^23 I) F m o q Q T ϱ ψ, I E^λ], 3, 1/2] (-1 + LaguerreL[I^n λ, (0. + 6.02214076*^23 I) F m o q Q T ϱ ψ, I E^λ]) LaguerreL[I^n λ, (0. + 6.02214076*^23 I) F m o q Q T ϱ ψ, I E^λ] (1 + LaguerreL[I^n λ, (0. + 6.02214076*^23 I) F m o q Q T ϱ ψ, I E^λ]) (2 + LaguerreL[I^n λ, (0. + 6.02214076*^23 I) F m o q Q T ϱ ψ, I E^λ]) Derivative[2, 0, 0] [ZernikeR] [Hypergeometric2F1Regularized[-LaguerreL[I^n λ, (0. + 6.02214076*^23 I) F m o q Q T ϱ ψ, I E^λ], 1 + LaguerreL[I^n λ, (0. + 6.02214076*^23 I) F m o q Q T ϱ ψ, I E^λ], 1, 1/2], (m δ θ^10 ψ Ψ Log[y] ^2)/(10000000000000000000000000000 E^((N Pi)/2)), r] + Hypergeometric2F1Regularized[1 - LaguerreL[I^n λ, (0. + 6.02214076*^23 I) F m o q Q T ϱ ψ, I E^λ], 2 + LaguerreL[I^n λ, (0. + 6.02214076*^23 I) F m o q Q T ϱ ψ, I E^λ], 2, 1/2] ^3 LaguerreL[I^n λ, (0. + 6.02214076*^23 I) F m o q Q T ϱ ψ, I E^λ] ^2 (1 + LaguerreL[I^n λ, (0. + 6.02214076*^23 I) F m o q Q T ϱ ψ, I E^λ])^2 Derivative[3, 0, 0] [ZernikeR] [Hypergeometric2F1Regularized[-LaguerreL[I^n λ, (0. + 6.02214076*^23 I) F m o q Q T ϱ ψ, I E^λ], 1 + LaguerreL[I^n λ, (0. + 6.02214076*^23 I) F m o q Q T ϱ ψ, I E^λ], 1, 1/2], (m δ θ^10 ψ Ψ Log[y] ^2)/(10000000000000000000000000000 E^((N Pi)/2)), r]))/48 + (x^4 LaguerreL[I^n λ, (0. + 6.02214076*^23 I) F m o q Q T ϱ ψ, I E^λ] (1 + LaguerreL[I^n λ, (0. + 6.02214076*^23 I) F m o q Q T ϱ ψ, I E^λ]) (Hypergeometric2F1Regularized[4 - LaguerreL[I^n λ, (0. + 6.02214076*^23 I) F m o q Q T ϱ ψ, I E^λ], 5 + LaguerreL[I^n λ, (0. + 6.02214076*^23 I) F m o q Q T ϱ ψ, I E^λ], 5, 1/2] (-3 + LaguerreL[I^n λ, (0. + 6.02214076*^23 I) F m o q Q T ϱ ψ, I E^λ]) (-2 + LaguerreL[I^n λ, (0. + 6.02214076*^23 I) F m o q Q T ϱ ψ, I E^λ]) (-1 + LaguerreL[I^n λ, (0. + 6.02214076*^23 I) F m o q Q T ϱ ψ, I E^λ]) (2 + LaguerreL[I^n λ, (0. + 6.02214076*^23 I) F m o q Q T ϱ ψ, I E^λ]) (3 + LaguerreL[I^n λ, (0. + 6.02214076*^23 I) F m o q Q T ϱ ψ, I E^λ]) (4 + LaguerreL[I^n λ, (0. + 6.02214076*^23 I) F m o q Q T ϱ ψ, I E^λ]) Derivative[1, 0, 0] [ZernikeR] [Hypergeometric2F1Regularized[-LaguerreL[I^n λ, (0. + 6.02214076*^23 I) F m o q Q T ϱ ψ, I E^λ], 1 + LaguerreL[I^n λ, (0. + 6.02214076*^23 I) F m o q Q T ϱ ψ, I E^λ], 1, 1/2], (m δ θ^10 ψ Ψ Log[y] ^2)/(10000000000000000000000000000 E^((N Pi)/2)), r] + (-1 + LaguerreL[I^n λ, (0. + 6.02214076*^23 I) F m o q Q T ϱ ψ, I E^λ]) LaguerreL[I^n λ, (0. + 6.02214076*^23 I) F m o q Q T ϱ ψ, I E^λ] (1 + LaguerreL[I^n λ, (0. + 6.02214076*^23 I) F m o q Q T ϱ ψ, I E^λ]) (2 + LaguerreL[I^n λ, (0. + 6.02214076*^23 I) F m o q Q T ϱ ψ, I E^λ]) (3 Hypergeometric2F1Regularized[2 - LaguerreL[I^n λ, (0. + 6.02214076*^23 I) F m o q Q T ϱ ψ, I E^λ], 3 + LaguerreL[I^n λ, (0. + 6.02214076*^23 I) F m o q Q T ϱ ψ, I E^λ], 3, 1/2] ^2 (-1 + LaguerreL[I^n λ, (0. + 6.02214076*^23 I) F m o q Q T ϱ ψ, I E^λ]) (2 + LaguerreL[I^n λ, (0. + 6.02214076*^23 I) F m o q Q T ϱ ψ, I E^λ]) + 4 Hypergeometric2F1Regularized[1 - LaguerreL[I^n λ, (0. + 6.02214076*^23 I) F m o q Q T ϱ ψ, I E^λ], 2 + LaguerreL[I^n λ, (0. + 6.02214076*^23 I) F m o q Q T ϱ ψ, I E^λ], 2, 1/2] Hypergeometric2F1Regularized[3 - LaguerreL[I^n λ, (0. + 6.02214076*^23 I) F m o q Q T ϱ ψ, I E^λ], 4 + LaguerreL[I^n λ, (0. + 6.02214076*^23 I) F m o q Q T ϱ ψ, I E^λ], 4, 1/2] (-2 + LaguerreL[I^n λ, (0. + 6.02214076*^23 I) F m o q Q T ϱ ψ, I E^λ]) (3 + LaguerreL[I^n λ, (0. + 6.02214076*^23 I) F m o q Q T ϱ ψ, I E^λ])) Derivative[2, 0, 0] [ZernikeR] [Hypergeometric2F1Regularized[-LaguerreL[I^n λ, (0. + 6.02214076*^23 I) F m o q Q T ϱ ψ, I E^λ], 1 + LaguerreL[I^n λ, (0. + 6.02214076*^23 I) F m o q Q T ϱ ψ, I E^λ], 1, 1/2], (m δ θ^10 ψ Ψ Log[y] ^2)/(10000000000000000000000000000 E^((N Pi)/2)), r] + 6 Hypergeometric2F1Regularized[1 - LaguerreL[I^n λ, (0. + 6.02214076*^23 I) F m o q Q T ϱ ψ, I E^λ], 2 + LaguerreL[I^n λ, (0. + 6.02214076*^23 I) F m o q Q T ϱ ψ, I E^λ], 2, 1/2] ^2 Hypergeometric2F1Regularized[2 - LaguerreL[I^n λ, (0. + 6.02214076*^23 I) F m o q Q T ϱ ψ, I E^λ], 3 + LaguerreL[I^n λ, (0. + 6.02214076*^23 I) F m o q Q T ϱ ψ, I E^λ], 3, 1/2] (-1 + LaguerreL[I^n λ, (0. + 6.02214076*^23 I) F m o q Q T ϱ ψ, I E^λ]) LaguerreL[I^n λ, (0. + 6.02214076*^23 I) F m o q Q T ϱ ψ, I E^λ] ^2 (1 + LaguerreL[I^n λ, (0. + 6.02214076*^23 I) F m o q Q T ϱ ψ, I E^λ])^2 (2 + LaguerreL[I^n λ, (0. + 6.02214076*^23 I) F m o q Q T

 doi:10.20944/preprints202403.0518.v1

ϱ ψ, I E^λ]) Derivative[3, 0, 0] [ZernikeR] [Hypergeometric2F1Regularized[-LaguerreL[I^n λ, (0. + 6.02214076*^23 I) F m o q Q T ϱ ψ, I E^λ], 1 + LaguerreL[I^n λ, (0. + 6.02214076*^23 I) F m o q Q T ϱ ψ, I E^λ], 1, 1/2], (m δ θ^10 ψ Ψ Log[y] ^2)/(10000000000000000000000000000 E^((N Pi)/2)), r] + Hypergeometric2F1Regularized[1 - LaguerreL[I^n λ, (0. + 6.02214076*^23 I) F m o q Q T ϱ ψ, I E^λ], 2 + LaguerreL[I^n λ, (0. + 6.02214076*^23 I) F m o q Q T ϱ ψ, I E^λ], 2, 1/2] ^4 LaguerreL[I^n λ, (0. + 6.02214076*^23 I) F m o q Q T ϱ ψ, I E^λ] ^3 (1 + LaguerreL[I^n λ, (0. + 6.02214076*^23 I) F m o q Q T ϱ ψ, I E^λ])^3 Derivative[4, 0, 0] [ZernikeR] [Hypergeometric2F1Regularized[-LaguerreL[I^n λ, (0. + 6.02214076*^23 I) F m o q Q T ϱ ψ, I E^λ], 1 + LaguerreL[I^n λ, (0. + 6.02214076*^23 I) F m o q Q T ϱ ψ, I E^λ], 1, 1/2], (m δ θ^10 ψ Ψ Log[y] ^2)/(10000000000000000000000000000 E^((N Pi)/2)), r]))/384 + O[x] ^5 V̈ ⊕ G⁞xi, [H] [∂] ~ [NM] edges conducted for the docked SARS-Cov2 protein and Gissitorviffirna_TM ligand complexes. [1-99,90,149-195] The delicacy of these Quantum Homeopathy States makes a practical path for a pharmacophore merging algorithm imperative where classical notions of resource utilizations can be directly applicable when trying to preserve the topological nature of CS theory for the generation of these unique drug designs with the highest Quantum Energy Negativities when compared to other known SARS - CoV - 2 antivirals. [11-99,118-195] In this context, the generalized fragments are viewed as external sources that have the ability to produce an effective description of Quantum Hall effect, and can be coupled to the Chern - Simons theory. [11–80,133-193] In this effort, I propose computer-aided and Quantum Homeopathy-directed rational drug design strategies efficient in computing docking usage, and powerful enough to achieve very high accuracy levels for this in-silico effort for the generation of Quantum Turing Homeopathy Ruled molecules of DRVYIHPF-mimetic, Gisitorviffirna_TM, Roccustyrna_gs, Gissitorviffirna_TM, Roccostyrna_ gs_consv, and Roccustyrna _fr ligands targeting the COVID-19-SARS-COV-2 SPIKE D614G mutation by unifying Quantum Homeopathy Molecular Pairs (QHMMP), Lindenbaum-Tarski logical spaces and Adaptive Weighted KNN Positioning for Matched Bemis and Murko (BM) driven eigenvalue statements into Shannon entropy quantities as composed by Tipping–Ogilvie driven Machine Learning potentials on a (DFT) ℓneuron (ι) (Eqs.1-400), ((Iconics1-4), (Eqs1-400), and (Schematics1a,1b,1c,1d,1e,1f,1g,1h,1i,1j,1k,1l,1m), (I-VI) Supplementary Material METHODS AND MATERIALS)) (SI Appendix XXXIX), (Cluster of BIOGENEA_ CONSENSUS_Eqs.1-26), (Supplement Material FUNCTIONS.1 - 20) improver for Chern-Simons Topology Euclidean Geometrics. (SI Appendix I), (SI Appendix VIII), (SI Appendix XII), (SI Appendix XIII), (SI Appendix IX), (SI Appendix XIV), (SI Appendix XV), (SI Appendix XVI), (SI Appendix XVII), (SI Appendix XVIII), (SI Appendix XIX), (SI Appendix XX), (SI Appendix XXI), (SI Appendix XXII), (SI Appendix XXIII), (SI Appendix XXIV), (SI Appendix XXV) (SI Appendix XXVI), (SI Appendix XXVII). (SI Appendix XXVIII), (SI Appendix XXIX), (SI Appendix XXX), (SI Appendix XXXI), (SI Appendix XXXII), (SI Appendix XXXIII), (SI Appendix XXXIV), (SI Appendix XXXV), (SI Appendix XXXVI), (SI Appendix XXXVII), (SI Appendix XXXV), (SI Appendix XXXVI), (SI Appendix XXXVII), (SI Appendix XVIII), ((Cluster Docking Energy TableS1), (SI Appendix I), (Cluster Docking Energy TableS2), SI Appendix I), (Docking Energy TableS1), (SI Appendix I), (Docking Energy TableS2), (SI Appendix I), (Docking Energy TableS3), (SI Appendix I)), and ((Iconics1-4), (Eqs1-400), Supplementary Material METHODS AND MATERIALS (1), (2)),(SI Appendix XXXIX), (SI Appendix XXXIX), ((Cluster of BIOGENEA_ CONSENSUS_Eqs.1-26), (Supplement Material FUNCTIONS.1 - 21)), (OUTPUTs1-3), (Ic1a), (Ic1b), (Ic1c), (Ic2a), (Ic2b), (Ic2c), (Ic2d), (Ic2e), (Ic2f), (Ic2g),(Ic2h), (Ic2c), (Ic2g), (Ic2k), (Ic2l), (Ic2m),(Ic2n),(Ic2o),(Ic2p),(Ic2q),(Ic2r), (Ic3a), (Ic3b) (Ic3c), (Ic3d), (Ic3d), (Ic3e), (Ic3f), (Ic3g), (Ic3h), (Ic3i), (Ic3j), (Ic3k), (Iconic4), and (Supplementary Material METHODS AND MATERIALS Figures S(1- 133)), ((Iconics1-4), (Eqs1-400), Supplementary Material METHODS AND MATERIALS)). [1–29-191] It should be emphasized that here we adhere to a phenomenological Quantum Thermodynamics and Quantum Homeopathy approach, under which the details of replicator dynamics are irrelevant, in contrast, for example, to the approach of Sella and Hirsh [13-169]. [2-195] Here, I describe the basic constructions of these drug designing problems and summarize relevant AiryAi, AiryAiPrime, AiryBi, AiryAiZero, AiryBiZero $E^{-z/2}$ z^{-k} (E^{z} (Γ(2 m+1)/Γ(-k+m+1/2)+((k-m+1/2) (k+m+1/2) Γ(2 m+1))/(Γ(-k+m+1/2) z)+((k-m+1/2) (k-m+3/2) (k+m+1/2) (k+m+3/2) Γ(2 m+1))/(2 Γ(-k+m+1/2) z^2)+((k-m+1/2) (k-m+3/2) (k-m+5/2) (k+m+1/2) (k+m+3/2) (k+m+5/2) Γ(2 m+1))/(6 Γ(-k+m+1/2) z^3)+((k-m+1/2)

 doi:10.20944/preprints202403.0518.v1

(k-m+3/2) (k-m+5/2) (k-m+7/2) (k+m+1/2) (k+m+3/2) (k+m+5/2) (k+m+7/2) Γ(2 m+1))/(24 Γ(-k+m+1/2) z^4)+((k-m+1/2) (k-m+3/2) (k-m+5/2) (k-m+7/2) (k-m+9/2) (k+m+1/2) (k+m+3/2) (k+m+5/2) (k+m+7/2) (k+m+9/2) Γ(2 m+1))/(120 Γ(-k+m+1/2) z^5)+O((1/z)^6))+$z^{2\,k}$ (((-1)^(k-m+3/2) Γ(2 m+1))/Γ(k+m+1/2)+((-1)^(k-m+3/2) (-k+m+1/2) (k+m-1/2) Γ(2 m+1))/(Γ(k+m+1/2) z)-(I (-1)^(k-m) (2 k-2 m-3) (2 k-2 m-1) (2 k+2 m-3) (2 k+2 m-1) Γ(2 m+1))/(32 Γ(k+m+1/2) z^2)+(I (-1)^(k-m) (2 k-2 m-5) (2 k-2 m-3) (2 k-2 m-1) (2 k+2 m-5) (2 k+2 m-3) (2 k+2 m-1) Γ(2 m+1))/(384 Γ(k+m+1/2) z^3)-(I (-1)^(k-m) (2 k-2 m-7) (2 k-2 m-5) (2 k-2 m-3) (2 k-2 m-1) (2 k+2 m-7) (2 k+2 m-5) (2 k+2 m-3) (2 k+2 m-1) Γ(2 m+1))/(6144 Γ(k+m+1/2) z^4)+(I (-1)^(k-m) (2 k-2 m-9) (2 k-2 m-7) (2 k-2 m-5) (2 k-2 m-3) (2 k-2 m-1) (2 k+2 m-9) (2 k+2 m-7) (2 k+2 m-5) (2 k+2 m-3) (2 k+2 m-1) Γ(2 m+1))/(122880 Γ(k+m+1/2) z^5)+O((1/z)^6))) quantum functions of ZernikeR[LegendreP[LaguerreL[λ I^n, (ψ o) 6.02214076 10^23 ϱ I Q F T q m, I Exp[λ]], x], ((ψ I^(N I)) Q F T^δ θ^10 Ψ Log[y] ^2 m)/10^27, r] GegenbauerC[n, m, x] ChebyshevT[n, x] {M^2 R sin^-1(r)^4+M^2 R x sin^-1(r)^4 (N LaguerreL$^{(1,0)}$(0,0) GegenbauerC$^{(0,1,0)}$(n,0,(E a)/4)+π c^4 δ G $θ^4$ M^2 r R S^{10} log(C(logG(z) $Q^{\cos(z)}$)))+1/2 M^2 R x^2 sin^-1(r)^4 (2 π c^4 δ G $θ^4$ M^2 N r R S^{10} LaguerreL$^{(1,0)}$(0,0) GegenbauerC$^{(0,1,0)}$(n,0,(E a)/4) log(C(logG(z) $Q^{\cos(z)}$))+N^2 LaguerreL$^{(2,0)}$(0,0) GegenbauerC^(0,1,0)(n,0,(E a)/4)^2+N^2 LaguerreL$^{(1,0)}$(0,0) GegenbauerC$^{(0,2,0)}$(n,0,(E a)/4)+2 N LaguerreL$^{(1,1)}$(0,0) GegenbauerC$^{(0,1,0)}$(n,0,(E a)/4)+$π^2$ c^8 $δ^2$ G^2 $θ^8$ M^4 r^2 R^2 S^{20} log^2(C(logG(z) $Q^{\cos(z)}$)))+M^2 R x^3 sin^-1(r)^4 (1/2 $π^2$ c^8 $δ^2$ G^2 $θ^8$ M^4 N r^2 R^2 S^{20} LaguerreL$^{(1,0)}$(0,0) GegenbauerC$^{(0,1,0)}$(n,0,(E a)/4) log^2(C(logG(z) $Q^{\cos(z)}$))+1/2 π c^4 δ G $θ^4$ M^2 r R S^{10} log(C(logG(z) $Q^{\cos(z)}$)) (N^2 LaguerreL$^{(2,0)}$(0,0) GegenbauerC^(0,1,0)(n,0,(E a)/4)^2+N^2 LaguerreL$^{(1,0)}$(0,0) GegenbauerC$^{(0,2,0)}$(n,0,(E a)/4)+2 N LaguerreL$^{(1,1)}$(0,0) GegenbauerC$^{(0,1,0)}$(n,0,(E a)/4))+1/6 (N^3 LaguerreL$^{(3,0)}$(0,0) GegenbauerC^(0,1,0)(n,0,(E a)/4)^3+3 N^3 LaguerreL$^{(2,0)}$(0,0) GegenbauerC$^{(0,1,0)}$(n,0,(E a)/4) GegenbauerC$^{(0,2,0)}$(n,0,(E a)/4)+N^3 LaguerreL$^{(1,0)}$(0,0) GegenbauerC$^{(0,3,0)}$(n,0,(E a)/4)+3 N^2 LaguerreL$^{(2,1)}$(0,0) GegenbauerC^(0,1,0)(n,0,(E a)/4)^2+3 N^2 LaguerreL$^{(1,1)}$(0,0) GegenbauerC$^{(0,2,0)}$(n,0,(E a)/4)+3 N LaguerreL$^{(1,2)}$(0,0) GegenbauerC$^{(0,1,0)}$(n,0,(E a)/4))+1/6 $π^3$ c^{12} $δ^3$ G^3 $θ^{12}$ M^6 r^3 R^3 S^{30} log^3(C(logG(z) $Q^{\cos(z)}$)))+M^2 R x^4 sin^-1(r)^4 (1/6 $π^3$ c^{12} $δ^3$ G^3 $θ^{12}$ M^6 N r^3 R^3 S^{30} LaguerreL$^{(1,0)}$(0,0) GegenbauerC$^{(0,1,0)}$(n,0,(E a)/4) log^3(C(logG(z) $Q^{\cos(z)}$))+1/4 $π^2$ c^8 $δ^2$ G^2 $θ^8$ M^4 r^2 R^2 S^{20} log^2(C(logG(z) $Q^{\cos(z)}$)) (N^2 LaguerreL$^{(2,0)}$(0,0) GegenbauerC^(0,1,0)(n,0,(E a)/4)^2+N^2 LaguerreL$^{(1,0)}$(0,0) GegenbauerC$^{(0,2,0)}$(n,0,(E a)/4)+2 N LaguerreL$^{(1,1)}$(0,0) GegenbauerC$^{(0,1,0)}$(n,0,(E a)/4))+1/6 π c^4 δ G $θ^4$ M^2 r R S^{10} log(C(logG(z) $Q^{\cos(z)}$)) (N^3 LaguerreL$^{(3,0)}$(0,0) GegenbauerC^(0,1,0)(n,0,(E a)/4)^3+3 N^3 LaguerreL$^{(2,0)}$(0,0) GegenbauerC$^{(0,1,0)}$(n,0,(E a)/4) GegenbauerC$^{(0,2,0)}$(n,0,(E a)/4)+N^3 LaguerreL$^{(1,0)}$(0,0) GegenbauerC$^{(0,3,0)}$(n,0,(E a)/4)+3 N^2 LaguerreL$^{(2,1)}$(0,0) GegenbauerC^(0,1,0)(n,0,(E a)/4)^2+3 N^2 LaguerreL$^{(1,1)}$(0,0) GegenbauerC$^{(0,2,0)}$(n,0,(E a)/4)+3 N LaguerreL$^{(1,2)}$(0,0) GegenbauerC$^{(0,1,0)}$(n,0,(E a)/4))+1/24 (N^4 LaguerreL$^{(4,0)}$(0,0) GegenbauerC^(0,1,0)(n,0,(E a)/4)^4+3 N^4 LaguerreL$^{(2,0)}$(0,0) GegenbauerC^(0,2,0)(n,0,(E a)/4)^2+6 N^4 LaguerreL$^{(3,0)}$(0,0) GegenbauerC^(0,1,0)(n,0,(E a)/4)^2 GegenbauerC$^{(0,2,0)}$(n,0,(E a)/4)+4 N^4 LaguerreL$^{(2,0)}$(0,0) GegenbauerC$^{(0,1,0)}$(n,0,(E a)/4) GegenbauerC$^{(0,3,0)}$(n,0,(E a)/4)+N^4 LaguerreL$^{(1,0)}$(0,0) GegenbauerC$^{(0,4,0)}$(n,0,(E a)/4)+4 N^3 LaguerreL$^{(3,1)}$(0,0) GegenbauerC^(0,1,0)(n,0,(E a)/4)^3+12 N^3 LaguerreL$^{(2,1)}$(0,0) GegenbauerC$^{(0,1,0)}$(n,0,(E a)/4) GegenbauerC$^{(0,2,0)}$(n,0,(E a)/4)+4 N^3 LaguerreL$^{(1,1)}$(0,0) GegenbauerC$^{(0,3,0)}$(n,0,(E a)/4)+6 N^2 LaguerreL$^{(2,2)}$(0,0) GegenbauerC^(0,1,0)(n,0,(E a)/4)^2+6 N^2 LaguerreL$^{(1,2)}$(0,0) GegenbauerC$^{(0,2,0)}$(n,0,(E a)/4)+4 N LaguerreL$^{(1,3)}$(0,0) GegenbauerC$^{(0,1,0)}$(n,0,(E a)/4))+1/24 $π^4$ c^{16} $δ^4$ G^4 $θ^{16}$ M^8 r^4 R^4 S^{40} log^4(C(logG(z) $Q^{\cos(z)}$)))+O(x^5)}, GegenbauerC[n, x] LegendreP [n, x] ZernikeR [n, m, r] LegendreP [n, m, x] HermiteH [n, x] JacobiP [n, a, b, x] LaguerreL [n, x] ChebyshevU [n, x] Hypergeometric0F1[a, z] Hypergeometric0F1[a, z] Hypergeometric2F1Regularized[a, b, c, z] ZernikeR[LegendreP [LaguerreL[λ n, D f z, g z (ψ^0 ϱ m), I Exp[λ]], x], m, r] $C_n^{(m)}(x)$ $T_n(x)$ $C_n(x)$ $P_n(x)$ ($R_n^m(r)$ Hypergeometric1F1Regularized[a^5,∂2($ϱ^6$ n^{73})/(∂y ∂x) b,g^8,exp(n)*6,δ $σ^2$,ε $θ^3$,Δ($α^4$)]) Hypergeometric1F1Regularized[a^5, D[ϱ^6 n^73, y, x] b, g^8, Exp[n] 6, δ σ^2, ε θ^3, Δ α^4] ${}_2F_1$◎(P δ,P r Ω;o ψ;γ) $Q^{\delta K Þ \cos(\mu)}_{-a\,b\,R\left(12\,g\,\psi\,j^C+\log(4)\log(\zeta(d))\right)}\left(j\,\delta\,\sigma\,\sin^{-1}(q\,\zeta(s))^{\Psi}\right)$ +N x LaguerreL$^{(1,0)}$(0,0) GegenbauerC$^{(0,1,0)}$(n,0,(E a)/4) ${}_2F_1$ ◎(P δ,P r Ω;o ψ;γ) $Q^{\delta K Þ \cos(\mu)}_{-a\,b\,R\left(12\,g\,\psi\,j^C+\log(4)\log(\zeta(d))\right)}\left(j\,\delta\,\sigma\,\sin^{-1}(q\,\zeta(s))^{\Psi}\right)$ +1/2 N x^2 (N LaguerreL$^{(2,0)}$(0,0) GegenbauerC^(0,1,0)(n,0,(E a)/4)^2+N LaguerreL$^{(1,0)}$(0,0) GegenbauerC$^{(0,2,0)}$(n,0,(E a)/4)+2 LaguerreL$^{(1,1)}$(0,0) GegenbauerC$^{(0,1,0)}$(n,0,(E a)/4)) ${}_2F_1$ ◎(P δ,P r Ω;o ψ;γ)

 doi:10.20944/preprints202403.0518.v1

$Q^{\delta K \text{Þ} \cos(\mu)}_{-a\,b\,R\left(12\,g\,\psi\,j^{C}+\log(4)\,\log(\zeta(d))\right)}\left(j\,\delta\,\sigma\,\sin^{-1}(q\,\zeta(s))^{\Psi}\right)$ +1/6 N x³ (N² LaguerreL⁽³,⁰⁾(0,0) GegenbauerC^(0,1,0)(n,0,(E a)/4)³+3 GegenbauerC⁽⁰,¹,⁰⁾(n,0,(E a)/4) (N² LaguerreL⁽²,⁰⁾(0,0) GegenbauerC⁽⁰,²,⁰⁾(n,0,(E a)/4)+LaguerreL⁽¹,²⁾(0,0))+3 N LaguerreL⁽²,¹⁾(0,0) GegenbauerC^(0,1,0)(n,0,(E a)/4)²+N (N LaguerreL⁽¹,⁰⁾(0,0) GegenbauerC⁽⁰,³,⁰⁾(n,0,(E a)/4)+3 LaguerreL⁽¹,¹⁾(0,0) GegenbauerC⁽⁰,²,⁰⁾(n,0,(E a)/4))) ${}_2F_1$ ⊚(P δ,P r Ω;o ψ;γ) $Q^{\delta K \text{Þ} \cos(\mu)}_{-a\,b\,R\left(12\,g\,\psi\,j^{C}+\log(4)\,\log(\zeta(d))\right)}\left(j\,\delta\,\sigma\,\sin^{-1}(q\,\zeta(s))^{\Psi}\right)$ +1/24 N x⁴ (N³ LaguerreL⁽⁴,⁰⁾(0,0) GegenbauerC^(0,1,0)(n,0,(E a)/4)⁴+4 N² LaguerreL⁽³,¹⁾(0,0) GegenbauerC^(0,1,0)(n,0,(E a)/4)³+6 N GegenbauerC^(0,1,0)(n,0,(E a)/4)² (N² LaguerreL⁽³,⁰⁾(0,0) GegenbauerC⁽⁰,²,⁰⁾(n,0,(E a)/4)+LaguerreL⁽²,²⁾(0,0))+N (3 N² LaguerreL⁽²,⁰⁾(0,0) GegenbauerC^(0,2,0)(n,0,(E a)/4)²+N (N LaguerreL⁽¹,⁰⁾(0,0) GegenbauerC⁽⁰,⁴,⁰⁾(n,0,(E a)/4)+4 LaguerreL⁽¹,¹⁾(0,0) GegenbauerC⁽⁰,³,⁰⁾(n,0,(E a)/4))+6 LaguerreL⁽¹,²⁾(0,0) GegenbauerC⁽⁰,²,⁰⁾(n,0,(E a)/4))+4 GegenbauerC⁽⁰,¹,⁰⁾(n,0,(E a)/4) (N³ LaguerreL⁽²,⁰⁾(0,0) GegenbauerC⁽⁰,³,⁰⁾(n,0,(E a)/4)+3 N² LaguerreL⁽²,¹⁾(0,0) GegenbauerC⁽⁰,²,⁰⁾(n,0,(E a)/4)+LaguerreL⁽¹,³⁾(0,0))) ${}_2F_1$⊚(P δ,P r Ω;o ψ;γ) $Q^{\delta K \text{Þ} \cos(\mu)}_{-a\,b\,R\left(12\,g\,\psi\,j^{C}+\log(4)\,\log(\zeta(d))\right)}\left(j\,\delta\,\sigma\,\sin^{-1}(q\,\zeta(s))^{\Psi}\right)$ +O(x⁵) Hypergeometric0F1 Regularized[a, z] within this theoretical framework where adaptive evolution involves primarily quantum entropy learning machine to predict their macro-environment, and accordingly when the entropy of the ligand-receptor micro-environment with respect to the ultra low quantum packages behaves as the one of the key determinants of Quantum Turing Machine Homeopathy Evolutions. [41-89,92-187] These evolving systems have to be sufficiently robust and resistant to fluctuations for the transitions occurred when using default parameters in this parallel docking algorithm (named BiogenetoligandorolTM) which are set in the KNIME-web server as follows: (i) 24 inverse docking runs, (ii) evaluations per parallel docking run, (iii) population of the Roccustyrna individuals, (iv) maximum of 20 cluster small molecule top leaders on each parallel inverse docking run. For illustration, since Quantum Teleportation raises profound issues about the nature of reality, especially at the quantum level of a system that can have a more fundamental meaning than the system's objective reality I consider this specific phenomenological model, in which the rate of adaptive evolution reflected in the value of the QFT Loss Quantum Function (QLQF) which depends exponentially on the number of adaptable variables and also shows a power law dependence on the entropy of the environment related to the adaptable variables in biological terms of the number of genes or sites that are available for positive selection in a given evolving population at a given time which is itself proportional to the entropy of the environment and to the log of the effective population size. Thus, this Quantum Homeopathy Information or Knowledge is even more starkly, when we only concern ourselves with what can be *known* about the reality of a similar system; not its presumed objective (ontological) 'reality-in-itself' for this sequential screening experiment where an alternative dataset of similar geometric parameters are co-factored to improve the Euclidean Space between the Roccustyrna and (PDB code: 6xs6) protein interacting chains without significantly losing binding site accuracy. This is named EuTHTS Euclidean Topology Virtual Screening and consists of: (i) 120 docking runs, (ii) evaluations per docking run, (iii) population of Roccustyrna individuals**, (**iv**)** maximum of 20 cluster leaders on each docking run. The validation of these docking experiments was performed on DockThor CPU nodes of the Dumont supercomputers**,** each one containing two processors Intel Xeon E5**-**2695v2 Ivy Bridge **(**12c@2**,**4 GHz**)** and 64 GB of RAM memory. The validation of these docking experiments was achieved through the re**-**docking of the non**-**covalent Roccustyrna ligand present in the 6W63 **(**Mpro**)** protein complexes using standard configuration which is successfully predicting co**-**crystallized conformations of each inserted complex as an ingenious system of using entangled states through the engineering of these QFT biologically inspired Quantum Homeopathy Drug Designing technologies. [2-100,122-195] Certainly, these similar Euclid Special Space solvable models that are taken advantage the homeopathy fact of the less the likelihood of material presence in the remedy, or, in homeopathic parlance, the higher the potency would guarantee a viability of fitting many measured N−plets of levels E, experimental values of n by the suitable N−plets, in a similar vein. The Euclid Spaced -index data structure [4-87.99-

 doi:10.20944/preprints202403.0518.v1

193] is leveraged in conjunction with the Burrows–Wheeler transformation as a Quantum advantage when using thermodynamic measures of performance that has been quantified for theirs principle's applicability to realistic biological structures demonstrated here and are based on the sum of the following terms from the MMFF94S force field. [9-100,133-195] This particular case of 20 steps for 11dimensions seems to be particularly suited to admit an anti-de Sitter ChernSimons formulation in future generalized relativity applications of supergravity for Quantum Homeopathy Frame Representations in more advanced pharmacophore merging schemes. [11–90,112-195] As shown**, in** this super anti de Sitter group**,** the OSp **(**32**)** supergroup is generalized in this path from QFT's Hidden Quantum Homeopathy Information as a Quantum Black Hole paradigm for the generation of unique drug designs with the highest docking energies of negative binding values when compared to other known SARS **-** CoV **-** 2 antiviral. [22-103,54-115] This Entanglement model of homeopathy translations is a quantum hypergeometric example of generalized entanglement predicted by weak quantum theory revealing its greatest strength and promise, not yet touched upon. [2-53,60-116] It has always been an intuition of Wolfgang Pauli, one of the founders of modern QM, that physics will only be complete if it has incorporated consciousness into a final theory of matter [33-120]. Until now, quantum algorithms to simulate QFT [13,14-139] have mainly used lattices. [2-73,100-140] Conversely, this transactional interpretation of quantum mechanics for each task (binding site prediction, binding pose generation, de novo molecule generation, linker design, and binding affinity prediction), including the problem setup, representative methods, datasets, and evaluation metrics could act as a qualitative and a non-local metaphor for quantum homeopathy and as based on quantum theory could be also resulting to more novel fuzzy sphere formations ((Iconics1-4), (Eqs1-400), Supplementary Material METHODS AND MATERIALS (1), (2)),(Figures S(1-99)) and Quantum Deep Geometry generated drug designing processes providing explanations of the success of quantum homeopathic therapeutic approaches and an equivocal evidence for the efficacy of homeopathy [18-140] in quantum entanglement in general. [2-23,72-144] This is an advantage within this quantum homeo-formalism, because differential operators are formally ill-defined [14-148], although recent developments have shown that good results can still be achieved [26-159] also for other macroentanglement formation project. [14-149] These macroentanglement formations for Quantum Homeopathy based chemical geometrics would be far more useful for drug designers and researchers when trying to explore generalized entanglement as a vehicle for geometry processes. [6–89-150] In this situation, where quantum similarities between famous double-slit experiment of quantum physics, and quantum information processing are proposed docking free energy expectation values proving this apparent relationship between quantum homeopathic efficacy and QFT to QM reductions which could be explained in general terms of information loss from small molecule quantum superposition states. [34-98,94-158] The next step was to incorporate geometrical consciousness into this Quantum Homeopathy Model (Maths1-12,13a,13b,13c,13d,13e,13f,13g, 13h,13i,13j,13k), ((Schematics1,2, (Supplementary Material METHODS AND MATERIALS)) (Eqs.1-400), ((Iconics1-4), (Eqs1-400), Supplementary Material METHODS AND MATERIALS (1), (2)),(Supplement Material FUNCTIONS.1-25), (Maths14a,14b,14c,14d,14e, 14f,14g,15,16,17,18, 19a,19b,19c, 19d,19e,19f,19g,19h,20a,20b,20c,20d,20e,20f1,20f2,20f3, 20g,20h,20i,20j,21a,21b,21c, 21d,21e,21f,21g, 21h,21i,21j,22a,22b,22c,22d,,22e,,22f,22g), (Cluster of BIOGENEA_ CONSENSUS_Eqs.1-26), and ((Figures S(1- 133)), (OUTPUTs1-3)), (Supplementary Material METHODS AND MATERIALS (2), MasterEquations1-34), Supplementary Material METHODS AND MATERIALS (1), (2)),(Ic1a), (Ic1b), (Ic1c), (Ic2a), (Ic2b), (Ic2c), (Ic2d,e,f,g,h,g,k,l,m,o,p,q,r), (Diagramm1, Diagramm2, Diagramm3), (Maths1-19) (Ic3a), (Ic3b) (Ic3c), (Ic3d), (Ic3d), (Ic3e), (Ic3f), (Ic3g), (Ic3h), (Ic3i), (Ic3j), (Ic3k) after translating this intimate relationship between water memory and protein folding issues, between drug substances in ultra low concentrations and the quantum geometrics which is also a complementary one [21-99,101-159] when generating hypergeometric druggable fuzzy spheres (Supplementary Material METHODS AND MATERIALS Figures S(1-100)), ((Iconics1-4), (Eqs1-400), and (Schematics1a,1b,1c,1d, 1e,1f,1g,1h,1i,1j,2a,2b,2c,2d,2e), (I-VI) Supplementary Material METHODS AND MATERIALS)) interacted with negative binding free energies accordingly. These functions can be deciphered through DockThor docking energy

 doi:10.20944/preprints202403.0518.v1

evaluations of the hydrophobic interactions among neighbored side-chains of an unfolded thermodynamic metastable state with great accuracy of the prediction. [1-195] Therefore, I suggest that the Practical consequences of this computational entanglement model for this quantum homeopathic research for mathematical chemistry practice could be more extended to new Generalised Entanglement Theoretical Drug Designing Models for understanding the effects of complementary and alternative medicine including Nano-and molecular events, thermodynamics/entropy, Quantum mechanisms and genetic instructions with the following inputs: ACE2 and AT1R receptors, Remdesivir's therapeutic mechanism for the COVID-19, Candesartan's role in ameliorating COVID-19 cytokine storm including Telmisartan's molecular mechanism as tentative angiotensin receptor blocker and therapeutic agent for COVID-19. [28-137,150-189] To be made practical, these theoretical quantum algorithms are expected to require both significant refinement and effort in translation in the near term, since these refinements could include (i) recasting them for WOLFRAM devices that use the VQA, QAOA or QA frameworks for (ii) integrating greater biological context of the generalized entangled state (a) depends on the proper production process and is intimately connected to the ritual of remedy producing. [28-137,150-169] (OUTPUTs1-3), (Ic1a), (Ic1b), (Ic1c), (Ic2a), (Ic2b), (Ic2c), (Ic2d), (Ic2e), (Ic2f), (Ic2g),(Ic2h), (Ic2c), (Ic2g), (Ic2k), (Ic2l), (Ic2m),(Ic2n),(Ic2o),(Ic2p),(Ic2q),(Ic2r), (Ic3a), (Ic3b) (Ic3c), (Ic3d), (Ic3d), (Ic3e), (Ic3f), (Ic3g), (Ic3h), (Ic3i), (Ic3j), (Ic3k), (Iconics4-6), and ((Iconics1-6), (Iconics1-4), (Eqs1-400), Supplementary Material METHODS AND MATERIALS)) Therefore, I hope that this work will stimulate the development of new directions in the study of the AT1R drug universe and other drug designing efforts. [40-162] Although it is less conclusive due to a large finite-size effect, we show that certain entanglement phases seem to exist even when a random state has permutation or translation symmetry for a non-vanishing boundary solution in a five-dimensional CS supergravity Quantum Foam [20-163] for all the poly-tetrahedron shaped pharmacophoric ligand provided here in the form of a Turing Machine Ruled Quantum Function which can carry U (1) charge among the unknown characteristics revealed in the cluster of the Gissitorviffirna_TM, Roccustyrna_gs, Roccustyrna_fr, and Roccustyrna_consv Quantum-computational structures. These AI-Quantum Homeopathy Entropy Negativities (QHEN) generated the highest total free energy values of negative docking energy factors and will be generalized into Spheroidal Wave Equations for Avogadro's Number SphericalHarmonicY, ChebyshevT, and LegendreP Fuzzy Sphere-like small molecules, (Ic1a), (Ic1b), (Ic1c), (Ic2a), (Ic2b), (Ic2c), (Ic3a), (Ic3b) (Ic3c), (Ic3d), (Ic3d), (Ic3e), (Ic3f), (Ic3g), (Ic3h), (Ic3i), (Ic3j), (Ic3k) geometrical descriptors and (Eqs.1-400) ((Iconics1-4), (Eqs1-400), Supplementary Material METHODS AND MATERIALS (1), (2)),which are ordinary differential equations (Eqs1-325), ((Iconics1-4), (Eqs1-400), and (Schematics1a,1b,1c,1d,1e,1f,1g,1h,1i,1j,2a,2b,2c,2d,2e), (I-VI) Supplementary Material METHODS AND MATERIALS)) with two regular singular points and one confluently irregular singular point. By incorporating Quantum Biological Evolution and QuantumTuring Deep Learning processes into this (Ic0a), (Ic0b), (Ic0c), (Ic1a), (Ic1b), (Ic1c), (Ic1d), (Ic2a), (Ic2b), (Ic2c), (Ic3a1), (Ic3a2), (Ic3b1), (Ic3b2), (Ic3c), (Ic3d), (Ic3d), (Ic3e), (Ic3f), (Ic3g), (Ic3h), (Ic3i), (Ic3j), and (Ic3k) Quantum Homeopathy Framework, this quantum homeopath of negative docking energy theory paradigm implying that this emergence of complexity with life which is an inherent feature of learning occurs throughout the history of the universe. With respect to these Quantum Homeopathy logic advantages, this led us to the Turing Machine Ruled Generalizations of Genetic, Homeopathic, and Clinical Data to Chemical Proteomic based Graph Translations (Ic3a), (Ic3c) as inputs into (Ic2e,f,g,h,g,k,l,m,o,p,q,r,q) these Quantum Circuit Generative Models of various number of qubits and quantum circuit layers discussed from above can yield operational docking energy advantages such as sample complexity advantages in particular which could have a great impact in future drug designing fields for the computer-aided designing of Hidden Druggable Pharmacophoric Subgroups and Small Molecule Triangularizations of N-{[(2S)-3-(aminomethyl)-2-[(1R,2S)- 2-methyldiaziridin-1-yl]-1,3- diazetidin-1-yl]({[(E)-{[(E)- (aminomethylidene)amino] methylidene}amino]amino})aziridin-1-yl-λ^5-phosphanyl}-3-{5-[(1E)-[2-(aminomethyl)-2-methylhydrazin-1-ylidene]methyl]-3,4-dihydroxyfuran-2-yl}-2-methyl-5-sulfanylidene-1,2,3,4-tetrazole-1-carboxa, {[(1S,2S,3S)-2-(4-amino-5-sulfanylidene-4H- 1,2,4-triazol-3-yl)-2-carboximidoyl-

 doi:10.20944/preprints202403.0518.v1

3-fluoro -1-oxo-1λ^5-phosphiran-1-yl]amino}[(Z)- ethylideneamino]iminomethanium, (6R)-6-[(3S)-2-[(1Z)-amino({1H- 1,3-benzodiazol-2-yl[(3R)-3-ethyloxolan-3-yl]methylidene})-λ^5- phosphanyl]-5-sulfanylidene-1,2,4- triazolidin-3-yl]-4-oxa-1-azabicyclo[3.1.0]hexane-3-thione, {1-[(R)-[(1S,3R)-3-[(R)- amino(carbamothioylamino)methyl]diaziridin-1- yl] ({6-oxo-2-[(2S,5R)-3,4,5-trifluoro-2,5-dihydrofuran-2-yl]-6,7-dihydro-1H-purin-8- yl}amino)phosphoroso] -1H-azirin-2-yl}thiourea, and (2R,4R,5S)-2-amino-3-{4-amino- 1-[(2R,3R,4R,5R)-5-[(2R)-3- (aminomethyl)-2-(2-methyldiaziridin-1-yl)-1,3- diazetidin-1-yl]-3,4-dihydroxyoxolan-2-yl]-5-sulfanylidene-4,5-dihydro-1H-1,2,4-triazole-3-carbonyl}-1-[(2S)-1-[(3R)-2-amino-1-methyl-5-sulfanylidene-1,2,4-triazolidin-3-yl]propan-2-yl]-octahydro-1H-purin-6-one (Highlights Supplementary Material, Maths14a,14b,14c,14d,14e,14f,14g,19a,19b,19c, 19d,19e,19f,19g,19h,20a,20b,20c,20d, 20e,20f1,20f2,20f3,20g, 20h,20i,20j,21a,21b,21c,21d,21e,21f,21g,21h,21i,21j,22a,22b,22c, 22d,,22e,,22f,22g), and (Cluster of BIOGENEA_ CONSENSUS_Eqs.1-26), (Diagramm1, Diagramm2, Diagramm3), (Highlights Supplementary Material, Maths1-21), and (Supplementary Material METHODS AND MATERIALS Figures S(1- 133)), (Ic2e,f,g,h,g,k,l,m,o,p,q,r), ((Iconics1-4), (Eqs1-400), Supplementary Material METHODS AND MATERIALS (1), (2)),and ((SI APPENDIX I Supplementary Material), (TableS1), (TableS2), (TableS3), (Figures S1), (Figure S2a), (Figure S2b), (Figure S2c), (Figure S2d), (Figure S2d), (Figure S2e), (Figure S3a), (Figure S3b), (Figure S3c), (Figure S3d), (Figure S3e), (Figure S3f), (Figure S3g), (Figure S3h), (Cluster Docking Energy TableS1), (SI Appendix I), (Cluster Docking Energy TableS2),SI Appendix I), (Docking Energy TableS1), (SI Appendix I), (Docking Energy TableS2), (SI Appendix I), (Docking Energy TableS3), (SI Appendix I)). With respect to these Quantum Homeopathy logic advantages, further experimental work is necessary to assess whether these diagonal-matrix potential advantages in variational (Ic2e,f,g,h,g,k,l,m,o,p,q,r) Quantum Circuit Generative Models of various number of qubits and quantum circuit layers for the Roccustyrna peptidemimetic Small Molecule Drug Discoveries discussed from above can yield operational docking energy advantages such as sample complexity advantages in particular which could have a great impact in future drug designing fields..These novel applications in the field of structure-based binding affinity prediction will have to address the points of criticism directed toward existing methods, therefore I will let your imaginations roam far outside the M87 supermassive rotating black hole in this structure-based molecular modeling section since only Avogadro's Quantum Uncertainity relations between Entangled Space-Time backgrounds and Euclid Special Meta-Logic-Black Hole-Chemical Spaces (Highlights Supplementary Material, Maths19a,19b,19c,19d, 19e,19f,19g,19h,20a,20b,20c,20d,20e,20f1,20f2,20f3,20g, 20h,20i,20j,21a,21b,21c,21d,21e,21f,21g,21h, 21i,21j,22a,22b,22c,22d,,22e,,22f,22g), and (Supplementary Material METHODS AND MATERIALS Figures S(1- 133)), (OUTPUTs1-3)), (Ic1a), (Ic1b), (Ic1c), (Ic2a), (Ic2b), (Ic2c), (Ic2d), (Ic2e), (Ic2f), (Ic2g),(Ic2h), (Ic2c), (Ic2g), (Ic2k), (Ic2l), (Ic2m),(Ic2n),(Ic2o),(Ic2p),(Ic2q),(Ic2r), (Ic3a), (Ic3b) (Ic3c), (Ic3d), (Ic3d), (Ic3e), (Ic3f), (Ic3g), (Ic3h), (Ic3i), (Ic3j), (Ic3k), ((Iconics4-6), (Supplementary Material METHODS AND MATERIALS)) for which the full Schwarzschild metric is required could be able of translating rare entropy signatures from Homeopathy Substances into 3D macromolecular structure representations for rational drug design, emphasizing to the most recent developments in both predictive and generative deep-learning methods.

Limitations of the Study

In this study, many amino acid features were utilized. Whether they are all actually beneficial for the prediction needs further exploration. In addition, all the information learned by these Quantum Deep Machine Learning approaches and Protein-ligand binding affinity prediction with edge awareness and supervised attention comes from the static crystal structure. How to integrate the dynamic behavior information of protein–ligand complex in the model structure is still not well solved. Finally, more datasets are needed to verify the generalization ability and interpretability of these Edge Graph convolution-based and Supervised Attention-based Drug-Target Affinity prediction methodologies, where the super edge graph convolution can comprehensively be combined to Geometric Deep Learning for Structure-based Drug Design modules. Intuitively, sample

 doi:10.20944/preprints202403.0518.v1

complexity and generalization error as Quantum Hormetic advantages may arise when quantum entanglement enables the modeling of classically intractable correlative structures even if such sample complexity advantages are achievable with classical data, which will likely be problem instance specific [2-195], highly dependent on the distribution of the input data [1-99,2-195] and are unlikely to be superpolynomial [2-11,3-195]. However, a diverse and growing body of evidence from recent and previous work on novel and more efficient error correcting codes is required [1-14,1-16], for the realization of dynamical topological phases [34,4-35] and for the early demonstrations of logical qubits [31–43] by utilizing node and edge information and multi-supervised attention to efficiently learn the attention distribution that are consistent with real protein-ligand interactions proposing general conditions for the emergence of Turing patterns in a domain that changes size through homogeneous growth/shrinkage based on the qualitative changes of a potential function. Based on the Kolmogorov complexity of real weights, evolving weights, and real probabilities, respectively an infinite hierarchy of Bell pair Qubits of analog networks defined in terms of the Kolmogorov complexity should be Quantum Mechanically distributed at each molecular location of the Telmisartan's chemical bonding that causes a semi Quantum negative downregulation effect inside the AT1 receptor at the mRNA and protein level apparently due to its action as a partial PPAR-gamma (Peroxisome Proliferator-Activated Receptor gamma) agonist. Moreover, while in the case of a Quantum Hormetic Regulator the limit of the continuum is reached **(**but not always**)** when the number of sites is huge and the spacing approaches zero**,** in our case there is the classic limit that is reached when the fluctuations of the quantum metrics vanish near the attractor. Moreover**,** while in the case of this Quantum Homeopathy Regulator the reduction of QFT to QM is not mathematically explicit**,** in this case it is**,** since the ansatz corresponds to the execution of a boson translation **(**as it was illustrated in Sections 1-3**)**. Depending on the precise form, polynomial quantum speedups could be associated with useful quantum advantage, as even a polynomial classical algorithm does not mean that solutions can be obtained in a practical time. Both aspects may prove important in the further development of quantum algorithms in quantum chemistry. Other barriers to quantum advantages include (i) the sophistication of existing classical heuristic algorithms and the inherent parallelism of many of the problems they solve in a polynomial time computable noise p.s.d. for which the computation of its capacity cannot be performed in polynomial time, i.e., the number of computational steps on a Turing Machine grows faster than all polynomials (ii) the scale of both existing classical hardware and practical problem instances within the context of contemporary [3-185] ,function described by a polynomial time classical Turing machine, which is public; the client would like to sample a random x as the function input and use a protocol to send f(x) to the server (iii) the broad institutional support and incumbent advantage benefiting existing classical approaches (including extensive clinical validation in the medical setting) by introducing the Counter Turing Test (CT^2), a benchmark consisting of techniques aiming to offer a comprehensive evaluation of the robustness of existing AGTD techniques, and (iv) the likely precondition of FTQC to realize polynomial advantages based on amplitude amplification in practice revealing that synthetic data that passed visual Turing tests, can also enhance the representation learning capability of VisionFM, and leading to substantial performance gains on downstream ophthalmic AI tasks [41-190]. Thus, while current research in this direction shows long-term promise and should be explored further, many of these quantum advantages appear unlikely to be practical in the near term, including Turing-complete programming elements, programming languages, and sophisticated document notations. On the contrary, regarding the potential biological usefulness of entanglement as a communication system [30], it would be strange if biological systems had not used it showing that this landscape of quantum advantages considers the benefits of quantum computing technologies relative to existing classical alternatives by indicating that these geometric topology-driven heuristic algorithms used in this project are capable of fragmenting and remerging small molecules that could not be fragmented by the algorithm of any of the known reference databases. In fact, this holomorphic twist is equivalent to holomorphic BF-like Quantum fields theory as said before, since the computational skeletons of these innovative drug designs that are tetrahedrically quantized can finally assign definite values to the negative docking energy observables represented by noncommutative operators in this von

 doi:10.20944/preprints202403.0518.v1

Neumann's scheme. Though still a controversial assertion, Quantum Homeopathy macroentanglement as a significant operational quantum advantage in the energy required to perform computations [4-27,4-36] gives much reason for optimism if the analysis offered here is at all useful and has some truth to it we have to suppose that the same Polynomial-time algorithms for prime factorization and discrete logarithms on a quantum computer process could play an important role in other therapeutic procedures as well. It is to be suspected that this meta-analysis of homeopathy supply the quantum entanglement base of what is termed the quantum therapeutic alliance or was called rapport by the early hypnotists. All that happens in the meanwhile is unknowable, and the only theory I can make concerns the correlations among input and output events. [61-73] Different physical theories (for example, SU (2) vs. SL (2, r) Chern-Simons theory) (Supplementary Material METHODS AND MATERIALS (2), MasterEquations31b1,31b2,31b3,31b4) correspond to quantizing different atoms that are hidden in QFT just like Quantum information does (remember that there is an uncertainty relationship between Quantum Geometrics and Quantum information) considering these CS equations (Highlights Supplementary Material, Maths19a,19b,19c,19d,19e,19f,19g,19h, 20a,20b,20c,20d,20e,20f1,20f2,20f3,20g,20h,20i,20j,21a,21b, 21c,21d,21e,21f,21g, 21h,21i,21j,22a,22b,22c,22d,,22e,,22f,22g), (Eqs1-325), ((Iconics1-4), (Eqs1-400), and (Schematics1a,1b,1c,1d,1e,1f, 1g,1h,1i,1j,2a,2b,2c,2d,2e), (I-VI) Supplementary Material METHODS AND MATERIALS)) as relative CS motion equations of nearby atoms, and a coordinate-independent measure of the wave's effects described by the geodesic deviation function. I claim that a quantum computer would be needed in order to simulate the hidden quantum network (HQN) of the designed quantum circuits under this study. But using a binary tree to trace the original QFT would mean not always recovering the Quantum Characteristics of the latter in four dimensions, whose field content consists of (ϕk) ((Supplement Material) FUNCTION1-28). For this reason, in particular, a regulator would be needed to play the role of a hidden quantum definitional function [53-72] to allow the switch from a classical metalanguage to a hypergeometric language logic in this quantum homeopathy version [43-73] of a definitional function that allows to pass from a QML to the quantum logic of quantum information (QLI). [39-73] More precisely, a 100 qubit quantum computer is required in order to be programmed to be in a one-to-one correspondence with the HQN as had already pointed out in these Quantum Functions and QFT Loss Quantum Function (QLQF) established here as a direct connection between processes of Quantum Chemical Biology and Turing Machine Learning Ruled Euclid Special Spaces which are consisted of a connected part, the molecular interaction of this disconnected part that calculates in parallel the total free energy fields. From a mathematical perspective, these quantum circuits could also recover Hilbert Symmetric Spaces as may be called by the Chern–Simon's theory. Thus the problem is in QP, the quantum analogue of the class P, and if we wish, more realistically, to model the oracle's size and running time, then we could assume the oracle size, in general f, to be O(N), this being the size of the oracle which simply contains a ROM list of the function values. With these results**,** I expect to take advantage of the knowledge accumulated in half a century of classical networking research and operation to create strong Quantum Homeopathy Network Architectures**,** and guide the experimental focus for the development of Quantum Negative Energy Repeaters for the implementation of real**-**world Quantum based Drug Design protocols. Implementation of these in**-**silico Quantum Homeopathic Phase Cryptographic Experiments led me to Quantum Turing Machine Networking Acceleration and fragmentations of the existed molecular networks into NPs occupying electronic orbitals that are involved in the endothelial damage of the cardiovascular system in an early stage of the COVID-19 disease as reflected by the release of highly sensitive troponin and natriuretic peptides **(**NPs**).** Notably, while Quantum Turing may yield superpolynomial Quantum Homeopathy, advantages on classically hard problems, whether these near-term algorithms can fully capitalize on the computational power afforded by quantum information remains a matter of theoretical investigation (e.g., [4-124]). Despite some advancement, [3-79,135-149], these Quantum Mechanics and Quantum-gravitational ideas provided us along only with a Theoretical Quantum Gravity background from Quantum Homeopathy Information into a Quantum Homeopath Folding Translation Scheme (Ics.3a,3b,3c) which is highly dependent on the folding of typical secondary structures as the means

 doi:10.20944/preprints202403.0518.v1

to hierarchically pave a negative docking energy and native folding pathway and still exhibit limitations in terms of prediction accuracy and require significant efforts in feature design. This research has highlighted the application of geometric deep learning methods, which represent the protein-ligand complex structure as 3D grids or 3D graphs for processing and predicting these Bell Pair Qubits at another chemical space solution if the intersect would reduce these negative docking energies to a finite set of Haag's theorem. [1-48] Since not all computational groups working in this field will have the expertise, equipment, or desire to perform the required synthesis and experimental testing, collaborations with experimentalists will be highly valuable. To comprehensively evaluate the utility of emerging new models in a real-world drug design context, experimental validation of the proposed molecular structures is paramount. Still we believe that quantum computing remains a potentially powerful model of computation. Quantum computers can quickly solve some problems not known complete such as factoring and the potential to solve quantum entanglement problems such as graph isomorphism (Supplementary Material METHODS AND MATERIALS (2), MasterEquations1-34), (Highlights Supplementary Material, Maths1-12,13a,13b,13c,13d,13e,13f,13g, 13h,13i,13j,13k,19a, 19b,19c,19d,19e,19f,19g,19h, 20a,20b,20c, 20d,20e,20f1,20f2,20f3,20g,20h,20i, 20j,21a,21b,21c,21d, 21e,21f,21g,21h,21i,21j,22a,22b, 22c,22d,,22e,,22f,22g), ((Iconics1-4), (Eqs1-400), and (Schematics1a,1b,1c,1d,1e,1f,1g, 1h,1i,1j,2a,2b,2c,2d,2e), (I-VI) Supplementary Material METHODS AND MATERIALS (1), (2)),(Ic0a), (Ic0b), (Ic0c), (Ic1a), (Ic1b), (Ic1c), (Ic1d), (Ic2a), (Ic2b), (Ic2c), (Ic3a1), (Ic3a2), (Ic3b1), (Ic3b2), (Ic3c), (Ic3d), (Ic3d), (Ic3e), (Ic3f), (Ic3g), (Ic3h), (Ic3i), (Ic3j), and (Ic3j) for finding a short vector in a lattice. Moreover, quantum computing can give a large increase in speed, for example a quadratic improvement in NP-like search problems.

Declaration

The paper reports annotated quantum functions, and cluster of equations regarding Avogadro Number's oriented HyperGeometric and ChebyshevT Functions on Black Hole Paradox Generalizations and Turing Machine Ruled Quantum Homeopathy Water Memory Entanglements for the Translation of COVID19 Homeopathy Remedies into the Neprilysin and ACE2/AT1R receptors targeted DRVYIHPFX- ligands. This study did generate new and unique drug designs. This project contains the following extended data: https://zenodo.org/records/10149911, https://zenodo.org/records/10724423, and https://doi.org/10.7910/DVN/I5YOMO.

 doi:10.20944/preprints202403.0518.v1

Ethical Approval and Consent to Participate

All methods were carried out in accordance with relevant ethical guidelines and regulations. The study was approved by the Biogenea's Drug Designing Organization Authorities. No human clinical trials involved or human subjects participated in this research effort.

Supplementary Materials: The following supporting information can be downloaded at the website of this paper posted on Preprints.org.

Author Contributions: Grigoriadis Ioannis's diverse contributions to the published work are accurate and agreed. Grigoriadis Ioannis wrote the whole manuscript and solely contributed to multiple roles: Conceptualization, Ideas, formulation, or evolution of overarching research goals and aims. Methodology, Development, or design of methodology; creation of models. Writing-Review & Editing, Preparation, creation, and presentation of the published work by those from the original research group, specifically critical review, commentary, or revision including pre-or post-publication stages. Visualization, Preparation, creation, and presentation of the published work, specifically visualization/data presentation. Supervision, Oversight, and leadership responsibility for research activity planning and execution, including mentorship external to the core team. Project administration, Management, and coordination responsibility for research activity planning, and execution.

Funding: No funding received for this research article.

Data Availability Statement: The paper reports annotated quantum functions, and cluster of equations regarding Avogadro Number's oriented HyperGeometric and ChebyshevT Functions on Black Hole Paradox Generalizations and Turing Machine Ruled Quantum Homeopathy Water Memory Entanglements for the Translation of COVID19 Homeopathy Remedies into the Neprilysin and ACE2/AT1R receptors targeted DRVYIHPFX- ligands. This study did generate new and unique drug designs. This project contains the following extended data: https://zenodo.org/records/10149911, https://doi.org/10.7910/DVN/I5YOMO, Avogadro Number's-oriented HyperGeometric and ChebyshevT Functions for Black Hole Paradox Generalizations and Turing Machine Ruled Quantum Homeopathy Water Memory Entanglements for the Translation of COVID19 Homeopathy Remedies into the Neprilysin and ACE2/AT1R receptors targeted DRVYIHPFX- ligands. - Harvard Dataverse, https://zenodo.org/records/10724423.

Acknowledgements: I would like to deeply express my special thanks of gratitude to my teacher (George Grigoriadis Pharmacist) as well as My CEO and principal (NikolAoΨos Grigoriadis Phd Pharmacist) who gave me the golden opportunity to do this wonderful project on Grover Search Quantum Deep Learning Chemistry topics, which also helped me in doing a lot of Original drug Repurposing and drug Combination Research and I came to know about so many new things I am thankful to them.

Conflicts of Interest: The authors declare competing interests.

Consent for publication: Informed consent was obtained from Biogenea's legal guardians for Biogenea's scientific committee members to participate in the main and the optional parts of this research project. All experimental protocols were approved by the Biogenea's Drug Designing Organization Authorities.

SI Appendices

SI Appendix Tables (I-XXXVIII): IUPAC NAMES, ADMET Analysis, PLIP REPORTS, and Docking Files and Comparative Docking Free Energy Analysis between Roccustyrna, Gissitorviffirna, RoccustyrnaDRVYIHPFXmimetic Drug Designs and FDA Drugs of Molnupiravir/Nirmatrelvir (PAXLOVID), Candesartan, Olmesartan, Telmisartan, Valsartan, and Losartan. Supplement Material FUNCTIONS (1-28), Supplementary Material Highlights qHBIOGENEA, Supplementary Material METHODS AND MATERIALS. SI Appendix XL (Docking Tables(FDA DRUGS, GissitofviffirnaTM, and DRVYIHPFXmimetic)), SI Appendix I (Roccustyrna structure fragments, Docking Tables(FDA DRUGS, Roccustyrna_fr, and DRVYIHPFXmimetic)), SI Appendix II (Docking Tables(FDA DRUGS, GissitofviffirnaTM, and DRVYIHPFXmimetic)), SI Appendix II (swissADMET physicochemistry and estimated pharmacokinetics, druglikeness and medicinal chemistry friendliness analysis of the cluster of Roccustyrna_gs, Roccustyrna_fr, and GissitorviffirnaTM drug designs), SI Appendix II IUPAC NAMES, SI Appendix III (FDAs, cav6w63_X77-Roccustyrna_fr, cav6w63_X77-GissitorviffirnaTM),

 doi:10.20944/preprints202403.0518.v1

SI Appendix IV (FDAs, cav7b3o_NAG-Roccustyrna_fr, cav7b3o_NAG-GissitorviffirnaTM), SI Appendix V (FDAs, model1_7b3d-Roccustyrna_fr, model1_7b3d-GissitorviffirnaTM), SI Appendix VI (FDAs, 7khp-Roccustyrna_fr, 7khp-GissitorviffirnaTM, 7khp-Roccustyrna_gs), SI Appendix I (Docking Tables(Valsartan, Telmisartan, Roccustyrna_fr, GissitofviffirnaTM, and DRVYIHPFXmimetic)) , SI Appendix I (Docking Tables(Candesartan, Olmesartan, Roccustyrna_fr, GissitofviffirnaTM, and DRVYIHPFXmimetic)), SI Appendix IX (6m2q-cav6wzu_GOL-Roccustyrna_gs, 6m2q-cav7b3o_NAG-Roccustyrna_fr, 6m2q-1xak-Roccustyrna_fr, 6m2q-cav6lu7_02J-Roccustyrna_fr, 6m2q-7bv2-Roccustyrna_gs),, SI Appendix XI (FDAs, 6xs6-Roccustyrna_frs, 6xs6-GissitorviffirnaTMs, 6xs6-Roccustyrna_gs) and (FDAs, 6m2q-Roccustyrna_frs, 6m2q-GissitorviffirnaTMs, 6m2q-Roccustyrna_gs), SI Appendix IXa (Docking Energies of the 6nur-GissitorviffirnaTM2, 2ghv-GissitorviffirnaTM, 1xak-GissitorviffirnaTM, 1xak-GissitorviffirnaTM2 cluster complexes) , SI Appendix XII (6nur-2ghv-Roccustyrna_fr, 6nur-1xak-Roccustyrna_gs, 6nur-2g9t-Roccustyrna_fr, 6nur-6m2q-Roccustyrna_fr), SI Appendix XIII (FDAs, cav6w63_X77-Roccustyrna_fr), SI Appendix XV (FDAs, 6xs6-Roccustyrna_gs, 6xs6-Roccustyrna_fr), SI Appendix XIV (FDAs, cav6woj_APR-Roccustyrna_fr, cav6woj_APR-GissitorviffirnaTM, cav6woj_APR-Roccustyrna_gs), SI Appendix X (FDAs, 6xs6-Roccustyrna_fr, 6xs6-Roccustyrna_gs), SI Appendix XIV (FDAs, 6xs6-Roccustyrna_gs), SI Appendix XVI (FDAs, model1_7b3d-Roccustyrna_fr, model1_7b3d-Roccustyrna_gs), SI Appendix XXII (RoccustyrnaTM_gs_convs)-5rem-1xak)), SI Appendix XVIII (FDAs, 7bv2-GissitorviffirnaTM, 7bv2-Roccustyrna_fr, 7bv2-Roccustyrna_gs), SI Appendix XIX (FDAs, 7bv2-GissitorviffirnaTM, 7bv2-Roccustyrna_gs, 7bv2-GissitorviffirnaTM), SI Appendix XX (7khp-Roccustyrna_fr, 7khp-Roccustyrna_gs, 7khp-GissitorviffirnaTM), SI Appendix XXI (NUBBEE Plants, 1xak-7bv2-Roccustyrna_fr, 1xak-7bv2-Roccustyrna_gs, 1xak-cav6woj_APR-Roccustyrna_fr, 1xak-cav7b3o_NAG-Roccustyrna_gs), SI Appendix XXII (RoccustyrnaTM_gs_convs)-5rlh)), SI Appendix XXII (RoccustyrnaTM_gs_convs)-5rle)), SI Appendix XXV (1xak-Roccustyrna_fr, 1xak-Roccustyrna_gs), SI Appendix XXII (RoccustyrnaTM_gs_convs)-7tx5)), SI Appendix XXVII (RoccustyrnaTM_gs)-5rem)), SI Appendix XXVI ((RoccustyrnaTM_gs)-7tx5), SI Appendix XXVII (RoccustyrnaTM_gs)-6wzu)), SI Appendix XXIX (Roccustyrna_(gs-fr)-1xak), SI Appendix XXV (Roccustyrna_fr)-1xak)), SI Appendix XXXI (RoccustyrnaTM_gs_convs)-7nij)), SI Appendix XXVIII (RoccustyrnaTM_gs)-6wzu)), SI Appendix XXII (RoccustyrnaTM_gs_convs)-5rlg), SI Appendix XXXIII (RoccustyrnaTM_gs_convs)-7e5x)), SI Appendix XXXII (RoccustyrnaTM_gs_convs)-5tlg)), SI Appendix XXXIV (RoccustyrnaTM_gs_consv)-6wzu)), SI Appendix XXXIV (RoccustyrnaTM_gs_consv)-5x8s)), SI Appendix XXXVI (RoccustyrnaTM_gs_convs)-7tx5)), SI Appendix XXXV (RoccustyrnaTM_gs_convs)-5x8s)), SI Appendix XXXVII (RoccustyrnaTM-Organic_Synthesis), SI APPENDIX XXXVIII (GissitorviffirnaTM-5rem), Abbreviations Roccustyrna Manuscript.

symbol	name	value
c	speed of light in a vacuum	299 792 458 m/s
G	gravitational constant	$6.674\ 30 \times 10^{-11}$ N m²/kg²
h	Planck constant	$6.626\ 070\ 15 \times 10^{-34}$ J s $4.135\ 667\ 696\ 9 \times 10^{-15}$ eV s
hc	h c	$1.986\ 445\ 857 \times 10^{-25}$ J m 1,239.841 984 eV nm
$\hbar = h$	h bar, reduced Planck constant, Dirac constant	$1.054\ 571\ 817 \times 10^{-34}$ J s $6.582\ 119\ 570 \times 10^{-16}$ eV s

 doi:10.20944/preprints202403.0518.v1

symbol	name	value
2π		
f_{Cs}	hyperfine transition of ^{133}Cs	9 192 631 770 Hz
e	elementary charge	$1.602\,176\,634 \times 10^{-19}$ C
ε_0	electric constant, permitivitty of free space, vacuum permitivitty	$8.854\,187\,812\,8 \times 10^{-12}$ $C^2/N\,m^2$
μ_0	magnetic constant, permeability of free space, vacuum permeability	$1.256\,637\,062\,12 \times 10^{-6}$ T m/A
N_A	Avogadro constant	$6.022\,140\,76 \times 10^{23}$ 1/mol
k	Boltzmann constant	$1.380\,649 \times 10^{-23}$ J/K
$R = N_A k$	gas constant	8.314 462 618 J/mol K
$\sigma = \frac{2\pi^5 k^4}{15 h^3 c^2}$	Stefan-Boltzmann constant	$5.670\,374\,419 \times 10^{-8}$ W/m^2K^4
b	Wien displacement constant	2.897 771 955 mm K 58.789 257 57 GHz/K
m_u	atomic mass constant	$1.660\,539\,066\,60 \times 10^{-27}$ kg 931.494 102 42 MeV/c^2 1 u
m_e	electron mass	$9.109\,383\,701\,5 \times 10^{-31}$ kg 0.510 998 950 00 MeV/c^2 $5.485\,799\,090\,65 \times 10^{-4}$ u
m_p	proton mass	$1.672\,621\,923\,69 \times 10^{-27}$ kg 938.272 088 16 MeV/c^2 1.007 276 466 621 u
m_n	neutron mass	$1.674\,927\,498\,04 \times 10^{-27}$ kg 939.565 420 52 MeV/c^2 1.008 664 915 95 u

 doi:10.20944/preprints202403.0518.v1

symbol	name	value
K_{cd}	luminous efficacy	683 lm/W
H_0	hubble constant*	69.3 km/s/Mpc 2.25×10^{-18} 1/s

References

1. Badanta B., García M.A., Jiménez A.E., Lucchetti G., de Diego-Cordero R. The use of complementary and traditional medicine for the treatment of patients with COVID-19: a systematic review. EXPLORE. 2023 [PMC free article] [PubMed] [Google Scholar]
2. Chaudhary A., Khurana A., et al. A review on the role of homoeopathy in epidemics with some reflections on COVID-19 (SARS-cov-2) Ind J Res Homoeopathy. 2020;14(2):100. [Google Scholar]
3. Gosik M.S., Mendes M.F.X., da Silva Barbas D., do Cabo D.J.V., Strastis H., Takeuti I.S.D., et al. Medicines for the new coronavirus in the view of classical systemic homeopathy. Complement Ther Clin Pract. 2021;45:101482. [PMC free article] [PubMed] [Google Scholar] Worldometer Covid-19 Info, Coronavirus update (live) [cited February 20, 2021], Available from: https://www.worldometers.info/coronavirus/.
4. Interactive web-based dashboard at the coronavirus Resource center at Johns Hopkins university [cited February 20, 2021], Available from: https://coronavirus. jhu.edu/map.html.
5. Gesundheitsministerium Austria, Amtliches dashboard (Ministry of health Austria. Official dashboard) COVID-19 [Internet]. [cited February 20, 2021], Available from: https://info.gesundheitsministerium.at/dashboard_Epidem.html?l=de.
6. R.T. Mathie, S.M. Lloyd, L.A. Legg, J. Clausen, S. Moss, J.R. Davidson, et al., Randomised placebo-controlled trials of individualised homeopathic treatment: systematic review and meta-analysis, Syst. Rev. 3 (2014) 142, https://doi.org/ 10.1186/2046-4053-3-142.
7. P. Weiermayer, M. Frass, T. Peinbauer, L. Ellinger, Evidence-based homeopathy and veterinary homeopathy, and its potential to help overcome the anti-microbial resistance problem - an overview, Schweiz. Arch. Tierheilkd. 162 (2020) 597–615, https://doi.org/10.17236/sat00273.2020.
8. J. Jacobs, Homeopathic prevention and management of epidemic diseases, Homeopathy 107 (2018) 157–160, https://doi.org/10.1055/s-0038-1649487.
9. M. Frass, M. Linkesch, S. Banyai, G. Resch, C. Dielacher, T. Lobl, ¨ et al., Adjunctive homeopathic treatment in patients with severe sepsis: a randomized, double-blind, placebo-controlled trial in an intensive care unit, Homeopathy 94 (2005) 75–80, https://doi.org/10.1016/j.homp.2005.01.002.
10. S. Conde Diez, A. Viejo Casas, J.L. Garcia Rivero, J.C. Lopez Caro, F. Ortiz Portal, G. Diaz Saez, Impact of a homeopathic medication on upper respiratory tract infections in COPD patients: results of an observational, prospective study (EPOXILO), Respir. Med. 146 (2019) 96–105, https://doi.org/10.1016/j. rmed.2018.11.011.
11. P.S. Chakraborty, C.D. Lamba, D. Nayak, M.D. John, D.B. Sarkar, A. Poddar, et al., Effect of individualized homoeopathic treatment in influenza like illness: a multicenter, single blind, randomized, placebo-controlled study, IJRH 7 (2013) 22–30.
12. S. Prajapati, M. Sharma, A. Kumar, P. Gupta, G.V. Narasimha Kumar, An update on novel COVID-19 pandemic: a battle between humans and virus, Eur. Rev. Med. Pharmacol. Sci. 24 (2020) 5819–5829, https://doi.org/10.26355/eurrev_202005_ 21377.
13. K.L.A. To, Y.Y.Y. Fok, Homeopathic clinical features of 18 patients in COVID-19 outbreaks in Hong Kong, Homeopathy 109 (2020) 146–162, https://doi.org/ 10.1055/s-0040-1710545. Epub 2020 Jun 5.
14. M. Oberbaum, Will we miss the opportunity again? Homeopathy 109 (2020) 176–178, https://doi.org/10.1055/s-0040-1713082. Epub 2020 Jun 5.
15. N. Basu, B.C. Das, S. Tandon, Interim management of COVID-19 by repurposed homeopathic medicines, Homeopathy 109 (2020) 182–183, https://doi.org/ 10.1055/s-0040-1713004. Epub 2020 Jun 9.
16. S. Hahnemann, Organon of Medicine, sixth ed., B. Jain Publishers Ltd., New Delhi, 1994.

Hui DS. Epidemic and Emerging Coronaviruses (Severe Acute respiratory Syndrome and Middle East respiratory Syndrome). Clin Chest Med.2017 Mar;38 (1): 71-86. doi: 10.1016/j. ccm.2016.11.007. Epub 2016 Dec 16. PMID: 28159163; PMCID: PMC7131795.

17. Zhu N, Zhang D, Wang W, Li X, Yang B, Song J, ZhAoΨo X, Huang B, Shi W, Lu r, NiuP, Zhan F, Ma X, Wang D, Xu W, Wu G, GAoΨo GF, Tan W; China Novel Coronavirus Investigating and research Team. A Novel Coronavirus from Patients with Pneumonia in China,2019. N Engl J Med.2020 Feb 20;382 (8): 727-733. doi: 10.1056/NEJ Moa2001017. Epub 2020 Jan 24. PMID: 31978945; PMCID: PMC7092803.
18. Paraskevis D, Kostaki EG, Magiorkinis G, Panayiotakopoulos G, Sourvinos G, Tsiodras S. Full-genome evolutionary analysis of the novel corona virus (2019-nCoV) rejects the hypothesis of emergence as a result of a recent recombination event. InfectGenet Evol.2020 Apr;79: 104212. doi: 10.1016/j. meegid.2020.104212. Epub 2020 Jan29. PMID: 32004758; PMCID: PMC7106301.
19. Hendriks-Balk, M. C., Tjon-Atsoi, M., Hajji, N. et al. LPS differentially affects vasoconstrictor responses: a potential role for RGS16?. J. Physiol. Biochem.65,71–83 (2009). https://doi. org/10.1007/BF03165971
20. Nardi, D. T., Casare, M. S., Teixeira, L. G., Nascimento, N., & Nakaie, C. R. (2008). Effect of gamma radiation on the structural and biological properties of angiotensin II. International journal of radiation biology,84 (11),937–944. https://doi. org/10.1080/09553000802460164
21. Lu r, ZhAoΨo X, Li J, Niu P, Yang B, Wu H, Wang W, Song H, Huang B, Zhu N, Bi Y, Ma X, Zhan F, Wang L, Hu T, Zhou H, Hu Z, Zhou W, ZhAoΨo L, Chen J, Meng Y, Wang J, Lin Y, Yuan J, Xie Z, Ma J, Liu WJ, Wang D, Xu W, Holmes EC, GAoΨo GF, Wu G, Chen W, Shi W, Tan W. Genomic characterisation and epidemiology of 2019 novel coronavirus: implications for virus origins and receptor binding. Lancet.2020 Feb 22;395 (10224): 565-574. doi: 10.1016/S0140-6736 (20) 30251-8. Epub 2020 Jan 30.PMID: 32007145; PMCID: PMC7159086.
22. Zhang, X. Measurement-based universal blind Quantum computation with minor resources. Quantum Inf Process 21,14 (2022). https://doi.org/10.1007/s11128-021-03365-w
23. Arndt M., Juffmann T., Vedral V. Quantum physics meets biology HFSP J.,3 (6) (2009), pp.386-400,10.2976/1.3244985
24. Nunn, A.V.W.; Guy, G.W.; Bell, J.D. Thermodynamics and Inflammation: Insights into Quantum Biology and Ageing. Quantum Rep.2022,4,47-74. https://doi.org/10.3390/Quantum4010005
25. Nunn, A.V.; Guy, G.W.; Bell, J.D. The Quantum mitochondrion and optimal health. Biochem. Soc. Trans.2016,44,1101–1110. [Google Scholar] [CrossRef] [PubMed] [Green Version]
26. Gilijamse JJ, Lock AJ, Bakker HJ. Dynamics of confined water molecules. Proc Natl Acad Sci U S A. 2005;102:3202–3207. doi: 10.1073/pnas.0404916102. [PMC free article] [PubMed] [CrossRef] [Google Scholar]
27. Rey LR. Thermoluminescence of ultra-high dilutions of lithium chloride and sodium chloride. Phys A. 2003;323:67–74. doi: 10.1016/S0378-4371(03)00047-5. [CrossRef] [Google Scholar]
28. van Wijk R, Bosman S, van Wijk EP. Thermoluminescence in ultra-high dilution research. J Altern Complement Med. 2006;12:437–443. doi: 10.1089/acm.2006.12.437. [PubMed] [CrossRef] [Google Scholar]
29. Roberston T. Homoeopathy and recent advances in science and semantics. Br Homoeopath J. 1949;39:27–36. doi: 10.1016/S0007-0785(49)80004-4. [CrossRef] [Google Scholar]
30. Walach H. Entanglement model of homeopathy as an example of generalized entanglement predicted by weak quantum theory. Forsch Komplementarmed Klass Naturheilkd. 2003;10:192–200. doi: 10.1159/000073475. [PubMed] [CrossRef] [Google Scholar]
31. Weingärtner O. The nature of the active ingredient in ultramolecular dilutions. Homeopathy. 2007;96:220–226. doi: 10.1016/j.homp.2007.05.005. [PubMed] [CrossRef] [Google Scholar]
32. Weingärtner O. The homeopathic mechanism from the viewpoint of a quantum mechanical paradoxon. J Altern Complement Med. 2005;11:773–774. doi: 10.1089/acm.2005.11.773. [PubMed] [CrossRef] [Google Scholar]
33. Milgrom L. Patient–Practitioner–Remedy (PPR) entanglement: Part 1. A qualitative, non-local metaphor for homeopathy based on quantum theory. Homeopathy. 2002;91:239–248. doi: 10.1054/homp.2002.0055. [PubMed] [CrossRef] [Google Scholar]
34. McFadden, J.; Al-Khalili, J. The origins of Quantum biology. Proc. R. Soc. A 2018,474. [Google Scholar] [CrossRef] [Green Version]
35. Cramer JG. The transactional interpretation of quantum mechanics. Rev Mod Phys. 1986;58:647–87. [Google Scholar]

36. Walach H. Entanglement model of homeopathy as an example of generalised entanglement predicted by weak quantum theory. Forsche Komplementarmed Klass Naturheilkd. 2003;10:192–200. [PubMed] [Google Scholar]
37. Milgrom LR. Patient–practitioner–remedy (PPR) entanglement. Part 5: Can homeopathic remedy reactions be outcomes of PPR entanglement? Homeopathy. 2004;93:94–8. [PubMed] [Google Scholar]
38. Wooters WK. Quantum entanglement as a quantifiable resource. Philos Trans R Soc London A. 1998;356:1717. [Google Scholar]
39. Zeilinger A. 2004. Quantum teleportation and the nature of reality. Available at: http://www.btgjapan.org/catalysts/anton.html. [Google Scholar]
40. Walach H. Entangled—and tied in knots! Practical consequences of an entanglement model for homeopathic research and practice. Homeopathy. 2005;94:96–9. [PubMed] [Google Scholar]
41. Walach H. Generalised entanglement: a new theoretical model for understanding the effects of complementary and alternative medicine. J Altern Complement Med. 2005;11:549–59. [PubMed] [Google Scholar]
42. Walach H. Magic of signs: a non-local interpretation of homeopathy. Br Hom J. 2000;89:127–40. [PubMed] [Google Scholar]
43. Valente, D.; Brito, F.; Werlang, T. Quantum dissipative adaptation. Commun. Phys.2021,**4**,11. [Google Scholar] [CrossRef]
44. Marais, A.; Adams, B.; Ringsmuth, A.K.; Ferretti, M.; Gruber, J.M.; Hendrikx, R.; Schuld, M.; Smith, S.L.; Sinayskiy, I.; Kruger, T.P.J.; et al. The future of Quantum biology. J. R. Soc. Interface 2018,**15**,640. [Google Scholar] [CrossRef] [Green Version]
45. Pulselli, R.M.; Simoncini, E.; Tiezzi, E. Self-organization in dissipative structures: A thermodynamic theory for the emergence of prebiotic cells and their epigenetic evolution. Biosystems 2009,**96**,237–241. [Google Scholar] [CrossRef] [PubMed]
46. Prigogine, I.; George, C. The second law as a selection principle: The microscopic theory of dissipative processes in Quantum systems. Proc. Natl. Acad. Sci. USA 1983,**80**,4590–4594. [Google Scholar] [CrossRef] [PubMed] [Green Version]
47. Vattay, G.; Salahub, D.; Csabai, I.; Nassimi, A.; Kaufmann, S.A. Quantum Criticality at the Origin of Life. J. Phys. Conf. Ser 2015,**626**, 012023. [Google Scholar] [CrossRef]
48. Trixler, F. Quantum Tunnelling to the Origin and Evolution of Life. Curr. Org. Chem.2013,**17**,1758–1770. [Google Scholar] [CrossRef]
49. Trevors, J.T. Origin of microbial life: Nano-and molecular events, thermodynamics/entropy, Quantum mechanisms and genetic instructions. J. Microbiol. Methods 2011,**84**,492–495. [Google Scholar] [CrossRef] [PubMed]
50. Xin, H.; Sim, W.J.; Namgung, B.; Choi, Y.; Li, B.; Lee, L.P. Quantum biological tunnel junction for electron transfer imaging in live cells. Nat. Commun.2019,**10**,3245. [Google Scholar] [CrossRef] [PubMed]
51. Valente, D. Self-replication of a Quantum artificial organism driven by single-photon pulses. Sci. Rep.2021,**11**,16433. [Google Scholar] [CrossRef] [PubMed]
52. Ababneh, O.; Qaswal, A.B.; Alelaumi, A.; Khreesha, L.; Almomani, M.; Khrais, M.; Khrais, O.; Suleihat, A.; Mutleq, S.; Al-olaimat, Y.; et al. Proton Quantum Tunneling: Influence and Relevance to Acidosis-Induced Cardiac Arrhythmias/Cardiac Arrest. Pathophysiology 2021,**28**,400–436. [Google Scholar] [CrossRef]
53. Vattay, G.; Kauffman, S.; Niiranen, S. Quantum biology on the edge of Quantum chaos. PLoS ONE 2014,**9**, e89017. [Google Scholar] [CrossRef] [Green Version]
54. Lloyd, J. A., Spraggins, J. M., Johnston, M. V., & Laskin, J. (2006). Peptide ozonolysis: product structures and relative reactivities for oxidation of tyrosine and histidine residues. Journal of the American Society for Mass Spectrometry,**17** (9),1289–1298. https://doi. org/10.1016/j. jasms.2006.05.009
55. Mueller S. On DNA Signatures, Their Dual-Use Potential for GMO Counterfeiting, and a Cyber-Based Security Solution. Front Bioeng Biotechnol.2019 Aug 7;7: 189. doi: 10.3389/fbioe.2019.00189. PMID: 31440503; PMCID: PMC6693310.
56. Ziebuhr J. Molecular biology of severe acute respiratory syndrome coronavirus. Curr Opin Microbiol.2004 Aug;7 (4): 412-9. doi: 10.1016/j. mib.2004.06.007. PMID: 15358261;PMCID: PMC7108451.
57. Susan r. Iiss, Julian L. Leibowitz, Chapter 4-Coronavirus Pathogenesis, Editor (s): Karl Maramorosch, Aaron J. Shatkin, Frederick A. Murphy, Advances in Virus research, Academic Press, Volume 81,2011, pages 85-164, iSSN 0065-3527, iSBN 9780123858856, https://doi. org/10.1016/B978-0-12-385885-6.00009-2.

58. Brian DA, Baric rS. Coronavirus genome structure and replication. Curr Top Microbiol Immunol.2005;287: 1-30.doi: 10.1007/3-540-26765-4_1.PMID: 15609507;PMCID: PMC7120446.
59. Rothlin, R. P., Vetulli, H. M., Duarte, M., & Pelorosso, F. G. (2020). Telmisartan as tentative angiotensin receptor blocker therapeutic for COVID-19. Drug development research,81 (7),768–770.https://doi. org/10.1002/ddr.21679
60. Elkahloun, A. G., & Saavedra, J. M. (2020). Candesartan could ameliorate the COVID-19 cytokine storm. Biomedicine & pharmacotherapie,131,110653. https://doi. org/10.1016/j. biopha.2020.110653
61. Duarte, M., Pelorosso, F., Nicolosi, L. N., Salgado, M. V., Vetulli, H., Aquieri, A., Azzato, F., Castro, M., Coyle, J., Davolos, I., Criado, I. F., Gregori, R., Mastrodonato, P., Rubio, M. C., Sarquis, S., Wahlmann, F., & Rothlin, R. P. (2021). Telmisartan for treatment of Covid-19 patients: An open multicenter randomized clinical trial. EClinicalMedicine,37,100962. https://doi. org/10.1016/j. eclinm.2021.100962
62. Siu KL, Chan CP, Kok KH, Chiu-Yat Woo P, Jin DY. Suppression of innate antiviral response by severe acute respiratory syndrome coronavirus M protein is mediated through the first transmembrane domain. Cell Mol Immunol.2014 Mar;11 (2): 141-9. doi: 10.1038/cmi.2013.61.Epub2014 Feb 10.PMID: 24509444; PMCID: PMC4003381.
63. Schoeman D, Fielding BC. Coronavirus envelope protein: current knowledge. Virol J.2019May 27;16 (1): 69. doi: 10.1186/s12985-019-1182-0.PMID: 31133031; PMCID: PMC6537279.
64. Al-Tawfiq JA, Al-Homoud AH, Memish ZA. Remdesivir as a possible therapeutic option for the COVID-19. Travel Med Infect Dis.2020 Mar-Apr;34: 101615. doi: 10.1016/j. tmaid.2020.101615. Epub 2020 Mar 5. PMID: 32145386; PMCID: PMC7129391.
65. Agostini ML, Andres EL, Sims AC, Graham rL, Sheahan TP, Lu X, Smith EC, Case JB, FengJY, Jordan r, ray AS, Cihlar T, Siegel D, Mackman rL, Clarke MO, Baric rS, Denison Mr. Coronavirus Susceptibility to the Antiviral Remdesivir (GS-5734) Is Mediated by the Viral Polymerase and the Proof reading Exoribonuclease. mBio.2018 Mar 6;9 (2): e00221-18. doi: 10.1128/mBio.00221-18. PMID: 29511076; PMCID: PMC5844999.
66. de Wit E, Feldmann F, Cronin J, Jordan r, Okumura A, Thomas T, Scott D, Cihlar T, Feldmann H. Prophylactic and therapeutic Remdesivir (GS-5734) treatment in the rhesus macaque model of MERS-CoV infection. Proc Natl Acad Sci U S A.2020 Mar 24;117 (12): 6771-6776. doi: 10.1073/pnas.1922083117. Epub 2020 Feb 13. PMID: 32054787; PMCID: PMC7104368.
67. Pilon AC, Valli M, Dametto AC, Pinto MEF, Freire rT, Castro-Gamboa I, Andricopulo AD, Bolzani VS. NuBBEDB: an updated database to uncover chemical and biological information from Brazilian biodiversity. Sci rep.2017 Aug 3;7 (1): 7215. doi: 10.1038/s41598-017-07451-x. PMID: 28775335; PMCID: PMC5543130.
68. Khot WY, Nadkar MY. The 2019 Novel Coronavirus Outbreak-A Global Threat. J AssocPhysicians India.2020 Mar;68 (3): 67-71.PMID: 32138488.
69. Zeng YM, Xu XL, He XQ, Tang SQ, Li Y, Huang YQ, Harypursat V, Chen YK. Comparative effectiveness and safety of ribavirin plus interferon-alpha, lopinavir/ritonavir plus interferon-alpha, and ribavirin plus lopinavir/ritonavir plus interferon-alpha in patients with mild to moderate novel coronavirus disease 2019: study protocol. Chin Med J (Engl).2020 May 5;133 (9): 1132-1134. doi: 10.1097/CM9.0000000000000790.PMID: 32149772; PMCID: PMC7213617.
70. McGraw PN, Menzinger M, Muñuzuri AP. Harmonic resonant excitation of flow distributed oscillation waves and Turing patterns driven at a growing boundary. Phys rev E Stat Nonlin SoftMatter Phys.2009 Aug; 80 (2 Pt 2): 026209. doi: 10.1103/PhysrevE.80.026209. Epub 2009 Aug20.PMID: 19792233.
71. Martinez MA. Compounds with Therapeutic Potential against Novel respiratory 2019Coronavirus. Antimicrob Agents Chem other.2020 Apr 21;64 (5): e00399-20.doi: 10.1128/AAC.00399-20.PMID: 32152082; PMCID: PMC7179632.
72. Gordon CJ, Tchesnokov EP, Feng JY, Porter DP, Götte M. The antiviral compound Remdesivir potently inhibits RNA-dependent RNA polymerase from Middle East respiratory syndrome coronavirus. J Biol Chem.2020 Apr 10;295 (15): 4773-4779. doi: 10.1074/jbc. AC120.013056. Epub2020 Feb 24. PMID: 32094225; PMCID: PMC7152756.
73. Sheahan TP, Sims AC, Leist Sr, Schäfer A, Won J, Brown AJ, Montgomery SA, Hogg A, Babusis D, Clarke MO, Spahn JE, Bauer L, Sellers S, Porter D, Feng JY, Cihlar T, Jordan r, DenisonMr, Baric rS. Comparative therapeutic efficacy of Remdesivir and combination lopinavir, ritonavir, and interferon beta against MERS-

CoV. Nat Commun.2020 Jan 10;11 (1): 222. doi: 10.1038/s41467-019-13940-6. PMID: 31924756; PMCID: PMC6954302.

74. Trott O, Olson AJ. AutoDock Vina: improving the speed and accuracy of docking with a new scoring function, efficient optimization, and multithreading. J Comput Chem.2010 Jan30;31 (2): 455-61.doi: 10.1002/jcc.21334. PMID: 19499576; PMCID: PMC3041641.
75. Van Meter, r., Satoh, T., Ladd, T. D. et al. Path selection for Quantum repeater networks. Netw. Sci.3,82–95 (2013). https://doi. org/10.1007/s13119-013-0026-2
76. Xin T, Che L, Xi C, Singh A, Nie X, Li J, Dong Y, Lu D. Experimental Quantum Principal Component Analysis via Parameterized Quantum Functions. Phys rev Lett.2021 Ma [r1] 9;126 (11): 110502. doi: 10.1103/PhysrevLett.126.11050.PMID: 33798351.
77. Henriques AG. What Chern-Simons theory assigns to a point. Proc Natl Acad Sci U S A.2017 Dec 19;114 (51): 13418-13423. doi: 10.1073/pnas.1711591114. Epub 2017 Dec 5. PMID: 29208715; PMCID: PMC5754777.
78. Honda M. Supersymmetric Solutions and Borel Singularities for N,2 Supersymmetric Chern-SimonsTheories. Phys rev Lett.2018 Jul 13; 121 (2): 021601.doi: 10.1103/PhysrevLett.121.02160.PMID: 30085688.
79. Simón J. Brane Effective Actions, Kappa-Symmetry and Applications. Living rev relativ.2012; 15 (1): 3. doi: 10.12942/lrr-2012-3. Epub 2012 Feb 27. PMID: 28179834; PMCID: PMC5256004.
80. Cavaglià A, Fioravanti D, Gromov N, Tateo R. Quantum spectral curve of the N,6 supersymmetric Chern-Simons theory. Phys rev Lett.2014 Jul 11; 113 (2): 021601.doi: 10.1103/PhysrevLett.113.021601.Epub 2014 Jul 11.PMID: 25062163.
81. Mabkhot YN, Alatibi F, El-Sayed NN, Al-Showiman S, Kheder NA, Wadood A, rauf A, Bawazeer S, HaddaTB. Antimicrobial Activity of Some Novel Armed Thiophene Derivatives andPetra/Osiris/Molinspiration (POM) Analyses. Molecules.2016 Feb 17; 21 (2): 222. doi: 10.3390/molecules21020222. PMID: 26901173; PMCID: PMC6273311.
82. Khan T, Lawrence AJ, Azad I, Raza S, Joshi S, Khan Ar. Computational Drug Designing and Prediction of Important Parameters Using in-silico Methods-A review. Curr Comput Aided Drug Des.2019; 15 (5): 384-397. doi: 10.2174/1573399815666190326120006. PMID: 30914032.
83. Ulrich H, Pillat MM. CD147 as a Target for COVID-19 Treatment: Suggested Effects of Azithromycin and Stem Cell Engagement. Stem Cell rev rep.2020 Jun;16 (3): 434-440.doi: 10.1007/s12015-020-09976-7. PMID: 32307653; PMCID: PMC7167302.
84. Chan JF, Kok KH, Zhu Z, Chu H, To KK, Yuan S, Yuen KY. Genomic characterization of the 2019 novel human-pathogenic coronavirus isolated from a patient with atypical pneumonia after visiting Wuhan. Emerg Microbes Infect.2020 Jan 28;9 (1): 221-236. doi: 10.1080/22221751.2020.1719902. Erratumin: Emerg Microbes Infect.2020 Dec;9 (1): 540.PMID: 31987001; PMCID: PMC7067204.
85. Kong r, Yang G, Xue r, Liu M, Wang F, Hu J, Guo X, Chang S. COVID-19 Docking Server: a meta server for docking small molecules, peptides and antibodies against potential targets of COVID-19. Bioinformatics.2020 Dec 22;36 (20): 5109-5111.doi: 10.1093/bioinformatics/btaa645. PMID: 32692801; PMCID: PMC7558834.
86. Shi Y, Zhang X, Mu K, Peng C, Zhu Z, Wang X, Yang Y, Xu Z, Zhu W. D3Targets-2019-nCoV: a webserver for predicting drug targets and for multi-target and multi-site based virtual screening against COVID-19. Acta Pharm Sin B.2020 Jul;10 (7): 1239-1248. doi: 10.1016/j. apsb.2020.04.006. Epub 2020 Apr 20.PMID: 32318328; PMCID: PMC7169934.
87. Camila Silva de Magalhães, Diogo Marinho Almeida, Helio José Correa Barbosa, Laurent Emmanuel Dardenne, A dynamic niching genetic algorithm strategy for docking highly flexible ligands. Information Sciences, Volume 289,2014, pages 206-224, iSSN 0020-0255, https://doi. org/10.1016/j. ins.2014.08.00.
88. Van Loock P, Ladd TD, Sanaka K, Yamaguchi F, Nemoto K, Munro WJ, Yamamoto Y. Hybrid Quantum repeater using bright coherent light. Phys rev Lett.2006 Jun 23;96 (24): 240501.doi: 10.1103/PhysrevLett.96.240501.Epub 2006 Jun 19. PMID: 16907223.
89. ZhAoΨo B, Chen ZB, Chen YA, Schmiedmayer J, Pan JW. robust creation of entanglement between remote memory qubits. Phys rev Lett.2007 Jun 15;98 (24): 240502. doi: 10.1103/PhysrevLett.98.240502. Epub 2007 Jun 15. PMID: 17677950.
90. Santos KB, Guedes IA, Karl ALM, Dardenne LE. Highly Flexible Ligand Docking: Benchmarking of the DockThor Program on the LEADS-PEP Protein-Peptide Data Set. J Chem Inf Model.2020 Feb 24;60 (2): 667-683. doi: 10.1021/acs. jcim.9b00905. Epub 2020 Jan 27. PMID: 31922754.

91. Iheagwam FN, rotimi SO. Computer-Aided Analysis of Multiple SARS-CoV-2 Therapeutic Targets: Identification of Potent Molecules from African Medicinal Plants. Scientifica (Cairo).2020 Sep 12;2020: 1878410.doi: 10.1155/2020/1878410.PMID: 32963884; PMCID: PMC7492903.
92. Müller S. Flexible heuristic algorithm for automatic molecule fragmentation: application to the UNIFAC group contribution model. J Cheminform.2019; 11: 57. Published 2019 Aug 20.doi: 10.1186/s13321-019-0382-3
93. Shi J, Chen S, Lu Y, et al. An Approach to Cryptography Based on Continuous-Variable Quantum Neural Network. Sci rep.2020;10 (1): 2107. Published 2020 Feb 7. doi: 10.1038/s41598-020-58928-1
94. Nalewajski, r. F. Quantum information descriptors and communications in molecules. JMath Chem 52,1292–1323 (2014). https://doi. org/10.1007/s10910-014-0311-7
95. Giribet, Gaston & Merino, Nelson & Miskovic, Olivera & Zanelli, Jorge. (2014). Black hole solutions in Chern-Simons AdS supergravity. Journal of High Energy Physics.2014.10.1007/JHEP08 (2014) 083.
96. Baianu, Ion & Glazebrook, James & Brown, ronald. (2009). Algebraic Topology Foundations of Supersymmetry and Symmetry Breaking in Quantum fields Theory and Quantum Gravity: A review. Symmetry, Integrability and Geometry: Methods and Applications.5.10.3842/SIGMA.2009.051.
97. Horvathy, Peter. (1999). Topology of non-topological Chern-Simons vortices.
98. Bañados, Máximo & Troncoso, ricardo & Zanelli, Jorge. (1996). Higher dimensional Chern-Simons supergravity. Physical review D.54.10.1103/PhysrevD.54.2605.
99. Bañados, Máximo & Gomberoff, Andres. (1996). Black Hole Entropy in the Chern-Simons Formulation of 2,1 Gravity.
100. Zizzi P. Quantum Information Hidden in Quantum fieldss. Quantum Reports.2020; 2 (3): 459-488. https://doi. org/10.3390/Quantum2030033
101. Nasser M, Salim N, Saeed F, Basurra S, Rabiu I, Hamza H, Alsoufi MA. Feature Reduction for Molecular Similarity Searching Based on Autoencoder Deep Learning. Biomolecules.2022; 12 (4):508. https://doi. org/10.3390/biom12040508
102. Mohammed MEA. The percentages of SARS-CoV-2 protein similarity and identity with SARS-CoVand BatCoV raTG13 proteins can be used as indicators of virus origin. J Proteins Proteom.2021 Apr 9: 1-11.doi: 10.1007/s42485-021-00060-3. Epub ahead of print. PMID: 33850392; PMCID: PMC8033097.
103. Schwarzschild K. Sitzungsberichte der Königlich Preußischenakademie der Wissenschaften; Berlin: 1916. Über das gravitationsfeld eines massenpunktes nach der einsteinschen theorie; pp.189–196. [Google Scholar]
104. Reissner H. Über die eigengravitation des elektrischen feldes nach der einsteinschen theorie. Ann. Phys.1916;355 (9):106–120. [Google Scholar]
105. Nordström G. On the energy of the gravitation field in Einstein's theory. Proc. K. Ned.akad. It., Ser. B, Phys. Sci.1918;20:1238–1245. [Google Scholar]
106. Kerr R.P. Gravitational field of a spinning mass as an example of algebraically special metrics. Phys. Rev. Lett.1963;11 (5):237. [Google Scholar]
107. Newman E.T., Couch E., Chinnapared K., Exton A., Prakash A., Torrence R. Metric of a rotating, charged mass. J. Math. Phys.1965;6 (6):918–919. [Google Scholar]
108. Vaidya P. The external field of a radiating star in general relativity. Curr. Sci.1943;12 (6):183. [Google Scholar]
109. Hawking S. Black-hole evaporation. Nature.1974;248 (5443):30–31. [Google Scholar]
110. Newman E.T., Adamo T. Kerr–Newman metric. Scholarpedia.2014;9 (10) [Google Scholar]
111. Brauer O., Camargo H., Socolovsky M. Newman–Janis algorithm revisited. Int. J. Theor. Phys.2015;54 (1):302–314. [Google Scholar]
112. Penrose R., Rindler W. Cambridge University Press; 1984. Spinors and Space-Time: Volume 1, Two-Spinor Calculus and Relativistic Fields, Vol.1. [Google Scholar]
113. Nerozzi A. A new approach to the Newman–Penrose formalism. arXiv:1109.4400 arXiv preprint.
114. Meinel R.1st Karl Schwarzschild Meeting on Gravitational Physics. Springer; 2016. A physical derivation of the Kerr–Newman black hole solution; pp.53–61. [Google Scholar]
115. Kramer D. The Ernst function in general relativity. Czechoslov. J. Phys. B.1987;37 (3):350–358. [Google Scholar]
116. Chou Y.-C. A derivation of the Kerr metric by ellipsoid coordinate transformation. Int. J. Phys. Sci.2017;12 (11):130–136. [Google Scholar]

117. Chou Y.-C. A derivation of the Kerr–Newman metric using ellipsoid coordinate transformation. J. Appl. Phys. Sci. Int.2018;10 (3):144–150. [Google Scholar]
118. Ibohal N. Rotating metrics admitting non-perfect fluids. Gen. Relativ. Gravit.2005;37 (1):19–51. [Google Scholar]
119. Ghosh S.G., Maharaj S.D. Radiating Kerr-like regular black hole. Eur. Phys. J. C.2015;75 (1):7. [Google Scholar]
120. Eddington A.S. A comparison of Whitehead's and Einstein's formula. Nature.1924;113 (2832):192. [Google Scholar]
121. Finkelstein D. Past-future asymmetry of the gravitational field of a point particle. Phys. Rev.1958;110 (4):965. [Google Scholar]
122. Boehmer C.G., Hogan P.A. A Vaidya-type generalization of Kerr spacetime. Mod. Phys. Lett. A.2017;32 (35) [Google Scholar]
123. Taub A. High frequency gravitational radiation in Kerr–Schild space-times. Commun. Math. Phys.1976;47 (2):185–196. [Google Scholar]
124. Reynolds C. The spin of supermassive black holes. Class. Quantum Gravity.2013;30 (244004):17. [Google Scholar]
125. Everitt C.F., DeBra D., Parkinson B., Turneaure J., Conklin J., Heifetz M., Keiser G., Silbergleit A., Holmes T., Kolodziejczak J. Gravity probe B: final results of a space experiment to test general relativity. Phys. Rev. Lett.2011;106 (22) [PubMed] [Google Scholar]
126. Petrov A.Z. The classification of spaces defining gravitational fields. Gen. Relativ. Gravit.2000;32 (8):1665–1685. [Google Scholar]
127. Erbin H. Janis–Newman algorithm: simplifications and gauge field transformation. Gen. Relativ. Gravit.2015;47 (3):19. [Google Scholar]
128. Bekenstein J.D. Black holes and entropy. Phys. Rev. D.1973;7 (8):2333. [Google Scholar]
129. Hawking S.W. Particle creation by black holes. Commun. Math. Phys.1975;43 (3):199–220. [Google Scholar]
130. Bardeen J.M., Carter B., Hawking S.W. The four laws of black hole mechanics. Commun. Math. Phys.1973;31 (2):161–170. [Google Scholar]
131. Raine D.J., Thomas E.G. Imperial College Press; 2010. Black Holes: An Introduction. [Google Scholar]
132. Page D.N. Hawking radiation and black hole thermodynamics. New J. Phys.2005;7 (1):203. [Google Scholar]
133. Williams D. Pluto fact sheet, NASA.2015. https://nssdc.gsfc.nasa.gov/planetary/factsheet/plutofact.html retrieved from.
134. Iorio L. Constraints on the location of a putative distant massive body in the solar system from recent planetary data. Celest. Mech. Dyn. Astron.2012;112 (2):117–130. [Google Scholar]
135. Faber A.,akiyama K., Alberdi A., Alef W., Asada K., Azulay R., Baczko A.-K., Ball D., Baloković M., Barrett J. First M87 event horizon telescope results. I. The shadow of the supermassive black hole. Astrophys. J. Lett.2019;875 (1) [Google Scholar]
136. Hawking S. Gravitationally collapsed objects of very low mass. Mon. Not. R. Astron. Soc.1971;152 (1):75–78. [Google Scholar]
137. Zolfaghari Emameh, r., Eftekhari, M., Nosrati, H. et al. Identification and characterization of a silent mutation in RNA binding domain of N protein coding gene fromSARS-CoV-2. BMC res Notes 14,10 (2021). https://doi. org/10.1186/s13104-020-05439-x
138. Neuman BW, Kiss G, Kunding AH, Bhella D, Baksh MF, Connelly S, Droese B, KlausJP, Makino S, Sawicki SG, Siddell SG, Stamou DG, Wilson IA, Kuhn P, Buchmeier MJ. A structural analysis of M protein in coronavirus assembly and morphology. J Struct Biol.2011 Apr;174 (1): 11-22. doi: 10.1016/j. jsb.2010.11.021.Epub 2010 Dec 3. PMID: 21130884; PMCID: PMC4486061.
139. M.Z. Teixeira, Clinical research protocol to evaluate the effectiveness and safety of individualized homeopathic medicine in the treatment and prevention of the COVID-19 epidemic, Rev. Assoc. Med. Bras. 66 (2020) 405–406, https://doi.org/ 10.1590/1806-9282.66.4.405.
140. E.G. Rossi, The experience of an Italian public homeopathy clinic during the COVID-19 epidemic, March-May 2020, Homeopathy 109 (2020) 167–168, https:// doi.org/10.1055/s-0040-1713618. Epub 2020 Jul 8.
141. B. Jethani, M. Gupta, P. Wadhwani, R. Thomas, T. Balakrishnan, G. Mathew, et al., Clinical characteristics and remedy profiles of patients with COVID-19: a retrospective cohort study, Homeopathy (2021 Feb 10), https://doi.org/10.1055/ s-0040-1718584 (Online ahead of print).

142. W. Boericke W, Pocket Manual of Homoeopathic Materia Medica Comprising the Characteristic and Guiding Symptoms of All Remedies, ninth ed., Boericke and Runyon, Boericke and Tafel, Inc., Philadelphia, PA, 1927.
143. A. Hofmann, Nosoden – status und Verfügbarkeit. (Nosodes - status and availability), Allg. Homoopathische ¨ Ztg. 259 (2014) 7–9.
144. Homoopathisches ¨ Arzneibuch, Vorschriften 43 und 44. Deutscher Apotheker Verlag, Stuttgart, Deutschland (Homeopathic Pharmacopoeia 2019, Regulations 43 and 44, Deutscher Apotheker Verlag, Stuttgart, Germany, 2019.
145. V.M. Corman, O. Landt, M. Kaiser, R. Molenkamp, A. Meijer, D.K. Chu, et al., Detection of 2019 novel coronavirus (2019-nCoV) by real-time RT-PCR, Euro Surveill. 25 (2020) 2000045, https://doi.org/10.2807/1560-7917. ES.2020.25.3.2000045.
146. C.D. Lamba, V.K. Gupta, R. van Haselen, L. Rutten, N. Mahajan, A.M. Molla, et al., Evaluation of the modified Naranjo criteria for assessing causal attribution of clinical outcome to homeopathic intervention as presented in Case reports, Homeopathy 109 (2020) 191–197, https://doi.org/10.1055/s-0040-1701251. Epub 2020 Mar 25.
147. Directive 2001/83/EC of the European parliament and of the Council of 6 november 2001 on the community code relating to medicinal products for human use, Brüssel, Belgium, https://www.ema.europa.eu/en/documents/regulatoryprocedural-guideline/directive-2001/83/ec-european-parliament-council-6-nove mber-2001-community-code-relating-medicinal-products-human-use_en.pdf (cited 2020 July 20).
148. S. Waisse, M. Oberbaum, M. Frass, The hydra-headed coronaviruses: implications of COVID-19 for homeopathy, Homeopathy 109 (2020) 169–175, https://doi.org/ 10.1055/s-0040-1714053. Epub 2020 Jul 22. PMID: 32698230.
149. I. Ali, O.M.L. Alharbi, COVID-19: disease, management, treatment, and social impact, Sci. Total Environ. 728 (2020) 138861, https://doi.org/10.1016/j. scitotenv.2020.138861. Epub 2020 Apr 22.
150. E. Bernstein and U. Vazirani, Quantum Complexity Theory, in Proceedings of 1993 ACM Symposium on Theory of Computing (1993), pp.11-20.
151. D. Deutsch, Quantum Theory, the Church-Turing Principle and the Universal Quantum Computer, Proceedings of the Royal Society of London, Vol. A 400 (1985), pp.97-117.
152. D. Deutsch and R. Jozsa, Rapid solution of problems by quantum computation, Proceedings of the Royal Society of London. Vol. A439, pp.553-558 (1992).
153. P. Shor, Algorithms for Quantuim Computation: Discrete Log and Factoring, in Proceedings 35th IEEE Symposium on Foundations of Computer Sciende, IEEE Press (1994), pp.124-134.
154. D. Simon, On the power of quantum computation, in Proceedings 35th IEEE Symposium on Foundations of Computer Sciende, IEEE Press (1994), pp.116-123.
155. A. Yao, Quantum Circuit Complexity, Proceedings of 34th Symposium on Foundations of Computer Science (1993), pp.352-361.
156. Shor, P.W.: Polynomial-time algorithms for prime factorization and discrete logarithms on a quantum computer. SIAM J. Comput 26,1484–1509 (1997)
157. Fisher P, Scott DL. A randomized controlled trial of homeopathy in rheumatoid arthritis. Rheumatology. 2001;40:1052–1055. doi: 10.1093/rheumatology/40.9.1052. [PubMed] [CrossRef] [Google Scholar]
158. Grabia S, Ernst E. Homoeopathic aggravations: a systematic review of randomised, placebo-controlled clinical trials. Homeopathy. 2003;92:92–98. doi: 10.1016/S1475-4916(03)00007-9. [PubMed] [CrossRef] [Google Scholar]
159. Davenas E, Beauvais F, Amara J, Oberbaum M, Robinzon B, Miadonna A, Tedeschi A, Pomeranz B, Fortner P, Belon P, Sainte-Laudy J, Poitevin B, Benveniste J. Human basophil degranulation triggered by very dilute antiserum against IgE. Nature. 1988;333:816–818. doi: 10.1038/333816a0. [PubMed] [CrossRef] [Google Scholar]
160. Maddox J, Randi J, Stewart WW. “High-dilution” experiments a delusion. Nature. 1988;334:287–290. doi: 10.1038/334287a0. [PubMed] [CrossRef] [Google Scholar]
161. Hirst SJ, Hayes NA, Burridge J, Pearce FL, Foreman JC. Human basophil degranulation is not triggered by very dilute antiserum against human IgE. Nature. 1993;366:525–527. doi: 10.1038/366525a0. [PubMed] [CrossRef] [Google Scholar]

162. Harvey W. Exercitatio Anatomica de Motu Cordis et Sanguinis in Animalibus (Anatomical account of the motion of the heart and blood in animals). Frankfurt; 1628.
163. Dean ME. 'An innocent deception': placebo controls in the St Petersburg homeopathy trial, 1829–1830. J R Soc Med. 2006;99:375–376. doi: 10.1258/jrsm.99.7.375. [PMC free article] [PubMed] [CrossRef] [Google Scholar]
164. Forbes J. Homoeopathy, allopathy and "young physic" Br Foreign Med Rev. 1846;21:225–265. [PMC free article] [PubMed] [Google Scholar]
165. Paris A, Gonnet N, Chaussard C, Belon P, Rocourt F, Saragaglia D, Cracowski JL. Effect of homeopathy on analgesic intake following knee ligament reconstruction. Br J Clin Pharmacol. 2007;65:180–187. doi: 10.1111/j.1365-2125.2007.03008. [PMC free article] [PubMed] [CrossRef] [Google Scholar]
166. Brien S, Lachance L, Prescott P, McDermott C, Lewith G. Homeopathy has clinical benefits in rheumatoid arthritis patients that are attributable to the consultation process but not the homeopathic remedy: a randomized controlled clinical trial. Rheumatology. 2011;50(13):1070–1082. doi: 10.1093/rheumatology/keq234. [PMC free article] [PubMed] [CrossRef] [Google Scholar]
167. Shang A, Huwiler-Müntener K, Nartey L, Jüni P, Dörig S, Sterne JA, Pewsner D, Egger M. Are the clinical effects of homoeopathy placebo effects? Comparative study of placebo-controlled trials of homoeopathy and allopathy. Lancet. 2005;366:726–732. doi: 10.1016/S0140-6736(05)67177-2. [PubMed] [CrossRef] [Google Scholar]
168. Rutten AL, Stolper CF. The 2005 meta-analysis of homeopathy: the importance of post-publication data. Homeopathy. 2008;97:169–177. doi: 10.1016/j.homp.2008.09.008. [PubMed] [CrossRef] [Google Scholar]
169. Wilson P. Analysis of a re-analysis of a meta-analysis: in defence of Shang et al. Homeopathy. 2009;98:127–128. doi: 10.1016/j.homp.2008.12.003. [PubMed] [CrossRef] [Google Scholar]
170. The Lancet The end of homoeopathy. The Lancet. 2005;366(9487):690. [PubMed] [Google Scholar]
171. National Health and Medical Research Council. NHMRC information paper: evidence on the effectiveness of homeopathy for treating health conditions. Canberra: National Health and Medical Research Council; 2015. [Google Scholar]
172. European Academies' Science Advisory Council. Homeopathic products and practices: assessing the evidence and ensuring consistency in regulating medical claims in the EU. 2017. https://easac.eu/publications/details/homeopathic-products-and-practices/. Accessed: 27 Oct 2019
173. Podolsky SH, Kesselheim AS. Regulating homeopathic products—a century of dilute interest. N Engl J Med. 2016;374:201–203. doi: 10.1056/NEJMp1513393. [PubMed] [CrossRef] [Google Scholar]
174. Cooper KL, Harris PE, Relton C, Thomas KJ. Prevalence of visits to five types of complementary and alternative medicine practitioners by the general population: a systematic review. Complement Ther Clin Pract. 2013;19:214–220. doi: 10.1016/j.ctcp.2013.06.006. [PubMed] [CrossRef] [Google Scholar]
175. Furnham A, Vincent C, Wood R. The health beliefs and behaviors of three groups of complementary medicine and a general practice group of patients. J Altern Complement Med. 1995;1:347–359. doi: 10.1089/acm.1995.1.347. [PubMed] [CrossRef] [Google Scholar]
176. Miller JD. The measurement of civic scientific literacy. Public Understand Sci. 1998;7:203–223. doi: 10.1088/0963-6625/7/3/001. [CrossRef] [Google Scholar]
177. Loudon I. A brief history of homeopathy. J R Soc Med. 2006;99:607–610. doi: 10.1258/jrsm.99.12.607. [PMC free article] [PubMed] [CrossRef] [Google Scholar]
178. Klein SD, Torchetti L, Frei-Erb M, Wolf U. Usage of complementary medicine in Switzerland: results of the Swiss health survey 2012 and development since 2007. PLoS ONE. 2015;10:e0141985. doi: 10.1371/journal.pone.0141985. [PMC free article] [PubMed] [CrossRef] [Google Scholar]
179. Belmi P, Neale MA, Reiff D, Ulfe R. The social advantage of miscalibrated individuals: the relationship between social class and overconfidence and its implications for class-based inequality. J Pers Soc Psychol. 2020;118:254–282. doi: 10.1037/pspi0000187. [PubMed] [CrossRef] [Google Scholar]
180. Snow CP. The two cultures. London: Cambridge University Press; 1959. [Google Scholar]
181. Avina RL, Schneiderman LJ. Why patients choose homeopathy. West J Med. 1978;128:366–369. [PMC free article] [PubMed] [Google Scholar]
182. Gunther M. The homeopathic patient: comparative results of homeopathic and conventional GP patient interviews. Med Ges Gesch. 1999;18:119–136. [PubMed] [Google Scholar]

183. Smith PJ, Clavarino A, Long J, Steadman KJ. Why do some cancer patients receiving chemotherapy choose to take complementary and alternative medicines and what are the risks? Asia Pac J Clin Oncol. 2014;10:1–10. doi: 10.1111/ajco.12115. [PubMed] [CrossRef] [Google Scholar]
184. Humpel N, Jones SC. Gaining insight into the what, why and where of complementary and alternative medicine use by cancer patients and survivors. Eur J Cancer Care. 2006;15:362–368. doi: 10.1111/j.1365-2354.2006.00667.x. [PubMed] [CrossRef] [Google Scholar]
185. Morant R, Jungi WF, Koehli C, Senn HJ. Warum benützen Tumorpatienten Alternativmedizin? (Why do cancer patients use alternative medicine?) Schweiz Med Wochenschr. 1991;121:1029–1034. [PubMed] [Google Scholar]
186. Boon H, Stewart M, Kennard MA, Gray R, Sawka C, Brown JB, McWilliam C, Gavin A, Baron RA, Aaron D, Haines-Kamka T. Use of complementary/alternative medicine by breast cancer survivors in Ontario: prevalence and perceptions. J Clin Oncol. 2000;18:2515–2521. doi: 10.1200/JCO.2000.18.13.2515. [PubMed] [CrossRef] [Google Scholar]
187. Angell M, Kassirer JP. Alternative medicine—the risks of untested and unregulated remedies. N Engl J Med. 1998;339:839–841. doi: 10.1056/NEJM199809173391210. [PubMed] [CrossRef] [Google Scholar]
188. Shor, P.W.: Fault-tolerant quantum computation. In: Proceedings of the 37th IEEE Symposium on Foundations of Computer Science, pp.56–65. IEEE Computer Society Press, Los Alamitos, CA (1996)
189. KARISSON, PER W., Hypergeometric functions with integral parameter differences, J. Math. Phys. 12, 270-271 (1971).
190. LUJCE, YIJDELL L., The special functions and their approximations, Vol. I (Academic Press, New York and London, 1969).
191. SNEDDON, IAN N., Special functions of mathematical physics and chemistry, Second edition (Oliver and Boyd, Ltd., Edinburgh and London, 1966).
192. Evaluation of the Modified Naranjo Criteria for Assessing Causal Attribution of Clinical Outcome to Homeopathic Intervention as Presented in Case Reports Chetna Deep Lamba et al., Homeopathy, 2020
193. A Co-morbid Condition of Warts and Vitiligo Treated with Individualized Homeopathy: An Evidence-Based Case Report
194. Akhyaya Kumar Prusty et al., Homeopathy, 2021 A Case Report of Idiopathic OAT Syndrome, Associated with Necrospermia and Hypospermia, Reversed with Individualized Homeopathy Vinitha Edavattath Ramanan et al., Homeopathy
195. Individualised Homeopathic Treatment of Nausea and Vomiting in the First Trimester and of COVID-19 in the Third Trimester of Pregnancy—A Case Report Katarina Lucija Glas, Homeopathy, 2022